UNIVERSIDAD COMPLUTENSE DE MADRID
FACULTAD DE CIENCIAS FÍSICAS
Departamento de Astrofísica y Ciencias de la Atmósfera

TESIS DOCTORAL

Análisis espacialmente resuelto de la tasa de formación estelar y su densidad cósmica en galaxias cercanas

Spatially-resolved analysis of the star formation rate and its cosmic density in nearbay galaxies

MEMORIA PARA OPTAR AL GRADO DE DOCTOR

PRESENTADA POR

Cristina Catalán Torrecilla

Directores

Armando Gil de Paz
África Castillo Morales

Madrid, 2018

Once upon a time, in a planet far, far away from the center of its galaxy, human beings raised their heads and looked up at the night sky admiring its immensity. The magnificence of the objects that they could see and the observational fact that they were constantly changing, set the beginning of this story.

UNIVERSIDAD COMPLUTENSE MADRID

9 788469 730041
ISBN 9788469730041

Spatially-resolved analysis of the Star Formation Rate and its Cosmic Density in nearby galaxies
Cristina Catalán Torrecilla - May 2017

UNIVERSIDAD COMPLUTENSE MADRID

FACULTAD DE CIENCIAS FÍSICAS

ANÁLISIS ESPACIALMENTE RESUELTO DE LA TASA DE FORMACIÓN ESTELAR Y SU DENSIDAD CÓSMICA EN GALAXIAS CERCANAS

SPATIALLY-RESOLVED ANALYSIS OF THE STAR FORMATION RATE AND ITS COSMIC DENSITY IN NEARBY GALAXIES

Ph.D. THESIS

Author:
Cristina Catalán Torrecilla

Supervisors:
Dr. Armando Gil de Paz
Dra. África Castillo Morales

Madrid, May 2017

UNIVERSIDAD COMPLUTENSE DE MADRID

FACULTAD DE CIENCIAS FÍSICAS
DEPARTAMENTO DE ASTROFÍSICA Y CIENCIAS DE LA ATMÓSFERA

Análisis espacialmente resuelto de la Tasa de Formación Estelar y su Densidad Cósmica en galaxias cercanas

Spatially-resolved analysis of the Star Formation Rate and its Cosmic Density in nearby galaxies

Dirigida por:

Dr. Armando Gil de Paz
Profesor Titular
UCM

Dra. África Castillo Morales
Profesor Contratado Doctor
UCM

Memoria presentada por
D.ª Cristina Catalán Torrecilla
para aspirar al grado de
Doctor en Astrofísica
Madrid, Mayo 2017

Back cover image credits:
Enrique Pérez - Instituto de Astrofísica de Andalucía (CSIC)
Mosaic of Van Gogh's "The Starry Night" (*De sterrennacht*) recreated with *SDSS* images for the CALIFA mother sample.

"The size of your dreams must always exceed your current capacity to achieve them."

Ellen Johnson Sirleaf, Nobel Peace Prize Winner & President of Liberia

"Nothing in life is to be feared, it is only to be understood.
Now is the time to understand more, so that we may fear less."

Marie Curie

This page was left intentionally blank.

A mis padres.
A Carlos.

This page was left intentionally blank.

Agradecimientos

He aquí mi secreto, que no puede ser más simple: solo con el corazón se puede ver bien; lo esencial es invisible a los ojos.
— Antoine de Saint-Exupéry, El principito

Y siguiendo la cita anterior, me dispongo a redactar estas líneas desde el cariño, siendo consciente de que son muchas las personas a las que quiero agradecer por haberme ayudado de una u otra forma a lo largo de esta etapa tan especial. Etapa que se ha caracterizado por un aprendizaje continuado, por algún que otro momento de estrés, pero sobre todo por la ilusión de llevar a buen puerto este proyecto. Sin vosotros, los que nombro a continuación y los que por descuido (espero que no sean muchos) olvide mencionar, el camino no hubiese sido igual.

En primer lugar, y para darles el crédito que sin duda merecen, quiero expresar mi más sincero agradecimiento a mis directores de tesis, al Dr. Armando Gil de Paz y a la Dra. África Castillo Morales. Armando, Afri, gracias por toda la ayuda y cariño que me habéis brindado durante estos años. Parece que fue ayer cuando comencé el trabajo académicamente dirigido con vosotros, después vino el trabajo fin de máster y como no podía ser de otra forma, la tesis. Gracias a ambos que me habéis acompañado en esta aventura, aportando tanto durante nuestras conversaciones científicas, respondiendo correos de madrugada y teniendo siempre una sonrisa disponible, pero sobre todo, por contagiarme vuestra ilusión y por vuestra calidad tanto humana como científica. Es un auténtico privilegio trabajar codo a codo con personas a las que admiras tanto. Gracias infinitas, *teachers*.

Gracias también a todos y cada uno de los miembros del Departamento de Astrofísica y Ciencias de la Atmósfera que siempre han estado disponibles, mostrando una amabilidad y apoyo inestimable. En especial a Pablo Pérez González, Sergio Pascual, Jaime Zamorano, Jesús Gallego, Nicolás Cardiel, Javier Gorgas, Ainhoa Sánchez, Antonio Hernán, Bililign T. Dullo, Carmen Eliche, Pilar Esquej, Helena Domínguez, Antonio Verdet, Carlos Tapia y Eugenia Carrascosa. Quiero hacer una mención especial para aquellos con los que he podido trabajar más de cerca, a Sergio por las innumerables veces que ha *salvado* a mi ordenador así como por animarme a conocer el mundo de la estadística bayesiana; a Pablo a quien en más de una ocasión he acudido y que siempre ha estado dispuesto a hablar de ciencia conmigo y ayudarme en lo que fuera necesario; a Jesús y Jaime a los que he tenido la suerte de tener como profesores por todo lo que he aprendido con vosotros. También quiero dar las gracias al resto de compañeros del Departamento incluyendo a Elisa de Castro, María José Fernández, Manuel Cornide y David Montes.

De manera especial quisiera expresar mi agradecimiento a todos los doctorandos con los que he tenido el privilegio de compartir estos años, por los ánimos y los buenos ratos compartidos, a los que ya no están y a quienes se les echa de menos como Alejandro, Paco, Lucía, Jaime, Raffaella, Néstor, Javier, Miriam, Víctor, y a los que siguen estando aquí, a Belén porque sus conversaciones me llenan de energía y a Alexandre por todos los congresos que hemos compartido juntos, y porque escuchar su *take it easy* es la mejor receta para darme ánimos. Y en especial con los que he tenido la suerte de compartir despacho en estos últimos años, Raúl, Lucía, Álex y Jaime. Las charlas sobre ciencia, las risas, vuestra disponibilidad para echar una mano cuando ha sido necesario y los innumerables cafés han sido vitales para terminar esta tesis.

I would like to offer my special thanks to Dr. Barry Madore for his valuable guidance during

my two stays at *The Carnegie Observatories* and for all of the opportunities I was given to conduct my research during those 6 months. My sincere thanks also goes to Erika who was always willing to help me, to Andy and Charllie who were excellent flatmates, to Gwen for her conversations and advices and to Vicky for giving me this special book that I have read a thousand times.

A la Dra. M. Carmen García Payo por animarme a aventurarme en el mundo de la investigación y por esos abrazos suyos que cargan las pilas. A los doctores Rafael Barrena y Jairo Méndez Abreu que fueron unos directores excelentes durante la beca de verano en el IAC y que me animaron también a seguir en este mundo. A todos los miembros de la colaboración CALIFA, haber formado parte de una colaboración internacional ha enriquecido con creces mi aprendizaje. Al Ministerio de Educación que ha financiado mi investigación gracias a la concesión de la beca de Formación de Profesorado Universitario.

Y en la parte más personal quiero empezar por mis amigos por ser un pilar fundamental en mi vida. A mis niñas, Lore, Paula y Gema. Gracias por los abrazos, las risas y nuestras escapadas. Me siento inmensamente afortunada de haber compartido tantos y tan buenos momentos con vosotras, espero que juntas sigamos sumando recuerdos. A Rus, que me has brindado tu amistad durante estos casi 20 años y me has enseñado que la valentía no tiene límites. A Lorenlay, por transmitirme esa paz. A Diana, que se ha convertido en un referente para mí. A Isa, por los fantásticos años que hemos vivido juntas en Madrid. A Judit y Maider que comenzaron siendo mis compañeras durante el máster y quien hoy son grandes amigas. Judit, como bien escribías en tus agradecimientos: 'ya estamos a un paso de ser doctoras'. A Edgar, Essalhi y Óscar por las innumerables comidas compartidas en la facultad. A mis amigos, los de siempre, por todo lo que hemos vivido juntos y por lo que nos queda; Pili, Yoli, Arancha, Elena, Luz, Bea, Fátima, Josele, Dani, Luis, Ángel, Clemente, Ramón y en especial, a Nieves que siempre ha creído en mí y porque como tú bien dices: '*tener amigos es saber que no estás sola*'. Y a los que han aparecido después para quedarse; Irina, Mario, Marta, Adrián, Vanessa, Ka, Carlos, Clara, Álvaro, Morla y Ángel.

A mi familia que tanto significa para mí, porque las experiencias compartidas con los que más quieres son las mejores. Siempre me habéis apoyado y habéis confiado plenamente en mí. Y en especial, a Valentina, la niña de mis ojos; a mis abuelos que tanto me han cuidado y sobre todo a mi abuela, que ya no está, pero que la siento como si estuviera; a mis primas, Eva y Nuria que nuestra complicidad siga siempre intacta; a mis primos, Alberto, Noelia y Beatriz que me llenan de alegría, y a Jessica, Harold, Mari y Rubén porque os habéis convertido ya en parte de la familia. Y como no podía ser de otra forma, a mis padres, Luis y Mari Carmen, sin los cuales hubiera sido imposible llegar hasta aquí. Por quererme de forma incondicional, por haberme enseñado la importancia del esfuerzo y por haberme dado no solamente lo que estaba a vuestro alcance, si no muchísimo más. A vosotros va dedicada esta tesis, os quiero. Gracias de corazón.

Finalmente, A Carlos, quien sin duda ha vivido más de cerca estos años, por haber compartido conmigo los buenos momentos haciéndolos aún mejores y por haber conseguido que los malos se desvanezcan. Gracias por alegrar mis días, por endulzarlos, y por conseguir que a tu lado sea mejor persona. Esta tesis también está dedicada a ti.

A todos, ¡muchas gracias por haberme acompañado en esta aventura!

Madrid, Mayo de 2017

Contents

Resumen

La formación estelar es uno de los procesos físicos más relevantes que determinan la formación de las galaxias, además de ser un factor esencial para su evolución.

Esta Tesis Doctoral tiene como objetivo abordar el tema de la formación estelar en galaxias cercanas explorando distintas escalas físicas que van desde las galaxias como sistemas completos hasta las diferentes componentes estructurales que las forman, tales como bulbos, barras, y discos. La manera de proceder ha sido la siguiente, (I) se ha determinado la tasa de formación estelar actual en galaxias externas desde una perspectiva global, (II) se ha analizado la variación de la tasa de formación estelar a lo largo de las distintas estructuras internas que moldean las galaxias (bulbos, barras, y discos) con el objetivo de caracterizar los procesos de activación y quenching presentes, (III) finalmente, se proporcionan los valores de la densidad de la tasa de formación estelar para las galaxias y para sus componentes. La aparición de técnicas de espectroscopía de campo integral (del inglés, *Integral Field Spectroscopy*), que combinan al mismo tiempo las ventajas de la imagen y la espectroscopía clásica, es especialmente apropiada para el estudio en dos dimensiones de la estructura de las galaxias. Esta técnica permite tener información espacial y espectral de manera simultánea. Por ello, a lo largo de esta tesis, hemos usado los datos IFS de la exploración de galaxias cercanas CALIFA (*Calar Alto Legacy Integral Field Area Survey*).

En la primera parte de esta tesis, se proporcionan un conjunto de trazadores de la tasa de formación estelar empíricamente calibrados y actualizados anclados al trazador Hα previamente corregido de extinción. La luminosidad de la línea de recombinación Hα es elegida como trazador de referencia ya que recupera de forma precisa la formación estelar más instantánea, trazando la emisión del gas ionizado en los alrededores de las estrellas jóvenes más masivas que son, a su vez, las que tienen un tiempo de vida más corto ($\sim 3 - 10$ Myr). Se proporcionan trazadores tanto de una sola banda como trazadores compuestos, también conocidos como trazadores híbridos. Estos últimos han sido derivados basándonos en la aproximación de balance energético analizando sus límites de aplicabilidad detalladamente. El empleo de datos de espectroscopía de campo integral proporciona los requisitos técnicos necesarios para asegurar una correcta determinación de la atenuación por polvo, una cobertura completa de la extensión de la galaxia así como una precisa sustracción del continuo estelar subyacente. Las conclusiones derivadas de este estudio permiten explorar la distribución de la tasa de formación estelar de forma espacialmente resuelta. Así, el análisis de la tasa de formación estelar se lleva a cabo aislando las componentes internas que componen las galaxias (bulbos, barras, y discos). El método aplicado es una combinación de la descomposición fotométrica multi-componente en dos dimensiones usando imágenes de SDSS con los datos de espectroscopía de campo integral de CALIFA. La motivación principal de este trabajo es aclarar cuales son los mecanismos que regulan, activan y finalizan los procesos de formación estelar dentro de las galaxias. También se analizan las relaciones fundamentales entre la formación estelar y otras propiedades físicas inherentes a las galaxias. Finalmente, construimos la Función de Luminosidad en Hα tratando las galaxias como un todo y, también, para sus componentes morfológicas con el objetivo principal de determinar los valores de la densidad de la tasa de formación estelar en el universo local. Estos valores son restricciones fundamentales a los modelos de formación y evolución de las galaxias que deberían ser capaces de reproducirlos.

A lo largo de este tesis, hemos demostrado la singularidad de usar datos IFS en combinación con una muestra que cubre un rango amplio de propiedades físicas relevantes, para proporcionar un conocimiento profundo en las procesos de formación estelar que dominan las galaxias.

This page was left intentionally blank.

Summary

Star Formation is one of the most relevant physical processes that determines the formation of galaxies, as well as, one of the main agents that drive their evolution.

This Ph.D. Thesis addresses the topic of star formation in nearby galaxies exploring a range of different physical scales ranging from entire galaxies to the different structural components that form them such as bulges, bars, and disks. The way of proceeding has been as follows, (I) we determine the current SFR in external galaxies from a global perspective, (II) we determine the variation of the SFR along the different internal structures that shape galaxies (bulges, bars, and disks) with the aim to characterize the activation and quenching process involved, (III) finally, the star formation rate density values are provided for entire galaxies and for their components. The advent of the integral field spectroscopy (IFS) technique, that combines at the same time the advantages of imaging and spectroscopy, is particularly suitable for studying the two-dimensional structure of galaxies. This technique allows us to have spatial and spectral information simultaneously. Thus, the majority of the data used along this thesis come from the CALIFA (*Calar Alto Legacy Integral Field Area Survey*) survey.

In the first part of this thesis, we provide a set of updated empirically calibrated star formation rate prescriptions anchored to the extinction-corrected Hα tracer with the physical motivation of accurately measure the amount of newly born stars. Scaling laws have been proposed as a way to characterize and measure the amount of star formation in galaxies. We proportionate single-band and composite tracers, with the latter ones being based on an energy-balance approach. The luminosity coming from the Hα recombination emission line is selected as our fiducial tracer as it properly recovers the current star formation. Hα traces the ionized gas surrounding massive young stars with the shortest lifetimes ($\sim 3 - 10$ Myr). We also emphasize the limits of applicability of these SFR estimators. Only the IFS technique assures a proper determination of the dust attenuation, a complete coverage of the galaxy extension and a proper subtraction of the stellar underlying continuum. The conclusions derived for this first study allow us to explore the distribution of the SFR in a spatially-resolved manner. Thus, the analysis of the star formation rate is performed by means of isolating the internal components that shape galaxies (bulges, bars, and disks). The method applied is a combination of a two dimensional multi-component photometric decomposition using *SDSS* images with wide-field CALIFA IFS data. The main motivation of this work is to shed some light on the mechanisms that regulate and shut down the star formation processes within galaxies. We also analyze fundamental relations between star formation and other physical properties inherit to galaxies. Finally, we construct the Hα Luminosity Function analyzing galaxies as a whole and also their different morphological components from which we determine the star formation rate density values (again, in entire galaxies and by galaxy components) in the Local Universe. These values are fundamental constraints for the models of galaxy formation and evolution, which should now aim to reproduce.

We have demonstrated along this thesis the uniqueness of using IFS data, in combination with a sample that covers a wide range of relevant physical properties, to provide deeper insights into the star formation processes that govern galaxies.

This page was left intentionally blank.

List of Figures

This page was left intentionally blank.

List of Tables

This page was left intentionally blank.

CHAPTER 1

Introduction

The beginning is the most important part of the work.
— Plato

Once upon a time, in a planet far, far away from the center of its galaxy, human beings raised their heads and looked up at the night sky admiring its immensity. The magnificence of the objects that they could see and the observational fact that they were constantly changing set the beginning of this story.

1.1 Deciphering galaxy evolution using observational properties

The modern scientific comprehension of the Universe was established in the early part of the 20th century. At this time, astronomers were facing one of the most important questions along the history of the Astronomy: revealing the extragalactic and true nature of galaxies. The majority of the questions formulated during The Great Debate or the Shapley-Curtis Debate, were answered by E. Hubble who was able to observe Cepheid variable stars in the Andromeda Galaxy revealing its distance in 1925.

The first visual classification of the galaxies was established in Hubble (1926), which later led to its modern version the "Hubble Tuning Fork" in Hubble (1936). This scheme separates systems in two main types, namely spiral (S) and elliptical (E) galaxies. The former ones, also known as late-type galaxies, present a disk composed of stars, a spiral structure and some of them a bar component. In contrast, ellipticals display a spheroidal morphology. Intermediate lenticular galaxies (S0) are disk systems with large spheroidal components. E and S0 galaxies are now commonly referred to as early-types galaxies (ETGs).

As more and more galaxies become accessible, other internal features such as rings, the shape of spiral arms or its cumpliness, the size of the bulge relative to the disk were progressively being taken into account. Although having a visual classification is extremely valuable and morphology has provided a descriptive framework, a more quantitative treatment of galaxies based on stellar masses, luminosities, colors, and other physical properties, was found to be needed. Especially, once it became clear that galaxies appear in a wide range of intrinsic luminosities and masses (Zwicky 1942).

Thus, a tight relationship between morphology and color was found. The local galaxy population exhibits a color distribution that is bimodal (see Kauffmann et al. 2003; Blanton et al. 2003; Baldry et al. 2006, for a recent quantification of this issue). On one hand, the existence of the so-called "blue cloud" of star-forming galaxies becomes associated with a disk-like morphology, i. e., mostly active spiral systems located at intermediate-to-low stellar masses (see Figure 1.1). On the other hand, early-type galaxies are found associated with passive, luminous and massive systems that constitute the "red sequence" of galaxies. The majority of these galaxies are characterized by an absent, or at least, a strongly reduced star formation activity compared to those in the blue cloud. Yet, another population of galaxies is found, the "green valley", a transition zone between the previous sequences. There are rare systems in the local Universe that do not obey the previous color-morphology relation. Some exceptions are the existence of early-type galaxies with bluer colors than expected and late-type objects with unusual red colors.

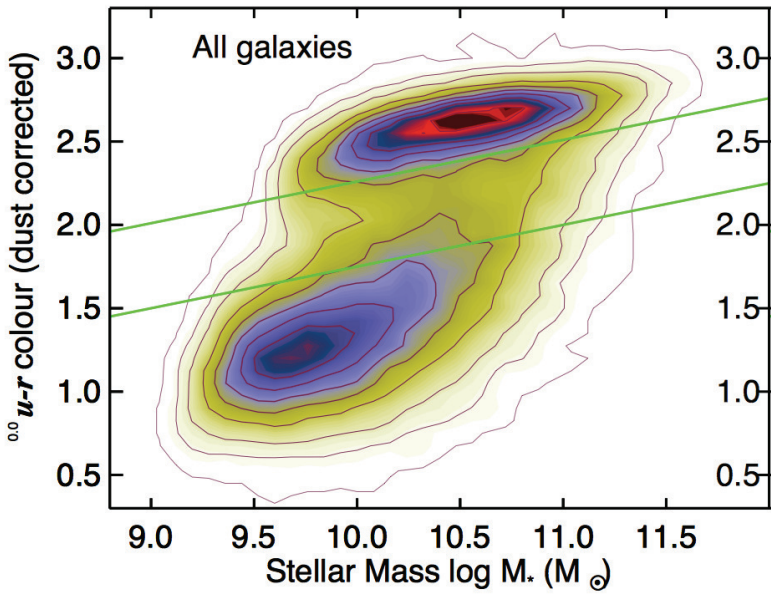

Figure 1.1: $u - r$ color-mass diagram from Schawinski et al. (2014). The location of the green valley is defined by the green lines. Early-type galaxies are mostly concentrated in the upper part of the diagram while bluer star-forming galaxies appeared mainly in the bottom part.

As previously outlined, there are clear morphological differences between galaxies undergoing star formation processes and passive systems. Clumpy spiral arms, asymmetric light distribution and knots of star formation are likely dominant structures associated with local star-forming galaxies. The degree of light concentration varies among galaxies undergoing star formation processes. It has been proved that blue star-forming galaxies tend to be less concentrated than passive systems in the local Universe and at higher redshifts (Strateva et al. 2001). In fact, the presence of a prominent disk is more likely to occur in less concentrated galaxies (Conselice 2003). This is a natural consequence of the relatively low SF efficiency in the process of formation of disks that allowed these galaxies (1) to distribute angular momentum to the outer parts of their disks and (2) to slowly but progressively reduce the total energy of these systems. Besides, the existence of both red spheroidal and disk components in most spirals indicates that star formation must have

varied significantly spatially and/or with time within galaxies. The previous issues explain why star formation is used as a key criteria for classifying galaxies into the well-known Hubble sequence.

The bimodality observed previously serves as an observational evidence that there should be mechanisms (triggering and quenching) regulating the formation of stars in galaxies and that their efficiency should vary from galaxy to galaxy and within different components in galaxies. Both enhancement and quenching mechanisms will be explored in Section 1.4. But before, we focus our attention on some observational properties associated with star-forming galaxies as a first step to understand the connection between star formation and other physical properties of the galaxies and to what degree these mechanisms are now at play or not.

1.2 Global properties of star-forming galaxies

Here we examine the topic of the rate at which stars form (SFR, Star Formation Rate). We focus on the main empirical relations that have served to shape our view of the galaxies and to improve our knowledge of the processes that regulate star formation. Taking into account the importance of having SFR measurements for this thesis, we will briefly introduce how SFR values can be obtained.

Different ways have been proposed to compute the SFR in galaxies. The most obvious way is by counting stars which implies to be able to resolve them individually. This method is restricted to our own Galaxy or to galaxies in the Local Group. To estimate the SFR in external galaxies indirect measurements are needed as individual stars are not accessible. Integrated light measurements are employed, and then, luminosity is converted into a total number of massive stars. The latter step makes use of stellar population synthesis modeling, i. e., a combination of simple stellar population (SSP) models that are able to reproduce the observed spectrum under some assumptions like the shape and limits of the Initial Mass Function (IMF). Accurate knowledge of the IMF, that tell us the expected distribution of stars, is crucial to the interpretation of integrated properties of galaxies. The functional form of the IMF has been investigated since the pioneer work of Salpeter (1955) in our solar neighborhood. The universality of the IFM has been questioned and efforts have been made to constrain the stellar mass limits. In the SFR tracers domain, and in the specific case of the Hα recombination emission line the bulk of the emission comes from short-lived massive stars. Nevertheless, if we assume a standard IMF these stars only account for about 5-20 % of the total stellar mass of the galaxy population. To infer the SFR a substantial interpolation to lower stellar masses is applied, revealing the sensitive of the SFR tracers to the massive end of the stellar mass spectrum. The variations of the IMF is an interesting topic that recalls attention, but a full discussion and extensive treatment of the IMF is beyond the scope of this work. Throughout this thesis a Kroupa (2001) IMF is adopted.

The continuous star formation approach is normally assumed in the case of integrated light measurements, i. e., the timescale over which the SFR process is supposed to remain constant is longer than the lifetimes of the stars that are generating the emission. Usually, this translates into a period of about 100 Myr for the UV continuum and a shorter interval of 10 Myr for the Hα recombination line. There is also another category of SFR estimators based on local scales within galaxies which mostly refers to regions limited to sub-kpc scales. The seminal work of Kennicutt (1998a) and the most recent version in Kennicutt & Evans (2012) are excellent reviews on this topic.

Accurate measurements of the SFR constitute the foundations of this thesis as they are essential to derive further results. Consequently, more details about SFR tracers are given in Chapter 3.

Star formation is not only an important driver of galactic evolution but, as commented above, how SFR has evolved with time and spatially also determines the galaxies present-day morphology. As a consequence, we examine in the following sections the correlations between SFR and other physical parameters that define galaxies and their evolutionary histories. Below, we start summarizing the global properties of galaxies in terms of their SFR and their corresponding scaling relations.

1.2.1 Star-Forming Main Sequence

The star-forming "main sequence" (SFMS) of galaxies is a tight correlation observed between the stellar mass of a galaxy and the rate at which it is forming new stars (see Figure 1.2). It is found both locally (SDSS sample; Elbaz et al. 2007; Salim et al. 2007; Peng et al. 2010) and at high-redshift galaxies as far back as z $\sim$ 6 (Steinhardt et al. 2014). The slope of the SFMS remains approximately constant along this redshift range while its normalization changes considerably. Galaxies at z $\sim$ 2 show larger values (up to a factor of 20) of their SFR values in comparison with the local galaxies (Lamastra et al. 2013).

Galaxies that are not longer forming stars, and, consequently, appear as red and dead systems lie outside this sequence. The physical meaning of the SFMS is that as galaxies increase its star formation rate they become more massive. Eventually, the galaxy will experience a shut down in its SFR and it will leave this sequence. The nature of this main sequence still remains unclear.

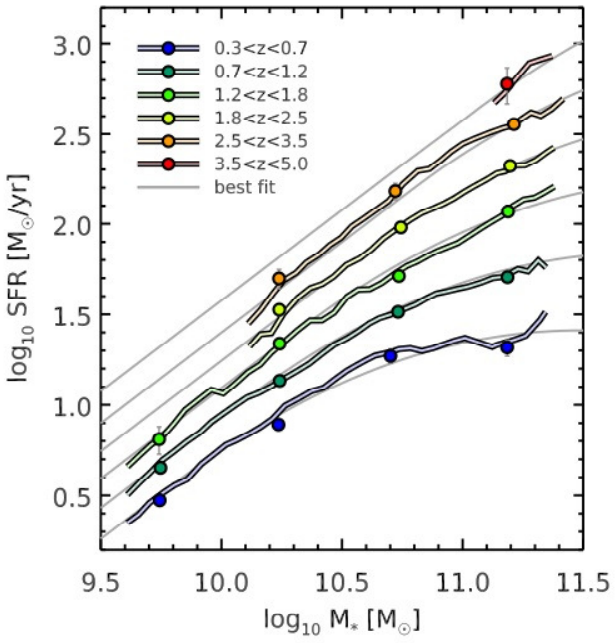

Figure 1.2: Star-forming SFR-M$_\star$ relation and its evolution with redsfhit from Schreiber et al. (2015). Light-gray curves shown the best fitting for the main sequence in each redshift interval.

1.2.2 sSFR-M$_\star$ relation

The previous figure (1.2) shows that there is a large dynamic range in the observed SFR values mainly due to the wide range in stellar masses. Exploring the behavior of the SFR normalized by stellar mass, i. e., the specific star formation rate (sSFR = SFR/M$_\star$), could be a more clarifying way of procedure; especially, because galaxies do not seem to follow lines of constant sSFR in the SFMS. The sSFR presents a similar bimodality dependence on stellar mass (Brinchmann et al. 2004; Schiminovich et al. 2007) with the prevalence of a blue and red sequences (blue and red fittings in Figure 1.3). Relatively less active star-forming systems such as disk of early-type galaxies and active bulges populate the space in between the previous blue and red trends. Overall, red galaxies tend to have larger stellar masses than bluer star-forming systems. The general trend observed in the blue sequence is that sSFR decreases at larger stellar masses. In fact, its peculiar tilt reflects the fact that lower-mass galaxies tend to be more efficient at forming new stars at the present moment than in the past in comparison with the more massive systems, pointing out to the concept of downsizing (Cowie et al. 1996).

The evolutionary properties of galaxies can be parametrized using variations of the sSFR-M$_\star$ diagram. For instance, the Hα equivalent width (EW) is another relevant parameter that scales with the sSFR. The trends show that EW(Hα) is lower for high-mass galaxies. This behavior is also observed for samples at different redshifts, massive galaxies present lower EW(Hα) than less massive objects (Fumagalli et al. 2012; Whitaker et al. 2014).

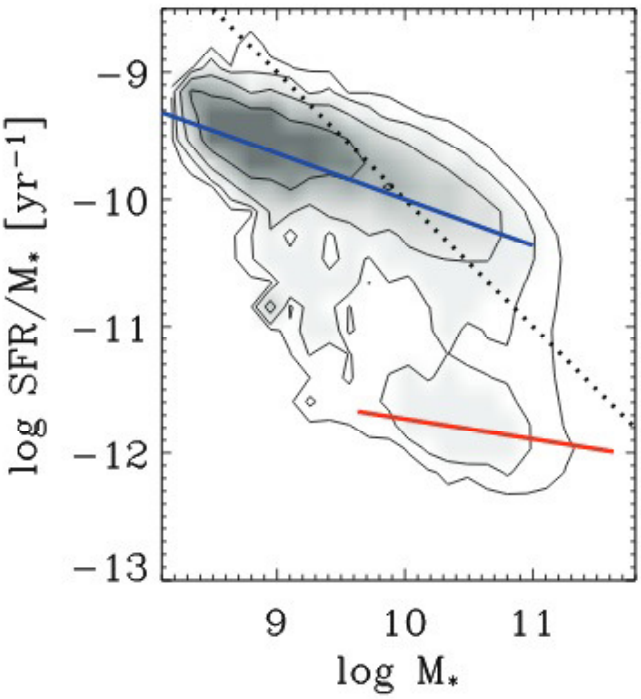

Figure 1.3: sSFR-M$_\star$ relation taken from Schiminovich et al. (2007). The blue and red solid lines represent the position of the star-forming galaxies and the red sequence in this diagram, respectively.

1.2.3 Kennicutt-Schmidt law

The strong trends in SFR and sSFR with stellar mass reveal fundamental insights into the processes that regulate the SFR. Exploring the connection between fundamental properties of galaxies and the global SFR will help to quantify the physical conditions of the SFR mechanisms, first globally and later with spatial resolution. The first idea was proposed by Schmidt (1959) who derived an empirical scaling relation where the star formation rate scaled as a power law of the gas mass. Nowadays, the relation between the average surface density of star formation and the average surface density of the total gas (atomic plus molecular) is well-known as the Kennicutt-Schmidt law of star formation. This observational recipe describes the fraction of gas that turns into stars within galaxies. The significant scatter present in this relation suggests possible variations in the star formation efficiency.

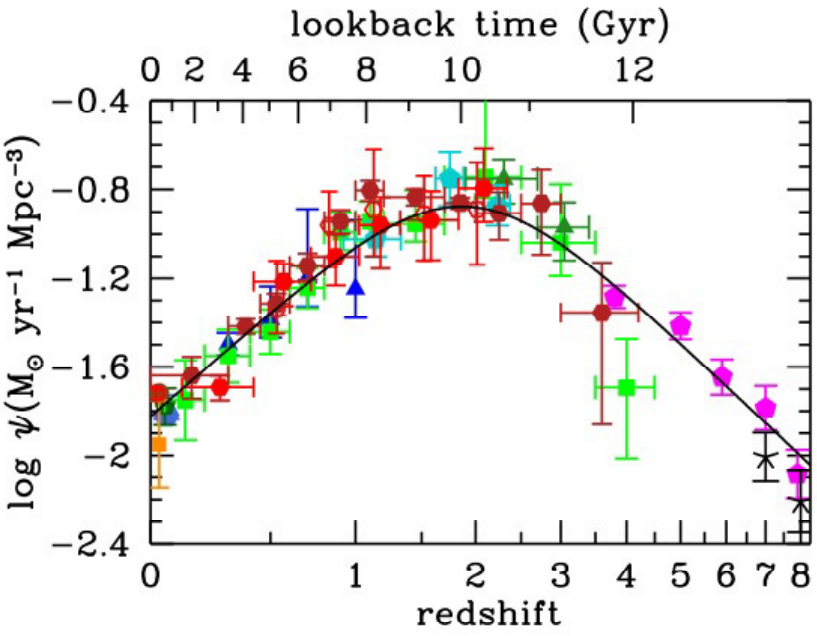

Figure 1.4: Evolution of the cosmic star formation history from a recent compilation of FUV + IR rest-frame measurements as illustrated in Figure 9 from Madau & Dickinson 2014. Two main phases characterized the shape of the SFRD, (a) a rising stage that peaks at z between 1.5 and 2.0 which corresponds to an age of $\sim$ 3.5 Gyr for the Universe, and (b) a decline phase that continues until the present day.

1.2.4 SFR density

As we have seen along this Section, among the multiple parameters that define what a galaxy is, probably, one of the most important ones is its SFR. Therefore, it is essential to know how efficiently has been the transformation of gas into stars in the galaxies throughout the history of the Universe. The analysis of the cosmic history of star formation, i. e., the variation of the Star Formation Rate Density (SFRD) with time (see Figure 1.4), could provide a reliable picture in that regard. Latest studies (for a recent review see Madau & Dickinson 2014) have proved that

the SFRD peaks at redshifts between 1.5 and 2, when the Universe was approximately 3.5 Gyr old. Then, it declined progressively until the present epoch. This framework points out that galaxies were able to sustain significant star formation processes at higher redshift suggesting the presence of large gas reservoirs. The way this gas was accreted into galaxies and the quantification of the relative importance of mergers and internal star formation processes are still a matter of concern.

In the following Sections, we present the most widely accepted views on the formation and evolution of galaxies of different types and masses.

1.3 The current standard paradigm of galaxy evolution

Hierarchical galaxy formation models are the current paradigm for structure formation. Collisions of smaller galaxies are among the processes proposed to form the grand spirals that we see today while the encounter and finally coalescence of larger galaxies are suggested as the mechanism responsible for creating colossal ellipticals. Through this thesis a Λ Cold Dark Matter (ΛCDM) cosmology is assumed, where the existence of dark energy and cold dark matter (cold reflects that the particle have small thermal velocities) in a non-baryonic form are the dominant components. This standard cosmological model postulates that baryonic matter accounts for only $\sim$ 4-5 % of the total content. The ΛCDM paradigm has been widely claimed to successfully reproduce observations. In this scenario, numerical simulations have shown the hierarchical assembly of massive halos through the merger of small halos, i. e., smaller structures are formed first and then, they merged into largest ones.

There is observational evidence that suggests a morphological and structural evolution of the galaxies over cosmic time. The stellar mass assembly histories of galaxies must be a complex process leading to the actual paradigm in which the number of massive galaxies has considerably increased in the present by a factor of $\sim$ 10. The so-called "downsizing" phenomenon is based on observations such as (i) the specific star formation (sSFR) decreases with cosmological time, (ii) the stellar mass assembly of galaxies shows that more massive systems assembled their stellar masses earlier than low-mass galaxies, and, (iii) the ages of the stellar populations in local galaxies by means of the analysis of the star formation histories reveals that the formation of the stellar populations has a different evolution, more massive systems mostly host older stellar populations. All these previous observations might or not reflect the same physical processes.

Galaxy structure can help to clarify how the more distant galaxies in the Universe have transformed into the local analogs that we see today.

1.3.1 Evolution of galaxies from the Blue Cloud to the Red Sequence and back

As shown in Section 1.1, attending to their inherent properties of color and luminosity, galaxies can be grouped into three categories: the blue cloud, the green valley, and the red sequence. A deeper understanding of the mechanisms that lead to this separation and the processes by which galaxies could migrate from the blue cloud to the red sequence, that comprises Es and S0s, are essential to decipher galaxy evolution. Moreover, these processes will shed some light on how the activation

and the quenching of the SF happens in galaxies. With this aim in mind, we explain below the actual paradigm that is believed to create this separation and potential evolutionary connections between these categories.

One galaxy formation scenario that emerged in the last decade is able to explain the build-up of the red sequence via mergers, in particular, with the existence of dissipational wet mergers and dissipationless dry mergers that form red elliptical galaxies with a physically motivated kinematical differentiation into fast and slow rotator systems (Emsellem et al. 2007, 2011). Wet mergers of gas-rich blue spirals are thought to be followed by a suppression of the star formation activity due to efficient gas consumption and feedback mechanisms arising from AGNs, moving the galaxy into the red sequence to form an intermediate-mass elliptical or S0 galaxy. These systems present a particular kinematical pattern consistent with a disk-like rotation as the gas concentration from the merging process tend to develop a disk before being removed. This process leads to the formation of systems known as fast rotators.

In the particular case of S0, these systems must be specially efficient at maintain or rebuild a stellar disk after the merging. Alternatively, it has been proposed that lenticulars might have evolved from massive disk galaxies that had lost their gas via ram pressure stripping processes. Nevertheless, this latter scenario is unable to explain the presence of S0 in the field. Other mechanisms such as starvation, that can happen at group environment (Kawata & Mulchaey 2008), might be responsible for the SFR cessation due to the removal of the gas reservoir onto the intergalactic medium.

On the other hand, more massive systems with negligible rotation in the red sequence will appear as a consequence of dissipationless (dry) mergers of galaxies with a poor content of gas corresponding to the formation of slow rotating ETGs.

Recently, the green valley has been explained as a mixture of reddish spirals and blue ellipticals and it has been pointed out that there is a significant difference among them in terms of their quenching time scales while they remain in the green valley (Schawinski et al. 2014). The concept of quenching here refers to galaxies that are in the process of shutting down their star formation. This study suggests that spirals turn red slowly forming some hot bright short-lived stars in the process that emit in the UV so the galaxy still remains blue. The gas needed to form stars comes mainly in two ways, a gas supply from the surrounding intergalactic medium (IGM) and the presence of gas reservoirs already available in galaxies. Once the cosmological supply of gas is shut off, spirals consume its gas reservoir slowly until the star formation is shut down or, at least, damped significantly. On the contrary, ellipticals undergo a more faster quenching without forming new young stars and suffering an aging of the stellar populations.

1.4 Physics of SF: activation and quenching

Cold dense gas is required to form new stars. Unfortunately, these mechanisms and the quenching ones are the least known ingredients of galaxy formation and evolution models (including in the scenario outlined above). Thus, the most relevant mechanisms proposed for triggering (Subsection 1.4.1) and shutting down the star formation in galaxies (Subsection 1.4.2) must be properly addressed and are explained in some detail in this Section.

1.4.1 SF triggering and activation mechanisms

Along this Section, we describe the most fundamental mechanisms that can affect the gas reservoir of galaxies and, ultimately, alter the process of star formation. Although feedback from newborn stars also alters the physical conditions of the gas in their vicinity, we focus here on mechanisms that have an impact on kiloparsec scales and beyond and mainly in relatively massive systems.

1.4.1.1 Galaxy interactions

As discused in Section 1.3, mergers and major interactions play a dominant role in the star formation history of the Universe as they constitute the basis hierarchical scenario for the formation of galaxies, and are thought to be responsible for the most intense star formation episodes especially in current-day ETGs (Sanders et al. 1988). Also, mergers are expected to influence the star formation histories of galaxies through their connection to AGN activity. Nevertheless, it is still far from being completely understood its direct relation with the cosmic star formation history and the evolution of the galaxy merger rate. On one hand, the decrease in the galaxy merger rate has been suggested as the potential cause for the SFRD decline from $z \sim 1$ until the present epoch. At low redshift, blue gas-rich mergers are thought to decrease while a higher merger fraction is present among red galaxies (Lin et al. 2008). On the other hand, it has also been claimed that their contribution to the SFRD is rather small (Robaina et al. 2009). Hα emission maps from galaxies with disk-like morphologies suggest high levels of star formation already present in extended disks at $z \sim 1$ (Nelson et al. 2013). Star forming disks at high redshift present a higher gas fraction with respect to their total mass than their low redshift counterparts as suggested by its clumpy morphology.

In the Local Universe, a mild star formation enhancement is also found in close pair galaxies that have experienced a recent encounter. The star formation is often concentrated in the central parts of the galaxies (Smith et al. 2007) or in the outer disks where signatures of interaction mainly include tidal tails and streams (Barton et al. 2000; Smith et al. 2010).

1.4.1.2 Perturbations: the role of disk instabilities and bars

Gravitational instabilities create dense clouds offering the conditions for gas cooling and its posterior fragmentation. At this state, the collapse of these gas clouds is not regulated by pressure which is commonly known as *free fall*. Once stars are formed, they heat and ionize the surrounding gas stooping this process and preventing new episodes of star formation. The main mechanisms that create gravitational instabilities in the disk are associated with secular processes such as spiral arms and bars. Spiral arms compress the gas and star formation takes place in cold gas dense complexes along them. Also, instabilities in the whole gas disk can drive gas towards the central parts of the galaxy after a significant loss of angular momentum. This mechanism triggers star formation activity in the center. Bar perturbations are able to move the gas around as well, quite far into the disk if coupled to the spiral structure.

1.4.2 Quenching mechanisms

Contrary to the previous mechanisms that enhance the star formation in galaxies, quenching mechanisms are associated with processes that prevent or shut down the star formation in galaxies. These processes mainly invoke the ejection of gas into the interstellar of intergalactic medium, processes that prevent galaxies from replenishing the gas supply, mechanisms that stabilize the disks, or the heating, removing and/or gas consumption at galactic scales. Thus, quenching processes can be divided in internally or externally induced.

1.4.2.1 Environmentally related quenching: starvation, ram pressure

It is well-known that morphology correlates with local environment (Dressler 1980). This so-called "morphology-density" relationship established that dense regions are populated mostly by ellipticals while disky spiral galaxies are most commonly present in low-density environments. Not only morphology but also other physical properties of galaxies are thought to be regulated by the environment. For instance, the gas content that provides the fuel necessary for the formation of stars and, ultimately, affects the amount of star formation in galaxies is also under-abundant in cluster galaxies (Cortese et al. 2011).

Thus, along this Section, we explore the "nurture" effects, i. e., how is the transformation of galaxies due to environmental effects as opposed to the intrinsic "nature" variations; galaxies in the most dense regions are red and dead as they have had more time to evolve since they started forming stars very early on (positive galaxy bias). The main plausible mechanisms proposed to quench the star formation in galaxies in dense environments are ram-pressure stripping as described in the seminal work from Gunn & Gott (1972), harassment, strangulation and starvation.

Ram-pressure stripping (Gunn & Gott 1972; Abadi et al. 1999): It is related to the additional pressure that a galaxy experiences as it moves through a hot dense medium, in particular, when the galaxy is moving within a cluster. The pressure of the intracluster medium is able to remove the gas content of spiral galaxies pushing it into the opposite direction of the galaxy movement. As a consequence of the gas removal, a shutdown of the star formation is expected, sometimes joined by star formation episodes along the tails of removal gas (see Jellyfish galaxies, Poggianti et al. 2016). A fast quenching of the star formation is produced overall as ram-pressure stripping processes remove the cold gas reservoir, but especially in the outskirts of galaxies. Chung et al. (2009) showed a variety of HI morphologies at different distances from the center of the Virgo cluster. In particular, galaxies nearest to the core cluster display HI disks smaller in size than their corresponding stellar disks while galaxies located at intermediate distances from the center display HI tails.

Galaxy strangulation or starvation: It was first proposed by Larson et al. (1980) to explain the transformation of spirals into lenticulars. Spiral galaxies are surrounded by a gaseous halo which supplies the gas needed for the formation of new stars. The cooling of the hot-gas component is essential to sustain the star formation processes. Thus, the stripping of the hot-gas component in the cluster environment prevent the cooling and lead to the formation of lenticulars. The cosmological chemodynamical simulations from Kawata & Mulchaey (2008) also showed the efficiency of strangulation at stripping the hot gas in low-mass galaxy groups. Recently, Peng et al.

(2015) pointed out the importance of strangulation as an important mechanism to shut down star formation in galaxies. The authors suggest a framework in which starvation results in a relatively slow quenching due to the suppression of gas accretion onto the galaxy. Then, the star formation continues until the cold gas reservoir is fully consumed.

1.4.2.2 Mass related quenching: Morphological quenching or other internal process

As we have shown in Section 1.4.1.2, one of the optimal conditions for the onset of star formation is the presence of a gravitational unstable gas disk. The gas cools to low temperatures until fragmentation takes place and, then, it leads to the formation of stars. Thus, an effective mechanism proposed to quench star formation is the existence of a disk that is stable against fragmentation. This mode of quenching is known as "morphological quenching" (MQ) (Martig et al. 2009). The basic idea behind MQ is the growth of a stellar spheroid component that becomes the dominant component of the galaxy. This could have happened via major or minor mergers or by the morphological transition from a rotating stellar disk to a stellar spheroid. Both cases are able to stabilize the gas disk against star formation without the complete removal of the cold gas. This process might explain the existence of red ETG (ellipticals or bulge-dominated lenticulars) galaxies that are very inefficient at forming new stars although having some amounts of cold gas.

1.4.3 AGN activity and star formation connection: negative and positive feedback at play

Nuclear activity itself is a relevant field in Astrophysics. AGN are compact, high-luminosity regions at the centers of some galaxies. Most of the radiation they emit is due to gas accretion onto a compact object, a black hole (BH), and this emission is thought to affect the evolution of the host galaxy even on galactic scales. Due to the broad nature of this research topic, here we will bring into focus the interplay between nuclear activity and star formation.

The main motivation for studying the AGN-SF connection are (a) the tight correlation between the massive BH masses and the stellar velocity dispersion of their host galaxy bulges, the M_{BH}-$\sigma_\star$ relation (Ferrarese & Merritt 2000; Gebhardt et al. 2000; Gültekin et al. 2009; Kormendy & Ho 2013), and (b) the evidence that the BH growth and the galaxy growth are intimately connected at all redshifts as shown in Figure 1.5. In that regard, the comparison between the total SFR density and the cosmic mass accretion history of massive BH shows similar trends although a considerable offset is present (a factor of ~ 1500 is needed to scale up the BH accretion). Both the massive BH mass growth rate and the cosmic SFH peak at $z \sim 2$. On the other hand, the total BH accretion density declines slightly more rapidly from $z \sim 1$ to 0 suggesting a change in the efficiency of the BH growth with respect to the galaxies SFR. At higher redshifts, $z > 3$, the total rate of BH mass growth also evolves (decreases) more rapidly than the SFR density.

Besides, galaxy formation models in cosmological context (Mo & White 2002) seem to require AGN to have a large impact on the galaxy host in order to reproduce the the bright end of the LF and the CMD. This impact includes preventing the cooling of gas and subsequent star formation, and, as the same time leading to the growth of the central black hole by accretion.

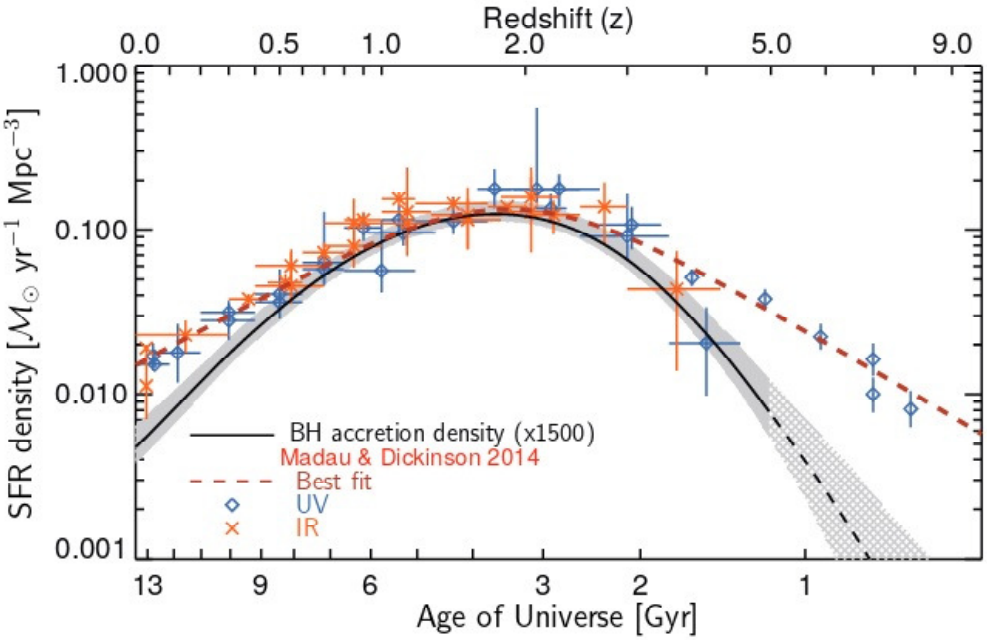

Figure 1.5: Comparison of the star formation history (thick solid curve) with the massive black hole accretion history (dashed orange line).

One of the plausible explanations to understand the previous scaling relation comes from AGN negative feedback mechanisms. Due to the significant difference in physical scales between the black hole and the host galaxy, complex regulation processes must be at play in this regard. In fact, supernovae-driven winds are proposed to be responsible for the suppression of the star formation in low mass galaxies (haloes with $M < 10^{12}$ $M_\star$) (Dekel & Silk 1986) while the more powerful outflows coming from AGNs are thought to be the cause of the star formation quenching at larger masses. These galactic outflows might suppress the cold gas supply and shut down the star formation. Two main modes for AGN feedback are invoked (see Fabian 2012):
(a) *radiative* or *quasar/wind* mode, which typically operates when the AGN luminosity is high, especially at high redshift where galaxies were gas rich. This mode explains the black hole mass - stellar velocity dispersion relation as it predicts a limit on the mass than can be concentrated on the bulge.
(b) *kinematic* or *radio/maintenance* mode. In this case, the energy is transferred by powerful jets and it prevents the gas from cooling keeping the gas hot and maintaining the heating/cooling balance. This mechanism is more common in massive galaxies at the centers of clusters and groups, especially at lower redshifts when the AGN luminosity is low.

On the other hand, positive feedback from AGNs has been also claimed to enhance the star formation process in galaxies. In that regard, the AGN might help to compress the gas that finally cools to form stars. Indeed, there is strong evidence that radio jets might trigger star formation (van Breugel et al. 2004; Zinn et al. 2013) when propagating through the gas reservoirs. The turbulence or shocks generated are thought to compress dense clouds inducing star formation in the host galaxy. Other possibilities come from AGN-driven outflows (Ishibashi & Fabian 2012).

The role that low-luminosity AGNs might play in nearby galaxies is examined in detail in Chapters 3 and 4 by analyzing, for the first time, the spatial distribution of SFR (computed with unprecedented precision) in a well-defined sample of nearby galaxies. In this kind of objects where both AGN activity and star formation are present, the widely known BPT diagram (BPT, Baldwin et al. 1981) has been the most commonly diagnostic method used to distinguish between AGN and star formation powered line emission. This classical diagram is based on the idea that star-forming regions and AGN present differences in the hardness of their ionizing spectra and, consequently, in some of their specific emission line ratios as well. High ionization forbidden emission lines such as [NII]λ6584 Å and [OIII]λ5007 Å are used in combination with Balmer lines. This commonly leads to high [NII]/Hα and [OIII]/Hβ ratios for AGN sources.

1.5 The relative role of enhancement and quenching mechanisms at different physical scales

The mechanisms that are able to activate and quench the star formation as explained above, could act at different physical scales affecting the components of the galaxy in a different manner. Here, we describe some open challenging questions that remain unsolved and that we will try to answer in the next Chapters of this thesis, where the distribution of the SFR in different components is studied for the first time in a systematic way.

AGN feedback: AGNs have been claimed to supply vast amounts of energy that might influence their host galaxy on large scales. The propose feedback mechanism will act both ways, the galaxy injects cold gas into the AGN via dense clouds of gas that are able to migrate to the center of the galaxy that collide and activate the AGN and, then, the AGN releases part of this energy through outflows or radio jets that are believed to be able to shut down star formation. Several possibilities appear at play to explain whether or not the AGN could have an effect on the gas distribution and the star formation in the host galaxy. On one hand, the removal of gas from the galaxy to feed the AGN might impact the star formation process over large scales. On the other hand, the large scale outflows delivered later from the AGN might be the cause of a possible quenching of the star formation in the wider host galaxy although some simulations have proposed that the AGN might affect only the central region surrounding the AGN as dense clouds will be able to block the outflow that emerges from the AGN (Gabor & Bournaud 2014). Whether or not an anti-correlation between AGN and star formation is present on bulges or disks could be analyzed by means of measuring the SFR on both components separately on galaxies with and without nuclear activity.

Internal secular processes: Internal secular processes also affect differently the distinct galaxy components. In particular, bars play a determining role in driving the secular evolution of disk galaxies altering their gas distribution. The growth of a secular (pseudo) bulge via gas inflow from the bar component is expected to occur in late-type spiral galaxies. These bulges manifest a higher level of star formation activity than classical bulges. Also, the transfer of angular momentum to the outer part of the galaxy allows to form ring-like structures. Thus, the presence of bars could significantly alter the bulge component although effects on global galaxy scales could be less crucial. On the contrary, other studies have suggested that if the process of funneling gas into the centers of galaxies is highly efficient and the amount of cosmological gas inflow is unable to compensate it,

then, the galaxy would appear as a quiescent system (Masters et al. 2011, 2012). In this context, Cheung et al. (2013) claim that secular evolution processes driven mainly by the effect of a bar are able to build high central densities which is a characteristic associated with quiescent galaxies. A detailed study is needed to firmly establish the connection between the presence of bars and the central star formation properties of the most inner regions in galaxies and to provide an in-depth understanding of the processes driving galactic evolution.

Another important aspect is the relation between the bulge prominence and the efficiency of the star formation processes within galaxies. It has been pointed out by Saintonge et al. (2011, 2012) that the efficiency of SF might vary as a function of the different galaxy properties, suggesting that lower star formation efficiency is related to redder colors and higher stellar mass concentrations. Ellipticals or bulge-dominated lenticulars with red colors that still contain a considerable amount of cold gas reservoirs are thought to be examples of this process. This low efficiency at forming new stars can be explained in terms of the morphological quenching that is able to increase the disk stability (as explained in Section 1.4.2.2). Thus, the study of the relation between the bulge prominence and the SFR associated with this component is essential to shed some light on the different mechanisms that will influence their evolution, although degeneracies with other mechanisms proposed are likely to occur.

Environmental processes: The processes that are responsible for the environmental quenching of disk galaxies (see Section 1.4.2.1), are expected to leave a clear imprint in the spatial distribution of the SFR. In particular, galaxies undergoing *ram pressure stripping* in a cluster environment are believed to experience a slowly quenched or a rapid cessation of the star formation due to the (partial) removal of low gas density mainly in their outer regions. On the contrary, recent hydrodynamical simulations (Steinhauser et al. 2016) have shown that the gas that still remains after the stripping process can be redistributed to the outer parts of disks and still form stars with only slightly modified rates. Asymmetries and gaseous tails are also indirect proof for processes of ram pressure stripping. The stripped gas present in tails does not become dense enough and it shows lower star formation efficiency in comparison with the one in the disk (Boissier et al. 2012). *Strangulation* mechanisms (Kawata & Mulchaey 2008) also work at stripping of the hot gas component and preventing the galaxy of its gas supply which lead to a quenching of the star formation even in low-mass groups. It is clear that the evolution of a galaxy and, especially, it most outer part regions, strongly depends on the strength of the environmental quenching processes that it experiences. Thus, the effects on the SFR need to be carefully examined to analyze at what level the globally SFR and the SFR in the disk component present lower values in group galaxies relative to the ones in the field.

The study of the empirical relationships presented in Section 1.2 also provides insights into the processes of star formation activation and quenching. In particular, important efforts have been made to understand the origin of the dispersion of the Star-Forming Main Sequence which reflects the variation in the level of star formation for galaxies with similar masses. The analysis of the specific SFR with stellar mass is also essential as it indicates the SFR variability on short time scales. As seen in Section 1.4, quenching processes involve either gas consumption or lack of gas supply from their halos which at the same time depends on the particular mass of the corresponding

halo. This effect might cause an impact on the disks of most massive galaxies in comparison with low-mass star-forming systems. Analyzing the variation of the specific SFR among disks and its entire galaxies can shed some light on this issue. Thus, the analysis of the empirical relationships presented in Section 1.2 in a spatially-resolved manner, by means of isolating the basic stellar components of the galaxies such as bulges or disks, will allow to characterize the contributions coming from different mechanisms at regulating or shutting down the star formation on galaxy scales.

1.6 Main objectives and outline of this thesis

To decipher the physical processes that govern galaxy formation there are two ways in which one can proceed, one is to make observations of galaxies at different cosmic epochs and try to identify their counterparts at different redshifts and the other one is to focus on the higher level of detail and depth offered by nearby galaxies, used here as fossil records of their evolution through time. The latter option is the approach we explore along this thesis. Most of the distant galaxies appear as small, clumpy objects usually undergoing star formation processes. It is essential to understand the mechanisms that are inherent to its evolution and make feasible to develop their current masses, colors, structure and dynamics. Nearby star-forming galaxies spanning a variety of shapes and sizes here serve as local laboratories for studying galaxy populations from the distant Universe to the present. Besides, local galaxies provide the opportunity of carrying out these studies with spatial resolution, which, as shown in Section 1.5, is critical to disentangle the role of the different triggering and quenching physical mechanisms in the evolution of galaxies.

Thus, the ultimate goal of this thesis is to describe and characterize the star formation processes that govern galaxies from an observational point of view. We address this goal using two complementary perspectives (a) treating galaxies as entire systems and (b) focussing on the basic stellar structures that shape galaxies (bulges, bars, and disks). The CALIFA galaxies constitute an excellent observational reference point in that regard as explained in Chapter 2. Finally, we derive the SFR density by galaxy components in the Local Universe. Through this work we rely on the use of the extinction-corrected Hα luminosity as our bona fide SFR tracer. The validity of this tracer is extensively tested in Chapter 3.

Studying the SFR by galaxy components will help us to shed some light on the different processes that are changing the mass, colors and structure of galaxies and to have an in-depth understanding of the evolution of the individual galaxy components at different cosmic epochs (see Section 1.5). The first step to achieve this goal involves a characterization of the distinct stellar structures that make up galaxies such as bulges, bars, and disks. One of the most promising ways of decompose galaxies is through the analysis of the optical continuum light distribution using two dimensional multi-component photometric decompositions codes such as GASP2D (Méndez-Abreu et al. 2008), among others. This decomposition method is explained in Section 2.3.2 of Chapter 2 and, then, applied to our sample in Chapter 4. By knowing the distribution of the SFR at multiple physical size scales and the role that external processes (including merging or accretion) and internal secular evolution processes (formation of bars/rings that influence the evolution of disks) play within galaxies, one can begin to understand how galaxies were built. In that regard, the goal of Chapter 4 is measuring the SFR in different structural components (using IFS data for the first time in the

literature) to see how active star formation can impact the evolution of the galaxy and how this impact depends on the galaxy internal and environmental properties.

Challenging questions that remain unsolved and that we aim to answer in this thesis are the following:

1. How precisely can we measure the SFR in galaxies? Star formation is an important driver of galactic evolution. Consequently, the need for accurate measurements is a must. Using CALIFA galaxies is an excellent opportunity to provide updated SFR calibrations and shed some light on the discrepancies between them. Moreover, we can analyze how good is Hα as a tracer of recent star formation in a well-define sample of nearby galaxies and whether or not there is a significant presence of highly obscured objects where recovering the star formation might be a difficult task.

2. How do the different morphological components that shape galaxies contribute to their current and past growth? Although integrated properties of galaxies are essential to have a deeper understanding of the birth and evolution of galaxies this necessarily also involves dealing with their basic structures. We aim to spatially segregate the locus of the SFR in a well-defined sample of galaxies in a reproducible way using two dimensional multi-component decomposition, but how feasible is to recover the SFR in the different galaxy components?

3. Regarding the most fundamental relationships between the SFR in galaxies and other physical parameters such as the stellar mass (i. e., the well-known Star-Forming Main) or the specific SFR and the stellar mass; how is the behavior of the galaxy components (bulges, bars, and disks) in these relations in comparison with galaxies as a whole? What are the main mechanisms responsible for the quenching o damping of the SFR in the different components that shape galaxies? Are bulges and disks equally affected by them?

4. Technical questions also appear in this context such as, which are the advantages that the use of Integral Field Spectroscopy technique offers to solve the previous questions? How critical is the use of a 2D multi-component decomposition approach in this regard?

This thesis is structured as follows, in Chapter 2 we focus our attention on the description of the Integral Field Spectroscopy (IFS) techniques as the majority of the work presented here is based on the analysis of IFS data. The benefits associated with this methodology, the characterization of the CALIFA survey as well as the state-of-the-art IFS facilities are described in detail. Chapter 3 is devoted to a profound analysis of the extinction-corrected Hα emission line as a SFR tracer. We compare this tracer with single-band and hybrid estimators using integrated luminosity values treating galaxies as entire systems. The use of a well-characterized sample of nearby galaxies allow us to shed some light on the validity and assumptions imposed to these tracers and allow us to provide updated SFR calibrators. In Chapter 4, we analyze the distribution of the SFR in the internal structures that form galaxies (bulges, bars, and disk) by means of applying the outcome from a 2D multi-component decomposition over the CALIFA IFS datacubes. We carefully study the relationship between the SFR in each component and the most significant physical properties that define galaxies such as stellar mass, morphological type or the presence of nuclear activity. The effects of the environment as well as the stellar kinematics are also treated. Once we are able to weight (in light) the different galaxy components and the amount of SFR they contain,

we construct their corresponding Hα Luminosity Functions (LF) in Chapter 5. From these LF we provide the SFR density value in the Local Universe for entire systems and, for the first time, for their basic stellar structures. Chapter 6 describes the extension of the work presented along this manuscript and give details about the future prospective. Mainly, we explain an ongoing project using high spatial resolution spectrophotometric datacube that will allow us to resolve a individual star forming region. In particular, we will be able to study in detail the physical properties within a nearby extended HII region, Hubble III, located in the Local Group dwarf galaxy NGC 6822 to investigate the escape fraction of ionizing photons. An additional future research line goes in the direction of improving the spatial resolution for galaxies in the local Universe and its complementary analysis at higher redshifts. Finally, the main conclusions derived from this thesis are summarized in Chapter 7.

This page was left intentionally blank.

CHAPTER 2

CALIFA: The Calar Alto Legacy Integral Field Area Survey

The important thing is to never stop questioning.
— Albert Einstein

Resumen

Nuestra concepción del Universo y de sus principales constituyentes, las galaxias, ha experimentado un avance sin precedentes en las últimas décadas gracias a la aparición de grandes exploraciones de galaxias. La necesidad de aunar las ventajas de las dos técnicas observacionales empleadas hasta el momento, imagen y espectroscopía, ha hecho emerger la espectroscopía de campo integral (IFS, por sus siglas en inglés Integral Field Spectroscopy). Esta nueva técnica proporciona información espacial y espectral simultáneamente en una sola exposición generando cubos de datos de 3 dimensiones (dos espaciales y una tercera en longitud de onda).

En este contexto, CALIFA (Calar Alto Legacy Integral Field Area) aparece como un proyecto de vanguardia con el objetivo de generar cubos de datos en una muestra amplia y representativa de galaxias del Universo Local, cubriendo un gran rango de propiedades físicas tales como la masa estelar, el tipo morfológico o el entorno. La unidad de campo integral (IFU, del inglés Integral Field Unit) que emplea es idónea para el estudio de objetos cercanos y extensos. CALIFA fue concebido como un proyecto de legado de tal modo que tras la culminación de las observaciones se ha puesto a disposición de la comunidad científica los datos correspondientes a las 667 galaxias observadas. La Figura 2.1 muestra el potencial de esta exploración de galaxias a modo de resumen.

A lo largo de este capítulo también se revisan las exploraciones de galaxias que precedieron a CALIFA y los ambiciosos proyectos que están siendo construidos en la actualidad o que se planean desarrollar en un futuro cercano. Así mismo, se describe CALIFA en profundidad con una mención especial a los hitos y resultados más relevantes a los que ha dado lugar. Mi contribución particular dentro del marco de la colaboración CALIFA es detallada. En concreto, se describe la fotometría llevada a cabo en el ultravioleta (UV) lejano y cercano para las galaxias de la muestra que tienen contrapartida en las imágenes del satélite GALEX así como mi participación en el proceso de descomposición fotométrica bidimensional (2D) usando múltiples componentes. Los productos resultantes de ambos trabajos son utilizados posteriormente en los estudios principales de esta tesis que se recogen en los capítulos 3 y 4. Por un lado, los datos UV se emplean para

derivar tasas de formación estelar mientras que el resultado de la descomposición 2D servirá para analizar la formación estelar reciente trazada por la línea de recombinación Hα en cada una de las componentes morfolólogicas que definen las galaxias (bulbos, barras, y discos). Finalmente, se analiza las principales ventajas que supone el uso de los datos de espectroscopía de campo integral para el desarrollo de esta tesis.

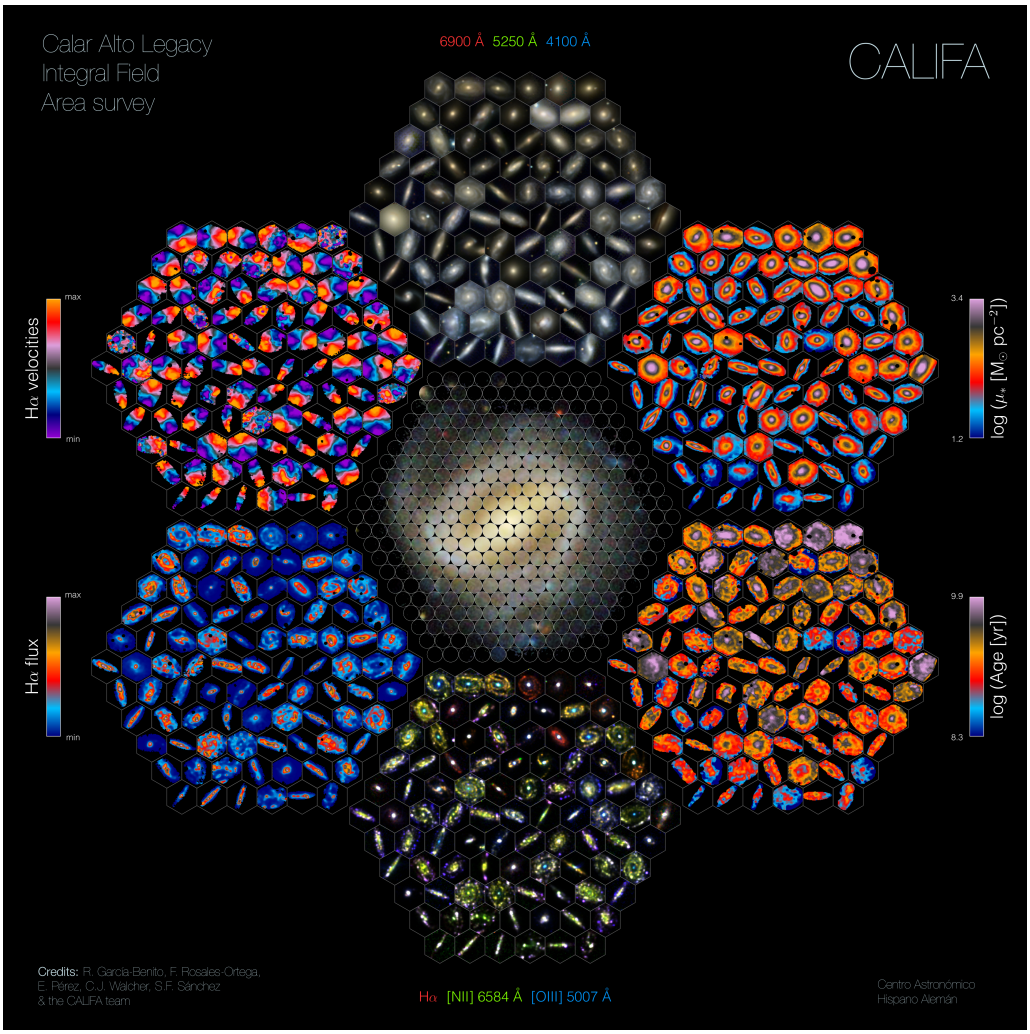

Figura 2.1: Mapas espacialmente resueltos que muestran algunas de las características espectroscópicas más relevantes de las galaxias, en particular, imágenes de falso color en banda ancha de SDSS (arriba en el centro), densidades superficiales de masa estelar (arriba a la derecha), promedio de edades estelares (abajo a la derecha), líneas empleadas en el diagnóstico de la actividad nuclear como Hα, [N II] λ 6584 Å y [O III] λ 5007 Å (abajo en el centro), mapas con la línea de emisión Hα (abajo a la izquierda) y mapas mostrando la cinemática de las galaxias (arriba a la izquierda) (***Crédito de la imagen: R. García-Benito, F. Rosales-Ortega, E. Pérez, C.J. Walcher y S.F. Sánchez***).

2.1 IFS surveys: needs and specifics

Large surveys have greatly contribute to improve our vision of the Universe by constraining the evolution of galaxies and the large-scale structure. Last decades have been specially fruitful thanks to outstanding surveys such as 2-degree Field Galaxy Redshift Survey (2dFGRS, Folkes et al. 1999), Sloan Digital Sky Survey (SDSS, York et al. 2000), Cosmic Evolution Survey (COSMOS, Scoville et al. 2007) and, more recently, Galaxy and Mass Assembly (GAMA, Driver et al. 2009) that have transformed our current understanding of the Universe leading to breakthrough discoveries. The majority of them were conceived as either imaging or spectroscopic surveys. Broad- and narrow-band imaging provides an excellent two dimensional sampling and detailed spatial information but it does not allow for realistic measurements of emission line ratios which are necessary to quantify properties such as SFR. Multi-band photometric surveys (even narrow-band ones) also present difficulties at accurately measure individual spectral lines. On the other hand, spectroscopic surveys give detailed information about individual spectral lines but they have limitations related to the coverage of the full galaxy, making the use of aperture corrections necessary, and, they are mostly limited to one spectrum per object.

In this context, Integral Field Spectroscopy (IFS) appears as a novel technique that combines at the same time the advantages of imaging and spectroscopy, providing resolved spectroscopy information. In fact, IFS is becoming a popular tool as its capabilities are particularly suitable for studying the two-dimensional structure of galaxies (see left panel in Figure 2.2 for a 3D datacube illustration). IFS technique benefit from the fact that (a) spatial and spectral information are obtained simultaneously. This advantage makes the observational process more efficient and assures the homogeneity in the data taken, (b) it is not necessary to adapt the slit width to the atmospheric conditions as the spectral resolution is already settled by the size of the fibers, (c) spectra can be corrected by differential atmospheric refraction effects, (d) this kind of data allows the use of adaptive spatial binning using Voronoi tessellations to reach a certain signal-to-noise ratio per bin as described in Cappellari & Copin (2003).

IFS technique makes use of an Integral Field Unit (IFU). It was G. Courtes who first propo the concept for an IFU in 1982. The development of the TIGER instrument (a lenslet array) was mounted on the 3.6-meter Canada-France-Hawaii Telescope (CFHT) on Mauna Kea, Hawaii, in 1987. The IFU divides the field of view into many little pieces, known as spaxels[1], to achieve a precise and comprehensive overview of the whole target. It is an excellent technique as it allows to study extended objects spectroscopically, such as galaxies, in just one shot. For the particular case of CALIFA, PPaK is the IFU used (it will be explained in detail in section 2.2). The way these IFU work can be briefly summarize as follows. The signal from each individual spaxel is carried to the spectrograph. Then, it produces the corresponding spectrum for each of the spaxels. The next step is to store and arrange spatially the previous spectra. A datacube is ultimately generated. Thus, the datacube is the final output of this process which is able to record a spectrum from each part of an extended object. As it can be seen in Figure 2.2, the datacube contains the spatial information and a third dimension which corresponds to the wavelength range.

The IFU could divide the spatial plane into a continuous (or pseudo-continuous) array using three main techniques as described below.

[1]Minimum resolution element resolved on the sky.

A microlens array: A microlens (lenslet) array is placed at the focal plane of the telescope so the image can be projected onto the lenslet array. The light is concentrated in each spatial element (lenslet) forming a small and independent (non-continuous) image at the entrance to the spectrograph. Then, the light is dispersed by the spectrograph obtaining a spectrum for each lenslet. To avoid the overlapping of the spectra coming from lenslets in the same row, the microlens array is slightly rotated. The main advantage of this technique is its high throughput. Potential disadvantages are the inefficient packing of the detector space and the limited wavelength coverage in order to avoid these to overlap.

A fiber bundle: The focal plane is discretized using a bundle (matrix) of optical fibers. In the other extreme of the bundle, the flexibility of the fibers makes possible to align them creating a pseudo-slit at the entrance of the spectrograph. Thanks to this process, light coming from different regions in the focal plane is rearranged into a common slit. Finally, a spectrum is obtained for each of the fibers in the spectrograph at the same time. The main disadvantages are the fiber loss mechanisms due to coupling issues and focal ratio degradation. The benefits of this design are the longer spectral bandpass just restricted by the properties of the spectrograph and the dimension of the detector and the full coverage of the detector. The fiber bundle technique can be also used in combination with a microlens array placed in front of the fiber bundle, that way the lenslets array focus the collected light into the fiber creating a fiber-lenslet IFU.

An image slicer: The input image hits a mirror array that is divided into several thin parallel segments. Then, these segments often called slices are reformatted on the detector thanks to a second segmented mirror. This step assures that the images are not above each other but instead they are organized end-to-end. This slicing arrangement creates a large pseudo slit in the spectrograph. The main advantages are (a) a highly efficient use of the detector surface. To avoid crosstalk between distinct regions of the sky, only a relatively small part of the detector (the space between contiguous slices) has to be masked off, (b) image slicer designs are especially suitable for the infrared range as they are relatively easy to implement in cooled instruments avoiding differential thermal expansion. On the down side, the complexity of the optical system and the number of mirrors required makes it hard to build. Also, they present a higher scatter for optical wavelengths.

As commented before, the IFU employed in CALIFA is PPak, a fiber-bundle IFU. Specific details about this particular IFU are given in section 2.2. The main advantages that fiber bundle systems offer, in comparison with microlens array and image-slices techniques, are the simplicity in the design and its flexibility. Also, fiber spectrograph could be placed at a reasonable distance from the focal plane, allowing thermal isolation and offering stability to face mechanical torsions.

2.1.1 Setting the scene: development of IFS surveys before and after CALIFA

2.1.1.1 Past

We have explained above the necessity for acquiring spectral and spatial information simultaneously in a single exposure in contrast to traditional techniques such as long-slit spectroscopy or imaging. In this section, we review state-of-the-art IFS surveys that most notably have contributed to transform our knowledge of the Universe. Although IFS data can be obtained for just a single

object or for a few of them, we focus here on IFS data that have been released in a survey mode.

Although CALIFA observations started back in summer 2010 other less ambitious IFS surveys pave the road. The most outstanding IFS surveys that preceded the advent of CALIFA or that were ongoing projects at this time are the following:

(i) The Spectrographic Area Unit for Research on Optical Nebulae survey (**SAURON** survey, Bacon et al. 2001; de Zeeuw et al. 2002) which main goal is the study of the stellar and gas kinematics and stellar populations of a representative sample of 72 nearby galaxies (24 ellipticals, 24 lenticulars, and 24 early-type spirals). The instrument SAURON is a lenslet array with a 33×41 arcsec^2 field mounted on the 4.2m William Herschel Telescope (WHT).

(ii) The **DiskMass** survey (DMS Bershady et al. 2010) mapped a sample of 146 nearby face-on spiral galaxies providing high spectral resolution using large-fiber IFUs like PPak and SparsePak (Bershady et al. 2004, 2005) both subtended a ~ 70 arcsec field of view in their core and are mounted in 3.5m class telescopes, the 3.5m at Calar Alto and WIYN at KPNO, respectively. One of the primary goals of this survey is to measure the mass surface-density in moderate-to-late type disks galaxies to break the disk-halo degeneracy.

(iii) The PPAK IFS Nearby Galaxies Survey (**PINGS**) project using the PPak IFU at the CAHA 3.5m of a 17 very nearby disk galaxies in the optical wavelength range (Rosales-Ortega et al. 2010).

(iv) The **ATLAS**^{3D} survey (Cappellari et al. 2011) mainly focused on the stellar kinematics and dynamic aspects of a volume complete sample of 260 early-type galaxies. This project is the extension of the SAURON survey. It will also derive the star formation history of these galaxies to shed some light on the mass-assembly processes. It is conceived as a multi-wavelength survey providing data from the optical (Optical IFS come from the SAURON IFU), the radio and the millimeter range.

(v) The VIRUS-P Exploration of Nearby Galaxies project (**VENGA** project, Blanc et al. 2013) that is observing a sample of 30 face-on nearby spiral galaxies sampling 3600-6800 Å range. The VIRUS-P IFU allows to map large portions of the disks out to ~ 0.7R$_{25}$ thanks to its large field of view of 1.7' $\times$ 1.7'. The main science drivers of this survey are the study of the star-formation processes on galactic scales, the assembly and the gas inflows in the central regions of spiral galaxies, among others.

2.1.1.2 Present

The high quality datacubes delivered by these surveys have contributed to answer most of the specific questions they were created for. Nevertheless, the particular criteria imposed at the moment of design the surveys lead to some constraints such as the limited size of the field of view for the case of the study of the central regions avoiding a complete coverage of the extent of the galaxy, the limited number of targets observed or the morphological types of the galaxies included.

Although it is essential to have a comprehensive study of a few individual galaxies, a survey providing observational properties of a large sample of galaxies in a more homogeneous way was

a necessity. In this scenery, CALIFA appears as the first survey that mapped a large number of relatively extended nearby objects covering almost all the galaxy subtypes in a wide range of stellar masses and in different environmental conditions allowing statistical conclusions. Additional advantages are the capacity to resolve the main structures presented in galaxies such as bulges, bars, or spiral arms due to its spatial resolution ($\sim$ 1 kpc at the mean distance of the survey), and, the spatial coverage of the targets up to 2.5 effective radii for at least 80% of the galaxies.

CALIFA has been the largest wide-field IFU survey of nearby galaxies carried out to date being a true revolution in the IFS field.

One of the main differences between CALIFA and other currently ongoing IFS surveys described below, is that CALIFA uses a single-IFU mode while the others use a multiplexing scheme. The use of monolithic IFUs naturally limits the capacity of observing more than a few hundred objects, at least in terms of telescope time. That is why, ongoing IFS surveys are making use of the multi-object IFS, also known as multiplexed IFUs, as a way of efficiently extent IF observations to a larger number of objects. Extracting the fundamental relations between different physical observed properties as well as tracing the formation history of individual galaxies in a statistically meaningful approach is the next step. A technical challenge inherent to the use of multiplexed IFUs is to achieve a coherent S/N ratio for all the observed objects at the same pointing, especially, for those targets with low surface brightness levels. In that regard, MaNGA and SAMI will increase notoriously the amount of galaxies observed, 10000(3000) galaxies for MaNGA(SAMI).

(i) Sydney Australian-Astronomical-Observatory Multi-object Integral-Field-Spectrograph survey (**SAMI**, Croom et al. 2012). The instrument is mounted on the 4m Anglo-Australian Telescope at Siding Spring Observatory. SAMI will observe 3000 galaxies in different environments in 260 clear nights. SAMI has 13 hexabundle IFUs (13 $\times$ 61-core hexabundles) that can be located over a 1-degree diameter field of view. The 61 optical fibers per IFU have a total active area of diameter 980 μm. Each hexabundle samples a 14.9 arcsec diameter field at 1.6 arcsec per fiber core matching the median optical seeing at the AAT ($\sim$ 1.5 arcsec). It has two wavelength channels, 3700-5700 Å and 6250-7350 Å, with a spatial resolution of 1-2 kpc.

(ii) Mapping Nearby Galaxies at Apache Point Observatory survey (**MaNGA**, Bundy et al. 2015). MaNGA aims to observe $\sim$ 10000 nearby galaxies representative for the local Universe with an intermediate redshift of $\sim$ 0.03 with stellar masses spanning over 3 orders of magnitude starting at $M_\star > 10^9$ $M_\odot$. The sample selection imposed cuts in redshift, *i*-band luminosity, and NUV-r color for a subset of galaxies while there are not cuts in size, inclination, morphology or environment. The data are taken using 17 simultaneous optical IFUs fiber bundles that vary in diameter from 12" (19 fibers) to 32" (127 fibers) and that can be placed anywhere within the 3 deg diameter focal plane. Some other technical details include its wavelength coverage that goes from 3600 to 10300 Å at a resolution of R $\sim$ 2000 with a spatial sampling of 1-2 kpc. The typical integration time is 3 hours.

2.1.1.3 Future

The future of IFS technique looks promising. Upcoming IFS surveys will pose a revolution. We briefly introduce two of the most important surveys.

(i) (**HECTOR**, Bland-Hawthorn 2015; Bryant & Bland-Hawthorn 2016) is designed to be a massively-multiplexed IFS instrument for the Anglo-Australian Telescope. It will observe a total amount of $\sim$ 100,000 galaxies at z $\sim$ 0.1. The main characteristics are its wide 3-degree-field, the high spectroscopic resolution (R=3000-5500) covering the wavelength range from 3727-7761 Å and a large number of IFUs (from 50 to 100). The goal of this survey is to understand galaxy evolution through a detailed study of individual nearby galaxies using an unprecedented sample of objects. Analyzing the accretion history of these galaxies and the effect of large-scale environment are among the main science goals of this ambitious project.

(ii) The Hobby-Eberly Telescope Dark Energy Experiment (**HETDEX**, Hill et al. 2008). The aim of HETDEX is to search for dark energy through the study of baryonic acoustic oscillations. Dark energy is extremely important as it is the force responsible for the expansion of the Universe in the cosmological paradigm, being responsible for up to three-quarters of all the matter and energy. It will observe almost a million of Lyman-alpha emitting (LAE) galaxies in a wide redshift interval (1.9 < z < 3.5) and [OII] emitting galaxies at z < 0.5. For that purpose, it will use a set of 150 VIRUS IFS. Each VIRUS unit covers a 1.8 arcsec^2 field on the sky with a spectral resolution of 5.7 Å covering the spectral range from 3500 to 5500 Å.

The future of IFS technique looks promising. Most of the large facilities such as the 10 meter class telescopes are or will be soon equipped with multi-object IFUs or wide-field IFS. Among the most impressive IFU currently working or designed for the near future are: (a) The Multi Unit Spectroscopic Explorer (**MUSE**, Bacon et al. 2010) is currently placed at the Very Large Telescope (VLT) of the European Southern Observatory (ESO). It is conceived as a panoramic integral-field spectrograph covering the optical range (4650-9300 Å). It is composed of 24 identical IFUs with an image slicer in from of each of them. MUSE can operate in a Wide Field Mode (WFM) with a 1 $\times$ 1 arcmin^2 field of view and a Narrow Field Mode (NFM) of 7.5 $\times$ 7.5 arcsec^2. The use of adaptive optics is highly implemented using four artificial laser guide stars, (b) Multi-Espectrógrafo en GTC de Alta Resolución para Astronomía (**MEGARA**, Gil de Paz et al. 2016) will be located on the Nasmyth A platform in the 10.4m GTC telescope in La Palma (Spain). MEGARA is composed of a Multi-Object Spectrograph (MOS) and an optical IFU. Up to 92 objects could be observed with the MOS mode covering an area of 3.5 x 3.5 arcmin^2 around the Large Compact Bundle IFU. The latter one covers a 12.5 $\times$ 11.3 arcsec^2 field of view on the sky with a spaxel size of 0.62 arcsec. Both modes will provide intermediate-to-high spectral resolutions (R $\sim$ 6,000, 12,000 and 18,700; for the Low-Resolution, Medium-Resolution, and High-Resolution spectral setups, respectively) with unprecedented throughput.

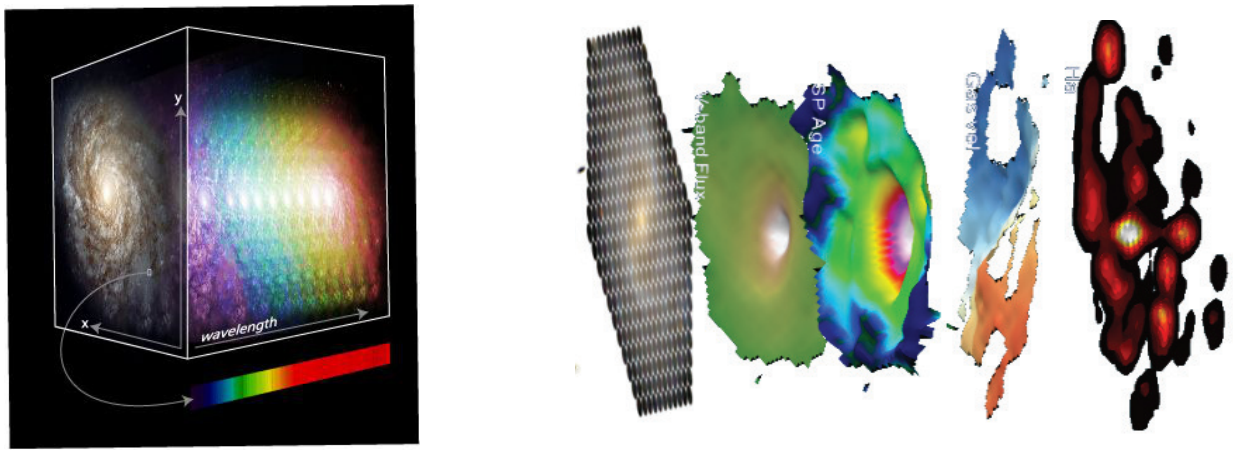

Figure 2.2: Left panel: Illustration showing a 3D datacube (***image credit: Marc White, RSAA-ANU***). The x and y axis provide the spatial coverage of the galaxy while the third axis gives the spectroscopic information. Each spaxel in the xy plane has its corresponding spectrum. Among the multiple uses of IFS data, it allows to extract a particular image of the object at a given wavelength, i. e, an Hα map. It is also possible to obtain the integrated spectrum for a specific region over the target, i. e., we can add all the spaxels in the central region and obtain its final integrated spectrum. Right panel: Diagram showing some of the information that can be extracted from the CALIFA datacubes. From left to right, example of a galaxy covering the PPaK field of view, its V-band light distribution, luminosity-weighted stellar population age, Hα line emission and velocity maps.

2.2 CALIFA in a nutshell: Survey description and characteristics

CALIFA[2] has been conceived as a legacy survey that aims to increase our knowledge about the intrinsic physical properties of a well characterized sample of nearby galaxies. The CALIFA observations have a great legacy value as data have been made public to the astronomical community through the following web page: `http://califa.caha.es`. In particular, fully reduced and quality controlled datacubes for 667 objects in total have been distributed as part of the third and final Data Release (DR3, Sánchez et al. 2016) on April 2016.

2.2.1 Technical constraints

The Integral Field spectrophotometer used by CALIFA is PMAS, the Potsdam Multi-Aperture Spectrophotometer, developed at the AIP. It covers a wide wavelength range going from the ultraviolet to the near infrared. It is currently mounted at 3.5m telescope in the Calar Alto Observatory and it has been mainly dedicated to the CALIFA survey in the last years. The fiber-bundle IFU unit employed is PPak. PPak comprises a central 72"-diameter hexagonal bundle with 331 optical science-fibers with a diameter of 2.7 arcseconds each. In order to accurately measure the sky background, an additionally set of six mini-IFUs composed of 36 fibers are located around the hexagon (see Figure 2.3). Also, there is the possibility to calibrate the IFU unit making use of an extra 15 fibers that can be illuminated by internal lamps. PPak offers a field of view of 74×65 arcseconds, making it an ideal instrument to observe extended objects.

[2] http://califa.caha.es

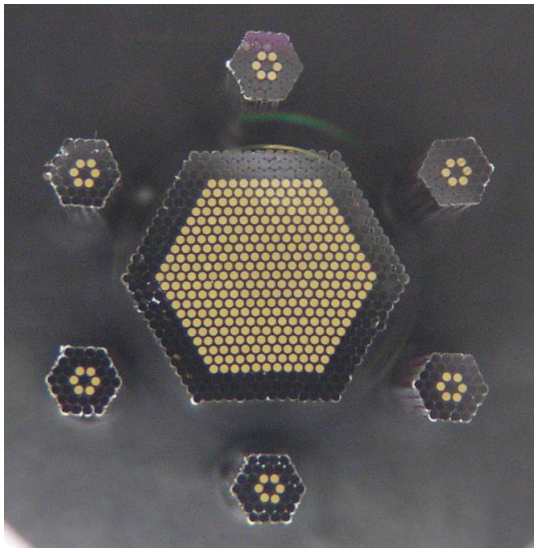

Figure 2.3: The PPak (IFU) fiber bundle showing its hexagonal FoV with a footprint of 65 × 74 arcsec. It is densely packed with 331 optical fibers with a 2.7 arcsec diameter per fiber and six surrounding sky fiber bundles (each consisting of 6 fibers).

In order to fully recover the whole galaxy in just one pointing there are restrictions imposed to the angular isophotal diameter of the galaxies and the redshift range. The limits in the latter one are also important to be able to recover all the important spectral features of the galaxies in the optical range. The redshifts values extend between $0.005 < z < 0.03$. The lower redshift restriction ensures that dwarf galaxies will not dominate the mother sample and, consequently, a lower completeness limit is imposed on the stellar mass range. The limits imposed to the angular isophotal diameter are $45\," < D_{25} < 79.2\,"$, where D_{25} refers to the isophotal diameter in the SDSS *r*-band. Thus, nearby and bright galaxies are favored targets.

Two overlapping spectral settings, the V500 and the V1200, guarantee an optimal coverage of the optical range. The V500 setup covers the wavelength range from 3745 to 7500 Å . Thus, the most relevant optical emission lines are included in this range ([OII] $\lambda\lambda$ 3726, 3729, Hβ, [OIII] $\lambda\lambda$ 4959, 5007, [NII] λ 6548, Hα, [NII] λ 6568, [SII] $\lambda\lambda$ 6717, 6731). It has a spectral resolution of 6.0 Å (FWHM) ($\sim$ 150 km s^{-1}). On the other hand, the V1200 setup has a more restricted wavelength range center in the bluer part of the optical spectrum from 3400 to 4840 Å but it offers a higher spectral resolution of 2.3 Å (FWHM) ($\sim$ 85 km s^{-1}). A total of 646 galaxies have been observed with the V500 setup while 484 of them have been observed with the V1200 setup.

2.2.2 Characterization of the mother sample

The CALIFA mother sample encompasses a sample of 937 galaxies selected from the SDSS DR7 photometric catalog (Abazajian et al. 2009) which assures the availability of multi-band photometry in the SDSS *u, g, r, i* -bands. The final observed sample includes 2/3 of these galaxies based exclusively on a visibility criteria. Early-type galaxies comprise 1/3 of the total number of galaxies observed while the remaining 2/3 are spiral, irregular and interacting systems. Figure 2.4 shows the distribution of a subsample of CALIFA galaxies spanning the complete color-magnitude diagram as an example. As we are interested in studying the local galaxy population, a wide range of

morphological types, luminosities, colors and stellar masses is desirable.

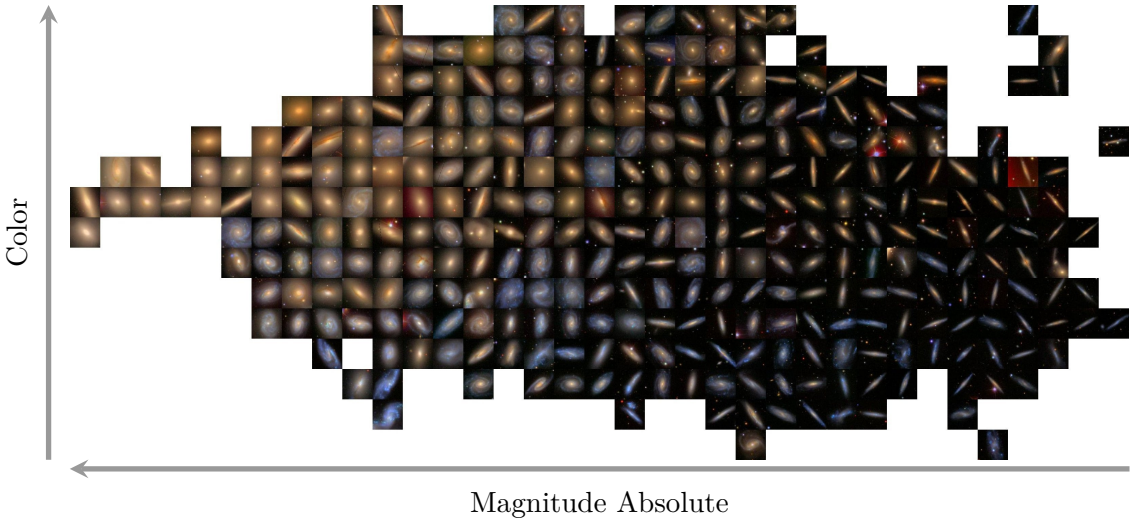

Figure 2.4: False color SDSS images of the CALIFA sample arranged according to their color and absolute magnitude.

Besides the restrictions imposed to the redshift range and the angular isophotal diameters, additional selection effects are applied over the SDSS DR7 photometric catalog: (a) the galactic latitude values must be $|b| > 20^\circ$ to avoid the Galactic plane, (b) declination values $\delta > 7^\circ$ for objects at northern Galactic latitudes to have a good visibility from the observatory location, (c) a flux limit of $petroMag_r < 20$ assures the exclusion of very faint objects.

Taking into account that CALIFA is a diameter-limited sample for a given redshift range and assuming that the SDSS survey is representative of the local galaxy population, it is possible to define the CALIFA completeness limit. Thus, only the linear isophotal size (D_{iso}) and the corresponding redshift of each galaxy will determine whether a particular object will be or not part of CALIFA. The values of the angular diameter limits 45 ” (79.2 ”) at the lowest (highest) redshift values 0.005 (0.03) in terms of their corresponding linear isophotal sizes are 4.7 (46) kpcs. This means that SDSS galaxies with a linear isophotal size lower than 4.7 kpc at a redshift of 0.005 or SDSS galaxies with a linear isophotal size larger than 46 kpc at a redshift of 0.03 will be excluded from CALIFA. The previous considerations make that CALIFA become a representative sample for the following domains, -19.0 > M_r > -23.1, 1.7 kpc < r_{50} < 11.5 kpc and 9.7 < $\log(M_\star/M_\odot)$ < 11.4, where M_r is the r-band absolute magnitude, r_{50} is the half light radii and $M_\star$ is the stellar mass of the galaxy.

Apart from the mother sample, which we often refer to as the “Main Sample”, there is also an “Extension Sample” delivered as part of the final Data Release (DR3). The “Extension Sample” mainly includes galaxies absent in the CALIFA Main Sample which allow also galaxies not even included in the SDSS DR7 imaging survey. As a consequence, the selection criteria applied could differ notably from the CALIFA ones making the previous completeness limits not suitable for the extended sample. The main extension programs focus on: dwarf galaxies, pairs and interacting galaxies, low- and high-mass early-type galaxies, supernova environments and compact early-type galaxies. As explained in Section 2.2.1, we will use the dwarf galaxies program to further constrain the faint-end slope of the luminosity function. All of them use the same CALIFA setup during

the observations including the same gratings, exposure times, etc. The detailed strategy for these observations goes beyond the scope of this thesis as they are not part of our main working sample.

2.3 Contribution to the CALIFA Survey

2.3.1 A UV look into the CALIFA sample: generating extra products

In this Section, I detail my contribution to the CALIFA Collaboration by providing FUV and NUV flux measurements for the galaxies in the CALIFA mother sample that do have a UV counterpart observed by GALEX. These values are used to further constrain the best-fitting Spectral Energy Distributions (SED) models that are used to derive the stellar masses of the galaxies in the sample.

Firstly, is it important to remember that stellar mass is a key parameter in driving galaxy evolution. A promising way of estimating the stellar masses is through the analysis of SEDs. In (Walcher et al. 2014), the authors make use of multi-band photometry measurements available at other wavelength ranges from the UV to the near-infrared for the CALIFA mother sample. In particular, the FUV and the NUV bands from the GALEX satellite, the SDSS *ugriz* growth curve magnitudes and the photometry carried out using NIR measurements in the J, H, K bands from the 2MASS All-Sky Extended Source Catalog (XSC) (Jarrett et al. 2000). The rest-frame SED of each galaxy was computed using the codes and algorithms as in Walcher et al. (2008). As a brief explanation, Bruzual & Charlot (2003) stellar population models combined with a Chabrier IMF (Chabrier 2003) are applied spanning a variety of underlying star formation histories (SFH) and amounts of dust attenuation. A Bayesian methodology is applied to obtain the probability density functions of the different parameters, in this case, stellar masses. The histogram showing the distribution of the stellar masses for the CALIFA mother sample is illustrated in Figure 2.5. Quoting from Walcher et al. (2014), "the CALIFA sample is representative of galaxies over a luminosity range of -19 $>$ M_r $>$ -23.1 and over a stellar mass range between $10^{9.7}$ and $10^{11.4}$ $M_\odot$".

I will explain now the UV photometry carried out using GALEX data, for FUV ($\lambda_{eff} \sim 1516$ Å) and NUV ($\lambda_{eff} \sim 2267$ Å) bands. In a few words, I describe the GALEX main characteristics to put it in context. The Galaxy Evolution Explorer (GALEX) satellite (Martin et al. 2005) performed the first all-sky survey including imaging and spectroscopic in the UV range. It was a NASA mission that was launched on 2003 April 28. Regarding its design, GALEX consisted of a 50 cm diameter modified Ritchey-Chrétien telescope with a circular field of view of 1.2 deg. It operated in two bands working simultaneously thanks to a dichroic beam splitter, the FUV band between 1350-1750 Å and the NUV band between 1750-2750 Å. The survey is limited at $m_{AB} \sim 23.5$ and the angular resolution of the images goes from 4.5" (FUV) to 6" (NUV) for the FWHM. Observations were performed in a pointed mode obtaining science data only during the night. As we are interested in the photometry, we briefly mentioned the main imaging surveys with their corresponding exposure time, sky coverage and depth of the images given in brackets: (a) AIS: All-sky Imaging Survey (100 s, 26000 deg^2, $m_{AB} \sim 20.5$), (b) MIS: Medium Imaging Survey (1500 s, 1000 deg^2, $m_{AB} \sim 23.5$), (c) DIS: Deep Imaging Survey (30000 s, 80 deg^2, $m_{AB} \sim 25.0$), (d) NGS: Nearby Galaxies Survey (1500 s, 300 deg^2, surface brightness of $m_{AB} \sim 27.5$ arcsec^{-2}) and (e) CAI: Calibration Imaging in which several white dwarf standards were observed for calibration.

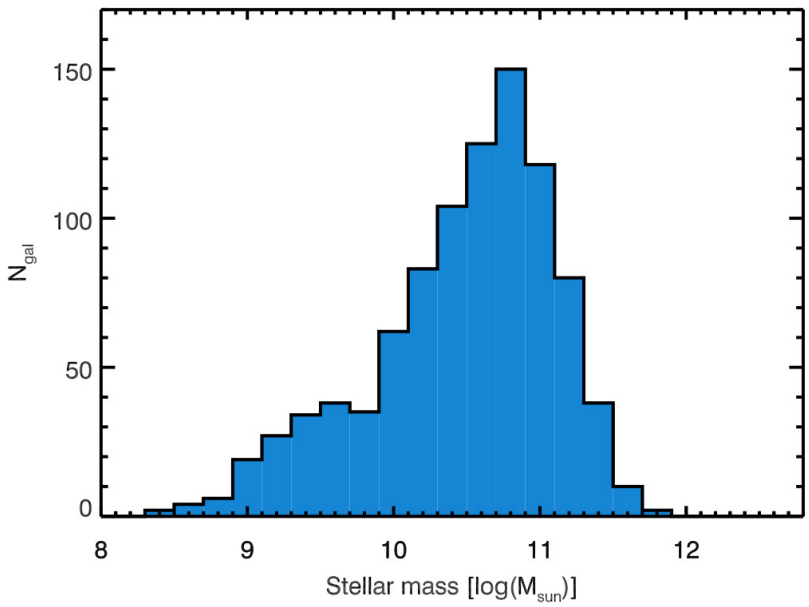

Figure 2.5: Stellar mass histogram as in Figure 14 in Walcher et al. (2014)

Among the previous mentioned surveys, we select the images taking into account two criteria, (a) selecting images with the maximum exposure time possible in the FUV band, and (b) having the entire galaxy located inside the detector with a maximum distance of 0.5 degrees from its center. Criterium (a) means that galaxies in the Deep Imaging Survey are optimal for our purpose, so we will choose them whenever possible. These images can be downloaded from the GalexView[3] service. The photometry is done for 663 galaxies of the CALIFA mother sample. Useful photometry is available for 655 of the 663 objects in the FUV and NUV bands while there are 52 objects for which there are not deep enough FUV data due to inefficient exposure time or to the redness of the galaxy. The steps followed to perform the surface photometry are extensively explained in Gil de Paz & Madore (2005); Gil de Paz et al. (2007a) and, also with a lower level of detail in Section 3.2 of Catalán-Torrecilla et al. (2015). The main steps are mentioned here as a short guidance. First, it is essential to determine the sky background level. Before that, we need to mask the target galaxy as well as the nearest objects, either galaxies or field stars. An elliptical area around the galaxy is divided into several smaller regions with the same number of pixels. In each of these regions, the mean and the typical deviation for the sky are computed. The use of the mean instead of the median or the mode is justified in terms of the low level of background in the image (typically, a non-Gaussian distribution is expected for the low count rates expected). Once the value of the sky is known, aperture photometry is performed using the ELLIPSE task in IRAF. The ellipticity and Position Angle of the elliptical apertures is the same as the one used for the CALIFA datacubes (more details in Catalán-Torrecilla et al. 2015). Asymptotic magnitudes are also obtained using 6 arcsec-width concentric elliptical apertures until the error in the surface photometry reached 0.8 mag. These asymptotic magnitudes (see Figure 2.6) are the ones employed for obtaining the stellar masses. Although the values of $L(FUV_{obs})$, $L(NUV_{obs})$ and FUV−NUV

[3] http://galex.stsci.edu/GalexView/

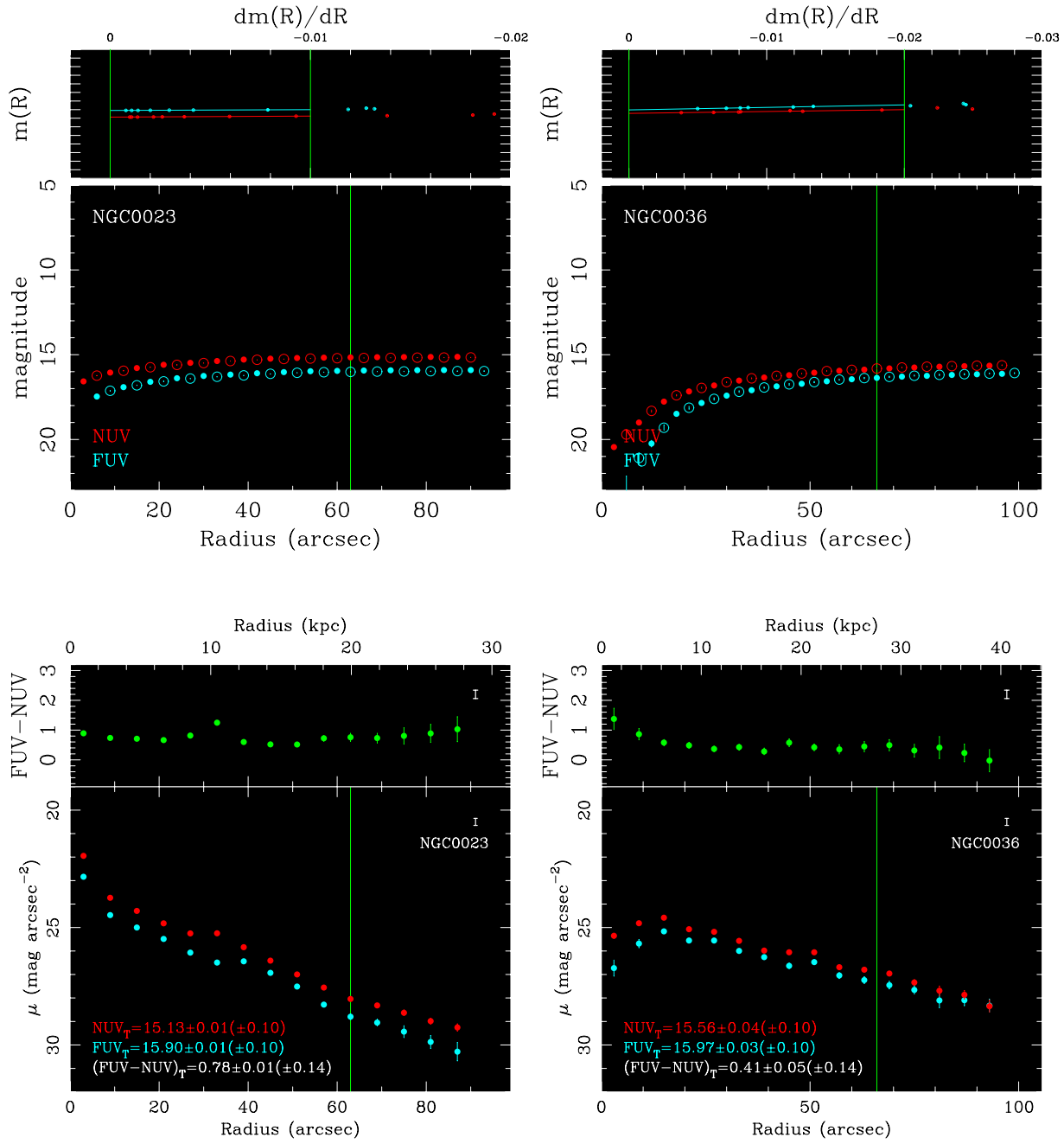

Figure 2.6: Examples of the GALEX photometry carried out for the galaxies NGC 0023 and NGC 0036. Bottoms panels: Surface brightness profiles in the FUV (blue) and NUV (red) bands. The green vertical line shows the position of the D25 ellipse. Top panels: Growth curves applied to obtain the asymptotic magnitudes in the FUV and NUV bands.

for the 272 galaxies included in Catalán-Torrecilla et al. (2015) are available through the article, for the sake of completeness, we include here the GALEX photometry for the 655 galaxies in the CALIFA mother sample that do have GALEX data. The UV byproducts have been used to derive extinction-correction UV SFRs, more details are given in Section 3. The table below (B.1) is

available in its entirety in the Appendix B while a portion is shown here for reference.

Table 2.1: (1) ID CALIFA identifier; (2) galaxy name; (3) & (4) major and minor axis radii, respectively, for the same common aperture. They correspond to the smallest of the last isophote for which the UV surface photometry can be properly computed in both bands (error < 0.8 mag/arcsec^2); (5) Position Angle that defines the shape of the concentric elliptical apertures used for the photometry (the RA and DEC coordinates that define the center of the galaxy are the ones provided by SDSS DR7); (6) & (8) FUV and NUV aperture magnitudes. The values are expressed in AB mag scale and are computed for the same common aperture. They are corrected for Milky Way attenuation assuming the following expressions between the attenuation in the different bands and the color excess, A(FUV) = 7.9×E(B-V) and A(NUV) = 8.0×E(B-V); (7) & (9) FUV and NUV magnitude errors. The errors in the aperture photometry are obtained after combining the photon noise and sky-subtraction uncertainty. A zero point error (common to all measurements) of 0.1mag commonly adopted for any GALEX measurement is not included in these numbers.

ID	name	a_{last} [arcsec]	b_{last} [arcsec]	PA [deg]	FUV [AB mag]	Δ FUV [AB mag]	NUV [AB mag]	Δ NUV [AB mag]
1	IC 5376	84.0	12.6	4.0	17.94	0.11	17.32	0.05
2	UGC 00005	54.0	27.0	45.0	16.71	0.06	16.21	0.03
3	NGC 7819	66.0	52.8	0.0	...	...	15.64	0.03
5	IC 1528	84.0	42.0	70.0	15.46	0.03	15.21	0.02
6	NGC 7824	42.0	31.5	-35.0	18.05	0.09	17.44	0.05
7	UGC 00036	42.0	19.4	18.0	18.14	0.09	17.55	0.04
9	NGC 0023	90.0	60.0	8.0	15.90	0.02	15.13	0.01
10	NGC 0036	96.0	61.1	21.0	16.12	0.04	15.65	0.02
11	UGC 00139	84.0	40.0	82.0	15.41	0.04	15.19	0.02
13	MCG-02-02-030	78.0	32.8	0.0	16.45	0.03	15.97	0.02
14	UGC 00312	60.0	30.0	7.0	15.29	0.01	14.99	0.01
15	ESO 539-G014	72.0	8.5	0.0	18.02	0.09	17.44	0.04
16	MCG-02-02-040	60.0	17.2	50.0	16.78	0.04	16.31	0.02
17	UGC 00335NED02	48.0	36.0	-10.0	...	...	18.49	0.15
18	NGC 0155	6.0	4.6	0.0	21.57	0.45	19.20	0.10
20	NGC 0160	84.0	47.6	45.0	17.09	0.03	16.57	0.04

2.3.2 Two-dimensional multi-component photometric decomposition

As part of the "Photometric decomposition" group formed by six members of the CALIFA collaboration (myself included) and led by Dr. Jairo Méndez-Abreu, I have contributed to create the photometric characterization of the multiple stellar components that shape galaxies such as bulges, bars, and disks. The set with all the structural components for the different galaxy components has been recently published Méndez-Abreu et al. (2017).

The way of characterizing the distinct stellar components that shape galaxies through photometric decompositions has greatly improved over the last forty years. Different approaches to model the surface brightness profile of the galaxy components can be found in the literature. The first attempt consists of one-dimensional SB profiles fittings (Freeman 1970) mostly focused on the bulge and disk components. Afterwards, the galaxy ellipticity profiles were also added to the former ones. More recently, the development of two-dimensional decomposition methods that fit the SB of the galaxy in a pixel-by-pixel basis have emerged. In particular, 2D multi-component codes such as GALFIT (Peng et al. 2002), BUDDA (de Souza et al. 2004), GASP2D (Méndez-Abreu et al.

2008) and IMFIT (Erwin 2015) have become popular as they are capable of fitting several stellar structures simultaneously. Among the variety of 2D multi-component codes, GASP2D is used for our purpose.

GASP2D makes use of a Leverg-Marquard algorithm to fit a composite model that combines the multiple stellar components available, bulge or nuclear point source, bar and disk (truncated or not). Additional complex structures such as ovals or lenses are not included to avoid degeneracy on the final parameters.

Calibrated *g*-,*r*-,*i*-band SDSS DR7 images are used as input files. Automatic initial conditions are applied over the intermediate wavelength *r*- band to initialize the fitting. The resulting best-fit parameters serve as initial conditions for the other bands. The Position Angles (PA) and the ellipticity (ϵ) that defined the elliptical isophotes are fixed for each photometric structure although their values can vary from one component to another. The photometric structures of the bulge, bar and disks components are parameterized by the following analytical functions that describe their surface brightness profiles.

For the bulge component a Sérsic profile Sersic (1968) is used:

$$I_b(r_b) = I_e 10^{-b_n\left(\left(\frac{r_b}{r_e}\right)^{1/n}-1\right)} \tag{2.1}$$

where r_e is the half-light or effective radius, I_e is the surface brightness at the corresponding r_e, n is the Sérsic index and b_n is equal to $0.868n$ - 0.142.

The bar component is described by the following expression:

$$I_{bar}(r_{bar}) = I_{0,bar}\left(1 - \left(\frac{r_{bar}}{a_{bar}}\right)^2\right)^{n_{bar}+0.5} \tag{2.2}$$

where $I_{0,bar}$ is the central surface brightness, a_{bar} is the length of the bar and n_{bar} represents the shape of the bar that it is fixed to a value of 2 to avoid degeneracies associated with this parameter in the fitting process.

The disk component is modeled using an exponencial profile that allows for the inclusion of Type I, Type II and Type III profiles.

$$I_d(r_d) = I_0\left(e^{\frac{-r_d}{h}}\theta + e^{\frac{-r_{break}(h_{out}-h)}{h_{out}h}} e^{\frac{-r_d}{h_{out}}}(1-\theta)\right) \tag{2.3}$$

where I_0 is the central surface brightness profile, h is the inner scale-length, h_{out} is the outer scale-length and r_{break} is the break radius of the disk. The θ parameter is 0 for r_d greater than the break radius while it is set to 1 for lower values.

The nuclear point source (NPS) is used when the bulge component is unresolved and its size is similar to the image PSF. Its parameterization using a Moffat function is the following:

$$I_{NPS}(r_{NPS}) = I_{NPS}\Big(1 + \Big(\frac{r_{NPS}}{\alpha}\Big)^2\Big)^{-\beta} \tag{2.4}$$

where α and β are interpreted in terms of the full width at half maximum (FHWM) by the expression FWHM $= 2\alpha\ 2\sqrt{2^{1/\beta} - 1}$.

Figure 2.7 shows an example of the 2D multi-component decomposition applied to the galaxy UGC 11228.

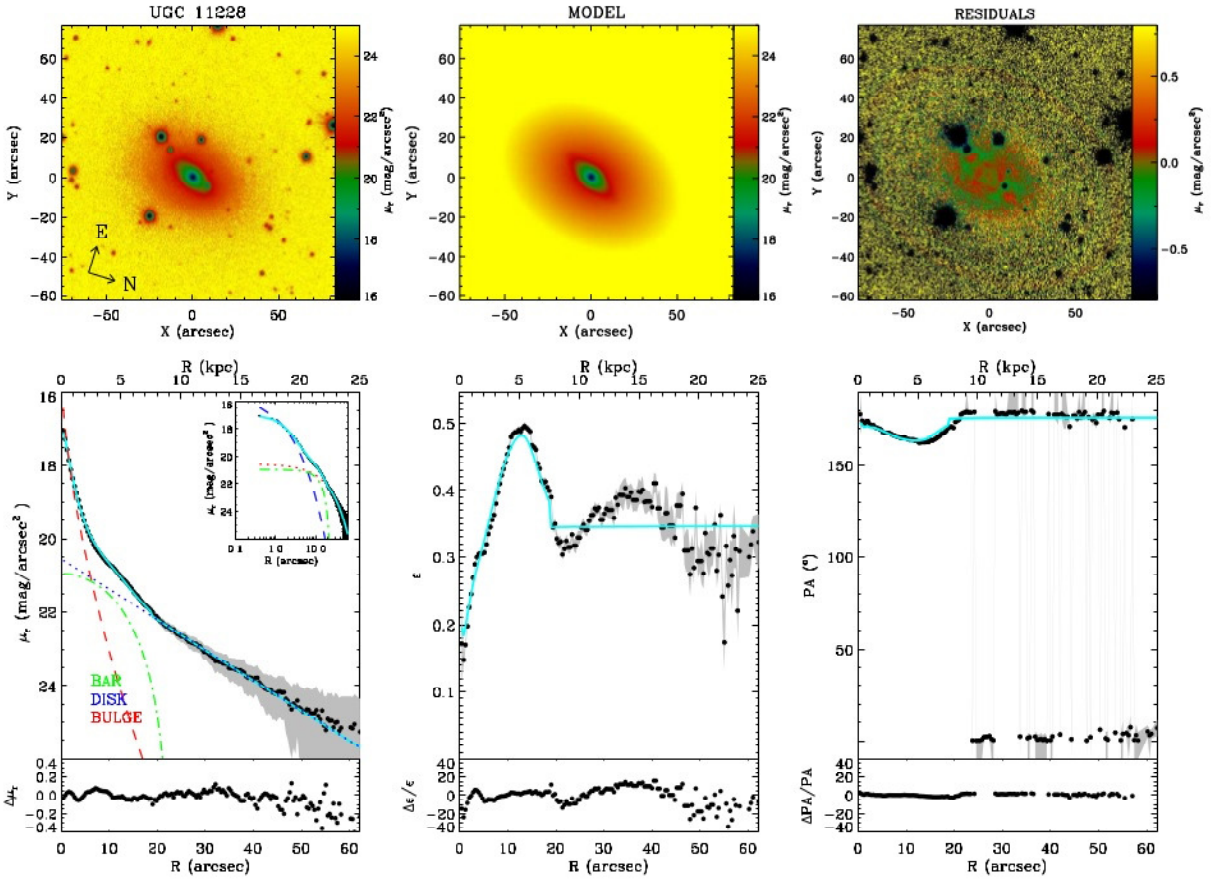

Figure 2.7: 2D decomposition method applied to the galaxy UGC 11228 as shown in Figure 3 from Méndez-Abreu et al. (2017).

In the particular case of this thesis, the 2D photometric multi-component decomposition using the *g*-band have been applied to the study of the SFR in the different morphological components that shaped the galaxies (bulges, bars, and disks). The results of this study are shown in Chapter 4.

2.3.3 SFR derivations

2.3.3.1 Measuring the SFR in entire systems

As a member of the *CALIFA SFR science working group* I led the initiative to discuss in detail the validity of the assumption that the SFR given by the extinction-corrected Hα is a good tracer of the total SFR by means of cross-comparing Hα with single (UV, 22μm and TIR) and hybrid SFR estimators (UV+22μm, UV+TIR, Hα +22μm and Hα+TIR). As described in Chapter 3, CALIFA allows us to determine that using a statistically large sample of galaxies, no significant fraction of the SFR is being missed when using the extinction-corrected Hα luminosity as an SFR estimator in the local Universe. Finally, we provide updated SFRs tracers using our integrated extinction-corrected Hα SFR as a reference (more details in Catalán-Torrecilla et al. 2015).

2.3.3.2 Measuring the SFR in different structural components

Once we have concluded that the extinction-corrected Hα luminosity is an excellent tracer of the SFR, we analyze the large-scale star formation that takes place in the different morphological components that shape galaxies, i. e., the extended disks of galaxies, the bar components and in the center of galaxies (the bulge component). Two dimensional multi-component photometric decompositions based on SDSS imaging (as explained in Section 2.3.2) are applied to CALIFA IFS datacubes for a sample of 219 galaxies. This is the first step in spatially resolving the SFR in galaxies from an observation point of view. The main goal is to analyze the SFR variations due to the contribution of several factors. In particular the nuclear emission, the environment, the presence of bars and the stellar mass, among others. The complete methodology as well as the main results are explained in detail in Chapter 4.

2.4 Scientific highlights

The current understanding of the physical processes that govern galaxies in the local Universe has improved significantly thanks to the CALIFA survey. It was created as a Legacy project which means that a scientific exploitation of the data acquired by members of the astronomical community beyond the CALIFA team is desirable. DR1 (Husemann et al. 2013), DR2 (García-Benito et al. 2015) and finally the last Data Release, DR3 (Sánchez et al. 2016) have already been distributed. The datacubes are fully reduced after a careful Quality Control process. Due to the number of galaxies available a proper statistical analysis can be done.

The main science drivers of the survey are: stellar populations, properties of the ionized gas, stellar and gas kinematics, galaxy mass distributions, nuclear activity in galaxies. I will summarize the most fundamental science cases addressed by the CALIFA collaboration until this moment.

1. **Stellar Populations**. The study of the star formation histories (SFH) of galaxies in a spatially resolved way shows us the imprints of the processes that contribute to their stellar mass assembly. In that regard, González Delgado et al. (2015) analyzed the stellar populations

properties as a function of the radial distance for different morphological types and stellar masses. Their findings about (a) negative radial stellar age gradients and (b) the mean stellar ages of disks and bulges showing that disks are younger and with low metallicities in comparison with the bulges, support the idea of an inside-out growth scenario. In González Delgado et al. (2016), they dealt with the study of the radial profiles of the SFR intensity and sSFR as a function of galaxy morphology. The authors found that sSFR values scale with Hubble type and increase radially outwards, with a steeper slope in the inner 1 half light radius (HLR). This behavior suggests that galaxies are quenched inside-out, and that this process is faster in the central, bulge-dominated part than in the disks. Sánchez-Blázquez et al. (2014) showed that the SFHs of spirals have not been largely affected by the presence of bars. Contrary to some numerical simulations predicting that the presence of bars will create a flattening of the metallicity gradient, the authors do not find significant differences between the stellar metallicity gradients or the age distributions in galaxies with and without bars.

2. **Physical properties of the ionized gas**. CALIFA offers an excellent opportunity to examine the nature of the ionized gas since many fundamental emission lines in the optical part of the spectrum are accessible through the CALIFA data. In particular, chemical abundances of the gas and SFR measurements are the two key goals in this spectral domain. The former ones are derived using direct temperature or empirically calibrated indicators while the latter case rely on the extinction-corrected Hα luminosity. Important efforts have been made to characterize the gas-phase metallicity in a large number of star-forming galaxies which the ultimate goal of understanding the chemical evolution of the Universe. One of the main steps is to be able to accurately measure the chemical abundances. With this aim in mind, Marino et al. (2013) present improved O3N2 and N2 empirical calibrators using an extensive compilation of HII regions from the literature with accurate measurements of the electron temperature and a total of 3423 HII regions provided by CALIFA. Sánchez et al. (2013, 2014) analyzed the radial abundance gradients and found that there is a characteristic slope for the oxygen abundance gradient of $\alpha_{O/H}$ = -0.1 dex/r$_e$ between 0.3 and 2 disk effective radii (r$_e$) in disk galaxies. Galaxies undergoing merging processes or with clear signals of interaction present a flatter gradient pointed towards an efficient mixing of metals in those galaxies. With respect to the SFR domain, progress has been made at (i) exploring the feasibility of different SFR estimators anchored to the extinction-correction Hα SFR tracer for extended objects and (ii) proving the suitability of Hα as an outstanding SFR tracer for recovering the recent SFR in the CALIFA sample (Catalán-Torrecilla et al. 2015). Finally, the nature of some global scaling laws relating star formation or metallicity to other galaxy parameter like stellar mass, i. e., the well-defined star formation main sequence and the mass-metallicity relation are found to be mimicked at lower scales (about 1 kpc) (see Sánchez et al. 2013; Cano-Díaz et al. 2016).

3. **Nuclear activity in galaxies**. The low-ionization nuclear emission-line region (LINER) has been traditionally associated with an AGN source. In Singh et al. (2013) the analysis of radial emission-line surface brightness profiles lead to the conclusion that LINER-like emission could be distributed over larger scales through the galaxies. Although the LINER emission is not strictly limited to the central parts of the galaxies where AGNs are placed, the contribution of some central radiation by the AGN is not discarded. Post-AGB stars are postulated as the potential source of photoionization as already suggested in Papaderos et al. (2013) and later on in Gomes et al. (2016).

4. **Galaxy mass distributions**. Measuring the growth of galaxies is key to understand galaxy evolution. Stellar masses are fundamental properties that define galaxies. Thus, it is essential to understand which processes allow galaxies to grow their stellar mass as these will provide information about the efficiency of star formation in them. In this context, Pérez et al. (2013) applied the fossil record method (i. e., finding the most suitable combination of single stellar populations that reproduce the observed present-day spectrum) to examine the spatially resolved star formation histories of individual galaxies. A growing inside-out scenario appears for the most massive galaxies while less massive galaxies ($M_\star < 10^{10}$ $M_\odot$) tend to grow outside-in (the outskirts of these galaxies grow faster than the central regions). Several studies have pointed out the existence of a critical stellar mass at which the SFR efficiency becomes higher. The authors found that the inner regions of massive galaxies could grow about twice faster than the outer regions at stellar masses around 7×10^{10} $M_\odot$.

5. **Stellar and gas kinematics**. CALIFA is providing valuable information in terms of both stellar absorption-line and ionized gas emission-line kinematics. Velocity and velocity dispersion maps of the stars and the ionized gas up to several effective radii can be created in a wide range of morphologies across the Hubble sequence. These products can be used to study a variety of phenomena linked with galaxy evolution. In particular, the first characterization of the ionized gas kinematics for the CALIFA galaxies was provided in García-Lorenzo et al. (2015) using a sample of 177 galaxies. They showed that the majority of the galaxies included in CALIFA present regular velocity fields. They also found that almost 70% of their galaxies show evidence of kinematically distinct gaseous components in the [O III] emission line profiles. Regarding the stellar kinematics, a carefully study of stellar motions is shown in Falcón-Barroso et al. (2017) where a set of 300 stellar kinematic maps covering galaxy types from ellipticals to late-spiral galaxies has been made public to the community. The authors were able to reach velocity dispersion values down to $\sigma \sim 40$ km s^{-1}. They also provided integrated velocity dispersion aperture corrections finding a different behavior between early-type and late-type spiral galaxies. The former ones show decreasing radial profiles while the latter ones have increasing profiles.

Other important studies that do not strictly belong to the previous fields of research are the following. Traditional surveys based on single fiber spectroscopy (e. g. SDSS) lost a considerable fraction of the total flux due to the limited size of the fiber that do not allow a complete coverage of the galaxy extension. In this context, Iglesias-Páramo et al. (2013) developed a new set of empirical aperture corrections in different magnitude and redshift intervals. The authors used growth curves for the Flux(Hα), the Flux(Hα)/Flux(Hβ) ratio and the Hα Equivalent Width (EW) as a function of the radius of the aperture using a sample of spiral galaxies from CALIFA. More recently, in Iglesias-Páramo et al. (2016) a similar approach is followed but extended to a larger sample of galaxies including also other emission lines used for the measurement of oxygen abundances. These empirical calibrators are O3N2 [log([O III] λ 5007/Hβ)/([N II] λ 6583/Hα)] and N2 [log[N II] λ 6583/Hα].

2.5 CALIFA as a valuable tool: the impact of using IFS data throughout this thesis

As mentioned in Section 2.2, CALIFA combines the advantages of narrow-band imaging and spectroscopic surveys in a large sample of local galaxies. One of the purposes of this thesis is to calculate precise extinction-corrected Hα SFR values.

The main benefits of using these IFS data in our work in comparison with previous techniques are listed below:

1. We have a direct way of measuring the extinction via the Balmer Decrement, i. e., using the ratio of Hα and Hβ emission lines. This is specially important for deriving a precise extinction-corrected Hα SFR value. Both emission lines are covered in the V500 CALIFA setup which ranges from 3700 to 7140 Å.

2. Problems associated to the determination of Hα fluxes using narrow-band imaging surveys are absent. These commonly include stellar absorption corrections, disentangling the contamination coming from [NII] to the Hα flux, isolating AGN contribution or, as commented before, direct measurements of the extinction correction.

3. Single-fiber spectroscopic surveys such as SDSS have a limited coverage of the galaxy extension. They lose a part of the total flux so aperture corrections are needed. In our case these aperture corrections are minimal as the sample was diameter-selected with that objective in mind.

4. Spectroscopy allows to remove the AGN contamination. Line-excitation diagnostics such as the BPT diagram help to distinguish between line emission due to AGN or SF.

5. The number of galaxies available together with a wide range of morphological types, luminosities and stellar masses covered by the sample, ensures statistically meaningful results derived from the CALIFA sample.

CHAPTER 3

Star formation in the local Universe: Calibrating the SFR using IFS data

When you can measure what you are speaking about, and express it in numbers, you know something about it.
— Lord Kelvin

Resumen

La tasa de formación estelar (SFR, por sus siglas en inglés *Star Formation Rate*) es uno de los principales parámetros empleados para analizar la evolución de las galaxias a distintas épocas cosmológicas. Su medida es fundamental ya que aporta información sobre la abundancia de gas y la eficiencia en la formación de nuevas estrellas. Como se discutió en el capítulo 1, uno de los mayores inconvenientes es que normalmente no se tiene acceso al número total de estrellas que se están formando en un momento dado, es más, es complicado conocer el instante preciso en el cual estas estrellas nacen, especialmente las más longevas. En su lugar, la luminosidad global de una población de estrellas suele usarse como una aproximación a la medida de la SFR. Así la mayoría de los indicadores de SFR analizan la luminosidad que proviene de las estrellas más masivas y con un tiempo de vida más corto. Este es el caso del continuo ultravioleta no ionizante (principalmente estrellas de tipo OB) o la luminosidad originada en las regiones ionizadas (Regiones H II, donde las estrellas de tipo O son capaces de ionizar el hidrógeno del Medio Interestelar circundante). Otra posibilidad es emplear la luz que proviene de estas estrellas después de ser re-emitida por el polvo en el IR. En las últimas décadas se ha hecho un esfuerzo especial por calibrar los trazadores de forma precisa explorando distintas escalas espaciales y distintos rangos en longitud de onda, gracias a la aparición de exploraciones multi-frecuencia tanto en el espacio (GALEX, HST, Spitzer) como en tierra (SDSS).

Sin embargo, en el uso de la luminosidad de la línea de recombinación Hα, las correcciones debidas a la extinción por el polvo han estado basadas en imagen de banda estrecha o espectroscopía de rendija larga imponiendo un límite a la utilidad de las exploraciones mencionados anteriormente. La manera óptima de superar esta limitación es mediante el uso de espectroscopía de campo integral (IFS, por sus siglas en inglés Integral Field Spectroscopy). La aparición de esta nueva técnica permitirá mejorar significativamente los estudios de trazadores ópticos con resolución espacial como el estudio aquí presentado y aclarar el origen de las discrepancias entre distintos trazadores. Con este propósito, se han derivado (a) luminosidades Hα corregidas de extinción mediante el Decremento

Balmer usando los datos IFS de la muestra CALIFA, (b) fotometría asintótica y superficial en el UV usando los datos de GALEX (Sección 5.1 del Capítulo 5.1) y (c) flujos integrados en el IR medio a 22 μm usando WISE y flujos totales en el IR (TIR) usando IRAS. Las valores anteriores nos permiten obtener medidas de la SFR para 272 galaxias con el objetivo final de proporcionar calibradores actualizados (de una sola banda e híbridos) de forma empírica anclados al trazador Hα que se ha tomado como estimador de referencia. Los criterios de selección de la muestra y el número de galaxias empleado nos permiten llevar a cabo este análisis tanto de forma global como centrándonos en distintas propiedades. De este modo se proporcionan trazadores compuestos por primera vez, en función de propiedades físicas como la masa estelar y el tipo morfológico. Entre los resultados a destacar en este trabajo cabe mencionar que (a) los calibradores híbridos proporcionan una medida de la SFR más robusta que los trazadores que emplean una sola banda en base a las bajas dispersiones que muestran los primeros (al menos en el caso de los trazadores empleados a lo largo de este trabajo), (b) las bajas dispersiones encontradas entre los trazadores compuestos y la línea de emisión Hα apuntan que las principales suposiciones realizadas a lo largo de este trabajo, como son el uso de la aproximación de pantalla de polvo para estimar las atenuaciones y la aproximación de balance energético, juegan un papel secundario, (c) existe una variación del coeficiente que mide la contribución de la cantidad de luminosidad IR (22 μm o TIR) respecto a las luminosidades observadas (Hα o UV) que disminuye para las galaxias más masivas y de tipo temprano, (d) la inclusión de galaxias que albergan AGNs de tipo-2 tiende a reducir los valores medios del coeficiente anterior.

Finalmente, podemos concluir que la luminosidad Hα derivada de observaciones IFS puede ser usada de forma óptima para medir la SFR de muestras de galaxias en el Universo Local y que la fracción de SFR completamente oscurecida es despreciable en el caso de galaxias del Universo Local (ver también Prescott et al. 2007). La sustracción del continuo estelar así como la corrección por efectos de atenuación del polvo son pasos claves en el proceso. Además, el análisis de los calibradores de SFR teniendo en cuenta las propiedades de las galaxias (masa y tipo morfológico en este caso particular) pueden ser usados potencialmente por otros trabajos para estudiar el impacto de los distintos criterios de selección en los valores derivados de la SFR.

3.1 Catalán-Torrecilla et al. (2015) A&A, 584, A87

This chapter is based on the article: "**Star formation in the local Universe from the CALIFA sample I. Calibrating the SFR using IFS data**" by Catalán-Torrecilla and collaborators published in *Astronomy & Astrophysics, Volume 584, id. A87, 34 pp, 2015.*

3.2 Introduction and Motivation

The measurement of the star formation rate (SFR) is crucial for understanding the birth and evolution of the galaxies (Kennicutt 1998a) as it provides information on the amount of gas in galaxies and the efficiency in the formation of stars inside them, which depends strongly on the conditions of the interstellar medium in which they are formed (Kennicutt & Evans 2012, and references therein). The SFR is, together with galaxy mass, one of the most important parameters that define galaxies and their evolution across cosmic times (Somerville & Davé 2014; Madau & Dickinson 2014). Several authors have tried to quantify the rate of ongoing star formation and its evolution with redshift (e.g., Madau et al. 1996; Lilly et al. 1996; Pérez-González et al. 2008; Bouwens et al. 2007, 2011, 2015) using different tracers. These works have shown that the SFR density has declined by roughly a factor of six from z=2 to present day (Hopkins & Beacom 2006).

Until now, the study of the evolution of the SFR has focused on the analysis of the integrated SFR in galaxies, with little attention being paid to where in galaxies (nuclei, bulges, disks) SFR takes places and how the SFR in each of these components evolves separately with redshift. It is remarkable that the use of NIR integral field spectroscopy on 8-10 m class telescopes is now allowing us to measure the SFR in these different components in distant galaxies, up to z=1-3 (e.g., Genzel et al. 2008; Förster Schreiber et al. 2009, 2011a,b; Nelson et al. 2012, 2013; Wuyts et al. 2013; Lang et al. 2014), while the local benchmark for these and possible future studies is still missing except for a few studies rather limited in number and completeness (e.g., Pérez-González et al. 2006; Kennicutt et al. 2007; Leroy et al. 2008; Bigiel et al. 2008; Blanc et al. 2009; Schruba et al. 2011; Leroy et al. 2012). In this regard, a correct determination of the calibrators we use to calculate the spatially-resolved SFR is essential to compare how the star formation of these different spatial components behave at different wavelength ranges and/or redshifts.

Although SFR calibrators have existed for almost 30 years, the last decade has been particularly fruitful thanks to the multiwavelength surveys of nearby and distant galaxies. The development of the integral field spectroscopy (IFS) technique has allowed us to combine the advantages of both imaging and spectroscopy at optical and near-infrared (NIR) wavelengths. In this study, we make use of a large and well-characterized sample of nearby galaxies from the Calar Alto Legacy Integral Field Area (CALIFA) survey (Sánchez et al. 2012), which spans the entire color-magnitude diagram to address this fundamental issue. The use of CALIFA allows us to properly determine the Hα and Hβ fluxes using IFS spectroscopic data. This is particularly important in the case of galaxies with low equivalent widths in emission, especially in Hβ, like many of the objects in the CALIFA sample and in the local Universe in general (Gallego et al. 1995; Brinchmann et al. 2004), where narrowband imaging is not feasible. Furthermore, using these data we can separate the Hα and [NII] flux, while imaging is only feasible in the narrowband if a [NII]/Hα ratio is assumed. The use of the unique

IFS data allows us to obtain precise Balmer-decrement measurements to compute Hα extinction-corrected luminosities. Various studies have shown the importance of computing the extinction using IFS data in nearby regions where the line ratios obtained from the integrated spectra are dominated by regions of lower surface brightness rather than by the brighter regions (Pellegrini et al. 2010; Relaño et al. 2010; Monreal-Ibero et al. 2011). Other advantages related to the IFS data is that we can cover the whole galaxy avoiding problems associated with the limited spatial coverage of long-slit spectroscopy. From these Balmer-corrected Hα luminosities, we compute their corresponding SFRs, which we use as a fiducial measure of the current SFR. However, it is critical to first determine that at least in a statistically sense, no significant fraction of the SFR is being missed when using the extinction-corrected Hα luminosity as SFR estimator. This requires of a combined analysis of this estimator with other SFR estimators, including the continuum ultraviolet (UV) emission, recombination lines of hydrogen and other atomic species together with other estimators less affected by dust attenuation, such as total infrared (TIR) luminosity, monochromatic infrared (IR) emission, or radio emission. The combination of different SFR estimators is also needed to evaluate the potential differences between the current-day SFR given by Hα and that given by tracers sensitive to intermediate-aged stellar population (Kennicutt & Evans 2012; Calzetti 2013). We order the SFR estimators from less to more sensitive to these populations as 22 μm, FUV, NUV, TIR. Whether 22 μm should precede FUV in this list is still controversial although some results indicate that should be the case (Pérez-González et al. 2006; Alonso-Herrero et al. 2006b; Calzetti et al. 2007, 2010; Kennicutt et al. 2009).

The SFR indicators we consider here come in two types: single-band and hybrid recipes (see Kennicutt & Evans 2012; Calzetti 2013, for a recent compilation). In the case of the recipes based on a single photometric band, we have used the extinction-corrected UV (with a extinction correction based on the UV slope; Treyer et al. (2007); Cortese et al. (2008); Muñoz-Mateos et al. (2009); a more precise dust-extinction correction is implicit to the use of UV+IR hybrid tracer), the extinction-corrected Hα and the observed mid-infrared (MIR) or TIR luminosities. The hybrid recipes combine luminosities measured directly (observed UV or Hα) with that of the light re-emitted by dust after being heated by young massive stars (in our case the MIR or TIR luminosities), assuming an approximate energy-balance approach (see Gordon et al. 2000; Inoue et al. 2001; Hirashita et al. 2003; Iglesias-Páramo et al. 2006; Calzetti et al. 2007; Kennicutt et al. 2007, 2009; Hao et al. 2011, for more details).

We derive integrated, extinction-corrected Hα-based SFRs from the analysis of CALIFA IFS data and compare them with measurements from other SFR tracers. We provide new single-band and hybrid updated SFRs tracers (with and without type-2 AGN being considered) using our integrated, extinction-corrected Hα SFR as a reference, thanks to the quality of our attenuation correction via Balmer decrement. We pay special attention on the hybrids recipes, providing for the first time, a set of hybrid calibrations for different morphological types and stellar masses. We also analyze the dependence with the color (SDSS $g-r$), axial ratio, and ionized-gas attenuation. This analysis is the starting point for a series of studies in which we will study how the SFR in the local Universe is distributed across galaxy components (bulges, bars, and disks) and in a spatially-resolved manner (see Chapter 4 of this thesis). Ultimately, we are interested in knowing how the local SFR density is spatially distributed over galaxies and how these results would compare to similar future studies at high redshift (more details in Chapter 5).

This Chapter is organized as follows: in Section 3.3 we describe the reference sample used in

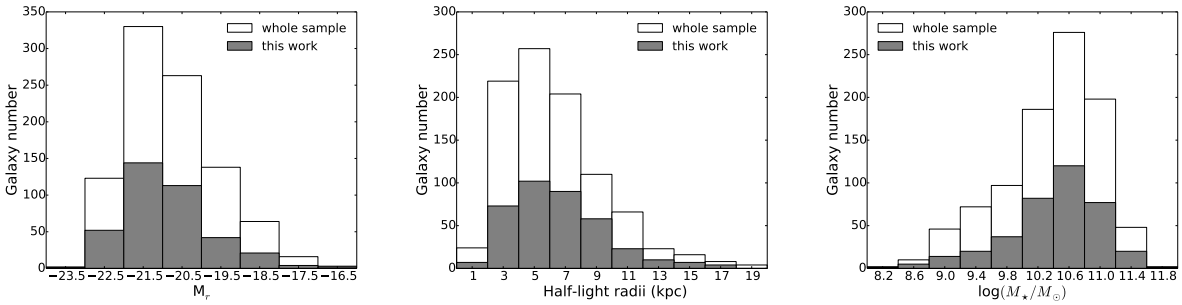

Figure 3.1: From left to right: distributions of the r-band absolute magnitude, half-light radius, and $\log(M_\star/M_\odot)$. The white histograms correspond to the complete CALIFA sample (939 galaxies), and the gray-filled areas correspond to our sample (380 galaxies). A visual inspection of these histograms together with the perform of the K-S test probability show that our sample is representative in terms of galaxy properties of the entire CALIFA sample.

this work, in Section 3.4 we describe the data and the analysis applied to the data, in Section 3.5 we discuss our results, and finally, in Section 3.6 we summarize the main conclusions.

3.3 The sample

The galaxies we studied are part of the CALIFA survey (Sánchez et al. 2012). The CALIFA mother sample includes 939 galaxies of all types. The survey and the characterization of the sample are described in detail in the presentation article (Sánchez et al. 2012) and in Chapter 2 of this thesis. As a summary, the CALIFA mother sample (Walcher et al. 2014) includes all galaxies in the DR7 SDSS photometric catalog (Abazajian et al. 2009) with declinations above 7°, spectroscopic redshifts (from the SDSS spectroscopic catalog or elsewhere) in the range $0.005<z<0.03$ and SDSS r-band diameters in the range 45"<D25<80", where D25 refers to the isophote major axis at 25 magnitudes per square arcsecond in the SDSS r-band. The observations cover the optical wavelength range 3700-7000 Å, including the most relevant optical emission lines, such as the [OII]$\lambda\lambda$3726,3729 Å doublet, Hα or the [NII]$\lambda\lambda$6549,6583 Å and [SII]$\lambda\lambda$6717,6731 Å doublets. The mother sample is representative of the general galaxy population with the following limits: -19.0 and -23.1 in r-band absolute magnitude, 1.7 and 11.5 kpc in half-light radius, and 9.7 and 11.4 in $\log(M_\star/M_\odot)$ (Walcher et al. 2014).

This study makes use of all 380 CALIFA galaxies that have been observed and processed up to Oct 27^{th} 2013, including all those released as part of the Data Release 1 (DR1, see Husemann et al. 2013) and Data Release 2 (DR2, see García-Benito et al. 2015). We refer to this as our reference sample even though some objects do not show detectable line emissions and are not used to derive the Hα-based SFR measurements. As this is a random subselection of the mother sample based only on visibility along the observing period, this should be representative in terms of galaxy properties of the entire CALIFA mother sample. To prove this statement we compare the whole mother sample (white areas in Figure 3.1) and the galaxies involved in this study (gray-filled areas). We use a K-S test to check whether the two data samples come from the same distribution. The K$-$S test probability is computed using the limits where the mother sample is representative of the general galaxy population as mentioned before. The values of the probabilities found by the K$-$S test are 40.25% in half-light radius, 70.95% in r-band absolute magnitude and, finally, 75.55% in

$\log(M_\star/M_\odot)$. From these values and from the visual inspection in Figure 3.1, we conclude that the subsample we are using is representative of the mother sample, except for a marginal deficiency of intermediate luminosity objects in the range M_r=(−20.5,−21.2), which might explain the low K−S values but certainly does not bias the results against these systems.

3.4 Data and analysis

3.4.1 CALIFA integral field spectroscopy

3.4.1.1 CALIFA Survey

The CALIFA spectra cover the range 3650-7500 Å in two overlapping setups, one in the red (3745-7500 Å) at a spectral resolution of R∼850 (V500 setup) and one in the blue (3650-4840 Å) at R∼1650 (V1200 setup), where the resolutions quoted are those at the overlapping wavelength range (λ∼4500 Å). For the purpose of deriving extinction-corrected Hα luminosities, we make use of the V500 setup as we are interested in having both Hβ λ4861 Å and Hα λ6563 Å emission lines in the same observing range. The spectral resolution (FWHM∼6 Å) is sufficient to deblend the Hα emission line from the nearest [NII]$\lambda\lambda$6548,6584 Å doublet lines. We are using the v1.3c data products, which yield the measured flux densities corrected for Galactic extinction. The data reduction is explained in detail in Sánchez et al. (2012) and Husemann et al. (2013).

3.4.1.2 Aperture spectrophotometry

For each galaxy for which the CALIFA V500 observations reached the full depth planned (3×900 seconds exposures in a three-point dithered scheme), we generate an integrated spectrum within the largest common aperture possible between the CALIFA and the other complementary data (UV, IR). This aperture has an elliptical shape with a major axis radius of 36 arcsec and the corresponding ellipticity of the galaxy, as given by the minor-to-major axis ratio listed in NED[1] for each object. The previous values and the position angle (PA) are measured at the 25.0 mag/arcsec^2 isophote at B-band provided by the RC3 catalog (de Vaucouleurs et al. 1991). When this information is not available, we use the SDSS g or r-band isophotal photometry. As the extracted aperture is significantly larger (∼4000×) than the CALIFA pixel size (1 arcsec^2), effects associated with the treatment of fractional pixels are negligible.

3.4.1.3 Continuum subtraction and line-flux measurements

To minimize systematics associated with the stellar continuum subtraction at low-S/N regimes, we decided to first spatially integrate the datacube within these apertures. This is a particularly interesting use of the IFS data that facilitates both covering the whole galaxy and having a high-S/N in the integrated spectrum. Then, we carry out the necessary corrections to derive total extinction-corrected Hα luminosities. The use of the Hα/Hβ ratio derived from the integrated

[1] https://ned.ipac.caltech.edu

spectra is justified instead of correcting for extinction spaxel to spaxel and then coadding the flux to minimize systematics when adding up signals from very noisy individual spaxels, as shown below. Thus, while Sánchez et al. (2011) and Marino et al. (2012) show that the dust attenuation from individual spaxels is a little larger than that derived from the integrated spectra (1.24/1.04 and 1.19/1.03, respectively), Castillo-Morales et al. (2011) obtain rather similar values in each case. Nevertheless, the interesting point here is how the luminosity-weighted attenuation compares when using individual spaxels with that from the integrated spectra. This question is more relevant as we are analyzing attenuation-corrected Hα luminosities rather than attenuations themselves. For this matter, we select the galaxy NGC 5668 in Marino et al. (2012) as it is a nearby spiral galaxy similar to those used in this work. We find that the difference between computing the average luminosity-weighted attenuation from individual spaxels and that derived from the integrated spectrum is less than 1%. From this result, we conclude that we can safely use the Hα/Hβ ratio derived from the integrated spectra to correct the Hα flux in each galaxy. Besides, this way of obtaining the extinction-corrected Hα luminosity would actually mimic what one could measure in more distant systems for which this work is intended to provide a local benchmark.

The first of those corrections to be applied to our data is to carefully remove the stellar continuum underlying the Hβ and Hα lines. This is done by means of adjusting a linear combination of two single stellar population (SSP) evolutionary synthesis models of Vazdekis et al. (2010) based on the MILES stellar library (Sánchez-Blázquez et al. 2006a) to the spectrum obtained for each aperture. Two set of models with a Kroupa IMF (Kroupa 2001) are combined. One set contains models (considered as a young stellar population) with ages of 0.10, 0.50, and 0.79 Gyr. A second set (considered as an old stellar population) involves ages of 2.00, 6.31, and 14.13 Gyr. For each age, we considered five different metallicities with [M/H] values equal to 0.00, 0.20, -0.40, -0.71, and -1.31 dex offset from the solar value.

Different wavelength ranges corresponding to the emission lines from the ionized gas and sky-lines are masked and not included in the fit. The basic steps applied in this method are the following: (1) shift the SSP templates to match the systemic velocity of the integrated spectrum, (2) convolve each stellar population model with a Gaussian profile so the absorption features could be broadened to match those of the integrated spectrum, (3) redden the spectrum using a $\mathrm{k}(\lambda) = \mathrm{R}_V\ (\lambda/5500\,\text{Å})^{-0.7}$ power law, where $\mathrm{R}_V = 5.9$, as given by Charlot & Fall (2000), and (4) finally, the best linear combination of SSPs is determined by a χ^2 minimization.

Once we obtain the best underlying continuum of the stellar population, we subtract it from the original integrated spectrum to derive the pure emission line spectrum. The emission line fluxes are computed from this residual spectrum. As some residual continuum could still be present in some cases, we do not simply add all the flux in fixed windows in wavelength. Instead, we compute the Hβ and Hα emission line fluxes by fitting Gaussian functions plus a low-order polynomial function. Figure 3.2 shows the original integrated spectrum for three galaxies with different levels of emission-line strength, IC 4215, NGC 2906, and NGC 5630 in black. The best fit to the spectrum of the underlying stellar population is shown in red and the emission-line spectrum produced by the ionized gas is shown in blue. Gray-colored wavelength ranges correspond to the emission lines and sky lines masked out in the fitting procedure.

A proper estimation of the Hβ emission line flux is crucial to obtain a reliable Balmer decrement and, from it, the correction for extinction of the Hα-based SFR. The method applied here is

expected to be a robust procedure as long as a relatively wide wavelength coverage is available (see Mármol-Queraltó et al. 2011) and the models contain an extensive range of ages and metallicities. When the whole spectral range (3750−7000) Å is used for the stellar continuum fitting, however, we still detect systematic residuals around the Hβ absorption line. The treatment of these spectral features is particularly critical. They could be real because of the limitation of the models in reproducing simultaneously a broad wavelength range and the Hβ region, or introduced during the data reduction. We have also checked that adding an intermediate age population in the linear combination of the SSPs does not change the overall results. For that reason, the stellar continuum fitting around the Hβ line is done for other wavelength ranges using the method explained before. The new spectral ranges used are (3700−5500) Å, (4100−5500) Å, and (4800−5500) Å. Given that the residual continuum around Hα and Hγ emission lines does not show systematic uncertainties, we determine the Hβ flux by anchoring to Hα and Hγ fluxes based on theoretical line ratios and extinction coefficients. In high S/N spectra, this Hβ emission line flux estimation is compared with the values obtained when different spectral ranges for the stellar continuum fitting are used. Finally, we obtain that the Hβ emission fluxes calculated using the spectral range (4800−5500) Å are in best agreement with the theoretical emission fluxes.

We impose a minimum S/N for both Hα and Hβ emission lines fluxes to obtain a precise measurement of the extinction using the Balmer decrement. The S/N emission line estimation is done using a formal method calculating the ratio between the Gaussian amplitude at Hβ and the root mean square in the near featureless continuum. A visual inspection of the continuum-subtracted spectra at Hβ is performed for all the analyzed galaxies and a minimum S/N$>$ 5 is considered for Hβ emission line detection. The number of galaxies with detected Hβ emission is 272 over the initial 380 galaxies. This is the sample (listed in Table 3.5 for reference) that will be used in the rest of the analysis.

The spectrophotometric accuracy in CALIFA DR1 was checked using SDSS g and r-band photometry, which are both entirely covered by the V500 setup. Husemann et al. (2013) found a systematic offset of Δ(g −r) = −0.06 mag (median) with a scatter of only 0.05 mag. This means that the spectrophotometric accuracy across most of the covered wavelength range is 6% for the CALIFA data. This value is included in our error estimation for the emission line fluxes.

3.4.1.4 Flux corrections and uncertainties

We also apply some corrections, such as aperture corrections and those associated with the spatial masking of field stars and background galaxies applied to the datacubes, to our data. We use aperture corrections for the galaxies whose line emission is expected to be more extended that the CALIFA field of view (FOV). Our main criterion is to select the band that would first trace the SFR, and second, that it would do it with the best spatial resolution possible. Also, we want to have them available for most galaxies in our sample. Here, we assume that the Hα light distribution beyond the FOV is similar to that of the ultraviolet light in each galaxy individually. Besides, the UV band has the highest spatial resolution within the bands we are using that are closely related to the SFR. Thus, for that purpose we use the GALEX NUV images (deeper and available for a few more objects than the FUV images). We compute the difference between the NUV magnitudes obtained for the 36-arcsec-aperture and the asymptotic magnitudes. We fit the aperture correction data for the whole mother sample (those galaxies having NUV data) as a function of the galaxy

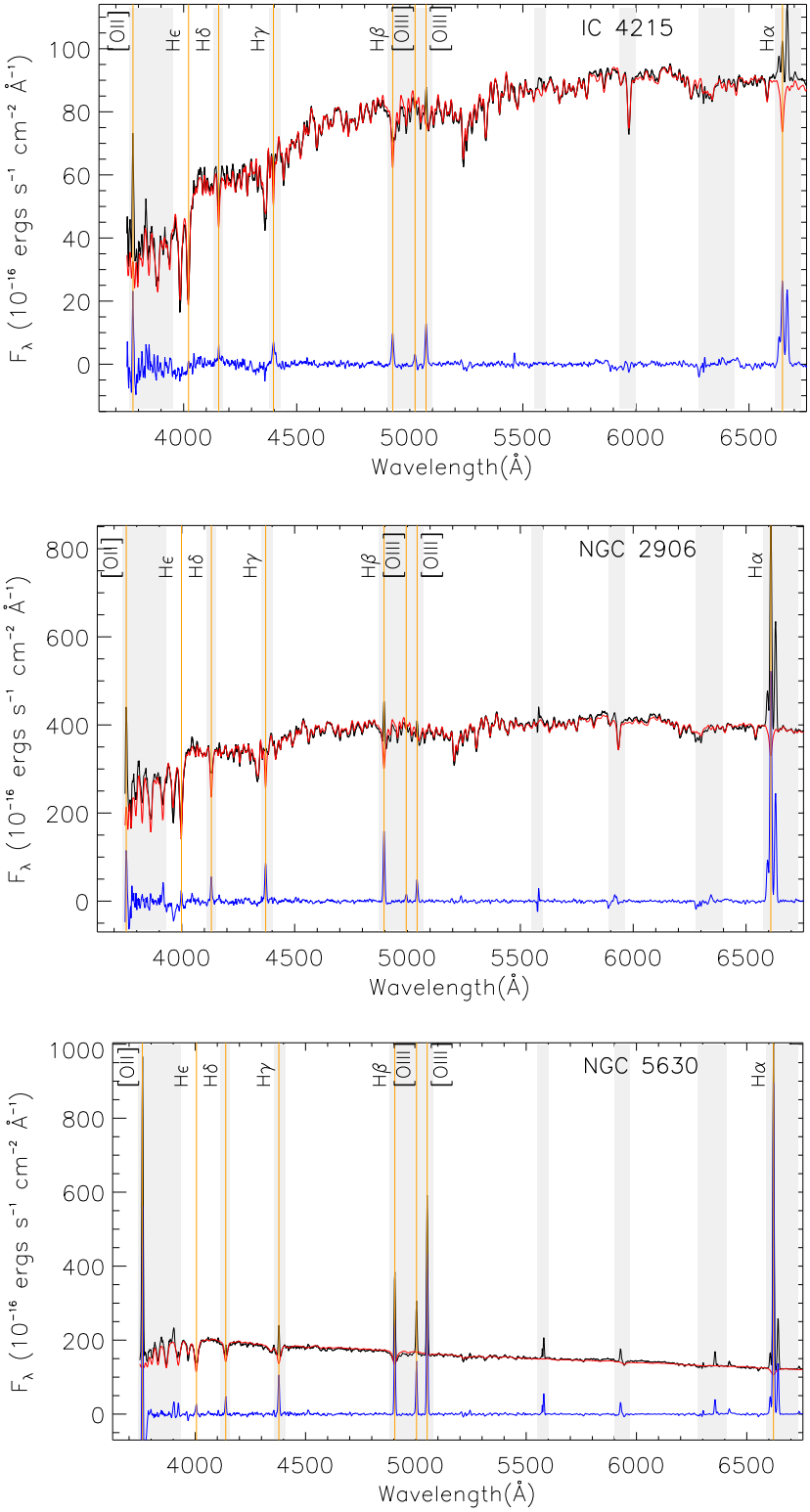

Figure 3.2: Top panel: the original integrated spectrum for galaxy IC 4215 is shown in black; the best fit to the stellar population appears in red (using the 3745−7500 Å entire spectral range), and the pure emission line spectrum (after the subtraction of a residual continuum shape applying a smooth function) is shown in blue. This galaxy shows a small equivalent width in the Hβ line. Center panel: same as top panel for the galaxy NGC 2906. Note that in this case the spectrum shows more prominent Hα and Hβ emission lines. Bottom panel: in this case, NGC 5630 shows a typical emission line dominated spectrum with very high EWs of Hα and Hβ emission lines. These spectra show the variety in levels of emission line strength in our galaxies. A proper subtraction of the underlying stellar population is required to obtain the estimation of the emission line fluxes.

size, given by the *isoA* in the *r*-band from the SDSS. The correlation between aperture correction and isophotal diameter is the strongest of all those analyzed and it will be used for galaxies without NUV magnitudes. The resulting median correction is around 1.4. The observed Hα luminosities already corrected for aperture effects are listed in Table 3.5.

The spatial masking is applied over the datacubes before performing the stellar continuum fitting. That means that the light from spaxels contaminated by field stars and background objects is not summed up at this stage. Then, we correct the emission-line fluxes for the flux coming from those missing spaxels. The mean value for the correction factor is 2.2 %. The corrections are only applied over 44.7 % of the galaxies, i.e., those that have contaminating sources. These correction factors are obtained comparing the aperture fluxes between two sets of synthetic continuum-subtracted narrowband images. One of them without the flux from the corresponding contaminated pixels and the other where the flux from those pixels is obtained by local interpolation.

Once Hα and Hβ emission line fluxes are computed, we correct the Hα flux for dust attenuation assuming that the relation between Hα reddening and extinction follows the foreground dust screen approximation. Although this could be a possible source of systematic error in the analysis, some models have shown that when applied to normal star-forming galaxies the dust geometry assumed does not introduce significant systematic errors (Jonsson et al. 2010). See a detail discussion about the use of attenuation corrections based on Balmer decrements with a Galactic extinction curve and a foreground screen dust geometry in sections 3.3 and 6.3 in Kennicutt et al. (2009). For the attenuation correction, we use an intrinsic Balmer ratio of 2.86 for case B recombination (Osterbrock 1989) at electron temperature T_e = 10,000 K and density n_e = 100 cm^{-3} (Hummer & Storey 1987) using the following expression 3.1, where $K_{H\alpha}$ = 2.53 and $K_{H\beta}$ = 3.61 are the extinction coefficients for the Galactic extinction curve from Cardelli et al. (1989):

$$A(H\alpha) = \frac{K_{H\alpha}}{-0.4 \times (K_{H\alpha} - K_{H\beta})} \times log_{10} \frac{F_{H\alpha}/F_{H\beta}}{2.86}. \quad (3.1)$$

As an example of how little this attenuation correction would vary among extinction curves and dust-to-stars geometries, we compare the ratio between the A(Hα) attenuations for the same A(Hβ) using the Cardelli et al. (1989) (R_V = 3.1) law above and the Calzetti et al. (2000) (R_V = 4.05) attenuation law. We obtain $A(H\alpha)_{Calzetti}/A(H\alpha)_{Cardelli}$ = 1.03.

Note that the standard Hα/Hβ ratio used in equation 3.1 is only valid for the particular ionization conditions indicated above, but values below 2.86 are also physically possible in HII regions, depending on the electron density, effective temperature, and, therefore, on the chemical abundance. This leads to a number of galaxies for which we assumed A(Hα) = 0. The computed extinction values A(Hα) are listed in Table 3.5. The Hα luminosity corrected by attenuation and by the effects mentioned along this section is referred to hereafter as $H\alpha_{corr}$.

We test whether the foreground dust screen approximation has an effect on edge-on galaxies. For that purpose, we plot the difference between A(Hα) derived from the Balmer decrement and the A(Hα) values derived from the ratio of IR/Hα as a function of galaxy axial ratio (see top panel in Figure 3.3). The expression used to derive the attenuation from the ratio of IR/Hα is A(Hα) = 2.5 $\times$ log[1+$a_{IR}\times$L(IR)/L($H\alpha_{obs}$)] (see Kennicutt et al. 2009, equation 2). In this case, L(IR) corresponds to L(22μm) available for a larger number of galaxies in our sample than L(TIR). The coefficient a_{IR} is equal to $0.015^{+0.018}_{-0.006}$ (average value derived from our sample in Section 3.5.5.2).

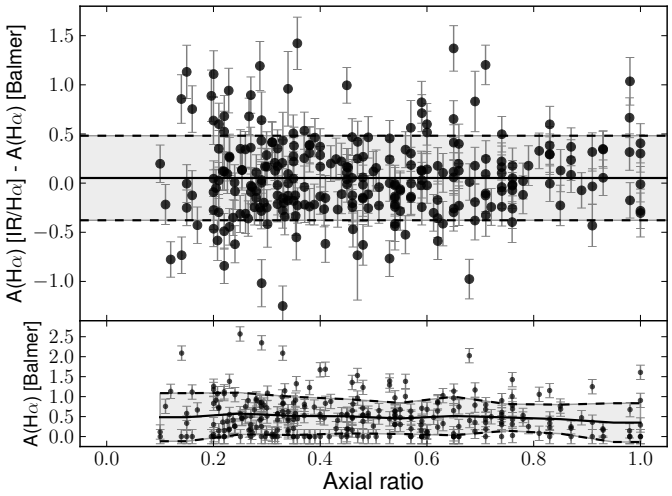

Figure 3.3: Top panel: difference between Hα attenuations derived from the ratio of IR/Hα and those obtained using the Balmer decrement as a function of galaxy axial ratio. Solid and dashed black lines correspond to the mean and 1σ values, (0.05 $\pm$ 0.43) mag, after applying a rejection of 4σ. Because of the good agreement between both attenuations computed from different methods, we can safely assume that our Balmer decrement attenuations yield proper results. Besides, we do not find any systematic residuals against the axial ratio parameter associated with highly-inclined galaxies. Bottom panel: A(Hα) derived from the Balmer decrement as a function of the axial ratio (used as a proxy for inclination). Gray shadow corresponds to the 1σ intervals around the mean value showed in black solid line.

The value given by Kennicutt et al. (2009) is a_{IR} = 0.020 $\pm$ 0.001r $\pm$ 0.005s, which is in good agreement with ours even taking into account that they are obtained from different samples. Finally, the difference between both A(Hα) estimations yields mean and 1σ values of (0.05 $\pm$ 0.43) mag after doing a rejection of 4σ. This value shows that both methods produce compatible results. As we do not see systematic residuals against the axial ratio parameter, we conclude that we do not find a different behavior in the case of highly-inclined galaxies.

Finally, the uncertainty in the Hα flux is estimated from a random redistribution of the residuals obtained after fitting a Gaussian function to the pure emission-line spectrum in the spectral range around Hα emission. The new residual spectrum is added to the pure emission-line spectrum and a new Gaussian fit is performed. This procedure is repeated 1000 times and the standard deviation of the computed Hα fluxes is considered as the error in the Hα flux. On the other hand, the comparison between the measured Hβ line fluxes and those expected from the Hα/Hγ Balmer decrements for the same ionized-gas physical conditions gives us an estimation of the Hβ flux uncertainty. A dispersion of σ = 7 % centered around unity is obtained across the whole sample. This method provides much larger uncertainties compared with the method using the redistribution of the residuals around the Hβ emission line. The reported error includes the potential uncertainties in the modeling of the stellar continuum and it is taken as a conservative upper limit for the error in the Hβ flux. This Hβ flux uncertainty propagates to a much larger one in the corrected Hα flux. A standard error propagation method is used to compute the uncertainties in other quantities, such as extinction or luminosity.

3.4.2 GALEX UV imaging

For nearly two thirds of the galaxies in the CALIFA mother sample, we were able to collect UV observations available from the Galaxy Evolution Explorer (GALEX[2]) archive (see Martin et al. 2005). In most cases (655 out of the 663 objects with GALEX UV data), this includes both far-ultraviolet (FUV, effective wavelength $\lambda_{\rm eff}\sim$1516 Å) and near-ultraviolet (NUV, $\lambda_{eff}\sim$2267 Å) bands, 200 of them included in the sample of the 272 galaxies we analyzed.

The GALEX archive provides simultaneous co-aligned FUV and NUV images with a pixel scale of 1.5 arcsec per pixel and a spatial resolution (FWHM) of $4-5$ arcsec. We selected galaxies located within the central 0.5-degree radius of the 1.2-degrees circular GALEX FOV. We also imposed that the whole galaxy is included in the GALEX FOV. To calculate the integrated mean flux of the galaxy, foreground stars and other targets in the field were identified and removed by averaging the interpolation along rows and columns from the GALEX images.

The typical background in the GALEX UV images is very low so the distribution of count rates in each image typically follows a non-Gaussian distribution. Because of this peculiarity, we estimate the background using the mean instead of the median or the mode used at high background levels, such as ground-based optical or NIR imaging (see Gil de Paz et al. 2007b). Surface and aperture photometry was then carried out for each galaxy, using the IRAF task ELLIPSE, as described in Gil de Paz et al. (2007b), within elliptical isophotes with fixed ellipticity and position angle (the same ones used for the extraction of the spectra from the CALIFA datacubes). Figure 2.6, in Chapter 2 of this thesis, shows the surface brightness profiles and the growth curves of two particular galaxies of the sample. In addition to the 36-arcsec aperture mentioned above, we also extracted UV photometry in other concentric elliptical apertures until the error in the surface photometry reached 0.8 mag (including both background-subtraction and photon noise). From each set of concentric elliptical apertures, we finally obtained asymptotic magnitudes for the whole sample (Gil de Paz et al. 2007b). These asymptotic magnitudes are those previously applied in Section 3.4.1.4 to obtain the aperture corrections.

As the UV luminosity suffers from severe attenuation by dust this has to be corrected to properly estimate the SFR. The most commonly accepted method to estimate the dust attenuation at UV wavelengths is to use the ratio between the IR (22-25 μm MIR, FIR, or TIR) and the UV flux (also known as infrared excess or simply IRX). This is equivalent to the use of hybrid SFR estimators, which includes information from these two wavelengths and is the approach used in Section 3.5.5.2. The IR/UV ratio is almost independent of the dust properties and the relative distribution of dust and stars (Buat et al. 2005). However, it depends on the age of the dust-heating populations (see Cortese et al. 2008). In the context of this section, we analyzed only the case when no IR data is available. Should that be the case, a relation between the FUV$-$NUV color and the infrared excess could be used instead (see Muñoz-Mateos et al. 2009, equation 2). For the sake of simplicity, and given the intrinsic large dispersion of the IRX-β relationship (see Section 3.5.5.2 for the IRX-β relationship in our sample), we make use of the following linear relation between A(FUV) and FUV$-$NUV and the corresponding $\pm1\sigma$ prediction intervals:

$$A(FUV) = 0.556 + 2.292 \times (FUV - NUV) \tag{3.2}$$

[2]http://galex.stsci.edu/GalexView/

This linear empirical relation is based on the analysis of UV and infrared surface photometry of the SINGS sample (Kennicutt et al. 2003) carried out by Muñoz-Mateos et al. (2009). These authors use FUV, NUV, and TIR luminosity profiles with the same spatial resolution to compute both, FUV−NUV colors and A(FUV) attenuations via the L(TIR)/L(FUV) ratio using the expression given by Buat et al. (2005). This is similar to the IRX-β relationship first studied by Meurer et al. (1995) and calibrated for starburst galaxies. However, Muñoz-Mateos et al. (2009) used star-forming galaxies that have lower values of the extinction for a given FUV-NUV color. We emphasize that these relations (based on the UV color alone) should only be used as a rough estimate of the UV light attenuation. These relations have some (limited) statistical meaning, but very little use in a case-by-case basis. More recently, Hao et al. (2011) provided a physical motivation for this linear relationship between UV color and attenuation and yielded a y-intercept of -0.084 mag (that corresponds to a FUV-NUV color in the absence of dust of 0.022 ± 0.024 mag) and a slope of 3.83. Taking into account that the intrinsic FUV−NUV color for zero attenuation is different in both cases (because of the noisy relation between A(FUV) and FUV−NUV color), we decide to use Equation 3.2 (J. C. Muñoz-Mateos, priv. comm.) as in this case we have prediction intervals as a function of the UV color.

We apply Equation 3.2 to galaxies that have a FUV-NUV color less or equal to 1 mag. Galaxies with colors FUV−NUV>1 could correspond to either red galaxies with old stellar populations or galaxies with large amounts of dust reddening. In our sample, the mean value of the dust attenuation in the FUV is 1.73 magnitudes and vary from 0.81 to 2.80 magnitudes, as is found by other authors (e.g., Buat et al. 2005; Burgarella et al. 2005). The FUV−NUV colors, L(FUV), and L(NUV) in ergs s^{-1} for 200 galaxies over the 272 galaxies we analyzed are listed in Table 3.5.

3.4.3 WISE MIR imaging

The Wide-field Infrared Survey Explorer (WISE, Wright et al. 2010) surveyed the entire sky at MIR wavelengths 3.4, 4.6, 12, and 22 μm (W1 through W4 bands) with five σ point-source sensitivities of $\sim$ 0.08, 0.11, 0.8, and 4 mJy, respectively. The WISE All-sky Data Release is available through the Infrared Science Archive (IRSA[3]). It includes imaging (Image Atlas) and PSF-photometry source catalogs (Source Catalog) for all four WISE bands for the entire CALIFA mother sample. We make use of the WISE 22 μm data (W4-band) for information on the amount of (mainly UV) photons being processed through dust absorption and re-emitted. The WISE Source Catalog is optimized for point sources and, in spite of the resolution of the 22 μm data (FWHM $\sim$ 11 arcsec) and the size of the CALIFA galaxies (limited in diameter to $\sim$ 1 arcmin), this photometry catalog might not be appropriate for our sample (see Figure 3.4). Therefore, we decided to perform aperture photometry using the Image Atlas to calculate the integrated 22 μm fluxes and magnitudes. We obtain aperture photometry in circular apertures that enclosed the entire flux from the source. A circular annulus around this aperture is used to compute the sky. We derive L(22 μm) in ergs s^{-1} for 265 objects out of the 272 galaxies with detected Hβ emission included in this work (see Table 3.5). It has been pointed out by several authors (Wright et al. 2010; Jarrett et al. 2013; Brown et al. 2014) that star-forming galaxies measured with the WISE 22 μm filter are systematically brighter by $\sim$ 10 % than that inferred from Spitzer IRS and 24 μm data. This factor has been applied in our 22 μm luminosities along the work. Values of L(22 μm) in Table 3.5 should be multiplied by this

[3] http://irsa.ipac.caltech.edu

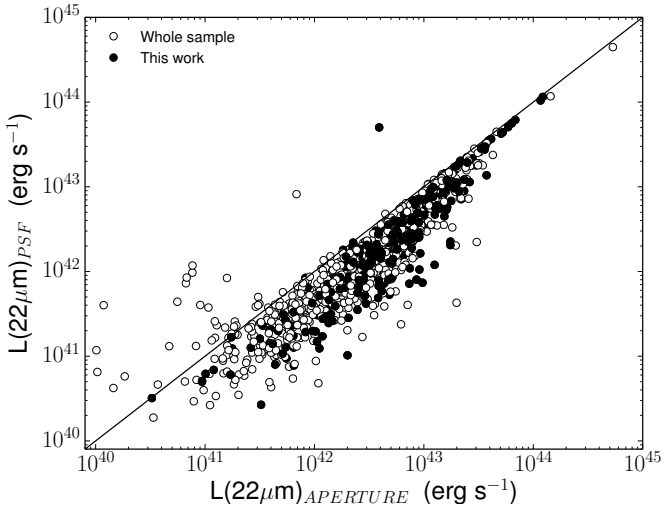

Figure 3.4: Comparison between the WISE 22 μm PSF and aperture photometry for the entire CALIFA mother sample (white points) and for the galaxies used in this work (black points). Solid line corresponds to the 1:1 line and is given for reference. Although the WISE Source Catalog is ideal for point sources and the resolution of the WISE 22 μm band is wide enough (FWHM $\sim$ 11 arcsec) it does not seems to be suitable for the CALIFA sample.

correction factor.

3.4.4 TIR fluxes: WISE, IRAS, and AKARI

Although the longest WISE band already provides relevant information on the attenuation of the UV light associated with regions of star formation, a significant fraction of the energy re-radiated in the IR by dust emerges at longer wavelengths. To account for possible differences in the dust temperature or grain-size distribution, which could hamper the use of WISE 22 μm alone, we have also collected IRAS photometry for the entire CALIFA mother sample.

The Infrared Astronomical Satellite (IRAS, Neugebauer et al. 1984) surveyed 96% of the sky in four wavelength bands at 12, 25, 60, and 100 μm. Our main data source is the IRAS Faint Source Catalog v2.0 (FSC) (Moshir et al. 1990) with a detection limit about one magnitude deeper than the Point Source Catalog (PSC) (Beichman et al. 1988), reaching a depth of $\sim$0.2 Jy at 12, 25, and 60 μm and greater than 1.0 Jy at 100 μm. The FSC is at least 98.5% reliable at 12 and 25 μm and $\sim$94% at 60 μm.

We performed a cross-match of the CALIFA mother sample with the IRAS Faint Source Catalog (closest IRAS source within 40 arcsec), finding 488 galaxies in common for the four IRAS bands. Within the IRAS FSC catalog, a flux density measurement can either be high quality (FQUAL=3), moderate quality (FQUAL=2), or just an upper limit (FQUAL=1) (Moshir et al. 1992). We make use of only high and moderate quality measurements available for the CALIFA mother sample galaxies, which yielded 12, 25, 60, and 100 μm detections for 200, 203, 486, and 443 sources, respectively. Note that poor spatial resolution of IRAS in any of these bands ensures that the flux measurements in the FSC are accurate for the CALIFA objects as long as the object is relatively isolated, but could have an impact on the TIR measurements of galaxies in pairs or close groups.

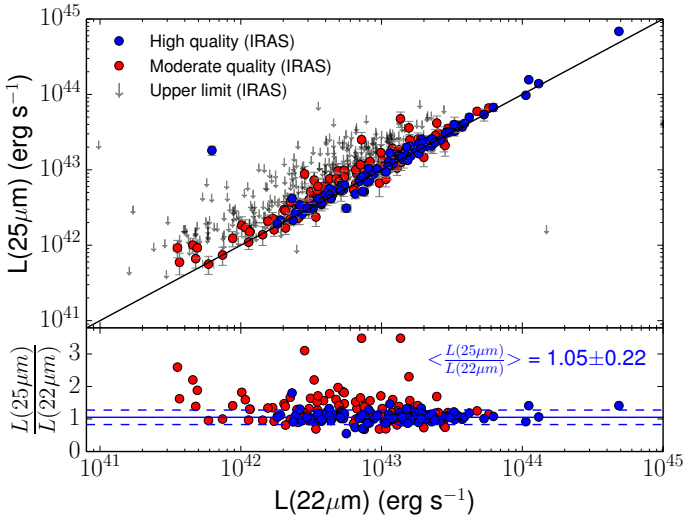

Figure 3.5: Comparison between 22 μm WISE and 25 μm IRAS luminosities for the CALIFA mother sample. Blue and red points correspond to high and moderate quality IRAS 25 μm data, respectively. Arrows represent upper limits for the same IRAS band. The solid line shows a linear 1:1 relation for reference. The average ratio between 25 μm and 22 μm luminosities is 1.05 $\pm$ 0.22 when using high quality 25 μm IRAS measurements. This tight relation allows us to use them interchangeably using the previous conversion factor.

As noted above, the fraction of galaxies with 25 μm measurements is significantly lower than that of galaxies with 60 μm and 60+100 μm measurements. This is due to the comparable detection limit of IRAS at 25 and 60 μm but larger flux densities of nearby star-forming galaxies at these latter wavelengths. To recover a larger fraction of galaxies with total infrared flux densities (TIR, i.e., 8-1000 μm) we decided to combine the WISE 22 μm photometry with that from IRAS to determine the galaxies TIR luminosity. The reliability of this procedure is demonstrated by the tight correlation between our WISE 22 μm luminosities and those detected at 25 μm with high and moderate quality flux by IRAS (blue and red points in Figure 3.5). Therefore, we can confidently use our WISE 22 μm photometry to increase the number of CALIFA galaxies with TIR measurements. In addition, we are going to use the WISE 22 μm measurements instead of the IRAS 25 μm in the corresponding IR SFR tracers, as both are found compatible, and there are significantly more measurements from WISE 22 μm. Previous studies (Kennicutt et al. 2009; Calzetti et al. 2010) show that the average ratio between 24 μm and 25 μm luminosities is 0.98 $\pm$ 0.06. In our case, we find that the average ratio between 25 μm and 22 μm luminosities is 1.05 $\pm$ 0.22 when using high quality 25 μm IRAS measurements. Note that the galaxies used in our work are more distant and, therefore, the photometric errors tend to be larger.

As we are interested in estimating the TIR luminosity for our sample of galaxies, we add AKARI photometry measurements at 140 and 160 μm from the AKARI/FIS All-Sky Survey Bright Source Catalogue (Yamamura et al. 2010). Using a cone search of 90 arcsec, we find 247 galaxies at 140 μm and 70 galaxies at 160 μm with high quality data, which implies confirmation of the source detection and a reliable flux estimation. By adding these measurements, we include information at wavelengths at the peak of the spectral energy distribution (SED) and beyond.

We test the consistency of the IRAS and AKARI measurements when possible (IRAS 60 μm vs. AKARI 65 μm and IRAS 100 μm vs. AKARI 90 μm). In general, AKARI gives lower flux

values than expected from the IRAS photometry measurements for those wavelengths in common. Besides, we also find that AKARI 140 and 160 μm fluxes tend to fall (quite systematically) below the values predicted by our best-fitting infrared SEDs at these wavelengths when data at all IRAS bands is also available. For this reason, we use AKARI 140 and 160 μm bands as lower limits to help discriminate between different dust SEDs, which still provides information for the fits in cases where some IRAS fluxes could be missing.

Finally, by fitting a set of IR templates from Chary & Elbaz (2001), Dale & Helou (2002) and Rieke et al. (2009) to the WISE 22 μm, IRAS, and AKARI photometry, we derive TIR fluxes for 547 (out of 939) galaxies in the CALIFA mother sample, 221 of them included in the sample of the 272 galaxies analyzed in this work. The fitting procedure used to derive TIR fluxes is described in detail in Pérez-González et al. (2008). As a brief explanation, the code carries out a template-fitting procedure using the rest-frame effective wavelengths (i.e., $\lambda_{eff}/(1+z)$). Then, it integrates the best-fit spectra in the wavelength range (8-1000) μm for a total of 100 Monte-Carlo simulated SEDs per galaxy. The average of the TIR individual MC-simulated SED luminosities obtained for each galaxy is listed in Table 3.5. We adopt these values as the best measure of the TIR luminosity.

3.5 Results

Our aim is to determine the different SFR estimators (single-band and hybrids) for the CALIFA sample and, in particular, ensure that Hα_{corr} can be safely used for future statistical spatially-resolved studies, at least in the local Universe.

There are three different ways to carry out this analysis: by comparing fluxes, luminosities (or SFRs), and surface brightnesses (or SFR surface densities). Ideally, we would also like to include in this comparison as many SFR tracers as possible. In the latter case, this implies having good spatial resolution to identify the area in the galaxy responsible for the current activity of star formation. Specifically, in the case of the IR measurements this is usually not possible as the WISE and IRAS data do not provide such a high spatial resolution. For this reason, the analysis of the SFR surface density cannot be carried out in all tracers. Therefore, for most of this section we rely on the comparison between integrated SFR measurements. The use of fluxes for this comparison is excluded as the correlations would be mainly driven by the wide range in distances spanned by our sample ($0.005<z<0.03$).

However, the linear correlation of the integrated SFR between different tracers, more than the similarity between the SFR tracers, could be partly due to galaxies with different total SFR but similar SFR surface density (scaled-up versions of low-SFR surface density objects). Using the tracers with higher spatial resolution, UV and Hα, (see Section 3.5.1 for a description of the SFR calibrators found in the literature), we compare in Section 3.5.2 the predictions of the SFR surface density.

In the majority of cases, the recipes used to determine the integrated SFR found in the literature are based on samples with ill-defined selection criteria, where the bias toward or against low-metallicity, low-extinction galaxies or highly extinct systems has not been accounted for. We compare their predictions for the CALIFA sample in Section 3.5.3. We describe the possible discrepancies among the different SFR tracers used until now in Section 3.5.4.

Finally, in Section 3.5.5 we provide updated calibrations for the CALIFA sample assuming that (as proven across this section) the Hα extinction-corrected SFR provides a reliable SFR estimator in the local Universe. Thus, we anchor both single-band and hybrid tracers to the Hα extinction-corrected SFR tracer. We also explore the origin of the difference between the SFR tracers used as a function of galaxy properties, such as morphological type, stellar mass, SDSS $g-r$ color, axial ratio, or attenuation.

As we are interested in separating star-forming galaxies from the galaxies hosting an AGN, the plots provided in the following sections show SF galaxies in blue and type-2 AGN host galaxies in orange. The same color-coding is used in the rest of this study. The information regarding the optical AGN classification can be found in Walcher et al. (2014). Briefly, the authors use the emission-line fluxes for all SDSS spectra of DR7. They create a classical [O III]λ5007/Hβ vs. [N II]λ6583/Hα diagram (Baldwin et al. 1981) to classify the objects and discriminate between different ionization sources at the center of CALIFA galaxies (see Walcher et al. 2014, Figure 17). For the galaxies with no classification, we extract the same 3"-diameter circular apertures in the nuclear part. Then, we follow the same criteria as described in Walcher et al. (2014) to classify them into their corresponding activity type: either SF or type-2 AGN host galaxies.

3.5.1 Recipes for determining the SFR in galaxies

The SFR indicators considered are of two types: single-band and hybrid. In the case of the recipes based on a single photometric band, we use the extinction-corrected UV (from the UV slope), extinction-corrected Hα (from the Balmer decrement), and the observed MIR or TIR luminosities. The hybrid tracers combine luminosities measured directly (observed UV or Hα) with that of the light emitted by dust after being heated by young massive stars (see Gordon et al. 2000; Inoue et al. 2001; Hirashita et al. 2003; Iglesias-Páramo et al. 2006; Calzetti et al. 2007; Kennicutt et al. 2007, 2009; Hao et al. 2011; Kennicutt & Evans 2012; Calzetti 2013; Domínguez Sánchez et al. 2014, for more details).

The most widely used recipes for SFR tracers are included in Calzetti (2013) and are listed here for convenience. These expressions are used to compute the SFR from different data, both for single-band and hybrid recipes, scaled to the same IMF (Kroupa 2001). The mass range varies from 0.1 to 100 $M_{\odot}$. The value of the timescale over which the star formation must remain constant depends on each tracer, up to 100 Myr for the UV, MIR or TIR and with a lower value for the Hα tracer, equal, or larger than 6 Myr. The expressions listed below are for global scales, as we are using integrated fluxes for the whole galaxy in each case. Also, recipes for determining the SFR at local scales could be found in the review of Calzetti (2013). For the case of Equations 3.6, 3.7, and 3.9, we have rescaled the coefficients that multiply L(22 μm) taking into account the L(25 μm)/L(22 μm) ratio obtained for our sample and the average ratio between L(24 μm) and L(25 μm) derived in previous studies (Kennicutt et al. 2009; Calzetti et al. 2010) as explained in Section 3.4.4. The nonlinear behavior for galaxies with L(22 μm) $> 5\times10^{43}$ erg s^{-1} present in the original recipe (see Calzetti 2013) is not included here as we only find four galaxies in that range. The total infrared emission in the range 8$-$1000 μm is L(TIR).

First we list those based on single-band, where all the luminosities are in units of ergs s^{-1} :

$$\text{SFR } (M_\odot\ yr^{-1}) = 4.6 \times 10^{-44} \times L(FUV_{corr}), \tag{3.3}$$

$$\text{SFR } (M_\odot\ yr^{-1}) = 5.5 \times 10^{-42} \times L(H\alpha_{corr}), \tag{3.4}$$

$$\text{SFR } (M_\odot\ yr^{-1}) = 2.8 \times 10^{-44} \times L(TIR), \tag{3.5}$$

$$\text{SFR } (M_\odot\ yr^{-1}) = 2.10 \times 10^{-43} \times L(22\mu m). \tag{3.6}$$

The hybrid tracers are obtained assuming an approximate energy-balance approach. The expressions for the hybrid tracers are shown below where the luminosities are observed and are in units of ergs s^{-1}. The global coefficients, 4.6×10^{-44} and 5.5×10^{-42} [$M_\odot yr^{-1}/ergs^{-1}$], correspond with the calibration of the single-band or monochromatic indicators shown before, UV and Hα respectively. On the other hand, the coefficients that multiply the IR luminosity, either L(22 μm) or L(TIR), are dependent on this tracer and on that used for the direct stellar light emission. We empirically calibrate these coefficients in Section 3.5.5.2 to create dust-corrected SFRs, i.e.,

$$\text{SFR } (M_\odot\ yr^{-1}) = 4.6 \times 10^{-44}\ [L(FUV_{obs}) + 4.08 \times L(22\mu m)] \tag{3.7}$$

$$\text{SFR } (M_\odot\ yr^{-1}) = 4.6 \times 10^{-44}\ [L(FUV_{obs}) + 0.46 \times L(TIR)] \tag{3.8}$$

$$\text{SFR } (M_\odot\ yr^{-1}) = 5.5 \times 10^{-42}\ [L(H\alpha_{obs}) + 0.021 \times L(22\mu m)] \tag{3.9}$$

$$\text{SFR } (M_\odot\ yr^{-1}) = 5.5 \times 10^{-42}\ [L(H\alpha_{obs}) + 0.0024 \times L(TIR)] \tag{3.10}$$

The original recipes for the hybrid tracers make use of the 25 μm luminosity, but we are interested in using our 22 μm luminosities instead as we have a large number of these measurements. In Section 3.4.4, we justify the use of L(22) instead of L(25) after a 1.05 $\pm$ 0.22 conversion factor is applied. This factor is computed as the average ratio between 25 μm and 22 μm luminosities when using high quality 25 μm IRAS measurements.

3.5.2 SFR surface density

As mentioned before, the only tracers with enough spatial resolution to compute SFR surface densities across the CALIFA sample are the UV (FWHM $\sim$ 4.5 arcsec) and Hα (FWHM $\sim$ 2.5 arcsec) measurements. We calculate the SFR surface density in both as the SFR per unit area measured in the largest elliptical apertures (semimajor axis = 36 arcsec) fitting the PPaK FOV with the ellipticity and PA of the corresponding galaxy. The Hα data are corrected for extinction

using the Balmer decrement measured within these apertures. In the case of the UV, we use the hybrid tracer (Equation 3.7). This tracer combines UV-observed luminosities with 22 μm luminosities (FWHM $\sim$ 11 arcsec). Because of the negative dust extinction gradients found in star-forming galaxies, virtually all the flux at 22 μm was found to come from inside these elliptical apertures (see Muñoz-Mateos et al. 2009). Nevertheless, to avoid systematic offsets we decorrected for aperture the total 22 μm fluxes using the same aperture correction as described in Section 3.4.1.4. This means that now all the fluxes, 22 μm, Hα, and FUV, are calculated for the same area.

Thus, the SFR surface density is computed using the following expression:

$$\Sigma_{SFR} = \frac{SFR}{\pi a^2 \left(\frac{d}{206265}\right)^2}, \tag{3.11}$$

where the expressions used for estimating the SFR values are Equations 3.4 and 3.7; see Section 3.5.1. The parameter a corresponds to the semimajor axis set to 36 arcsec in all cases as described in Section 3.4.1.3 and d is the distance in Mpc to the galaxy calculated from its redshift (listed in Table 3.5).

Figure 3.6 compares the hybrid star formation surface density using the observed FUV and 22 μm fluxes with their corresponding Hα attenuation-corrected star formation surface density. We have excluded elliptical and lenticular galaxies in this plot where part of the UV emission could come from HB stars responsible for the UV upturn (Brown et al. 1997; Yi et al. 1997).

We found a good linear correlation between both measurements in a wide range of values of $\sim$2 dex, especially at $\Sigma_{SFR[H\alpha_{corr}(36)]}>10^{-9}$ $M_{\odot}yr^{-1}pc^{-2}$. A mean value of 0.04 is found for $<\log(\Sigma_{SFR[FUV_{obs}(36)+22\mu m]}/\Sigma_{SFR[H\alpha_{corr}(36)]})>$, while the dispersion is $\pm$0.24 dex r.m.s. (see Figure 3.6). There are a number of galaxies at low-surface brightnesses, which correspond to galaxies with null A(Hα) values.

The consistency between the two star formation surface density values and the large range involved shows that there are no systematic differences between the two tracers when SFR surface densities are used or, at least, these are of the order of the object-to-object variation. Thus, from now on we use the SFR instead of SFR density surface , which allows us to use all TIR measurements confidently.

3.5.3 Comparison of the different SFR tracers

As CALIFA provides an excellent Hα-integrated luminosity and a precise Balmer decrement, we are going to study the SFR tracers found in the literature and provide updated calibrations (Section 3.5.5).

Once we have verified that the extinction-corrected Hα SFR surface density behaves linearly with the hybrid SFR surface density (FUV$_{obs}$ + 22μm) within the errors (previous section), we can safely assume that any correlation between the integrated SFR is not primarily driven by scaling effects.

Thus, in the rest of Section 3.5 we describe the results from the analysis of the galaxies' total

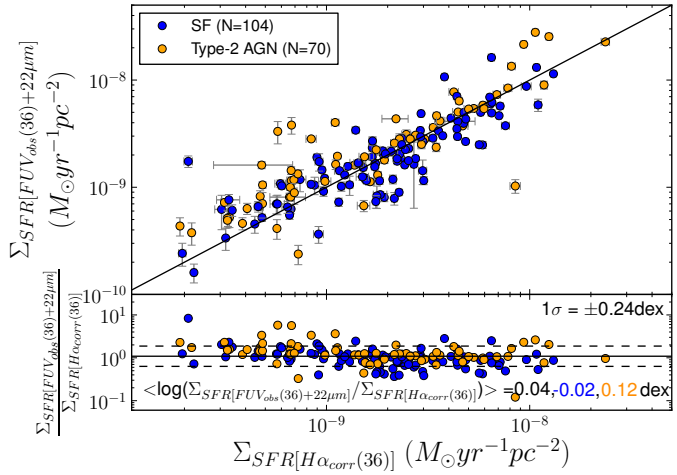

Figure 3.6: Star formation rate surface density derived using a combination of observed-FUV and 22 μm luminosities compared to Balmer attenuation-corrected Hα star formation rate surface density. The values are obtained within an area of semimajor axis equal to 36 arcsec. The solid line corresponds to equal Σ_{SFR} on both axes. The bottom part of this plot represents the residuals as a function of the Balmer-corrected Hα star formation rate surface density. The mean value is shown with the solid line, while dashed lines correspond to the 1σ dispersion in dex around the mean value. Black, blue, and orange numbers correspond to the mean values for the whole sample, SF, and type-2 AGN host galaxies, respectively. The tight relation found for these two SFR density tracers shows that there are not systematic differences between them, hence, we can safely use the SFR measurements.

SFR. We first analyze the behavior when using different SFR indicators independently, including the UV and IR-continuum luminosities and, of course, extinction-corrected emission-line Hα luminosity. Then, we compare the results of the different tracers among themselves, assuming that those combining directly observable luminosities (either UV or Hα) and those associated with dust re-emission (monochromatic or TIR) should be able to recover the entire energy budget from recently-formed massive stars.

3.5.3.1 Single-band SFR tracers

Comparison between Mid-IR and extinction-corrected Hα

In this section, we compare the SFRs using warm-dust sensitive 22 μm WISE luminosities with Balmer attenuation-corrected Hα SFRs (Equations 3.6 and 3.4, respectively) in Figure 3.7. We find that at high luminosities 22 μm reproduces the SFR measured with extinction-corrected Hα. Nevertheless, L(22 μm) underestimates the SFR expected at low luminosities, where these galaxies are supposed to have very little dust and consequently weak L(22 μm) emission. This could be the reason why the mean value of the residuals, expressed as <log(SFR[22 μm]/SFR[Hα_{corr}])> in the subpanel of Figure 3.7, is equal to -0.08.

We not have included the nonlinear behavior for galaxies with L(22 μm) $> 5\times10^{43}$ erg s^{-1} present in the original recipe (see Calzetti 2013), as we only find four galaxies in that range. Three of them have similar values of the SFR(22 μm), 11.22, 12.14, and 13.07, making this SFR range too small to determine whether a nonlinear fit would be more appropriate in this case.

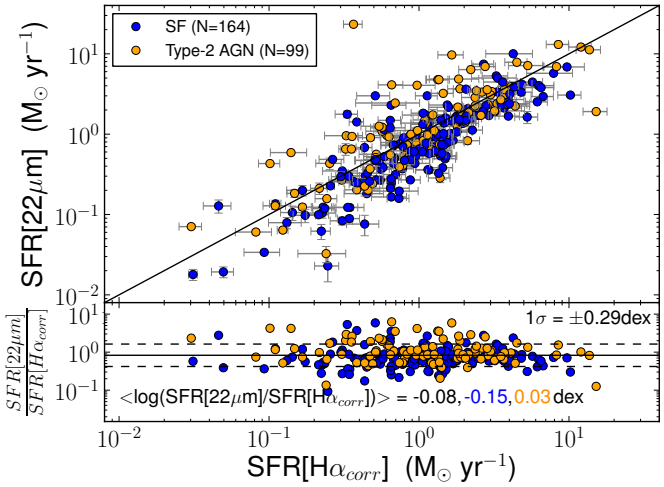

Figure 3.7: Comparison between the MIR (22 μm) and the Balmer-corrected Hα SFR tracers; recipes from Calzetti (2013); see Equations 3.6 & 3.4. Solid line corresponds to the 1:1 line. Orange points show type-2 AGN galaxies and blue points represent star-forming galaxies. The legend gives the number of objects available in both cases. Residuals appear in the bottom part of this figure as a function of the Balmer-corrected Hα SFR tracer. Solid line shows the mean value of -0.08 when all the galaxies are included and the dashed lines are referred to the 1σ dispersion (±0.29 dex) around it. For SF galaxies, the mean values is -0.15, while for type-2 AGN host galaxies is 0.03.

Comparison between β-based extinction-corrected UV and extinction-corrected Hα

We analyze the FUV continuum and the Hα emission-line luminosities as tracers of recent star formation (Equations 3.3 and 3.4) since both are linked to the presence and amount of massive (i.e., young) stars (see top left panel in Figure 3.8). The nonionizing UV emission is mainly photospheric direct emission from O and B stars formed over the past 10−200 Myr and the optical emission lines from ionized gas surrounding massive young stars with lifetimes of $\sim$ 3−10 Myr. We apply the attenuation relation given by Equation 3.2 mentioned in Section 3.4.2 to correct the FUV luminosity.

We find a rather noisy relation of ±0.36 dex around the mean which has a value equal to $<\log(\mathrm{SFR}[\mathrm{FUV}_{corr}]/\mathrm{SFR}[\mathrm{H}\alpha_{corr}])> = 0.14$. This likely reflects the large uncertainties in the correction for dust attenuation at UV wavelengths using only UV data. They are associated with uncertainties in our knowledge of the slope of the attenuation curve in the UV and with the slope of the underlying stellar continuum. Besides, whether the reddening of the UV continuum can recover all dust-processed SFR is not free for systematics. Figure 3.8 (top left panel) shows that at high $\mathrm{L}(\mathrm{H}\alpha)_{corr}$ ($\mathrm{SFR}[\mathrm{H}\alpha_{corr}] > 5$ M$_\odot$ yr^{-1}) the SFR derived from the UV alone is underestimated. This fact could be explained by taking into account that higher SFRs are associated with higher values of the attenuation (Kennicutt 1998b; Calzetti et al. 2007). It might be that the extinction correction using the FUV−NUV color traces only the most superficial and less extinct part of the SFR. Consequently, the higher SFRs associated with higher values of the extinction are being underestimated.

In order to establish whether other effects could be present, such as an intrinsic discrepancy between the light emitted in the ionizing and nonionizing UV light from galaxy to galaxy, we also compare the $\mathrm{SFR}[\mathrm{H}\alpha_{obs}]$ and the $\mathrm{SFR}[\mathrm{FUV}_{obs}]$ in the top right panel of Figure 3.8. Although one

might think that dust attenuation should erase any linear correlation between these quantities, the fact that one comes from emission from stars and the other from the ionized-gas should partly compensate for the difference in wavelength. In principle, this makes the two quantities not very different for the whole range of SFRs involved with a slope close to unity. We emphasize that this numerical agreement does not imply, of course, that there is physical reason for them to be equal in any galaxy.

As these luminosities are observed quantities, we can estimate the expected extinction for these measurements to match. We assume that the color excess of the stellar continuum is related to the color excess of the gas by E(B-V)$_s$ = 0.44 E(B-V)$_g$ (Calzetti 1997; Calzetti et al. 2000). For the color excess of the ionized gas we use a standard extinction curve, such as the Galactic extinction curve proposed by Cardelli et al. (1989) and R_V = 3.1. For the case of the color excess of the stellar continuum, we use the attenuation law derived by Calzetti et al. (2000) and $R_V = 4.05 \pm 0.80$. Finally, we obtain the relation for the stars attenuation in FUV and that of the gas in Hα as A(FUV)$_s$ = 1.79 A(Hα)$_g$. This value is similar to those obtained by other authors using different samples, such as the case of Hao et al. (2011) that found A(FUV)$_s$ = 1.82 A(Hα)$_g$.

If we suppose that the SFR deduced from the FUV continuum and the SFR from Hα emission line (Equations 3.3 & 3.4 in Section 3.5.1), both corrected by extinction, are equal, then,

$$\log(\mathrm{SFR}[FUV_{obs}]) = \log(\mathrm{SFR}[H\alpha_{obs}]) + 0.4[A(H\alpha)_g - A(FUV)_s]. \tag{3.12}$$

Using the previous relation between the corresponding attenuations yields

$$\log(\mathrm{SFR}[FUV_{obs}]) = \log(\mathrm{SFR}[H\alpha_{obs}]) - 0.32A(H\alpha)_g. \tag{3.13}$$

The light green dashed line in Figure 3.8 (top right panel) corresponds to values of A(Hα) equal to 0 magnitudes. Nearly every galaxy falls below this line. As expected, having no attenuation correction applied to neither Halpha nor to FUV luminosities implies lower values of the SFR(FUV) as it suffers from higher attenuation. Dark green and black dashed lines in the same figure correspond to values of Hα attenuation of 1 and 2 magnitudes, respectively. It seems like values of A(Hα) around 1 magnitude are in relatively good agreement with our data. However, our A(Hα) values vary from 0 to 2.57 magnitudes (Table 3.5) with a mean value of 0.49 magnitudes, which does not match the expected value. One possibility for this offset could be that the assumption E(B-V)$_s$ = 0.44 E(B-V)$_g$ is not obeyed for our galaxy sample. Alternatively, the corrected SFR could be different when the UV and Hα tracers are used. As we see in Section 3.5.3.2, the latter does not appear to be the cause. In constrast, as pointed out previously, the main aim with this comparison is to show that the real problem when comparing SFR[Hα_{corr}] and SFR[FUV$_{corr}$] is the difficult estimation of the A(FUV) and also the importance of the attenuation corrections.

To explore the possibility that our sample might have a different assumption than E(B-V)$_s$ = 0.44 E(B-V)$_g$, we compare de A(Hα) from the Balmer decrement and the A(FUV)[IRX] in the bottom left panel in Figure 3.8. The blue dashed line shows the relation between these two quantities when the expression applied for the stellar continuum and the gas color excess is E(B-V)$_s$ = 0.44 E(B-V)$_g$. The red dashed line is plotted assuming that the color excess from the stellar continuum and the gas are equal, E(B-V)$_s$ = E(B-V)$_g$. This comparison suggests that we

could apply a higher value than that found by Calzetti et al. (2000) for our sample, and that the values of A(Hα) would not be as higher as those expected from the top right panel in Figure 3.8. Nevertheless, as we find many points below the blue line that could be due to a deviation from the screen foreground model used to compute the ionized gas extinction, we decided to explore this behavior using another parameter such as the SFR surface density. The light green points show where the galaxies with higher values of the SFR surface density are located in this plot. Clearly, these galaxies are between both lines and they never appear below the red line. This result underscores that galaxies with higher values of SFR surface density (starburst-like) have a relation between the color excess of the stellar continuum and the gas that is more similar to that found by Calzetti et al. (2000) than galaxies with lower values of the SFR surface density.

Finally, we compare A(FUV) derived using the UV-slope (FUV−NUV color) with those obtained using the IR/FUV flux ratio (IRX) in Figure 3.8 (bottom right panel). For the IRX case, we use the expression by Buat et al. (2005) (star-like symbols) and that in Hao et al. (2011) (open circles). It is clear from this representation that A(FUV)[FUV−NUV] gives higher values than A(FUV)[IRX] for the lowest values of attenuations. On the other hand, A(FUV)[FUV−NUV] gives lower values than A(FUV)[IRX] when the highest values of attenuations are involved. Both expressions, Buat et al. (2005) and Hao et al. (2011), yield similar results. As explained before, this plot suggests that using the FUV−NUV color to recover the dust-processed SFR is not the best option.

Comparison between TIR and extinction-corrected Hα

The main problem with using the SFR only based on TIR luminosity is that we are assuming that there is a negligible fraction of the light coming directly from the stars without being reprocessed by dust. Besides, even if there are no UV photons escaping directly (without being processed by dust) to the observer, the calibration of the SFR[TIR] assumes that the light reprocessed by dust comes from young stars, i.e. those linked to the current SF we want to trace. Nevertheless, optical photons from old stars contribute to the heating of the dust (see Johnson et al. 2007) and thus, to the TIR luminosity. Indeed, based on constant star formation (CSF) models, Calzetti (2013) found a reduction in this constant of almost a factor of 2 from models with a CSF lasting for 100 Myr compared to those CSF models lasting for over 10 Gyr. Besides, according to Cortese et al. (2008), for star formation timescales (equivalently the age of the Universe at which the SFR peaks in their 'a la Sandage' SFH) larger than ∼6-7 Gyr the UV radiation dominates the dust heating with a contribution of >75% to the total energy absorbed and then re-emitted in the infrared. On the other hand, the same authors derive that if $\tau < 5$ Gyr, the UV light contributes less than 50% to the TIR emission.

The comparison between the SFR[TIR] and SFR[Hα_{corr}] (Figure 3.9) shows that at low TIR luminosities the SFR[TIR] are underestimated (in the line of the results of Rieke et al. 2009). We find that for values of the SFR[TIR] below 0.3 $M_\odot$ yr^{-1} the average value of $A_{H\alpha}$ is 0.28 ± 0.04 mag. On the other hand, at high luminosities (SFR[TIR] > 1 $M_\odot$ yr^{-1}) the TIR seems to provide SFRs somewhat higher than those obtained from Hα. In fact, a large number of galaxies appear in this regime making the mean value of the ratio between these tracers larger than zero in the residuals, $<\log(\mathrm{SFR[TIR]}/\mathrm{SFR[H}\alpha_{corr}\mathrm{]})> = 0.11$. This is either because the contribution of

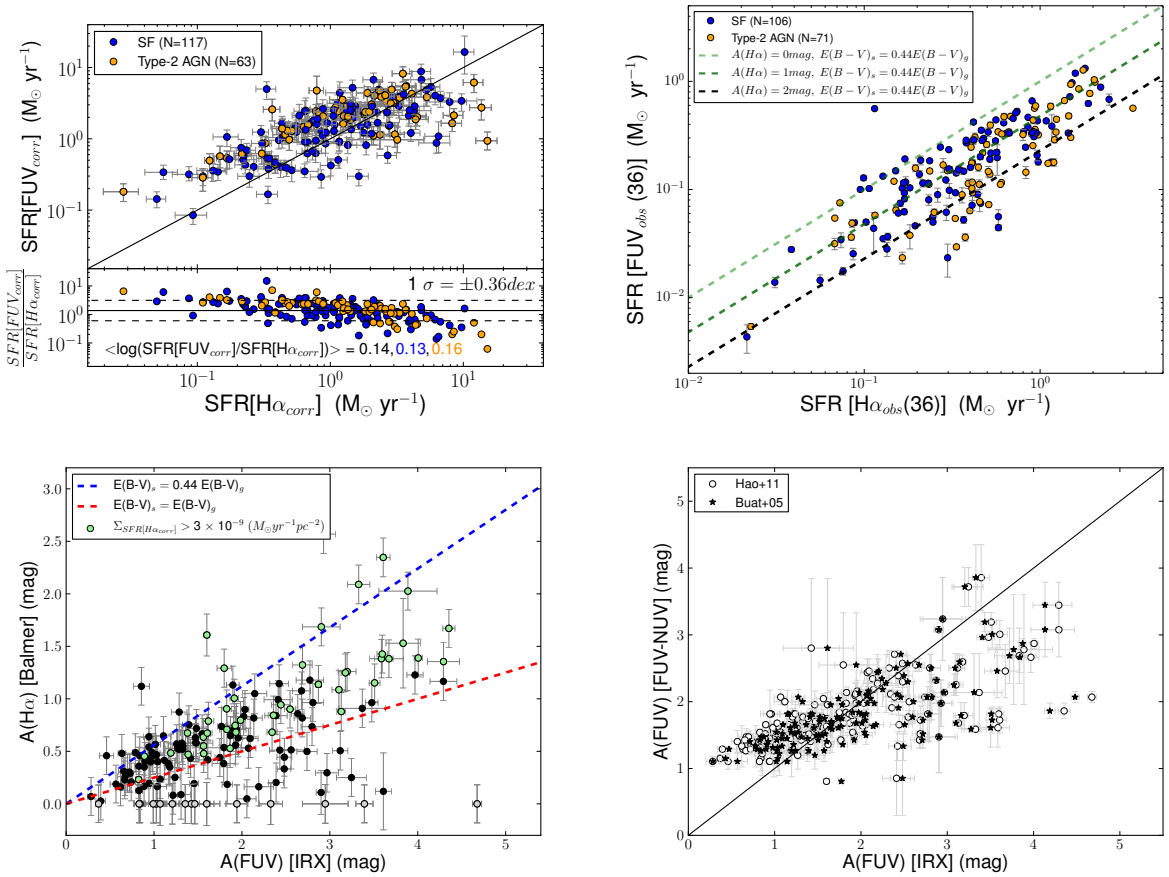

Figure 3.8: Top left panel: FUV-corrected SFR as a function of Balmer-corrected Hα SFR, using Equations 3.3 & 3.4, respectively. Color-coding, solid, and dashed lines have the same meaning as in Figure 3.7. At high L(Hα)$_{corr}$ the SFR derived from the UV alone is underestimated. It might be that the extinction correction using the FUV−NUV color traces only the most superficial and less extinct part of the SFR. Consequently, the higher SFRs associated with higher values of the extinction are being underestimated. Top right panel: relation between observed-FUV SFR and observed-Hα SFR. Light green, dark green, and black dashed lines correspond to values of A(Hα) equal to 0, 1, and 2 magnitudes, respectively. All cases are based on the assumption that the relation between the color excess of the stars and the gas is E(B-V)$_s$=0.44E(B-V)$_g$. Bottom left panel: comparison between A(Hα) from the Balmer decrement (Equation 3.1) and A(FUV) from IR/FUV flux ratio using the expression by Hao et al. (2011). Blue dashed line represents a relation between color excess of E(B-V)$_s$=0.44E(B-V)$_g$ while red dashed line assumes that the relation is E(B-V)$_s$=E(B-V)$_g$. Gray points show cases of A(Hα) equal to zero magnitudes, while light green points show galaxies with the highest values of the SFR surface density. This plot suggest that we might apply a higher value for the relation between the color excess of the gas and the stellar continuum than that found by Calzetti et al. (2000) for our sample, although galaxies with higher values of the SFR surface density are more similar to this previous relation. Bottom right panel: comparison between A(FUV) derived using the FUV−NUV color (Equation 3.2) and A(FUV) from IR/FUV flux ratio. A discrepancy between these two expressions is found for the lowest and highest values of the attenuation. Star-like symbols show the values when the expression used to compute the A(FUV) is that from Buat et al. (2005), while open circles show the values from Hao et al. (2011). The solid line shows the 1:1 line for reference.

heating due to optical photons or nuclear activity becomes relevant at those luminosities and/or because a fraction of the Hα recombination line luminosities are not recovered when correcting for dust attenuation using the Balmer decrement. The analysis of the hybrid calibrations (see section below) favors the former scenario.

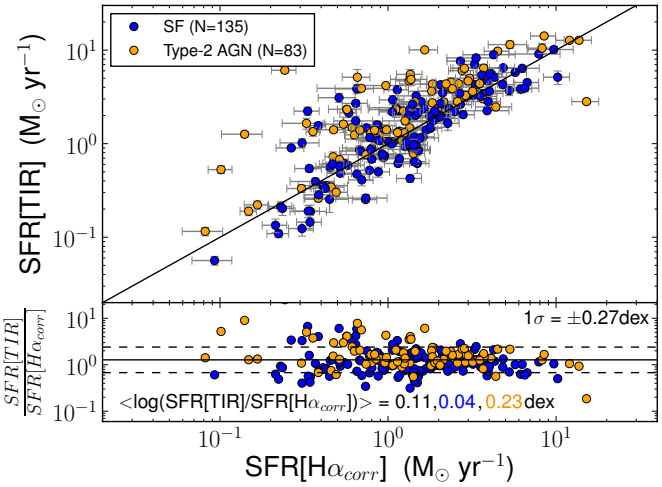

Figure 3.9: Comparison between the SFR tracer using the TIR luminosity and the extinction-corrected Hα SFR tracer, after applying Equations 3.5 and 3.4, respectively. Color-coding, solid, and dashed lines have the same meaning as in Figure 3.7.

3.5.3.2 Hybrid SFR tracers

A powerful way of determining the SFR is to combine a photometric band that is sensitive to the light directly emitted by young stars (i.e., observed UV or Hα fluxes) with that reprocessed by dust, usually in the mid- or far-infrared (or, alternatively, the TIR emission). This is an alternative approach to correct the UV or Hα fluxes for attenuation.

In both cases, the validity of these hybrid tracers is that the observed IR emission comes from light whose optical depth (or attenuation) is of the order of that in the UV or Hα, otherwise it would not be possible to write the total SFR as a sum of the two luminosities, observed and dust-processed (see Kennicutt et al. 2009).

This assumption would not be valid if the heating of the dust were dominated by (1) optical photons, which are particularly important at long IR wavelengths where the contribution of low-temperature dust emission is most relevant; or (2) by UV photons; which are more energetic than those observed directly (e.g., if the bluest observed band is in the NUV); or (3) in the case of a significant AGN contamination, where any of these bands could be actually tracing a UV radiation field that is not merely due to recently-formed massive stars. If there is a significant difference between the τ_{FUV} (or $\tau_{H\alpha}$) and the opacity of the photons that lead to the IR emission used in the corresponding tracer, a linear relation between the SFR and the two (emitted and dust-absorbed) luminosities should not be present. In the particular case of UV and Hα, the τ are similar to the one that comes from the dust component so the approach of using a linear relation between L(FUV$_{obs}$) or L(Hα_{obs}) combined with the L(IR) luminosity can safely be done. That implies that for the IR tracer both bands should suffer the same attenuation (see a detail analysis in Kennicutt et al. 2009; Hao et al. 2011)

Once we have explained the assumptions imposed on the use of the hybrid tracers, we compare them with our Hα extinction-corrected SFR tracer. In the first place, we examine the behavior using Hα observed luminosity combined with 22 μm and TIR luminosity. Figure 3.10 shows that,

applying the method explained in Kennicutt et al. (2009), we now obtain very similar results to theirs but using a larger sample and IFS data for the first time. Secondly, we replace Hα observed luminosity with FUV observed luminosity combined with the IR luminosities (Figure 3.11). In both cases, we find a very good correlation across 2.5 dex in SFR, but with an offset in the mean ratio of SFRs of 25 per cent. This offset goes in the sense that SFR derived from the hybrid Hα+IR and FUV+IR SFR tracers is larger than for the extinction-corrected Hα one. As explained before, one possibility could be the presence of optical photons from old stellar populations heating the dust, especially at long IR wavelengths, or the effects of AGN. In particular, if we discriminate between star-forming and type-2 AGN galaxies when computing these ratios, type-2 AGN host galaxies yield larger offsets than those reported for SF galaxies. Section 3.5.5.2 provides an extensive discussion on this issue.

We conclude that when comparing the hybrid calibrators with Balmer decrement attenuation-corrected Hα SFR tracer, we find tighter correlations than those obtained with single-band tracers (see the 1σ dispersions around the mean values in Figures 3.7, 3.8, 3.9, 3.10, and 3.11.)

3.5.4 Origin of the discrepancies among SFR tracers

As we have seen in the previous section, there is generally good agreement between the SFR tracers considered, single-band and especially hybrids, compared to the attenuation-corrected Hα SFR tracer. Nevertheless, we can appreciate some differences if we take a closer look at these relations. In the case of the single-band tracers the main problems appear when using FUV$_{corr}$ luminosities as the extinction correction is a big problem to deal with, in particular, for high SFR values. However, we can mitigate this effect using hybrid tracers combining the FUV$_{obs}$ luminosity with the IR luminosity, both 22 μm and TIR. In the latter case we are assuming that we can recover all the light that it has been re-emitted by the dust. Similar cases appear when using the single-band tracers for 22 μm or TIR luminosities, where we apparently lose some SF in galaxies with low values of the SFR. Again, when using hybrid tracers the agreement between calibrators improves.

One of the main reasons behind these discrepancies is the different selection criteria used in the process of determining the SFR calibrators in the literature. Now, we have the opportunity to recalibrate these tracers for a diameter-limited sample of 380 galaxies. Moreover, we are able to use integral field spectroscopy data to assure a proper determination of the attenuation using the Balmer decrement, and thereby, avoiding the problems associated with narrowband imaging. Thus, we are going to provide updated SFR tracers based on our state-of-the-art, attenuation-corrected Hα luminosities.

3.5.5 Updated SFR tracers for the diameter-limited CALIFA sample

We now provide updated calibrations for the global current SFR in external galaxies by means of anchoring the different tracers (single-band and hybrid ones) to the SFR derived from the

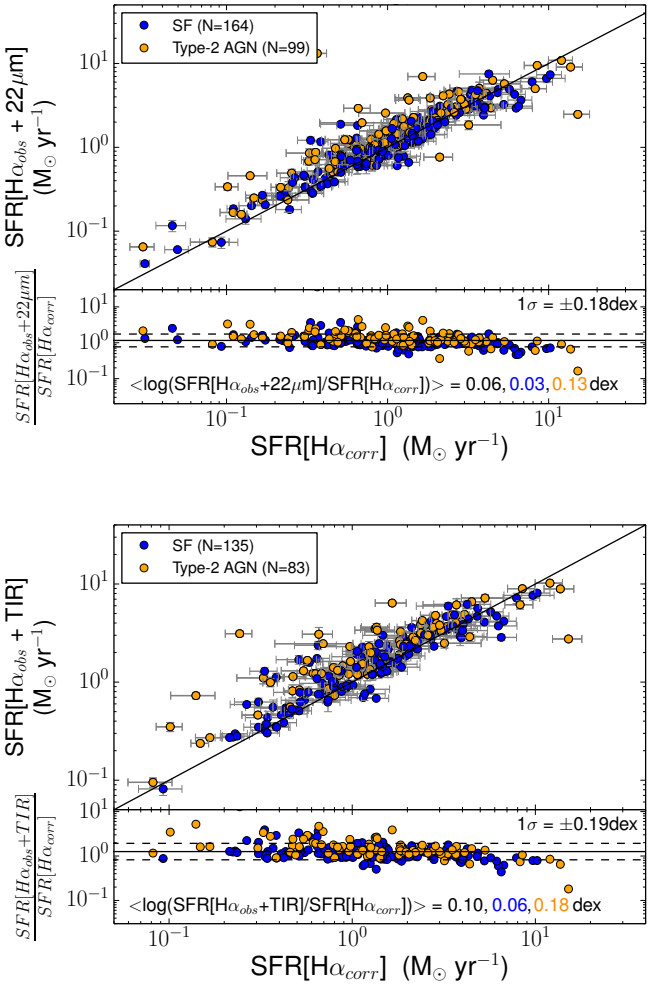

Figure 3.10: Top panel: Hα_{obs} + 22 μm hybrid tracer as a function of Balmer-corrected Hα SFR, using Equations 3.9 and 3.4, respectively. Color-coding and lines have the same meaning as in Figure 3.7. Bottom part shows the residuals as a function of Hα-corrected SFR being the mean value 0.06, 0.03, and 0.13 for all the galaxies, SF galaxies, and type-2 AGN host galaxies, respectively. Dashed lines represent the 1σ dispersion in dex around the mean value. Bottom panel: same as the top panel but showing the Hα_{obs} + TIR hybrid tracer as a function of Balmer-corrected Hα SFR instead (Equations 3.10 and 3.4).

extinction-corrected Hα luminosity measured in our sample of CALIFA galaxies. Seminal works in this context include Kennicutt (1998a), Kennicutt et al. (2009), and Hao et al. (2011).

As we are interested in calibrating the SFR tracers, we need to exclude galaxies that have type-1 AGN signatures to avoid contamination of sources that are not star-forming (only galaxies UGC 00987 and UGC 03973 are classified as type-1 AGN within our sample). As explained in Section 3.5.3, the information regarding the optical AGN classification can be found in Walcher et al. (2014). We provide separate calibrations for the sample when type-2 AGN galaxies are included and when they are not. The reason for this is that, despite numerous efforts (Alonso-Herrero et al. 2006a; Díaz-Santos et al. 2008, 2010; Castro et al. 2014), the fraction of UV or line emission arising from circumnuclear star formation in type-2 AGN is still highly uncertain. We remind the reader that the nuclear emission in type-2 AGN includes the contribution of both a dusty torus (external radius of a few parsecs, see Ramos Almeida et al. 2009) and a circumnuclear region that could

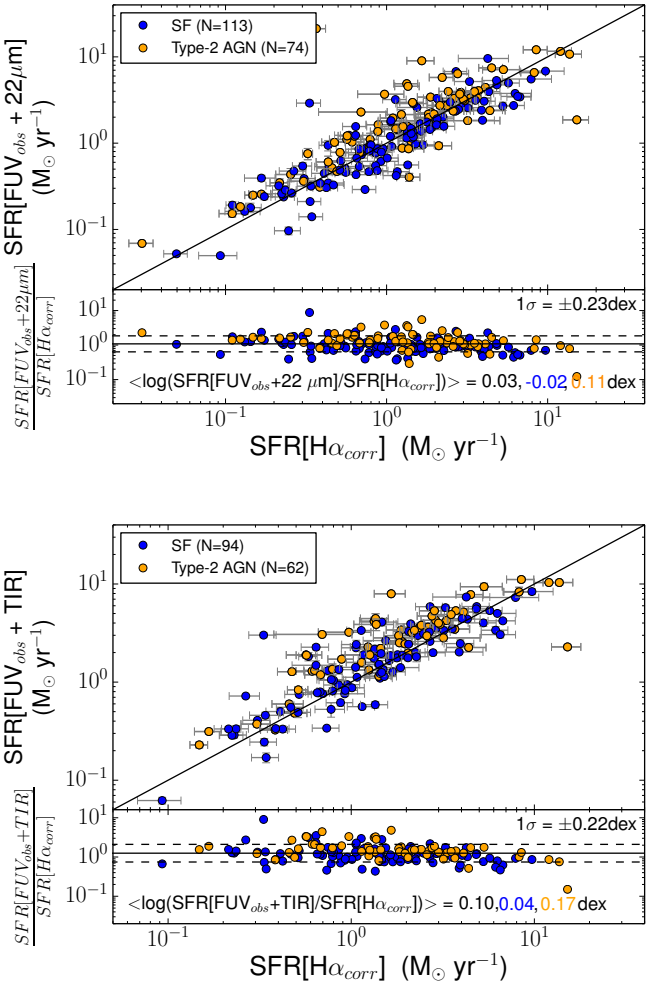

Figure 3.11: Top panel: comparison between FUV$_{obs}$ + 22 μm hybrid tracer and the Balmer-corrected Hα SFR, using Equations 3.7 and 3.4, respectively. Color-coding, lines, and residuals have the same meaning as in Figure 3.10. Bottom panel: same as the top panel, except showing FUV$_{obs}$ + TIR hybrid tracer as a function of Balmer-corrected Hα SFR (Equations 3.8 and 3.4). The hybrid tracers shown here and in Figure 3.10 reduce the dispersion when compared with single-band tracers.

expand up to 1kpc from the central region. We estimate the level of contamination of the emission from the AGN host galaxies to the total SFR. We find that the contribution of the attenuation-corrected Hα luminosity in the nucleus (measured in a 3"-diameter aperture) over the total for galaxies classified as type-2 AGN is 8.3%, while for the purely SF galaxies this contribution is 5.1%. Galaxies classified as type-2 AGN are shown in our plots as orange points.

We first provide updated calibrations in the case of the single-band tracers. We do not perform this analysis in the case of the SFR[FUV$_{corr}$] because, as we have explained before, the attenuation correction is highly uncertain and the SFR tracer proposed would not be reliable. On the other hand, we pursue the estimation of the hybrid tracers using FUV$_{obs}$ luminosity in Section 3.5.5.2.

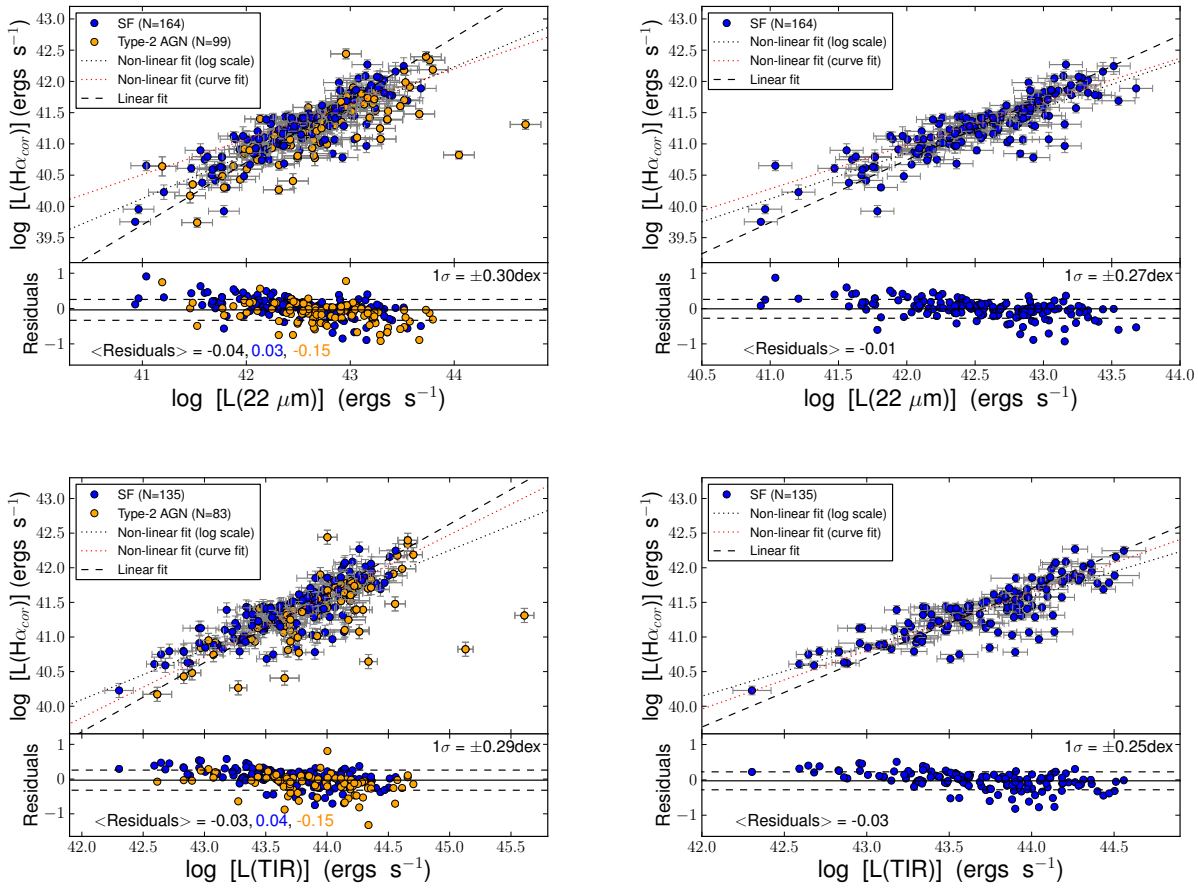

Figure 3.12: Updated calibrations for the 22 μm and TIR single-band SFR tracers anchoring them to extinction-corrected Hα luminosity (Equation 3.4). Orange points in left panels correspond to type-2 AGN, while blue points refer to star-forming galaxies. Linear fits are shown with dashed lines, while nonlinear fits are shown with dotted lines. The results for these calibrations appear in table 3.1. The residuals are computed as the average value of the log[$5.5\times10^{-42}\times$L(Hα_{corr})/a$\times$L(IR)] where L(IR) could be 22 μm or TIR for the case of the linear fits, after applying a 4 σ rejection. These values are computed for all galaxies (black), star-forming (blue), and type-2 AGN host galaxies (orange).

3.5.5.1 Single-band tracers

In this section, we provide calibrations for the observed 22 μm and TIR luminosities as tracers of the SFR anchoring them to the SFR given by the extinction-corrected Hα luminosity, according to Equation 3.4. Figure 3.12 shows the relation between L(Hα_{corr}) and the observed infrared luminosities. We include in these plots both nonlinear [4], $\log[\mathrm{L}(\mathrm{H}\alpha_{corr})]=\mathrm{b}\times\log\left[\frac{L(IR)}{10^{43}}\right]+\log\left[\frac{a'}{5.5\times10^{-42}}\right]$ and linear fits, $\log[\mathrm{L}(\mathrm{H}\alpha_{corr})]=\log[\mathrm{L}(\mathrm{IR})]+\log\left[\frac{a}{5.5\times10^{-42}}\right]$; (see Calzetti 2013). The use of nonlinear calibrations should be restricted to studies using similar (1) selection criteria, (2) apertures, and (3) corrections, or the resulting SFRs could be affected by severe systematics. Linear fits are shown in dashed line, while nonlinear fits are shown in dotted lines. The coefficients for these fits are given in Table 3.1. In the case of the linear fit, we name the constant a, which is expressed in

[4] We normalize the luminosities to 10^{43} ergs s^{-1} to ensure that the y-intercept for these nonlinear fits is located near the values covered by our sample.

units of $M_{\odot}yr^{-1}/ergs\,s^{-1}$, and for the nonlinear fit we use a' because it lacks the physical meaning of a. We are going to use a_{IR} for the hybrid tracers as in this case it is dimensionless and has a different physical meaning than the previous constants (see Section 3.5.5.2 for more details). The values for a' and the exponent b are obtained with two different methods, a least-squares linear fit in log scale and a nonlinear least-squares fit using the Python task *curve_fit*. Both methods yield similar values for these fitting parameters with 22 μm and TIR luminosities.

Figure 3.12 also shows the results of this analysis after including (left panels) or excluding (right panels) type-2 AGN from the sample. In all cases, with and without type-2 AGN and using either the 22 μm or TIR luminosity, a nonlinear behavior is clearly present, especially at low luminosities ($\log[L(22\mu m)]<41.8$ or $\log[L(TIR)]<43.3$), where most galaxies are located above the best linear fit (see Figure 3.12). On the other hand, galaxies with high 22 μm luminosities ($\log[L(22\mu m)]>43.4$) are all found below the linear fit, similar to the behavior observed at 24μm luminosities above $5\times10^{43}\,ergs\,s^{-1}$ by Rieke et al. (2009). The best-fitting global slope for our nonlinear SFR calibrations based on 22 μm luminosity, 0.733 (0.702) when type-2 galaxies are (not) included in the sample, is somewhat smaller (less linear) than the local value (500 pc scale) of 0.885 obtained by Calzetti et al. (2007) and than the value of 0.82 given by Cluver et al. (2014) from the analysis of the GAMA survey. Regarding a', the values can be very different from those in the literature (even their units are different, obviously) but the uncertainties are of the order of 5-18%, similar to the value quoted by Calzetti (2013), when the log is computed in normalized luminosities. The 22 μm or TIR luminosities explored by our sample are significantly lower than those of the sample studied by Rieke et al. (2009), which explains why these authors only needed to make use of a nonlinear fit at their high-luminosity end.

For the case of the linear fit, the difference between the a coefficients with and without type-2 AGN is very small, leading to smaller a coefficient when these objects are included by roughly 7 percent in the case of the 22 μm and 18 percent in the TIR. This is likely due to the enhanced contribution of an AGN or, alternatively, obscured circumnuclear star formation to the infrared emission compared to Hα. In the former case, the use of this calibration would remove, statistically speaking at least, part of the AGN contamination, although some fraction of the Hα could still arise from the AGN. Regarding the latter possibility, the use of a calibration anchored to the extinction-corrected Hα luminosity would slightly underestimate the total SFR, as the star formation due to highly-obscured circumnuclear regions in type-2 AGN could be missed. In general, independent of its origin (star formation or not), the total UV light emitted in these regions is hardly recovered using the UV slope or even the Balmer decrement as a measure of its dust attenuation, especially in type-2 AGN where the BLR is completely hidden from us. The difference here is that if the emission is due to either a BLR or NLR is something that should not be accounted for in terms of the SFR anyway. Finally, we cannot rule out at this stage that, since we are dealing with single-band tracers, this difference arises from a dependence of the attenuation with the level of nuclear activity at a given SFR.

The analysis of the hybrid tracers and the dependence of the a_{IR} coefficient with the attenuation presented later in this work favors the scenario in which it is the contribution of the AGN itself that leads to these small changes in the single-band SFR calibrations. This is studied in more detail in the spatially-resolved analysis presented in Chapter 4. Although, as mentioned before, we will still be unable to disentangle the relative contribution of AGN or circumnuclear star formation to the nuclear emission of type-2 AGN host galaxies using these data (see Alonso-Herrero et al. 2006a;

Díaz-Santos et al. 2010; Castro et al. 2014, for alternative approaches).

3.5.5.2 Hybrid tracers

In the case of the hybrid indicators we assume a simple energy balance (see Kennicutt et al. 2009, for more details), i.e.,

$$\text{SFR } (M_{\odot} yr^{-1}) = 5.5 \times 10^{-42} \, [L(H\alpha_{obs}) + a_{IR} \times L(IR)] \tag{3.14}$$

$$\text{SFR } (M_{\odot} yr^{-1}) = 4.6 \times 10^{-44} \, [L(FUV_{obs}) + a_{IR} \times L(IR)], \tag{3.15}$$

where L(FUV$_{obs}$) and L(Hα_{obs}) are the observed luminosities in ergs s^{-1} and L(IR) could be either L(22 μm) or L(TIR), also in ergs s^{-1} .

We calculate the value of the dimensionless a_{IR} coefficient in the previous hybrid relations as the median of the following ratio for the L(Hα) case (Equation 3.9 & 3.10) and for the L(FUV) case (Equation 3.7 & 3.8):

$$a_{IR} = \frac{L(H\alpha_{corr}) - L(H\alpha_{obs})}{L(IR)} \tag{3.16}$$

$$a_{IR} = \frac{\frac{C_{H\alpha}}{C_{FUV}} L(H\alpha_{corr}) - L(FUV_{obs})}{L(IR)}, \tag{3.17}$$

where C$_{H\alpha}$ and C$_{FUV}$ are the constants that multiply the L(Hα) and L(FUV) in Equations 3.4 and 3.3 (5.5×10^{-42} and 4.6×10^{-44} [M$_{\odot}$yr^{-1}/ergs^{-1}]), respectively.

Histograms in Figure 3.16 show the distribution of the a_{IR} coefficient for different hybrid SFR tracers. The end of this section and Sections 3.5.5.3 through 3.5.5.7 give an extensive analysis of the nature of the variation of a$_{IR}$.

In the case of the combined UV + IR SFR tracers, there are several ways of estimating the calibration. The most common methods are (1) using an energetic balance approach once we have corrected for attenuation in the UV, or (2) anchoring our data to other SFRs measurements.

With regard to (1), we must keep in mind that the estimation of the FUV attenuation is challenging so several methods have been put forward for that purpose. The most common approaches are the use of the β slope of the UV continuum (similar, but not identical to the FUV−NUV color) or the ratio of IR to UV luminosity. We obtained the FUV−NUV-corrected FUV luminosity (using the β slope) in Section 3.5.3.1, but the results show that with this method recovering the SFR is complicated, especially for the highest values of the SFR where the attenuation appears to be underestimated. Other expressions for the FUV attenuation using the FUV−NUV color can be found in the literature (e.g., Kong et al. 2004; Seibert et al. 2005; Salim et al. 2007; Hao et al. 2011). As an example, Hao et al. (2011) use their own expression for the A(FUV) (equation 16 in their paper) to calibrate the TIR + FUV hybrid tracer obtaining that the FUV−NUV-corrected FUV luminosity also underestimates the highest SFRs. As explained before, the other way of deriving the attenuation uses the ratio of IR to UV luminosity. We can use the IRX-corrected

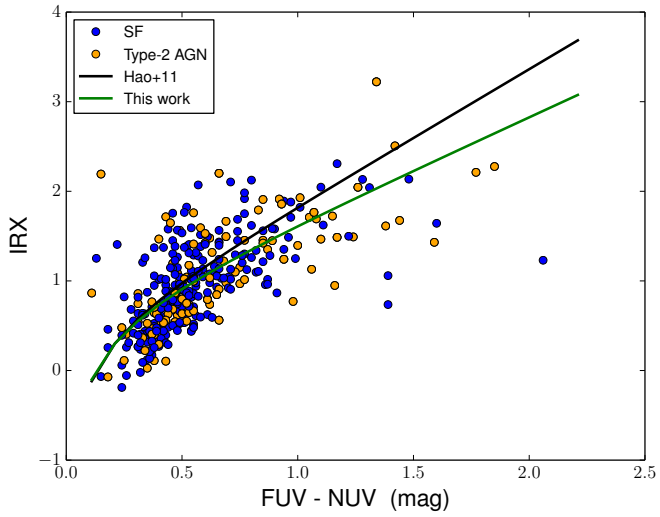

Figure 3.13: IRX-β relation for the galaxies that have FUV and TIR measurements in the CALIFA mother sample. Blue points represent star-forming galaxies while orange points correspond to type-2 AGN host galaxies. Black line shows the fit from Hao et al. (2011), while the green line shows our fit. We obtain a value of $a_{IR} = 0.33 \pm 0.08$ for our fit.

FUV luminosity to calibrate the TIR + FUV and the 22 μm + FUV hybrid tracers as done in sections 4.1 and 4.3 in Hao et al. (2011). The authors obtain a relation (equation 13 in their paper) between the IRX and the FUV−NUV observed color. An important parameter that appears in the former equation is the a_{IR} value linked directly to the IRX by $A(FUV) = 2.5\log(1+a_{IR} \times 10^{IRX})$. (See Hao et al. 2011, equation 2, where the authors name it a_{FUV} instead of a_{IR}; we used a_{IR} for consistency along this work). For the IRX, they use the definition of Meurer et al. (1995): $IRX = \log[L(TIR)/L(FUV)_{obs}]$. To see the differences from Hao et al.'s sample and this work, we have derived our own IRX−β relation for the galaxies that have FUV and TIR measurements in the CALIFA mother sample, including SF and type-2 AGN host galaxies (see Figure 3.13). We use the intrinsic FUV−NUV color obtained by Gil de Paz et al. (2007b), 0.025 ± 0.049 mag, which is very similar to that obtained by Hao et al. (2011), 0.022 ± 0.024 mag. The black line shows Hao et al.'s fit and the green line is our own fit. This fit gives us a value for the coefficient a_{IR} of 0.33 ± 0.08, in comparison with their value $a_{IR} = 0.46 \pm 0.12$. There is a large dispersion in the previous figure, so even if we account for the fact that our measure of the a_{IR} coefficient is in good agreement with that found by Hao et al. (2011), we trust method (2) more, and we discuss this next.

Finally, method (2) relies on anchoring the data we want to calibrate to other SFRs measurements, i.e., we establish a reference SFR against which we can compare the hybrid tracers. One possibility would be to use the SFR provided by the extinction-corrected Paα line emission (see Calzetti et al. 2007). This line is only moderately influenced by dust extinction and gives us a good measure of the current SFR. The problems related with this emission line are due to its faintness and to the difficulty of observing a large number of nearby galaxies, as it is only accessible from space.

In our case, we are going to use the extinction-corrected Hα SFR tracer measurements obtained for the first time from IFS data as a reference. These data are required to obtain a proper estimation of the stellar continuum and, therefore, to estimate a reliable measurement of the ionized-gas dust attenuation via the Balmer decrement. Besides, we count on a homogeneous large survey that

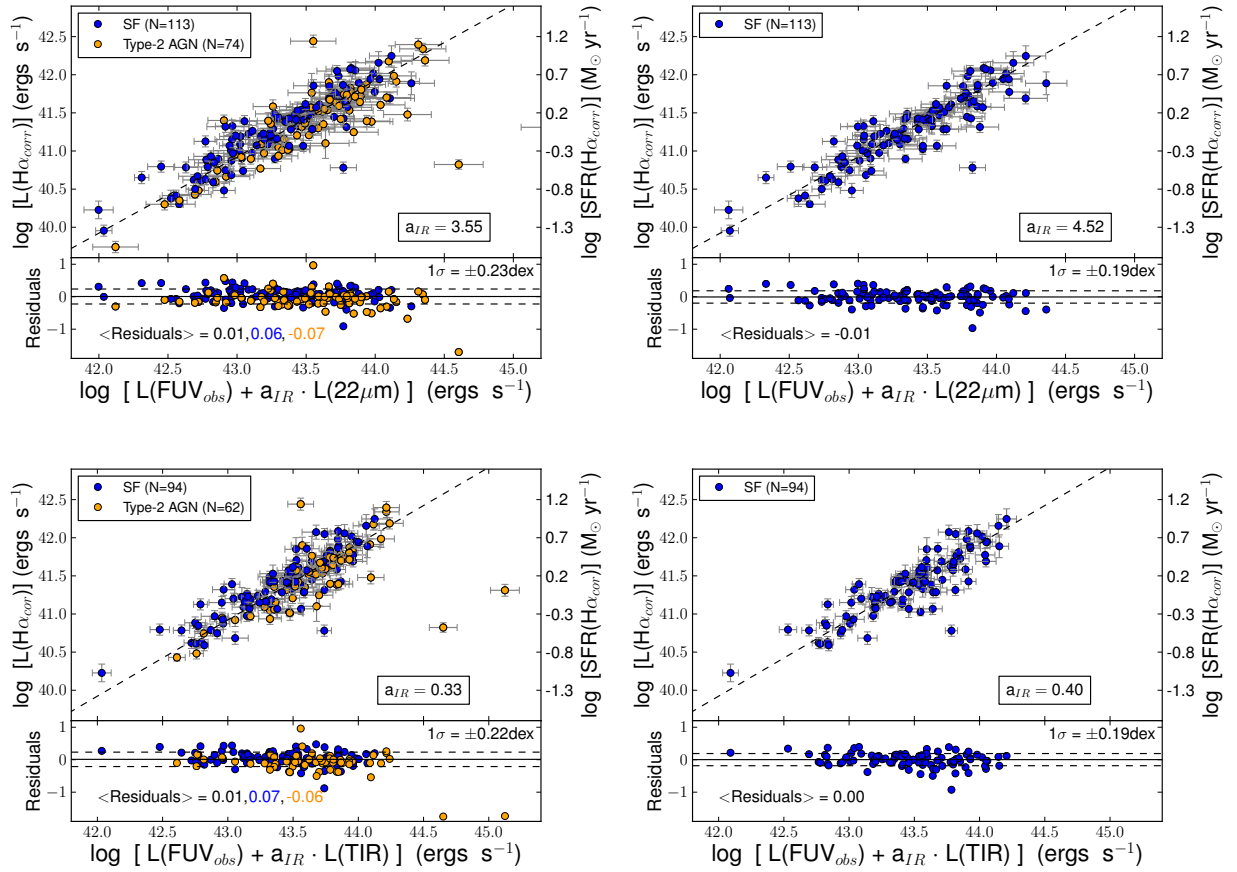

Figure 3.14: Updated calibrations for the hybrids tracers that combine FUV observed luminosity and IR luminosity. Top panels show the FUV$_{obs}$ + 22 μm hybrid tracer, while the FUV$_{obs}$ +TIR hybrid tracers appear on the bottom panels. Galaxies hosting type-2 AGN (orange points) are included on the left panels. Blue points refer to star-forming galaxies. Dashed lines correspond to the 1:1 line taking into account the $C_{H\alpha}$ and C_{FUV} constants (5.5×10^{-42} and 4.6×10^{-44}) given in Equations 3.3 and 3.4, respectively. The best-fitting a_{IR} coefficients calculated as the median value of the expression 3.17 are shown for clarity. These a_{IR} values and their corresponding errors appear in Table 3.2. The residuals are computed as the average value of the log[$C_{H\alpha}\times$L[Hα_{corr}]/($C_{FUV}\times$(L[FUV$_{obs}$] + $a_{IR}\times$L[IR]))], where L(IR) could be 22 μm or TIR, after applying a 4 σ rejection. These hybrid tracers show a trend with the a_{IR} coefficient, so when type-2 AGN host galaxies are included the value of a_{IR} decreases.

provides us with good statistics on the properties of nearby star-forming galaxies. For these reasons (and others explained in Section 3.5.4), we consider this tracer as a robust estimator of the SFR. Using this method we obtain the updated calibrations for FUV + 22 μm, FUV + TIR, Hα + 22 μm, and Hα + TIR hybrid tracers that appear in Table 3.2.

The resulting hybrid-tracer calibrations obtained using FUV and Hα as observed luminosities are shown in Figures 3.14 and 3.15. The dispersions found for FUV + 22 μm, FUV + TIR, Hα + 22 μm, and Hα + TIR tracers are 0.23 (0.19), 0.22 (0.19), 0.17 (0.14), and 0.17 (0.15) dex when type-2 AGN are (not) included, respectively. The single best-fitting parameter in each of these plots is the median of the distribution of the coefficients that multiply the corresponding infrared luminosity in each galaxy (a_{IR}) to match the SFR based on the extinction-corrected Hα luminosity. As explained before, a_{IR} has been obtained using expressions 3.16 and 3.17 and can be found on these plots. The line shown in these figures corresponds to the 1:1 relation in SFR. This

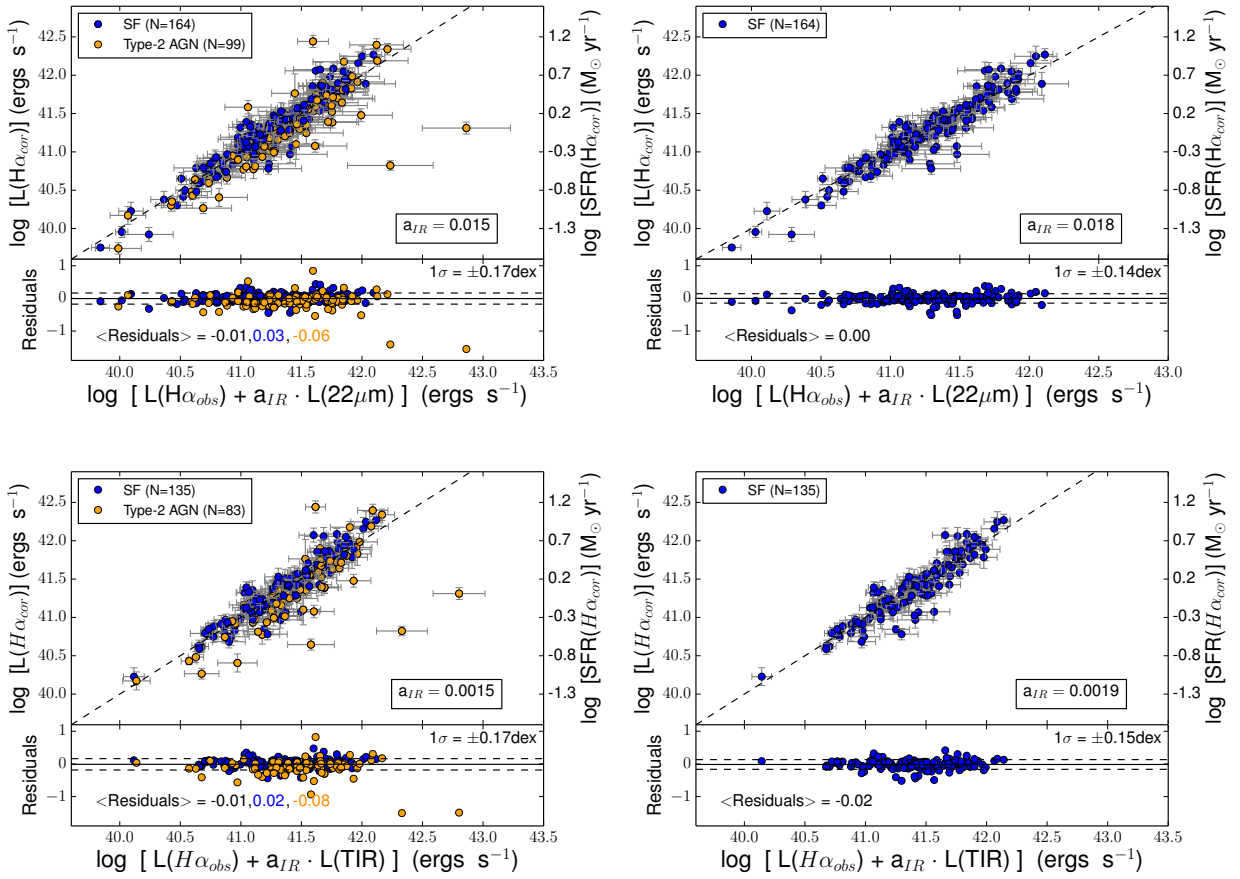

Figure 3.15: Updated calibrations for the hybrid tracers, which combine Hα observed luminosity and infrared emission. Those with 22 μm luminosity appear at the top, while the tracers that used TIR luminosity are shown at the bottom. Galaxies hosting type-2 AGN (orange points) are included on the left panels. Blue points refer to star-forming galaxies. Dashed lines correspond to the 1:1 line. The best-fitting a_{IR} coefficients calculated as the median value of the expression 3.16 are shown for clarity. These a_{IR} values and their corresponding errors appear in Table 3.2. The residuals are computed as the average value of the log[L(Hα_{corr})/(L(Hα_{obs}) + a$_{IR}$×L(IR))], where L(IR) could be 22 μm or TIR, after applying a 4 σ rejection. The hybrid tracers show dispersions lower than in the case of the single-band tracers. These hybrid tracers show the same pattern as the ones in Figure 3.14, the a$_{IR}$ coefficient decreases when galaxies hosting type-2 AGN are considered. These calibrations and those in Figure 3.14 show that applying an energy balance approximation is a good approach for obtaining reliable SFR tracers for integrated measurements of nearby galaxies. Here, we use IFS data for the first time to achieve this goal.

line corresponds to the 1:1 line also in luminosity in the case of the Hα + IR tracers (Figure 3.15) but takes into account the different constant for FUV and Hα given in Equations 3.3 and 3.4, respectively (Figure 3.14). An interesting result found is a nearly constant difference ($\sim$ 9 %) in the coefficients of the infrared term, a$_{IR}$, 3.55 (4.52) in the FUV + 22 μm and 0.33 (0.40) in FUV + TIR tracers with (and without) type-2 AGN host galaxies. A $\sim$ 10 % difference also appears when we compare the a$_{IR}$ coefficients between the Hα + 22 μm, 0.015 (0.018) and Hα + TIR, 0.0015 (0.0019), calibrators with (and without) type-2 AGN, respectively. If we compare the ratio between these a$_{IR}$ coefficients for the combinations of 22 μm and TIR data with the luminosity ratio expected for infrared SEDs with different interstellar radiation fields, starlight intensities, dust chemical composition, etc., we can estimate the ratio of the energy absorbed by dust at $\lambda <$ or $>$ 4000 (see Figure 2 of Cortese et al. 2008). The most optimal models for carrying out this kind of study, those by Draine & Li (2007), assume a specific and fixed shape for the interstellar

radiation field (the local one) so the effect of optical photons is hidden in the variation of the factor γ, which parameterize the fraction of dust heated by intense radiation fields. The comparison of the a_{IR} for 22 μm and a_{IR} for TIR coefficients yields a factor of 0.1 between L(22) and L(TIR), which (according to Figure 19 of Draine & Li 2007) corresponds to $\gamma = 0.02$, independent of the fractional abundance of PAHs.

In Figures 3.14 and 3.15 we also show the results of this analysis after including (left panels) or excluding (right panels) type-2 AGN from the sample to establish whether the behavior of the hybrid calibrators changes in each case. The four hybrid tracers show the same pattern, the a_{IR} coefficient decreases when galaxies hosting type-2 AGN are considered. As for the case of the single-band tracers (see Section 3.5.5.1) this decrease in the value of the a_{IR} coefficient implies that we need to slightly reduce the contribution of the infrared emission in type-2 AGN to match that measured in Hα. This implication means that either (1) galaxies hosting type-2 AGN are emitting more light in the infrared, which is not associated with the sites or processes that lead to the Hα emission, both at 22 μm and TIR luminosities, as normal star-forming galaxies, or (2) the Balmer-corrected Hα luminosity underestimates the actual SFR in these galaxies.

The distribution of the a_{IR} coefficient appears in the histograms of Figure 3.16 where red dashed lines are referred to its median value. This coefficient has a large dispersion even when only star-forming galaxies are studied. In Table 3.2 we give the resulting median values of a_{IR} and the corresponding dispersions (measured as the interval that includes 68% of the data points around the median). These dispersions appear as red tick marks at the top panels in Figure 3.16, while black tick marks indicate the standard error of the median computed from the asymptotic variance formula (which assumes that the underlying distribution is Gaussian) using the previous 1 σ dispersions. These values are in good agreement with those reported in the literature for integrated measurements of galaxies. Kennicutt et al. (2009) found 0.020 $\pm$ 0.005 and 0.0024 $\pm$ 0.0006 for L(Hα) + a_{IR} $\times$ L(24 μm) and L(Hα) + a_{IR} $\times$ L(TIR), respectively. For the case of the UV luminosity, Hao et al. (2011) found 3.89 $\pm$ 0.15 and 0.46 $\pm$ 0.12 for L(FUV) + a_{IR} $\times$ L(25 μm) and L(FUV) + a_{IR} $\times$ L(TIR), respectively.

In the rest of this section, we study the value of the a_{IR} coefficient as a function of galaxy properties to obtain insights on the origin of this spread. As we show below, the change in the a_{IR} coefficient with galaxy properties appears when studying nuclear activity as well as galaxy morphology, stellar mass, color, axial ratio, and attenuation.

3.5.5.3 Morphological-type dependence of a_{IR} in hybrid tracers

Given the large number of galaxies in our sample, we can now explore the origin of the differences between the various SFR tracers. In particular, we analyze the origin of the variation of the a_{IR} with different galaxy properties. Here we focus on the study of its dependence with galaxy morphology (see Walcher et al. 2014). Figure 3.17 shows the distribution of the a_{IR} coefficient in bins of morphological type. In the four top plots of this figure, we can see a trend toward the median value of the a_{IR} coefficient (vertical dashed lines) with the galaxy morphology for Hα + IR tracers. Star-forming galaxies of early type, considered here as S0/a, Sa, and Sab, have lower median values for a_{IR} (red dashed line) than intermediate-type spirals such as Sb and Sbc (gray dashed line). The last group of galaxies, Sc-Sd-Sm-Irr, shows the largest median value for the a_{IR}

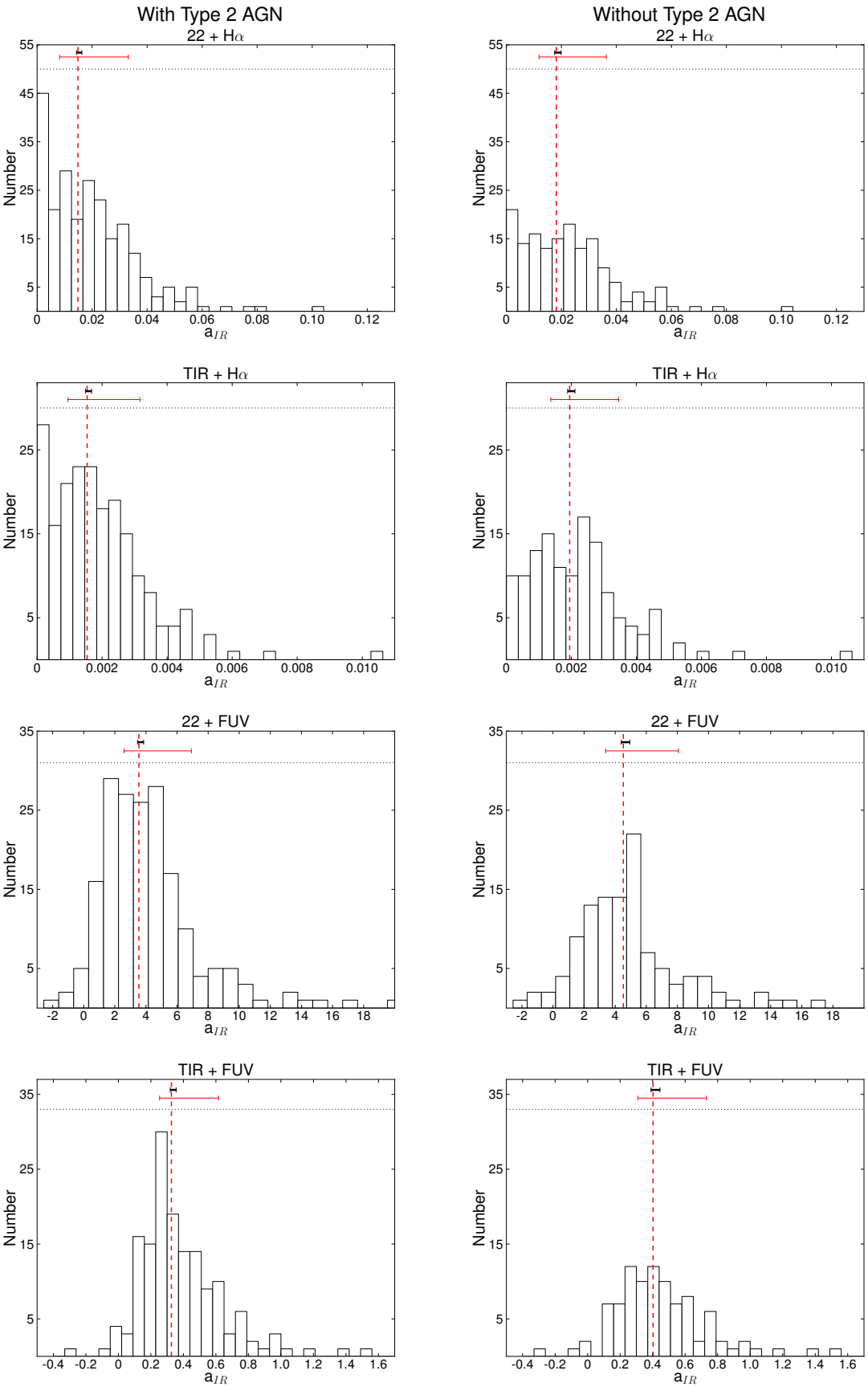

Figure 3.16: Histograms showing the distribution of the a_{IR} coefficient values obtained for the different hybrid tracers. The parameter a_{IR} is computed using the expressions 3.16 and 3.17. The red dashed line corresponds to the median value of this coefficient. The red tick marks shown at the top refers to the 1 σ dispersions measured as the interval that includes 68% of the data points around the median quoted in Table 3.2, while black tick marks indicate the standard error of the median computed from the asymptotic variance formula using these 1 σ dispersions. Type-2 AGN galaxies are excluded from the histograms at right.

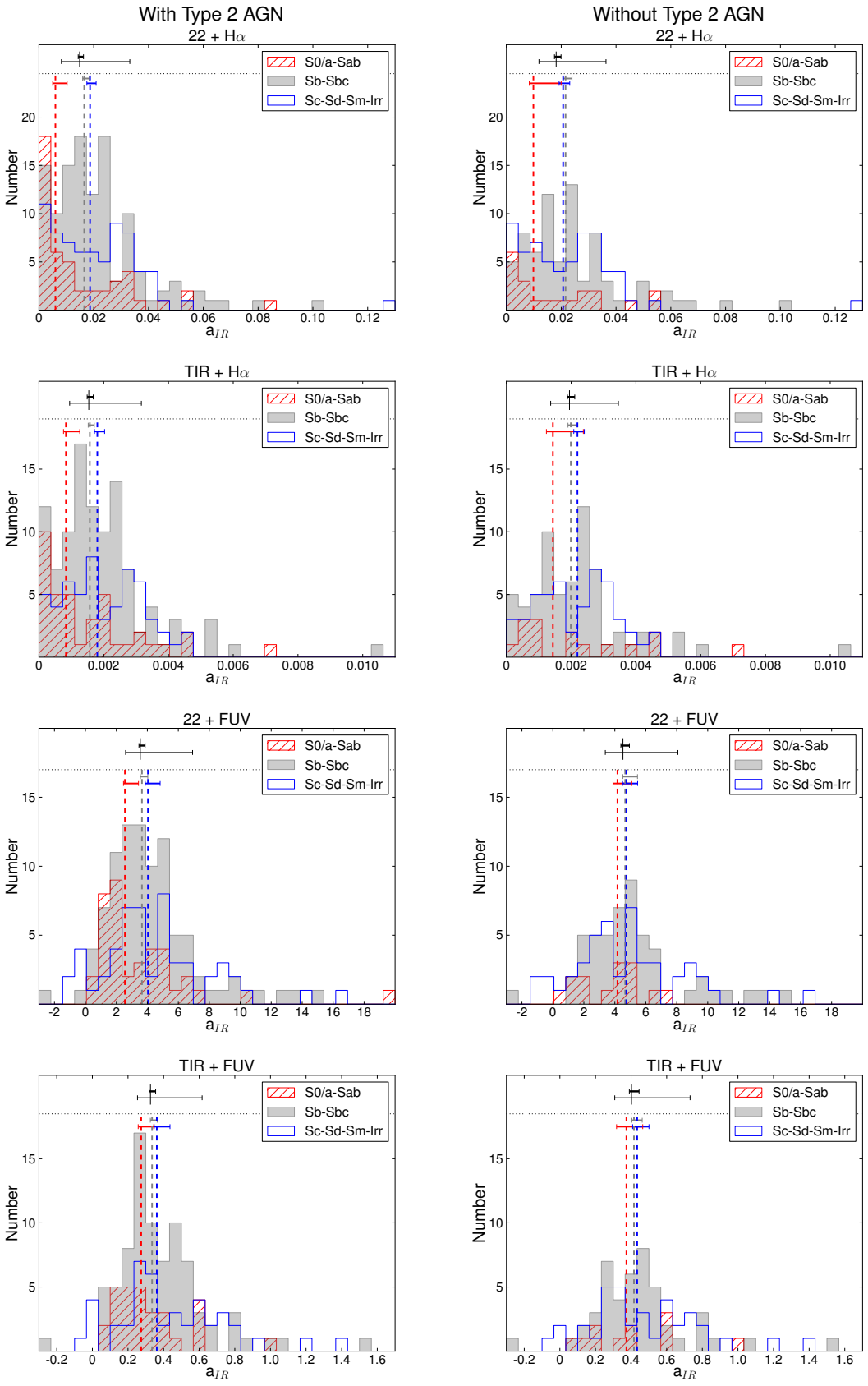

Figure 3.17: Four left panels: histograms showing the values of the coefficient that multiply the IR luminosity, a_{IR}, in the hybrid tracers using bins of morphological types. Early-type, star-forming galaxies, considered here as S0/a, Sa, and Sab, are shown in red, intermediate-type spirals such as Sb and Sbc appear in gray, and Sc-Sd-Sm-Irr galaxies are represented in blue. Vertical dashed lines correspond to the median value of each galaxy group. Black top marks show the median value for all the galaxies as in Figure 3.16. There is a clear trend with the morphological type, late-type galaxies need a higher value of the a_{IR} coefficient than early-type galaxies. This trend could be explained in terms of the contribution of an obscured AGN, a missing fraction of the Hα extinction-corrected SFR, or heating by optical photons. Four right panels: same histograms as before, except removing the type-2 AGN. There is still a trend with the morphological type, although it is less obvious that in the previous case.

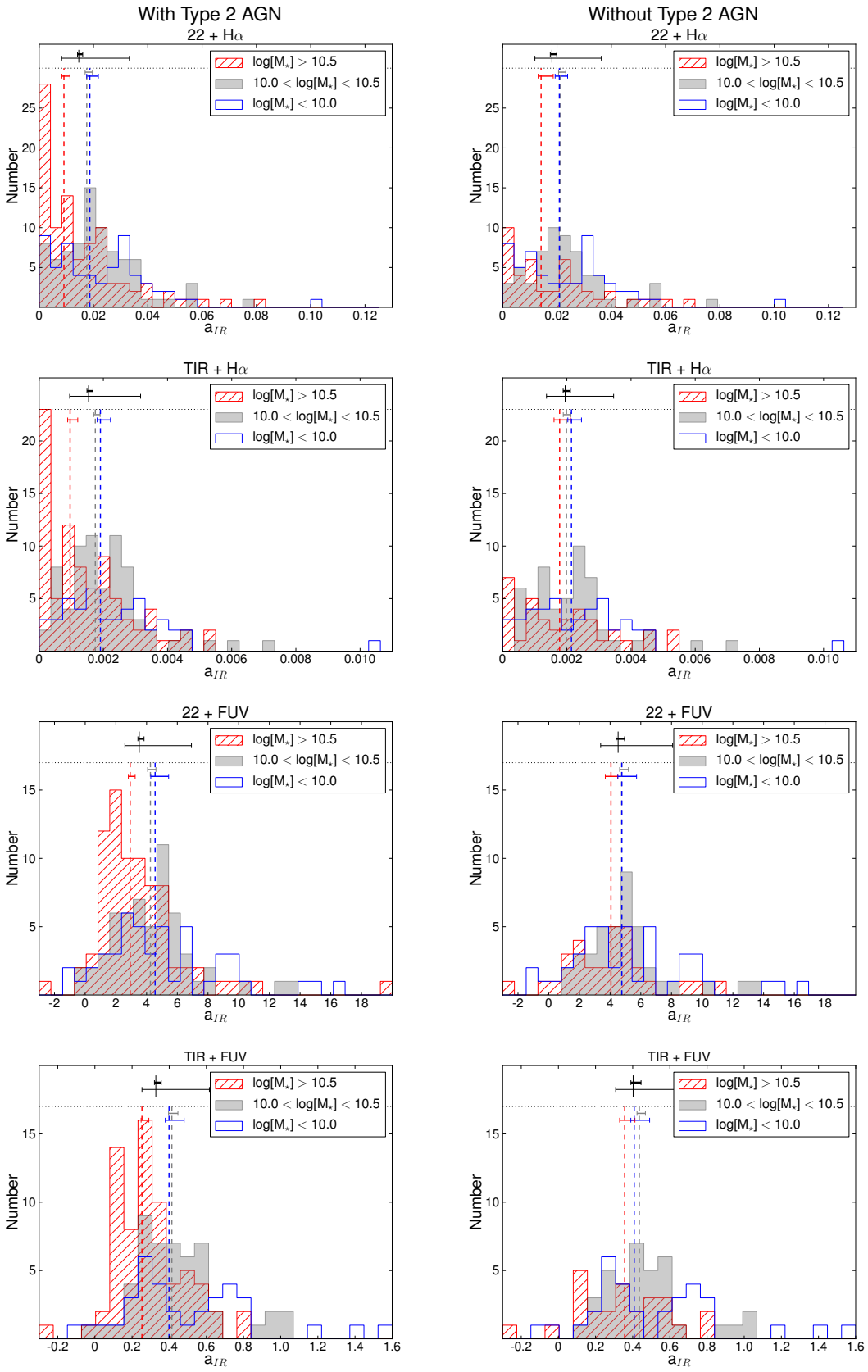

Figure 3.18: Left four panels: frequency histograms of a_{IR} for different hybrid tracers as a function of stellar mass. Massive galaxies ($\log[M_*/M_\odot]>10.5$) appear in red, intermediate-mass galaxies ($10<\log[M_*/M_\odot]<10.5$) are shown in gray, and low-mass galaxies ($\log[M_*/M_\odot]<10$) in blue. Dashed vertical lines correspond to the median value of each galaxy group. Black top marks show the median value for all the galaxies as in Figure 3.16. There is a clear trend with the stellar mass that less massive galaxies need a higher value of the a_{IR} coefficient compared with massive galaxies. Right four panels: same as in left panels, except this time type-2 AGNs are excluded for the sample. The distribution of the a_{IR} coefficient with the stellar mass and morphological type (Figure 3.17) allow us to provide, for the first time, a set of hybrid calibrations in terms of these galaxy properties. If the sample to be analyzed is biased toward morphology or, more commonly, luminosity or stellar mass, these tracers would be particularly useful (see Tables 3.3 and 3.4).

coefficient (blue dashed line). When type-2 AGN galaxies are excluded (right panels in Figure 3.17), the trend is less obvious, mainly because of a drastic increase in the median a_{IR} of early-type spirals.

Regarding the FUV+IR hybrid tracers (four bottom panels in Figure 3.17), we find that the median values for a_{IR} are more similar between S0/a-Sab and Sb-Sbc galaxies. However, the Sc-Sd-Sm-Irr galaxies still show the highest value for the a_{IR} coefficient. Table 3.3 lists the resulting median values and their corresponding errors.

These trends are likely the combination of multiple effects (especially given the large dispersion in the value of a_{IR} within a given subsample), namely:

(1) The contribution of obscured AGN to the IR luminosity (both at 22 μm and in the TIR). This partly explains the fact that the average a_{IR} decreases when type-2 AGN are included in the sample. The fraction of type-2 AGN is larger within early-type galaxies, so part of the IR luminosity (without an equivalent extinction-corrected Hα luminosity counterpart) is arising from the (obscured) AGN itself.

(2) A fraction of the SFR (that assumed to be in this case accurately measured using a hybrid tracer with a nominal, large, value of the a_{IR} coefficient) is missed when using the extinction-corrected Hα luminosity. This happens, especially, in early-type spirals so the a_{IR} coefficient decreases in these objects to compensate for the reduced amount of SFR derived from Hα. When the Hα emission missed is exclusively due to an obscured AGN we are in case (1) and Hα would be a fair measure of the SFR.

(3) There is a fraction of the infrared emission that is due to heating by optical photons. One would expect that this effect would be more notorious when the a_{IR} coefficient refers to the TIR band, as optical photons are expected to heat the dust at low temperatures, where the emission at 22 μm is small. As discussed above, the value of a_{IR} is smaller for S0/a-Sab galaxies, which are galaxies that have older stellar populations and optically bright bulges. Li et al. (2013) also found that the coefficient that multiply the IR luminosity in the L(Hα) + a $\times$ L(70 μm) hybrid tracer is smaller when larger apertures around star-forming regions are used. The authors attribute this effect to the larger associated star formation timescale and the consequent dust heated by old stellar populations.

The fact that by removing type-2 AGN we reduce but not completely eliminate the morphological-type dependence of a_{IR} indicates that while (1) appears to have some role, the other possibilities are also at play. Disentangling the contribution of different mechanisms listed above is not easy. In particular, the change observed in a_{IR} when type-2 AGN are excluded from the sample could be also because of a decrease in the number of red massive star-forming galaxies in each morphological-type bin. These galaxies are expected to suffer from mechanism (3) as well. The analysis of the variation of a_{IR} with other properties, mass, color, axial ratio, and ionized-gas attenuation helps us to understand the relative contribution of these mechanisms and, therefore, the specific limitations of the different SFR hybrid tracers.

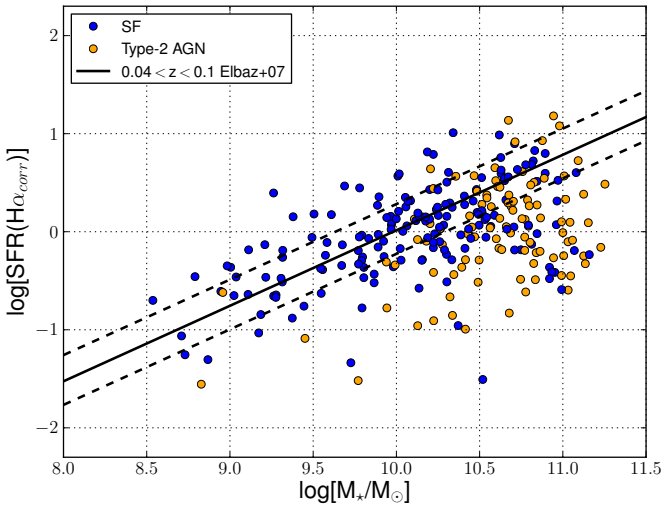

Figure 3.19: Correlation between the extinction-corrected Hα SFR and the total stellar mass of the galaxies. Solid line represents the fit of Elbaz et al. (2007) with a slope of 0.77 for galaxies in the $0.04<z<0.1$ range, while dashed lines correspond to the dispersion of this fit. Type-2 AGN host galaxies dominate the high-mass end in the main sequence plot for our galaxies. They show somewhat smaller SFR values for the same stellar mass. This fact could be because of a fraction of Hα emission absorbed by the AGN or in the circumnuclear region or, alternatively, the presence of the type-2 AGN might impact the internal evolution of the galaxy quenching the SF.

3.5.5.4 Stellar mass dependence of a_{IR} in hybrid tracers

Since morphology alone is not able to establish the origin of the variation of a_{IR} from galaxy to galaxy and within subsamples, we now explore its dependence with stellar mass. We use the total stellar masses for the CALIFA galaxies from Walcher et al. (2014), Section 6.3. (J. Walcher, priv. comm.). The masses are publicly available on the CALIFA DR2 webpage[5]. The procedure for determining them is based on the fitting of UV-optical-NIR SEDs as described in detail in Walcher et al. (2014).

Figure 3.18 shows the frequency histograms of a_{IR} for different hybrid tracers (with and without type-2 AGN in the sample) as a function of stellar mass. As for Figure 3.17, we find a large dispersion within each mass bin, so clearly mass is not the only driver behind the variation of a_{IR} from galaxy to galaxy. We find that most massive galaxies ($\log[M_*/M_\odot]>10.5$) have lower median values of a_{IR} (red dashed line) than intermediate mass ($10<\log[M_*/M_\odot]<10.5$) (gray dashed line). In general, low-mass galaxies ($\log[M_*/M_\odot]<10$) show the largest median value for a_{IR} (blue dashed line). Table 3.4 compiles the resulting median values and their corresponding errors.

Besides the relation between mass and color or attenuation, the presence of intense nuclear star formation (such as that found in the classical starburst nuclei, SBN; e.g. Gonzalez-Delgado et al. 1995; Gallego et al. 1996) is also far more common among massive star-forming systems than in low-mass systems (see Pérez-González et al. 2003). It is precisely in these objects where complete obscuration effects in Hα (that would reduce the value a_{IR}) might occur.

Figure 3.19 compares SFR (derived from the extinction-corrected Hα luminosity) with the total

[5]http://www.caha.es/CALIFA/public_html/?q=content/califa-2nd-data-release

stellar mass of the galaxies in the sample, the so-called main sequence of galaxies (Brinchmann et al. 2004). This figure shows that type-2 AGN host galaxies (orange dots) dominate the high-mass end of those in our diameter-limited sample. Besides, for the same stellar mass, active galaxies show somewhat smaller star formation rates. Some simulations show that when including the AGN feedback, most massive galaxies show a decrease in the specific SFR (Taylor & Kobayashi 2015). This could be due to a fraction of Hα emission being completely absorbed either at the AGN or in circumnuclear star formation or to correlations between nuclear activity and other properties, besides mass, such as morphological type or environment. The latter is related with the fact that the presence of an AGN might impact the internal evolution of the galaxy quenching the SF by feedback mechanisms (for a complete review on this topic see Alexander & Hickox 2012). The analysis of potential effects of the AGN on the current level of star formation at fixed mass (e.g., preference of type-2 AGN for the Green Valley; see Kauffmann et al. 2003; Sánchez et al. 2004) is beyond the scope of this work, but it is analyzed in detail in Chapter 4.

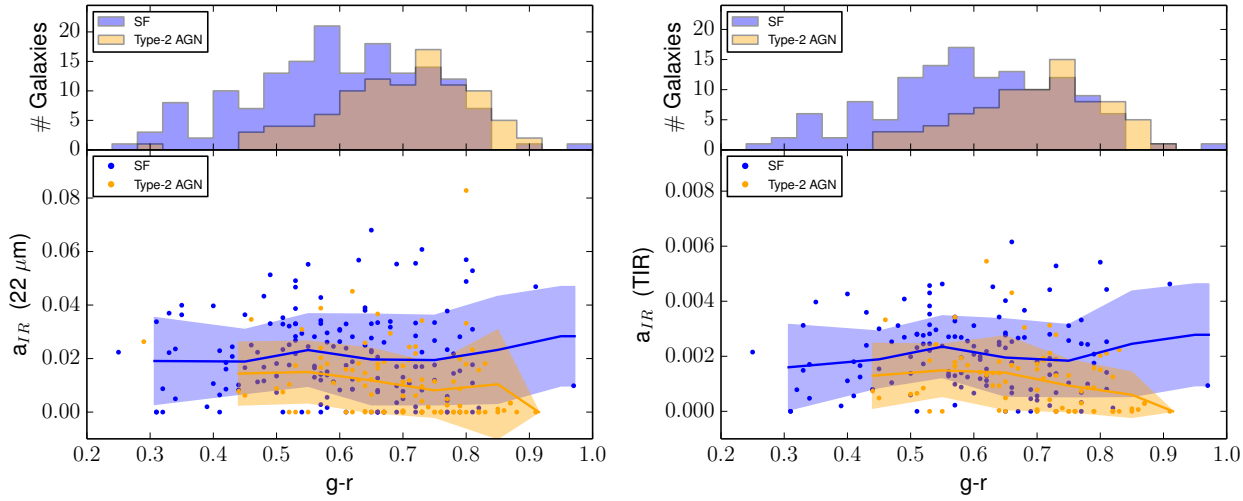

Figure 3.20: Left panel: distribution of a_{IR} coefficients as a function of the galaxies $g-r$ *SDSS* color for the Hα+22 μm hybrid tracer. Orange points show type-2 AGN galaxies while blue points represent star-forming galaxies. Filled contours represent the 1 σ dispersion after applying a 5 σ rejection around the mean value expressed as a blue (orange) solid line for the SF (type-2 AGN) galaxies. The corresponding histogram with the distribution of the number of galaxies for each $g-r$ *SDSS* color is plotted on the top for reference applying the same color-coding. Right panel: same as the left panel, except showing the Hα+TIR hybrid tracer. There is a clear offset between the star-forming and type-2 AGN host galaxies with the a_{IR} coefficient at any $g-r$ *SDSS* color.

3.5.5.5 Color dependence of a_{IR} in hybrid tracers

We address here the dependence of the a_{IR} coefficient with the color of the integrated stellar population (as traced by the global SDSS $g-r$ color; see Walcher et al. 2014). Figure 3.20 shows the distribution of a_{IR} coefficients as a function of the galaxies $g-r$ color in the case of the Hα+22 μm (left panel) and Hα+TIR (right panel) hybrid tracers. In these plots, type-2 AGN galaxies are shown as orange points and star-forming objects as blue. A clearer picture is obtained when looking separately at star-forming and type-2 AGN galaxies, as traced by the blue- and orange-shaded areas in the bottom panels (mean $\pm 1\sigma$ curves computed after an initial 5σ

rejection). We see here that most of the decrease in a_{IR} with color is driven by type-2 AGN host galaxies that appeared to be a little redder than SF galaxies in the top histogram. We find a trend for redder type-2 AGN host galaxies to show a lower value of a_{IR} especially at colors $g - r > 0.6$, although with a large scatter. This trend could be because redder colors are likely related to galaxies with more massive bulges, and these with systems where the IR emission of a (luminous) obscured AGN could effectively dominate over that due to star formation alone. With regard to the pure star-forming galaxies in the sample, we find a relatively flat trend considering the scatter.

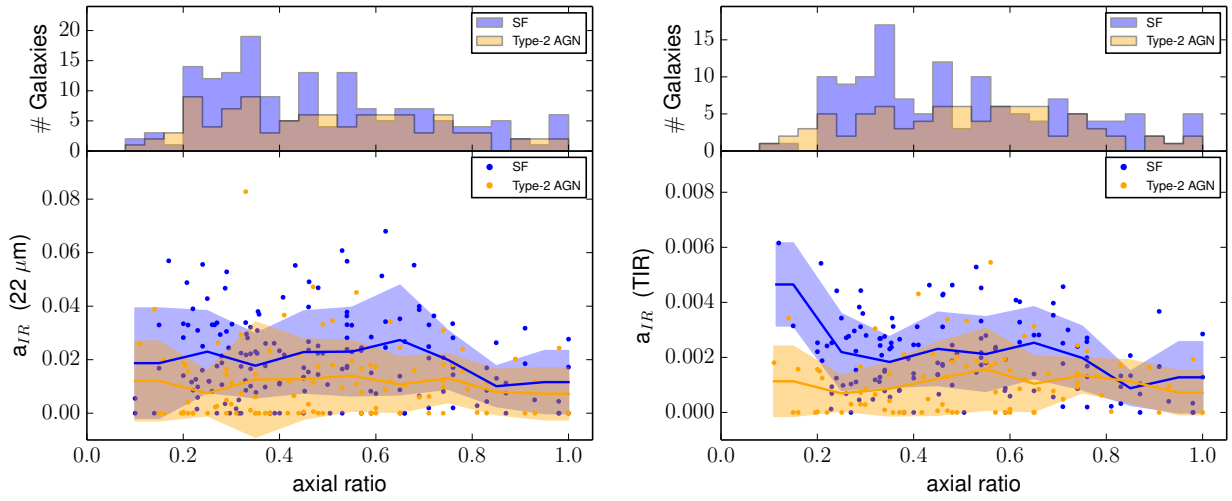

Figure 3.21: Left panel: distribution of a_{IR} coefficients as a function of the galaxies axial ratio for the Hα+22 μm hybrid tracer. Orange points show type-2 AGN galaxies while blue points represent star-forming galaxies. Filled contours represent the 1 σ dispersion after applying a 5 σ rejection around the mean value expressed as a blue (orange) solid line for the SF (type-2 AGN) galaxies. The corresponding histogram with the distribution of the number of galaxies for each axial ratio is plotted on the top for reference applying the same color-coding. Right panel: same as the left panel, except showing the Hα+TIR hybrid tracer. The SF objects with low axial ratios (where highly-inclined disk galaxies would be located) show similar a_{IR} values as the rest of the galaxies. Lower a_{IR} would be expected if a fraction of the Hα emission is completely obscured.

3.5.5.6 Axial ratio dependence of a_{IR} in hybrid tracers

Since highly-inclined systems might be subject to important obscuration effects in the derivation of the SFR, we have explored the dependence between the a_{IR} coefficient and the axial ratio, as a proxy for the galaxy inclination. Figure 3.21 shows the histograms of both star-forming and type-2 AGN host galaxies as a function of the axial ratio as given by the RC3 catalog, i.e., measured in the D25 B−band isophote. In addition to a clear offset between the two samples at any axial ratio, we find a nearly flat distribution within each sample at axial ratios below ∼0.65. An apparent decrease of a_{IR} appear for face-on SF systems, although statistics are poor in this case. This is true both for the Hα+22μm and the Hα+TIR hybrid tracers (left and right panel in Figure 3.21, respectively). We do not find star-forming objects with low axial ratios (where highly-inclined disk galaxies would be located) to show lower a_{IR}. One would expect this if a fraction of the dust-absorbed Hα emission is not recovered by our Balmer decrement based extinction correction (in other words, the Hα emission will be completely obscured.) Therefore, if Hα is missing a fraction of the SFR in some galaxies, these are not necessarily the most inclined systems. Alternatively,

missed SFR (if present) could arise from dense nuclear regions, such as (circum)nuclear starbursts.

Prescott et al. (2007) studied the incidence of obscured SF in a large sample of infrared-selected star-forming regions in normal galaxies. They used the 24 μm flux as a tracer of the obscured emission due to SF and the uncorrected Hα flux as a tracer of the unobscured portion (the same way we use our 22 μm + Hα hybrid tracer, but we compute integrated measurements of galaxies). These authors conclude that the fraction of highly obscured regions in normal, star-forming disk galaxies is small on 500 pc scales. They are more luminous and tend to be closer to the center of the host galaxy. The analysis of obscuration effects is the subject of Section 3.5.5.7 below which efforts had been made to further explore this issue.

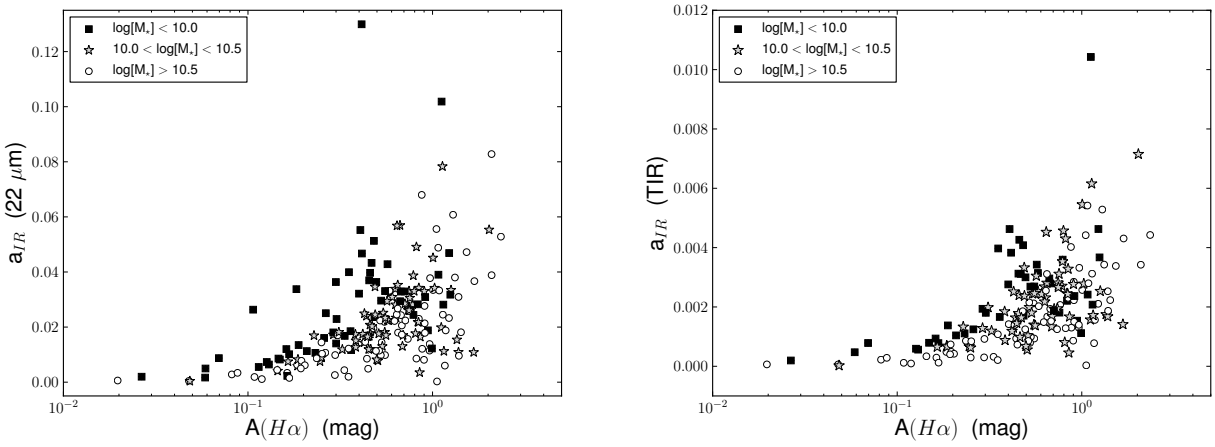

Figure 3.22: Left panel: variation of the a_{IR} coefficient with the Hα attenuation derived using the Balmer decrement for the Hα+22 μm hybrid tracer. Black squares show galaxies with stellar masses lower than log[M$_\star$] < 10.0; gray stars represent galaxies with stellar masses in the range of 10.0 < log[M$_\star$] < 10.5; and finally, open circles are for the most massive galaxies with log[M$_\star$] > 10.5. Right panel: same as previous panel, except this time for the a_{IR} coefficient, which corresponds to the Hα+TIR hybrid tracer.

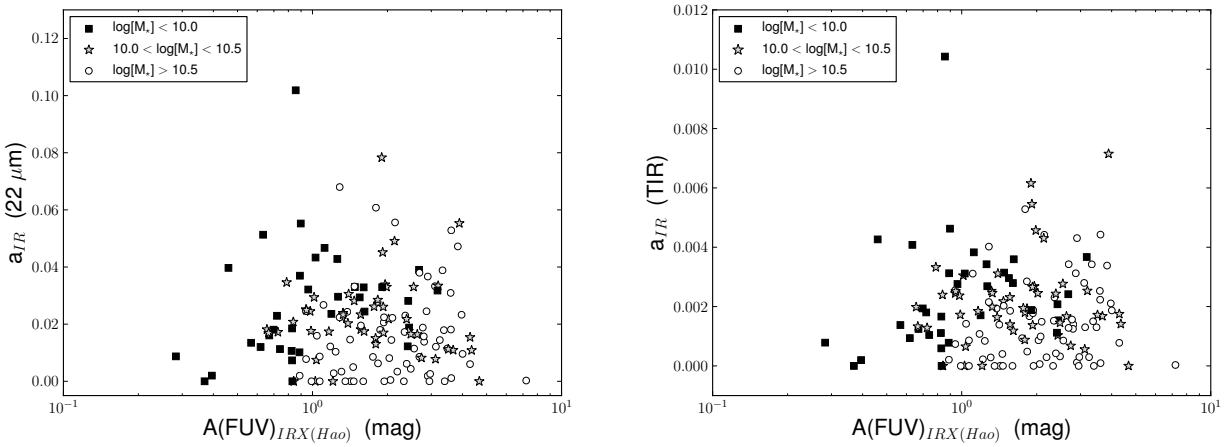

Figure 3.23: Left panel: variation of the a_{IR} coefficient with the FUV attenuation derived using the IRX from Hao et al. (2011) for the Hα+22 μm hybrid tracer. Same symbol-coding as in Figure 3.22. Right panel: same as previous panel, except this time for the a_{IR} coefficient that corresponds to the Hα+TIR hybrid tracer.

3.5.5.7 Attenuation dependence of a_{IR} in hybrid tracers

To determine whether local obscuration effects in Hα might be behind the decrease of a_{IR} in galaxies of specific types, masses or colors (as this coefficient should be reduced to compensate by the SFR missed in Hα), we finally analyze its variation as a function of ionized-gas attenuation. This attenuation is derived from the Hα/Hβ Balmer decrement as described in Section 3.4.1.4. Figure 3.22 shows the variation of the a_{IR} coefficient with the attenuation measured in magnitudes in Hα (the use of log scale in the abscissa is justified by the large concentration of points at low attenuations). The most remarkable feature in this plot is that there is a number of galaxies with low global ionized-gas attenuations that show very small values of a_{IR}. We interpret this as consequence of dust emission that is caused by the heating of photons different from those arising in sites of current star formation. In galaxies where the attenuation derived in Hα is compatible with no attenuation even a small amount of dust emission would lead to a null value for a_{IR}, which results in the number of galaxies with low attenuations and low values of a_{IR} seen in Figure 3.22. These galaxies with very small values of a_{IR} indicate that, at this level, we are in the limit where A(Hα) can be properly derived, given the low global, ionized-gas attenuations found. The variation of the a_{IR} coefficient using the FUV attenuation, applying the IRX given by Hao et al. (2011), is shown in Figure 3.23 for comparison.

Except for this tail at low attenuation, A(Hα)<0.2 mag, we find no correlation between the two parameters. Should a significant fraction of the SFR being missed when the extinction corrected Hα luminosity is used, one would expect to find a clear decrease in a_{IR} as the ionized-gas attenuation gets larger. Only when low-mass galaxies are analyzed separately they seem to show a decline in their a_{IR} values above A(Hα)=0.4 mags, although with some discrepant points at A(Hα) > 1 mag. This decline in a_{IR} might be due to the fact that in some of these naturally low-metallicity galaxies only, high attenuations are due to the presence of active nuclear star formation events. Nevertheless, the average and scatter obtained for the a_{IR} coefficient in these galaxies are not very different from those obtained at higher masses, and do not a_{IR} reach very low values.

3.6 Summary and conclusions

In this work, we present the analysis of the SFR in a sample of 380 galaxies from the diameter-limited CALIFA survey. A total of 272 galaxies show detected emission in both Hβ and Hα and are listed in Table 3.5 for reference. The availability of wide-field IFS for all the galaxies in the sample is a major advantage over other techniques. Using IFS data we can recover the flux in galaxies with low equivalent widths and separate Hα and the [NII] without assuming a [NII]/Hα ratio; thus we avoid problems associated with narrowband imaging or long-slit spectroscopy. It also ensures a proper determination of the underlying stellar continuum and, consequently, of the extinction-corrected Hα luminosity.

We combined the aperture-corrected Hα measurements from CALIFA with those measured in other bands, which are also used to estimate the SFR, including luminosity measurements in the UV from GALEX (200 galaxies), 22 μm from WISE (265 galaxies), and TIR luminosities from WISE+IRAS+AKARI SED fitting (221 galaxies).

We first compare the extinction-corrected Hα SFR with measurements from single-band (FUV, 22 μm and TIR) and hybrid-tracers (Hα+22 μm, Hα+TIR, FUV+22 μm, FUV+TIR). In this part of the work, we use recent compilations of SFR recipes by Calzetti (2013). The good correlation between the SFR surface density obtained with extinction-corrected Hα tracer and FUV+22 μm hybrid tracer guarantees that potential linear correlations between different SFR tracers (some of them not resolved, such as those relying on TIR measurements) are not driven by scaling effects and that global values of the SFR can be used reliably. Our results indicate that, overall, the extinction-corrected Hα luminosity (once underlying stellar absorption and dust-attenuation effects are properly accounted for) matches the SFR obtained from hybrid tracers combining the observed FUV or Hα and the IR (22 μm and TIR) luminosities with dispersions found around $\sim$0.20 dex. In the case of the comparison with single-band tracers, we conclude (1) that the use of IR measurements clearly underestimates the SFR below $\sim$1 $M_{\odot}$ yr^{-1} , and (2) the large uncertainty in the correction for attenuation when only FUV$-$NUV color (similar to the UV slope, β) information is available. This factor introduces a very large scatter, particularly at SFR$>$5 $M_{\odot}$yr^{-1}, where the β-corrected FUV luminosity also tends to underestimate the SFR. This prevents the use of the UV luminosity alone as a SFR tracer.

We also provide a new set of single-band calibrators anchored to the extinction-corrected Hα luminosities. The values for these coefficients appear in Table 3.1. In the case of the hybrid calibrators ,we determine the best (median) fit for the coefficient that weights the amount of IR luminosity reprocessed by dust, a_{IR}. We assume an energetic balance and calculate the a_{IR} coefficients for different combinations of observed (UV or Hα) and dust-reprocessed (22 μm or TIR) SFR contributions anchored to the extinction-corrected Hα luminosities. These values appear in Table 3.2 and are calculated with and without galaxies hosting type-2 AGN being considered.

- This analysis allows us to provide, for the first time, a set of hybrid calibrations for different morphological types and masses. These are particularly useful in case that the sample to be analyzed shows a different bias in terms of morphology or, more commonly, luminosity or stellar mass (see Tables 3.3 and 3.4).

- We also study the dependence of this coefficient with morphological type and mass and with color (SDSS $g-r$), axial ratio, and ionized-gas attenuation.

- The distributions of a_{IR} values (for each of the hybrid tracers) are quite wide in all cases. While part of the spread can be attributed to changes in morphological type, stellar mass, color, and attenuation among the galaxies in the sample, there is no single physical property that can by itself explain the entire variation in a_{IR} from galaxy to galaxy.

- The analysis of the dependence of a_{IR} with galaxy properties indicates that galaxies hosting type-2 AGN tend to reduce the median value of a_{IR}, likely due to the contribution of obscured AGN to the infrared emission. The fact that a_{IR} does not show a particularly low value at high ionized-gas attenuations nor low axial ratios, suggests that obscured star formation is, comparatively, playing a minor role. Part of the dependence of the median value of a_{IR} with the morphological type disappears once the AGN contribution is removed, although early spirals still show a somewhat lower a_{IR} than intermediate- and late-type spirals. This behavior, also present when comparing massive with less massive systems, can be explained

in part as due to the enhanced contribution of optical photons to the heating of the dust in both early-type spirals and massive systems.

These conclusions will allow us to make use of the CALIFA IFS data to explore the distribution of the SFR with spatial resolution in the next Chapter. We emphasize that the impact of potential differences in the selection criteria should be addressed carefully when extrapolating these results to other samples of galaxies and, particularly, to other redshifts.

Table 3.1: Values of the a, a′ , and b coefficients for the calibration of single-band tracers: Linear and nonlinear fits, as explained in Section 3.5.5.1. The numbers in brackets refer to the number of galaxies used in each case (same notation applied in Tables 3.2, 3.3, and 3.4). The luminosities are expressed in erg s^{-1} and the values of the SFR are in $M_{\odot}yr^{-1}$.

Single-band Tracers	Without type-2 AGN	With type-2 AGN
SFR = a × L(22 μm)	a = $\left(3.0^{+2.1}_{-0.4}\right) \times 10^{-43}$ [164]	a = $\left(2.8^{+1.6}_{-0.6}\right) \times 10^{-43}$ [263]
SFR = a × L(TIR)	a = $\left(2.8^{+1.7}_{-0.5}\right) \times 10^{-44}$ [135]	a = $\left(2.3^{+1.6}_{-0.5}\right) \times 10^{-44}$ [218]
SFR = a′ × [L(22 μm)/10^{43}]^b (log scale fit)	a′ = 2.12 ± 0.18 ; b = 0.733 ± 0.053	a′ = 1.86 ± 0.11 ; b = 0.702 ± 0.039
SFR = a′ × [L(22 μm)/10^{43}]^b (curve_fit)	a′ = 2.60 ± 0.12 ; b = 0.697 ± 0.051	a′ = 2.38 ± 0.12 ; b = 0.564 ± 0.043
SFR = a′ × [L(TIR)/10^{43}]^b (log scale fit)	a′ = 0.403 ± 0.032 ; b = 0.720 ± 0.042	a′ = 0.359 ± 0.028 ; b = 0.719 ± 0.038
SFR = a′ × [L(TIR)/10^{43}]^b (curve_fit)	a′ = 0.350 ± 0.063 ; b = 0.845 ± 0.064	a′ = 0.285 ± 0.054 ; b = 0.881 ± 0.061

Table 3.2: Values of the a_{IR} coefficients for the calibration of hybrid tracers: GLOBAL VALUES (see Section 3.5.5.2 for a detailed explanation)
The errors quoted here are the 1 σ dispersions measured as the interval that includes 68% of the data points around the median, and correspond with the spread of the histograms in Figure 3.16. Note that the standard error of the median, computed from the asymptotic variance formula as $1.253\times\sigma/\sqrt{N}$, where σ is referred to the values listed here and N is the number of galaxies shown in brackets, decreases these errors considerably (black tick marks shown at the top in Figure 3.16). The luminosities in these expressions are in erg s^{-1} and the values of the SFR are expressed in $M_{\odot}yr^{-1}$.

Hybrid Tracers	Without type-2 AGN	With type-2 AGN
SFR = 5.5 × 10^{-42} [L(Hα)$_{obs}$ + a_{IR} × L(22 μm)]	$0.018^{+0.018}_{-0.006}$ [164]	$0.015^{+0.018}_{-0.006}$ [263]
SFR = 5.5 × 10^{-42} [L(Hα)$_{obs}$ + a_{IR} × L(TIR)]	$0.0019^{+0.0015}_{-0.0005}$ [135]	$0.0015^{+0.0016}_{-0.0006}$ [218]
SFR = 4.6 × 10^{-44} [L(FUV)$_{obs}$ + a_{IR} × L(22 μm)]	$4.52^{+3.55}_{-1.14}$ [113]	$3.55^{+3.38}_{-0.95}$ [187]
SFR = 4.6 × 10^{-44} [L(FUV)$_{obs}$ + a_{IR} × L(TIR)]	$0.40^{+0.33}_{-0.09}$ [94]	$0.33^{+0.29}_{-0.07}$ [156]

Table 3.3: Values of the a_{IR} coefficients for the calibration of hybrid tracers: BY MORPHOLOGICAL TYPE (see Sections 3.5.5.2 and 3.5.5.3 for a detailed explanation). The recipes to compute the SFR in $M_{\odot}yr^{-1}$ shown in the left column are the same as in Table 3.2. The luminosities are in units of erg s^{-1}.

Hybrid Tracers	Without type-2 AGN			With type-2 AGN		
	S0/a-Sab	Sb-Sbc	Sc-Irr	S0/a-Sab	Sb-Sbc	Sc-Irr
$L(H\alpha)_{obs} + a_{IR} \times L(22\,\mu m)$	$0.010^{+0.037}_{-0.005}$ [21]	$0.022^{+0.016}_{-0.007}$ [76]	$0.021^{+0.016}_{-0.009}$ [67]	$0.006^{+0.026}_{-0.006}$ [58]	$0.017^{+0.017}_{-0.005}$ [131]	$0.019^{+0.015}_{-0.008}$ [74]
$L(H\alpha)_{obs} + a_{IR} \times L(TIR)$	$0.0014^{+0.0029}_{-0.0006}$ [16]	$0.0020^{+0.0013}_{-0.0006}$ [68]	$0.0022^{+0.0012}_{-0.0006}$ [51]	$0.0008^{+0.0022}_{-0.0004}$ [44]	$0.0016^{+0.0012}_{-0.0004}$ [116]	$0.0018^{+0.0013}_{-0.0005}$ [58]
$L(FUV)_{obs} + a_{IR} \times L(22\,\mu m)$	$4.17^{+2.76}_{-0.86}$ [14]	$4.67^{+4.52}_{-0.88}$ [51]	$4.75^{+3.97}_{-1.37}$ [48]	$2.55^{+4.37}_{-0.46}$ [39]	$3.65^{+2.90}_{-0.78}$ [93]	$4.04^{+4.61}_{-1.04}$ [55]
$L(FUV)_{obs} + a_{IR} \times L(TIR)$	$0.37^{+0.24}_{-0.15}$ [11]	$0.42^{+0.25}_{-0.06}$ [46]	$0.43^{+0.32}_{-0.12}$ [37]	$0.27^{+0.31}_{-0.07}$ [30]	$0.34^{+0.21}_{-0.07}$ [82]	$0.36^{+0.39}_{-0.08}$ [44]

Table 3.4: Values of the a_{IR} coefficients for the calibration of hybrid tracers: BY STELLAR MASS (see Sections 3.5.5.2 and 3.5.5.4 for a detailed explanation). The stellar masses are in units of $M_{\star}/M_{\odot}$. Expressions to compute the SFR ($M_{\odot}yr^{-1}$) appeared in the left column. These recipes are the same as those in Table 3.2. The luminosities are in units of erg s^{-1}.

Hybrid Tracers	Without type-2 AGN			With type-2 AGN		
	$\log[M_{\star}]>10.5$	$10.0<\log[M_{\star}]<10.5$	$\log[M_{\star}]<10.0$	$\log[M_{\star}]>10.5$	$10.0<\log[M_{\star}]<10.5$	$\log[M_{\star}]<10.0$
$L(H\alpha)_{obs} + a_{IR} \times L(22\,\mu m)$	$0.014^{+0.024}_{-0.006}$ [44]	$0.021^{+0.012}_{-0.004}$ [60]	$0.021^{+0.018}_{-0.010}$ [60]	$0.009^{+0.019}_{-0.007}$ [108]	$0.017^{+0.016}_{-0.005}$ [88]	$0.019^{+0.020}_{-0.007}$ [66]
$L(H\alpha)_{obs} + a_{IR} \times L(TIR)$	$0.0018^{+0.0017}_{-0.0008}$ [37]	$0.0020^{+0.0008}_{-0.0006}$ [54]	$0.0021^{+0.0017}_{-0.0006}$ [44]	$0.0010^{+0.0018}_{-0.0006}$ [92]	$0.0018^{+0.0011}_{-0.0004}$ [77]	$0.0019^{+0.0018}_{-0.0005}$ [48]
$L(FUV)_{obs} + a_{IR} \times L(22\,\mu m)$	$4.06^{+1.93}_{-1.61}$ [30]	$4.75^{+2.21}_{-0.63}$ [39]	$4.77^{+5.07}_{-1.39}$ [44]	$2.93^{+2.34}_{-0.84}$ [81]	$4.25^{+2.17}_{-1.09}$ [57]	$4.55^{+4.87}_{-1.56}$ [48]
$L(FUV)_{obs} + a_{IR} \times L(TIR)$	$0.36^{+0.22}_{-0.11}$ [26]	$0.44^{+0.16}_{-0.06}$ [36]	$0.41^{+0.37}_{-0.08}$ [32]	$0.25^{+0.25}_{-0.03}$ [70]	$0.41^{+0.18}_{-0.10}$ [50]	$0.40^{+0.38}_{-0.10}$ [35]

Table 3.5: Integrated measurements for the CALIFA galaxies. (1) ID CALIFA identifier; (2) galaxy name; (3) morphological type; (4) distance in Mpc calculated from redshift; (5) minor-to-major axis ratio as given by the RC3 catalog, i.e., measured in the D25 B-band isophote; (6) observed-Hα flux using an elliptical aperture with a semimajor axis of 36 arcsec; (7) attenuation obtained using the Balmer decrement. As explained in Section 3.4.1.4, we have assumed an intrinsic Hα/Hβ ratio of 2.86 (although lower values are also physically possible in HII regions, depending on the electron density, effective temperature, and therefore on the chemical abundance. This leads to a number of galaxies for which we assumed A(Hα) = 0 that also appeared in this table). The errors listed here only use the Hα flux uncertainty, an additional 7% uncertainty in the Hβ flux have been taken into account for the errors in the Hα luminosities, col. (8), and SFRs, col. (9) and in the attenuations used in this work; (8) observed Hα luminosity corrected for aperture effects; (9) Balmer-corrected and aperture-corrected Hα SFR values; (10) observed FUV luminosity; (11) observed NUV luminosity; (12) UV color in AB system; (13) TIR luminosity defined as the total infrared emission in the range $8-1000\,\mu$m; (14) $22\,\mu$m (aperture photometry) luminosity. As explained in Section 3.4.3, it has been pointed out by several authors (Wright et al. 2010; Jarrett et al. 2013; Brown et al. 2014) that SF galaxies measured with the WISE $22\,\mu$m filter are systematically brighter by ~ 10 % than that inferred from Spitzer IRS and $24\,\mu$m data. For that reason, the $22\,\mu$m luminosity values given in column (14) have to be multiplied by 1/1.1. Note that galaxies UGC 00987 and UGC 03973 are classified as type-1 AGN within our sample. As a consequence, they have been excluded from the SFR analysis.

ID	Name	Type	Dist (Mpc)	b/a	F(Hα_{obs}) ($\times 10^{-16}$ cgs)	A(Hα) (mag)	L(Hα_{obs}) ($\times 10^{40}$ erg s^{-1})	SFR[Hα_{corr}] (M$_\odot$ yr^{-1})	L(FUV$_{obs}$) ($\times 10^{42}$ erg s^{-1})	L(NUV$_{obs}$) ($\times 10^{42}$ erg s^{-1})	F–N (AB mag)	L(TIR) ($\times 10^{43}$ erg s^{-1})	L(22μm) ($\times 10^{42}$ erg s^{-1})
(1)	(2)	(3)	(4)	(5)	(6)	(7)	(8)	(9)	(10)	(11)	(12)	(13)	(14)
1	IC 5376	Sb	71.97	0.17	719.75 ± 10.36	0.67 ± 0.07	11.47 ± 0.88	1.17 ± 0.22	3.20 ± 0.44	5.71 ± 0.18	0.63	…	1.88 ± 0.18
2	UGC 00005	Sbc	104.31	0.51	2676.95 ± 22.90	0.65 ± 0.05	40.99 ± 1.87	4.10 ± 0.71	20.10 ± 0.19	31.57 ± 0.78	0.49	20.08 ± 0.66	20.55 ± 0.66
3	NGC 7819	Sc	71.47	0.76	2617.25 ± 7.13	0.43 ± 0.04	25.42 ± 0.75	2.07 ± 0.35	…	…	…	9.42 ± 1.80	9.33 ± 0.22
5	IC 1528	Sbc	54.77	0.48	3146.26 ± 12.74	0.54 ± 0.03	19.78 ± 0.40	1.79 ± 0.30	17.37 ± 0.16	21.66 ± 0.13	0.24	5.22 ± 0.24	5.58 ± 0.17
7	UGC 00036	Sab	89.82	0.46	839.79 ± 10.40	0.16 ± 0.11	9.57 ± 0.66	0.61 ± 0.11	3.74 ± 0.62	7.47 ± 0.28	0.75	5.31 ± 0.33	5.03 ± 0.29
8	NGC 0001	Sbc	64.92	0.76	4068.14 ± 22.32	1.01 ± 0.04	28.22 ± 6.26	3.92 ± 1.09	…	…	…	16.75 ± 0.95	14.16 ± 0.34
9	NGC 0023	Sb	65.26	0.65	12029.28 ± 138.27	1.14 ± 0.03	76.62 ± 1.15	12.01 ± 2.04	15.99 ± 0.15	32.50 ± 0.20	0.77	45.41 ± 1.54	63.64 ± 0.94
10	NGC 0036	Sb	87.09	0.62	1933.46 ± 21.73	0.87 ± 0.07	42.82 ± 1.84	5.27 ± 0.92	26.70 ± 0.74	38.95 ± 0.96	0.41	13.16 ± 1.52	8.56 ± 1.55
11	UGC 00139	Scd	56.45	0.46	2209.21 ± 5.91	0.46 ± 0.03	17.8 ± 0.93	1.49 ± 0.26	19.14 ± 0.18	23.87 ± 0.73	0.24	2.19 ± 0.48	2.59 ± 0.19
12	UGC 00148	Sc	59.88	0.26	5192.47 ± 14.94	0.75 ± 0.02	33.83 ± 8.67	3.70 ± 1.13	…	…	…	12.31 ± 1.22	11.11 ± 0.33
14	UGC 00312	Sd	62.13	0.46	5977.27 ± 13.19	0.48 ± 0.01	34.07 ± 0.34	2.93 ± 0.48	25.89 ± 0.24	34.45 ± 0.21	0.31	11.22 ± 1.90	8.93 ± 0.38
15	ESO539-G014	Scd	101.16	0.1	255.45 ± 2.36	0.11 ± 0.07	7.18 ± 0.56	0.44 ± 0.08	5.71 ± 0.37	9.74 ± 0.36	0.58	…	1.59 ± 0.32
16	MCG-02-02-040	Scd	50.38	0.28	2379.79 ± 9.65	0.94 ± 0.02	8.92 ± 1.60	1.17 ± 0.29	4.36 ± 0.24	6.78 ± 0.04	0.48	8.03 ± 0.74	7.22 ± 0.18
19	ESO540-G003	Sb	47.63	0.4	1559.81 ± 20.22	0.0 ± 0.09	6.72 ± 1.82	0.37 ± 0.11	…	…	…	1.41 ± 0.12	1.34 ± 0.13
20	NGC 0160	Sa	75.09	0.57	443.08 ± 33.11	0.0 ± 0.55	7.88 ± 0.61	0.43 ± 0.05	7.27 ± 0.27	11.74 ± 0.14	0.52	…	3.57 ± 0.69
21	NGC 0165	Sb	84.19	0.83	1770.5 ± 9.19	0.44 ± 0.06	18.7 ± 3.43	1.54 ± 0.38	11.51 ± 0.53	19.28 ± 0.12	0.56	10.02 ± 0.43	12.08 ± 0.38
22	NGC 0169	Sab	66.2	0.25	1159.63 ± 17.74	2.57 ± 0.10	25.9 ± 1.54	15.17 ± 2.77	3.34 ± 0.43	5.92 ± 0.22	0.62	10.06 ± 0.44	10.01 ± 0.34
23	NGC 0171	Sb	56.14	0.87	2358.23 ± 14.08	0.25 ± 0.08	13.05 ± 3.20	0.90 ± 0.27	…	…	…	4.96 ± 0.42	4.84 ± 0.45
25	NGC 0180	Sb	75.65	0.81	2267.29 ± 14.99	0.08 ± 0.05	35.61 ± 0.73	2.11 ± 0.35	27.81 ± 0.77	46.15 ± 0.57	0.55	12.49 ± 0.83	10.89 ± 0.56
26	NGC 0192	Sab	60.17	0.47	2532.58 ± 34.39	0.96 ± 0.06	14.03 ± 0.25	1.87 ± 0.32	3.00 ± 0.03	7.90 ± 0.05	1.05	15.40 ± 1.04	19.23 ± 0.43
27	NGC 0216	Sd	22.3	0.34	5110.81 ± 10.96	0.17 ± 0.01	3.58 ± 0.06	0.23 ± 0.04	2.78 ± 0.03	3.80 ± 0.02	0.34	0.76 ± 0.09	0.65 ± 0.05
28	NGC 0214	Sbc	64.66	0.74	6034.21 ± 58.51	0.55 ± 0.07	40.79 ± 0.79	3.73 ± 0.63	27.53 ± 0.25	42.06 ± 0.26	0.46	19.27 ± 0.80	16.33 ± 0.41
30	NGC 0237	Sc	59.5	0.57	4649.69 ± 12.55	0.64 ± 0.02	27.27 ± 0.50	2.69 ± 0.45	13.41 ± 0.74	21.66 ± 0.13	0.52	9.37 ± 0.26	10.20 ± 0.27
31	NGC 0234	Sc	63.73	1.0	8268.97 ± 16.74	0.9 ± 0.02	45.09 ± 1.39	5.71 ± 0.96	21.64 ± 1.00	36.24 ± 0.67	0.56	20.59 ± 0.89	23.33 ± 0.56
33	NGC 0257	Sc	75.17	0.71	5054.03 ± 48.01	0.68 ± 0.06	47.0 ± 1.04	4.84 ± 0.82	21.61 ± 0.40	40.05 ± 0.25	0.67	23.13 ± 1.27	21.94 ± 0.61
38	NGC 0447	Sa	79.94	0.98	634.8 ± 5.97	0.0 ± 0.11	6.99 ± 1.67	0.38 ± 0.04	…	…	…	5.56 ± 0.48	7.44 ± 0.24
39	NGC 0444	Scd	69.18	0.31	973.51 ± 4.42	0.0 ± 0.06	10.04 ± 0.39	0.55 ± 0.09	5.90 ± 0.43	10.06 ± 0.06	0.58	…	1.40 ± 0.15
40	UGC 00809	Scd	60.04	0.15	980.49 ± 3.06	0.58 ± 0.02	8.28 ± 0.66	0.78 ± 0.14	2.93 ± 0.19	4.61 ± 0.17	0.49	1.86 ± 0.42	1.95 ± 0.09
41	UGC 00841	Sbc	79.83	0.2	725.9 ± 3.37	0.3 ± 0.06	7.69 ± 0.46	0.56 ± 0.10	2.85 ± 0.50	6.12 ± 0.04	0.83	…	1.92 ± 0.12
42	NGC 0477	Sbc	83.83	0.54	1597.8 ± 10.14	0.46 ± 0.07	27.51 ± 0.94	2.31 ± 0.39	26.14 ± 0.24	38.85 ± 0.48	0.43	8.42 ± 0.31	9.07 ± 0.37
43	IC 1683	Sb	69.36	0.46	1829.71 ± 7.21	1.35 ± 0.04	10.74 ± 0.66	2.06 ± 0.36	1.37 ± 0.21	3.77 ± 0.12	1.1	15.24 ± 1.04	19.03 ± 0.35
45	NGC 0496	Scd	85.95	0.54	3039.25 ± 9.26	0.63 ± 0.04	32.59 ± 0.38	3.20 ± 0.53	18.84 ± 0.17	29.31 ± 0.18	0.48	11.77 ± 1.64	10.01 ± 0.31
48	NGC 0523	Sd	69.53	0.29	1628.81 ± 20.50	0.86 ± 0.04	21.66 ± 0.65	2.63 ± 0.45	6.96 ± 0.26	15.52 ± 0.10	0.87	15.63 ± 0.97	17.49 ± 0.84
49	UGC 00987	Sa	66.53	0.3	1340.65 ± 11.35	0.72 ± 0.06	12.06 ± 0.65	1.29 ± 0.23	5.21 ± 0.72	7.88 ± 0.15	0.45	3.30 ± 0.24	4.35 ± 0.14
52	NGC 0551	Sbc	74.37	0.44	2131.63 ± 14.69	0.55 ± 0.04	19.75 ± 4.51	1.80 ± 0.51	…	…	…	6.13 ± 0.27	6.53 ± 0.37
53	UGC 01057	Sc	90.68	0.32	1716.37 ± 12.49	0.16 ± 0.05	21.04 ± 0.29	1.35 ± 0.23	15.19 ± 0.14	20.21 ± 0.12	0.31	5.28 ± 0.82	5.07 ± 0.27

ID	Name	Type	Dist (Mpc)	b/a	$F(\mathrm{H}\alpha_{\mathrm{obs}})$ ($\times 10^{-16}$ cgs)	$A(\mathrm{H}\alpha)$ (mag)	$L(\mathrm{H}\alpha_{\mathrm{obs}})$ ($\times 10^{40}$ erg s^{-1})	$SFR[\mathrm{H}\alpha_{\mathrm{corr}}]$ ($M_\odot$ yr^{-1})	$L(\mathrm{FUV}_{\mathrm{obs}})$ ($\times 10^{42}$ erg s^{-1})	$L(\mathrm{NUV}_{\mathrm{obs}})$ ($\times 10^{42}$ erg s^{-1})	F−N (AB mag)	L(TIR) ($\times 10^{43}$ erg s^{-1})	$L(22\,\mu\mathrm{m})$ ($\times 10^{42}$ erg s^{-1})
(1)	(2)	(3)	(4)	(5)	(6)	(7)	(8)	(9)	(10)	(11)	(12)	(13)	(14)
56	UGC 01110	Sc	40.23	0.36	824.77 ± 14.38	0.0 ± 0.04	2.60 ± 0.01	0.14 ± 0.02	1.84 ± 0.05	2.73 ± 0.03	0.43	…	0.55 ± 0.07
61	NGC 0681	Sa	25.16	0.63	4494.5 ± 39.20	1.03 ± 0.04	5.66 ± 1.61	0.80 ± 0.26	…	…	…	3.20 ± 0.17	2.86 ± 0.08
65	NGC 0716	Sb	65.66	0.42	5263.42 ± 51.60	0.88 ± 0.08	36.34 ± 0.55	4.49 ± 0.76	9.49 ± 0.09	14.90 ± 0.09	0.49	34.78 ± 1.67	41.14 ± 0.83
66	UGC 01368	Sab	114.74	0.33	324.27 ± 6.31	2.09 ± 0.05	5.6 ± 0.56	2.11 ± 0.43	4.19 ± 0.62	7.21 ± 0.31	0.59	…	4.34 ± 0.43
70	IC 1755	Sb	113.21	0.22	276.5 ± 6.49	0.0 ± 0.14	5.89 ± 0.22	0.32 ± 0.02	3.72 ± 0.10	6.06 ± 0.07	0.53	…	3.42 ± 0.60
71	NGC 0768	Sc	100.01	0.48	3116.02 ± 104.59	0.38 ± 0.09	47.04 ± 1.94	3.68 ± 0.74	25.74 ± 0.71	40.06 ± 0.49	0.48	10.74 ± 0.67	12.55 ± 0.45
73	NGC 0776	Sb	70.29	0.98	4594.42 ± 12.53	0.67 ± 0.04	32.37 ± 0.81	3.31 ± 0.55	25.84 ± 1.67	34.38 ± 0.21	0.31	14.42 ± 1.15	12.61 ± 0.34
77	NGC 0825	Sa	48.52	0.39	475.93 ± 6.08	0.0 ± 0.10	2.01 ± 0.28	0.11 ± 0.01	1.52 ± 0.24	2.30 ± 0.18	0.45	…	0.71 ± 0.08
78	NGC 0833	Sa	54.94	0.48	829.28 ± 8.20	0.0 ± 0.09	4.42 ± 1.09	0.24 ± 0.04	0.66 ± 0.10	114.38 ± 10.16	5.59	21.77 ± 1.45	0.83 ± 0.04
88	UGC 01938	Sbc	91.36	0.23	1433.02 ± 11.37	0.19 ± 0.05	17.9 ± 3.32	1.17 ± 0.29	…	…	…	4.85 ± 0.33	6.24 ± 0.27
100	NGC 1056	Sa	22.14	0.48	9129.11 ± 23.11	1.23 ± 0.02	7.34 ± 1.62	1.25 ± 0.35	…	…	…	3.34 ± 0.19	3.63 ± 0.06
108	NGC 1093	Sbc	75.85	0.65	1646.19 ± 11.59	0.0 ± 0.07	16.12 ± 0.63	0.89 ± 0.14	17.16 ± 1.26	21.80 ± 0.27	0.26	4.36 ± 0.32	4.97 ± 0.22
115	UGC 02403	Sb	58.73	0.4	2022.92 ± 13.47	1.67 ± 0.05	10.52 ± 0.17	2.70 ± 0.45	2.31 ± 0.11	3.91 ± 0.02	0.57	27.24 ± 1.25	38.99 ± 0.72
116	UGC 02405	Sbc	110.12	0.38	1712.66 ± 23.12	0.0 ± 0.07	34.38 ± 7.71	1.89 ± 0.51	…	…	…	7.95 ± 0.46	7.47 ± 0.45
131	NGC 1542	Sab	53.38	0.37	603.47 ± 7.10	0.81 ± 0.10	2.66 ± 0.53	0.31 ± 0.08	…	…	…	3.64 ± 0.40	1.83 ± 0.08
132	UGC 03038	Sab	115.71	0.23	647.4 ± 12.22	0.55 ± 0.14	12.2 ± 3.07	1.12 ± 0.34	…	…	…	8.66 ± 0.44	9.06 ± 0.58
133	UGC 03107	Sb	121.24	0.28	1205.67 ± 37.35	0.91 ± 0.11	26.17 ± 4.78	3.32 ± 0.88	…	…	…	15.33 ± 0.47	17.58 ± 0.58
134	NGC 1645	S0a	69.65	0.45	645.37 ± 11.18	0.00 ± 0.12	11.89 ± 1.12	0.65 ± 0.04	8.88 ± 0.98	15.72 ± 1.18	0.62	…	1.31 ± 0.21
141	IC 2095	Sc	40.89	0.22	986.85 ± 2.46	0.06 ± 0.02	3.43 ± 1.02	0.20 ± 0.07	…	…	…	…	…
143	NGC 1677	Scd	39.57	0.34	2771.85 ± 7.53	0.45 ± 0.04	6.59 ± 1.26	0.55 ± 0.14	…	…	…	2.19 ± 0.26	2.23 ± 0.06
146	UGC 03253	Sb	59.0	0.63	2236.96 ± 13.16	0.32 ± 0.06	12.90 ± 2.89	0.96 ± 0.27	…	…	…	3.77 ± 0.25	4.17 ± 0.15
147	NGC 2253	Sbc	51.24	0.74	2418.9 ± 8.81	0.9 ± 0.03	9.01 ± 0.16	1.13 ± 0.19	11.21 ± 0.10	19.85 ± 0.12	0.62	13.44 ± 0.62	15.73 ± 0.30
149	NGC 2347	Sbc	63.67	0.71	5451.42 ± 87.09	0.18 ± 0.06	36.28 ± 1.38	2.37 ± 0.42	14.54 ± 0.27	27.45 ± 0.51	0.69	13.93 ± 0.87	11.80 ± 0.30
150	UGC 03899	Sd	55.53	0.27	1473.73 ± 3.57	0.18 ± 0.03	6.67 ± 1.18	0.43 ± 0.11	6.02 ± 0.22	8.62 ± 0.11	0.39	…	0.40 ± 0.12
151	NGC 2410	Sb	66.82	0.29	2201.04 ± 27.36	0.45 ± 0.05	22.12 ± 7.09	1.84 ± 0.67	…	…	…	15.48 ± 0.91	25.43 ± 0.47
152	UGC 03944	Sbc	55.82	0.45	1854.12 ± 7.28	0.19 ± 0.04	10.67 ± 0.22	0.70 ± 0.12	9.82 ± 0.63	13.81 ± 0.09	0.37	1.46 ± 0.20	1.65 ± 0.12
153	UGC 03969	Sb	117.84	0.2	908.47 ± 13.14	0.91 ± 0.09	18.62 ± 1.39	2.37 ± 0.44	3.51 ± 0.81	6.63 ± 0.20	0.69	16.23 ± 1.80	14.99 ± 0.59
154	UGC 03973	Sbc	94.29	1.0	5742.33 ± 196.92	1.61 ± 0.17	75.27 ± 13.73	18.20 ± 4.91	69.74 ± 0.64	77.17 ± 0.48	0.11	51.06 ± 1.90	116.55 ± 2.25
155	UGC 03995	Sb	68.28	0.45	1535.73 ± 14.38	0.05 ± 0.09	23.21 ± 0.36	1.33 ± 0.23	13.65 ± 0.13	21.24 ± 0.13	0.48	16.75 ± 1.89	24.97 ± 0.48
156	NGC 2449	Sab	70.01	0.48	1278.65 ± 32.52	0.53 ± 0.10	8.32 ± 0.42	0.75 ± 0.14	4.22 ± 0.31	8.97 ± 0.22	0.82	5.27 ± 0.28	3.98 ± 0.22
165	UGC 04132	Sbc	74.46	0.3	4701.41 ± 75.78	1.09 ± 0.05	52.74 ± 15.33	7.89 ± 2.67	9.09 ± 0.59	17.96 ± 0.11	0.74	32.44 ± 1.36	29.99 ± 0.69
186	IC 2247	Sab	61.8	0.16	1008.76 ± 7.90	1.11 ± 0.06	7.25 ± 1.94	1.11 ± 0.35	…	…	…	8.27 ± 1.45	7.20 ± 0.20
208	UGC 04461	Sbc	71.31	0.35	2548.35 ± 7.99	0.58 ± 0.02	23.91 ± 0.28	2.24 ± 0.37	12.97 ± 0.24	18.92 ± 0.12	0.41	6.66 ± 0.58	8.28 ± 0.25
213	NGC 2623	Scd	79.17	0.42	606.17 ± 6.15	0.00 ± 0.20	6.65 ± 1.62	0.37 ± 0.05	8.47 ± 0.23	15.55 ± 0.19	0.66	134.64 ± 5.25	122.22 ± 2.25
219	NGC 2639	Sa	46.52	0.6	2892.4 ± 124.48	0.11 ± 0.13	9.32 ± 0.41	0.57 ± 0.12	2.84 ± 0.03	7.83 ± 0.05	1.1	8.32 ± 0.45	5.71 ± 0.15
226	UGC 04659	Sdm	25.97	0.47	341.16 ± 2.69	0.25 ± 0.08	0.4 ± 0.10	0.03 ± 0.01	1.12 ± 0.03	1.55 ± 0.01	0.36	…	…
231	UGC 04722	Sdm	24.66	0.33	1556.99 ± 3.91	0.11 ± 0.03	1.43 ± 0.27	0.09 ± 0.02	2.57 ± 0.02	3.18 ± 0.02	0.23	…	…
232	NGC 2730	Scd	54.95	0.74	4530.91 ± 12.11	0.46 ± 0.02	19.26 ± 0.28	1.62 ± 0.27	16.69 ± 0.31	22.62 ± 0.14	0.33	4.22 ± 0.19	5.35 ± 0.20
273	IC 2487	Sc	62.25	0.33	1731.12 ± 12.33	0.63 ± 0.06	17.2 ± 0.52	1.69 ± 0.29	4.56 ± 0.29	8.69 ± 0.05	0.7	5.02 ± 0.46	4.38 ± 0.23
274	IC 0540	Sab	29.6	0.27	393.61 ± 3.56	0.16 ± 0.1	0.47 ± 0.02	0.03 ± 0.01	0.13 ± 0.01	0.36 ± 0.01	1.15	…	0.37 ± 0.02
275	NGC 2906	Sbc	30.59	0.59	5416.94 ± 35.66	0.71 ± 0.02	6.41 ± 0.13	0.68 ± 0.11	3.20 ± 0.03	5.67 ± 0.03	0.62	3.06 ± 0.30	2.28 ± 0.11
277	NGC 2916	Sbc	53.31	0.68	3630.93 ± 54.72	0.4 ± 0.06	23.85 ± 0.48	1.90 ± 0.33	21.49 ± 0.20	33.13 ± 0.20	0.47	7.52 ± 0.37	7.36 ± 0.54
278	UGC 05108	Sb	116.19	0.65	1008.07 ± 8.14	0.96 ± 0.11	24.48 ± 2.40	3.27 ± 0.63	9.40 ± 0.95	17.26 ± 1.06	0.66	25.07 ± 1.68	27.82 ± 0.72
306	UGC 05358	Sd	41.59	0.62	1331.74 ± 5.13	0.13 ± 0.03	3.56 ± 0.70	0.22 ± 0.06	3.35 ± 0.25	4.54 ± 0.17	0.33	…	…
307	UGC 05359	Sb	121.27	0.35	686.14 ± 7.68	0.0 ± 0.12	19.9 ± 0.97	1.09 ± 0.18	13.25 ± 0.85	20.61 ± 0.51	0.48	…	7.88 ± 0.81
309	UGC 05396	Sbc	77.51	0.45	1171.19 ± 11.36	0.19 ± 0.10	10.51 ± 1.94	0.69 ± 0.17	…	…	…	2.98 ± 0.33	2.62 ± 0.38
310	UGC 05391	Sm	22.41	0.90	1159.09 ± 34.93	0.0 ± 0.06	1.01 ± 0.24	0.06 ± 0.01	2.58 ± 0.98	3.28 ± 0.76	0.26	…	…
311	NGC 3106	Sab	88.75	1.0	1005.35 ± 17.58	0.0 ± 0.19	14.36 ± 2.06	0.79 ± 0.10	7.92 ± 3.14	19.54 ± 1.80	0.98	4.67 ± 0.49	4.33 ± 0.73
312	NGC 3057	Sdm	21.79	0.59	3416.93 ± 8.27	0.0 ± 0.02	4.06 ± 0.06	0.22 ± 0.03	4.44 ± 0.08	5.64 ± 0.03	0.26	0.39 ± 0.04	0.33 ± 0.07

ID	Name	Type	Dist (Mpc)	b/a	$F(\mathrm{H}\alpha_{\mathrm{obs}})$ ($\times 10^{-16}$ cgs)	$A(\mathrm{H}\alpha)$ (mag)	$L(\mathrm{H}\alpha_{\mathrm{obs}})$ ($\times 10^{40}$ erg s^{-1})	$SFR[\mathrm{H}\alpha_{\mathrm{corr}}]$ ($M_\odot$ yr^{-1})	$L(\mathrm{FUV}_{\mathrm{obs}})$ ($\times 10^{42}$ erg s^{-1})	$L(\mathrm{NUV}_{\mathrm{obs}})$ ($\times 10^{42}$ erg s^{-1})	F−N (AB mag)	L(TIR) ($\times 10^{43}$ erg s^{-1})	$L(22\,\mu\mathrm{m})$ ($\times 10^{42}$ erg s^{-1})
(1)	(2)	(3)	(4)	(5)	(6)	(7)	(8)	(9)	(10)	(11)	(12)	(13)	(14)
314	UGC 05498NED01	Sa	90.12	0.2	345.63 ± 4.43	0.0 ± 0.10	5.95 ± 1.81	0.33 ± 0.09	…	…	…	5.89 ± 0.79	5.02 ± 0.32
326	UGC 05598	Sb	80.39	0.25	1013.28 ± 5.61	0.46 ± 0.04	10.33 ± 2.13	0.87 ± 0.23	…	…	…	5.58 ± 0.55	5.04 ± 0.27
340	NGC 3303	S0a	85.71	0.71	1056.24 ± 11.80	0.0 ± 0.10	25.13 ± 0.75	1.38 ± 0.23	3.23 ± 0.48	9.74 ± 0.12	1.2	…	1.49 ± 0.20
353	NGC 3381	Sd	23.21	0.91	6641.87 ± 13.79	0.36 ± 0.01	5.36 ± 0.06	0.41 ± 0.07	5.08 ± 0.05	7.55 ± 0.05	0.43	1.26 ± 0.11	1.25 ± 0.03
361	UGC 05990	Sc	23.13	0.25	1187.42 ± 15.85	0.57 ± 0.19	1.00 ± 0.20	0.09 ± 0.02	0.42 ± 0.03	0.65 ± 0.00	0.46	0.20 ± 0.02	0.18 ± 0.01
364	UGC 06036	Sa	93.57	0.21	315.62 ± 8.19	0.0 ± 0.26	4.62 ± 0.50	0.25 ± 0.05	1.00 ± 0.27	2.79 ± 0.10	1.11	…	2.27 ± 0.40
381	IC 0674	Sab	107.44	0.44	561.39 ± 5.75	0.0 ± 0.09	14.18 ± 1.43	0.78 ± 0.10	11.94 ± 1.21	18.40 ± 1.13	0.47	…	2.14 ± 0.33
388	NGC 3614	Sbc	33.15	0.61	2513.2 ± 11.34	0.48 ± 0.04	16.76 ± 0.28	1.44 ± 0.24	13.29 ± 0.24	17.85 ± 0.11	0.32	2.29 ± 0.20	2.00 ± 0.62
414	NGC 3687	Sb	35.75	1.0	3223.0 ± 9.14	0.29 ± 0.03	7.23 ± 0.10	0.52 ± 0.09	8.34 ± 0.15	11.51 ± 0.07	0.35	1.73 ± 0.11	1.41 ± 0.09
436	NGC 3811	Sbc	43.92	0.76	5634.04 ± 63.11	0.78 ± 0.04	17.4 ± 3.68	1.96 ± 0.53	…	…	…	6.76 ± 0.49	7.15 ± 0.18
437	NGC 3815	Sbc	53.08	0.54	3007.07 ± 22.02	0.52 ± 0.03	12.12 ± 0.42	1.08 ± 0.18	7.19 ± 0.33	11.39 ± 0.21	0.5	3.73 ± 0.14	3.43 ± 0.14
475	NGC 3991	Sm	46.46	0.28	12687.14 ± 21.54	0.23 ± 0.01	36.46 ± 0.46	2.48 ± 0.41	31.67 ± 0.29	39.51 ± 0.24	0.24	7.83 ± 0.46	8.96 ± 0.22
476	NGC 3994	Sbc	44.16	0.56	11022.62 ± 97.94	1.01 ± 0.02	31.51 ± 5.58	4.38 ± 1.07	8.41 ± 0.15	13.45 ± 0.17	0.51	8.82 ± 0.46	11.72 ± 0.21
479	NGC 4003	S0a	93.86	0.59	496.7 ± 7.42	0.0 ± 0.12	6.5 ± 1.19	0.36 ± 0.03	…	…	…	4.80 ± 0.52	4.91 ± 0.21
486	UGC 07012	Scd	43.78	0.54	3001.7 ± 6.44	0.3 ± 0.02	9.02 ± 1.84	0.65 ± 0.17	…	…	…	…	0.87 ± 0.05
489	NGC 4047	Sbc	49.2	0.85	7567.21 ± 28.13	0.76 ± 0.03	31.30 ± 7.36	3.48 ± 1.00	…	…	…	15.45 ± 0.87	13.34 ± 0.27
502	NGC 4149	Sa	44.02	0.2	792.2 ± 13.11	0.05 ± 0.06	2.44 ± 0.51	0.14 ± 0.04	…	…	…	4.50 ± 0.32	3.09 ± 0.08
515	NGC 4185	Sbc	55.52	0.74	1811.94 ± 11.78	0.3 ± 0.08	11.73 ± 3.53	0.85 ± 0.29	…	…	…	4.00 ± 0.50	4.12 ± 0.31
518	NGC 4210	Sb	38.85	0.78	3446.38 ± 14.31	0.44 ± 0.03	8.99 ± 2.15	0.74 ± 0.22	…	…	…	2.73 ± 0.21	2.05 ± 0.15
520	NGC 4211NED02	S0a	95.62	0.29	311.56 ± 2.79	0.85 ± 0.14	4.24 ± 0.78	0.51 ± 0.13	…	…	…	11.06 ± 1.24	15.74 ± 0.44
528	IC 0776	Sdm	34.89	0.66	2147.53 ± 5.77	0.0 ± 0.02	4.12 ± 0.84	0.23 ± 0.05	…	…	…	…	0.55 ± 0.08
548	NGC 4470	Sc	33.71	0.72	8400.82 ± 14.94	0.5 ± 0.01	16.05 ± 3.68	1.39 ± 0.39	…	…	…	3.10 ± 0.25	2.81 ± 0.08
569	NGC 4644	Sb	70.52	0.31	1054.53 ± 5.80	0.0 ± 0.07	9.43 ± 2.38	0.52 ± 0.12	…	…	…	…	2.95 ± 0.17
580	NGC 4711	Sbc	58.25	0.57	2460.2 ± 13.15	0.45 ± 0.04	12.78 ± 2.48	1.07 ± 0.27	…	…	…	3.72 ± 0.25	4.38 ± 0.17
593	UGC 08107	Sa	118.66	0.43	1929.57 ± 27.48	0.2 ± 0.07	56.23 ± 16.72	3.71 ± 1.27	…	…	…	22.91 ± 1.81	18.79 ± 0.57
603	NGC 4961	Scd	36.64	0.69	4494.24 ± 13.10	0.13 ± 0.02	9.28 ± 1.82	0.58 ± 0.15	…	…	…	2.10 ± 0.17	2.02 ± 0.06
606	UGC 08231	Sd	35.38	0.5	3228.46 ± 8.91	0.0 ± 0.02	6.28 ± 1.26	0.35 ± 0.08	…	…	…	0.67 ± 0.12	0.64 ± 0.05
608	NGC 5000	Sbc	79.99	0.85	1520.88 ± 13.82	0.69 ± 0.09	15.2 ± 3.07	1.57 ± 0.41	…	…	…	10.04 ± 0.60	11.33 ± 0.27
609	UGC 08250	Sc	75.41	0.22	757.06 ± 4.07	0.36 ± 0.05	6.61 ± 1.29	0.51 ± 0.13	…	…	…	…	2.47 ± 0.14
610	UGC 08267	Sb	103.64	0.23	618.61 ± 6.58	0.17 ± 0.09	10.15 ± 1.97	0.65 ± 0.17	…	…	…	13.75 ± 1.54	12.03 ± 0.35
611	NGC 5016	Sbc	37.37	0.74	5183.36 ± 36.60	0.6 ± 0.05	12.59 ± 3.04	1.21 ± 0.35	…	…	…	3.86 ± 0.23	3.34 ± 0.10
613	UGC 08322	S0a	108.76	0.2	371.21 ± 18.63	0.0 ± 0.15	6.44 ± 1.18	0.35 ± 0.06	…	…	…	…	3.42 ± 0.37
614	NGC 5056	Sc	79.41	0.57	4232.77 ± 29.45	0.19 ± 0.03	43.88 ± 0.67	2.89 ± 0.48	38.94 ± 0.36	48.57 ± 0.30	0.24	11.70 ± 1.01	12.22 ± 0.29
615	IC 4215	Sb	55.7	0.15	299.29 ± 2.54	0.0 ± 0.11	1.84 ± 0.53	0.10 ± 0.02	…	…	…	1.89 ± 0.18	2.26 ± 0.08
624	NGC 5157	Sab	104.68	0.72	576.79 ± 8.05	0.0 ± 0.24	14.9 ± 1.38	0.82 ± 0.05	10.63 ± 2.54	17.00 ± 0.94	0.51	…	…
630	NGC 5205	Sbc	25.31	0.57	1614.02 ± 9.62	0.0 ± 0.08	3.04 ± 0.07	0.17 ± 0.03	3.17 ± 0.09	4.50 ± 0.06	0.38	0.79 ± 0.08	0.65 ± 0.06
634	NGC 5218	Sab	41.41	0.69	1846.77 ± 14.41	1.17 ± 0.07	6.03 ± 1.64	0.97 ± 0.31	1.35 ± 0.19	4.29 ± 0.03	1.26	14.94 ± 0.56	21.27 ± 0.37
651	NGC 5267	Sab	84.69	0.37	1051.8 ± 20.30	0.0 ± 0.07	11.47 ± 0.43	0.63 ± 0.08	8.21 ± 0.76	11.97 ± 0.07	0.41	4.43 ± 0.46	4.85 ± 0.33
652	UGC 08662	Scd	28.9	0.3	700.48 ± 2.96	0.0 ± 0.04	0.9 ± 0.03	0.05 ± 0.01	0.76 ± 0.03	1.13 ± 0.01	0.43	…	0.10 ± 0.02
653	NGC 5289	Sab	36.18	0.32	1336.39 ± 5.69	0.57 ± 0.04	4.15 ± 0.11	0.38 ± 0.06	2.78 ± 0.05	3.83 ± 0.05	0.35	0.93 ± 0.08	1.06 ± 0.05
657	UGC 08733	Sdm	33.42	0.65	1737.45 ± 4.95	0.07 ± 0.03	5.25 ± 0.18	0.31 ± 0.05	6.83 ± 0.06	8.53 ± 0.16	0.24	0.44 ± 0.07	0.44 ± 0.05
659	NGC 5320	Sbc	37.49	0.51	3216.34 ± 14.83	0.49 ± 0.02	16.42 ± 0.30	1.42 ± 0.24	12.09 ± 0.11	16.38 ± 0.10	0.33	2.80 ± 0.15	2.96 ± 0.16
663	IC 0944	Sab	100.11	0.34	625.43 ± 78.03	0.12 ± 0.37	11.3 ± 1.57	0.69 ± 0.32	2.40 ± 0.18	6.42 ± 0.16	1.07	13.95 ± 0.63	12.81 ± 0.41
664	UGC 08778	Sb	46.38	0.21	596.48 ± 5.80	0.14 ± 0.07	1.75 ± 0.06	0.11 ± 0.02	0.82 ± 0.05	1.60 ± 0.01	0.72	…	0.67 ± 0.07
665	UGC 08781	Sb	108.38	0.5	655.29 ± 14.79	0.26 ± 0.14	16.82 ± 2.00	1.18 ± 0.25	14.47 ± 3.07	26.57 ± 1.96	0.66	…	4.72 ± 0.88
676	NGC 5378	Sb	42.89	0.83	704.07 ± 9.59	0.0 ± 0.16	3.94 ± 0.18	0.22 ± 0.03	3.43 ± 0.22	5.00 ± 0.03	0.41	…	1.11 ± 0.19
680	NGC 5394	Sbc	48.73	0.56	3805.28 ± 15.39	1.38 ± 0.04	14.05 ± 0.52	2.76 ± 0.47	3.48 ± 0.55	7.48 ± 0.18	0.83	21.54 ± 0.62	36.41 ± 0.57
684	NGC 5406	Sb	77.16	0.74	2406.29 ± 19.18	0.35 ± 0.05	28.21 ± 0.51	2.14 ± 0.36	23.41 ± 0.22	33.53 ± 0.21	0.39	9.99 ± 0.70	9.72 ± 1.09
707	NGC 5480	Scd	27.05	0.66	9886.46 ± 18.44	0.74 ± 0.01	11.87 ± 2.62	1.30 ± 0.36	…	…	…	4.15 ± 0.14	4.80 ± 0.09
714	UGC 09067	Sbc	112.16	0.49	2150.23 ± 24.56	0.52 ± 0.05	40.11 ± 7.29	3.56 ± 0.88	23.24 ± 0.64	33.91 ± 0.42	0.41	11.44 ± 0.35	12.10 ± 0.36
715	NGC 5520	Sbc	26.83	0.55	7436.51 ± 30.18	0.67 ± 0.02	9.01 ± 2.07	0.92 ± 0.26	3.77 ± 0.03	6.08 ± 0.04	0.52	2.77 ± 0.18	2.59 ± 0.06
718	UGC 09113	Sb	45.59	0.22	985.09 ± 4.50	1.08 ± 0.05	5.76 ± 0.26	0.85 ± 0.15	1.72 ± 0.08	2.45 ± 0.03	0.38	4.04 ± 0.37	2.75 ± 0.07

ID	Name	Type	Dist (Mpc)	b/a	$F(\mathrm{H}\alpha_{\mathrm{obs}})$ ($\times 10^{-16}$ cgs)	$A(\mathrm{H}\alpha)$ (mag)	$L(\mathrm{H}\alpha_{\mathrm{obs}})$ ($\times 10^{40}$ erg s^{-1})	$SFR[\mathrm{H}\alpha_{\mathrm{corr}}]$ ($M_\odot$ yr^{-1})	$L(\mathrm{FUV}_{\mathrm{obs}})$ ($\times 10^{42}$ erg s^{-1})	$L(\mathrm{NUV}_{\mathrm{obs}})$ ($\times 10^{42}$ erg s^{-1})	F−N (AB mag)	L(TIR) ($\times 10^{43}$ erg s^{-1})	$L(22\,\mu\mathrm{m})$ ($\times 10^{42}$ erg s^{-1})
(1)	(2)	(3)	(4)	(5)	(6)	(7)	(8)	(9)	(10)	(11)	(12)	(13)	(14)
720	NGC 5522	Sb	65.58	0.21	1594.71 ± 14.97	0.73 ± 0.04	16.79 ± 0.44	1.82 ± 0.31	4.92 ± 0.41	10.77 ± 0.07	0.85	13.00 ± 1.22	11.38 ± 0.25
725	IC 0995	Scd	45.2	0.24	1122.24 ± 3.96	0.26 ± 0.03	3.37 ± 0.08	0.24 ± 0.04	3.92 ± 0.18	5.66 ± 0.07	0.4	0.73 ± 0.12	0.62 ± 0.05
737	NGC 5602	S0a	31.78	0.53	323.8 ± 8.32	0.0 ± 0.17	0.57 ± 0.05	0.03 ± 0.01	…	…	…	…	0.09 ± 0.02
740	NGC 5614	Sa	55.59	0.83	1490.19 ± 11.72	0.33 ± 0.09	8.6 ± 0.31	0.64 ± 0.11	5.02 ± 0.18	11.29 ± 0.21	0.88	9.63 ± 0.64	7.78 ± 0.24
741	NGC 5616	Sc	122.17	0.2	1434.33 ± 18.79	1.18 ± 0.06	32.62 ± 6.29	5.31 ± 1.37	15.87 ± 2.05	26.33 ± 1.78	0.55	40.92 ± 3.61	37.42 ± 1.03
742	NGC 5610	Sb	72.39	0.33	3307.52 ± 20.42	0.82 ± 0.02	36.38 ± 10.95	4.25 ± 1.46	13.49 ± 1.12	19.86 ± 0.24	0.42	31.86 ± 1.32	52.50 ± 0.87
743	NGC 5622	Sbc	55.54	0.57	2352.76 ± 13.80	0.49 ± 0.03	11.03 ± 0.31	0.95 ± 0.16	8.31 ± 0.15	12.70 ± 0.16	0.46	2.65 ± 0.20	2.82 ± 0.15
747	UGC 09262	Sab	122.33	0.14	992.55 ± 16.32	2.09 ± 0.06	21.9 ± 0.45	8.25 ± 1.44	8.43 ± 0.16	12.75 ± 0.08	0.45	37.44 ± 4.53	36.30 ± 0.77
748	NGC 5633	Sbc	33.24	0.62	8369.48 ± 30.71	0.84 ± 0.02	14.89 ± 3.18	1.78 ± 0.48	…	…	…	5.33 ± 0.24	5.62 ± 0.11
749	NGC 5630	Sdm	37.98	0.36	6765.18 ± 10.41	0.45 ± 0.01	18.14 ± 0.28	1.52 ± 0.25	10.91 ± 0.10	16.06 ± 0.10	0.42	3.01 ± 0.12	2.80 ± 0.08
750	NGC 5635	Sa	61.7	0.49	1392.19 ± 16.59	0.58 ± 0.09	13.25 ± 0.58	1.25 ± 0.22	7.43 ± 0.21	11.78 ± 0.07	0.5	4.67 ± 0.54	3.13 ± 0.14
751	UGC 09291	Scd	41.31	0.59	2057.09 ± 7.59	0.15 ± 0.04	6.86 ± 1.92	0.43 ± 0.14	…	…	…	1.27 ± 0.09	1.35 ± 0.11
753	NGC 5656	Sb	45.13	0.78	6985.15 ± 75.32	0.53 ± 0.03	20.49 ± 0.44	1.83 ± 0.31	9.81 ± 0.09	16.27 ± 0.20	0.55	9.75 ± 0.34	9.01 ± 0.19
754	NGC 5657	Sbc	56.06	0.41	2452.82 ± 9.47	0.83 ± 0.03	14.98 ± 4.17	1.77 ± 0.57	5.97 ± 0.05	9.20 ± 0.06	0.47	7.04 ± 0.66	8.71 ± 0.17
755	NGC 5659	Sb	64.36	0.27	1074.51 ± 5.47	0.51 ± 0.05	9.72 ± 0.79	0.86 ± 0.16	3.10 ± 0.14	6.48 ± 0.24	0.8	5.66 ± 0.64	3.65 ± 0.16
756	NGC 5665	Sc	31.75	0.71	15687.1 ± 20.27	0.8 ± 0.01	33.94 ± 10.43	3.89 ± 1.36	7.08 ± 0.07	12.89 ± 0.08	0.65	8.03 ± 0.18	12.22 ± 0.20
757	NGC 5675	Sa	56.62	0.35	1185.3 ± 22.43	0.20 ± 0.11	10.25 ± 0.36	0.68 ± 0.12	2.86 ± 0.03	6.80 ± 0.08	0.94	4.99 ± 0.43	3.78 ± 0.10
758	NGC 5682	Scd	32.47	0.34	2441.9 ± 4.40	0.4 ± 0.02	4.22 ± 0.04	0.34 ± 0.06	2.19 ± 0.02	3.64 ± 0.02	0.55	0.68 ± 0.10	0.64 ± 0.03
763	NGC 5714	Sb	32.28	0.12	1105.81 ± 4.72	1.13 ± 0.03	7.35 ± 0.29	1.15 ± 0.20	2.13 ± 0.12	3.50 ± 0.04	0.54	2.19 ± 0.13	1.90 ± 0.06
764	NGC 5720	Sbc	111.3	0.66	940.15 ± 10.36	0.0 ± 0.11	17.37 ± 3.20	0.96 ± 0.20	…	…	…	…	5.15 ± 0.92
765	UGC 09448	Sb	31.61	0.11	460.05 ± 1.63	0.76 ± 0.04	0.74 ± 0.16	0.08 ± 0.02	…	…	…	0.41 ± 0.04	0.32 ± 0.02
766	NGC 5730	Scd	36.15	0.2	1920.86 ± 5.54	0.83 ± 0.02	3.82 ± 0.74	0.45 ± 0.11	…	…	…	1.99 ± 0.23	1.71 ± 0.05
767	NGC 5731	Sd	36.07	0.32	3391.82 ± 8.35	0.06 ± 0.01	7.72 ± 1.88	0.45 ± 0.13	…	…	…	0.91 ± 0.25	0.95 ± 0.04
768	NGC 5732	Sbc	53.88	0.54	2352.9 ± 6.56	0.55 ± 0.02	10.26 ± 1.92	0.94 ± 0.23	…	…	…	2.53 ± 0.17	2.27 ± 0.08
769	UGC 09476	Sbc	46.77	0.65	3659.45 ± 8.84	0.65 ± 0.03	12.84 ± 2.73	1.28 ± 0.35	…	…	…	3.73 ± 0.34	3.27 ± 0.12
770	NGC 5739	S0a	79.11	0.91	785.48 ± 9.81	0.0 ± 0.13	8.58 ± 2.08	0.47 ± 0.05	…	…	…	2.59 ± 0.33	1.94 ± 0.10
771	NGC 5735	Sbc	53.61	0.79	2522.88 ± 12.10	0.25 ± 0.04	12.02 ± 2.70	0.83 ± 0.23	…	…	…	4.97 ± 0.62	3.86 ± 0.55
774	UGC 09537	Sb	126.22	0.22	484.34 ± 18.49	0.0 ± 0.16	43.89 ± 2.4	2.41 ± 0.30	18.92 ± 1.05	29.16 ± 0.18	0.47	13.82 ± 1.13	18.17 ± 0.92
775	UGC 09542	Sc	78.41	0.29	1130.64 ± 6.60	0.75 ± 0.04	13.05 ± 0.40	1.44 ± 0.24	7.37 ± 0.20	10.85 ± 0.07	0.42	4.20 ± 0.37	4.70 ± 0.18
777	NGC 5772	Sab	69.77	0.62	1801.35 ± 28.99	0.24 ± 0.07	16.67 ± 0.47	1.14 ± 0.20	12.88 ± 0.59	19.14 ± 0.12	0.43	4.70 ± 0.20	5.12 ± 0.23
778	NGC 5784	S0	77.68	0.98	1305.07 ± 43.32	0.0 ± 0.12	10.62 ± 0.81	0.58 ± 0.07	4.65 ± 0.39	10.17 ± 0.44	0.85	7.61 ± 0.85	5.99 ± 0.17
779	UGC 09598	Sbc	79.89	0.38	964.16 ± 7.38	0.0 ± 0.07	9.34 ± 0.35	0.51 ± 0.07	7.04 ± 0.32	10.37 ± 0.19	0.42	2.41 ± 0.30	2.68 ± 0.21
783	UGC 09665	Sb	36.56	0.27	2797.73 ± 7.19	0.9 ± 0.02	7.99 ± 0.22	1.01 ± 0.17	1.82 ± 0.07	2.97 ± 0.02	0.53	3.74 ± 0.20	3.45 ± 0.08
784	NGC 5829	Sc	81.11	0.87	2667.82 ± 35.54	0.0 ± 0.10	26.71 ± 5.14	1.47 ± 0.33	35.70 ± 4.93	47.50 ± 2.34	0.31	11.57 ± 1.28	7.22 ± 0.29
787	NGC 5876	S0a	46.7	0.49	472.87 ± 18.06	0.0 ± 0.15	2.69 ± 0.18	0.15 ± 0.02	1.86 ± 0.07	3.41 ± 0.06	0.66	0.68 ± 0.07	0.96 ± 0.11
788	UGC 09759	Sab	49.29	0.35	541.31 ± 8.72	0.51 ± 0.22	3.03 ± 0.22	0.27 ± 0.05	0.89 ± 0.07	1.94 ± 0.06	0.85	3.22 ± 0.13	2.54 ± 0.07
789	NGC 5888	Sb	124.62	0.6	985.88 ± 24.54	0.0 ± 0.10	22.46 ± 4.02	1.24 ± 0.25	12.88 ± 1.07	22.58 ± 0.14	0.61	7.98 ± 1.59	9.10 ± 1.57
790	UGC 09777	Sbc	67.16	0.59	1769.6 ± 8.74	0.38 ± 0.05	17.15 ± 1.04	1.34 ± 0.24	9.05 ± 0.83	14.22 ± 0.53	0.49	8.28 ± 0.98	5.31 ± 0.15
791	NGC 5908	Sa	47.86	0.38	2489.7 ± 29.70	1.23 ± 0.06	17.93 ± 0.87	3.06 ± 0.54	2.18 ± 0.18	5.09 ± 0.13	0.92	17.86 ± 0.47	17.77 ± 0.33
792	UGC 09842	Sbc	127.36	0.36	1775.46 ± 12.74	1.32 ± 0.04	52.15 ± 13.32	9.70 ± 2.96	15.30 ± 1.27	24.47 ± 0.30	0.51	36.23 ± 2.70	35.95 ± 0.76
793	UGC 09849	Sd	49.64	0.22	585.91 ± 5.58	0.15 ± 0.17	2.77 ± 0.06	0.17 ± 0.03	3.33 ± 0.06	4.55 ± 0.06	0.34	…	0.51 ± 0.10
795	NGC 5930	Sab	37.5	0.53	4311.22 ± 13.33	1.39 ± 0.02	11.2 ± 0.37	2.21 ± 0.37	1.83 ± 0.02	4.64 ± 0.09	1.01	15.53 ± 0.66	33.34 ± 0.43
796	NGC 5934	Sb	79.8	0.47	1274.0 ± 192.02	1.53 ± 0.45	14.17 ± 4.05	3.19 ± 1.87	1.80 ± 0.30	4.23 ± 0.03	0.93	12.95 ± 1.07	10.21 ± 0.27
797	UGC 09873	Sb	80.52	0.25	805.85 ± 3.18	0.45 ± 0.05	8.08 ± 0.46	0.67 ± 0.12	4.27 ± 0.12	5.68 ± 0.17	0.31	…	3.84 ± 0.12
798	UGC 09892	Sbc	81.13	0.23	706.62 ± 4.29	0.38 ± 0.04	7.5 ± 1.61	0.59 ± 0.16	…	…	…	…	2.76 ± 0.15
799	NGC 5951	Scd	25.42	0.43	3010.59 ± 16.33	0.41 ± 0.07	9.19 ± 0.12	0.73 ± 0.12	3.23 ± 0.03	5.02 ± 0.03	0.48	0.90 ± 0.05	0.83 ± 0.04
800	UGC 09901	Sc	45.44	0.15	573.54 ± 1.98	0.33 ± 0.05	1.76 ± 0.32	0.13 ± 0.03	1.98 ± 0.07	2.89 ± 0.02	0.41	…	0.41 ± 0.07
801	NGC 5953	Sa	28.29	0.83	6257.23 ± 30.83	1.15 ± 0.02	9.12 ± 0.18	1.45 ± 0.24	1.90 ± 0.10	5.47 ± 0.07	1.15	10.03 ± 0.20	16.87 ± 0.19
802	ARP 220	Sd	77.74	0.81	905.5 ± 9.93	1.06 ± 0.18	7.73 ± 0.46	1.13 ± 0.20	2.44 ± 0.31	8.39 ± 0.26	1.34	407.08 ± 25.2	534.17 ± 3.94
803	NGC 5957	Sb	26.19	0.93	3272.14 ± 15.06	0.16 ± 0.03	7.18 ± 0.73	0.46 ± 0.09	7.36 ± 0.54	10.06 ± 0.68	0.34	1.23 ± 0.13	1.05 ± 0.06

ID	Name	Type	Dist (Mpc)	b/a	$F(\mathrm{H}\alpha_{\mathrm{obs}})$ ($\times 10^{-16}$ cgs)	$A(\mathrm{H}\alpha)$ (mag)	$L(\mathrm{H}\alpha_{\mathrm{obs}})$ ($\times 10^{40}$ erg s^{-1})	$SFR[\mathrm{H}\alpha_{\mathrm{corr}}]$ ($M_\odot$ yr^{-1})	$L(\mathrm{FUV}_{\mathrm{obs}})$ ($\times 10^{42}$ erg s^{-1})	$L(\mathrm{NUV}_{\mathrm{obs}})$ ($\times 10^{42}$ erg s^{-1})	F−N (AB mag)	L(TIR) ($\times 10^{43}$ erg s^{-1})	$L(22\,\mu\mathrm{m})$ ($\times 10^{42}$ erg s^{-1})
(1)	(2)	(3)	(4)	(5)	(6)	(7)	(8)	(9)	(10)	(11)	(12)	(13)	(14)
804	NGC 5971	Sb	48.3	0.35	473.6 ± 6.45	0.0 ± 0.11	2.25 ± 0.08	0.12 ± 0.01	2.74 ± 0.18	4.00 ± 0.05	0.41	…	0.34 ± 0.03
805	UGC 09919	Sc	45.53	0.28	1237.27 ± 6.61	0.67 ± 0.05	4.16 ± 0.23	0.42 ± 0.07	1.73 ± 0.11	2.83 ± 0.09	0.53	1.19 ± 0.12	1.32 ± 0.06
807	IC 4566	Sb	79.79	0.65	974.58 ± 7.29	0.0 ± 0.10	8.63 ± 0.35	0.47 ± 0.08	4.64 ± 0.56	8.21 ± 0.10	0.62	5.03 ± 0.33	4.74 ± 0.38
809	NGC 5987	Sa	42.86	0.32	464.21 ± 10.16	0.0 ± 0.16	4.67 ± 0.34	0.26 ± 0.02	1.34 ± 0.25	4.04 ± 0.15	1.2	…	1.19 ± 0.08
810	NGC 5980	Sbc	58.41	0.35	6441.01 ± 93.74	0.84 ± 0.04	36.04 ± 0.92	4.31 ± 0.75	10.85 ± 0.40	18.69 ± 0.12	0.59	18.35 ± 0.90	20.22 ± 0.35
811	UGC 10043	Sab	31.0	0.33	490.3 ± 2.72	1.14 ± 0.06	2.15 ± 0.15	0.34 ± 0.06	1.07 ± 0.08	1.46 ± 0.05	0.34	1.94 ± 0.16	1.57 ± 0.04
813	NGC 6004	Sbc	54.8	0.93	3553.6 ± 9.97	0.19 ± 0.05	16.14 ± 0.37	1.06 ± 0.18	12.71 ± 0.47	19.42 ± 0.24	0.46	7.81 ± 0.40	6.96 ± 0.19
817	IC 1151	Scd	31.1	0.41	4574.39 ± 8.56	0.47 ± 0.01	10.34 ± 0.17	0.87 ± 0.15	5.20 ± 0.05	8.17 ± 0.05	0.49	1.79 ± 0.22	1.41 ± 0.05
818	UGC 10123	Sab	53.85	0.23	1924.86 ± 26.16	1.38 ± 0.05	8.33 ± 0.41	1.64 ± 0.29	1.49 ± 0.16	2.27 ± 0.06	0.46	8.48 ± 0.54	7.63 ± 0.15
820	NGC 6032	Sbc	62.1	0.45	1030.17 ± 14.81	0.53 ± 0.17	8.79 ± 0.39	0.79 ± 0.14	3.38 ± 1.06	7.53 ± 0.09	0.87	3.10 ± 0.22	4.72 ± 0.15
821	NGC 6060	Sb	64.56	0.53	3361.37 ± 35.04	1.29 ± 0.10	37.21 ± 0.75	6.73 ± 1.14	17.48 ± 1.29	27.45 ± 0.17	0.49	16.11 ± 0.90	15.40 ± 0.37
822	UGC 10205	S0a	93.98	0.59	705.13 ± 12.28	0.0 ± 0.22	10.35 ± 0.57	0.57 ± 0.07	2.71 ± 0.67	7.95 ± 0.15	1.17	8.30 ± 0.55	6.39 ± 0.25
823	NGC 6063	Sbc	40.86	0.59	2146.08 ± 11.62	0.29 ± 0.04	6.83 ± 0.14	0.49 ± 0.08	5.51 ± 0.15	7.96 ± 0.05	0.4	1.08 ± 0.12	1.27 ± 0.11
824	IC 1199	Sb	67.71	0.34	1880.03 ± 18.29	0.62 ± 0.04	13.63 ± 0.84	1.33 ± 0.24	5.55 ± 0.26	11.91 ± 0.44	0.83	7.09 ± 0.61	5.23 ± 0.23
825	UGC 10257	Sbc	54.57	0.22	1180.6 ± 4.77	1.12 ± 0.04	8.77 ± 0.29	1.35 ± 0.23	5.81 ± 0.75	7.59 ± 0.09	0.29	1.52 ± 0.13	1.71 ± 0.08
827	UGC 10297	Sc	32.89	0.29	1910.39 ± 7.48	0.41 ± 0.02	4.26 ± 0.12	0.34 ± 0.06	1.32 ± 0.01	2.36 ± 0.03	0.63	0.52 ± 0.09	0.47 ± 0.04
828	UGC 10331	Sc	65.1	0.29	3409.89 ± 5.27	0.79 ± 0.01	24.61 ± 0.38	2.80 ± 0.46	9.77 ± 0.09	13.48 ± 0.08	0.35	7.30 ± 0.53	11.82 ± 0.24
830	UGC 10337	Sb	125.4	0.3	881.95 ± 51.75	0.09 ± 0.17	21.18 ± 1.93	1.26 ± 0.34	12.34 ± 1.25	17.51 ± 0.65	0.38	6.26 ± 0.60	5.79 ± 0.50
831	NGC 6132	Sbc	71.21	0.32	2417.63 ± 18.34	0.42 ± 0.03	18.0 ± 0.37	1.46 ± 0.24	9.63 ± 0.71	16.89 ± 0.10	0.61	7.14 ± 0.80	5.33 ± 0.22
833	NGC 6154	Sab	85.3	0.93	1076.34 ± 5.66	0.0 ± 0.12	11.72 ± 2.17	0.64 ± 0.10	…	…	…	…	2.89 ± 0.27
834	UGC 10380	Sb	125.22	0.16	326.25 ± 2.79	0.0 ± 0.14	9.86 ± 2.71	0.54 ± 0.13	…	…	…	5.77 ± 1.08	6.58 ± 0.38
836	NGC 6155	Sc	34.59	0.69	6598.14 ± 12.22	0.79 ± 0.02	13.65 ± 3.27	1.55 ± 0.45	…	…	…	4.11 ± 0.22	4.13 ± 0.08
837	UGC 10384	Sb	70.75	0.2	2961.0 ± 22.74	1.26 ± 0.02	22.98 ± 0.87	4.03 ± 0.69	5.08 ± 0.37	8.36 ± 0.15	0.54	19.88 ± 1.32	16.56 ± 0.40
841	NGC 6168	Sc	36.84	0.35	3470.4 ± 11.17	0.91 ± 0.02	6.94 ± 1.24	0.88 ± 0.22	…	…	…	3.86 ± 0.19	3.25 ± 0.09
842	NGC 6186	Sb	42.12	0.76	4712.9 ± 13.45	0.69 ± 0.04	14.46 ± 3.46	1.50 ± 0.44	…	…	…	7.67 ± 0.59	8.33 ± 0.17
843	UGC 10650	Scd	42.31	0.24	2549.51 ± 5.30	0.26 ± 0.01	9.2 ± 2.66	0.65 ± 0.22	5.24 ± 0.05	7.51 ± 0.05	0.39	…	1.11 ± 0.06
847	UGC 10710	Sb	119.82	0.24	1017.53 ± 21.59	1.05 ± 0.06	27.25 ± 1.25	3.94 ± 0.73	7.44 ± 0.75	14.31 ± 0.09	0.71	10.05 ± 1.06	8.79 ± 0.39
848	NGC 6310	Sb	48.74	0.25	969.33 ± 26.78	0.0 ± 0.10	5.55 ± 0.25	0.31 ± 0.06	2.67 ± 0.12	4.35 ± 0.05	0.53	1.18 ± 0.11	1.41 ± 0.08
849	NGC 6301	Sbc	119.74	0.62	1680.26 ± 35.09	0.64 ± 0.11	48.57 ± 1.50	4.81 ± 0.87	50.94 ± 2.35	72.95 ± 0.45	0.39	15.27 ± 1.24	17.46 ± 1.69
852	UGC 10796	Scd	43.82	0.76	1348.1 ± 7.69	0.03 ± 0.05	3.8 ± 0.04	0.21 ± 0.04	5.04 ± 0.05	6.76 ± 0.04	0.32	0.48 ± 0.08	0.52 ± 0.03
853	NGC 6361	Sab	54.69	0.29	2842.15 ± 46.81	2.35 ± 0.05	13.15 ± 2.62	6.28 ± 1.66	3.93 ± 0.29	6.29 ± 0.12	0.51	22.83 ± 0.30	21.04 ± 0.39
854	UGC 10811	Sb	124.67	0.29	591.91 ± 12.25	0.0 ± 0.18	16.04 ± 0.37	0.88 ± 0.09	10.33 ± 0.10	15.78 ± 0.10	0.46	…	5.22 ± 0.65
856	IC 1256	Sb	68.16	0.71	2185.2 ± 12.20	0.43 ± 0.05	17.98 ± 0.78	1.47 ± 0.25	11.42 ± 1.58	18.95 ± 0.47	0.55	3.45 ± 0.36	3.83 ± 0.14
857	NGC 6394	Sbc	121.81	0.27	931.74 ± 14.07	0.3 ± 0.05	18.8 ± 0.34	1.36 ± 0.24	6.28 ± 0.12	11.86 ± 0.07	0.69	19.63 ± 2.52	25.01 ± 0.60
861	UGC 10972	Sbc	66.5	0.27	1063.16 ± 11.10	0.0 ± 0.06	9.41 ± 2.70	0.52 ± 0.15	…	…	…	2.03 ± 0.29	2.47 ± 0.41
862	NGC 6478	Sc	97.15	0.37	2381.38 ± 123.99	0.52 ± 0.14	37.49 ± 8.72	3.34 ± 1.11	…	…	…	29.47 ± 0.95	26.19 ± 0.63
863	NGC 6497	Sab	44.99	0.46	1204.58 ± 22.75	0.65 ± 0.07	3.87 ± 0.20	0.39 ± 0.07	2.63 ± 0.22	3.81 ± 0.09	0.4	1.02 ± 0.09	1.30 ± 0.09
866	UGC 11262	Sc	79.81	0.38	499.54 ± 3.34	0.0 ± 0.06	5.48 ± 0.36	0.30 ± 0.04	6.06 ± 0.50	9.35 ± 0.29	0.47	…	1.55 ± 0.24
868	MCG-02-51-004	Sb	80.7	0.35	2679.21 ± 35.86	0.43 ± 0.05	24.03 ± 1.03	1.97 ± 0.35	14.47 ± 0.93	20.34 ± 0.38	0.37	8.44 ± 0.89	8.84 ± 0.37
869	NGC 6941	Sb	88.94	0.71	220.02 ± 2.58	0.35 ± 0.12	4.38 ± 0.07	0.33 ± 0.06	28.89 ± 0.53	41.38 ± 0.25	0.39	7.95 ± 0.82	9.28 ± 0.95
871	NGC 6978	Sb	85.44	0.47	1293.92 ± 23.82	0.02 ± 0.11	17.47 ± 4.59	0.98 ± 0.31	…	…	…	5.02 ± 0.46	5.82 ± 0.35
872	UGC 11649	Sab	54.24	0.74	1009.84 ± 8.11	0.0 ± 0.10	7.89 ± 0.73	0.43 ± 0.07	8.78 ± 1.78	12.11 ± 0.67	0.35	…	1.18 ± 0.31
873	UGC 11680NED01	Sb	111.39	0.65	978.61 ± 8.08	0.0 ± 0.09	30.06 ± 5.54	1.65 ± 0.32	7.59 ± 0.70	28.59 ± 3.34	1.44	35.91 ± 0.75	50.78 ± 1.17
876	NGC 7047	Sbc	82.85	0.55	2744.54 ± 22.46	0.48 ± 0.07	23.88 ± 0.33	2.04 ± 0.34	10.17 ± 0.28	18.50 ± 0.11	0.65	7.13 ± 0.69	7.45 ± 0.87
877	UGC 11717	Sab	90.72	0.36	836.95 ± 14.24	0.0 ± 0.10	11.95 ± 2.88	0.66 ± 0.12	…	…	…	18.30 ± 3.85	21.55 ± 0.42
878	MCG-01-54-016	Scd	42.09	0.14	1451.01 ± 3.55	0.34 ± 0.01	4.61 ± 0.09	0.35 ± 0.06	2.93 ± 0.03	4.28 ± 0.05	0.41	…	…
879	UGC 11740	Sbc	92.19	0.32	895.94 ± 8.73	0.57 ± 0.06	11.97 ± 2.45	1.11 ± 0.29	…	…	…	…	4.04 ± 0.38
880	UGC 11792	Sbc	68.78	0.21	957.31 ± 7.33	1.07 ± 0.06	7.9 ± 1.92	1.17 ± 0.34	0.66 ± 0.10	2.66 ± 1.02	1.52	2.46 ± 0.27	3.01 ± 0.14
884	UGC 11982	Scd	69.6	0.14	111.21 ± 1.48	0.0 ± 0.14	0.84 ± 0.17	0.05 ± 0.01	…	…	…	…	0.67 ± 0.13
885	UGC 12054	Sc	29.92	0.24	1738.99 ± 4.42	0.41 ± 0.02	3.06 ± 0.24	0.25 ± 0.05	1.65 ± 0.11	2.41 ± 0.12	0.41	…	0.12 ± 0.05
886	NGC 7311	Sa	64.46	0.48	3342.64 ± 212.32	0.71 ± 0.18	19.4 ± 1.34	2.06 ± 0.56	8.89 ± 0.57	16.64 ± 0.10	0.68	9.58 ± 0.60	8.83 ± 0.43
887	NGC 7321	Sbc	101.84	0.66	2977.12 ± 29.39	0.25 ± 0.05	50.61 ± 0.89	3.51 ± 0.59	33.92 ± 1.87	56.29 ± 0.35	0.55	15.69 ± 0.88	14.06 ± 0.52

ID	Name	Type	Dist (Mpc)	b/a	$F(\mathrm{H}\alpha_{\mathrm{obs}})$ ($\times 10^{-16}$ cgs)	$A(\mathrm{H}\alpha)$ (mag)	$L(\mathrm{H}\alpha_{\mathrm{obs}})$ ($\times 10^{40}$ erg s^{-1})	$SFR[\mathrm{H}\alpha_{\mathrm{corr}}]$ ($M_{\odot}$ yr^{-1})	$L(\mathrm{FUV}_{\mathrm{obs}})$ ($\times 10^{42}$ erg s^{-1})	$L(\mathrm{NUV}_{\mathrm{obs}})$ ($\times 10^{42}$ erg s^{-1})	F–N (AB mag)	L(TIR) ($\times 10^{43}$ erg s^{-1})	$L(22\,\mu\mathrm{m})$ ($\times 10^{42}$ erg s^{-1})
(1)	(2)	(3)	(4)	(5)	(6)	(7)	(8)	(9)	(10)	(11)	(12)	(13)	(14)
889	NGC 7364	Sab	69.41	0.6	3883.28 ± 49.73	0.68 ± 0.05	29.08 ± 0.49	3.00 ± 0.51	10.03 ± 0.18	18.77 ± 0.12	0.68	16.69 ± 0.95	16.20 ± 0.36
890	UGC 12185	Sb	95.05	0.54	705.74 ± 11.54	0.31 ± 0.10	12.04 ± 1.10	0.88 ± 0.17	9.34 ± 1.89	16.54 ± 0.92	0.62	…	2.54 ± 0.38
891	UGC 12224	Sc	50.42	0.87	2270.75 ± 9.86	0.21 ± 0.06	12.01 ± 0.21	0.80 ± 0.13	11.47 ± 0.53	16.13 ± 0.10	0.37	2.44 ± 0.19	2.48 ± 0.17
892	VV488NED02	Sb	70.49	0.53	1255.21 ± 9.41	0.44 ± 0.05	22.99 ± 1.80	1.90 ± 0.35	4.16 ± 0.27	8.37 ± 0.31	0.76	7.99 ± 0.46	7.74 ± 0.56
895	UGC 12308	Scd	32.37	0.27	1738.61 ± 3.71	0.11 ± 0.02	3.96 ± 1.23	0.24 ± 0.08	…	…	…	…	0.17 ± 0.04
896	NGC 7466	Sbc	107.4	0.3	1590.85 ± 16.84	0.51 ± 0.06	32.26 ± 1.12	2.85 ± 0.49	10.98 ± 1.31	19.61 ± 0.24	0.63	22.82 ± 2.28	18.74 ± 0.47
897	UGC 12348	Sb	107.14	0.29	1168.95 ± 9.62	0.25 ± 0.05	19.77 ± 3.54	1.37 ± 0.34	4.23 ± 0.35	15.08 ± 0.84	1.38	17.36 ± 2.47	3.90 ± 0.07
898	NGC 7489	Sbc	89.12	0.54	4720.99 ± 27.00	0.64 ± 0.03	102.89 ± 5.92	10.22 ± 1.80	29.28 ± 1.20	70.23 ± 10.17	0.95	18.33 ± 3.02	16.07 ± 0.53
899	NGC 7536	Sc	67.15	0.39	3062.51 ± 15.18	0.74 ± 0.04	24.59 ± 6.14	2.67 ± 0.80	13.82 ± 0.25	19.62 ± 0.12	0.38	12.29 ± 0.63	10.08 ± 0.3
901	NGC 7549	Sbc	67.42	0.46	3865.33 ± 19.06	0.82 ± 0.03	52.61 ± 0.58	6.15 ± 1.02	10.28 ± 0.09	21.09 ± 0.13	0.78	13.74 ± 1.40	13.24 ± 0.35
904	NGC 7591	Sbc	70.82	0.41	3622.21 ± 24.33	1.69 ± 0.03	52.69 ± 4.24	13.68 ± 2.53	15.52 ± 3.14	22.43 ± 1.10	0.4	45.53 ± 2.71	58.82 ± 0.92
906	IC 5309	Sc	60.03	0.45	1694.21 ± 5.96	0.56 ± 0.04	8.46 ± 0.12	0.78 ± 0.13	3.90 ± 0.11	6.48 ± 0.04	0.55	4.16 ± 0.29	3.69 ± 0.16
907	NGC 7608	Sbc	50.31	0.33	1169.96 ± 5.55	0.84 ± 0.06	4.3 ± 0.14	0.51 ± 0.09	1.19 ± 0.01	2.18 ± 0.04	0.66	2.07 ± 0.27	2.54 ± 0.20
909	UGC 12519	Sc	62.6	0.37	3204.47 ± 22.32	0.75 ± 0.03	18.66 ± 0.68	2.04 ± 0.35	6.54 ± 0.30	9.54 ± 0.18	0.41	6.94 ± 0.56	7.79 ± 0.27
913	NGC 7625	Sa	23.23	0.91	12721.06 ± 24.44	1.25 ± 0.01	10.7 ± 2.15	1.86 ± 0.48	1.64 ± 0.06	3.72 ± 0.05	0.89	6.29 ± 0.18	8.00 ± 0.12
914	NGC 7631	Sb	53.67	0.4	1942.46 ± 10.78	0.55 ± 0.05	10.13 ± 0.14	0.93 ± 0.15	5.27 ± 0.10	8.59 ± 0.05	0.53	2.75 ± 0.41	3.18 ± 0.20
915	NGC 7653	Sb	61.04	0.89	5614.42 ± 15.50	0.47 ± 0.02	30.52 ± 0.31	2.59 ± 0.43	17.94 ± 0.17	28.96 ± 0.18	0.52	10.10 ± 0.78	8.98 ± 0.29
918	UGC 12633	Sab	59.65	0.68	2474.82 ± 20.76	2.03 ± 0.08	18.33 ± 2.38	6.51 ± 1.38	1.84 ± 0.56	4.51 ± 0.39	0.97	14.00 ± 1.07	19.90 ± 0.40
920	NGC 7691	Sbc	57.66	0.76	2563.25 ± 24.82	0.31 ± 0.15	19.33 ± 0.34	1.42 ± 0.24	17.88 ± 0.16	25.37 ± 0.16	0.38	3.23 ± 0.39	3.88 ± 0.27
921	UGC 12653	Sc	57.48	0.31	456.04 ± 17.30	0.06 ± 0.51	2.88 ± 0.18	0.17 ± 0.04	4.67 ± 0.13	7.55 ± 0.19	0.52	…	1.05 ± 0.16
922	UGC 12688	Scd	74.68	0.33	2457.96 ± 11.65	0.53 ± 0.04	25.39 ± 0.74	2.27 ± 0.38	12.27 ± 1.02	15.88 ± 0.10	0.28	5.90 ± 0.93	5.89 ± 0.20
924	NGC 7716	Sb	36.63	0.83	3426.16 ± 13.45	0.23 ± 0.05	9.61 ± 0.10	0.65 ± 0.11	9.17 ± 0.17	12.19 ± 0.08	0.31	1.69 ± 0.10	1.46 ± 0.14
926	UGC 12723	Sc	78.11	0.33	536.26 ± 5.71	0.99 ± 0.11	4.68 ± 0.92	0.64 ± 0.17	3.50 ± 0.39	3.94 ± 0.51	0.13	6.25 ± 0.77	6.28 ± 0.34
927	NGC 7738	Sb	97.92	0.76	1757.99 ± 12.15	1.43 ± 0.11	41.51 ± 1.25	8.49 ± 1.44	8.80 ± 0.08	14.60 ± 0.27	0.55	50.58 ± 2.86	68.51 ± 1.20
929	UGC 12810	Sbc	115.57	0.4	2053.33 ± 26.06	0.49 ± 0.05	41.76 ± 8.04	3.62 ± 0.93	…	…	…	19.29 ± 1.21	23.34 ± 0.75
930	UGC 12816	Sc	76.21	0.55	1902.54 ± 9.78	0.3 ± 0.04	19.56 ± 0.41	1.42 ± 0.24	17.01 ± 0.47	22.83 ± 0.14	0.32	3.48 ± 0.50	3.01 ± 0.24
931	NGC 7782	Sb	76.87	0.54	2350.61 ± 79.35	0.97 ± 0.12	29.81 ± 9.22	4.01 ± 1.47	…	…	…	12.96 ± 0.92	12.53 ± 1.15
933	NGC 7787	Sab	95.22	0.26	553.26 ± 2.94	0.5 ± 0.08	12.24 ± 0.28	1.07 ± 0.18	4.21 ± 0.04	7.73 ± 0.10	0.66	10.49 ± 1.21	9.56 ± 0.30
934	UGC 12857	Sbc	35.15	0.21	1920.31 ± 6.56	0.71 ± 0.04	4.44 ± 0.05	0.47 ± 0.08	2.08 ± 0.02	3.09 ± 0.02	0.43	2.16 ± 0.34	1.36 ± 0.07
935	UGC 12864	Sc	66.83	0.6	1591.1 ± 4.25	0.13 ± 0.05	17.1 ± 1.32	1.06 ± 0.19	14.34 ± 0.79	19.08 ± 0.94	0.31	3.57 ± 0.16	3.17 ± 0.13
937	NGC 7800	Ir	24.88	0.69	7629.71 ± 14.52	0.35 ± 0.01	9.69 ± 2.85	0.74 ± 0.25	…	…	…	0.94 ± 0.09	1.02 ± 0.07
938	NGC 5947	Sbc	84.84	0.98	2426.3 ± 10.09	0.14 ± 0.05	22.31 ± 2.59	1.40 ± 0.28	…	…	…	9.39 ± 1.18	7.84 ± 0.22

This page was left intentionally blank.

CHAPTER 4

Activation and quenching mechanisms of the SFR in bulges, bars, and disks.

Measure what is measurable, and make measurable what is not so.
— Galileo Galilei

Resumen

En el capítulo anterior se ha demostrado que la luminosidad Hα corregida de extinción es un buen trazador para la muestra de galaxias analizada con una presencia escasa de galaxias altamente oscurecidas donde parte de la emisión Hα podría no recuperarse. En este capítulo vamos a ir un paso más allá en el análisis de la SFR, con el propósito de conocer la distribución de la SFR a diferentes escalas físicas para comprender cómo las galaxias fueron adquirieron su masa y como su crecimiento futuro en masa se distribuirá en éstas. En definitiva, pasamos de explorar las propiedades globales (es decir, tratando la galaxia como un único sistema) a propiedades locales mediante el uso de componentes morfológicas.

En primer lugar, es necesaria la caracterización de las distintas estructuras estelares que componen las galaxias, tales como los bulbos, las barras y los discos (truncados o no). Para ello empleamos una descomposición fotométrica en dos dimensiones (2D) que permite incorporar múltiples componentes usando las imágenes de SDSS en bandas *g, r, i*. Para nuestro objetivo usamos los parámetros obtenidos empleando la banda *g* por ser la que nos ofrece una mejor aproximación a la distribución de la luz proveniente de las poblaciones estelares jóvenes. El uso de otras bandas ha sido descartado en base a las siguientes razones: (i) las bandas UV son problemáticas para ajustar componentes en 2D salvo en las galaxias de tipo temprano, (ii) la banda *u* de SDSS es menos profunda que la banda *g* y a su vez presenta problemas similares a los del UV mencionados anteriormente; (iii) por otra parte, las bandas más rojas (*r, i* de SDSS) trazan poblaciones estelares más evolucionadas. Por lo tanto, la banda *g* se usa para obtener los parámetros que definen las distintas componentes morfológicas de las galaxias así como para estimar los pesos relativos de cada una de ellas en aquellas regiones donde compiten en brillo superficial, tales como el disco interno, las regiones de la barra, etc. El proceso por el cual se obtienen los mapas de pesos relativos de cada componente se detalla a continuación. En primer lugar se generan los modelos 2D en banda *g* que mejor reproducen cada una de las componentes estructurales (bulbo, barra y disco). Después, se construyen mapas de pesos para cada una de ellas definidos como el cociente de luminosidades en banda *g* de cada componente particular y la luminosidad en banda *g* total (suma de las luminosidad

individuales de cada componente). De este modo, cada spaxel del cubo tiene una contribución de una, dos o tres componentes en mayor o menor medida sin descartar que la contribución pueda deberse enteramente a una sola componente (las partes más centrales tienden a estar dominadas por los bulbos mientras que en las partes más externas la contribución en muchos casos es debida únicamente al disco). Los cubos de datos originales de CALIFA se multiplican por los mapas de pesos generados de modo que tenemos disponible un nuevo cubo (pesado) para cada una de las componentes estructurales (bulbo, barra y disco). Finalmente, de cada uno de estos cubos se obtiene el espectro integrado correspondiente a cada componente. Por lo tanto, queremos recalcar que el valor de la SFR medido viene determinado por la luminosidad Hα presente en los cubos pesados de cada una de estas componentes. Del total de 667 galaxias observadas por CALIFA, la muestra final de este estudio está compuesta por 219 galaxias (aquellas que son aptas para la descomposición 2D) y que presentan emisión de Hα (las galaxias elípticas se han descartado).

La metodología anterior permite obtener valores de formación estelar para las distintas estructuras morfológicas que componen las galaxias. De este modo, se investigan las relaciones entre la SFR de cada componente en función de propiedades físicas como la tasa de formación estelar específica (sSFR del inglés, *specific Star Formation Rate*), la masa estelar, el entorno, la presencia de barras y la emisión nuclear con el objetivo de determinar cual/cuales de estos factores afecta de manera más significativa las variaciones de la SFR. Las conclusiones más importantes derivadas de este trabajo se describen a continuación. Este análisis revela un aumento de la SFR y la sSFR en galaxias barradas en concordancia con otros estudios observacionales (de Jong et al. 1984; Devereux 1987; Ellison et al. 2011; Wang et al. 2012; Florido et al. 2015). La relación entre la SFR y la masa estelar, también conocida como Secuencia Principal de las galaxias con formación estelar activa (SFMS, de sus siglas en inglés *Star-Forming Main Sequence*) es analizada usando propiedades globales y también empleando las propiedades derivadas de la descomposición multi-componente. Entre los resultados obtenidos en este trabajo cabe destacar que no solamente las galaxias más masivas tienen su formación estelar suprimida de forma más eficiente sino también los discos más masivos. Entre los mecanismos que podrían ser responsables de este proceso de 'quenching' aparece la posibilidad de que los AGNs tipo 2 puedan jugar un papel a la hora de disminuir la sSFR de los bulbos y también, de manera menos eficiente, podrían afectar también a la disminución de la sSFR de los discos.

Este trabajo muestra el potencial de combinar una descomposición multi-componente basada en imágenes con datos de espectroscopía de campo integral para llevar a cabo un estudio detallado de los mecanismos que afectan a la formación estelar.

4.1 Catalán-Torrecilla et al. (submitted to *ApJ*)

This chapter is based on the article: "**Star formation in the local Universe from the CALIFA sample II. Activation and quenching mechanisms in bulges, bars, and disks.**" by C. Catalán-Torrecilla and collaborators submitted to *Astrophysical Journal*.

4.2 Introduction

Among the multiple open issues on galaxy formation and evolution probably the most fundamental ones are related to the evolution of the baryonic component and, more specifically, on the relative role of the different mechanisms that can trigger and quench star formation (SF) in galaxies.

Regarding the processes that can activate and regulate SF, these might vary depending on the location within the galaxy. Secular internal evolution (Kormendy & Kennicutt 2004) and the accretion of gas (Dekel et al. 2009; Sánchez Almeida et al. 2014) are most likely dominant in galaxy disks, with the latter process being progressively more important as we move outwards in the disks. In the case of the central regions, in-situ SF is strongly affected by the amount of gas inflow that is driven to the center thanks to the presence of bars (Sakamoto et al. 1999; Sheth et al. 2005) or by galaxy mergers (Barnes & Hernquist 1991).

With respect to the quenching of in-situ SF in galaxies, these are also expected to differ depending on whether we are talking about the formation of stars associated with bulges, bars or disks. Some of the mechanisms that have been proposed to be responsible for the star formation shutdown are related to the gas consumption, such as the termination of gas supply, i. e., strangulation (Kawata & Mulchaey 2008; Peng et al. 2015), or ram-pressure stripping (Book & Benson 2010; Steinhauser et al. 2016). The previous mechanisms that transform galaxies are related to the influence of the environment in regulating the SFR in galaxies (Hashimoto et al. 1998; Koyama et al. 2013). Galaxy harassment (Moore et al. 1996, 1998; Bialas et al. 2015) or morphological quenching (Martig et al. 2009) are also important.

The role of active galactic nuclei (AGN) at enhancing (Silk 2005, 2013) or suppressing the star formation in the host galaxy (Oppenheimer et al. 2010; Page et al. 2012; Shimizu et al. 2015; Hopkins et al. 2016; Carniani et al. 2016), the effect of SNe-driven winds (Stringer et al. 2012; Bower et al. 2012) and the feedback from massive stars (Dalla Vecchia & Schaye 2008; Hopkins et al. 2012) have important implications for the evolution of galaxies as well.

Different mechanisms act on different spatial scales and are sensitive to the presence of specific structural components (spiral arms, bars, etc.). That is why having high spatial resolution is crucial to solve the problem. Besides, it is also important to quantify how these mechanisms compete not only as a function of different galaxy properties but also as a function of redshift. In previous chapters, we have seen that one of the most fundamental parameters that characterize galaxies is its Star Formation Rate (SFR). A better understanding of the distribution of the SFR in the different stellar structures that shaped galaxies in the local Universe will shed some light on their formation and evolution processes. The advance of Integral Field Spectroscopy (IFS) techniques give us the opportunity to accurately measure the SFR at the different components that are forming

the galaxies such as unresolved nuclear sources, bulges, bars, and disks. We can also explore the capacity of forming new stars with respect to the stellar mass in each of these stellar structures. This is a determining path if we want to know the different contributions of each component to the integrated value of the SFR in each galaxy. The Calar Alto Legacy Integral Field Area (CALIFA) survey (Sánchez et al. 2012) provides us with excellent data to answer these questions in a spatially resolved manner. Some early attempts based on radial profiles of the SFR as a function of galaxy morphology suggests that galaxies are quenched inside-out, and that this process is faster in the central, bulge-dominated part than in the disks (González Delgado et al. 2016). Here, we do a more precise analysis by isolating the galaxies in their basic stellar structures. We combine for the first time in a large sample of galaxies the two dimensional (2D) photometric decomposition of the CALIFA galaxies (Méndez-Abreu et al. 2017) with IFS data to measure the SFR in the different morphological components of galaxies.

This Chapter is organized as follows: in Section 4.3 we describe the CALIFA reference sample used in this study, in Section 4.4 we describe the analysis and methodology applied to the data, including the 2D photometric decomposition in bulges, bars, and disks and the derivation of the corresponding IFS-based SFRs. Results are discussed in Section 4.5. Finally, in Section 4.6 we summarize the main conclusions of this work. Throughout this Chapter, we use a cosmology defined by $H_0 = 70\ \mathrm{km\,s^{-1}\,Mpc^{-1}}$, $\Omega_\Lambda = 0.7$ and a flat universe.

4.3 CALIFA Sample

The galaxies used along this work are part of the Calar Alto Legacy Integral Field Area (CALIFA) Survey (Sánchez et al. 2012). Data were obtained with the Potsdam Multi-Aperture Spectrophotometer (PMAS, Roth et al. 2005) in the PPak mode (Kelz et al. 2006) mounted on the 3.5m telescope at the Calar Alto Observatory. As a brief summary, galaxies have spectroscopic redshifts in the range $0.005 < z < 0.03$ and angular isophotal diameter in the range $45" < D25 < 80"$ in the SDSS r-band. The properties of the CALIFA mother sample are described in more detail in Chapter 2 of this thesis.

The observations span the whole optical wavelength range in two overlapping setups. The V500 grating covers the range 3745-7500 Å at a spectral resolution of $R \sim 850$ while the V1200 grating is restricted to 3650-4840 Å with a higher resolution ($R \sim 1650$). As our aim is to calculate extinction-corrected Hα luminosities in each stellar galaxy component is desirable to have both Hβ and Hα emission lines in the same observing range. This is the reason why we use the V500 setup thorough this work. The V1200 data are restricted to the analysis of the line-of-sight velocity dispersions (Section 4.5.4.1).

We make use of 545 CALIFA galaxies that have been observed and processed with the V500 grating, are part of the Data Release 3 (DR3) (Sánchez et al. 2016) and belong to the CALIFA mother sample. This criterion should guarantee that we maintain the limits where the mother sample is representative of the general galaxy population: 9.7 and 11.4 in $\log(M_\star/M_\odot)$, -19.0 and -23.1 in r-band absolute magnitude and 1.7 and 11.5 kpc in half-light radius (Walcher et al. 2014). As we are interested in the SFR properties of these galaxies in their different components, our sample is further constrained to those galaxies that are eligible for the 2D photometric decomposition.

Galaxies meeting any of the following criteria were excluded: (1) if they are forming a pair, an interacting system or they have a heavily distorted morphology and (2) if they are highly inclined galaxies as the projection effects might affect the results (typically $i > 70°$). More details about the sample selection are given in Méndez-Abreu et al. (2017). A total of 204 galaxies were excluded in this way. We also reject 122 galaxies that do not show detectable Hα emission based on a signal-to-noise (S/N) criteria, including also galaxies classified as elliptical in the 2D decomposition analysis. We impose a minimum of S/N > 5 for the detection of both Hβ and Hα emission lines in each photometric structure of the galaxies (more details are given in Section 4.4.3). This leads to the final sample of 219 CALIFA galaxies used for this work.

4.4 Analysis

In this Section, we describe the method applied to obtain a extinction-corrected Hα SFR value for each galaxy morphological component (nuclear point source, bulge, bar, and disk). This method relies on the combination of 2D decomposition of multi-band photometry on IFU spectral datacubes. Consequently, our galaxy components are defined based exclusively on the fitting to the photometry. Our objective is to determine how these components will grow in stellar mass due to in-situ star formation which ultimately dominates the total mass growth in the local Universe. We aim to identify the mechanism(s) that either trigger or quench star formation in each of these regions, and, therefore, in galaxies as a whole, but going beyond the use of simple spectro-photometric apertures on the datacubes.

4.4.1 Assigning SFR values to morphological components

Different approaches can be used to perform a spatially-resolved analysis of the SFR in galaxies, including individual pixels, full 2D maps, radial profiles or, as in this study, multi-component decomposition. The analyses based on 2D maps or individual pixels have strong difficulties in combining information from different galaxies and are also limited in our case by the coarse spatial resolution of the CALIFA datacubes. A simplified approach would have been to identify the transition radius between the bulge and disk components in one-dimensional (1D) surface brightness profiles and use this radius (and the galaxy ellipticity and position angle at that radius) to define spectro-photometric apertures for those two components. However, early tests already showed that this 1D approach does not allow to properly isolate the emission coming from the bulge and the disk, neither to deal with objects where a clear bar is present. In fact, some studies (Aguerri et al. 2005; Weinzirl et al. 2009; Meert et al. 2015) have demonstrated the importance of including the bar to obtain the precise parameters for the bulge component. The previous limitations and the availability of 2D structural fits to the optical continuum light distribution in our galaxies have led us to use a decomposition based on structural components as the optimal option in our case. The use of multi-component decomposition has been widely probed to be the best way of recovering the stellar structure parameters (de Souza et al. 2004; Gadotti 2009; Weinzirl et al. 2009; Salo et al. 2015; Meert et al. 2015, 2016).

An alternative would have been to use the distinct kinematic features of bulge, disk, and bar main-sequence stars to separate between components. However, it is quite likely that the

stars currently being formed do not follow the same balance but they have might formed in a kinematically cold component and are being heated up afterwards. In addition, for this particular aim the CALIFA spectral resolution is at the limit of what is needed to perform such multi-component kinematical fitting. Future IFS facilities working at R $>$ 5000 such as MEGARA (at GTC; Gil de Paz et al. 2016) or WEAVE (at WHT; Dalton et al. 2014) might help in that regard. Our method (see Section 4.4.2) is based on assigning bulge and disk SFR values as those measured in regions where the stellar content is dominated by stars that follow either a bulge or disk light profile and possibly are also either dynamically hot or cold. Consequently, these are also the regions where the SFR is expected to later contribute to the growth of the stellar mass of these components.

4.4.2 2D Photometric decomposition analysis

We use the structural parameters derived for the CALIFA galaxies in Méndez-Abreu et al. (2017). These values were obtained by applying the 2D photometric decomposition code GASP2D (Méndez-Abreu et al. 2008, 2014) over the *g*-, *r*- and *i*-band images from the Sloan Digital Sky Survey Data Release 7 (SDSS-DR7, Abazajian et al. 2009). The use of SDSS images is justified in terms of their higher spatial resolution in comparison with CALIFA, making the method more precise. GASP2D makes use of a Leverberg-Marquard algorithm to fit the 2D surface brightness distributions of galaxies. This code allows the simultaneous fitting of different galaxy structures such as nuclear point sources, bulges, bars, and disks (including breaks). The reader is referred to Méndez-Abreu et al. (2017) and to Chapter 2 of this thesis for more details about the methodology of the fitting algorithm.

For the purpose of this work, we use the parameters derived using the SDSS *g*-band images. This band is the one that provides the best compromise between image depth and being able to fit analytical functions to the light distribution of the youngest possible stellar populations. We have discarded the use of other bands for the following reasons: (a) trying to fit these 2D analytic components to the UV bands leads to catastrophic failures in all but the very early type systems, (b) the *u*-band is significantly less deep than the *g*-band in SDSS (and it is subject to the same problems than the UV, especially in late-type spirals), (c) redder bands would progressively trace older stellar populations. It is worth emphasizing here that the main objective of the use of the *g*-band data is to provide relative weights for the different components in those regions where they compete in surface brightness (inner disk, outer regions of the bar, etc.). However, the actual SFR is dominated by the amount of extinction-corrected Hα luminosity provided by the CALIFA datacubes to which these weights are applied.

The process followed to create the datacubes for each of the stellar components in each galaxy is the following. Firstly, we create the photometric characterization of the multiple stellar structures (nuclear point source, bulge, bar or disk), i. e., their best-fitting 2D *g*-band models as illustrated in the left panels of Figure 4.1. Then, we create weight maps for each stellar component. The weight maps are defined as the ratio between the light in each galaxy structure (nuclear point source, bulge, bar or disk) and the total luminosity of the galaxy, as given by the SDSS *g*-band best-fitting models. These weight maps are computed for each individual CALIFA spaxel. Finally, the original CALIFA datacube of the galaxy is multiplied by these weight maps. This means that a 3D datacube is now created for each of the photometric structures.

Figure 4.1 illustrates the process. The complete figure set (219 images) is available in the Appendix C of this thesis. Once we have created the final weighted-datacube for each component, we can obtain the corresponding distribution of the continuum-subtracted Hα luminosity. Middle panels of Figure 4.1 show the continuum-subtracted Hα luminosity for the disk, the bar, and the bulge (from top to bottom). We emphasize that these Hα maps are given as a visual tool to prove the goodness of the method but the actual Hα luminosity is computed using the corresponding spectrum per component as explained in the next paragraph. We have identified 15 galaxies (7 % of the bulge components) in the figure set (Appendix C) that show a clear contamination coming from the internal parts of the disks. These objects are marked with a nuclear 3-arcsec green aperture (see Section 4.4.5).

Finally, we obtain the integrated spectrum for each galaxy structure (right panels of Figure 4.1) and for it the corresponding Hα flux to derive the SFR. The analysis of the spectra extracted from the CALIFA datacubes is explained with detail in the following Section 4.4.3 and it is similar to that described in Section 3.4 of Chapter 3. We emphasize here that the spectra obtained for each component might not be optimal for the study of intermediate-to-old stellar populations in each of these regions since these (more evolved) populations do show distinct kinematical properties in bulges, bars, and disks. Indeed, these properties are the ones that ultimately define what bulges, bars and disks truly are.

4.4.3 CALIFA: Extinction-corrected Hα luminosities, continuum subtraction and line-flux measurements

Once we have the final datacube for each component, we obtain the integrated spectra (see below) and the corresponding Hα fluxes.

For each component (nuclear point source, bulge, bar, and disk), we spatially integrate their corresponding datacube to generate an integrated spectrum using an elliptical aperture with a major axis radius of 36 arcsec. The use of 36 arcsec apertures is justified in terms of assuring a homogenous way for computing the aperture effects that are mentioned at the end of this section. The minor-to-major axis ratio of the elliptical aperture is given by the isophotal major and minor axis in the g-band from SDSS-DR7 as well as the isophotal position angle (PA). Before extracting the integrated spectra, a spatial masking over the datacubes is performed to avoid light coming from spaxels contaminated by field stars or background objects.

The complete description of the methodology applied to obtain the Hα and Hβ fluxes is explained in detail in Section 3.4 of Chapter 3. For the sake of completeness, we briefly describe here the main steps. Once we have the integrated spectrum of each component, we carefully remove the stellar continuum using a linear combination of two single stellar population (SSP) evolutionary synthesis models of Vazdekis et al. (2010) based on the MILES stellar library (Sánchez-Blázquez et al. 2006b). Two sets of models with a Kroupa IMF (Kroupa 2001) are combined. One set contains models (considered as a young stellar population) with ages of 0.10, 0.50 and 0.79 Gyr. A second set (considered as an old stellar population) involves ages of 2.00, 6.31 and 14.13 Gyr. For each age we considered five different metallicities with [M/H] values equal to 0.00, 0.20, -0.40, -0.71 and -1.31 dex offset from the solar value. The basic steps applied to obtain the Hα and Hβ fluxes are the following: (1) to shift the SSP templates to match the systemic velocity of the

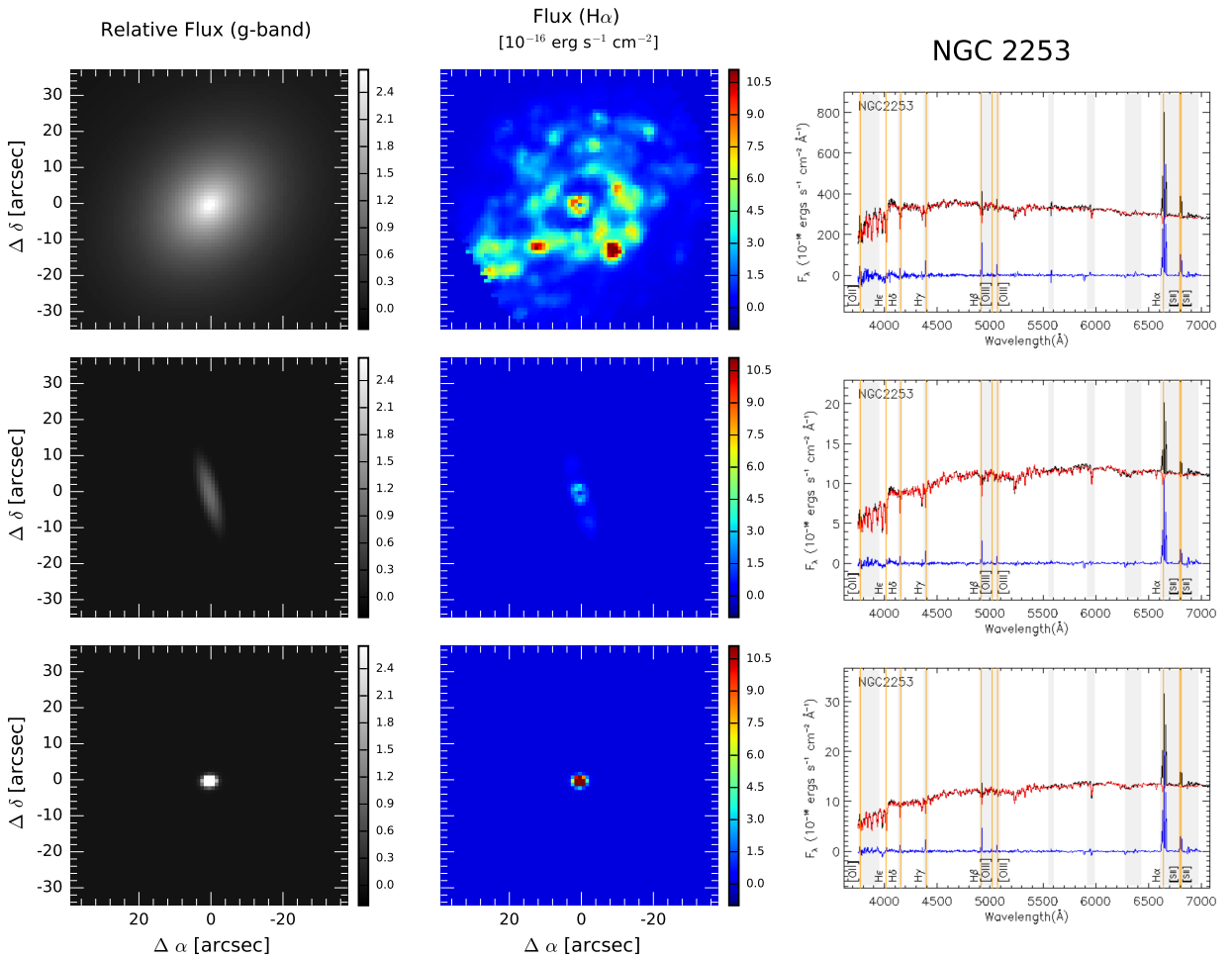

Figure 4.1: Left panels: 2D g-band models derived from the multi-component photometric decomposition. Disk, bar, and bulge components are shown from top to bottom, respectively. Units for the flux are given relative to the central surface brightness of the bar component (if the bar is not present the central surface brightness of the disk component is used instead). Central surface brightness and the rest of the parameters needed to create these g-band models are provided in Méndez-Abreu et al. (2017). Middle panels: Distribution of the continuum-subtracted Hα luminosity in the different stellar galaxy components. To create these Hα maps, the original CALIFA datacubes have been multiplied by the corresponding weight maps in each morphological component, i. e., there is a weighted-datacube for each galaxy component, and then, analyzed spaxel by spaxel. Right panels: the integrated spectrum extracted for the weighted-datacube for each galaxy structure (bulge, bar, and disk) is shown in black. Gray-colored vertical ranges correspond to the emission lines and sky lines masked out during the fitting procedure. The red spectrum corresponds to the best fit for the underlying stellar population. The emission-line spectrum originated by the ionized gas is shown in blue. The latest is the one used to measure the Hα and Hβ fluxes associated with each component. The complete figure for the 219 galaxies used in this work, showing the models, Hα maps and their corresponding spectra for each of the galaxies, appears in the Appendix C.

integrated spectrum, (2) to convolve each stellar population model with a Gaussian profile so the absorption features could be broadened to match those of the integrated spectrum, (3) to redden the spectrum using a $k(\lambda) = R_V\ (\lambda/5500\,\text{Å})^{-0.7}$ power law, where $R_V = 5.9$, as given by Charlot & Fall (2000) (4) to determine the best linear combination of SSPs by a χ^2 minimization. Finally, Hα and Hβ fluxes are obtained from fitting Gaussians to the pure emission line spectra. The fluxes uncertainties are estimated from a random redistribution of the residuals after the Gaussian fittings mentioned before. The procedure, that consists of adding this new residual spectrum to the pure emission-line spectrum and perform afterwards the Gaussian fittings, is repeated 1000 times. The

standard deviation of the computed fluxes is taken as the error in the Hα and Hβ fluxes.

An important parameter to take into account is the amount of dust attenuation for our measured Hα luminosities. In particular, we use Balmer decrements with a Galactic extinction curve and a foreground screen dust geometry approximation to estimate the attenuation. Although there is not a considerable number of edge-on galaxies in this work due to the selection criteria imposed for the 2D photometric decomposition, we refer the reader to the extensive analysis in Catalán-Torrecilla et al. (2015) where we test that the foreground dust screen approximation does not have an important impact on the SFR derived for these galaxies.

As some galaxies could extend beyond the PPak Field of View (FoV), we have applied aperture corrections to our extinction-corrected Hα measurements. Among all the morphological components analyzed, the light coming from disk is the only one that might extend beyond the FoV. As a consequence, we have applied these aperture corrections to the spectrum of the disk only. We have derived dust-corrected Hα growth curves using elliptical integrated apertures centered at the center of mass of the galaxy with radii increasing by steps of 3 arcsec up to a maximum radius of 36 arcsec (a similar methodology is used in Gil de Paz et al. 2007a). The last aperture corresponds to the 36 arcsec aperture that is the one used previously to compute the integrated disk spectra. This method allows to estimate the aperture effects in all the disks that create our sample in a uniform way. Then, we calculate the gradients of the extinction-corrected Hα growth curves as the ratio between the flux in each aperture and the corresponding radial interval. This gradient decreases and becomes nearly zero when it approaches the maximum radius as the flux tend to be constant in the last apertures. Finally, if we plot the flux as a function of these gradients, the intercept of this relation gives us the value of the aperture correction. The mean and the median values for the aperture correction multiplicative factors in our sample are 1.19 and 1.08, respectively. The extinction-corrected Hα SFR measurements for each galaxy component are given in Table 4.1.

4.4.4 CALIFA: Stellar masses

Stellar mass is a key parameter on the process of formation and evolution of galaxies. For this study, we rely on the CALIFA total stellar masses that were calculated by Walcher et al. (2014) using Bruzual & Charlot (2003) stellar population models with a Chabrier (2003) stellar IMF to construct UV to NIR SEDs. In particular, FUV (GALEX, Martin et al. 2005), *u*, *g*, *r*, *i*, *z* (SDSS-DR7, Abazajian et al. 2009) and J, H, K (2MASS Extended Source Catalog, Jarrett et al. 2000) photometric data were used (for more details see Section 2.3.1 of Chapter 2).

We are interested in determining the stellar masses not only for the galaxies as a whole but also for their different structural components. For that reason, we apply the recipe below that allows deriving the mass in each component using the *i*-band mass-to-light relation of each component, $(M_*/L)_{comp,i}$, the galaxy total stellar mass, $M_{*,total}$, and the bulge-to-total (B/T), bar-to-total (Bar/T) and disk-to-total (D/T) luminosity ratios in the *i*-band. The luminosity ratios are derived as by-products of the 2D photometric decomposition for our galaxies in *i* and *g*-bands (see Section 4.4.2 for more details). We use the *i*-band values as they will better reproduce the stellar mass distribution than the *g*-band. Thus, we obtain:

$$\frac{M_{*,comp}}{M_{*,total}} = \frac{\left(\frac{M_*}{L}\right)_{comp,i}}{\left(\frac{M_*}{L}\right)_{total,i}} \cdot \frac{L_{comp,i}}{L_{total,i}} \tag{4.1}$$

We make use of the color-dependent M_*/L_i ratio given by equation 7 in Taylor et al. (2011) where the authors also assume a Chabrier (2003) IMF. The authors proposed the following empirical relation between M_*/L_i and $(g-i)$ color:

$$logM_*/L_i = -0.68 + 0.70(g-i) \tag{4.2}$$

In our case, the $(g-i)$ colors correspond to either $(g-i)_{disk}$, $(g-i)_{bar}$ or $(g-i)_{bulge}$. The following expression is used to obtain the $(g-i)$ colors for each galaxy component:

$$(g-i)_{comp} = (g-i)_{total} - 2.5 \cdot log\frac{\left(\frac{L_{comp}}{L_{total}}\right)_g}{\left(\frac{L_{comp}}{L_{total}}\right)_i} \tag{4.3}$$

The $(g-i)_{total}$ color measurements came from the analysis of the growth curve magnitudes performed in Walcher et al. (2014).

To verify the goodness of our stellar mass values per component, we have checked that the sum of the stellar masses for the different components obtained via the previous equations reproduces the total stellar mass derived from SED fitting for each galaxy. Both methods yield similar results for 82 % of the galaxies, with the difference between the sum of the stellar components and the SED stellar mass being less than ± 15 %. For the remaining 18 % of the galaxies, a larger difference arises due to significant variations in the $^{(B/T)_i}/_{(B/T)_g}$ ratio. The latter case has a mean value of 2.26 for the $^{(B/T)_i}/_{(B/T)_g}$ ratio in contrast to a 1.30 value for the cases in which the sum of the derived stellar masses of the components and the SED total stellar mass are similar. The former case is a consequence of the non-linearity between the luminosity ratios in both bands and the mass-luminosity relation in equation 4.2.

As a final remark, we note here that the Hα extinction-corrected SFR tracer used along this work and the stellar population models applied for the continuum subtraction (Section 4.4.3) are both based on a Kroupa (2001) IMF. For the sake of consistency, we rescale the stellar masses derived in this section to the Kroupa (2001) IMF applying the factor 1.08 as obtained in Madau & Dickinson (2014). This value is almost independent of the stellar population age and has a very weak dependence on metallicity. The stellar masses derived for each galaxy component are provided in Table 4.1.

4.4.5 AGN optical classification

AGN feedback is one of the mechanisms proposed to explain the quenching of the star formation in classical bulges and in massive galaxies, as it has been put forward to explain the differences between models and observations mainly at the high-end of the galaxy luminosity function (Silk

& Mamon 2012). Therefore, it is critical to determine which of our CALIFA galaxies host an AGN. We apply a classical emission-line diagnostic to classify the objects into star-forming or type-2 AGN. For that purpose, we use the [OIII]/Hβ vs. [NII]/Hα diagram introduced by Baldwin et al. (1981) with the demarcation lines of Kauffmann et al. (2003) and Kewley et al. (2001). We extract the spectrum centered within 3 arcsec of the nucleus and we imposed a S/N $>$ 4 for the previous emission lines. We obtain that 74 out of 219 galaxies are Seyfert/LINER. From now on, we refer to Seyfert/LINER as type-2 AGN objects. We highlight that galaxies that have type-1 AGN signatures are excluded from the sample completely. In the Unified Model, the emission from the AGN in Seyfert 1 galaxies outshine that due to recently formed stars as the Broad Line Region (BLR) is directly observable, while in Seyfert 2 galaxies the BLR is highly obscured and the line emission from the AGN competes with that due to star formation. Alternatively, several studies have pointed out a new scenario where Seyfert 1 and Seyfert 2 might be indeed a different class of objects and the existence of "true Seyfert" which lack a BLR (Tran 2001; Tran et al. 2011). Since the spatial resolution in our data is not enough to disentangle whether the central contribution is coming totally from the AGN or it has some contamination from (or even dominated by) star formation, for the type-2 AGN objects we have decided to include them in our sample and to distinctly mark them as type-2 AGN when necessary. Table 4.1 provides information about the galaxies classified as AGN in our sample.

Although LINERs have been traditionally associated with low-luminosity active galactic nuclei (LLAGN, Ho et al. 1993; Terashima et al. 2000), some authors have recently claimed the importance of differentiating between galaxies hosting a weakly active nuclei and galaxies that could be ionized by hot low-mass evolved stars (a recent discussion about the nature of LINER galaxies is provided by Singh et al. 2013). In that regard, Stasińska et al. (2008); Cid Fernandes et al. (2010, 2011) have proposed to use the observed Hα equivalent widths ($EW_{H\alpha}$) versus the [NII]/Hα ratio in the so-called WHAN diagram in which the division between weak AGNs and galaxies that are ionized by their hot low-mass evolved stars is fixed at 3 Å. We restrict the estimation of the $EW_{H\alpha}$ to the center of our galaxies, i. e., the 3 central arcsec, instead of using the total integrated spectrum as we want to know whether or not the AGN is the dominant photoionization mechanism in the nuclear regions. The 3 Å criterion admittedly overestimates the number of galaxies classified as "retired galaxies" as diluted bona fide AGNs could be also included in this category (Cid Fernandes et al. 2011). For that reason, we analyze the trend for the 6-arcsec and 9-arcsec apertures in these objects. Radial $EW_{H\alpha}$ profiles using CALIFA data have been previously probed to be optimal for the study of the nuclear and extranuclear nebular emission of the warm ionized gas (Gomes et al. 2016). We find that there are two distinct types. On one hand, some galaxies show an increase in the $EW_{H\alpha}$ and a reduction in the [NII]/Hα ratio at larger apertures reflecting the presence of a star-forming component. Even more, the integrated spectrum shows values of the $EW_{H\alpha}$ larger than 3 Å. On the other hand, there are galaxies for which the $EW_{H\alpha}$ decreases while the [NII]/Hα ratio maintains a roughly constant value when using larger apertures. There are two possibilities for this case: (a) the evolved stars that are responsible for the photoionization of these regions exhibit a gradient which might explain the radial variation in $EW_{H\alpha}$ and/or (b) there is actually an AGN in the central region and the older populations in their surroundings create a decline in the $EW_{H\alpha}$ measurements. Whether one or both of these possibilities is the responsible mechanism is beyond the scope of this work. There are still, however, a fraction of 39.2% of the galaxies initially classified as AGN (33.5% of the sample) where an homogeneous population of evolved stars could generate, according to the predictions of Cid Fernandes et al. (2011), the $EW_{H\alpha}$ values and distribution observed (at least

at the spatial resolution of CALIFA). Thus, galaxies that have a Seyfert/LINER central spectrum are referred as type-2 AGN even though a fraction of these could be actually powered by a source distinct from a truly AGN.

4.5 Results

Along this work we use extinction-corrected Hα (Hα_{corr}) as our SFR reference indicator following the recipe given by Kennicutt & Evans (2012). From now on we will use Hα instead of Hα_{corr} to shorten the term along the text although we emphasize that all the Hα SFR measurements used here are extinction-corrected.

We have previously investigated the goodness of Hα as a SFR tracer for a representative sample of 272 CALIFA galaxies (for more details see Catalán-Torrecilla et al. 2015, and Chapter 3 of this thesis). For that purpose, we compared extinction-corrected Hα integrated measurements with single band (FUV$_{corr}$, 22 μm and TIR) and hybrid (22 μm + Hα_{obs}, TIR + Hα_{obs}, 22 μm + FUV$_{obs}$, TIR + FUV$_{obs}$) tracers. The latter shows an excellent agreement with dispersions around 0.18 dex. We also find that only 1 % of our objects host highly-obscured SF. Bearing in mind the above considerations, we can safely conclude that the use of extinction-corrected Hα is appropriate for our sample. Whether or not this calibration can be applied to other samples in the local Universe or to higher redshifts depends strongly on the expected fraction of galaxies and SFR that could be locked into completely-obscured star-forming sites and also on the percentage of nuclear line emission in Sy2 coming from either SF or AGN (or even ionization from evolved stars).

In this Section, we show the correlations found between the SFR in the different morphological components of the galaxies and other physical properties such as stellar mass, morphological type, the presence of an AGN, environment and stellar velocity dispersion. Among other aspects, we investigate the so-called "Main Sequence" of galaxies using not only integrated values but also the values in each galaxy morphological component (i. e., nuclear point sources, bulges, bars, and disks).

4.5.1 SFR ratios by components: SFR central enhancement due to the presence of bars

In this section, we explore the connection between the central SFR(Hα) with other parameters such as the morphological type and the B/T in the g-band. The analysis is performed only for galaxies that do show Hα emission in the central regions. For the discussion below, central regions refer to either the bulge component alone (green and orange points in plots) or the bulge plus bar components together (blue points) in Figures 4.2 and 4.3. We also analyze if the presence of a bar could trigger the star formation in the centers of galaxies. Galaxy morphologies were inferred by a combination of independent visual classifications carried out by members of the CALIFA collaboration as described in Walcher et al. (2014) while B/T values in the g-band came from the analysis of the 2D decomposition (Section 4.4.2).

In order to investigate the impact of the bar on the central SFR, galaxies are classified into two

main types, barred and unbarred. Simultaneously, the formers could include the SFR just in the bulge or include the SFR in the bar component as well. Obviously, the amount of the SFR in the central component increases when we add the contribution of the bar to it.

The variation of the SFR[Hα(central)]/SFR[Hα(total)] ratio as a function of the morphological type is shown in Figure 4.2. It can be seen that the median values of the fraction of SFR contained in bulges is higher for the Sb/c barred galaxies (orange points) in comparison with unbarred galaxies (green points). This result points out that SFR in the central parts of these galaxies may be enhanced by the presence of a bar. Nevertheless, this trend is not found for other morphological types, perhaps due to much lower-number statistics in those types.

As the majority of our galaxies are concentrated in the bin of Sb/c objects which makes the dynamic range of our morphological classification smaller, we also explore the behavior of the SFR[Hα(central)]/SFR[Hα(total)] ratio with the B/T parameter (left panel in Figure 4.3). As commented before, B/T is obtained from the 2D decomposition analysis and does not depend on a visual classification.

In order to quantify whether or not the presence of the bar is affecting the SFR in the bulge component, we split the sample in three bins: $\log(\mathrm{B/T}) < -1.5$, $-1.5 < \log(\mathrm{B/T}) < -1.0$ and $-1.0 < \log(\mathrm{B/T}) < -0.5$. Big squares represent the logarithm of the mean value for the SFR[Hα(central)]/SFR[Hα(total)] ratios in each bin for purely star-forming galaxies while big stars refer to galaxies that have been classified as type-2 AGN. The 1:1 (dotted) line corresponds to the locus of galaxies that having only bulge and disk components would show the same extinction-corrected Hα-to-optical (g-band) luminosity ratio among these two components. The main result of this figure is that star-forming galaxies present higher mean SFR central values for barred galaxies (orange squares) than for unbarred ones (green squares). This effect is especially important for the cases of B/T smaller than 0.1. The enhancement of the central SFR due to the presence of bars has been pointed out by several authors using observational data (de Jong et al. 1984; Devereux 1987; Ellison et al. 2011; Wang et al. 2012; Florido et al. 2015) and also in recent dynamical simulations such as in Carles et al. (2016). As a result, a rejuvenation of the stellar populations in the center of barred galaxies has been also claimed by Fisher (2006) and Coelho & Gadotti (2011) among others.

We can also analyze the connection between the presence of bars and AGN activity. We find that the optical bar fractions are similar for star-forming objects and type-2 AGN host galaxies, 43.9 % and 52.2 %, respectively. This result is in accordance with previous works (Mulchaey & Regan 1997; Hao et al. 2009). Nevertheless, galaxies hosting a type-2 AGN show less difference between the mean central SFR values for barred (orange stars) and unbarred (green stars) galaxies in comparison with purely star-forming objects. If bars and AGNs are simultaneously present, the effect of the bar in triggering the central SFR is reduced. Finally, it is also clear that type-2 AGNs are quenching the central SFR in their host galaxies, at least for small values of the B/T parameter.

To better understand the increase in the SFR in the central parts of star-forming barred galaxies we examine the behavior of the sSFR (sSFR = SFR/$M_\star$) in fixed bins of B/T values. Right panel in Figure 4.3 shows that barred galaxies tend to have higher mean values of their sSFRs in the central regions compared to unbarred galaxies. The horizontal dotted line here represents the location of galaxies that having only bulge and disk components would have the same sSFR in these two components. From this plot it is clear that the disks of low B/T galaxies (with only bulge and disk

components) have higher sSFR values than their bulges. This is possibly related to blue optical-to-infrared colors and the presence of significant intermediated-aged stellar populations in their disks.

From this section, we can conclude that there is a clear relation between the SFR and sSFR in the central parts of the galaxies and the presence of bars. Star-forming barred galaxies show higher values of their central SFR and sSFR than unbarred galaxies. This trend is present when we analyze the variation of the SFR with the B/T ratio while it is not as clear with the morphological type, probably, due to the low statistics for early-types and Sd/m galaxies. Besides, morphological type is also related to other aspects such as the definition of the spiral arms or the surface brightness. In contrast, the B/T is a more robust parameter to quantify the variation of the SFR in the central parts of the galaxies as it is related to the bulge prominence. This finding supports the idea of bars driving gas efficiently toward the central regions of galaxies causing an enhancement of the SFR and the importance of the internal secular processes for the evolution of galaxies. On the contrary, in type-2 AGN we do not find a significant difference in the central SFR between barred and unbarred galaxies. Thus, nuclear activity should play a role at quenching the central SFR.

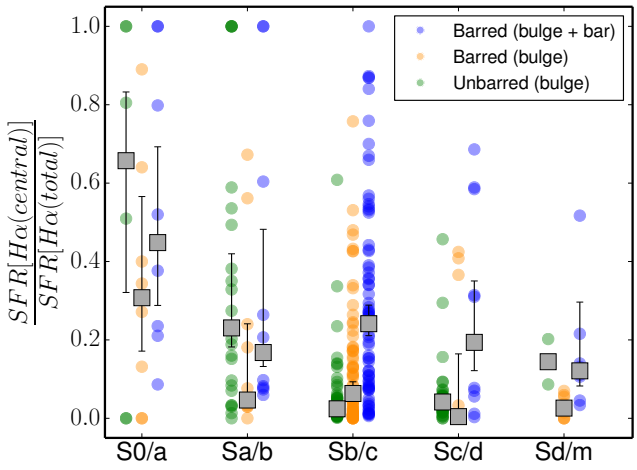

Figure 4.2: Distribution of the SFR[Hα(central)]/SFR[Hα(total)] ratio with the morphological type. Green points correspond to unbarred galaxies. Orange and blue points represent barred galaxies. In the former case the contribution of the SFR in the bar component is not added while in the latter case this contribution is included. The gray squares show the median value for each bin of measurements and the errors correspond to the standard error of the median, i./,e., 1.253×σ/sqrt(N), where σ is the interval that includes 68 % of the data points around the median.

4.5.2 Main Sequence

The correlation observed between SFR and stellar mass (M_*) often referred to as the galaxy "Main Sequence" (MS) has been extensively studied in the local Universe and at higher redshifts (Noeske et al. 2007; Daddi et al. 2007; Elbaz et al. 2007, 2011; Wuyts et al. 2011; Whitaker et al. 2012, 2014, 2015; Speagle et al. 2014; Magnelli et al. 2014; Renzini & Peng 2015; Catalán-Torrecilla et al. 2015; Lee et al. 2015; Cano-Díaz et al. 2016; Duarte Puertas et al. 2016).

Top left panel in Figure 4.4 shows the MS for the galaxies in our sample classified according to their morphological type. For the sake of clarity, we include here the fitting by Elbaz et al. (2007)

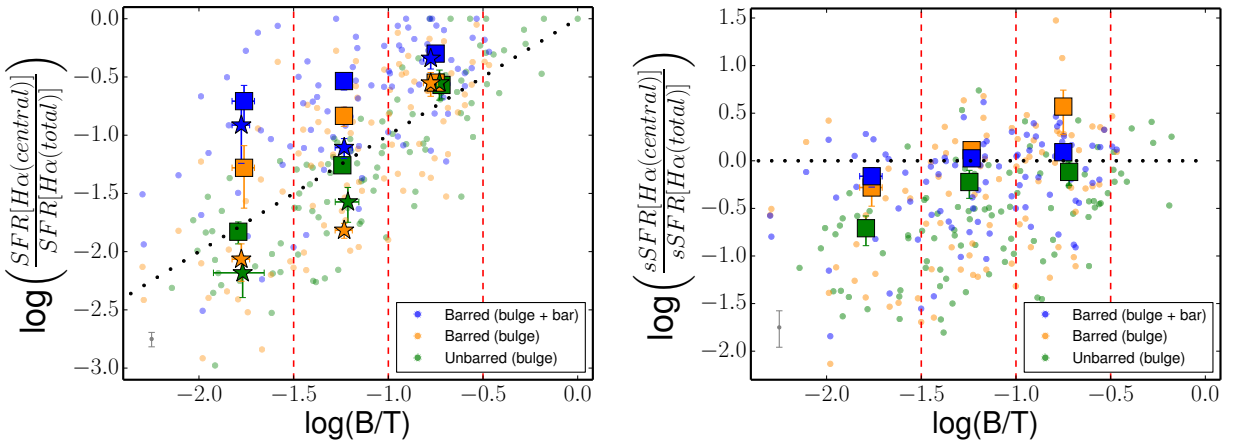

Figure 4.3: Left panel: Variation of the SFR[Hα(central)]/SFR[Hα(total)] ratio with the B/T parameter obtained for the *g*-band. The central SFR could be referred to the amount of SFR in the bulge component for unbarred galaxies (green points) or for barred ones (orange points). Blue points represent the SFR measured in the bulge and bar components at the same time. Squares correspond to purely star-forming galaxies while stars are referred to type-2 AGN objects. The previous symbols correspond to the logarithm of the mean value for the SFR[Hα(central)]/SFR[Hα(total)] ratio and the errors represent the standard deviation of the mean. Right panel: Variation of the sSFR[Hα(central)]/sSFR[Hα(total)] ratio with the B/T parameter in *g*-band.

that shows the region of the diagram where star-forming galaxies are placed. Most of the late-type galaxies in our sample are located in this region. On the other hand, S0/S0a, Sa/Sab and some Sb/Sbc galaxies are comparatively less efficient at forming stars at the present time, meaning that for the same stellar mass they are placed outside the MS as shown in this diagram.

Some of the previously mentioned studies claimed that there is a turn over of the MS for stellar masses $M_* > 10^{10}$ $M_\odot$. We analyze whether or not this particular trend is also present in our sample. Instead of imposing a stellar mass cut, we divide the sample into two groups: i) Sb/Sbc objects and ii) Sc/Scd together with Sd/Sdm galaxies. Nevertheless, this morphological type cut-off is quite similar to the one used for stellar mass as the majority of Sb/Sbc galaxies tend to have stellar masses larger than 10^{10} $M_\odot$ while most of the Sc/Scd and Sd/Sdm objects have masses below 10^{10} $M_\odot$. Moreover, the fact that massive late-type spirals are clearly on the MS while early-type ones of the same mass are significantly offset does advice on the use of other criteria besides mass to perform the analysis of the MS. The fittings for both cases are shown in the top left panel of Figure 4.4 (green and blue lines, respectively). Star-forming galaxies in Figure 4.4 are represented by circles while AGN objects appeared as star symbols. The fittings are only done for star-forming galaxies. There is an offset between them in the sense that Sb/Sbc galaxies tend to have lower SFR values for the same stellar mass. It is also important the change in the slope (0.74 ± 0.09 for Sc/Scd/Sd/Sdm, 0.63 ± 0.12 for Sb/Sbc) that goes in the direction of an extra flattening in the case of the Sb/Sbc objects [1]. As our sample does not contain highly inclined disks (due to the criteria imposed for the 2D decomposition, Section 4.4.2) we avoid effects that might be associated with an underestimate of the SFR which would affect the slope and width of the MS (Morselli et al. 2016). Therefore, we are in agreement with the authors that find a turn over of the MS and we confirm this result for our sample. We go beyond this as we find that is not only mass driven but also related to the galaxy morphological type.

[1]The relation given by Elbaz et al. (2007) is already tilted relative to the lines of constant sSFR

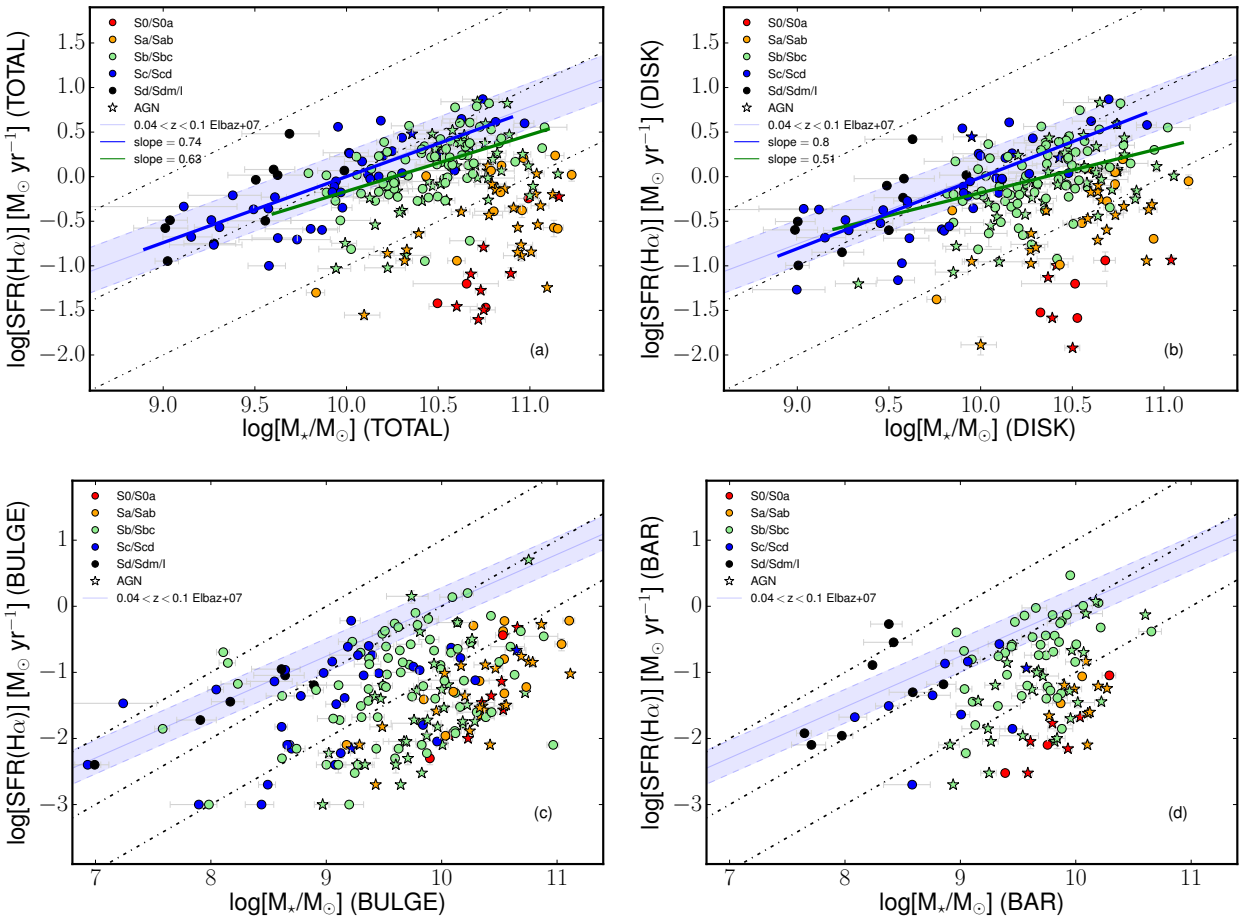

Figure 4.4: Top left panel (a): SFR(Hα)-M$_\star$ plane for integrated values of the galaxies in our sample. The blue shaded area in this diagram shows the position of the Main Sequence (MS) using the fit by Elbaz et al. (2007). Star-forming galaxies are represented by circles and AGNs by star symbols. The green line shows the fitting to Sb/Sbc star-forming objects while the blue line is the fitting to Sc/Scd/Sd/Sdm star-forming galaxies. The slope of the previous fittings appeared in the legend. The color-coding is used to distinguish the different morphological types of the galaxies. The dot-dashed lines indicate lines of constant sSFR (10^{-9}, 10^{-10} and 10^{-11} yr^{-1} from top to bottom, respectively). Top right panel (b): SFR(Hα)-M$_\star$ plane for the disk component. Symbols, fits and color-coding are as in panel (a). Bottom left panel (c): SFR(Hα)-M$_\star$ plane for the bulge component. Lines, symbols and colors are the same as in the panel (a). Bottom right panel (d): SFR(Hα)-M$_\star$ plane for the bar component. Lines, symbols and colors are the same as in the panel (a).

Although the analysis of the MS for integrated properties of galaxies is extremely valuable, we highlight the necessity of studying if the MS is also present when galaxies are separated in their stellar structures (bulges, bars, and disks). In fact, there is a key question that still remains unsolved, do disks of galaxies that are quenched (i. e., are found away from the MS) populate the MS?

To shed some light on this issue we analyze the "Disks MS", that is, the relation between the SFR in the disk component and the stellar mass of the disk (top right panel of Figure 4.4). As we have done in the case of integrated values, we focus our attention on intermediate-to-late-type galaxies. We find that the global trend for the MS is also reproduced in the case of the disks.

What is more, the fittings for the different morphological types, Sb/Sbc and Sc/Scd-Sd/Sdm, show a similar behavior when compare with the integrated values. There is an offset between both fits and the slope is also steeper for Sc/Scd-Sd/Sdm galaxies (0.80 ± 0.10 for Sc/Scd/Sd/Sdm, 0.51 ± 0.14 for Sb/Sbc). Then, we conclude that the current-to-past SFR has decreased in more massive disks and in earlier-type spirals relative to less massive and later-type systems. Not only entire galaxies but also disks in more massive systems have been more efficiently quenched. We note here that the dynamical range of stellar masses is quite similar for disks and for integrated galaxies, so when we refer to more massive systems, in general, we are referring to more massive disks as well. We appreciate in the same figure that many of the disks, mainly S0/S0a and Sa/Sab, are still away from the MS on their own.

The position of the bulges in the SFR(bulge)-$M_\star$(bulge) plane is shown in the bottom left panel of Figure 4.4 while in the case of the bars the SFR(bar)-$M_\star$(bar) plane is shown in the bottom right panel of the same Figure. Bulges and bars are clearly much less efficient than disks in terms of their SFR even less if we take into account that in type-2 AGN some of the SFR associated with the central components might not be related to recent SF.

Until now we have shown the SFR trend of each galaxy component with their corresponding stellar mass (bulges, bars, and disks). Now, we focus on the analysis of the SFR of each component with the total galaxy stellar mass instead. Left panel in Figure 4.5 shows the trends for the variation of the SFR in the bulge, bar, and disk component in bins of 0.5 dex in stellar mass. We have combined at the same time all the morphological types for each component (which will obviously increase the dispersion as early-type spiral have lower values of their SFR specially for the disk component). It can be seen from this figure that most of the actual SFR in galaxies is located in the disk component as it is expected while bars and bulges show a smaller contribution for a fixed stellar mass. As seen previously for the disks, not only by morphological type but also with stellar mass there is a clear decrease in the SFR for more massive disk galaxies (i. e., more massive systems in general due to the similar range in total and disk stellar masses).

To conclude, we have demonstrated in this section that more massive star-forming disks and earlier-type spiral disks show a higher level of quenching. Previous studies have shown that more massive star-forming galaxies (understanding galaxies as entire systems) tend to be less efficient at forming new stars. Here, the important fact is that we treat disks as separate components of the galaxies.

4.5.3 sSFR-$M_\star$ relation for bulges and disks: a clue for the quenching of massive systems

In the previous Section 4.5.2, we have explored in detail the Main Sequence and the fact that the same relation that applies to star-forming galaxies as a whole is also valid for the disk component of the same galaxies. More surprisingly, however, galaxies that are offset from the main sequence have disks that are also forming stars at present at a lower rate than in the past compared to MS galaxies (i. e., they do not fall on the MS), so the position of galaxies relative to the MS is not only due to a larger contribution of the bulge component but also to a decrease in the recent SFR normalized to their mass (see below). This is true even for well-defined Sb/Sbc spirals. In other words, there is what we have called the "Disk Main Sequence" and galaxies that are away the MS

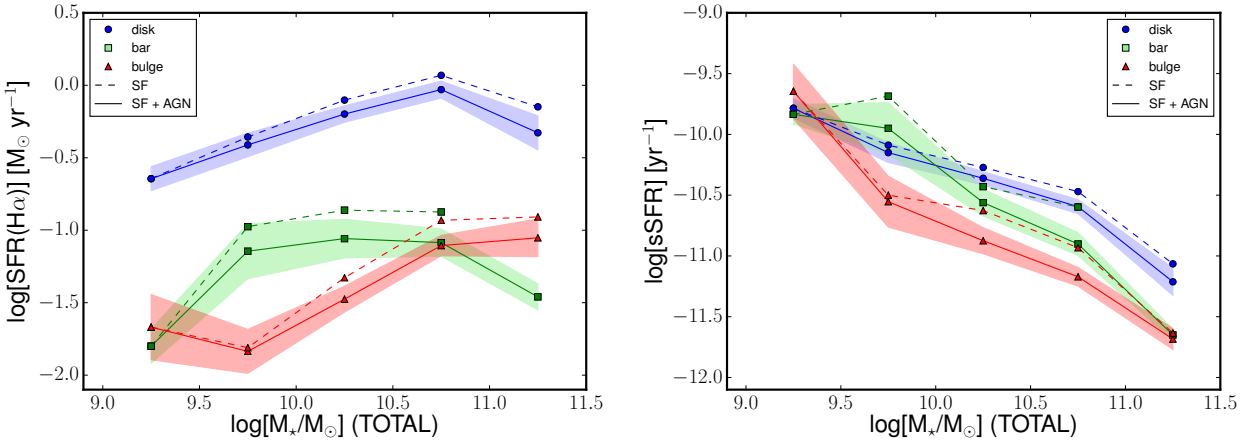

Figure 4.5: Left panel: Variation of the Hα-based SFR for the different morphological components of the galaxies (bulge, bar, and disk) with the total stellar mass of the galaxy. The trends for bulges, bars, and disks are shown in red triangles, green squares and blue circles, respectively. Filled contours represent the 1σ dispersion around the mean value expressed as a red, green and blue solid line for the bulge, bar, and disk, respectively. Dashed lines show the trends just for the star-forming galaxies. Right panel: Same description as the top panel this time for the sSFR.

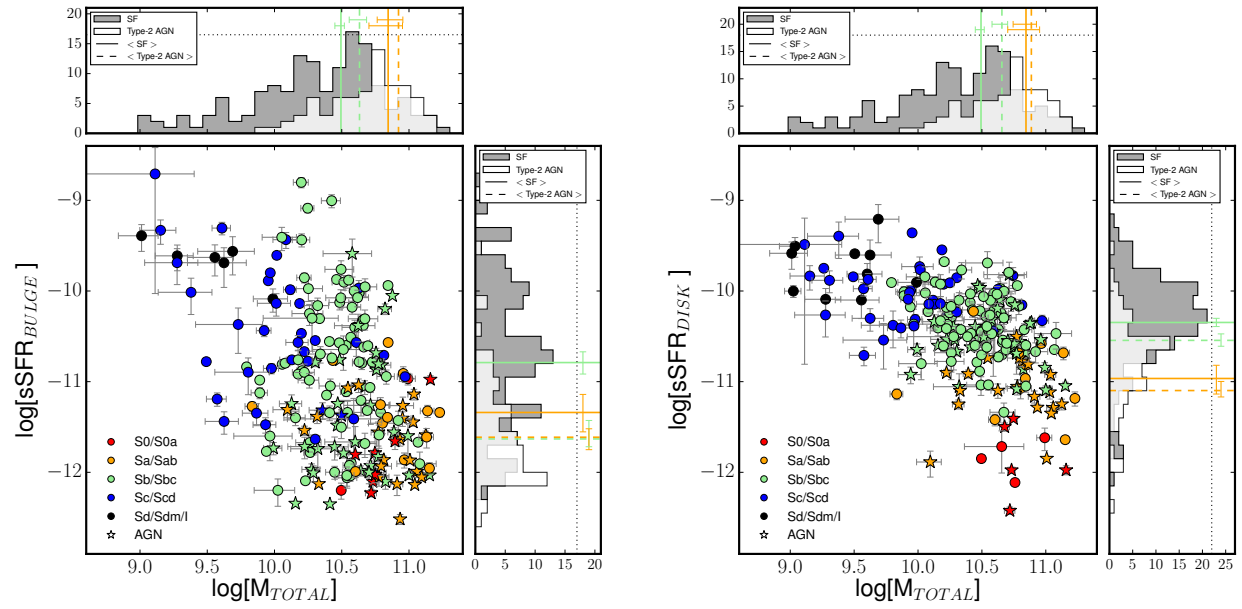

Figure 4.6: Left panel: sSFR for the bulge component as a function of the total stellar mass. The circles refer to the star-forming galaxies in our sample while the stars indicate the AGNs objects. The color of each symbol indicate the corresponding morphological type of the galaxy. The top histogram shows the distribution of the bulges with the total stellar mass of the corresponding galaxy that could be classified as star-forming or type-2 AGN. Vertical solid (dashed) lines represent the median value of SF (AGN) galaxies while the errors bars are computed using the standard error of the median, i./,e., 1.253×σ/sqrt(N) where σ is the interval that contains 68% of the points. Sb/Sbc (Sa/Sab) types appeared in light-green (orange). The right histogram shows the distribution of the galaxies as a function of the sSFR in the bulge component. Vertical lines represent median values and their errors. Right panel: same description as the left panel this time for the disk component.

have disks that are also away from the MS. To associate this finding with the capacity for galaxies to form stars at present time (compared with that in the past), we analyze here the specific SFR

of both bulges and disks as a function of the galaxy total stellar mass. Ultimately, we aim to answer the following question, what are the mechanisms responsible for the quenching of the most luminous and massive galaxies and their disks?

Abramson et al. (2014) declared that sSFR(disk) is approximately constant with stellar mass for $M_\star > 10^{10}$ $M_\odot$ and B/T < 0.6. The authors assume sSFR(disk) = SFR(total)/$M_\star$(disk) and that nuclear and bulge regions might have small contributions to the SF. If this was the case, the growth of bulges may be the potential cause to create the flattening in the MS for the higher stellar masses. Nevertheless, we argue here that bulges also contribute to the SFR in those galaxies with higher values of their stellar masses (as shown in the previous Section). Figure 4.6 shows the relation of the sSFR(disk) and sSFR(bulge) with the total stellar mass of the galaxies in our sample. From this figure, we conclude that sSFR(disk) is not constant with stellar mass, meaning that disks are not equally active at forming stars in terms of their sSFR. Besides, from left panel in Figure 4.6 it can be seen that the sSFR(bulge) spans a wide range (more than 2 dex) of values and the importance of the contribution coming from the bulges to the star formation. The bulges in our sample could be either classical bulges or pseudobulges (for an extensive review see Kormendy & Kennicutt 2004). Although with limitations, one can broadly discriminate between classical and pseudo-bulges using the Sérsic index n_b (see Fisher & Drory 2008, 2016), where classical bulges are characterized by n_b values greater than 2 while pseudobulges have values lower than 2. Using the n_b parameters derived from the 2D photometric decomposition, 72 % of our bulges would be classified as pseudobulges while the remaining 28 % would appear as classical bulges. Fisher & Drory (2016) established that bulges should be forming stars actively for sSFR $> 10^{-11}$ yr^{-1} while they might be either pseudobulges or classical for lower values of the sSFR. We find a median value of $1.66\ 10^{-11}$ ($8.95\ 10^{-12}$) yr^{-1} for pseudobulges (classical bulges). Determining whether or not sSFR provide an accurate separation between bulges or pseudobulges is beyond the scope of this study and would require of high-resolution imaging of the nuclear regions, which is not available for the vast majority of the galaxies in our sample.

Another potential mechanism to quench the star formation of the most massive galaxies could be the presence of an AGN. Although many studies include only galaxies that are strictly star-forming, we also include here type-2 AGN to study their relative position in the sSFR-stellar mass plane. The power of IFS data will certainly help us to resolve whether or not the presence of an AGN contributes to the quenching of the massive galaxies. We recently reported in Catalán-Torrecilla et al. (2015) (Figure 3.19 of Chapter 3) that AGN might have an impact at suppressing the total SFR in their host galaxies. Other works corroborate the idea of the suppression of the star formation by AGNs in the host galaxies (Shimizu et al. 2015; Leslie et al. 2016). In this Section, we investigate the role of AGN in the quenching of the SFR, not only in global terms but also in their bulges and disks separately. This is particularly important considering that, as shown above, galaxies that are away from the MS host disks that have their star formation depressed/suppressed, so AGN quenching should thus work at galactic-wide scales. The alternative is that AGN quenching is not the dominant mechanism but it is coeval with another mechanism(s) that has an impact on the star formation at those scales. One possibility is the removal of a fraction of the high-angular momentum gas of the disks due to interactions towards the nucleus (leading to an AGN) becoming unavailable for star formation in the disk component.

To investigate this possibility, we examine the sSFR-stellar mass plane shown in Figure 4.6 for bulges and disks, separately. Some interesting results emerge from these plots. First, type-2

AGN are not homogeneously distributed in the plane. They tend to be in high mass end. Indeed, type-2 AGN are mostly found in galaxies with stellar mass values in the range between [10^{10} - $10^{11.5}$] $M_{\odot}$ (white histograms on the top of both panels in Figure 4.6). We also find that there is a clear decrease in the sSFR values when a type-2 AGN is present. Bulges of AGN hosts show a median sSFR(bulge) that is 0.87 dex below that of star-forming galaxies when the difference in median stellar mass is +0.30 dex. For the case of the disks there is a −0.42 dex difference in median sSFR(disk) and +0.35 dex in median mass. Nevertheless, it is important to quantify whether this effect is still present in terms of the same morphological type or not. Thus, due to the lack of type-2 AGN in most of our late-type galaxies, in agreement with previous works (Moles et al. 1995), we restrict the following analysis to Sa/Sab and Sb/Sbc objects. Bulges of Sa/Sab (Sb/Sbc) show a median sSFR that is 0.27 (0.84) dex below that of star-forming galaxies while the difference in the median value of the stellar mass is 0.08 (0.14) dex. For the case of the disks, Sa/Sab (Sb/Sbc) galaxies exhibit a difference in the median values of sSFR for star-forming and AGNs of 0.13 (0.20) dex while the difference in stellar masses is 0.04 (0.16) dex (solid and dashed vertical lines in the top and right histograms of right panel in Figure 4.6). This result suggests a possible damping of the SFR in both components due to the presence of AGNs. We prefer the term damping here as compared to quenching. It is not clear whether this decrease in the sSFR is enough (neither if it lasts enough) to make these galaxies evolve towards and remain in the red sequence, something for which galaxy evolution models require of a strong quenching of the star formation in massive galaxies at high redshift (Weinberger et al. 2017, and references therein). Also, we find that bulges show a constant decline of the sSFR across the entire stellar mass range. On the contrary, the decrease in the disk component is more dramatic when galaxies reach a certain stellar mass, typically around $10^{10.5}$ $M_{\odot}$. Finally, a significant trend with the morphological type is also found. Late-type galaxies have higher values of their sSFR for both components, bulges and disks.

To clarify the previous trends, right panel in Figure 4.5 shows the variation of the sSFR in the different morphological components (bulge, bar, and disk) in bins of 0.5 dex in total stellar mass. As done previously with the case of the SFR (top panel in the same figure), all the morphological types of each component are combined at the same time (spreading the dispersion as early-type spiral present lower sSFR values). Again, it is clear from this figure that the disk component is significantly more effective than the bulge at forming new stars, specially for $M_{\star} > 10^{9.5}$ $M_{\odot}$, and the stepper decline for the bulges at the lower stellar mass bin.

From the results in this section, we conclude that the presence of an AGN might be linked with the damping of the SFR in both the bulge and the disk component. In both cases, the sSFR decreases when an AGN is present being this effect higher for the bulges in competition with the effect of the bars. We identify the same behavior among different morphological types such as Sa/Sab and Sb/Sbc. Again, due to the short timescale traced by the Hα line emission we cannot infer whether the AGN phase is cause, consequence or co-eval with the star formation quenching process. Besides, as discussed in Section 4.4.5, we cannot exclude that a fraction of these low-luminosity AGN could be powered by hot evolved stars in regions with basically null star formation.

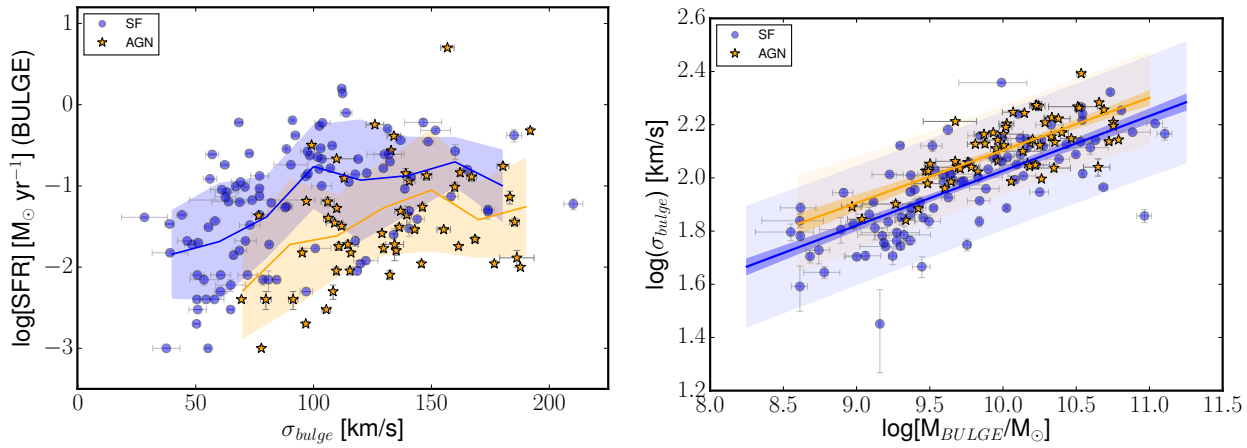

Figure 4.7: Left panel: SFR in the bulge component versus the line-of-sight stellar velocity dispersion. Galaxies are plotted using different colours and symbols, blue circles for star-forming objects and orange stars for type-2 AGN. Blue (orange) filled contours represent the 1σ dispersion around the mean value showed in blue (orange) solid line for SF (type-2 AGN) galaxies. Right panel: Faber-Jackson relation for the bulges in our sample. The blue (orange) solid line shows the best-fitting for SF (AGN) galaxies. Dark shaded areas correspond to the error bands of the fittings when only errors associated with slope and intercept are taking into account. Light shaded areas mark the global uncertainty bands once an additional s parameter that takes into account the intrinsic variation of the points is also included.

4.5.4 Relation with other parameters

As discussed previously in Sections 4.5.2 and 4.5.3, stellar mass seems to be the main driver of the star formation, and, after it, AGN activity also plays an important role. Nevertheless, it is worth exploring the role of other (possibly secondary) parameters that are known to either trigger or quench star formation. In that regard, the following subsections aim to shed some light on the effect that stellar kinematics and the environment have on the star formation processes taking place in our sample.

4.5.4.1 Stellar kinematics

In this section, we explore how stellar kinematics could regulate the star formation in the inner regions of our galaxies. With this aim in mind, we analyze the line-of-sight (LOS) stellar velocity dispersions for the bulge component. We have restricted the analysis of the LOS velocity dispersions to the bulge component due to the fact that the LOS velocity dispersion distribution for each component (bulge, bar, and disk) is quite distinct in the regions where they coexist. This case is especially important for the internal parts of the disks, where the values could be affected by the bulge contamination as this component tend to be the most prominent there. Thus, measuring the stellar velocity dispersion of only the disk component presents an intrinsic uncertainty. For the previous reason, we will focus here on the possible impact of the stellar velocity dispersion in bulges on their SFR.

We employ the CALIFA stellar velocity dispersion maps created by Falcón-Barroso et al. (2017) using V1200 grating data. In order to calculate the integrate velocity dispersions for the bulge, we first multiply the stellar velocity dispersion map by the luminosity-weight map of the bulge

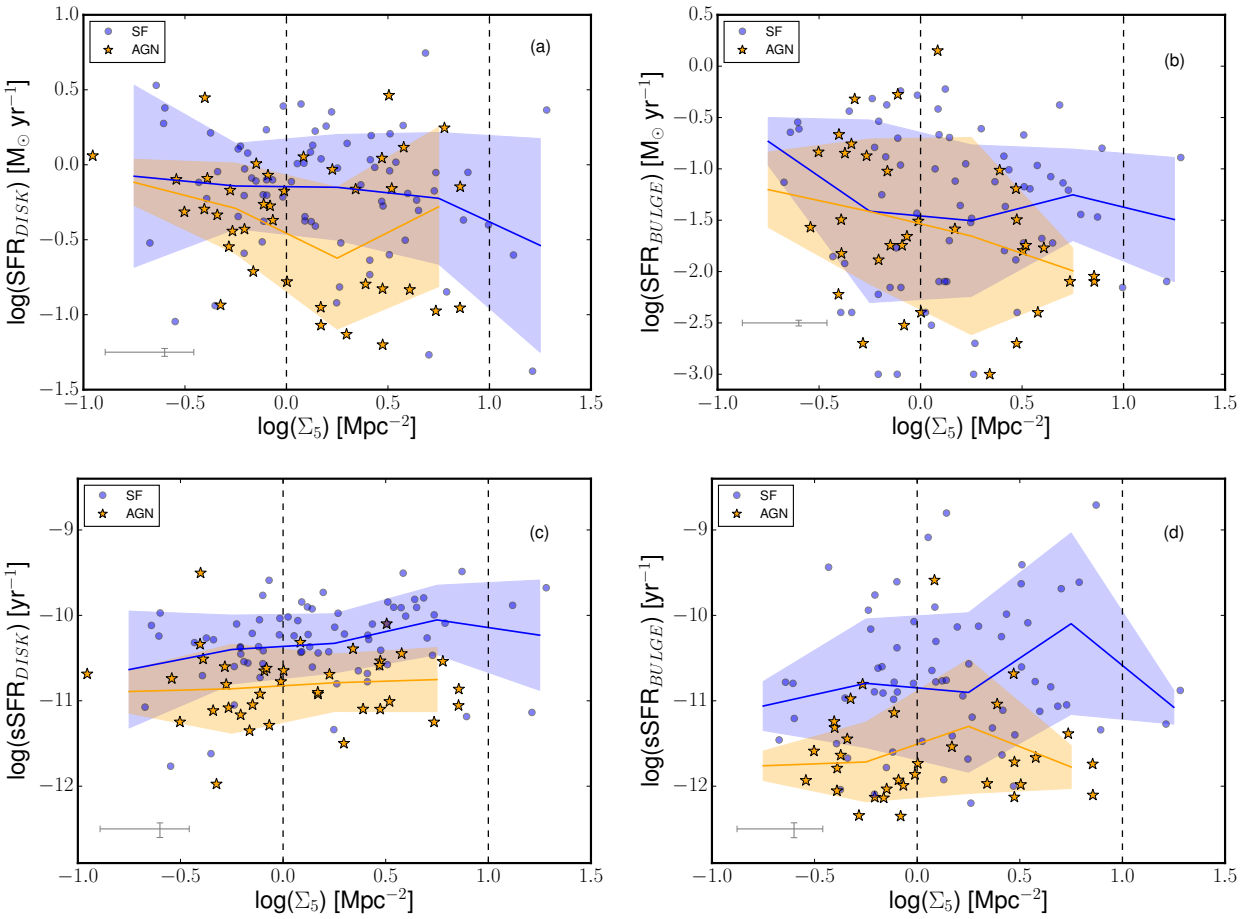

Figure 4.8: Top left panel (a): Variation of the SFR in the disk component with the Σ_5 parameter. Blue (orange) points denote star-forming (type-2 AGN) galaxies. Blue (orange) filled contours represent the 1σ dispersion around the mean value expressed as blue (orange) solid line for the star-forming (type-2 AGN) galaxies. Vertical dashed lines correspond to $\log(\Sigma_5) = 0.0$ and $\log(\Sigma_5) = 1.0$, i. e., the demarcation between low-medium and medium-high density environments, respectively. Top right panel (b): Same description as panel (a) but for the SFR in the bulge component. Bottom left panel (c): Variation of the sSFR in the disk component as a function of the Σ_5 parameter. Color-coding and symbols are the same as in previous panels. Bottom right panel (d): sSFR in the bulge component as a function of the Σ_5 value. Same color-coding and symbols as in previous panels.

component in the *g*-band (previously derived as explained in Section 4.4.2). Then, we divide it by the *g*-band luminosity taking into account only those pixels where the dispersion values are greater than zero. The method applied to obtain the luminosity-weight maps is the same as the one explained in Section 4.4.2. The only difference is that here we used Voronoi bins instead of spaxels as each Voronoi bin provides its own velocity dispersion for the stars. Thus, the expression used to obtain the LOS stellar velocity dispersion for each bulge component is the following:

$$\sigma_{bulge} = \frac{\sum_{i=1}^{N} F_i \cdot \sigma_i}{\sum_{i=1}^{N} F_i} \tag{4.4}$$

where the i subscript refers to the Voronoi bin used in each case. The values of the σ_{bulge} calculated in this Section are given in Table 4.1. The methodology followed in this work is similar to the one used in the literature to derive other kinematical parameters based on 2D spectroscopic data (see e.g. Emsellem et al. (2011) for a similar recipe for $\lambda_{\rm R}$) and it is easily reproducible by other authors using data from different instruments. Moreover, it allows to go beyond the standard method as we apply the luminosity-weight maps for the bulge component that should restrict in a better way the calculation of the LOS velocity dispersions.

In Figure 4.7 (left panel), we show the relation between the SFR in bulges and the stellar velocity dispersions computed as in Equation 4.4. The sample is separated by spectral class (AGN and SF). We find that for the same LOS velocity dispersion, star-forming galaxies show higher bulge SFRs that those of AGN hosts. This, in principle, might be simply due to the correlation between stellar mass and stellar velocity dispersion found in ellipticals and bulges (Faber & Jackson 1976; Chilingarian et al. 2008; Falcón-Barroso et al. 2011) and the noisy correlation between the former and the SFR (see bottom left panel in Figure 4.4).

Additionally, a higher σ_{bulge} (even for the same stellar mass) could also contribute to dynamically heating the gas and to reduce the efficiency of star formation. In order to test whether both effects (or only the stellar mass) are at play, we compare the σ_{bulge} and stellar mass values of our bulges in Figure 4.7 (right panel). The blue (orange) solid line shows the best-fitting for SF (AGN) galaxies. We have employed the Markov chain Monte Carlo (MCMC) method to sample the probability density function of our model parameters. The *Pymc3* code (Salvatier et al. 2016) is used to implement the analysis. Slope and intercept of a line are computed considering uncertainties in both axes. Also, an additional s parameter that takes into account intrinsic variations of the individual points is included. The best-fitting for SF galaxies is -0.035 ($\pm$ 0.180) + 0.206 ($\pm$ 0.018) $\times$ log[$M_{BULGE}/M_{\odot}$] with a $s = 0.110 \pm 0.009$ while for the AGNs is 0.130 ($\pm$ 0.253) + 0.197 ($\pm$ 0.025) $\times$ log[$M_{BULGE}/M_{\odot}$] with a $s = 0.082 \pm 0.008$. A similar value for the slope is found in both cases, while there is a slighter higher value for the intercept of AGNs. A priori, this indicates higher σ_{bulge} values for the AGNs at stellar masses larger than $10^{9.5}$ $M_{bulge}/M_{\odot}$ (the bulge stellar mass range where most of the SF and AGN coexist). Dark shaded area corresponds to the error bands of the fitting when only errors associated with the slope and the intercept are taking into account. Light shaded area marks the global uncertainty bands once the additional s is also included. If we fix the slope of the fits to both datasets to 1/4, then, the mean difference in σ_{bulge} between the two samples would be 0.03 dex. This Faber-Jackson relation shows that even for the same stellar mass, star-forming galaxies tend to have a lower σ_{bulge}, suggesting that a dynamically cooler stellar population in the bulges can host star formation more easily.

4.5.4.2 Environment

Environment is another parameter that can strongly affect the SFR and further stellar mass growth of galaxies and components within galaxies. It is also thought to be the cause of the well known morphology-density relation (Dressler 1980). The main three broad mechanisms proposed to play a role in this sense are mergers/interactions (sometimes referred as galaxy harassment), ram pressure and viscous stripping of cold gas and strangulation in the supply of warm/hot gas (see Kawata & Mulchaey 2008). As these mechanisms act differently in different regions of galaxies and on different timescales, the study of the distribution of the current SFR is key to determine whether

or not they are contributing on specific objects and which one dominates in each case. Moreover, in the case of mergers and interactions, they might lead to either quenching or triggering of the star formation depending on the type of interaction (mass ratios, impact parameters) and on the region considered (nuclear regions, outer disks or even tidal tails). Thus, to investigate whether or not the environment is playing a significant role on the SFR or sSFR of the different structural components of our galaxies, we use the local density values from the projected comoving distance to the 5^{th} nearest neighbor of the target galaxy. The projected galaxy density, Σ_5, in number of galaxies per Mpc^2 is calculated as:

$$\Sigma_5 = \frac{N}{\pi(d_5)^2} \tag{4.5}$$

We have reliable measurements for a total of 140 objects while we lack Σ_5 measurements for 87 galaxies (see Table 4.1). This is mainly because the area enclosing the nearest neighbor lies outside the footprint of the SDSS survey. This means that for these galaxies we cannot obtain a reliable measurement of the density, since we do not know whether there is another close galaxy outside the survey area.

In Figure 4.8 (top panels), we present the variation of the H$\alpha-$based SFR in the disk and in the bulge components as a function of galaxy density, Σ_5. We appreciate a weak trend between both parameters. Galaxies tend to have lower values of their SFR in both components (bulges and disks) for higher values of the galaxy density. These Σ_5 values are associated with medium and high density environments although the latter case is not well-sampled due to a lack of galaxies in this position of the diagram. The previous trend is consistent with other works that used galaxy density to estimate environmental effects associated with SFR but using integrated values, e.g., Gómez et al. (2003), and with high resolution cosmological simulations that show a reduction of the SFR in high-density environments at z=0 (Tonnesen & Cen 2014).

In order to properly assess this effect, which is also related to the mass of the galaxies, the bottom panels of Figure 4.8 represent the relationship between sSFR and galaxy density for bulges and disks. The evidence for a decrease in the SFR and sSFR in bulges and disks with the presence of type-2 AGN has been already discussed in Sections 4.5.2 and 4.5.3. We will focus here in the case of the SFR and sSFR measured in the disks of star-forming galaxies (left panels), as the trends found for bulges are clearly more noisy, albeit having similar slopes. It is clear that disks in star-forming galaxies with intermediate-to-high values of Σ_5 show higher sSFR values. The analysis of the morphological types that are responsible for the increase in the sSFR at intermediate densities (groups) indicates that this is due to a larger number of Sd (or later) galaxies being found in groups than in the field for our galaxy sample. The number of galaxies when split by environment and type is not large enough to drive firm conclusions. Despite that fact, an enhancement in the disk star formation activity for galaxies located in groups could increase the number of these objects in the sample due to either a positive bias towards actively star-forming systems being included in CALIFA or by means of a morphological transformation towards later types.

4.6 Conclusions

The uniqueness of combining IFS data and a 2D multi-component photometric decomposition makes possible to disentangle the distribution of the extinction-corrected Hα-based SFR within different stellar structures in galaxies (bulges, bars, and disks). It also allows to determine how these morphological components would grow in stellar mass due to in-situ star formation. With this aim in mind, we have analyzed which mechanisms might either trigger or quench the star formation in a sample of 219 CALIFA nearby galaxies.

This work led to the following main conclusions:

1. There is an enhancement of the central SFR and sSFR due to the presence of bars for star-forming galaxies in agreement with the results found in previous works (de Jong et al. 1984; Devereux 1987; Ellison et al. 2011; Wang et al. 2012; Florido et al. 2015). This finding supports the idea that gas might be funneled into the central part of the galaxies triggering the star formation processes. On the other hand, this effect is reduced when a type-2 AGN is present making the SFR values in barred and unbarred galaxies more similar between them (Section 4.5.1).

2. We examine the SFR-$M_\star$ plane focusing on the Star-Forming Main Sequence treating galaxies as entire systems and also analyzing this sequence for their basic stellar structures (bulges, bars, and disks). The results indicate that there is a turnover in the Main Sequence not only for integrated values but also for disks, i. e., in the correlation between the SFR(disk) and the $M_\star$(disk). This fact means that more massive disks have been more efficiently quenched (Section 4.5.2).

3. The correlation between sSFR in the stellar components of the galaxies (bulge, bar, and disk) and the total stellar mass is analyzed to identify which mechanism(s) might be damping the star formation in more massive systems. First, we observe a decline associated with the sSFR(bulge) that is present across the entire stellar mass range while in the case of the sSFR(disk) the decrease becomes significantly for $M_\star > 10^{10.5}$ $M_\odot$. We also find that galaxies hosting a type-2 AGN tend to have lower values of their sSFR in both bulges and disks, separately. We previously reported this behavior for entire systems in Catalán-Torrecilla et al. (2015). This effect is more important for the case of the bulge component in comparison with the disk component, $-0.87(-0.42)$ dex lower in the median value of the sSFR bulge(disk) and $+0.30(+0.35)$ dex more massive in terms of the median value of the total stellar mass. As type-2 AGN tend to be in the most massive systems in our sample, [10^{10} - $10^{11.5}$] $M_\odot$, we analyze if this trend is also present in terms of the morphological type. We restrict the analysis to the most abundant objects with these morphological type and stellar masses, i. e, Sa/Sab and Sb/Sbc objects. Bulges of Sa/Sab (Sb/Sbc) show a median sSFR that is 0.27 (0.84) dex below that of star-forming galaxies while the difference in the median value of the stellar mass is 0.08 (0.14) dex. For the case of the disks, Sa/Sab (Sb/Sbc) galaxies exhibit a difference in the median values of sSFR for star-forming and AGNs of 0.13 (0.20) dex while the difference in stellar masses is 0.04 (0.16) dex (Section 4.5.3).

4. The previous point supports the idea of negative feedback produced by type-2 AGN galaxies. We cannot exclude, however, that other possibilities might be at a play. On one hand, at least

a fraction of the LLAGN that are classified as LINERs could be powered by hot evolved stars. In those cases, the low SFR and sSFR values derived would indicate that these galaxies define a lower photoionization envelope (i.e. a minimum $EW_{H\alpha}$) associated with evolved (non-star-forming) stellar populations in very massive systems (Cid Fernandes et al. 2011). Thus, for these galaxies mass would be solely the parameter driving the level of current SFR in galaxies and in components within galaxies. On the other hand, AGN damping might be coeval with another mechanism(s) that are regulating the star formation processes (Section 4.5.3).

5. The role that stellar kinematics could have in regulating the star formation processes is analyzed by means of the light-weighted LOS stellar velocity dispersion of the bulge component, σ_{bulge}. Type-2 AGN galaxies show higher values of the σ_{bulge} than star-forming objects. This bimodality is also displayed in the Faber-Jackson relation where type-2 AGN galaxies present higher values of the σ_{bulge} for the same stellar mass than star-forming objects (Section 4.5.4.1).

6. The effect that environment has on the star formation processes is studied using the project galaxy density, Σ_5. We find that galaxies have lower values of the SFR in both bulges and disks when they are located in intermediate- and high-density environments (Section 4.5.4.2).

In brief, this study concludes that the parameter that is affecting more strongly the current SFR of a galaxy, even the SFR associated with their basic stellar structures, is the stellar mass. Star formation damping by type-2 AGN plays also a significant role for bulges but also for disks. Nevertheless, we do not discard the possibility that AGN might be coeval with other processes affecting the star formation processes in the galaxies. In addition to the stellar mass and the nuclear activity, it seems that kinematics and environment act as a secondary parameter in regulating the SFR, at least, in our sample of galaxies. We emphasize the importance of applying 2D multi-component photometry decomposition over IFS data to understand the role that different mechanisms play at quenching or triggering the star formation in the structural components that form galaxies.

Table 4.1: Col. (1): ID CALIFA identifier. Col. (2): Galaxy name. Cols. (3) − (5): Stellar mass of the bulge, bar, and disk component, respectively. Stellar masses have been derived as explained in Section 4.4.4. Cols. (6) − (8): Extinction-corrected Hα SFR for the bulge, bar, and disk component, respectively. The value provided for the SFR in the disk component has been corrected by aperture effects. Col. (9): Morphological type. Col. (10): Projected galaxy density (Σ_5). Col. (11): Type-2 AGN candidate using the BPT diagram to obtain the nuclear activity classification. Col. (12): Line-of-sight dispersion for the bulge component (σ_{bulge}). (*) These galaxies have a nuclear point source component instead of a bulge component. † These quantities have errors that are smaller than the last digit of the corresponding magnitude measured. Instead of adding more precision to the quantities quoted in this column, and for the sake of clarity in the formatting of the table, we have not included their errors here.

ID	name	M_{BULGE} [$\times10^{10}$ $M_\odot$]	M_{BAR} [$\times10^{10}$ $M_\odot$]	M_{DISK} [$\times10^{10}$ $M_\odot$]	SFR(Hα_{BULGE}) [$M_\odot$ yr^{-1}]	SFR(Hα_{BAR}) [$M_\odot$ yr^{-1}]	SFR(Hα_{DISK}) [$M_\odot$ yr^{-1}]	HT	Σ_5 [Mpc^{-2}]	AGN	σ_{bulge} [km s^{-1}]
(1)	(2)	(3)	(4)	(5)	(6)	(7)	(8)	(9)	(10)	(11)	(12)
2	UGC 00005	0.30±0.02	...	5.54±0.30	0.040±0.003	...	3.890±0.155	Sbc	...	yes	106.24±1.98
3	NGC 7819	0.16±0.03	0.22±0.04	0.85±0.17	0.605±0.008	0.268±0.009	0.609±0.021	Sc	...	no	68.29±1.55
5	IC 1528	0.20±0.00	...	1.07±0.01	0.031±0.001	...	1.017±0.023	Sbc	...	no	55.40±1.60
6	NGC 7824	5.41±0.12	...	8.78±0.20	0.060±0.009	...	0.201±0.017	Sab	...	no	210.19±4.03
7	UGC 00036	1.26±0.04	1.14±0.03	4.89±0.15	0.051±0.003	0.087±0.006	0.530±0.052	Sab	...	no	173.99±2.70
8	NGC 0001	1.68±0.20	...	2.70±0.33	1.586±0.051	...	1.021±0.042	Sbc	...	no	111.93±1.42
10	NGC 0036	0.65±0.08	0.92±0.11	5.58±0.65	0.411±0.027	0.215±0.012	1.210±0.105	Sb	...	yes	134.06±2.90
11	UGC 00139	0.01±0.00	...	0.40±0.06	0.055±0.001	...	0.534±0.013	Scd	...	no	...
13	MCG-02-02-030	0.26±0.02	...	1.75±0.13	0.043±0.003	...	0.376±0.027	Sb	...	yes	76.72±0.56
14	UGC 00312	0.04±0.02	0.03±0.01	0.43±0.19	0.112±0.002	0.285±0.004	2.632±0.044	Sd	...	no	68.99±3.88
19	ESO 540-G003	0.09±0.00	0.20±0.00	0.46±0.01	0.000±0.000	0.070±0.005	0.177±0.018	Sb	...	no	...
21	NGC 0165	0.31±0.06	0.34±0.06	2.78±0.51	0.383±0.006	0.044±0.002	1.024±0.058	Sb	1.22±0.00	no	...
23	NGC 0171	0.47±0.12	0.42±0.11	2.02±0.53	0.009±0.001	0.055±0.003	0.819±0.032	Sb	...	yes	115.44±0.61
25	NGC 0180	0.34±0.02	0.56±0.03	3.83±0.21	0.165±0.004	0.040±0.002	0.758±0.038	Sb	...	no	107.11±0.91
26	NGC 0192	1.88±0.04	...	5.41±0.12	0.509±0.019	...	0.825±0.065	Sab	...	no	131.38±0.85
28	NGC 0214	0.58±0.01	0.28±0.01	2.37±0.05	0.019±0.002	0.259±0.018	2.723±0.200	Sbc	...	yes	114.53±4.37
30	NGC 0237	0.28±0.01	...	1.36±0.03	0.097±0.002	...	1.621±0.035	Sc	...	no	70.90±0.53
31	NGC 0234	0.23±0.05	...	4.00±0.84	0.251±0.004	...	4.194±0.074	Sc	...	no	72.72±1.07
33	NGC 0257	1.21±0.03	...	5.54±0.13	0.236±0.012	...	3.882±0.235	Sc	...	no	98.35±0.49
34	NGC 0309	0.91±0.21	0.28±0.06	4.99±1.12	0.009±0.001	0.014±0.001	7.389±0.076	Scd	...	no	118.50±1.71
38	NGC 0447	2.93±0.46	0.97±0.15	5.41±0.85	0.115±0.011	0.056±0.004	0.000±0.000	Sa	...	yes	140.60±2.39
42	NGC 0477	0.34±0.01	...	2.33±0.10	0.093±0.003	...	1.739±0.082	Sbc	...	no	77.05±1.17
43	IC 1683	0.59±0.02	0.76±0.02	1.61±0.05	0.794±0.016	0.597±0.018	0.264±0.026	Sb	...	no	113.82±2.44
45	NGC 0496	0.14±†	...	1.93±0.04	0.041±0.001	...	2.696±0.084	Scd	...	no	28.25±9.74
49	UGC 00987	1.47±0.03	...	2.28±0.05	0.125±0.010	...	0.415±0.022	Sa	...	yes	113.05±1.68
50	NGC 0528	3.42±0.23	...	2.46±0.16	0.027±0.005	...	0.026±0.001	S0	...	yes	246.98±2.61
52	NGC 0551	0.39±0.03	0.13±0.01	3.37±0.24	0.005±†	0.036±0.001	1.243±0.043	Sbc	...	no	96.85±2.64
58	IC 0159	0.04±0.02	...	0.38±0.18	0.090±0.001	...	0.951±0.017	Sdm	...	no	...
60	UGC A021	0.0010 ± 0.0003	0.01±†	0.10±0.03	0.004±†	0.008±0.001	0.253±0.016	Sdm	...	no	...
65	NGC 0716 (*)	0.20±0.01	0.90±0.04	3.03±0.15	0.199±0.011	2.943±0.168	2.846±0.184	Sb	...	no	132.38±1.52
66	UGC 01368	0.70±0.12	...	5.46±0.97	0.039±0.003	...	1.129±0.162	Sab	...	no	143.99±2.95
69	NGC 0755	...	...	0.18±†	...	...	0.326±0.007	Scd	...	no	...
71	NGC 0768	4.46±0.91	...	0.89±0.18	0.216±0.007	...	2.799±0.161	Sc	0.40±0.14	yes	109.76±8.15
73	NGC 0776	0.79±0.16	0.42±0.08	2.89±0.57	0.314±0.006	0.341±0.007	1.791±0.055	Sb	...	no	107.88±1.28
75	NGC 0787	3.49±0.65	...	3.84±0.71	0.031±0.003	...	0.339±0.017	Sa	...	yes	...
80	NGC 0842	1.83±0.04	0.57±0.01	3.37±0.08	0.000±0.000	0.008±†	0.026±0.002	S0	...	no	138.68±0.85
81	UGC 01659	0.17±0.01	0.37±0.03	2.68±0.22	0.007±0.001	0.116±0.008	1.626±0.099	Sc	...	yes	...
84	NGC 0873	0.25±0.01	...	1.43±0.03	0.182±0.005	...	4.067±0.082	Scd	...	no	90.37±7.19
85	NGC 0924	2.69±0.19	0.63±0.04	2.58±0.18	0.044±0.001	0.017±†	0.101±0.001	S0	...	yes	...
86	UGC 01918	0.32±0.02	0.28±0.02	3.20±0.24	0.425±0.026	0.263±0.015	0.295±0.030	Sb	...	no	...
89	NGC 0941 (*)	0.00086±0.00025	...	0.14±0.04	0.004±†	...	0.207±0.004	Scd	...	no	54.43±2.71
94	NGC 0976	3.15±0.07	0.63±0.01	3.69±0.08	0.144±0.014	0.737±0.049	2.507±0.474	Sbc	...	no	122.57±1.24
95	NGC 0991 (*)	0.00019±0.00004	0.02±0.01	0.35±0.08	0.000±0.000	0.031±0.001	0.069±0.001	Scd	...	no	37.60±4.67
97	UGC 02134	0.08±0.01	0.11±0.02	3.70±0.59	0.054±0.002	0.056±0.002	1.251±0.039	Sb	...	no	87.94±2.91
102	NGC 1070	0.74±0.05	...	5.36±0.40	0.011±0.001	...	1.153±0.053	Sb	...	yes	145.77±0.72
107	NGC 1094	1.53±0.03	...	3.64±0.08	0.016±0.002	...	2.903±0.164	Sb	3.20±1.41	yes	135.04±1.26

ID	name	M_{BULGE} [$\times10^{10}$ $M_\star/M_\odot$]	M_{BAR} [$\times10^{10}$ $M_\star/M_\odot$]	M_{DISK} [$\times10^{10}$ $M_\star/M_\odot$]	SFR(Hα_{BULGE}) [$M_\odot$ yr^{-1}]	SFR(Hα_{BAR}) [$M_\odot$ yr^{-1}]	SFR(Hα_{DISK}) [$M_\odot$ yr^{-1}]	HT	Σ_5 [Mpc^{-2}]	AGN	σ_{bulge} [km s^{-1}]
(1)	(2)	(3)	(4)	(5)	(6)	(7)	(8)	(9)	(10)	(11)	(12)
108	NGC 1093	1.14±0.01	0.25±†	1.91±0.01	0.065±0.004	0.140±0.007	0.579±0.027	Sbc	...	yes	96.92±0.73
109	UGC 02311	0.86±0.07	0.72±0.06	3.44±0.28	0.214±0.007	0.288±0.011	0.911±0.062	Sbc	3.22±0.47	no	118.90±1.63
113	UGC 02367	12.74±1.49	...	5.41±0.63	0.605±0.060	...	1.122±0.122	Sab	...	no	146.51±7.86
115	UGC 02403	2.67±0.05	0.84±0.02	1.70±0.03	0.717±0.020	0.744±0.034	0.221±0.011	Sb	...	no	...
116	UGC 02405	0.88±0.16	...	2.13±0.38	0.040±0.002	...	1.988±0.115	Sbc	...	no	...
117	UGC 02443	0.03±0.01	...	0.41±0.11	0.001±†	...	0.204±0.005	Scd	...	no	...
121	NGC 1211	2.23±0.66	0.64±0.19	1.35±0.40	0.035±0.003	0.000±0.000	0.000±0.000	S0a	...	yes	108.90±3.53
122	MCG-01-09-006	3.94±1.28	...	2.24±0.73	0.245±0.010	...	2.394±0.176	Sbc	0.25±0.07	no	130.00±7.33
123	IC 0307	3.41±0.24	...	5.97±0.41	0.420±0.072	...	0.000±0.000	Sab	0.68±0.13	no	185.05±3.18
125	UGC 02690	0.11±†	...	0.79±0.02	0.146±0.007	...	3.481±0.136	Scd	...	no	...
126	NGC 1324	4.28±0.11	...	8.85±0.23	0.092±0.009	...	1.999±0.131	Sb	...	no	138.69±0.76
127	NGC 1349	3.24±1.19	...	4.03±1.48	0.036±0.004	...	0.443±0.042	E6	...	yes	185.28±2.03
129	MCG-01-10-015	0.05±0.01	...	0.91±0.12	0.007±†	...	0.442±0.018	Sc	...	no	...
130	MCG-01-10-019	0.23±0.02	...	1.03±0.09	0.037±0.002	...	0.610±0.035	Sbc	0.96±0.58	no	58.16±2.23
134	NGC 1645	1.17±0.18	1.09±0.17	3.47±0.54	0.011±0.001	0.021±0.002	0.000±0.000	S0a	...	yes	176.69±0.63
137	NGC 1659	0.01±†	0.24±0.04	3.00±0.48	0.139±0.004	0.198±0.006	1.858±0.070	Sbc	...	no	117.69±3.54
139	NGC 1666	0.79±0.02	0.24±0.01	2.12±0.05	0.005±0.001	0.003±†	0.030±0.001	S0a	...	no	...
140	NGC 1667	1.00±0.37	0.52±0.19	4.47±1.64	0.055±0.006	0.088±0.007	6.783±0.285	Sbc	...	yes	146.13±1.17
146	UGC 03253	0.33±0.01	0.60±0.02	1.99±0.08	0.060±0.004	0.053±0.004	0.000±0.000	Sb	...	no	...
147	NGC 2253	0.46±0.01	0.75±0.02	2.97±0.07	0.142±0.005	0.048±0.002	2.339±0.055	Sbc	...	no	97.62±1.01
149	NGC 2347	7.67±2.49	0.11±0.03	0.73±0.24	0.351±0.015	0.211±0.014	1.485±0.101	Sbc	...	no	148.59±2.45
151	NGC 2410	1.79±0.30	0.48±0.08	4.30±0.72	0.272±0.017	0.106±0.007	1.188±0.084	Sb	...	yes	132.87±0.91
152	UGC 03944 (*)	0.01±†	0.09±†	0.71±0.02	0.001±†	0.403±0.013	0.631±0.016	Sbc	0.77±0.46	no	37.53±5.79
154	UGC 03973	0.55±0.22	1.22±0.48	2.34±0.92	1.415±0.303	0.773±0.078	1.130±0.122	Sbc	1.21±0.27	yes	...
155	UGC 03995	0.86±0.02	0.88±0.02	4.36±0.10	0.134±0.017	0.052±0.004	0.361±0.027	Sb	0.54±0.34	yes	147.94±2.24
156	NGC 2449	2.26±0.05	0.59±0.01	3.98±0.09	0.031±0.003	0.022±0.002	0.667±0.081	Sab	0.98±0.63	yes	136.32±1.62
164	NGC 2487	1.52±0.09	0.46±0.03	3.80±0.23	0.018±0.002	0.099±0.006	0.851±0.052	Sb	0.81±0.32	yes	110.71±1.63
165	UGC 04132	4.85±0.35	0.21±0.02	3.47±0.25	0.419±0.015	0.175±0.008	5.564±0.341	Sbc	4.84±0.39	no	92.25±1.56
167	UGC 04145	1.06±0.12	1.22±0.14	2.00±0.23	0.097±0.012	0.147±0.020	0.160±0.022	Sa	2.45±0.49	yes	159.91±1.00
176	UGC 04195	0.13±0.07	0.21±0.12	1.59±0.90	0.064±0.002	0.031±0.001	0.498±0.035	Sb	...	no	...
179	NGC 2530	0.08±0.02	0.07±0.02	0.84±0.24	0.064±0.002	0.066±0.002	1.040±0.032	Sd	3.46±2.30	no	63.90±7.10
183	NGC 2540 (*)	0.17±0.04	0.45±0.11	2.66±0.64	0.291±0.009	0.945±0.025	0.938±0.045	Sbc	0.62±0.36	no	102.98±1.63
187	UGC 04308	0.12±0.02	0.10±0.02	1.31±0.25	0.033±0.001	0.023±0.001	0.950±0.024	Sc	1.78±0.46	no	72.99±4.43
190	UGC 04262	2.41±0.44	...	2.05±0.37	0.021±0.003	...	0.832±0.038	Sbc	...	no	117.68±1.28
192	NGC 2565	1.44±0.32	0.69±0.15	2.61±0.58	0.030±0.006	0.041±0.005	0.120±0.017	Sb	1.77±0.34	no	140.51±0.84
194	NGC 2572	1.75±0.18	1.56±0.16	5.43±0.57	0.013±0.003	0.062±0.004	0.372±0.041	Sa	0.62±0.45	yes	186.24±7.31
196	UGC 04375	0.16±0.05	...	0.97±0.32	0.001±†	...	0.153±0.005	Sbc	1.83±1.63	no	55.21±0.78
208	UGC 04461 (*)	0.02±†	...	1.12±0.32	0.067±0.002	...	1.610±0.044	Sbc	3.24±1.17	no	73.95±26.67
209	NGC 2604 (*)	0.00023±0.00007	0.02±0.01	0.38±0.12	0.084±0.001	0.538±0.008	0.581±0.009	Sd	4.38±3.34	no	63.19±4.93
219	NGC 2639	5.67±0.13	...	8.60±0.20	0.146±0.015	...	0.485±0.065	Sa	0.31±0.25	yes	162.19±0.38
232	NGC 2730	0.06±0.02	...	0.97±0.27	0.044±0.001	...	1.811±0.023	Scd	1.57±0.80	no	44.14±2.29
260	NGC 2805	0.21±0.11	...	0.37±0.19	0.090±0.004	...	0.107±0.006	Sc	...	no	61.06±4.81
275	NGC 2906	0.67±0.02	...	2.21±0.05	0.003±†	...	0.532±0.018	Sbc	0.83±0.65	yes	105.39±1.84
277	NGC 2916	0.92±0.09	...	2.63±0.25	0.015±0.001	...	0.811±0.052	Sbc	0.41±0.32	yes	115.86±0.99
278	UGC 05108 (*)	0.42±0.03	1.64±0.12	5.06±0.36	0.484±0.025	0.477±0.020	0.000±0.000	Sb	0.58±0.32	no	151.76±6.35
307	UGC 05359	1.31±0.13	0.11±0.01	3.01±0.30	0.012±0.001	0.006±0.001	1.631±0.143	Sb	0.42±0.20	no	122.16±5.12
309	UGC 05396	0.06±0.01	0.13±0.02	1.63±0.30	0.007±0.001	0.157±0.009	0.627±0.046	Sbc	0.80±0.65	no	53.50±6.01
311	NGC 3106	4.89±0.17	...	6.04±0.21	0.175±0.016	...	0.463±0.073	Sab	0.46±0.17	yes	180.34±2.53
312	NGC 3057	...	0.0044±0.0006	0.10±0.01	...	0.012±†	0.101±0.002	Sdm	...	no	...
353	NGC 3381	0.01±†	0.04±0.01	0.32±0.12	0.019±†	0.050±0.001	0.251±0.003	Sd	3.21±0.01	no	48.44±3.14
381	IC 0674	2.13±0.45	0.74±0.16	3.57±0.76	0.074±0.007	0.034±0.004	0.301±0.028	Sab	0.21±0.09	no	158.30±3.06
386	UGC 06312	6.15±0.14	...	3.90±0.09	0.142±0.022	...	0.000±0.000	Sab	0.42±0.26	yes	139.14±1.03
388	NGC 3614	0.68±0.31	...	0.71±0.33	0.017±0.001	...	0.306±0.007	Sbc	0.76±0.61	no	100.73±6.64

ID	name	M_{BULGE} [$\times 10^{10}$ $M_\star/M_\odot$]	M_{BAR} [$\times 10^{10}$ $M_\star/M_\odot$]	M_{DISK} [$\times 10^{10}$ $M_\star/M_\odot$]	SFR($H\alpha_{BULGE}$) [$M_\odot$ yr^{-1}]	SFR($H\alpha_{BAR}$) [$M_\odot$ yr^{-1}]	SFR($H\alpha_{DISK}$) [$M_\odot$ yr^{-1}]	HT	Σ_5 [Mpc^{-2}]	AGN	σ_{bulge} [km s^{-1}]
(1)	(2)	(3)	(4)	(5)	(6)	(7)	(8)	(9)	(10)	(11)	(12)
414	NGC 3687	0.44±0.01	0.09±†	1.13±0.03	0.002±†	0.002±†	0.284±0.006	Sb	0.52±0.25	yes	96.69±1.21
436	NGC 3811	0.23±0.05	0.38±0.08	1.68±0.34	0.162±0.007	0.063±0.004	1.331±0.055	Sbc	0.59±0.51	no	102.35±1.03
437	NGC 3815	0.42±0.04	0.57±0.06	1.27±0.13	0.007±†	0.061±0.002	0.780±0.023	Sbc	0.71±0.34	no	84.33±0.75
476	NGC 3994	0.98±0.09	...	1.10±0.10	0.129±0.005	...	2.318±0.094	Sbc	19.14±2.95	no	141.36±1.44
479	NGC 4003	3.39±0.46	1.96±0.26	4.78±0.65	0.365±0.021	0.090±0.012	0.115±0.028	S0a	0.45±0.10	no	136.83±2.21
486	UGC 07012	0.0017±0.0016	...	0.13±0.12	0.034±†	...	0.428±0.008	Scd	7.44±0.00	no	38.91±2.00
489	NGC 4047	1.78±0.26	...	3.29±0.49	0.285±0.007	...	1.886±0.048	Sbc	0.25±0.07	no	88.46±0.36
515	NGC 4185	0.18±0.08	0.17±0.07	3.67±1.49	0.004±0.001	0.014±0.001	1.308±0.028	Sbc	3.78±0.00	yes	79.77±2.24
518	NGC 4210	0.09±0.01	0.18±0.03	1.70±0.26	0.001±†	0.003±†	0.688±0.016	Sb	2.19±0.78	yes	77.83±0.83
528	IC 0776	0.01±†	...	0.18±0.06	0.036±0.001	...	0.142±0.002	Sdm	6.15±2.91	no	...
548	NGC 4470	...	...	0.88±0.02	...	...	0.887±0.011	Sc	5.45±3.73	no	...
569	NGC 4644	0.69±0.12	...	1.97±0.34	0.062±0.005	...	0.670±0.028	Sb	5.35±1.46	no	82.04±1.27
580	NGC 4711	0.19±0.04	...	1.74±0.37	0.004±†	...	0.900±0.038	Sbc	0.46±0.29	no	57.96±4.03
581	UGC 08004	0.12±0.02	...	0.81±0.16	0.004±†	...	0.772±0.026	Scd	1.06±0.37	no	...
603	NGC 4961	0.03±0.01	0.07±0.01	0.28±0.05	0.002±†	0.136±0.002	0.301±0.008	Scd	1.85±1.59	no	50.35±1.26
606	UGC 08231	...	0.01±†	0.10±0.02	...	0.011±†	0.314±0.005	Sd	3.85±3.58	no	...
608	NGC 5000	0.33±0.05	0.50±0.08	2.30±0.38	0.246±0.010	0.262±0.015	1.389±0.083	Sbc	1.99±0.00	no	132.00±6.44
611	NGC 5016 (*)	0.0038±0.0006	...	1.59±0.24	0.014±0.001	...	0.763±0.038	Sbc	0.37±0.12	no	66.03±0.87
624	NGC 5157	2.16±0.24	1.27±0.14	8.24±0.92	0.022±0.002	0.024±0.002	0.426±0.036	Sab	0.86±0.03	yes	168.49±1.43
630	NGC 5205	0.11±0.02	0.08±0.02	0.71±0.14	0.000±0.000	0.008±0.001	0.085±0.004	Sbc	1.48±0.81	yes	69.93±0.52
651	NGC 5267	1.40±0.02	1.87±0.02	4.36±0.05	0.000±0.000	0.057±0.006	0.676±0.057	Sab	0.53±0.28	yes	175.17±1.11
653	NGC 5289	0.90±0.08	...	0.89±0.08	0.026±0.002	...	0.112±0.003	Sab	1.48±0.10	yes	129.00±0.55
659	NGC 5320	0.10±0.02	...	1.36±0.25	0.004±†	...	0.531±0.012	Sbc	2.99±0.22	no	50.49±1.05
663	IC 0944	3.48±0.08	...	13.61±0.31	0.159±0.017	...	0.890±0.157	Sab	7.83±0.00	no	165.17±1.57
665	UGC 08781	2.52±0.27	0.90±0.10	6.09±0.65	0.000±0.000	0.020±0.004	1.761±0.130	Sb	6.00±1.42	yes	148.13±2.51
673	NGC 5379	0.15±0.02	...	0.58±0.07	0.008±†	...	0.042±0.003	Sab	16.30±11.85	no	60.58±4.24
676	NGC 5378	0.50±0.18	0.35±0.13	1.26±0.47	0.009±0.001	0.011±0.001	0.111±0.013	Sb	7.16±1.72	yes	109.68±0.85
684	NGC 5406	1.42±0.07	2.06±0.11	7.08±0.37	0.018±0.004	0.067±0.003	0.694±0.040	Sb	3.30±0.00	yes	...
690	NGC 5443	0.19±0.02	...	1.88±0.20	0.008±0.001	...	0.106±0.005	Sab	5.44±1.40	yes	...
707	NGC 5480	0.09±0.01	...	1.21±0.13	0.098±0.002	...	0.961±0.017	Scd	2.72±1.31	no	67.00±0.93
714	UGC 09067	0.44±0.18	...	2.93±1.20	0.100±0.003	...	2.543±0.141	Sbc	1.18±0.00	no	103.42±4.25
715	NGC 5520 (*)	0.13±†	0.30±0.01	0.40±0.01	0.019±†	0.579±0.017	0.496±0.014	Sbc	4.47±2.51	no	81.15±0.49
719	NGC 5519	1.38±0.03	0.55±0.01	2.92±0.07	0.574±0.017	0.361±0.015	0.794±0.057	Sb	0.80±0.16	no	...
720	NGC 5522	1.56±0.13	1.01±0.09	3.27±0.28	0.075±0.004	0.266±0.014	0.735±0.041	Sb	2.33±0.00	no	...
724	NGC 5533	7.32±0.72	...	4.56±0.45	0.531±0.048	...	0.545±0.043	Sab	0.77±0.36	yes	...
732	NGC 5559	0.55±0.05	...	3.00±0.28	0.043±0.003	...	1.567±0.056	Sb	2.61±1.62	no	...
736	NGC 5587	0.27±0.01	...	1.87±0.04	0.002±†	...	0.149±0.005	Sa	2.97±2.57	yes	...
742	NGC 5610	1.20±0.13	1.57±0.16	2.24±0.23	0.199±0.008	1.124±0.052	0.420±0.017	Sb	0.77±0.04	no	...
743	NGC 5622	0.74±0.02	...	1.45±0.03	0.006±†	...	0.623±0.019	Sbc	0.62±0.49	no	...
748	NGC 5633 (*)	0.00037±0.00004	...	1.77±0.20	0.003±†	...	1.018±0.021	Sbc	1.13±0.55	no	64.79±1.06
749	NGC 5630	...	0.02±†	0.31±0.01	...	0.129±0.002	0.793±0.010	Sdm	0.85±0.54	no	...
750	NGC 5635	13.04±0.24	...	4.35±0.08	0.095±0.008	...	0.194±0.017	Sa	0.69±0.06	yes	...
751	UGC 09291	0.01±†	0.04±0.02	0.61±0.27	0.001±†	0.002±†	0.257±0.006	Scd	0.62±0.19	no	...
753	NGC 5656	0.67±0.07	...	3.15±0.33	0.008±0.001	...	1.349±0.057	Sb	1.35±0.37	no	...
754	NGC 5657	0.43±0.02	0.66±0.02	1.20±0.05	0.215±0.006	0.359±0.009	0.451±0.023	Sbc	1.23±0.57	no	103.54±0.65
755	NGC 5659	1.30±0.19	...	2.27±0.32	0.013±0.001	...	0.570±0.018	Sb	2.95±0.00	no	...
756	NGC 5665	0.04±†	...	1.00±0.02	0.109±0.001	...	1.712±0.021	Sc	0.80±0.37	no	...
758	NGC 5682	...	0.01±†	0.19±0.05	...	0.021±†	0.250±0.003	Scd	13.13±11.20	no	...
764	NGC 5720	0.92±0.16	0.69±0.12	5.58±0.98	0.000±0.000	0.010±0.003	1.149±0.101	Sbc	0.11±0.04	yes	138.74±1.08
768	NGC 5732	0.28±0.04	...	0.66±0.09	0.021±†	...	0.644±0.019	Sbc	3.96±1.66	no	46.35±4.15
769	UGC 09476	0.11±0.03	...	1.41±0.38	0.020±0.001	...	1.678±0.020	Sbc	1.39±0.88	no	50.97±1.92
771	NGC 5735	0.11±0.02	0.20±0.04	1.10±0.21	0.006±0.001	0.064±0.002	0.506±0.014	Sbc	0.39±0.17	yes	...

ID	name	M_{BULGE}	M_{BAR}	M_{DISK}	SFR($H\alpha_{BULGE}$)	SFR($H\alpha_{BAR}$)	SFR($H\alpha_{DISK}$)	HT	Σ_5	AGN	σ_{bulge}
		[$\times10^{10}$ $M_\star/M_\odot$]	[$\times10^{10}$ $M_\star/M_\odot$]	[$\times10^{10}$ $M_\star/M_\odot$]	[$M_\odot$ yr^{-1}]	[$M_\odot$ yr^{-1}]	[$M_\odot$ yr^{-1}]		[Mpc^{-2}]		[km s^{-1}]
(1)	(2)	(3)	(4)	(5)	(6)	(7)	(8)	(9)	(10)	(11)	(12)
772	UGC 09492	3.62±0.02	1.32±0.01	7.78±0.04	0.032±0.003	0.025±0.001	0.000±0.000	Sab	0.41±0.06	yes	...
775	UGC 09542	0.69±0.02	...	1.84±0.06	0.016±0.001	...	1.080±0.054	Sc	2.59±1.77	no	68.54±3.13
777	NGC 5772	2.31±0.45	...	4.38±0.85	0.027±0.002	...	0.798±0.041	Sab	0.29±0.01	yes	...
778	NGC 5784	4.53±0.10	...	10.95±0.25	0.479±0.046	...	0.116±0.013	S0	0.47±0.18	yes	191.94±0.95
779	UGC 09598	0.13±†	...	3.02±0.07	0.004±0.001	...	0.595±0.027	Sbc	0.40±0.13	no	...
782	UGC 09629	6.43±0.01	...	5.25±0.01	0.000±0.000	...	0.090±0.006	E7	0.28±0.04	no	179.38±0.92
784	NGC 5829	1.96±1.33	...	3.02±2.05	0.076±0.005	...	1.095±0.097	Sc	1.48±0.71	no	...
787	NGC 5876	1.67±0.15	0.86±0.08	2.33±0.21	0.000±0.000	0.007±†	0.074±0.004	S0a	1.98±1.36	yes	186.70±1.02
789	NGC 5888	1.94±0.09	1.67±0.07	11.32±0.51	0.018±0.001	0.036±0.005	1.017±0.088	Sb	0.71±0.02	yes	161.50±0.94
790	UGC 09777	0.01±†	0.28±0.04	1.57±0.20	0.202±0.004	0.245±0.005	0.390±0.015	Sbc	1.39±1.06	no	...
792	UGC 09842	0.62±0.13	1.16±0.24	2.67±0.55	0.522±0.018	1.017±0.027	2.463±0.141	Sbc	0.96±0.52	no	...
803	NGC 5957	0.22±0.03	0.18±0.03	0.74±0.11	0.004±†	0.009±†	0.166±0.004	Sb	1.01±0.14	yes	69.38±0.51
804	NGC 5971	1.66±0.42	...	0.22±0.05	0.032±0.003	...	0.063±0.004	Sb	2.98±1.80	yes	111.86±1.73
807	IC 4566	1.02±0.12	0.66±0.08	5.21±0.62	0.008±0.001	0.009±0.001	0.713±0.067	Sb	7.18±5.67	yes	132.38±0.86
810	NGC 5980	1.38±0.29	...	4.44±0.95	0.227±0.007	...	3.387±0.166	Sbc	0.23±0.12	no	101.69±0.60
813	NGC 6004	0.23±0.01	0.25±0.01	4.17±0.20	0.056±0.003	0.092±0.002	1.197±0.028	Sbc	0.64±0.38	no	88.64±2.46
817	IC 1151	0.05±†	...	0.29±0.01	0.008±†	...	0.422±0.007	Scd	1.23±1.01	no	50.67±2.78
820	NGC 6032	0.24±0.06	0.55±0.14	1.11±0.29	0.133±0.005	0.181±0.024	0.231±0.067	Sbc	2.57±0.66	no	77.11±3.81
821	NGC 6060	0.98±0.15	...	6.01±0.89	0.112±0.011	...	2.252±0.138	Sb	1.67±0.24	no	114.99±1.26
823	NGC 6063	0.18±0.01	...	0.80±0.05	0.003±†	...	0.533±0.010	Sbc	...	no	50.85±3.71
824	IC 1199	0.52±0.05	...	2.95±0.27	0.131±0.004	...	0.816±0.041	Sb	0.67±0.38	no	96.72±2.21
830	UGC 10337	0.75±0.02	...	9.11±0.21	0.019±0.007	...	1.303±0.169	Sb	...	yes	134.37±3.81
831	NGC 6132	9.25±1.08	...	0.97±0.11	0.008±†	...	1.215±0.049	Sbc	1.31±0.39	no	71.96±4.08
833	NGC 6154	1.59±0.18	0.79±0.09	3.86±0.44	0.044±0.012	0.064±0.008	1.212±0.067	Sab	...	yes	139.56±2.05
836	NGC 6155	0.05±†	...	1.31±0.12	0.008±†	...	0.935±0.015	Sc	...	no	...
838	UGC 10388	1.08±0.12	0.23±0.02	2.70±0.30	0.011±0.001	0.000±0.000	0.103±0.010	Sa	...	no	119.84±1.06
842	NGC 6186	0.77±0.17	0.73±0.17	1.89±0.43	0.643±0.013	0.555±0.016	0.174±0.008	Sb	...	no	91.03±0.60
844	NGC 6278	1.69±0.16	0.38±0.04	3.17±0.30	0.010±†	0.003±†	0.012±†	S0a	...	yes	187.72±0.85
849	NGC 6301	0.27±0.01	...	5.79±0.16	0.007±0.002	...	6.640±0.222	Sbc	...	no	80.86±4.04
850	NGC 6314	10.94±1.36	...	5.09±0.63	0.268±0.056	...	0.000±0.000	Sab	...	no	160.03±1.56
852	UGC 10796	0.04±0.02	0.06±0.02	0.10±0.04	0.073±0.002	0.045±0.002	0.054±0.002	Scd	5.03±3.50	no	62.57±4.50
854	UGC 10811	0.47±0.19	1.04±0.41	4.56±1.81	0.000±0.000	0.035±0.006	0.930±0.089	Sb	1.68±0.67	yes	163.05±1.83
856	IC 1256 (*)	0.04±0.01	...	1.76±0.48	0.044±0.002	...	0.828±0.033	Sb	...	no	77.15±3.35
857	NGC 6394	0.31±0.01	1.49±0.03	4.25±0.10	0.064±0.008	1.187±0.088	1.107±0.101	Sbc	2.95±0.31	yes	105.97±2.78
862	NGC 6478	1.46±0.18	...	8.08±1.01	0.165±0.009	...	3.801±0.301	Sc	...	no	129.60±1.47
863	NGC 6497	2.63±0.06	1.26±0.03	4.87±0.11	0.008±0.001	0.008±0.001	0.253±0.021	Sab	...	yes	...
865	UGC 11228	3.31±0.23	0.40±0.03	4.33±0.30	0.073±0.013	0.009±0.002	0.000±0.000	S0	...	yes	183.26±0.74
866	UGC 11262	0.13±0.03	...	0.63±0.14	0.006±0.001	...	0.247±0.014	Sc	...	no	64.85±6.37
867	NGC 6762	0.31±0.07	...	1.00±0.22	0.015±0.001	...	0.013±0.003	Sab	...	yes	95.18±0.98
868	MCG-02-51-004	0.61±0.09	...	4.27±0.62	0.053±0.005	...	2.173±0.126	Sb	...	yes	109.84±1.14
869	NGC 6941	1.31±0.32	0.76±0.19	6.57±1.61	0.049±0.005	0.014±0.002	1.408±0.070	Sb	...	no	140.64±1.22
871	NGC 6978	5.28±0.31	...	6.97±0.41	0.049±0.004	...	0.562±0.054	Sb	...	yes	136.91±2.52
872	UGC 11649	0.32±0.03	0.35±0.03	1.89±0.16	0.000±0.000	0.000±0.000	0.230±0.012	Sab	...	yes	112.77±0.91
876	NGC 7047	0.40±0.01	...	4.75±0.11	0.004±0.001	...	1.340±0.072	Sbc	...	yes	91.33±1.98
879	UGC 11740	0.20±0.04	0.99±0.17	1.01±0.18	0.021±0.001	0.144±0.009	0.685±0.037	Sbc	...	no	71.09±4.59
886	NGC 7311	3.49±0.08	...	5.96±0.14	0.048±0.009	...	1.569±0.131	Sa	...	no	174.01±1.24
887	NGC 7321	1.05±0.10	1.17±0.12	6.08±0.60	0.029±0.002	0.200±0.008	2.723±0.144	Sbc	...	yes	155.20±2.85
890	UGC 12185	2.71±0.35	0.64±0.08	1.29±0.17	0.025±0.005	0.205±0.014	0.309±0.031	Sb	...	no	133.98±1.63
891	UGC 12224	0.04±0.01	...	0.81±0.10	0.015±0.001	...	0.656±0.024	Sc	...	no	39.07±7.57
894	UGC 12274	2.14±0.05	...	8.04±0.18	0.029±0.002	...	0.114±0.005	Sa	...	yes	142.90±1.41
896	NGC 7466	1.37±0.46	...	2.88±0.96	0.567±0.024	...	1.846±0.104	Sbc	...	yes	126.00±3.77
898	NGC 7489 (*)	0.31±0.06	...	2.14±0.43	0.063±0.003	...	3.655±0.160	Sbc	...	no	68.62±3.80
899	NGC 7536	0.64±0.05	...	1.48±0.12	0.108±0.004	...	1.829±0.048	Sc	3.76±0.59	no	...

ID	name	M_{BULGE} [$\times 10^{10}$ $M_\star/M_\odot$]	M_{BAR} [$\times 10^{10}$ $M_\star/M_\odot$]	M_{DISK} [$\times 10^{10}$ $M_\star/M_\odot$]	SFR($H\alpha_{BULGE}$) [$M_\odot$ yr^{-1}]	SFR($H\alpha_{BAR}$) [$M_\odot$ yr^{-1}]	SFR($H\alpha_{DISK}$) [$M_\odot$ yr^{-1}]	HT	Σ_5 [Mpc^{-2}]	AGN	σ_{bulge} [km s^{-1}]
(1)	(2)	(3)	(4)	(5)	(6)	(7)	(8)	(9)	(10)	(11)	(12)
901	NGC 7549	0.39±0.05	0.36±0.04	0.95±0.12	0.548±0.015	0.723±0.025	0.627±0.019	Sbc	...	no	102.46±1.20
904	NGC 7591	1.24±0.27	4.52±1.00	2.27±0.50	1.375±0.053	0.415±0.013	2.259±0.128	Sbc	...	no	112.31±0.55
906	IC 5309	0.57±0.03	...	1.25±0.07	0.122±0.003	...	0.658±0.021	Sc	...	no	56.02±2.86
914	NGC 7631	1.06±0.02	...	1.47±0.03	0.075±0.003	...	0.460±0.017	Sb	...	no	77.04±1.43
915	NGC 7653	1.83±0.04	...	1.60±0.04	0.318±0.008	...	1.740±0.037	Sb	...	yes	99.14±1.54
916	NGC 7671	0.98±0.48	0.33±0.16	3.27±1.60	0.000±0.000	0.000±0.000	0.063±0.001	S0	...	no	228.13±1.50
920	NGC 7691	0.04±†	0.13±†	1.40±0.03	0.005±†	0.016±0.001	0.655±0.090	Sbc	...	no	60.43±2.37
924	NGC 7716	0.51±0.01	0.14±†	1.23±0.03	0.005±0.001	0.037±0.001	0.354±0.013	Sb	...	yes	108.28±0.52
925	NGC 7722	2.39±0.48	...	6.76±1.37	0.130±0.017	...	0.000±0.000	Sab	...	yes	167.02±2.12
927	NGC 7738	5.67±0.13	4.01±0.09	1.98±0.05	5.035±0.230	0.744±0.055	0.867±0.074	Sb	...	yes	156.79±2.82
929	UGC 12810	0.54±0.13	0.48±0.12	3.83±0.95	0.266±0.009	0.182±0.009	1.934±0.138	Sbc	...	no	97.39±2.93
930	UGC 12816	0.19±0.08	...	0.11±0.05	0.182±0.005	...	0.436±0.017	Sc	...	no	62.32±1.77
931	NGC 7782	2.01±0.65	...	10.48±3.40	0.025±0.003	...	3.558±0.118	Sb	...	no	...
933	NGC 7787	3.50±0.08	...	0.70±0.02	0.599±0.030	...	0.418±0.032	Sab	1.32±0.49	no	103.75±3.26
935	UGC 12864	0.15±†	0.12±†	0.67±0.02	0.244±0.005	0.146±0.004	0.277±0.011	Sc	...	no	57.00±2.77

This page was left intentionally blank.

CHAPTER 5

SFR Cosmic Density

Not everything that can be counted counts, and not everything that counts can be counted.
— Albert Einstein

Resumen

El estudio de la función de luminosidad (LF, del inglés *Luminosity Function*) aporta información valiosa sobre la distribución de los distintos tipos de galaxias del Universo en base a su luminosidad. Su análisis es clave para poder constreñir los modelos cosmológicos de formación y evolución de galaxias así como para poder reconstruir la historia de la formación estelar en el Universo.

Uno de los objetivos principales de este trabajo es derivar la función de luminosidad basada en la línea de emisión Hα corregida de extinción para una muestra amplia de galaxias en el Universo local. En particular, el uso de la línea de recombinación Hα (corregida de efectos de atenuación) constituye una medida directa de la cantidad de estrellas nuevas que se están formando y, por tanto, de la tasa de formación estelar actual en las galaxias. Por primera vez, se obtendrá dicha función de luminosidad para las principales estructuras internas que constituyen las galaxias (bulbos, barras, y discos). La disponibilidad de imágenes de SDSS y de datos de espectroscopía de campo integral de la exploración CALIFA, permiten realizar una descomposición multi-componente como se mostró en el Capítulo 4. Una vez construidas las funciones de luminosidad, estamos en disposición de obtener los valores de la densidad de la tasa de formación estelar tanto para las galaxias como un todo como para sus distintas componentes. Este estudio revela que los valores de la densidad de la tasa de formación estelar de las galaxias y de la suma de discos y barras son bastante similares, arrojando valores medios de $(4.64 \pm 0.15) \times 10^{-3}$ y $(4.12 \pm 0.15) \times 10^{-3}$ $M_\odot$ yr^{-1} Mpc^{-3}, respectivamente. Los discos (sin incluir la presencia de barras) tienen un valor de $(3.41 \pm 0.11) \times 10^{-3}$ $M_\odot$ yr^{-1} Mpc^{-3} mientras que la componente de bulbo muestra un valor más reducido de $(2.64 \pm 0.23) \times 10^{-4}$ $M_\odot$ yr^{-1} Mpc^{-3}.

Los valores de la densidad de la tasa de formación estelar para las distintas estructuras que componen las galaxias presentados en este trabajo, pretenden servir como referencia local para trabajos futuros con galaxias situadas a más altos desplazamientos al rojo con el objetivo final de revelar cuales son los procesos físicos fundamentales que impulsan la formación de estrellas en discos y bulbos y el crecimiento en masa de éstos.

5.1 Introduction and motivation

Luminosity Functions (hereafter, LF) are excellent observational constraints for models of galaxy formation and evolution. Their shape and normalization factors and the evolution of these with redshift contain relevant information about the mechanisms that transform one type of galaxy into another and the evolution of the stellar populations within galaxies. The accurate characterization of the LF in a band sensitive to the emission from recently formed stars allows determining the star formation rate density (SFRD) of the Universe, i. e., the distribution of the star-forming galaxies as a function of their current SFR. As commented previously in Chapter 1 (Section 1.2.4), the study of the star formation history of the Universe provides a deeper understanding on both the evolution of galaxies and the physical processes that drive star formation. This has been traced out up to redshift ~ 10 using different SFR tracers covering a broad part of the electromagnetic spectrum (from X-ray and gamma-ray burst to radio emission).

In this Chapter, we construct the LF for the CALIFA sample in the extinction-corrected Hα luminosity as it provides a direct measure of the amount of newly formed stars and of the current SFR in galaxies. The Hα LF has been previously determined using narrow-band surveys (Pascual et al. 2001; Ly et al. 2007, 2011). These surveys suffer from some limitations, and assumptions need to be done about extinction and stellar absorption corrections or AGN contamination, among others. To avoid these systematic uncertainties, some authors used long-slit spectroscopic Hα measurements to derive the parameters of the Hα LF (Gallego et al. 1995; Pérez-González et al. 2003; Westra et al. 2010; Gunawardhana et al. 2013).

The use of CALIFA IFS data makes possible to yield a better constraint on the Hα LF in the local Universe as it assures an accurate estimation of the dust attenuation and a proper subtraction of the underlying stellar continuum in a well-defined sample of nearby galaxies. Moreover, the availability of both SDSS imaging and IFS data allows us to decompose the galaxies in their basic structures (bulges, bars, and disks) following the procedure described in Chapter 4. Thus, our main goal is to derive the Hα LF using integrated properties of the galaxies and, for the first time, for their morphological components as well. This is also the first time that a precise value for the present-day SFR density in the local Universe both for galaxies as a whole and for their components is obtained. With this work, we aim to provide a local benchmark for future high redshift studies that could mimic the procedure followed here.

The rest of this Section is structured as follows; the concept of the LF, its analytical approximation together with the corresponding main parameters, and how to obtain the SFRD from it are introduced in Section 5.2. The description of the V_{max} method, the analysis performed to obtain the V_{max} values, the sample used and the main selection criteria that could influence the derivation of the LF appear in Section 5.3. Finally, Section 5.4 shows the main results derived from this study and the main conclusions are summarized in Section 5.5.

5.2 Analytical approximation to the LF: The Schechter function

The first step of this analysis is to construct the Hα LF associated to galaxies as a whole and also to their components for the redshift interval of the CALIFA sample, $0.005 < z < 0.03$. Once

the LF is fitted to an analytical function and the best parameters that define it are obtained, the SFR density can be estimated as the integral of that function multiplied by the luminosity (this is explained in detail in Section 5.4.1, where the SFR density is derived).

The LF, $\phi(L)$, is defined as the number density of galaxies per luminosity interval. The determination of the LF in the Local Universe is a key constraint for the galaxy evolution models as it tells us about the final result of the evolution of the galaxy population through the Universe lifetime. It is commonly described analytically using a three-parameter ($\phi^\star$, $\mathrm{L}^\star$ and α) function known as the Schechter function (Schechter 1976). Thus,

$$\phi(L)dL = \phi^\star \left(\frac{L}{L^\star}\right)^\alpha e^{\left(-\frac{L}{L^\star}\right)} \frac{dL}{L^\star} \tag{5.1}$$

This expression reflects two distinctive regimes delimited by a characteristic luminosity ($\mathrm{L}^\star$), the low and the high luminosity parts of the LF. Luminosities lower than $\mathrm{L}^\star$ are characterized by a power law, where the α parameter, also known as the faint-end slope, is the power law slope which is driven by the abundance of low luminosity galaxies. The typical range of values for α is $-0.5 < \alpha < -1.5$, going from flatter to steeper. This part of the analytic function tell us that lower luminosity galaxies are more common in number than higher luminosity ones. For luminosities greater than $\mathrm{L}^\star$ there is an exponential decrease in the LF indicating that very luminous galaxies become progressively rare. $\phi^\star$ is the normalization constant but it does not affect the shape of the LF. Along this work, the units for the parameters $\mathrm{L}^\star$ and $\phi^\star$ are erg s^{-1} and Mpc^{-3}, respectively. The α parameter is dimensionless.

The LF might vary with the type of galaxy, environment and redshift of the sample analyzed. The fact that galaxy types are correlated with their environment (Dressler 1980) might further affect the resulting LF of different sample of galaxies. This result was shown in Binggeli et al. (1988), where the authors compared the LF for two different samples, one of them included galaxies in the vicinity of the Milky Way while the other sample of galaxies corresponded to the Virgo cluster. The authors show that the total LFs (defined as the sum of the individual LF associated to each Hubble type) for each sample of galaxies present slightly different values of their α and $\mathrm{L}^\star$ parameters. When early-type galaxies are the predominant objects in the sample, the values of $\mathrm{L}^\star$ tend to be higher in comparison with the values associated to a sample where late-type or irregular galaxies are the majority. De Propris et al. (2003) also established that the LF in clusters is significantly different from the field LF. The characteristic luminosity tends to be higher in denser regions, suggesting a dependence with the environment. Recent studies have pointed out that the LF is strongly affected by the environment in the case of the ellipticals while the LF of spirals do not present a remarkable dependence with environment (Tempel et al. 2011).

5.3 Vmax: a classical method for computing the number density of galaxies

In this Section, we describe one of the most common classical estimators used in the literature to derive the number of galaxies per luminosity interval, the V_{max} method.

The V_{max} method was originally used for quasars (Schmidt 1968) and later applied to field galaxies (Huchra & Sargent 1973). The goal of this technique is the derivation of the maximum volume within which a galaxy in the sample is detectable given its own absolute magnitude or luminosity and some detectability criteria. This volume, V_{max}, is calculated using such maximum distance at which a galaxy can be observed as part of the survey. This is a non-parametric method and it gives both the shape and the normalization of the LF without assuming any form for it. The LF can be expressed as:

$$\phi(L) = \sum_{i=1}^{N} \frac{1}{V_{max}(i)} \tag{5.2}$$

The V_{max} uncertainty can be computed using the following expression:

$$\sigma[\phi(L)] = \left[\sum_{i=1}^{N} \frac{1}{V_{max}^2(i)}\right]^{1/2} \tag{5.3}$$

The final contribution of each galaxy to the LF will be weighted by its corresponding $1/V_{max}$ quantity. V_{max} should compensate the fact that brighter galaxies can be seen at higher distances and, thus, they will be over-represented when compared with fainter galaxies.

In the following subsection, we describe the main steps for estimating the V_{max} values for our galaxies as a whole (treating them as entire systems) and, for the different morphological components that shape these galaxies (bulges, bars, and disks). We also explore the selection criteria of the sample, and, how to take them into account for computing the corresponding V_{max} values.

5.3.1 CALIFA galaxy sample and selection criteria

The galaxies used in this work are part of the diameter-limited CALIFA sample. This sample was created as a diameter-limited survey to optimize the use of the PPaK IFU, i. e. the size distribution of the observed objects is chosen to fill the IFU FoV. The selection criteria are well understood and are the following: (a) The galaxies are restricted to a diameter size of $45\," < isoA_r < 79.2\,"$, where $isoA_r$ is the major axis of the 25 magnitudes per square arcsecond isophote in the SDSS r-band. The previous limits correspond to 4.7 kpc and 46 kpc in linear isophotal size at the nearest and furthest limits of the survey, respectively. (b) There is also a redshift restriction in the range $0.005 < z < 0.03$. (c) Finally, a flux limit of $petroMag_r < 20$ mag ensures that faintest objects are excluded from the sample. To properly recover the LF of these galaxies, the selection function of the sample need to be accounted for. Otherwise, the final results derive from this study would be biased.

Out of the total number of observed galaxies in CALIFA, we make use of the ones described in Chapter 4. This selection is motivated by the fact that we are interested in construct the Hα LF of both entire galaxies and their components. The use of a 2D multi-component decomposition imposes some restrictions to the eligible galaxies. In particular, galaxies with an extremely distorted

morphology are discarded as they are not compatible with the use of symmetric models. In that regard, irregulars and interacting systems of projected pairs are not suitable for the photometric analysis. Also, highly inclined galaxies with an inclination value typically larger than 70 degrees are avoided due to projection effects. This leads to a final sample composed of 219 lenticular and spiral galaxies. The fluxes, luminosities and SFR values of the entire galaxies and their different morphological components were derived in Chapter 4 and are the ones used through this chapter. The selected galaxies were observed using the V500 set-up which allows to measure Hα and Hβ emission line fluxes at the same time.

5.3.2 Derivation of V_{max} measurements

As we have seen above, V_{max} is a reliable method for computing the unbiased number density of galaxies allowing the derivation of the LF. In this Section, we explain the methodology applied to estimate the V_{max} values. As the CALIFA survey is based on a diameter-limited selection, the main parameters that affect the V_{max} estimation are the angular isophotal values of the galaxies and the redshift range of the sample, which are defined by the following intervals $45\," < isoA_r < 79.2\,"$ and $0.003 < z < 0.05$.

V_{max} is defined using the following expression:

$$V_{max} = \frac{4}{3}\pi(d_{max}^3 - d_{min}^3) \tag{5.4}$$

where d_{max} and d_{min} are the maximum and minimum distance at which each galaxy in our sample would be observed, respectively. Thus, the first step is to estimate these distances. Bearing in mind that the information we have about the galaxies is their angular isophotal measurements, we need to calculate their corresponding diameter physical sizes in units of kpc (D_{iso}). D_{iso} can be derived as:

$$D_{iso}[kpc] = 10^3\, isoA_r\, \frac{c\, z}{206265\, H_0} \tag{5.5}$$

where c is the speed of light in units of $\mathrm{km\,s^{-1}}$, H_0 is the Hubble constant (we are assuming a value of 70 km/s/Mpc), and z is the corresponding redshift of the galaxy.

Then, the minimum and maximum distance can be calculated as:

$$d_{min}[Mpc] = 10^{-3}\, 206265\, \frac{D_{iso}}{isoA_{r\,max}} \tag{5.6}$$

$$d_{max}[Mpc] = 10^{-3}\, 206265\, \frac{D_{iso}}{isoA_{r\,min}} \tag{5.7}$$

The angular isophotal diameter limits in the sample are $45\," < isoA_r < 79.2\,"$, i. e., $\mathrm{isoA}_{r\,min} = 45\,"$ and $\mathrm{isoA}_{r\,max} = 79.2\,"$.

The derived distances need to be included within the redshift interval of the sample ($0.005 < z < 0.03$). Thus, if the minimum distance calculated is lower than the predicted by the specific lower limit redshift, the value of the minimum distance is fixed to this one. In other words, the minimum distance is limited by the following value: $d_{min}(\text{limit}) = \frac{z_{min}\, c}{H_0}$. Consequently, d_{max} could not be larger than $d_{max}(\text{limit}) = \frac{z_{max}\, c}{H_0}$. In the previous expressions, the corresponding values of z_{min} and z_{max} are 0.005 and 0.03, respectively. Note that at the redshifts of the CALIFA sample, angular and luminosity distances are almost identical (2% different at z = 0.01).

Other important quantity to determine is the solid angle subtended on the sky by the sample. A substancial sky coverage is desirable to overcome large-scale structure effects. Ideally, observing galaxies from the full sky, i. e., $4\,\pi$ steradians, will give us a non-bias distribution of the objects but this is difficult to achieve. For that reason, the percentage of the sky covered by the survey has to be taken into account and corrected for when computing V_{max}. In this case, the area of sky covered by CALIFA is 8700 deg^2. Thus, the real volume occupied by our galaxies could be estimated taking into account that $\Omega_{subsample} = \Omega_{CALIFA} \times \textit{factor}$, where $\Omega_{CALIFA} = 8700$ deg^2. In our case, this *factor* corresponds to the ratio 254/937, i. e, the ratio of the number of galaxies eligible to be used in this work and the total galaxies in the CALIFA mother sample. This value allows to scale the value of the V_{max} previously inferred. This procedure assumes that there is an isotropic distribution of galaxies in the sampled volume and that is not affected by the random observability criteria applied to go from the 937 mother sample targets to the 667 finally observed (Sánchez et al. 2016). Besides, the applied 2D decomposition imposes some extra criteria to the galaxies eligible for the study. In particular, our sample is avoiding galaxies with (a) a highly distorted morphology, and, (b) a high inclination. The latter criterion might affect the V_{max} measurements due to the relation between inclination and the possibility that a galaxy is observed within a diameter-limited sample. Although having the same intrinsic dimension, projection effects might favor the inclusion of inclined galaxies over face-on ones. This effect is especially important for systems with lower values of their extinction, while larger attenuated galaxies do not present significant differences. The total amount of galaxies available from the 2D decomposition is 254. A total of 219 galaxies are lenticulars and spirals (the ones with a considerable amount of star formation) while the other 35 are ellipticals. We remind that the number 937 that appears in the 254/937 ratio includes the total amount of galaxies in the CALIFA mother sample without excluding any morphological type. Thus, ellipticals need to be taken into account in the numerator of the previous ratio as well, although they do not contribute to the LF due to its negligible Hα luminosity, especially if only the emission associated to recent star formation is to be included.

To assure (a) bona fide measurements of our estimated V_{max} in comparison with the ones derived from CALIFA and (b) to verify whether or not the previous assumption ($\Omega_{subsample} = \Omega_{CALIFA} \times \textit{factor}$) is valid for our case, we construct the *r*-band LF as shown in Figure 5.1. The verification of issue (a) is done by means of demonstrating that our values are in concordance with the ones derived in Figure 8 in Walcher et al. (2014). Walcher et al. (2014) already compared the agreement of their derived LF with the Schechter function fit to the LF obtained from a sample of 150000 SDSS galaxies at $z \sim 0.1$ from Blanton et al. (2003), evolved to the mean redshift of the CALIFA sample. As already explained in Walcher et al. (2014), the incompleteness at the low luminosity bins is due to the low-redshift limit imposed for CALIFA that excludes galaxies with $D_{iso} < 4.6$ kpc, i. e., mostly dwarf galaxies, while the mild incompleteness at high luminosity values is a consequence of the upper redshift limit meaning that too extended galaxies might be absent

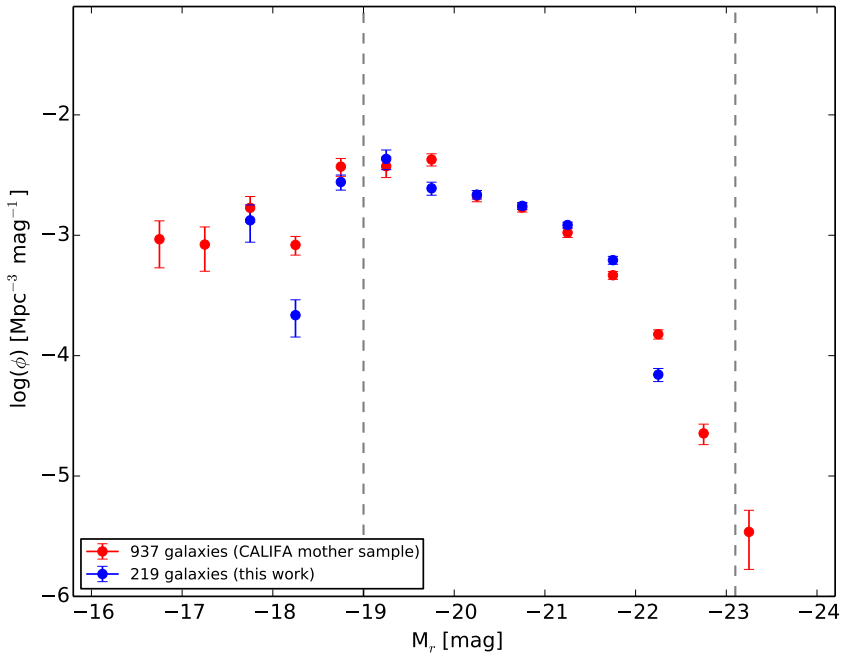

Figure 5.1: *r*-band Luminosity Function. Red points represent the LF for the entire CALIFA mother sample while blue points are referred to the subsample of 219 galaxies analyzed in this work. Vertical gray dashed lines correspond to the completeness limits of the entire CALIFA sample derived in Walcher et al. (2014).

(this is a minor source of incompleteness as relatively large objects are not part of the survey due to the volume sampled). The limits where the CALIFA sample is complete were derived in Walcher et al. (2014), -23.1 $<$ M$_r$ $<$ -18.6, and are shown as vertical gray dashed lines in Figure 5.1.

On the other hand, we aim to verify issue (b), i. e., whether the $\Omega_{subsample} = \Omega_{CALIFA} \times factor$ expression can be safely applied to our case. Thus, Figure 5.1 serves as a comparison between the CALIFA mother sample V$_{max}$ measurements and the V$_{max}$ values for the subsample derived in this work. It can be seen that there is a good agreement between them. Only the bins at the most extreme values of the M$_r$ magnitude present a disagreement. This is mostly due to a reduce dynamical range in the M$_r$ values for the 219 galaxies subsample in comparison with the complete CALIFA mother sample and to the fact that our bins contain a reduced number of objects. In particular, there are two low luminosities bins outside the limits where the sample is complete (M$_r$ $<$ -18.6) and two high luminosities bins without measurements as elliptical galaxies are not part of the subsample of star-forming galaxies. We can conclude that the expression $\Omega_{subsample} = \Omega_{CALIFA} \times factor$ can be used in our case under the assumption of an isotropic distribution of galaxies in the sampled volume. Consequently, the use of a 2D decomposition should act as a secondary effect that should not alter significantly the measurements of the V$_{max}$ values.

In the case of the different morphological components that form galaxies (bulges, bars, and disks) we examine whether or not the same V$_{max}$ values obtained for entire systems can be applied to them. Although CALIFA was not created as a magnitude-limited survey where galaxies below a threshold apparent brightness or flux are excluded, it is inherited to the nature of galaxies that

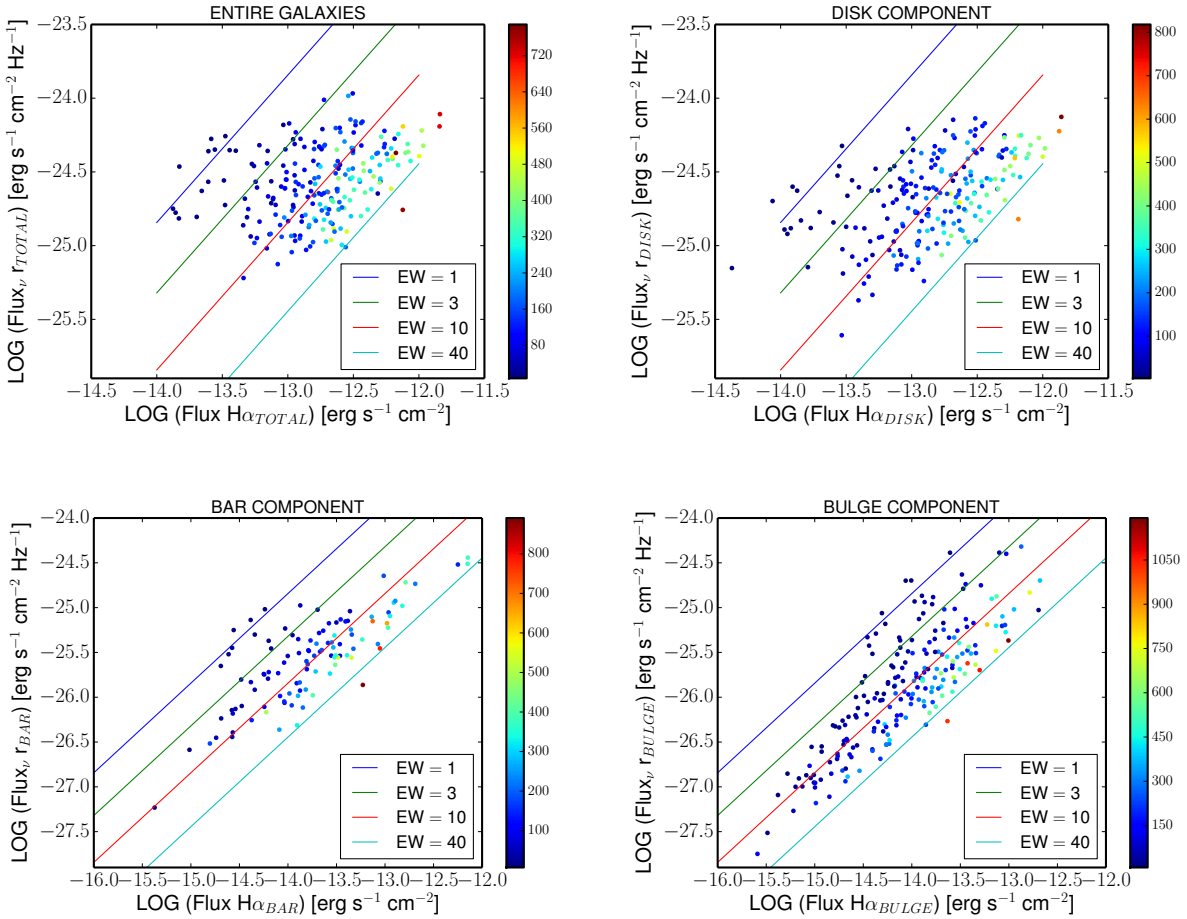

Figure 5.2: Variation of the r-band flux with the observed Hα flux for entire galaxies (upper left), the disk component (upper right), the bar component (bottom left) and the bulge component (bottom right). Constant equivalent width (EW) lines are shown as parallel lines (same slope and different offsets as a function of the corresponding EW value). The color-coding represents the S/N of the emission lines. All these values are above the threshold value of S/N > 5 imposed for both Hα and Hβ emission lines. The plots show that the S/N selection criterion imposed translates into a minimum EW value.

intrinsically bright objects will be easier to detect, i. e., the selection bias known as Malmquist bias. The basis of this phenomenon resides in the fact that objects with the same luminosity (their intrinsic brightness) but located at different distances will be seen dimmer if they are further away in comparison with the closer objects that will appear brighter. The decreasing of flux with distance ($1/\mathrm{d}^2$) makes harder to discriminate between a bright galaxy at a far distance and a faint object located closer resulting in a bias towards luminous galaxies. In that regard, besides the corrections taking into account the physical size of the galaxy, we explore if there is also a limit imposed by the observed Hα and Hβ fluxes and the continuum flux around them using the g and r asymptotic SDSS bands. We use growth curve magnitudes obtained from the SDSS DR7 images. This step is applied to the entire galaxies and also to the morphological components of the galaxies. The objetive behind this idea is to clarify if the observed Hα and Hβ fluxes limit the available volume for each galaxy more than the previous V_{max} calculations using the diameter of the galaxies.

Figure 5.2 shows the relation between the observed Hα and the r-band fluxes while the same

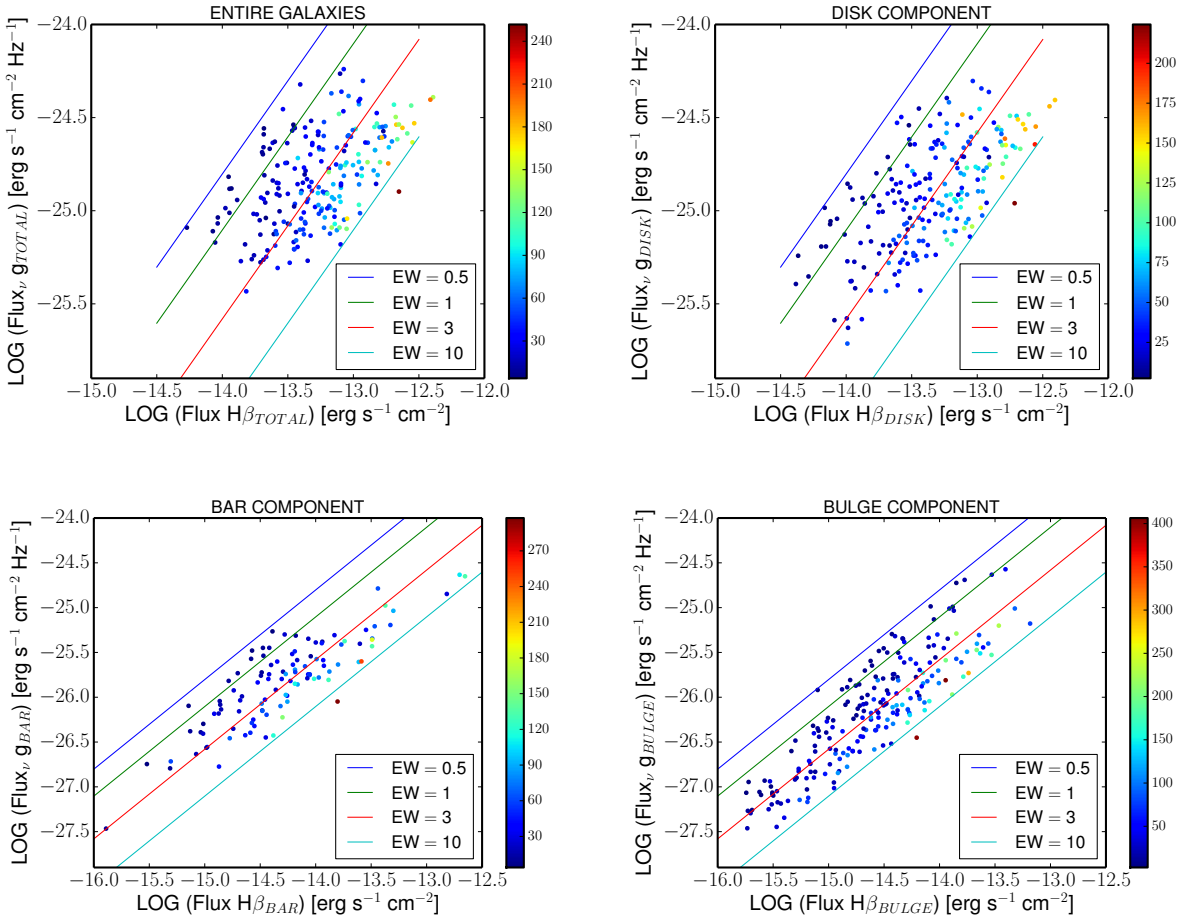

Figure 5.3: Same description as Figure 5.2 for the relation between the g-band and the observed Hβ flux.

relation for the observed Hβ and the g-band fluxes is shown in Figure 5.3 including the corresponding diagrams for entire galaxies, disks, bars and bulges. The g and r fluxes have been calculated from the asymptotic g and r-band magnitudes which assures a complete coverage of the galaxy and from the relative contribution of the components obtained from our 2D decomposition. Equivalent widths (EW) can be estimated in these figures as the ratio between the values on the x axis and the y axis, i. e., the ratio between the flux in the emission line and the adjacent continuous. Thus, constant EW lines are shown in Figures 5.2 and 5.3 as parallel lines (same slope and different offsets as a function of the corresponding EW value). There is a natural cut imposed by the lowest value of the EW measurable (parallel lines in the upper part of the previous Figures). In particular, galaxy components present a minimum EW ~ 0.5 Å and a maximum of EW ~ 10 Å for the Hβ/g-band ratio while the maximum value typically increases up to 40 Å for the Hα/r-band case. The plots show that the selection criterion imposed by limiting the galaxies to those which a S/N > 5 for both Hα and Hβ emission lines, translates into a minimum EW value. Thus, there is not an additional flux cut that might modify the criteria used to derive the V$_{max}$ values. We remind the reader that the EW is distance independent at the low redshifts of our sample. We can safely apply the V$_{max}$ values derived for galaxies as a whole (taking into account the redshift of the galaxy and its angular size as explained before) to the case of the galaxy components.

5.4 Results

Once we have explained the methodology used to estimate the V_{max} measurements, we construct the Hα LF for galaxies as a whole and for their different stellar components (bulges, bars, and disks) as explained in Section 5.3 using equations 5.2 and 5.3.

5.4.1 Hα Luminosity Function and SFR Density

The values of the Hα luminosities of every individual galaxy in our sample and their corresponding attenuations (both integrated and by-component values) used along this Chapter are the ones derived in Chapter 4.

The histograms of the extinction-corrected Hα luminosities for entire galaxies and also for their components give us an idea of the optimal width and the numbers of bins needed to computed the LF via the V_{max} method. Figure 5.4 shows these histograms. It can be seen that the dynamical range of galaxies as a whole and disks is quite similar, while bulges and bars display lower values of the luminosity.

The number of galaxies in each category and the luminosity range covered by each of them is as follows (in log scale and in units of erg s^{-1}), 219 galaxies in total ($39.66 < \log[L(H\alpha_{corr})] < 42.64$), 217 disk components ($39.34 < \log[L(H\alpha_{corr})] < 42.58$), 206 bulge components ($38.13 < \log[L(H\alpha_{corr})] < 41.96$) and 117 bar components ($38.61 < \log(H\alpha_{corr}) < 41.73$). We use a constant bin of 0.2 dex for entire galaxies and disks while a 0.3 dex is used for the case of the bulges. The bar component (which obviously shows poorer statistics than the rest of the components) has been included together with the disk component. We consider this decision is supported by the bar location within the galaxies and its true nature since the star formation is activated in the disk due to an increase in the rate of cloud-cloud collisions caused by the enhanced potential of the bar (Athanassoula 1992; Ohishi et al. 2012).

To constrain the faint-end slope of the LF is fundamental that the sample spans a large range of luminosities. In our case, α is not well sampled at the lowest values of the luminosity. This is, again, consequence of the exclusion of dwarfs by the diameter limits set as part of the CALIFA survey selection. Some lower limit cuts are also imposed to perform the fitting. The final luminosity ranges used (in log scale and in units of erg s^{-1}) are the following, entire galaxies from $40.5 < \log[L(H\alpha_{corr})] < 42.3$, disks and bars together from $40.5 < \log[L(H\alpha_{corr})] < 42.3$, disks from $40.1 < \log[L(H\alpha_{corr})] < 42.3$ and bulges from $38.8 < \log[L(H\alpha_{corr})] < 40.9$.

Other important aspect is the presence of AGNs in the sample. The CALIFA spatial resolution is not enough to spatially remove the contribution coming from unresolved AGNs. As we have shown in Chapter 4, the sSFR of the bulges is affected by the presence of AGNs. Thus, galaxies that host AGNs might play a role in the LF of the bulge component. In contrast, the effect of low-luminosity AGNs over large scales in the galaxy might be negligible. That means that in the particular case of the LF for entire galaxies and disks, the contamination to the Hα luminosity coming from type-2 AGNs will have a lower impact.

The V_{max} values obtained from the galaxies in this study and their corresponding components

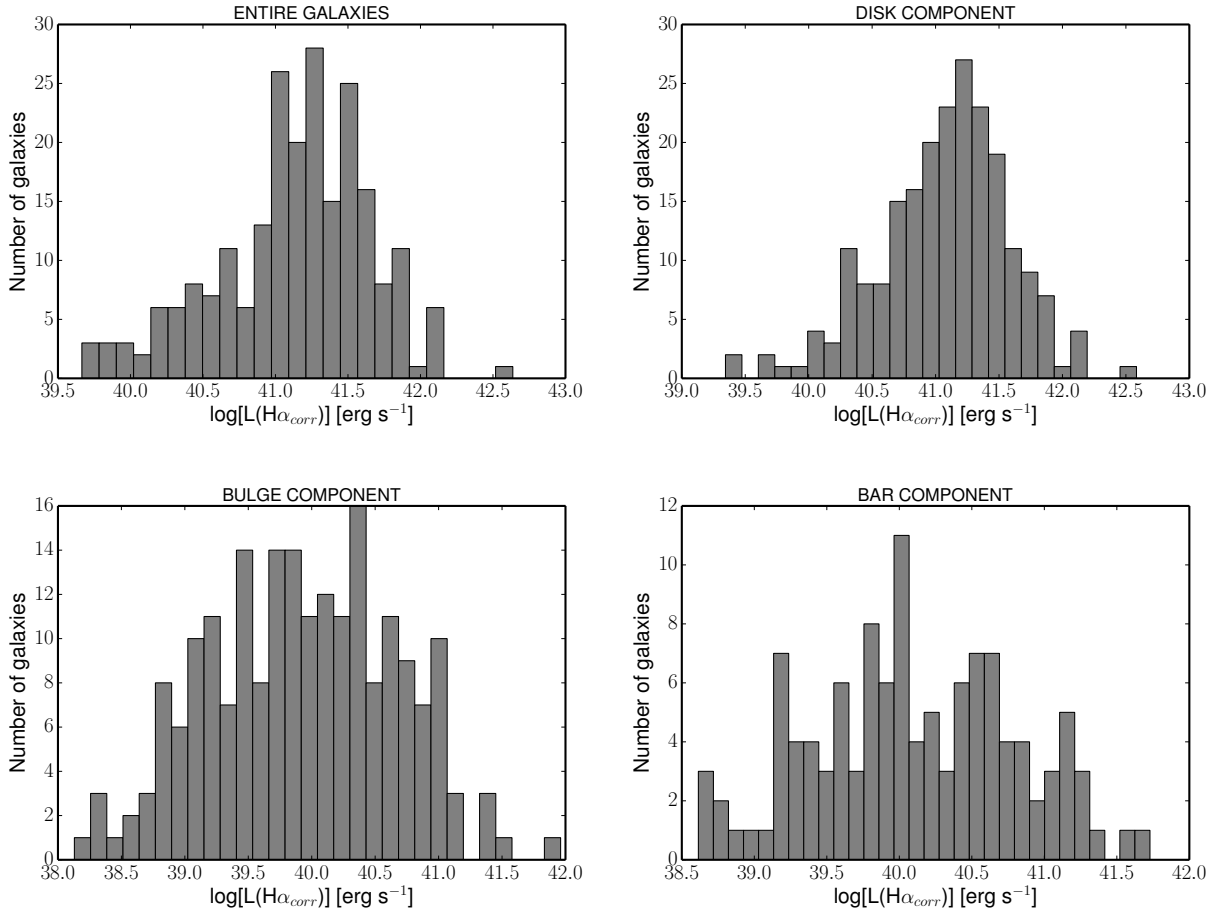

Figure 5.4: Histograms showing the distribution of the extinction-corrected Hα luminosity for whole galaxies (upper left), disk component (upper right), bulge component (bottom left) and bar component (bottom right). These histograms serve as a proxy for the number of bins used in the calculation of the LF.

(disks + bars, disks, and bulges) are shown as red points in the top panels of Figures 5.5, 5.6, 5.7 and 5.8. The V_{max} measurements and its uncertainties have been derived through equations 5.2 and 5.3 as commented above.

The extinction-corrected Hα LF is assumed to follow a Schechter parametric form with the α parameter fixed to -1.2 as the lowest luminosity range is not well-sample due to the lack of dwarf galaxies in the sample. The estimation of the best-fitting Schechter parameters is done using 20000 random realizations of each of the previous points of the LF estimated using the V_{max} method. In this process, we assume that the errors of the different bins are independent. Thus, a total of 20000 LFs are constructed. The mean value of the $\phi^\star$ and $L^\star$ Schechter parameters from the 20000 realizations are used as the final best-fitting parameters to represent the extinction-corrected Hα LF for the entire galaxies and its corresponding components. The best-fitting to the Schechter function is shown by the blue solid line in the top panels of Figures 5.5, 5.6, 5.7 and 5.8. The mean values of the $\phi^\star$ and $L^\star$ parameters and their corresponding uncertainties appeared in Table 5.1.

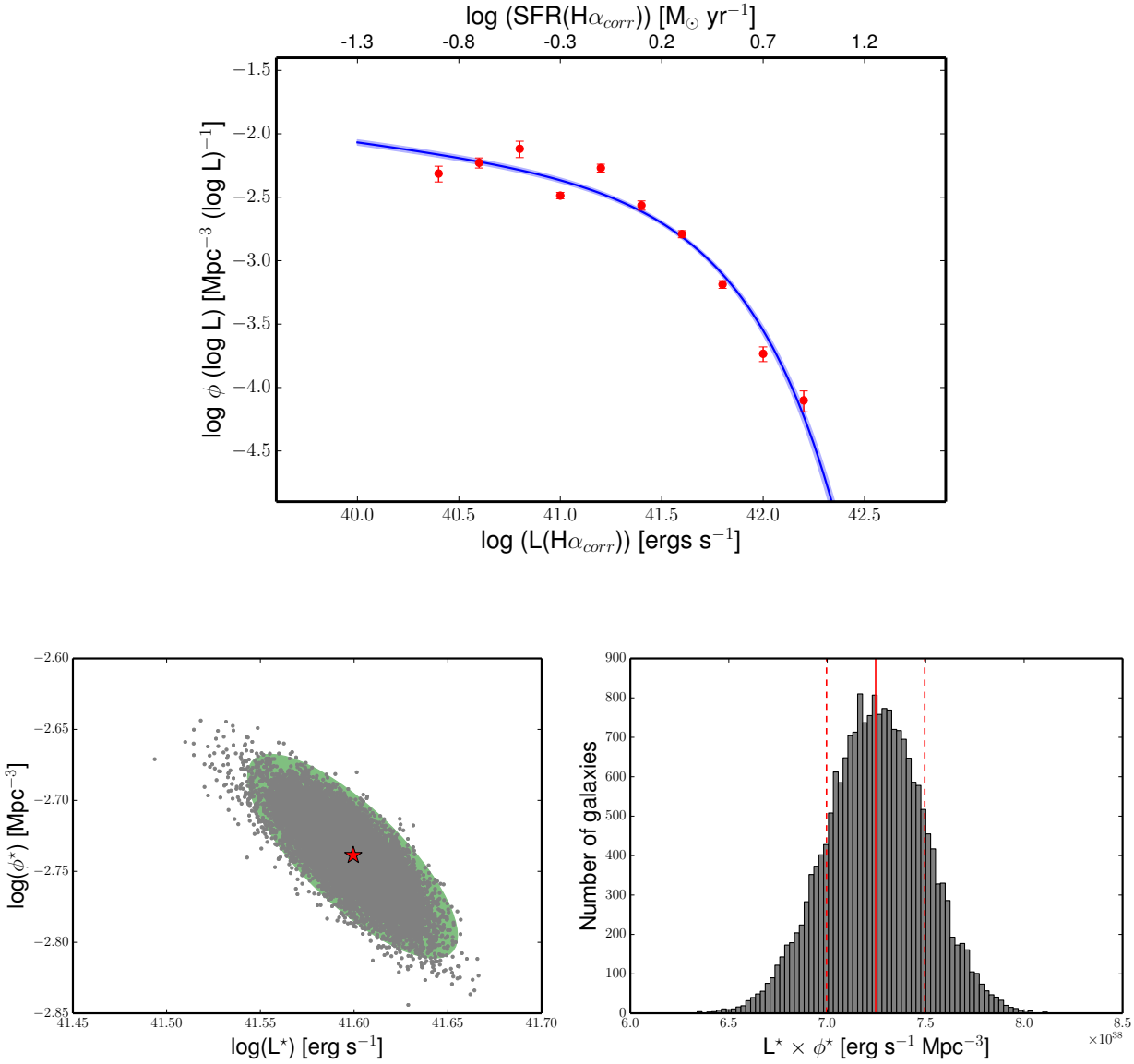

Figure 5.5: Top panel: Hα LF for galaxies as a whole. Red points and its errors are obtained using the V_{max} method. The blue solid line represents the best-fitting to the Schechter LF while the shaded blue region refers to the 1σ uncertainty band. The $\phi^\star$ and $L^\star$ Schechter parameters are obtained as the mean values of the 20000 random realizations of each point of the LF while α is fixed to -1.2 due to the incompleteness at the lowest luminosities values. Left bottom panel: Gray points show the variation of the $L^\star$ and $\phi^\star$ parameters obtained through 20000 random realizations of each point of the LF while the red star corresponds to their mean values, i. e., the ones used to derive the fitting to the LF in the top panel of this Figure. The shaded green region shows the distribution of the covariance ellipse for the individual points. Right bottom panel: Distribution of the $L^\star \times \phi^\star$ used to estimate the SFR density value (ρ_{SFR}). Red solid line shows the mean value while the red dashed lines correspond to the 1σ interval around the mean. To recover the real value of ρ_{SFR}, the previous values need to be multiplied by the corresponding Γ function.

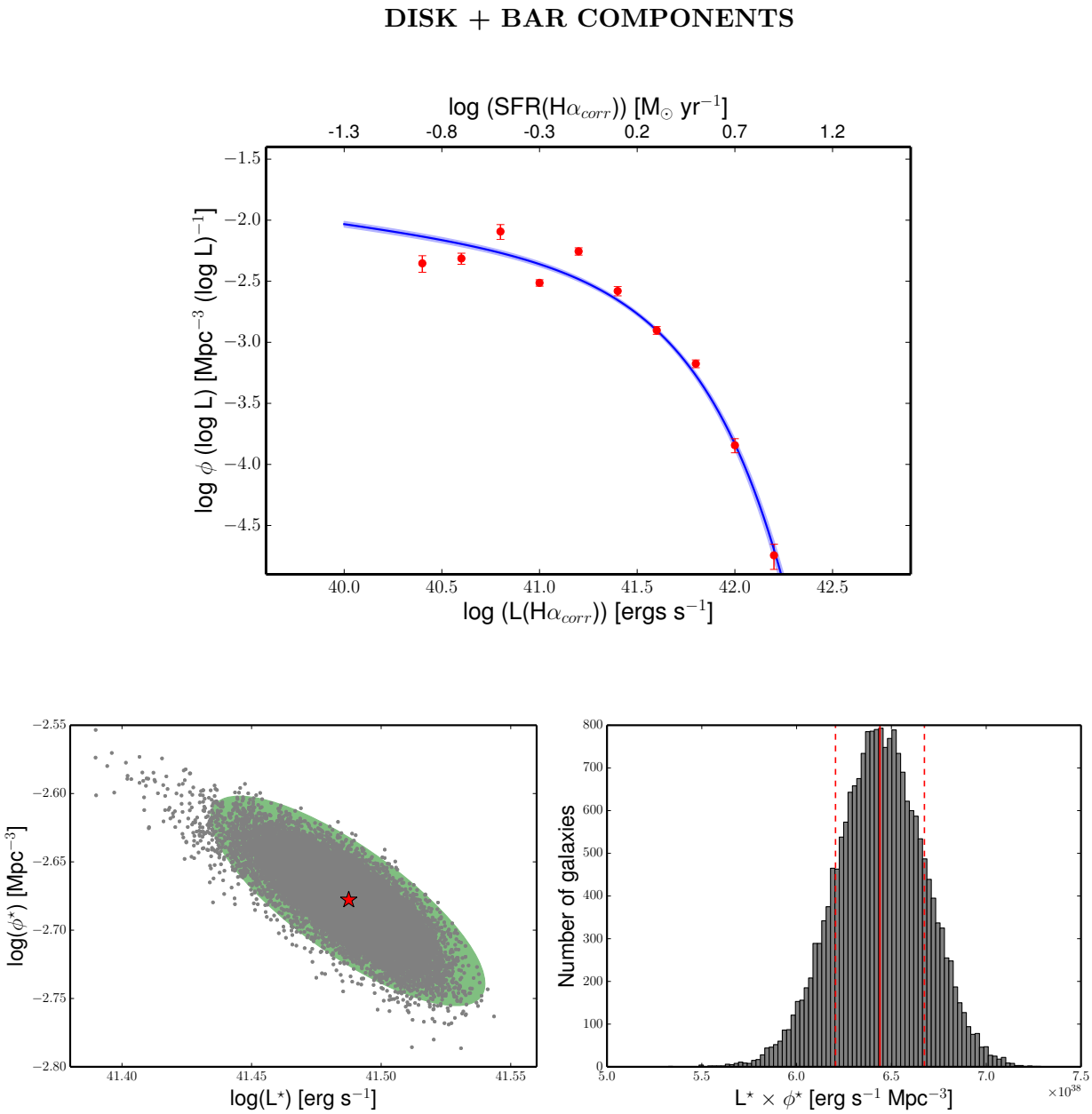

Figure 5.6: Top panel: Hα LF for the case of the bar and disk components together. Red points and its errors are obtained using the V_{max} method. The blue solid line represents the best-fitting to the Schechter LF while the shaded blue region refers to the 1σ uncertainty band. The $\phi^\star$ and $L^\star$ Schechter parameters are obtained as the mean values of the 20000 random realizations of each point of the LF while α is fixed to -1.2 due to the incompleteness at the lowest luminosities values. Left bottom panel: Gray points show the variation of the $L^\star$ and $\phi^\star$ parameters obtained through 20000 random realizations of each point of the LF while the red star corresponds to their mean values, i. e., the ones used to derive the fitting to the LF in the top panel of this Figure. The shaded green region shows the distribution of the covariance ellipse for the individual points. Right bottom panel: Distribution of the $L^\star \times \phi^\star$ used to estimate the SFR density value (ρ_{SFR}). Red solid line shows the mean value while the red dashed lines correspond to the 1σ interval around the mean. To recover the real value of ρ_{SFR}, the previous values need to be multiplied by the corresponding Γ function.

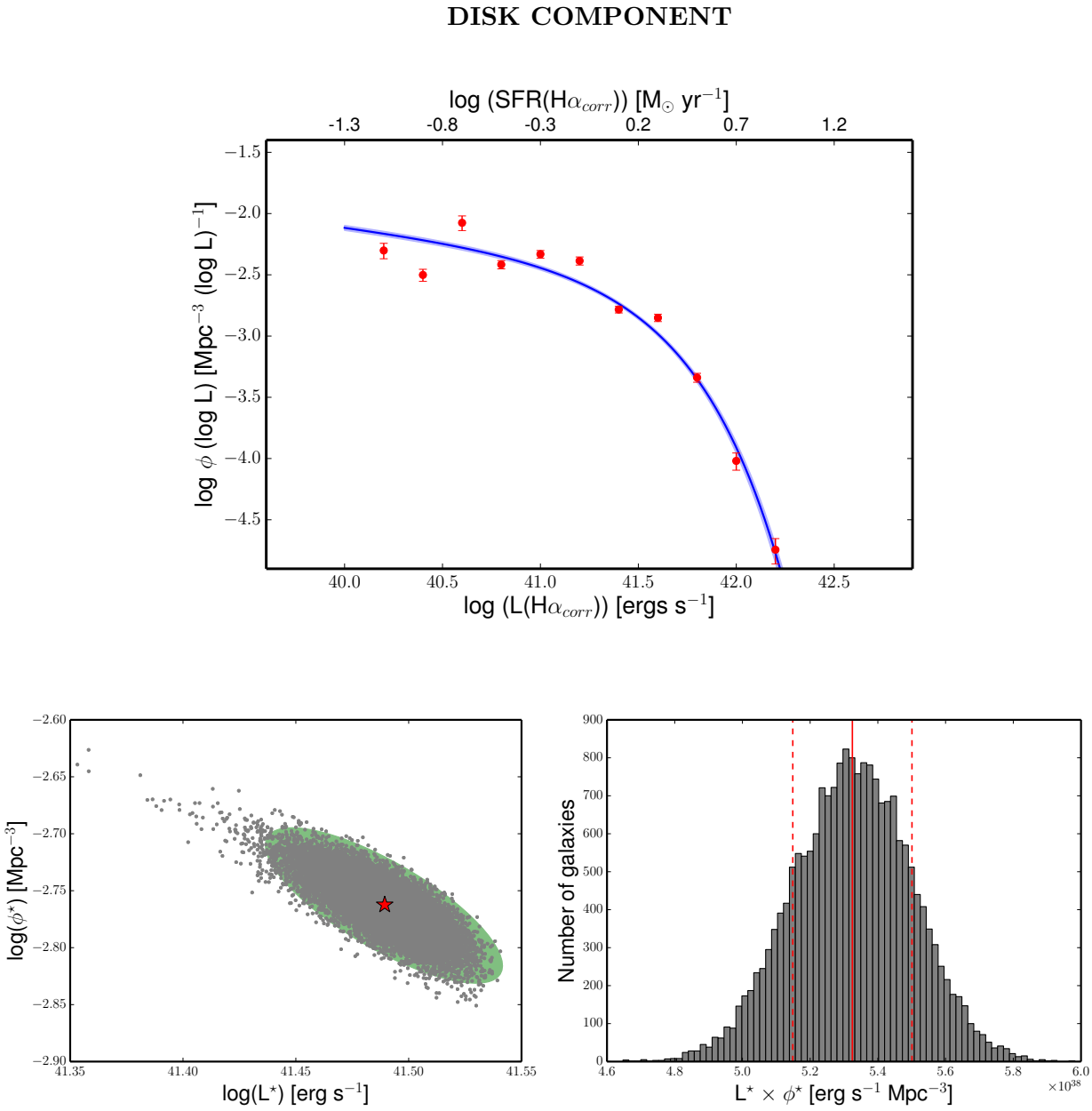

Figure 5.7: Top panel: Hα LF for the case of the disk component. Red points and its errors are obtained using the V_{max} method. The blue solid line represents the best-fitting to the Schechter LF while the shaded blue region refers to the 1σ uncertainty band. The $\phi^\star$ and $L^\star$ Schechter parameters are obtained as the mean values of the 20000 random realizations of each point of the LF while α is fixed to -1.2 due to the incompleteness at the lowest luminosities values. Left bottom panel: Gray points show the variation of the $L^\star$ and $\phi^\star$ parameters obtained through 20000 random realizations of each point of the LF while the red star corresponds to their mean values, i. e., the ones used to derive the fitting to the LF in the top panel of this Figure. The shaded green region shows the distribution of the covariance ellipse for the individual points. Right bottom panel: Distribution of the $L^\star \times \phi^\star$ used to estimate the SFR density value (ρ_{SFR}). Red solid line shows the mean value while the red dashed lines correspond to the 1σ interval around the mean. To recover the real value of ρ_{SFR}, the previous values need to be multiplied by the corresponding Γ function.

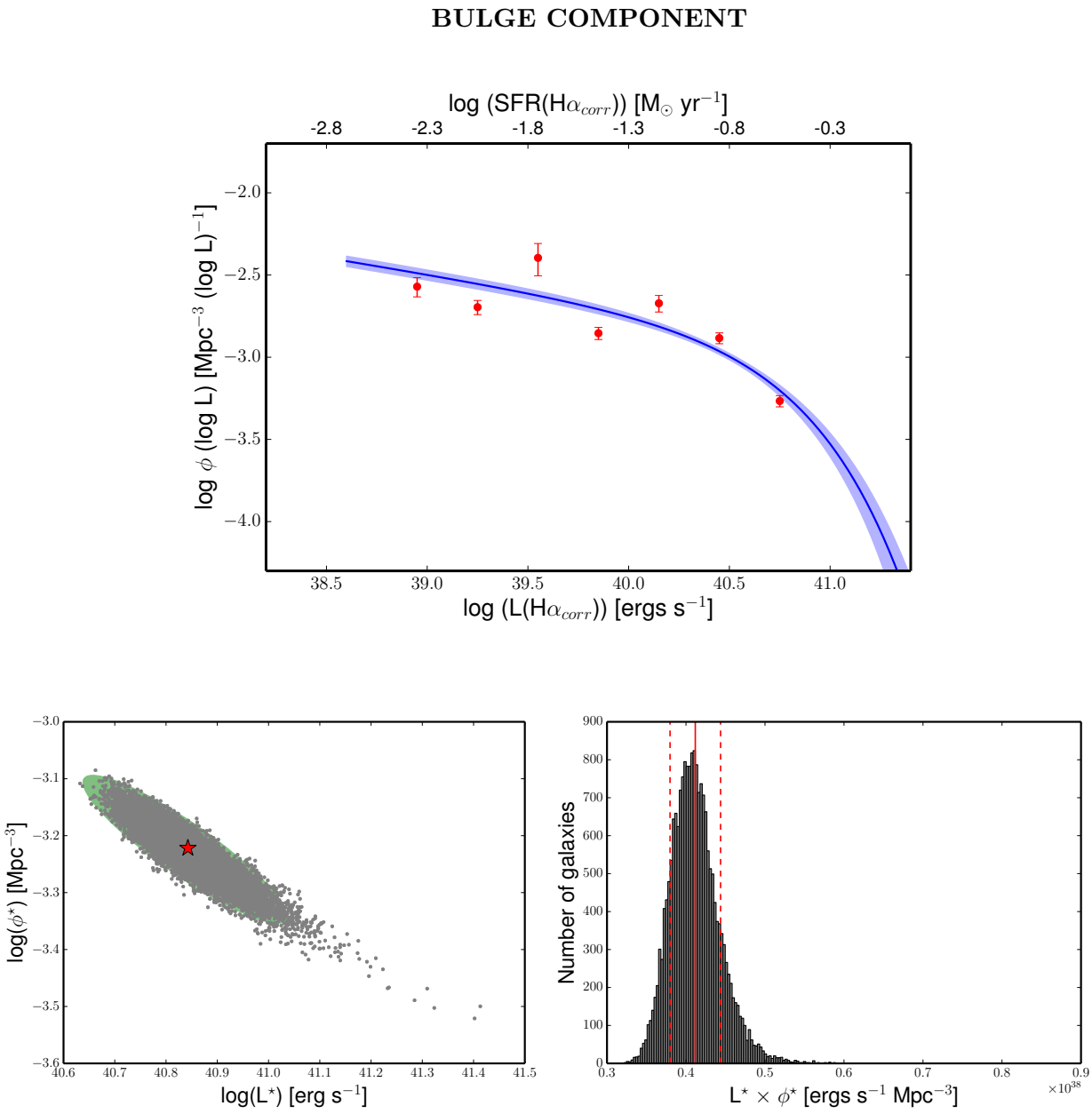

Figure 5.8: Top panel: Hα LF for the case of the bulge component. Red points and its errors are obtained using the V_{max} method. The blue solid line represents the best-fitting to the Schechter LF while the shaded blue region refers to the 1σ uncertainty band. The $\phi^\star$ and $L^\star$ Schechter parameters are obtained as the mean values of the 20000 random realizations of each point of the LF while α is fixed to -1.2 due to the incompleteness at the lowest luminosities values. Left bottom panel: Gray points show the variation of the $L^\star$ and $\phi^\star$ parameters obtained through 20000 random realizations of each point of the LF while the red star corresponds to their mean values, i. e., the ones used to derive the fitting to the LF in the top panel of this Figure. The shaded green region shows the distribution of the covariance ellipse for the individual points. Right bottom panel: Distribution of the $L^\star \times \phi^\star$ used to estimate the SFR density value (ρ_{SFR}). Red solid line shows the mean value while the red dashed lines correspond to the 1σ interval around the mean. To recover the real value of ρ_{SFR}, the previous values need to be multiplied by the corresponding Γ function.

Figure 5.9 shows the comparison of the extinction-corrected Hα LFs for entire galaxies and its components. It can be seen that the LF of entire galaxies is quite similar to the LF obtained with the combination of disks and bars together. As expected, the bulge LF presents lower values.

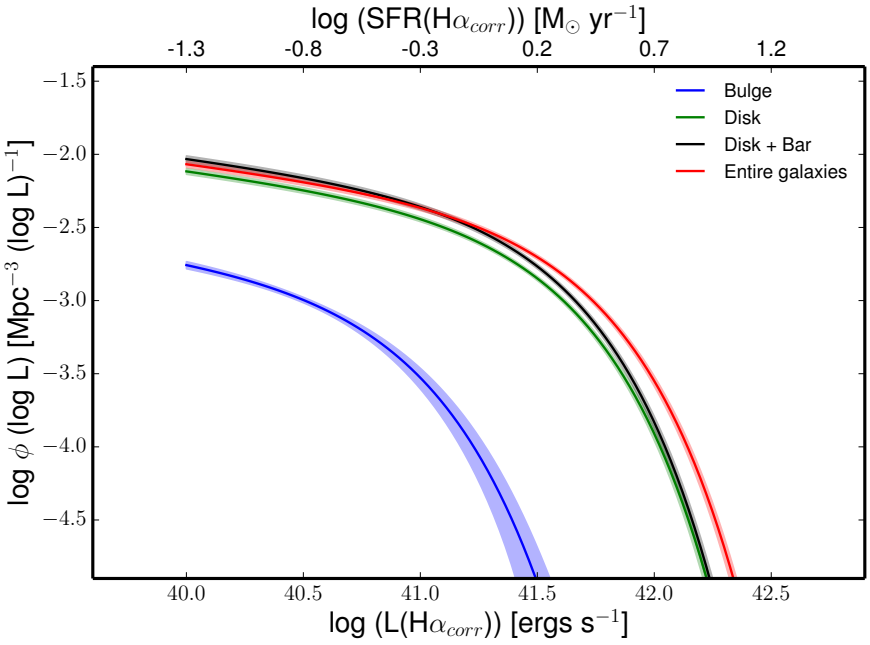

Figure 5.9: Hα LFs for the CALIFA sample. The different solid lines are for whole galaxies (red line), disk and bar components together (black line), disk component (green line) and bulge component (blue line). Shaded regions show the 1 σ uncertainty bands around them.

The way of deriving the SFR density is through the calculation of the total luminosity density. The LF can be integrated over the entire range in luminosity to obtain the integrated luminosity density. This parameter can be compared directly with the models of galaxy evolution that should successfully reproduce this value. Thus,

$$\mathcal{L}(> L_{lim}) = \int_{L_{lim}}^{\infty} L\phi(L)dL = \phi^{\star}L^{\star}\Gamma(\alpha + 2, L_{lim}/L^{\star}) \tag{5.8}$$

where Γ represents the incomplete gamma function. The choice of the luminosity limit, L_{lim}, affects the total luminosity density being the effects more severe for steeper values of the faint-end slope (α). We use $L_{lim} = 0$ which reduces equation 5.8 to $\phi^{\star}$ $L^{\star}$ $\Gamma(\alpha + 2)$, where now Γ is the complete Gamma function. We apply the complete Gamma function with a fixed value of -1.2 for the α parameter (as explained earlier in this Section).

One of the disadvantages of applying expression 5.8 is that the uncertainties in $\phi^{\star}$ and $L^{\star}$ are correlated. This fact immediately implies that if the individual errors in $\phi^{\star}$ and $L^{\star}$ are used to estimate the final uncertainty in the ρ_{SFR} quantity using the error propagation method, the errors in ρ_{SFR} would be overestimated. Here, since we have estimated the LF parameters doing 20000 random realizations, the ρ_{SFR} and its uncertainty is estimated using the mean and the sigma values of the $\phi^{\star} \times L^{\star}$ distribution, respectively. Bottom left panels of Figures 5.5, 5.6, 5.7 and 5.8 show

the correlation between the $\phi^\star$ and L* parameters while the distribution of $\phi^\star \times$ L* (which we use to estimate ρ_{SFR}) appears in the bottom right panels.

For the conversion between the Hα luminosity and the SFR we assume the following expression provided by Kennicutt et al. (2009):

$$SFR[M_\odot\, yr^{-1}] = 5.5 \times 10^{-42} L(H\alpha)[erg\, s^{-1}] \tag{5.9}$$

Thus, the values of ρ_{SFR} can be estimated as $\phi^\star \times$ L$^\star \times \Gamma(0.8) \times 5.5 \times 10^{-42}$. The derived values of ρ_{SFR} with their corresponding uncertainties for entire galaxies and their components are shown in Table 5.1. The small uncertainties mainly results from the low scatter present in the V$_{max}$ measurements and the large number of realizations done.

Table 5.1: Schechter parameters for the CALIFA galaxies

type	α	$\phi^\star$ [Mpc^{-3}]	L* [erg s^{-1}]	ρ_{SFR} [M$_\odot$ yr^{-1} Mpc^{-3}]
whole galaxies	-1.2	$(1.83 \pm 0.10) \times 10^{-3}$	$(3.98 \pm 0.17) \times 10^{41}$	$(4.64 \pm 0.15) \times 10^{-3}$
disk + bar	-1.2	$(2.10 \pm 0.12) \times 10^{-3}$	$(3.08 \pm 0.12) \times 10^{41}$	$(4.12 \pm 0.15) \times 10^{-3}$
disk	-1.2	$(1.73 \pm 0.10) \times 10^{-3}$	$(3.09 \pm 0.12) \times 10^{41}$	$(3.41 \pm 0.11) \times 10^{-3}$
bulge	-1.2	$(6.01 \pm 0.60) \times 10^{-4}$	$(6.97 \pm 1.37) \times 10^{40}$	$(2.64 \pm 0.23) \times 10^{-4}$

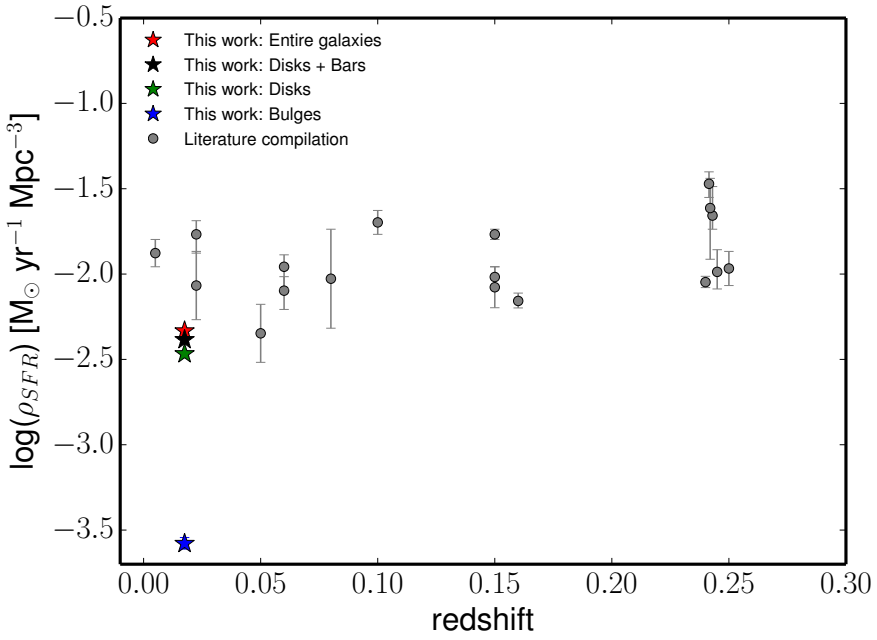

Figure 5.10: Evolution of the ρ_{SFR} with redshift. Gray points come from the recent compilation of Gunawardhana et al. (2013) and they are referred to measurements of entire galaxies. Red, black, green, and blue star symbols are the values derived in this work for entire galaxies, disks and bars, disks, and bulges, respectively.

We can compare our results with the ones from other surveys to see whether or not the parameters of the LF and the values of the ρ_{SFR} are in well agreement with them. So far, existing surveys

have been focussed on integrated properties of galaxies that is why the comparison is restricted to the values of entire systems (although we have also included our values for the different galaxy components in the following Figures to show where they are expected to appear; red, black, green, and blue star symbols for entire galaxies, disks and bars, disks, and bulges, respectively). Figure 5.10 shows the comparison between our ρ_{SFR} value and the ones found in the literature using the recent compilation of Gunawardhana et al. (2013) included in their Appendix B. In particular, we have included the values that have also been derived using Hα measurements and with redshifts lower than 0.3. As the majority of the data presented in their compilation were obtained applying the conversion between Hα luminosity and SFR given by Kennicutt (1998a) that are based on a Salpeter (1955) IMF, Gunawardhana et al. (2013) gave the final values of ρ_{SFR} converted to a Salpeter (1955) IMF. In our case, we have applied the more recent relation between Hα luminosity and SFR given by Kennicutt et al. (2009) based on a Kroupa (2001) IMF. The reference from Kennicutt et al. (2009) is lower than the one from Kennicutt (1998a) by a factor of 1.44. We apply this factor to the measurements in the Gunawardhana et al. (2013) compilation to be consistent with our own value, so the measurements in Figure 5.10 are consistent with the Kennicutt et al. (2009) calibration using a Kroupa (2001) IMF. Thus, Figure 5.10 shows the gradual decline of the ρ_{SFR} to the present-day epoch. The spread in the ρ_{SFR} values at lower redshifts reflects the fact that each measurement has been obtained sampling different volumes and covering different ranges of luminosities, i. e., the influence of the selection criteria that ultimately affect the constraints of the faint and bright end of the LF.

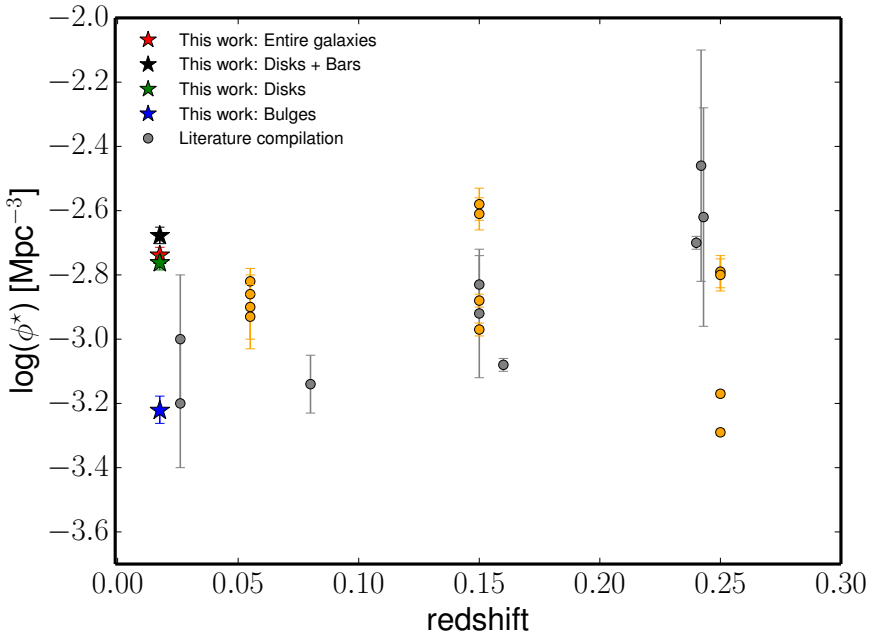

Figure 5.11: Evolution of the $\phi^\star$ Schechter parameter with redshift. Red, black, green, and blue star symbols are the values derived in this work for entire galaxies, disks and bars, disks, and bulges, respectively. Gray and orange points come from the literature, in particular orange points are from the analysis of Westra et al. (2010). Westra et al. (2010) obtained different values for $\phi^\star$ as (i) the α parameter can be fixed to -1.2 or unconstrained and (ii) the sample can include pure star-forming galaxies or pure star-forming and AGNs.

We have also searched in the literature for the values of $\phi^\star$ and L* that correspond to the

measurements in the compilation made by Gunawardhana et al. (2013) and we have included the ones that were available in the corresponding articles. Figures 5.11 and 5.12 show the evolution of the $\phi^{\star}$ and $L^{\star}$ Schechter parameters with redshift, respectively. There is a trend with the $L^{\star}$ parameter which point out to the idea of the downsizing in the evolution of the star-forming galaxies. In that regard, the galaxies that dominate the SFR in the Local Universe tend to be less massive and, comparatively, are less efficient at forming new stars, especially in the most inner parts of their disks.

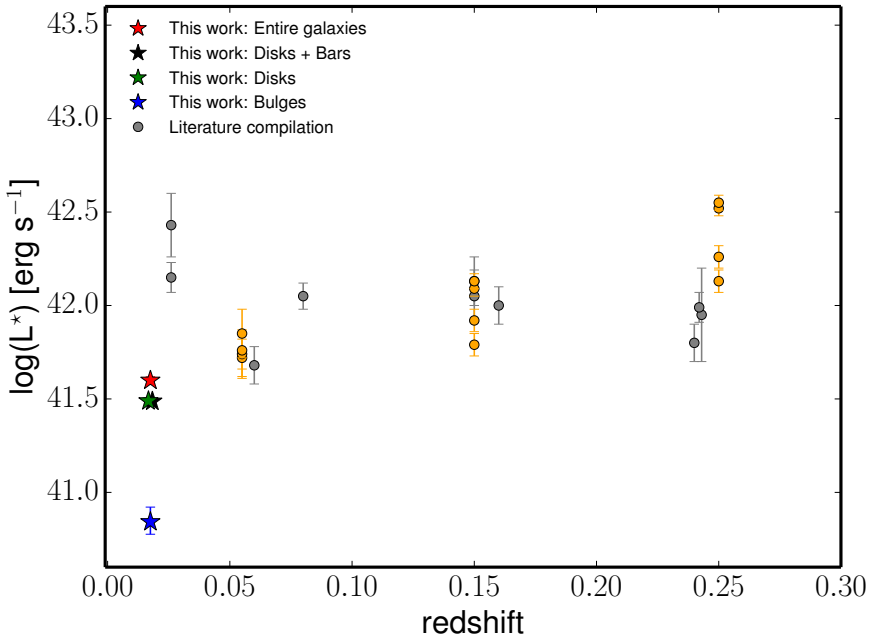

Figure 5.12: Evolution of the $L^{\star}$ Schechter parameter with redshift. Red, black, green, and blue star symbols are the values derived in this work for entire galaxies, disks and bars, disks, and bulges, respectively. Gray and orange points come from the literature, in particular orange points are from the analysis of Westra et al. (2010). Westra et al. (2010) obtained obtained different values for $L^{\star}$ as (i) the α parameter can be fixed to -1.2 or unconstrained and (ii) the sample can include pure star-forming galaxies or pure star-forming and AGNs. Thus, orange points reflects their different values.

Although there are not available ρ_{SFR} measurements in the literature for the different galaxy components, we can compare our results with the estimations from González Delgado et al. (2016) where CALIFA data are also used. The method employed by these authors consists of decomposing the optical continuum spectrum of the galaxy by a combination of stellar populations of different ages, i. e., applying stellar population synthesis. As the Hα luminosity traces the light coming from stars with lifetimes < 10 Myr, González Delgado et al. (2016) chose 32 Myr as the age of the oldest stars that can be included to compute their SFRs to have a similar order of magnitude than the estimation from the Hα luminosity. Thus, the mean SFR is obtained as the sum of all the populations younger than $t_{SF} = 32$ Myr as $SFR_{xy} = (1/\ t_{SF}) \times \sum_{t<t_{SF}} M_{txy}$, where xy refers to each Voronoi and M_{txy} is the amount of mass turned into stars which an age equal to t at the present moment. Their SFR are transformed into the volume density of SFR by adding SFR/V_{max}, using the V_{max} measurements from Walcher et al. (2014). They obtained a slightly higher value of $\rho_{SFR} = 0.0105 \pm 0.0008$ $M_{\odot}$ yr^{-1} Mpc^{-3} for galaxies as a whole than our derived value of $\rho_{SFR} = 0.00464 \pm 0.00015$ $M_{\odot}$ yr^{-1} Mpc^{-3}.

Due to the limitations of their method, instead of deriving measurements for the different galaxy components they analyze the spatial origin of the ρ_{SFR} in terms of the half light radius (HLR). Several values of HLR are imposed to discrimine between the disk dominated regions and the inner part of the galaxies. In particular, they obtained that 18% of the contribution to ρ_{SFR} comes from regions inside 0.5 HLR, 29% from $0.5 < R < 1$ HLR and 53% from regions outside 1 HLR. If we add all the contribution outside the central 0.5 HLR we have a total of 82 % contribution to the ρ_{SFR}. In our case, disks and bars together contribute up to 89% to the ρ_{SFR} while disks alone with 73%. In contrast, for the innermost componentes, these authors obtain a fraction of 18% of the ρ_{SFR} in the central 0.5 HLR regions while the fraction of the ρ_{SFR} for the bulge component that we obtain is 6%. While it is clear that in both cases most of the ongoing star formation occurs outside the central component, the total values obtained are slighter different. We remind the reader that in our case the SFR is estimated directly from the measurement of the Hα emission line while in the case of González Delgado et al. (2016) is a more indirect method that is subject to the degeneracies in the derivation of the complete star formation history of the galaxies analyzed by these authors.

5.5 Conclusions

We have addressed the fundamental question about which are the best parameters that define the Hα LF in the Local Universe for entire galaxies and also for their components using the well-defined sample of CALIFA nearby galaxies. The decomposition of the galaxies in their basic structures as well as the derivation of their extinction-corrected Hα luminosity values was done in Chapter 4. Once we have the Hα LF, we estimate the SFRD. The main conclusions derived from this study can be summarized as follows:

- The extinction-corrected Hα LF recovered for galaxies as a whole is quite similar to the one obtained for the case of the disk and the bar together which translates into similar values of the mean value of ρ_{SFR} being $(4.64 \pm 0.15) \times 10^{-3}$ M$_\odot$ yr^{-1} Mpc^{-3} and $(4.12 \pm 0.15) \times 10^{-3}$ M$_\odot$ yr^{-1} Mpc^{-3}, respectively. The values for entire galaxies are in agreement with the ones found in the literature using similar redshift ranges and Hα luminosities corrected for the effect of dust attenuation.

- The Hα LF of the disk component without including the presence of bars shows a slightly smaller value of ρ_{SFR}, equal to $(3.41 \pm 0.11) \times 10^{-3}$ M$_\odot$ yr^{-1} Mpc^{-3}, in comparison with the values for entire galaxies.

- As expected, the Hα LF of the bulge component samples the lower range of luminosities and there is a considerable offset between it and the LF for total galaxies (~ 0.8 dex). The ρ_{SFR} value derived for bulges is $(2.64 \pm 0.23) \times 10^{-4}$ M$_\odot$ yr^{-1} Mpc^{-3}.

To our knowledge, this is the first time that LFs are constructed for the different components that shape galaxies, and, thus, it is also a reference value of the ρ_{SFR} for the different internal structures of the galaxies in the Local Universe. These values can help to constrain the models of galaxy formation and evolution that should reproduce them. Moreover, the extension of this work at different redshifts is extremely important. It will allow to shed some light on the precise

moment at which the spheroidal component and the disk component would equally contribute to the total ρ_{SFR}. It is expected that in the epoch where bulges were forming (by dissipative, i. e., actively star-forming *wet* mergers), the ρ_{SFR} would be strongly dominated by them.

This page was left intentionally blank.

CHAPTER 6

Future work

The future belongs to those who believe in the beauty of their dreams.
— Eleanor Roosevelt

Resumen

La mayor parte del trabajo realizado a lo largo de esta tesis está basado en datos que emplean la técnica de espectroscopía de campo integral. Consideramos que el uso de este método es un camino prometedor, por lo tanto, proponemos extender su uso al resto de los proyectos de trabajo futuro descritos en este capítulo. Las posibilidades más interesantes que surgen pueden agruparse principalmente en las siguientes dos categorías. Por un lado, se sugiere un estudio detallado de galaxias en el Universo Local empleando instrumentos de última generación como MUSE. El objetivo es aprovechar las ventajas que brinda el incremento de la resolución espacial permitiendo realizar un análisis detallado de los principales mecanismos asociados a la formación estelar a distintas escalas físicas. Por otro lado, el estudio de la formación estelar en las distintas componentes que componen las galaxias (bulbos, barras y discos) descrito en el Capítulo 4, supone un punto de referencia que puede extrapolarse a muestras de galaxias a distintas distancias cosmológicas, especialmente, al momento en el que las galaxias eran jóvenes y estaban ensamblando la mayor parte de su masa.

A lo largo de este capítulo, también se describe el análisis (actualmente en desarrollo) de la región H II conocida como Hubble III, situada en una de nuestras galaxias vecinas, la enana irregular NGC 6822. Siguiendo la línea de lo descrito anteriormente, la técnica empleada para su observación es la espectroscopía de campo integral. En este caso particular, se emplea una rendija larga que se mueve perpendicularmente al campo del objeto para cubrirlo por completo. La elección de esta región con forma de burbuja se hace en base a su proximidad ($\sim$ 474 kpc) que permite resolver estrellas individualmente al tiempo que el cubo de datos proporciona información sobre las principales líneas de emisión del rango óptico. El análisis de este objeto esta íntimamente relacionado con el hilo conductor de esta tesis, la formación estelar. En concreto, con este trabajo se pretende estimar la fracción de fotones ionizantes que escapan de dicha región y cuya pérdida se ha postulado como uno de los mecanismos responsables que afectan al cálculo de la tasa de formación estelar.

6.1 Future work: spatially resolved star-formation properties across a wide range of environments at both low and high redshift

The work carried out along this thesis is intended to provide a local benchmark for future research studies. Being able to isolate the different morphological components that shape galaxies and measure their relative contribution to the total SFR in each object is a promising way to have an in-depth understanding about the processes associated with the star formation and the physical processes which drive galaxy formation and evolution in general. To achieve this goal it is essential to explore different environments going from dense clusters to low-density field objects. There are mainly two interesting possibilities at play that we are going to justify in this Section and in planned future works that we can combine to improve the knowledge of the distribution of the SFR at multiple physical size scales. Our ultimate goal is to understand how galaxies were built. First, we could (a) increase the spatial resolution of the data taken (Section 6.2) to investigate the ionized gas properties in a spatially resolved manner. This will allow us to focus on the different mechanisms associated to SFR acting on galaxies. In that regard, we analyze an ongoing project based on a new technique devoted to create high-spatial-resolution spectroscopic datacubes from long-slit spectroscopy. The aim of this study is to shed some light on the mechanisms that cause star formation at local scales, and, (b) extrapolate the study to galaxy samples at different cosmic epochs (Section 6.3) handling IFS data that allow us to spatially resolve [NII]/Hα and significantly increase the samples.

This thesis is based mainly on IFS data and we consider that this is a promising way of pursuing studies on large samples of intermediate and high-redshift objects. For that purpose, we can exploit the capabilities of state-of-the-art facilities such as MUSE[1], KMOS[2] and/or SINFONI[3] on the 8-meter Very Large Telescopes (VLT) and the future instrument generation such as NIRSpec[4] at the James Webb Space Telescope (JWST) that will open an unexplored territory of deep NIR IFS from space. Especially, the ones that could observe multiple targets simultaneously.

6.2 Increasing the spatial resolution in the local Unvierse

The work presented in Section 4 based on CALIFA data, has a physical scale of 0.4 kpc/arcsec that corresponds to a spatial resolution of ~ 1 kpc assuming an average redshift for the sample of 0.017 and a standard ΛCDM cosmology. The aim of this future work is to increase the spatial resolution to provide a detailed analysis of the galaxies morphology and to shed some light on the details of the mechanisms that power and regulate the SFR. We can take advantage of outstanding instruments such as MUSE, a powerful wide-field, optical IFS with unprecedented sensitivity already presented in Section 2. For that purpose, archival MUSE science products can be used in combination with the proposal of new observations of local star-forming galaxies.

[1] http://www.eso.org/sci/facilities/paranal/instruments/muse.html
[2] http://www.eso.org/sci/facilities/paranal/instruments/kmos.html
[3] http://www.eso.org/sci/facilities/paranal/instruments/sinfoni.html
[4] https://jwst.stsci.edu/instrumentation/nirspec

6.2.1 Hubble III: A extended H II Region in the nearby dwarf galaxy NGC 6822. The importance of photon leaking

The project presented here is an on-going work carried out as part of my research stays at Carnegie Observatories under the supervision of Dr. Barry Madore. The synergy between the previous work based on CALIFA IFS data and this new project is excellent, allowing to extend the study of the star formation to lower scales such as those only accessible to nearby extragalactic H II regions.

This study is motivated by the still open question about the leakage of Lyman continuum photons escaping their parent H II region and how this phenomena might affect the properties of the Diffuse Ionized Gas (DIG) and the SFR inferred from the Hα emission line in galaxies.

The existence of the DIG also referred to as the Warm Interstellar Medium (WIM) was first proposed by Hoyle & Ellis (1963), who characterized it by its warm temperature (10^4 K) and its low density (10^{-1} cm^{-3}) that surrounds the plane of our own galaxy in an ionized hydrogen state. The youngest, hottest and most luminous stars, O stars, are known to ionize their surrounding medium and have been postulated as the presumable ionizing sources for the DIG. The Lyman continuum radiation is able to escape from the luminous HII regions that surround massive O stars reaching not only the closer regions but it also propagates to large distances. Questions about the properties of the DIG and the source of its ionization still remain as it is a less well-understood component of nearby galaxies. We will be testing different photon escape laws that take into account how the clumpiness of the medium could affect the escape fraction and how the ionizing spectrum might vary from a pure massive stars once it escape the H II region. Other potential mechanisms that might contribute to the ionization or heating of the DIG will be also explored. As we will show later, we can use our 2D spectroscopy data to investigate and map the spatial distribution and the characteristics of ionized gas and, in particular, the DIG through a spectroscopic approach using line ratios. The amount of UV leakage measured in this particular H region will allow us to determine the potential contribution of the leakage to the heating of the DIG.

The leakage of Lyman continuum photons from star-forming regions is an interesting topic by itself as it has been claimed to be a potential mechanism to affect the measurement of the SFR in galaxies (Oey & Kennicutt 1997; Relaño et al. 2012). The wide-spread Hα emission line tracer applied to calculate SFR implicitly assumes that the neutral hydrogen absorbs all the ionizing radiation and, consequently, each Lyman continuum photon will generate their corresponding Hα photon (for the classical derivation of the relation between N_{Ly} and Hα luminosity see Brocklehurst 1972). The debate arises when some of the ionizing photons are able to escape the galaxy or when they are not detected as part of the DIG component. In fact, some studies have found that a non-negligible amount of the integrated Hα emission (up to a fraction of 50 %) is measured outside star-forming regions (van Zee 2000; Oey et al. 2007). This is specially important in dwarf galaxies, with low values of their SFRs (Hunter et al. 2010), such is the case of NGC 6822 with a SFR ~ 0.015 M$_\odot$ yr^{-1} (Efremova et al. 2011). Here, we can analyze whether dwarf galaxies and its surroundings might have particular conditions that favor the Lyman continuum photons escape from the H II region. Recently, Lee et al. (2016) have investigated the possibility that previous Hα surveys might have missed a fraction of the ionized emission in a sample of three dwarf galaxies reaching a flux limit of $\sim 8 \times 10^{-18}$ erg s^{-1} cm^{-2}. Leakage of photons has been postulated as one of the possible sources for explaining the under-predict SFR values derived using the Hα luminosity in comparison with the expected values of the UV continuum luminosity SFR tracer

for SFR below a characteristic threshold (typically stablished at SFR $\sim 10^{-3}$ $M_{\odot}\,yr^{-1}$, Lee et al. 2009). Nevertheless, applying general SFR recipes that assume a constant star formation history for systems that might be better reproduced by bursts of star formation is another possibility at play to explain this difference (Iglesias-Páramo et al. 2004). As the Hα emission line traces relatively short-lived stars (1-10 Myr) while the FUV continuum mainly traces long-lived stars (until 200 Myr), a deficiency in the former ones might explain the lower Hα values found.

Apart from the previous main points, the detailed 2D study of the line emission in nearby H II regions can also provide insights into the sources responsible for the ionization in every particular H II region. Some earlier studies have used CALIFA IFS data to study the Lyman continuum photon escape fraction in these galaxies (Papaderos et al. 2013; Morisset et al. 2016). We can measure quantities such as the ionization parameter using emission lines ratios such as [S II]$\lambda\lambda$6717,6731/[O III]λ5007 (Pellegrini et al. 2012). Also, proximity and isolation makes it ideal to perform studies of the high-mass end of the IMF via counting individual massive stars.

The Hubble III region located in the outskirts of the dwarf galaxy NGC 6822 is an optimal choice to carry out the previous analysis. Morphologies described with a shell shape using Hα images might present a higher escape fraction as suggested in Oey & Kennicutt (1997) due to the fragmentation of the interstellar medium (ISM) and the presence of gas unfilled regions. These shell-like regions, as it is the case of Hubble III, are often referred as bubbles.

6.2.1.1 Overview of the project

The study of the Hubble III H II region in the nearby dwarf galaxy NGC 6822 is part of a local survey lead by Dr. Barry Madore and their collaborators at The Observatories of the Carnegie Institution of Science (former Carnegie Institution of Washington). The team is currently creating spectrophotometric datacubes for a sample of large nearby galaxies in the southern hemisphere on the Irénée du Pont 2.5 m Telescope at Las Campanas Observatory. The goal of this project is to characterize the star formation processes in local galaxies under different conditions and over a large range of physical scales going from individual regions up to galaxy-wide areas.

Conventional spectrographic capabilities are applied to generate high-spatial-resolution spectroscopic datacubes. The methodology consists on moving a conventional (very) long-slit that is placed along the major axis perpendicular to it, which ultimately generates a 2D spectrum. After the first spectrum is taken, the slit is carefully moved to a new position using entire units of the slit width. This way of proceeding allows observations of targets that require of several nights. This technique is called PrISM, which stands for Progressive Integral Stepping Method. Among the multiple advantages of this methodology that it has a very simple design as it uses existent technology that it is optimized for large angular size galaxies. PrISM is especially suitable for large and bright objects with a surface brightness limit of $\mu = 21.1$ AB mag arcsec^2. The majority of the actual IFUs are not optimal for the study of large angular size galaxies due to the limited size of their field of views. In contrast, PrISM is conceived as a methodology able to resolve a median physical scale of 0.05 kpc. It also allows sky measurement simultaneously. The wavelength range coverage goes from 3650 to 9000 Å.

Hubble III has been observed with the alt-azimuth 6.5m Magellan Baade Telescope at Las

Campanas. The methodology is exactly as the one explained for the galaxies observed at the Du Pont telescope but using the spectroscopy mode provided by the Inamori-Magellan Areal Camera & Spectrograph (IMACS) instead. IMACS is mounted permanently on the Magellan Baade Telescope. Long-slit spectroscopy of up to 27 arcmin can be carried out in the f/4 channel. The wavelength coverage is 3650-6750 Å with a dispersion of 0.378 Å/pixel using the 600 lines/mm grating.

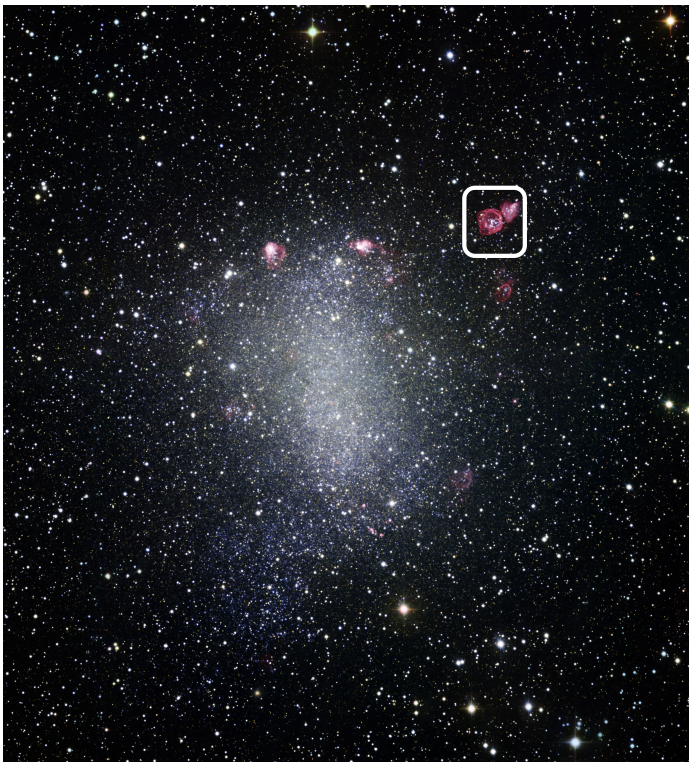

Figure 6.1: Image of the neighboring dwarf galaxy NGC 6822. White rectangle on the top right of the image shows the relative position of the bubble-shaped H II region known as Hubble III which is the target of this study. This image was made using four different filters (B, V, R, and Hα) and it has a field of view of 35 × 34 arcmin (***image credit: ESO***).

In particular, Hubble III is very suitable to study star formation at high resolution as it is a prominent and isolated extragalactic H II region hosting massive O-stars. This bubble-shaped H II region is part of the dwarf galaxy NGC 6822, which is also known as Barnard's Galaxy due to its discovery by E.E. Barnard in 1884. Later on, E.P. Hubble (1925) classified it as a nearby galaxy in 1925 (*NGC 6822. A Remote Stellar System. Astrophysical Journal, Vol. 62, pp. 409-433*). This object is a low metallicity (12 + log O/H = 8.02 ± 0.05, García-Rojas et al. 2016) dwarf irregular galaxy that is part of our Local Group and is located at a distance of 474 ± 13 kpc (Rich et al. 2014) with a stellar mass of 1.5 × 10^8 $M_\odot$ (Madden et al. 2013). Present day dwarf galaxies are particularly interesting as they resemble early-universe objects which are believed to have formed in similar physical conditions. An image of NGC 6822 with the position of Hubble III is shown in Figure 6.1.

6.2.1.2 First results

Available imaging data ranges from the UV to the NIR, including (a) *F170W* and *F255W* (UV range), *F336W*, *F449W* and *F555W* (optical range) and *F814W* (NIR range) HST bands, (b) the Massey catalog of the U, B, V, R, and I-band images and, (c) images taken specifically for this project in the B, V, R and I bands at the 6.5m Baade Telescope that are shown in Figure 6.2.

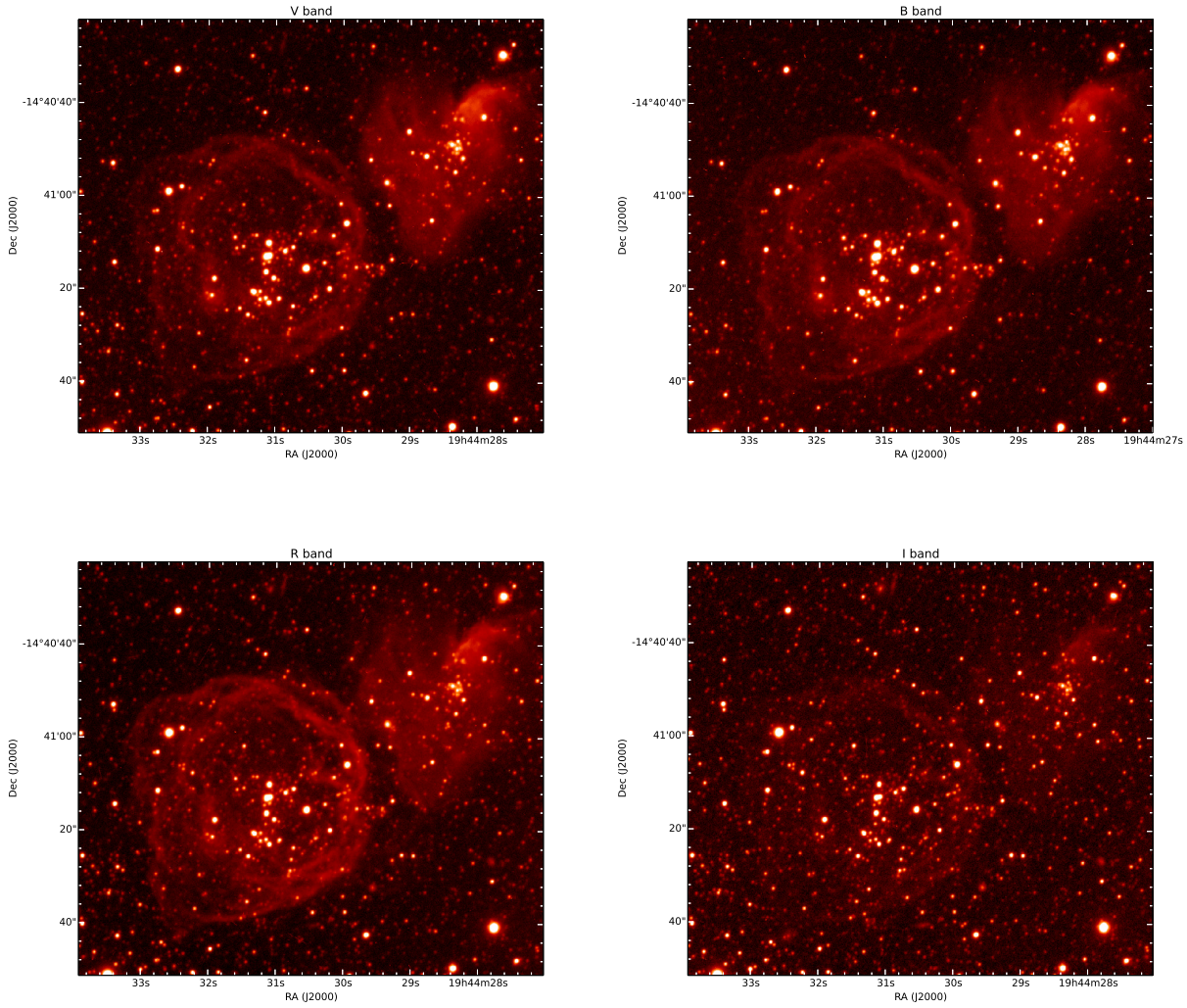

Figure 6.2: Images of Hubble III and Hubble I using the Bessel B, V, R, and CTIO-I filters obtained with the IMACS instrument at the 6.5m Baade Telescope in its wide-field imaging mode.

Some of the steps already perform in the analysis of the Hubble III datacube are listed below:

(i) Astrometry and wavelength calibration.

(ii) Obtaining aperture extractions and the corresponding stellar spectra for each of the stars in the datacube. Circular apertures are used as the optimal shape for recovering the spectrum

of each star. Due to the limited size of the objects and the relatively coarse sampling of the datacube it is necessary to account for fractional pixels to avoid flux losses. For that purpose, the images of the datacube have been extracted with a 2 Å separation. Then, the *daophot* routine inside the *IRAF* package is applied over the previous images to obtain the spectrum for each aperture. The majority of the stars are located in the central part of the H II region, making difficult to select the right position of the stars. To minimize this problem, we match each of the previous images with a high spatial resolution reference image. The *F170W* HST image from the WFPC2 camera is chosen for this purpose as it is the one that provides information at the bluest wavelengths where young, massive stars such as O and B stars are easy to identify. These stars are key to determine the star formation and the escape fraction of the H II region. Stellar spectra are essential to determine both the spectral type and the effective temperature of the stars. As a sanity check to assure the quality of the extracted spectra, the flux calibration of the datacube is verified by means of the available photometry in the literature and using photometry specifically obtained for this project. In particular, we have employed the *F170W* and *F255W* (UV range), the *F336W*, *F449W* and *F555W* (optical range) and *F814W* (NIR range) HST imaging bands and photometry from the Massey et al. (2007) optical catalog. B, V, R and I images taken from the 6.5m Baade Telescope specifically for this project were also used.

The codes of photoionization models are extremely sensitive to the input stellar Spectral Energy Distributions (SEDs) specially to their ionizing fractions. In our case, we are able to obtain the individual stellar spectrum instead of inferring it from stellar atmosphere models using an integrated spectrum for the whole region.

The next logical steps will be to derive the stellar parameters and the amount of dust attenuation from the photometry and the stellar spectra. For that purpose, the Chi-square cOde for parameteRized modeling and characterIZarion of phOtometry and Spectrophotometry code (CHORIZOS, Maíz-Apellániz 2004; Maíz Apellániz 2012) is going to be used. Then, the effective temperature and the spectral type of each star can be determined using the stellar models from TLUSTY. The effective temperature will be the initial input to find the gravity, dust and, finally, the amount of ionizing photons responsible for the escape fraction of the Hubble III region.

Finally, additional fundamental parameters of the ionized gas can be map such as the chemical abundance or extinction. In particular, the spatial distribution of the young massive stars is going to be compared with the ionized Hα emission maps.

6.3 Spatially-resolved SFR in galaxies at high redshift

The aim of this project is to perform a 2D multi-component decomposition over a large sample of galaxies at different cosmic epochs when galaxies were young and still assembling their masses. This will help to investigate the growth of young galaxies at high redshift where most of their mass was indeed assembled.

Gathering larger samples of galaxies over a broad range of stellar masses in the redshifted Hα line to trace the evolution of the SFR by components with redshift it is now achievable thanks to

the new generation of NIR instruments. Multi-IFU and multis-lit spectrographs, such as KMOS at ESO-VLT and MOSFIRE at Keck, respectively, are an excellent example. Ongoing surveys such as KMOS^{3D} survey (Wisnioski et al. 2015) are an excellent opportunity to achieve spatially resolved star formation. This survey employs the unique capabilities of the near-infrared multi-object spectrometer KMOS (K-band Multi-Object Spectrograph, Sharples et al. 2004, 2013), a second generation instrument for the VLT. It will observe over 600 star-forming galaxies creating a fairly representative sample of object in the redshift range from 0.7 to 2.7. The targets are drawn from the 3D-HST survey (Brammer et al. 2012; Skelton et al. 2014) and can be considered as a mass-selected sample with $M\star > 10^{9.5}$ $M\odot$.

The previous data will allow us to shed some light on the complex structures of intermediate-to-high redshift galaxies and they will help to solve some question such as, how is the behavior of the "Disk Star-Forming Main Sequence (SFMS)" presented in Section 4.5.2 (Chapter 4) at higher redshifts? Some studies have shown that rotation-dominated disk galaxies are the predominant objects that populated the main sequence at higher redshifts (Förster Schreiber et al. 2009; Genzel et al. 2014). Still important questions arise, which are the physical mechanisms that maintain galaxies on this SFMS? How is the balance between the physical mechanisms that sustain the star formation such as gas accretion and the processes that drive the star formation quenching (AGN)? How was the building up of the disks and what are they analogies with present-day disks? How was the connection between the onset of the clumpy structure and the development of the bulge component?

CHAPTER 7

Conclusions

It always seems impossible until it is done.
— Nelson Mandela

In this thesis, we present a comprehensive characterization of one of the most fundamental physical properties that define galaxies, its star formation rate. The main goal is to provide observational constraints on the general picture of galaxy assembly and evolution by means of analyzing the spatial distribution of the star formation within galaxies. A detailed study of this parameter is performed by treating galaxies as whole systems and, also, by analyzing the different structural components of galaxies, such as bulges, bars, and disks. Finally, we have been able to infer the corresponding star formation rate density values which are important observational constraints for models of galaxy formation and evolution. For that purpose, we make use of wide-field Integral Field Spectroscopy data in a large and well-defined sample of nearby galaxies.

We have first carried out a detailed study aim at accurately quantifying the star formation rate parameter in a statistically-significant sample of 272 local galaxies, using a set of panchromatic measurements including the UV continuum from GALEX, the Hα recombination emission line luminosity from CALIFA and IR luminosities (22 μm from WISE and TIR luminosities from WISE, IRAS and AKARI SED fitting). The fact that different selection criteria haven been used in the process of deriving the SFR tracers in the literature is believed to be the reason for some of the discrepancies found between them. Now, we have the opportunity to provide updated empirical SFR tracers anchoring the previous data to the Balmer decrement corrected Hα emission line from wide-field IFS. This study is described in detail in Chapter 3 and published in Catalán-Torrecilla et al. (2015). The main conclusions derived from this work can be summarized as follows.

- We present updated empirical prescriptions for measuring the SFRs of galaxies using single-band and composite multi-wavelength tracers.
- Hybrid calibrators provide more robust SFRs than the single-band tracers over the full range of SFRs ($0.03 - 20$ M$_\odot$ yr^{-1}), at least, the ones used along this work. The relatively large dispersions that arise from the use of single-band tracers (~ 0.28 dex) disappear if composite tracers are applied instead (~ 0.17 dex). In the particular case of the FUV single-band tracer, the dust attenuation correction is essential since attenuation can vary from zero to several magnitudes. This effect can be mitigated by combining the observed FUV and the 22 μm or TIR luminosities, i. e. using a composite tracer.

- We demonstrated the validity of the assumption of an energetic balance approach, which is the base of the hybrid calibrators. In that regard, linear combinations of observed luminosities without internal extinction corrections (Hα or UV) with the light reprocessed by dust (22 μm or TIR) provide accurate measurements of extinction-corrected Hα and SFRs. The best-fitting coefficients along with its uncertainty are provided below. The values of a_{IR} on the left are for purely star-forming galaxies while the values on the right are computed including also galaxies classified as type-2 AGN,

  - $\mathrm{SFR} = 5.5 \times 10^{-42}\ [\mathrm{L(H}\alpha)_{obs} + a_{IR} \times \mathrm{L(22}\,\mu\mathrm{m)}]$

    $a_{IR} = 0.018^{+0.018}_{-0.006}$; $a_{IR} = 0.015^{+0.018}_{-0.006}$

  - $\mathrm{SFR} = 5.5 \times 10^{-42}\ [\mathrm{L(H}\alpha)_{obs} + a_{IR} \times \mathrm{L(TIR)}]$

    $a_{IR} = 0.0019^{+0.0015}_{-0.0005}$; $a_{IR} = 0.0015^{+0.0016}_{-0.0006}$

  - $\mathrm{SFR} = 4.6 \times 10^{-44}\ [\mathrm{L(FUV)}_{obs} + a_{IR} \times \mathrm{L(22}\,\mu\mathrm{m)}]$

    $a_{IR} = 4.52^{+3.55}_{-1.14}$; $a_{IR} = 3.55^{+3.38}_{-0.95}$

  - $\mathrm{SFR} = 4.6 \times 10^{-44}\ [\mathrm{L(FUV)}_{obs} + a_{IR} \times \mathrm{L(TIR)}]$

    $a_{IR} = 0.40^{+0.33}_{-0.09}$; $a_{IR} = 0.33^{+0.29}_{-0.07}$

- The values of the a_{IR} coefficient (that weights the amount of energy produced by newly-born stars that is reprocessed by dust) are in agreement with the predictions from Kennicutt et al. (2009) for Hα and IR values and from Hao et al. (2011) for UV and IR measurements.
- For the first time, a set of hybrid calibrations for different morphological types and stellar masses is provided. These tracers are especially useful for samples with selection effect bias affecting the previous physical properties.
- The tight relations found between composite and extinction-corrected Hα tracers show that the main assumptions such as (1) the application of a Galactic foreground dust screen approximation to compute Balmer attenuations, and, (2) the energy balance approach method might play a secondary role.
- The large number of galaxies available in our sample allows exploring the origin of the variation of the a_{IR} coefficient in terms of the different galaxy properties listed below:
  - morphological type: a_{IR} presents a trend with the morphological type in the sense that star-forming galaxies of early-types (S0/a, Sa and Sab) have lower median values than

intermediate-type spirals (Sb and Sbc), and these, lower values than the most late-type spirals (Sc, Sd and Sm). The exclusion of type-2 AGN makes this trend less obvious, mainly because of a drastic increase in the median values of early-type spiral galaxies.

- stellar mass: most massive galaxies ($\log[M_\star/M_\odot] > 10.5$) have lower median values of a_{IR} than intermediate mass ($10 < \log[M_\star/M_\odot] < 10.5$). Low-mass galaxies ($\log[M_\star/M_\odot] < 10$) show the largest median value for a_{IR}.
- $g - r$ color: purely star-forming galaxies display a relatively flat trend for the variation of a_{IR} as a function of the g - r color. In contrast, type-2 AGN host galaxies (that tend to be redder than purely star-forming systems) show lower values of a_{IR} especially at colors g - $r > 0.6$ although with a large scatter.

- Although there is not a single physical property that can explain by itself the entire variation in a_{IR} from galaxy to galaxy, general conclusions can be drawn for the previous analysis, (a) galaxies hosting type-2 AGN tend to reduce the median values of a_{IR} probably due to the contribution of obscured AGN to the IR emission, and, (b) the fact that by removing these AGNs still early-type spiral galaxies and massive systems still show a somewhat smaller value of a_{IR} suggests an enhanced contribution of optical photons to the heating of the dust. The latter issue is related with the fact that massive, ionizing O stars which a lifetime typically less than 5 Myr in the case of Hα are the dominant stars that ionize the gas but stars older than this age can also contribute to the heating of the dust. The difference in the coefficient that weight the IR contribution on the composite calibrators is associated with the different stellar ages of the population that is contributing to the heating. We cannot completely discard the possibility that a fraction of the SFR is missed when using the extinction-corrected Hα luminosity, although the fact that does not show a particularly low value at high ionized-gas attenuations nor low axial ratios, suggests that obscured star formation is, comparatively, playing a minor role.

As a general remark, we can conclude that the composite tracers obtained in this work can be reliably applied to other galaxies that present similar properties of the ones used here. The applicability of these tracers to another type of galaxies is not a straightforward step. Objects in which the IR emission is not associated to regions of recent star formation do not obey the assumption of dust being heated by young stars producing high (unreliable) SFR values. We also highlight the improvements associated to the use of IFS data in the specific case of recovering a proper value of the Balmer Decrement corrected Hα luminosity. Thanks to that, we are able to recover the flux in galaxies with low equivalent width in emission (particularly important for the case of the Hβ line) where narrowband imaging is not feasible, we can also separate the contribution coming from Hα and the [NII] without assuming a particular ratio for [NII]/Hα, and, the stellar underlying continuum can be properly removed which is specially critical to recover the effects of the dust attenuation. Finally, the results derived from this study allows us to ensure that Hα (once it has been corrected by stellar absorption and dust attenuation) can be safely used since, in our sample of galaxies, the presence of highly-obscured systems where this tracer would fail, is negligible.

While integrated properties of galaxies are essential to have an in-depth understanding of the processes that govern star formation, the different components of galaxies provide valuable clues on the process of galaxy evolution. As commented in the Introduction of this thesis, one of the

questions we aim to solve is, *How do the different morphological components that shape galaxies contribute to the growth of this system?* For that purpose, we isolate the basic stellar structures of the galaxies by means of combining the 2D multi-component photometric decomposition of the CALIFA galaxies with IFS data. The complete study appears in Chapter 4 and it has been already submitted to the *ApJ* journal. The major conclusions concerning this study are summarized here:

- We corroborate the idea that bars produce an enhancement of the SFR in the central part of the galaxies supporting the idea that the amount of gas inflow that is driven to the center is highly influenced by the presence of bars.

- The tight correlation of the SFR and stellar masses, also known as Star-Forming Galaxies Main Sequence, is explored. The main finding is that not only more massive galaxies but also more massive disks have had their star formation more efficiently suppressed. We conclude that more massive star-forming disks and earlier-type spiral disks show a higher level of quenching.

- Nuclear activity is among the main mechanisms where we aim to identify whether or not it can play a dominant role in the previous quenching process. The variation of the sSFR as a function of galaxy mass is also analyzed for both bulges and disks, separately. The major findings are that the sSFR(bulge) decreases monotonically with stellar mass while the sSFR(disk) declines more rapidly beyond a certain stellar mass threshold, $M_\star > 10^{10.5}$ $M_\odot$. The decrease in the sSFR with the presence of a type-2 AGN indicates that these objects might be connected to the damping of the SFR, especially in the bulge component. The same behavior is observed among Sa/Sab and Sb/Sbc morphological types, the ones which allow a proper statistic to account for this effect. The term damping is used here to point out that although there is a mild shutdown of the star formation this does not necessarily imply a process that would move galaxies from the Blue Cloud to the Red Sequence. We highlight the necessity of having high spatial resolution to clearly probe the role of type-2 AGNs in damping the SFR. Due to the short timescale traced by the Hα emission line whether the AGN phase is cause, consequence or co-eval with the star formation damping process cannot be properly inferred.

- The Faber-Jackson relation is also analyzed for the bulge component. It shows that star-forming galaxies tend to display lower values of the bulge line-of-sight velocity dispersion compared to type-2 AGN host galaxies. This finding suggests the presence of a dynamical cooler stellar population in these bulges that are expected to host star formation processes more easily.

- The role that environment could have in regulating the star formation is analyzed by means of the project galaxy density, Σ_5. Galaxies located at intermediate- and high-density environments present lower values of their SFR in both the bulge and disk components.

The study of the SFR in the resolved structures of galaxies provides clues about their efficiency at forming new stars. The results derived from this work are used to construct the Hα Luminosity Functions of the galaxies as a whole and also for the different galaxy components. Luminosity Functions provide valuable constrains to the models of galaxy formation and evolution, thus, its

study is utterly important. From its analysis, we have been able to derive the values of the SFR density as described in detail in Chapter 5. The main conclusions of this work are the following:

- The classical V_{max} method is used to determine the Hα LFs for entire galaxies and for its different components. Then, we have been able to recover the Schechter parameters that best fit our Hα LFs doing 2000 random realizations of each point of the LF (obtained from the V_{max} method) assuming that the error of the different bins are independent. Due to the incompleteness at the lower luminosity range, the faint-end slope is fixed to $\alpha = -1.2$. The values of $\phi^\star$ [Mpc^{-3}] and $L^\star$ [erg s^{-1}] for entire galaxies and its components are:

  - Entire galaxies: $\phi^\star = (1.83 \pm 0.10) \times 10^{-3}$ and $L^\star = (3.98 \pm 0.17) \times 10^{41}$
  - Disks + bars: $\phi^\star = (2.10 \pm 0.12) \times 10^{-3}$ and $L^\star = (3.08 \pm 0.12) \times 10^{41}$
  - Disks: $\phi^\star = (1.73 \pm 0.10) \times 10^{-3}$ and $L^\star = (3.09 \pm 0.12) \times 10^{41}$
  - Bulges: $\phi^\star = (6.01 \pm 0.60) \times 10^{-4}$ and $L^\star = (6.97 \pm 1.37) \times 10^{40}$

- The values of the ρ_{SFR} [M$_\odot$ yr^{-1} Mpc^{-3}] have been obtained through the distribution of the product $\phi^\star \times L^\star$ multiplied by the Γ function and are the following:

  - Entire galaxies: $(4.64 \pm 0.15) \times 10^{-3}$
  - Disks + bars: $(4.12 \pm 0.15) \times 10^{-3}$
  - Disks: $(3.41 \pm 0.11) \times 10^{-3}$
  - Bulges: $(2.64 \pm 0.23) \times 10^{-4}$

  The comparison of our results for entire galaxies with the ones derived from other surveys with similar redshift and Hα luminosity ranges in terms of the parameters of the LF and the values of the ρ_{SFR} show a reasonable agreement. This study highlight the importance of treating galaxies and its principal morphological components separately to determine its relative contribution to the total ρ_{SFR}.

7.1 Concluding remarks

The Local Universe constitutes an excellent laboratory to measure fundamental properties of galaxies. In particular, the galaxies used along this work cover a broad range of galaxy morphologies and physical properties. We have addressed how the star formation rate variations reveal important information about galaxy formation processes. Thus, this thesis is intended to provide a local benchmark for future distant galaxies studies at analyzing the spatial distribution of the star formation within galaxies that only a multi-component photometric decomposition analyses can provide. The SFR measurements data set generated along this thesis are among the main CALIFA science data-products delivered to the community and are publicly accessible through the CALIFA website[1].

[1] http://califa.caha.es/?q=content/science-dataproducts

We have demonstrated that IFS data provide unique information to perform a detailed study of extended nearby galaxies. In that sense, this thesis aims to provide the foundations needed to understand the star formation processes that govern galaxies on galactic scales and over the different morphological components that constitute them. The future looks promising thanks to the advent of new generation IFS instruments that will provide access to a large number of galaxies covering different environments opening up an era of new possibilities.

APPENDIX A

List of publications and research stays

A.1 List of publications and research stays

This Appendix provides a brief overview of the main articles derived in the context of this thesis and the temporary stays carried out to complement the research experience. Articles in refereed journals as well as non-refereed conference contributions are listed below.

A.1.1 Articles in refereed journals (First author)

- " Star formation in the local Universe from the CALIFA sample. I. Calibrating the SFR using integral field spectroscopy data "
  Catalán-Torrecilla, C.; Gil de Paz, A.; Castillo-Morales, A.; Iglesias-Páramo, J.; Sánchez, S. F.; Kennicutt, R. C.; Pérez-González, P. G.; Marino, R. A.; Walcher, C. J.; Husemann, B.; García-Benito, R.; Mast, D.; González Delgado, R. M.; Muñoz-Mateos, J. C.; Bland-Hawthorn, J.; Bomans, D. J.; Del Olmo, A.; Galbany, L.; Gomes, J. M.; Kehrig, C.; López-Sánchez, Á. R.; Mendoza, M. A.; Monreal-Ibero, A.; Pérez-Torres, M.; Sánchez-Blázquez, P.; Vílchez, J. M.
  Astronomy & Astrophysics, Volume 584, id. A87, 34 pp, 2015.

- " Star Formation in the Local Universe from the CALIFA Sample. II. Activation and Quenching Mechanisms in Bulges, Bars, and Disks "
  Catalán-Torrecilla, C.; Gil de Paz, A.; Castillo-Morales, A.; Méndez-Abreu, J.; Falcón-Barroso, J.; Bekeraite, S.; Costantin, L.; de Lorenzo-Cáceres, A.; Florido, E.; García-Benito, R.; Husemann, B.; Iglesias-Páramo, J.; Kennicutt, R. C.; Mast, D.; Pascual, S.; Ruiz-Lara, T.; Sánchez-Menguiano, L.; Sánchez, S.F.; Walcher, C. J.; Duarte Puertas, S.; Marino, R. A.; Masegosa, J.; Sánchez-Blázquez, P.
  Submitted to ApJ

A.1.2 Articles in refereed journals (Co-author)

◇ " Two-dimensional multi-component photometric decomposition of CALIFA galaxies "
Méndez-Abreu, J.; Ruiz-Lara, T.; Sánchez-Menguiano, L.; de Lorenzo-Cáceres, A.; Costantin, L.; **Catalán-Torrecilla, C.** and 17 coauthors.
Astronomy & Astrophysics, Volume 598, id. A32, 18 pp, 2017.

◇ " Space density distribution of galaxies in the absolute magnitude - rotation velocity plane: a volume-complete Tully-Fisher relation from CALIFA stellar kinematics "
Bekeraité, S.; Walcher, C. J.; Falcón-Barroso, J.; García Lorenzo, B.; Lyubenova, M.; Sánchez, S. F.; Spekkens, K.; van de Ven, G.; Wisotzki, L.; Ziegler, B.; Aguerri, J. A. L.; Barrera-Ballesteros, J.; Bland-Hawthorn, J.; **Catalán-Torrecilla, C.**; García-Benito, R.
Astronomy & Astrophysics, Volume 593, id. A114, 16 pp, 2016.

◇ " Aperture Effects on the Oxygen Abundance Determinations from CALIFA Data "
Iglesias-Páramo, J.; Vílchez, J. M.; Rosales-Ortega, F. F.; Sánchez, S. F.; Duarte Puertas, S.; Petropoulou, V.; Gil de Paz, A.; Galbany, L.; Mollá, M.; **Catalán-Torrecilla, C.**; and 16 coauthors.
The Astrophysical Journal, Volume 826, Issue 1, article id. 71, 26 pp., 2016.

◇ " Spectroscopic aperture biases in inside-out evolving early-type galaxies from CALIFA "
Gomes, J. M.; Papaderos, P.; Vílchez, J. M.; Kehrig, C.; Iglesias-Páramo, J.; Breda, I.; Lehnert, M. D.; Sánchez, S. F.; Ziegler, B.; Dos Reis, S. N.; Bland-Hawthorn, J.; Galbany, L.; Bomans, D. J.; Rosales-Ortega, F. F.; Walcher, C. J.; García-Benito, R.; Márquez, I.; Del Olmo, A.; Mollá, M.; Marino, R. A.; **Catalán-Torrecilla** and 2 coauthors.
Astronomy & Astrophysics, Volume 586, id.A22, 6 pp, 2016.

◇ " Spiral-like star-forming patterns in CALIFA early-type galaxies "
Gomes, J. M.; Papaderos, P.; Vílchez, J. M.; Kehrig, C.; Iglesias-Páramo, J.; Breda, I.; Lehnert, M. D.; Sánchez, S. F.; Ziegler, B.; Dos Reis, S. N.; Bland-Hawthorn, J.; Galbany, L.; Bomans, D. J.; Rosales-Ortega, F. F.; Walcher, C. J.; García-Benito, R.; Márquez, I.; Del Olmo, A.; Mollá, M.; Marino, R. A.; **Catalán-Torrecilla, C.** and 2 coauthors.
Astronomy & Astrophysics, Volume 585, id. A92, 6 pp, 2016.

◇ " Outer-disk reddening and gas-phase metallicities: The CALIFA connection "
Marino, R. A.; Gil de Paz, A.; Sánchez, S. F.; Sánchez-Blázquez, P.; Cardiel, N.; Castillo-Morales, A.; Pascual, S.; Vílchez, J.; Kehrig, C.; Mollá, M., Méndez-Abreu, J.; **Catalán-Torrecilla, C.**; and 17 coauthors.
Astronomy & Astrophysics, Volume 585, id. A47, 29 pp, 2016.

◇ " CALIFA, the Calar Alto Legacy Integral Field Area survey. III. Second public data release "

García-Benito, R.; Zibetti, S.; Sánchez, S. F.; Husemann, B.; de Amorim, A. L.; Castillo-Morales, A.; Cid Fernandes, R.; Ellis, S. C.; Falcón-Barroso, J.; Galbany, L.; Gil de Paz,

A.; González Delgado, R. M.; Lacerda, E. A. D.; López-Fernandez, R.; de Lorenzo-Cáceres, A.; Lyubenova, M.; Marino, R. A.; Mast, D.; Mendoza, M. A.; Pérez, E.; Vale Asari, N.; Aguerri, J. A. L.; Ascasibar, Y.; Bekeraité, S.; Bland-Hawthorn, J.; Barrera-Ballesteros, J. K.; Bomans, D. J.; Cano-Díaz, M.; **Catalán-Torrecilla, C.** and 46 coauthors.
Astronomy & Astrophysics, Volume 576, id.A135, 30 pp, 2015.

◇ " Stellar population gradients in galaxy discs from the CALIFA survey. The influence of bars "

Sánchez-Blázquez, P.; Rosales-Ortega, F. F.; Méndez-Abreu, J.; Pérez, I.; Sánchez, S. F.; Zibetti, S.; Aguerri, J. A. L.; Bland-Hawthorn, J.; **Catalán-Torrecilla, C.** and 21 coauthors.
Astronomy & Astrophysics, Volume 570, id. A6, 85 pp2014

◇ " CALIFA: a diameter-selected sample for an integral field spectroscopy galaxy survey "
Walcher, C. J.; Wisotzki, L.; Bekeraité, S.; Husemann, B.; Iglesias-Páramo, J.; Backsmann, N.; Barrera Ballesteros, J.; **Catalán-Torrecilla** and 43 coauthors.
Astronomy & Astrophysics, Volume 569, id. A1, 18 pp, 2014

◇ " The Mice at play in the CALIFA survey. A case study of a gas-rich major merger between first passage and coalescence "
Wild, V.; Rosales-Ortega, F.; Falcón-Barroso, J.; García-Benito, R.; Gallazzi, A.; González Delgado, R..; Bekeraité, S.; Pasquali, A.; Johansson, P. H.; García Lorenzo, B.; van de Ven, G.; Pawlik, M.; Peréz, E.; Monreal-Ibero., A.; Lyubenova, M.; Cid Fernandes, R.; Méndez-Abreu, J.; Barrera-Ballesteros, J.; Kehrig, C.; Iglesias-Páramo, J.; Bomans, D. J.; Márquez, I.; Johnson, B, D.; Kennicutt, R. C.; Husemann, B.; Mast, D.; Sánchez, S. F.; Walcher, C. J.; Alves, J.; Aguerri, A. L.; Alonso Herrero, A.; Bland-Hawthorn, J.; **Catalán-Torrecilla, C.** and 13 coauthors.
Astronomy & Astrophysics, Volume 567, id. A132, 21 pp, 2014.

◇ " Fossil group origins. IV. Characterization of the sample and observational properties of fossil systems "
Zarattini, S.; Barrena, R.; Girardi, M.; Castro-Rodriguez, N.; Boschin, W.; Aguerri, J. A. L.; Méndez-Abreu, J.; Sánchez-Janssen, R.; **Catalán-Torrecilla, C.**; and 9 coauthors.
Astronomy & Astrophysics, Volume 565, id. A116, 13 pp, 2014.

◇ " Aperture corrections for disk galaxy properties derived from the CALIFA survey. Balmer emission lines in spiral galaxies "
Iglesias-Páramo, J.; Vílchez, J. M.; Galbany, L.; Sánchez, S. F.; Rosales-Ortega, F. F.; Mast, D.; García-Benito, R.; Husemann, B.; Aguerri, J. A. L.; Alves, J.; Bekeraité, S.; Bland-Hawthorn, J.; **Catalán-Torrecilla, C.** and 28 coauthors.
Astronomy & Astrophysics, Volume 553, id. L7, 5 pp, 2013.

◇ " CALIFA, the Calar Alto Legacy Integral Field Area survey. II. First public data release "
Husemann, B.; Jahnke, K.; Sánchez, S. F.; Barrado, D.; Bekeraité, S.; Bomans, D. J.; Castillo-Morales, A.; **Catalán-Torrecilla, C.**; and 68 coauthors.
Astronomy & Astrophysics, Volume 549, id. A87, 25 pp, 2013.

A.1.3 Non-Refereed conferences contributions (First author only)

- "Spatially-resolved SFR in nearby disk galaxies using IFS data"
  Catalán-Torrecilla, C.; de Paz, A. Gil; Castillo-Morales, A.; Méndez-Abreu, J., Pascual, S.; Ruiz-Lara, T.; de Lorenzo-Cáceres, A.; Sánchez-Menguiano, L.
  Formation and Evolution of Galaxy Outskirts, Proceedings of the International Astronomical Union, IAU Symposium, Volume 321, pp. 273-273, 2017.

- "A comprehensive study of the spatially-resolved SFR in nearby disk galaxies using CALIFA IFS data"
  Catalán-Torrecilla, C.; de Paz, A. Gil; Castillo-Morales, A.; Méndez-Abreu, J.
  Highlights on Spanish Astrophysics IX, Proceedings of the XII Scientific Meeting of the Spanish Astronomical Society held on July 18-22, 2016, Bilbao (Spain), p.125-130, 2017.

- "SFR bulge-to-disk ratios from the CALIFA IFS nearby galaxies survey"
  Catalán-Torrecilla, C.; de Paz, A. Gil; Castillo-Morales, A.; Méndez-Abreu, J.; Iglesias-Páramo, J.; Madore, B. F.; Pascual, S.; Ruiz-Lara, T.; de Lorenzo-Cáceres, A.; Sánchez-Menguiano, L.; Sánchez, S.
  From Interstellar Clouds to Star-Forming Galaxies: Universal Processes? Hawaii, (03/08/2015-07/08/2015). Proceedings of the International Astronomical Union, IAU Symposium, Volume 315, article id. E11, 2016.

- "Star Formation in the Local Universe from the CALIFA sample: calibration and contribution of disks to the SFR density"
  Catalán-Torrecilla, C.; Gil de Paz, A.; Castillo-Morales, Á.; Iglesias-Páramo, J.; Sánchez, S. F.
  Galaxies in 3D across the Universe, (07/07/2014-11/07/2014), Vienna (Austria). Proceedings of the International Astronomical Union, IAU Symposium, Volume 309, pp. 305-305, 2015.

- "Star Formation Rates in the Local Universe from CALIFA Integral Field Spectroscopy"
  Catalán-Torrecilla, C.; Gil de Paz, A.; Castillo-Morales, Á.; Iglesias-Páramo, J.; Sánchez, S. F.
  Oral presentation at the congress: Gas, Dust and Star-Formation in Galaxies from the Local to Far Universe, Crete, (25/05/15 - 29/05/15) Session: Measurements of the star-formation rates: consistency of IR, UV, Hα, and radio SFR estimates, accuracy of these tracers

- "Star formation rate at multiple physical scales using CALIFA and TYPHOON data"
  Catalán-Torrecilla, C.; Gil de Paz, A.; Castillo-Morales, A.; Iglesias-Páramo, J.; Sánchez, S. F.; Madore, B. F.; Sturch, L.
  Highlights of Spanish Astrophysics VIII, Proceedings of the XI Scientific Meeting of the Spanish Astronomical Society, 2014.

◇ " Contribution of the Disks to the SFR in the Local Universe using Integral Field Spectroscopy from CALIFA "
Catalán-Torrecilla, C.; Gil de Paz, A.; Castillo-Morales, Á..; Iglesias-Páramo, J.
Structure and Dynamics of Disk Galaxies. Proceedings of the Conference held 12-16 August, 2013 at the Winthrop Rockefeller Institute, Petit Jean Mountain, Arkansas, USA. ASP Conference Series, Vol. 480, 2014, p.231, 2014.

◇ " Comparison between different tracers of SFR in the CALIFA sample "
Catalán-Torrecilla, C.; Gil de Paz, A.; Castillo-Morales, Á.; Iglesias-Páramo, J.; Alonso-Herrero, A.
Highlights of Spanish Astrophysics VII, Proceedings of the X Scientific Meeting of the Spanish Astronomical Society (SEA) held in Valencia, July 9-13, 2012, pp.435-435, 2013.

A.1.4 Research stays

◇ Host Institution: *The Carnegie Observatories* (Pasadena, California)
Supervisor: Dr. Barry Madore
Stay duration: 7 September - 5 December (2014)

◇ Host Institution: *The Carnegie Observatories* (Pasadena, California)
Supervisor: Dr. Barry Madore
Stay duration: 27 July - 23 October (2015)

This page was left intentionally blank.

APPENDIX B

UV byproducts

The following table shows the UV byproducts created as described in Chapter 2. They have been used to derive extinction-corrected UV SFRs (see Chapter 3 for more details).

ID	name	a_{last} [arcsec]	b_{last} [arcsec]	PA [deg]	FUV [AB mag]	Δ FUV [AB mag]	NUV [AB mag]	Δ NUV [AB mag]
1	IC 5376	84.0	12.6	4.0	17.94	0.11	17.32	0.05
2	UGC 00005	54.0	27.0	45.0	16.71	0.06	16.21	0.03
3	NGC 7819	66.0	52.8	0.0	...	...	15.64	0.03
5	IC 1528	84.0	42.0	70.0	15.46	0.03	15.21	0.02
6	NGC 7824	42.0	31.5	-35.0	18.05	0.09	17.44	0.05
7	UGC 00036	42.0	19.4	18.0	18.14	0.09	17.55	0.04
9	NGC 0023	90.0	60.0	8.0	15.90	0.02	15.13	0.01
10	NGC 0036	96.0	61.1	21.0	16.12	0.04	15.65	0.02
11	UGC 00139	84.0	40.0	82.0	15.41	0.04	15.19	0.02
13	MCG-02-02-030	78.0	32.8	0.0	16.45	0.03	15.97	0.02
14	UGC 00312	60.0	30.0	7.0	15.29	0.01	14.99	0.01
15	ESO 539-G014	72.0	8.5	0.0	18.02	0.09	17.44	0.04
16	MCG-02-02-040	60.0	17.2	50.0	16.78	0.04	16.31	0.02
17	UGC 00335NED02	48.0	36.0	-10.0	...	...	18.49	0.15
18	NGC 0155	6.0	4.6	0.0	21.57	0.45	19.20	0.10
20	NGC 0160	84.0	47.6	45.0	17.09	0.03	16.57	0.04
21	NGC 0165	54.0	38.6	14.0	16.87	0.06	16.29	0.03
22	NGC 0169	114.0	30.7	88.0	18.16	0.07	17.46	0.06
24	NGC 0177	96.0	21.8	9.0	16.66	0.04	16.30	0.02
25	NGC 0180	102.0	80.8	-20.0	15.69	0.02	15.09	0.05
26	NGC 0192	84.0	39.8	-13.0	17.54	0.03	16.52	0.02
27	NGC 0216	90.0	31.5	27.0	15.47	0.03	15.14	0.02
28	NGC 0214	78.0	57.5	35.0	15.30	0.03	14.84	0.02
29	NGC 0217	60.0	13.9	-65.0	18.07	0.09	17.12	0.03
30	NGC 0237	72.0	40.5	-5.0	15.94	0.04	15.42	0.02
31	NGC 0234	54.0	54.0	0.0	15.54	0.03	14.99	0.02
32	MCG-02-03-015	54.0	15.9	20.0	17.22	0.06	16.75	0.03
33	NGC 0257	78.0	53.4	-75.0	15.89	0.05	15.21	0.02
34	NGC 0309	132.0	110.0	0.0	14.51	0.01	14.16	0.01
35	NGC 0364	30.0	27.9	30.0	20.24	0.08	18.78	0.03
36	NGC 0429	42.0	9.0	19.0	21.99	1.33	19.39	0.18
37	IC 1652	48.0	13.1	-11.0	...	...	18.54	0.12
39	NGC 0444	66.0	13.9	-23.0	17.19	0.07	16.58	0.03
40	UGC 00809	66.0	10.2	23.0	17.58	0.10	17.18	0.05
41	UGC 00841	48.0	9.6	54.0	18.25	0.16	17.47	0.06
42	NGC 0477	78.0	42.5	-45.0	15.95	0.05	15.53	0.03

ID	name	a_{last} [arcsec]	b_{last} [arcsec]	PA [deg]	FUV [AB mag]	Δ FUV [AB mag]	NUV [AB mag]	Δ NUV [AB mag]
43	IC 1683	36.0	16.6	-3.0	18.81	0.17	17.62	0.04
44	NGC 0499	72.0	58.5	82.0	17.89	0.15	17.26	0.06
45	NGC 0496	72.0	40.5	28.0	16.31	0.02	15.84	0.01
46	NGC 0504	72.0	21.2	47.0	...	...	18.75	0.06
47	NGC 0517	30.0	15.0	20.0	20.60	0.13	18.65	0.02
48	NGC 0523	102.0	28.6	-72.0	16.98	0.07	16.14	0.04
49	UGC 00987	72.0	22.9	32.0	17.22	0.09	16.75	0.05
50	NGC 0528	60.0	38.8	55.0	...	...	18.74	0.20
51	NGC 0529	6.0	5.3	-20.0	20.92	0.44	18.72	0.06
53	UGC 01057	66.0	22.0	-27.0	16.67	0.02	16.37	0.01
54	NGC 0570	36.0	31.2	-5.0	18.35	0.08	17.51	0.04
55	UGC 01062	48.0	25.8	60.0	...	...	18.53	0.09
56	UGC 01110	90.0	18.0	-6.0	17.22	0.05	16.79	0.03
57	UGC 01123	36.0	11.1	71.0	18.93	0.15	17.99	0.06
58	IC 0159	60.0	34.3	45.0	15.94	0.01	15.54	0.01
59	UGC 01271	24.0	15.5	-85.0	20.56	0.16	19.20	0.05
62	UGC 01274	36.0	12.9	-72.0	...	...	19.44	0.07
63	NGC 0677	48.0	36.0	14.0	18.62	0.07	17.34	0.02
64	NGC 0693	90.0	42.8	-74.0	16.19	0.02	15.62	0.01
65	NGC 0716	72.0	25.4	57.0	16.51	0.02	16.01	0.01
66	UGC 01368	36.0	12.9	53.0	18.71	0.16	18.09	0.08
67	NGC 0731	36.0	36.0	0.0	19.40	0.18	17.73	0.04
68	NGC 0741	126.0	121.8	90.0	17.64	0.20	16.70	0.10
69	NGC 0755	150.0	57.3	45.0	14.66	0.01	14.39	0.01
70	IC 1755	60.0	12.8	-26.0	18.71	0.04	18.17	0.02
71	NGC 0768	72.0	33.9	30.0	16.32	0.03	15.89	0.02
72	NGC 0774	30.0	24.0	-15.0	18.78	0.05	18.05	0.02
73	NGC 0776	42.0	42.0	0.0	15.70	0.05	15.32	0.02
74	NGC 0781	42.0	8.4	13.0	20.71	0.43	18.39	0.07
75	NGC 0787	84.0	63.8	0.0	16.70	0.02	16.24	0.02
76	NGC 0810	42.0	32.1	25.0	19.31	0.20	18.35	0.08
77	NGC 0825	48.0	19.6	53.0	18.27	0.16	17.58	0.07
78	NGC 0833	66.0	30.8	75.0	18.53	0.11	17.15	0.04
79	IC 0210	96.0	25.1	51.0	16.59	0.03	16.01	0.02
80	NGC 0842	48.0	36.0	-35.0	19.49	0.07	18.03	0.02
81	UGC 01659	48.0	18.0	38.0	17.09	0.04	16.59	0.02
82	KUG 0210-078	72.0	55.1	-51.0	16.22	0.02	15.97	0.01
83	UGC 01749	36.0	9.8	-45.0	18.74	0.20	18.44	0.13
84	NGC 0873	60.0	48.7	0.0	15.35	0.02	14.71	0.01
85	NGC 0924	90.0	50.8	53.0	...	...	16.37	0.13
86	UGC 01918	24.0	12.0	-62.0	18.45	0.11	17.91	0.05
87	NGC 0932	42.0	35.4	0.0	16.88	0.11	16.36	0.05
90	NGC 0938	60.0	45.0	-80.0	...	...	17.70	0.17
91	NGC 0955	120.0	30.0	19.0	16.83	0.03	16.20	0.02
92	NGC 0962	42.0	29.4	-5.0	...	...	18.33	0.17
94	NGC 0976	66.0	52.8	0.0	15.40	0.04	14.94	0.02
95	NGC 0991	120.0	106.7	0.0	14.37	0.01	14.12	0.01
96	UGC 02099	30.0	12.5	-40.0	18.72	0.32	18.06	0.14
98	NGC 1026	54.0	48.6	0.0	...	...	17.68	0.09
99	NGC 1041	72.0	50.8	0.0	...	...	18.02	0.16
101	NGC 1060	24.0	17.7	75.0	18.67	0.13	17.53	0.04
102	NGC 1070	102.0	88.7	-5.0	15.51	0.08	14.95	0.02
103	UGC 02222	48.0	28.0	-75.0	...	...	18.61	0.26

ID	name	a_{last} [arcsec]	b_{last} [arcsec]	PA [deg]	FUV [AB mag]	Δ FUV [AB mag]	NUV [AB mag]	Δ NUV [AB mag]
104	UGC 02229	36.0	14.8	-5.0	20.02	0.10	18.74	0.03
105	UGC 02239	48.0	11.1	13.0	18.42	0.25	18.07	0.14
106	MCG-01-08-008	54.0	12.5	0.0	18.29	0.04	17.69	0.02
107	NGC 1094	66.0	39.6	88.0	16.07	0.01	15.60	0.01
108	NGC 1093	60.0	40.0	-80.0	16.28	0.08	15.97	0.04
109	UGC 02311	66.0	50.8	-60.0	16.29	0.02	15.88	0.01
110	UGC 02319	36.0	8.3	47.0	18.40	0.11	17.98	0.06
111	MCG-02-08-014	60.0	8.6	-85.0	18.97	0.05	18.48	0.03
112	NGC 1132	90.0	50.4	-40.0	18.67	0.46	17.55	0.20
114	NGC 1142	48.0	30.5	-50.0	16.50	0.01	15.94	0.01
115	UGC 02403	54.0	20.8	-25.0	17.87	0.03	17.24	0.01
118	UGC 02465	24.0	6.6	-36.0	...	...	19.07	0.28
119	NGC 1167	108.0	88.7	70.0	...	...	16.39	0.43
120	NGC 1194	60.0	33.4	-40.0	19.21	0.13	17.92	0.03
121	NGC 1211	90.0	77.1	30.0	16.81	0.04	16.26	0.04
122	MCG-01-09-006	54.0	16.6	10.0	17.17	0.02	16.67	0.01
123	IC 0307	72.0	33.9	73.0	17.65	0.03	17.02	0.01
124	UGC 02628	54.0	18.0	-53.0	17.39	0.02	16.88	0.01
125	UGC 02690	54.0	24.9	-37.0	16.09	0.01	15.72	0.01
126	NGC 1324	90.0	34.3	-30.0	16.63	0.04	16.06	0.04
128	NGC 1361	72.0	63.0	0.0	19.47	0.54	18.26	0.17
130	MCG-01-10-019	72.0	38.1	10.0	16.09	0.05	15.75	0.03
132	UGC 03038	42.0	10.5	35.0	...	...	17.72	0.14
133	UGC 03107	24.0	7.2	72.0	...	...	18.20	0.18
134	NGC 1645	90.0	39.2	70.0	16.60	0.16	16.19	0.12
139	NGC 1666	30.0	23.6	0.0	18.24	0.21	17.25	0.07
140	NGC 1667	60.0	46.7	0.0	14.99	0.03	14.40	0.01
144	IC 2101	54.0	13.5	-30.0	16.80	0.07	16.35	0.03
147	NGC 2253	66.0	48.4	-44.0	15.75	0.04	15.14	0.02
149	NGC 2347	60.0	43.3	-4.0	15.98	0.06	15.33	0.02
150	UGC 03899	48.0	13.1	46.0	16.63	0.04	16.23	0.02
152	UGC 03944	60.0	26.6	-50.0	16.14	0.03	15.78	0.02
153	UGC 03969	42.0	8.4	-45.0	18.85	0.14	18.28	0.06
154	UGC 03973	48.0	48.0	63.0	15.14	0.02	15.05	0.01
155	UGC 03995	90.0	39.6	85.0	16.17	0.01	15.70	0.01
156	NGC 2449	48.0	22.2	-43.0	17.51	0.07	16.72	0.03
157	UGC 04029	90.0	19.5	63.0	16.99	0.07	16.48	0.03
158	UGC 04054	78.0	23.4	-10.0	16.94	0.06	16.32	0.03
159	IC 0480	96.0	15.2	-8.0	18.13	0.03	17.27	0.01
160	NGC 2476	18.0	11.3	-49.0	20.41	0.28	18.48	0.06
165	UGC 04132	48.0	12.0	28.0	16.88	0.06	16.22	0.02
168	UGC 04136	36.0	7.7	-38.0	20.04	0.09	19.24	0.04
169	IC 0485	36.0	9.0	-27.0	18.92	0.13	18.23	0.06
171	NGC 2513	72.0	57.6	-10.0	18.25	0.12	17.38	0.10
172	UGC 04176	78.0	21.7	-68.0	16.60	0.02	16.24	0.01
174	UGC 04197	84.0	17.7	-47.0	18.57	0.03	17.78	0.01
176	UGC 04195	72.0	36.0	21.0	16.61	0.05	16.05	0.02
177	NGC 2522	36.0	10.8	32.0	19.39	0.05	18.61	0.02
179	NGC 2530	60.0	42.8	-10.0	15.82	0.01	15.34	0.01
180	UGC 04240	66.0	13.2	-3.0	18.81	0.04	18.29	0.02
181	UGC 04245	90.0	24.0	-70.0	17.11	0.02	16.56	0.01
195	NGC 2577	54.0	33.0	-75.0	18.76	0.21	17.54	0.04
196	UGC 04375	108.0	69.1	0.0	15.73	0.05	15.18	0.02

ID	name	a_{last} [arcsec]	b_{last} [arcsec]	PA [deg]	FUV [AB mag]	Δ FUV [AB mag]	NUV [AB mag]	Δ NUV [AB mag]
197	IC 2341	30.0	13.9	1.0	20.29	0.36	18.62	0.06
198	UGC 04386	54.0	14.2	21.0	18.70	0.12	17.76	0.04
200	UGC 04405	54.0	16.6	28.0	18.48	0.16	18.10	0.10
201	NGC 2592	24.0	19.8	45.0	18.67	0.13	17.84	0.05
202	UGC 04416	78.0	35.5	-15.0	16.17	0.04	15.71	0.03
203	NGC 2596	60.0	24.0	65.0	16.69	0.05	16.21	0.03
204	NGC 2595	138.0	103.5	45.0	15.30	0.01	14.86	0.02
205	UGC 04425	60.0	21.4	-50.0	...	...	17.03	0.01
206	NGC 2598	30.0	10.9	3.0	18.76	0.04	17.78	0.01
208	UGC 04461	72.0	21.2	43.0	16.34	0.01	15.94	0.01
210	UGC 04468	66.0	39.6	-15.0	...	...	18.69	0.08
211	UGC 04505	36.0	10.8	60.0	18.23	0.12	17.62	0.05
212	NGC 2620	84.0	21.0	-87.0	17.64	0.02	17.16	0.01
213	NGC 2623	144.0	54.0	40.0	16.97	0.04	16.28	0.03
214	UGC 04515	66.0	26.4	-5.0	17.23	0.02	16.77	0.01
215	UGC 04532	66.0	8.8	34.0	17.65	0.08	17.29	0.05
216	NGC 2638	30.0	10.6	72.0	19.15	0.13	18.18	0.05
217	UGC 04548	48.0	8.7	50.0	18.83	0.15	18.19	0.07
218	UGC 04550	84.0	19.1	4.0	17.27	0.05	16.60	0.03
219	NGC 2639	78.0	47.7	-40.0	17.06	0.02	15.98	0.01
220	UGC 04546	54.0	8.3	25.0	20.02	0.06	19.09	0.02
221	UGC 04551	84.0	29.4	-67.0	19.14	0.06	17.79	0.02
222	UGC 04559	132.0	20.6	50.0	17.39	0.03	16.90	0.02
223	IC 2393	30.0	22.5	20.0	19.75	0.25	18.59	0.09
224	UGC 04587	42.0	21.0	8.0	18.85	0.15	18.03	0.07
225	IC 2407	48.0	8.0	86.0	18.42	0.12	17.88	0.06
226	UGC 04659	72.0	21.2	-65.0	16.88	0.02	16.50	0.01
227	NGC 2692	54.0	20.8	-15.0	19.73	0.07	18.41	0.03
228	NGC 2693	96.0	66.4	-20.0	18.01	0.06	17.01	0.08
229	NGC 2710	90.0	45.0	-55.0	15.81	0.01	15.48	0.01
230	NGC 2719	72.0	42.3	-45.0	15.64	0.01	15.20	0.01
231	UGC 04722	126.0	22.2	30.0	15.77	0.02	15.55	0.01
232	NGC 2730	54.0	41.3	80.0	15.49	0.02	15.17	0.01
233	NGC 2735	126.0	42.0	-86.0	16.63	0.05	16.27	0.03
234	NGC 2738	60.0	25.7	55.0	16.14	0.01	15.61	0.01
235	UGC 04753	90.0	13.5	45.0	18.06	0.07	17.55	0.04
236	UGC 04773	66.0	22.0	67.0	18.90	0.05	18.16	0.02
237	IC 2434	48.0	22.4	13.0	17.41	0.09	16.96	0.04
238	NGC 2764	54.0	36.0	15.0	17.14	0.07	16.36	0.03
239	UGC 04800	72.0	22.5	-60.0	16.77	0.01	16.41	0.01
240	NGC 2742A	54.0	21.6	90.0	17.47	0.09	16.64	0.03
241	NGC 2769	24.0	5.6	-34.0	20.03	0.24	18.96	0.07
242	NGC 2776	132.0	118.8	0.0	14.14	0.02	13.76	0.01
243	NGC 2778	54.0	38.6	40.0	...	...	17.74	0.08
244	UGC 04845	72.0	27.0	-82.0	16.96	0.06	16.43	0.03
245	UGC 04851	36.0	26.2	-35.0	19.46	0.08	18.51	0.03
246	NGC 2783	90.0	64.3	-12.0	18.05	0.11	17.11	0.08
247	UGC 04869	84.0	22.1	35.0	18.53	0.11	17.55	0.05
248	NGC 2794	30.0	30.0	0.0	17.19	0.06	16.61	0.03
249	NGC 2795	36.0	25.7	-10.0	19.35	0.21	18.12	0.08
250	NGC 2796	48.0	30.5	80.0	19.80	0.26	18.57	0.09
252	UGC 04906	90.0	22.5	48.0	17.81	0.08	16.97	0.03
253	NGC 2800	42.0	27.0	15.0	20.10	0.39	18.41	0.07

ID	name	a_{last} [arcsec]	b_{last} [arcsec]	PA [deg]	FUV [AB mag]	Δ FUV [AB mag]	NUV [AB mag]	Δ NUV [AB mag]
254	UGC 04926	60.0	12.8	-26.0	17.95	0.02	17.48	0.01
255	CGCG151-054	42.0	29.4	-20.0	...	...	19.31	0.18
256	UGC 04938	42.0	10.5	-33.0	19.06	0.16	18.46	0.06
257	NGC 2826	66.0	13.2	-37.0	20.57	0.12	19.05	0.04
258	NGC 2832	102.0	84.3	-20.0	18.06	0.07	16.85	0.04
260	NGC 2805	276.0	210.3	-55.0	13.33	0.02	13.14	0.03
262	UGC 04970	48.0	6.0	-75.0	18.48	0.13	17.96	0.06
263	UGC 04982	42.0	11.5	4.0	16.74	0.05	16.32	0.02
264	NGC 2854	72.0	33.6	50.0	16.38	0.01	15.89	0.01
265	NGC 2860	48.0	20.6	-72.0	18.31	0.09	17.39	0.03
266	NGC 2872	90.0	77.1	22.0	17.78	0.11	16.57	0.04
267	NGC 2874	102.0	29.8	12.0	17.06	0.03	16.12	0.01
268	UGC 05020	90.0	17.1	79.0	17.01	0.02	16.58	0.01
269	NGC 2882	66.0	35.2	80.0	16.44	0.01	15.75	0.01
270	UGC 05048	66.0	16.5	11.0	16.71	0.04	16.35	0.02
271	NGC 2894	84.0	44.2	27.0	16.96	0.03	16.20	0.04
273	IC 2487	72.0	16.0	-16.0	17.18	0.05	16.51	0.02
274	IC 0540	42.0	11.2	-10.0	19.47	0.07	18.39	0.02
275	NGC 2906	54.0	34.7	75.0	15.99	0.05	15.38	0.02
276	NGC 2919	72.0	25.4	-21.0	16.04	0.01	15.54	0.01
277	NGC 2916	90.0	61.2	20.0	15.16	0.02	14.69	0.01
278	UGC 05108	54.0	33.2	-37.0	17.83	0.06	17.23	0.04
279	NGC 2918	42.0	30.0	65.0	...	...	18.31	0.07
280	UGC 05111	72.0	9.0	-60.0	19.06	0.26	18.27	0.11
281	UGC 05113	48.0	8.7	43.0	...	...	19.51	0.25
282	NGC 2927	100.0	100.0	-25.0	16.61	0.04		
283	NGC 2929	48.0	12.0	-36.0	16.40	0.03	16.00	0.02
284	NGC 2939	108.0	38.9	-26.0	16.08	0.04	15.56	0.02
285	NGC 2943	96.0	52.3	-50.0	18.94	0.28	17.67	0.12
286	NGC 2942	78.0	63.8	-15.0	15.49	0.02	15.17	0.01
289	UGC 05164	48.0	8.7	22.0	17.67	0.08	17.20	0.04
290	UGC 05157	72.0	16.9	18.0	16.64	0.04	16.20	0.02
291	NGC 2955	72.0	38.1	-18.0	16.13	0.03	15.67	0.02
294	NGC 2959	54.0	54.0	0.0	16.61	0.02	16.01	0.02
295	UGC 05215	54.0	30.3	23.0	16.19	0.04	15.77	0.02
296	IC 0565	72.0	8.5	50.0	18.25	0.03	17.89	0.02
297	UGC 05244	72.0	9.0	31.0	17.18	0.07	16.75	0.03
298	UGC 05267	42.0	5.3	44.0	20.51	0.46	18.89	0.08
299	NGC 3021	72.0	40.5	-70.0	15.25	0.02	14.72	0.01
300	UGC 05315	48.0	8.0	59.0	17.87	0.07	17.46	0.04
301	UGC 05320	72.0	32.0	-78.0	16.13	0.04	15.82	0.02
302	NGC 3053	72.0	36.0	-40.0	17.33	0.06	16.61	0.03
303	NGC 3043	66.0	23.3	84.0	16.01	0.04	15.56	0.02
304	NGC 3060	78.0	21.3	78.0	16.82	0.06	16.33	0.03
305	NGC 3070	36.0	36.0	0.0	...	...	17.81	0.08
306	UGC 05358	66.0	17.6	77.0	16.67	0.05	16.39	0.03
307	UGC 05359	60.0	20.0	-83.0	17.52	0.05	17.05	0.03
308	NGC 3075	72.0	29.7	-55.0	15.93	0.04	15.57	0.02
310	UGC 05391	96.0	34.9	-10.0	15.56	0.03	15.31	0.02
311	NGC 3106	78.0	78.0	0.0	16.70	0.06	16.30	0.05
312	NGC 3057	90.0	53.2	6.0	14.95	0.02	14.69	0.01
313	UGC 05481	24.0	8.0	-89.0	19.91	0.24	19.21	0.12
315	UGC 05499	120.0	25.7	42.0	16.51	0.05	16.13	0.03

ID	name	a_{last} [arcsec]	b_{last} [arcsec]	PA [deg]	FUV [AB mag]	Δ FUV [AB mag]	NUV [AB mag]	Δ NUV [AB mag]
318	NGC 3158	60.0	54.0		17.99	0.11	17.34	0.07
319	NGC 3160	54.0	10.3	-34.0	21.36	0.72	19.76	0.21
321	UGC 05529	60.0	12.8	21.0	17.48	0.09	16.87	0.04
322	NGC 3179	42.0	11.0	48.0	...	...	18.91	0.11
323	NGC 3182	54.0	45.0	-25.0	16.98	0.05	16.30	0.03
324	NGC 3209	48.0	40.6	80.0	18.87	0.14	18.06	0.07
325	UGC 05597	48.0	8.0	-12.0	18.11	0.07	17.43	0.03
327	UGC 05604	84.0	43.8	47.0	16.37	0.05	15.99	0.03
328	NGC 3230	30.0	14.3	-65.0	19.63	0.26	17.96	0.04
329	UGC 05642	84.0	13.3	-82.0	16.98	0.02	16.48	0.01
330	NGC 3237	48.0	48.0	0.0	18.42	0.12	17.71	0.07
332	NGC 3251	90.0	18.0	55.0	17.10	0.05	16.47	0.02
334	UGC 05695	54.0	20.8	-84.0	16.87	0.06	16.44	0.03
336	UGC 05713	54.0	15.9	5.0	18.31	0.08	17.92	0.05
337	UGC 05727	66.0	18.9	29.0	16.83	0.04	16.58	0.03
338	UGC 05760	60.0	17.2	1.0	17.25	0.07	16.68	0.04
339	NGC 3300	42.0	22.1	-7.0	19.60	0.38	17.96	0.08
340	NGC 3303	96.0	67.2	0.0	18.35	0.09	17.33	0.20
341	UGC 05771	30.0	22.0	60.0	19.08	0.14	18.28	0.07
342	NGC 3304	42.0	14.8	-22.0	18.17	0.09	17.60	0.05
343	NGC 3320	90.0	40.9	20.0	15.18	0.02	14.77	0.01
345	NGC 3334	30.0	27.3	0.0	...	...	18.37	0.08
347	NGC 3352	54.0	40.5	0.0	...	...	18.23	0.08
349	UGC 05859	36.0	22.1	25.0	18.95	0.11	18.20	0.04
350	NGC 3363	54.0	33.2	0.0	17.26	0.06	16.61	0.03
351	UGC 05894	48.0	25.6	-25.0	17.03	0.06	16.60	0.02
352	IC 0642	48.0	44.6	0.0	18.86	0.21	17.75	0.08
353	NGC 3381	84.0	79.8	0.0	14.91	0.02	14.48	0.01
354	UGC 05924	54.0	14.4	52.0	18.43	0.11	17.92	0.05
355	NGC 3395	90.0	51.4	50.0	13.63	0.01	13.33	0.01
356	UGC 05957	42.0	10.5	-58.0	18.43	0.13	17.73	0.04
357	NGC 3419A	78.0	8.7	-43.0	16.77	0.01	16.28	0.01
358	NGC 3426	30.0	21.8	0.0	18.50	0.16	17.60	0.06
359	NGC 3415	84.0	52.0	10.0	17.01	0.03	16.07	0.01
360	NGC 3406NED01	66.0	35.2	-80.0	...	...	17.99	0.08
361	UGC 05990	30.0	8.0	14.0	17.60	0.09	17.27	0.04
362	NGC 3440	102.0	38.9	48.0	15.66	0.01	15.31	0.02
363	NGC 3462	54.0	38.1	60.0	...	...	17.80	0.04
364	UGC 06036	42.0	7.9	-79.0	19.65	0.25	18.83	0.10
365	NGC 3468	42.0	26.3	8.0	19.67	0.26	18.64	0.12
366	UGC 06062	30.0	22.5	25.0	19.82	0.35	18.60	0.06
367	UGC 06063	66.0	8.8	65.0	18.35	0.10	17.77	0.06
369	NGC 3488	84.0	57.5	-5.0	15.60	0.01	15.26	0.02
370	UGC 06104	72.0	16.9	50.0	16.35	0.04	15.90	0.02
371	UGC 06106	48.0	20.6	-20.0	17.67	0.09	17.08	0.04
372	UGC 06136	84.0	22.1	8.0	16.80	0.05	16.31	0.03
373	UGC 06148	54.0	8.3	-4.0	18.92	0.11	18.39	0.06
375	NGC 3540	30.0	25.7	0.0	19.95	0.29	19.18	0.16
376	UGC 06199	54.0	12.5	-23.0	17.14	0.05	16.86	0.03
378	NGC 3547	72.0	36.0	7.0	15.27	0.01	14.79	0.01
379	NGC 3543	60.0	18.8	20.0	17.80	0.07	17.27	0.04
380	UGC 06219	42.0	8.4	85.0	19.59	0.19	18.39	0.08
381	IC 0674	72.0	29.7	-60.0	17.33	0.08	16.90	0.04

ID	name	a_{last} [arcsec]	b_{last} [arcsec]	PA [deg]	FUV [AB mag]	Δ FUV [AB mag]	NUV [AB mag]	Δ NUV [AB mag]
382	NGC 3561	54.0	27.0	5.0	19.36	0.25	18.13	0.07
383	UGC 06256	36.0	5.5	89.0	19.95	0.19	19.24	0.09
385	UGC 06273	54.0	10.2	29.0	18.87	0.14	18.23	0.07
386	UGC 06312	36.0	16.4	45.0	19.62	0.08	18.54	0.03
387	NGC 3615	60.0	38.6	40.0	...	...	17.96	0.07
388	NGC 3614	174.0	98.3	80.0	14.67	0.02	14.34	0.01
389	NGC 3610	84.0	71.6	0.0	18.29	0.07	16.00	0.01
391	NGC 3619	120.0	102.2	0.0	16.69	0.02	15.90	0.02
392	UGC 06336	48.0	7.4	-22.0	19.41	0.14	19.13	0.09
393	NGC 3625	90.0	27.0	-32.0	16.35	0.01	15.93	0.01
394	NGC 3629	96.0	66.8	30.0	14.64	0.01	14.29	0.01
396	CGCG126-035	48.0	14.4	10.0	18.13	0.11	17.81	0.06
397	UGC 06380	60.0	30.0	58.0	17.34	0.05	16.87	0.02
398	UGC 06383	60.0	10.0	59.0	17.28	0.06	16.72	0.03
399	NGC 3649	48.0	24.0	-40.0	...	...	17.41	0.02
400	NGC 3642	240.0	199.9	-75.0	13.75	0.02	13.60	0.02
401	IC 2763	54.0	8.3	-81.0	17.55	0.02	16.98	0.01
402	NGC 3648	30.0	18.5	75.0	19.20	0.17	18.23	0.07
403	NGC 3650	42.0	7.4	54.0	20.08	0.21	19.00	0.08
405	UGC 06397	60.0	9.0	0.0	19.40	0.23	18.49	0.05
406	NGC 3656	72.0	72.0	7.0	17.17	0.02	16.08	0.04
407	UGC 06414	90.0	5.3	51.0	...	...	19.16	0.13
408	NGC 3668	66.0	54.4	0.0	15.88	0.03	15.33	0.02
409	UGC 06433	48.0	30.5	79.0	15.85	0.02	15.58	0.01
410	NGC 3674	42.0	13.3	33.0	19.47	0.15	18.20	0.05
411	UGC 06455	54.0	21.6	83.0	17.80	0.07	17.31	0.04
412	NGC 3683	84.0	30.9	-52.0	16.72	0.04	15.97	0.02
413	NGC 3682	72.0	44.0	-85.0	16.29	0.04	15.59	0.02
414	NGC 3687	84.0	84.0	0.0	15.34	0.02	14.97	0.01
415	NGC 3697	102.0	35.5	-87.0	16.08	0.01	15.71	0.01
416	NGC 3683A	102.0	75.4	75.0	15.30	0.03	14.89	0.02
417	NGC 3712	96.0	33.9	-20.0	16.68	0.06	16.31	0.04
418	NGC 3752	48.0	19.8	-25.0	16.39	0.04	15.90	0.02
419	UGC 06526	72.0	18.0	90.0	16.56	0.04	16.07	0.01
420	NGC 3728	90.0	67.5	25.0	16.45	0.04	16.09	0.03
421	NGC 3725	48.0	36.0	-35.0	16.14	0.04	15.69	0.02
422	UGC 06545	36.0	10.8	-47.0	17.65	0.07	17.04	0.03
423	UGC 06588	36.0	13.9	-36.0	17.32	0.07	16.99	0.04
424	NGC 3762	60.0	15.8	-13.0	19.57	0.28	18.26	0.09
425	NGC 3772	48.0	26.2	16.0	18.86	0.05	17.94	0.02
426	NGC 3753	72.0	21.2	-60.0	18.94	0.17	17.80	0.07
427	UGC 06617	18.0	6.0	-22.0	20.52	0.23	19.53	0.10
428	NGC 3780	120.0	92.9	90.0	14.52	0.02	14.15	0.01
429	NGC 3786	66.0	39.0	72.0	16.52	0.05	15.85	0.02
432	NGC 3801	156.0	93.6	-60.0	17.79	0.15	16.54	0.09
433	NGC 3805	48.0	37.7	60.0	19.62	0.08	18.07	0.02
435	NGC 3809	42.0	33.6	0.0	18.20	0.10	17.49	0.05
437	NGC 3815	66.0	34.9	72.0	16.29	0.05	15.83	0.02
438	UGC 06653	66.0	17.6	11.0	18.21	0.02	17.47	0.01
439	NGC 3816	60.0	34.7	70.0	20.00	0.10	18.08	0.02
440	NGC 3825	30.0	23.1	-20.0	18.47	0.15	17.50	0.06
441	UGC 06677	30.0	5.0	-38.0	20.61	0.34	20.21	0.22
442	IC 2951	60.0	30.0	80.0	...	...	18.94	0.22

ID	name	a_{last} [arcsec]	b_{last} [arcsec]	PA [deg]	FUV [AB mag]	Δ FUV [AB mag]	NUV [AB mag]	Δ NUV [AB mag]
443	NGC 3832	78.0	56.3	14.0	15.75	0.04	15.27	0.02
444	UGC 06697	198.0	62.6	-50.0	14.95	0.01	14.76	0.01
445	NGC 3842	60.0	42.8	5.0	18.33	0.03	17.53	0.01
446	NGC 3853	18.0	10.6	-40.0	19.68	0.20	18.46	0.03
447	NGC 3862	54.0	54.0	0.0	18.16	0.14	17.40	0.11
448	NGC 3867	42.0	16.8	-7.0	19.65	0.25	18.77	0.12
449	NGC 3869	30.0	7.9	-45.0	20.58	0.64	18.58	0.09
451	NGC 3884	90.0	60.0	10.0	16.95	0.02	16.47	0.04
452	NGC 3883	132.0	105.6	0.0	15.81	0.02	15.42	0.03
455	NGC 3888	72.0	55.1	-60.0	15.05	0.01	14.57	0.01
456	NGC 3891	78.0	66.3	70.0	15.60	0.03	15.09	0.02
458	NGC 3897	78.0	78.0	0.0	15.80	0.04	15.40	0.03
459	UGC 06791	78.0	12.3	1.0	17.44	0.06	16.96	0.03
460	UGC 06794	54.0	15.9	80.0	16.43	0.04	16.02	0.02
466	NGC 3937	66.0	58.7	15.0	19.13	0.41	17.70	0.12
467	NGC 3944	42.0	33.0	25.0	...	...	18.17	0.10
468	NGC 3947	60.0	51.4	0.0	16.29	0.05	15.80	0.02
469	IC 2973	60.0	34.3	-55.0	15.94	0.04	15.58	0.02
470	NGC 3958	60.0	28.0	28.0	17.22	0.07	16.75	0.02
471	UGC 06891	66.0	15.5	-80.0	17.75	0.10	17.25	0.05
472	NGC 3968	108.0	76.0	10.0	15.42	0.03	14.90	0.02
473	UGC 06905	30.0	5.5	41.0	18.88	0.13	18.68	0.07
474	NGC 3987	90.0	16.4	58.0	17.98	0.09	17.26	0.05
475	NGC 3991	66.0	18.9	33.0	14.43	0.02	14.19	0.01
476	NGC 3994	54.0	24.9	10.0	15.76	0.04	15.27	0.02
477	NGC 3993	48.0	13.3	-39.0	17.27	0.06	16.80	0.03
478	NGC 3995	102.0	64.5	33.0	13.89	0.02	13.53	0.01
614	NGC 5056	72.0	42.3	0.0	15.37	0.02	15.12	0.01
616	NGC 5057	18.0	16.6	0.0	20.88	0.31	19.41	0.09
617	NGC 5081	96.0	34.9	-77.0	16.81	0.04	16.39	0.04
618	IC 0881	42.0	10.5	11.0	19.55	0.21	18.94	0.06
619	IC 4225	24.0	7.2	-47.0	...	...	20.00	0.16
620	NGC 5127	60.0	44.0	75.0	19.43	0.07	17.87	0.02
621	NGC 5125	66.0	50.5	-10.0	15.96	0.04	15.58	0.02
622	NGC 5129	54.0	44.5	10.0	19.01	0.27	17.79	0.09
623	UGC 08451	60.0	30.0	65.0	16.63	0.05	16.28	0.03
624	NGC 5157	54.0	37.4	0.0	17.46	0.07	17.09	0.04
625	UGC 08457	42.0	7.6	38.0	18.65	0.12	18.10	0.04
626	NGC 5169	102.0	39.9	-77.0	15.77	0.02	15.41	0.01
627	NGC 5166	60.0	10.4	67.0	19.93	0.24	18.44	0.07
628	IC 4263	90.0	22.5	-75.0	16.89	0.02	16.48	0.01
629	NGC 5165	54.0	25.2	-1.0	...	...	18.64	0.03
630	NGC 5205	138.0	77.6	10.0	15.64	0.03	15.28	0.02
631	NGC 5198	90.0	77.1	0.0	18.29	0.11	17.06	0.07
632	UGC 08498	114.0	40.7	3.0	16.91	0.06	16.42	0.03
633	NGC 5216	102.0	61.2	0.0	18.75	0.32	17.31	0.09
634	NGC 5218	78.0	41.0	-80.0	17.60	0.09	16.36	0.03
635	NGC 5207	66.0	34.9	-40.0	16.71	0.05	16.26	0.04
639	NGC 5223	48.0	41.6	0.0	18.79	0.16	17.93	0.07
641	NGC 5222NED01	60.0	41.2	11.0	18.49	0.16	17.86	0.09
642	UGC 08564	36.0	14.8	20.0	20.50	0.37	19.49	0.15
643	NGC 5233	30.0	13.6	80.0	19.32	0.16	18.77	0.09
644	NGC 5240	66.0	48.6	60.0	16.11	0.04	15.68	0.02

ID	name	a_{last} [arcsec]	b_{last} [arcsec]	PA [deg]	FUV [AB mag]	Δ FUV [AB mag]	NUV [AB mag]	Δ NUV [AB mag]
646	NGC 5250	42.0	37.8	0.0	...	...	18.36	0.10
647	UGC 08600	42.0	5.3	56.0	21.01	0.41	19.34	0.11
648	NGC 5249	36.0	26.4	-10.0	19.30	0.23	18.08	0.05
650	NGC 5263	72.0	18.0	26.0	16.61	0.04	16.14	0.02
651	NGC 5267	42.0	15.0	56.0	17.42	0.06	16.90	0.03
652	UGC 08662	60.0	9.2	74.0	17.47	0.05	17.06	0.03
653	NGC 5289	84.0	26.5	-80.0	16.58	0.03	16.22	0.02
654	NGC 5308	138.0	26.1	60.0	18.49	0.20	16.97	0.03
655	UGC 08726	90.0	16.4	-57.0	16.52	0.04	16.12	0.02
656	NGC 5305	48.0	35.2	30.0	17.21	0.06	16.80	0.04
657	UGC 08733	84.0	54.8	12.0	15.38	0.03	15.16	0.02
658	UGC 08739	72.0	15.2	-58.0	17.13	0.09	16.65	0.05
659	NGC 5320	132.0	66.0	18.0	15.03	0.02	14.69	0.02
660	NGC 5318NED01	60.0	36.0	-15.0	...	...	18.04	0.06
661	IC 4336	66.0	18.3	-22.0	17.72	0.05	17.14	0.03
662	NGC 5326	54.0	27.0	-43.0	18.96	0.11	17.42	0.03
663	IC 0944	66.0	24.8	-72.0	18.83	0.18	17.90	0.06
664	UGC 08778	42.0	7.6	-60.0	18.39	0.07	17.74	0.03
665	UGC 08781	54.0	27.0	-20.0	17.17	0.07	16.62	0.04
666	UGC 08794	42.0	14.0	68.0	18.65	0.15	17.99	0.07
667	NGC 5349	60.0	17.6	82.0	18.02	0.07	17.47	0.03
668	UGC 08806	72.0	33.6	80.0	16.81	0.04	16.37	0.02
669	NGC 5347	72.0	55.1	-50.0	16.01	0.04	15.58	0.02
670	NGC 5350	144.0	103.5	40.0	14.80	0.07	14.35	0.04
671	NGC 5353	90.0	45.0	-35.0	17.49	0.26	16.38	0.05
672	NGC 5376	72.0	44.6	70.0	16.14	0.03	15.49	0.01
673	NGC 5379	36.0	16.4	60.0	17.93	0.07	17.17	0.02
674	IC 0959	60.0	35.3	0.0	17.53	0.09	17.07	0.05
675	UGC 08858	54.0	24.9	53.0	17.48	0.06	16.84	0.03
676	NGC 5378	78.0	63.0	90.0	16.69	0.05	16.26	0.04
677	UGC 08873	60.0	12.0	30.0	17.35	0.06	17.07	0.02
678	UGC 08881	48.0	8.0	-17.0	17.39	0.06	17.01	0.03
679	NGC 5402	48.0	11.1	-13.0	17.08	0.05	16.64	0.02
680	NGC 5394	72.0	42.3	-10.0	16.82	0.01	16.05	0.01
681	UGC 08896	66.0	9.4	71.0	17.65	0.08	17.05	0.04
682	UGC 08902	48.0	16.0	-25.0	16.75	0.05	16.25	0.02
683	NGC 5401	66.0	13.2	81.0	...	...	18.68	0.13
684	NGC 5406	78.0	57.5	-60.0	15.87	0.03	15.47	0.02
685	NGC 5425	66.0	17.4	-53.0	16.16	0.03	15.77	0.02
686	NGC 5421NED02	84.0	35.4	-20.0	16.83	0.07	16.56	0.03
688	NGC 5439	60.0	22.5	9.0	...	...	16.81	0.03
690	NGC 5443	120.0	44.4	34.0	16.81	0.01	16.19	0.02
691	NGC 5417	60.0	24.0	-60.0	18.03	0.09	17.32	0.04
692	NGC 5433	72.0	18.0	3.0	16.75	0.05	16.24	0.03
693	UGC 08955	24.0	10.8	-5.0	...	...	18.33	0.10
694	UGC 08960	102.0	12.8	-5.0	18.90	0.17	18.20	0.07
696	NGC 5448	180.0	81.0	-65.0	15.23	0.01	14.78	0.02
697	UGC 08988	60.0	8.6	-6.0	18.27	0.12	17.80	0.04
698	NGC 5444	78.0	68.3	90.0	...	...	17.19	0.11
700	NGC 5445	48.0	22.4	27.0	...	...	18.77	0.16
701	NGC 5436	36.0	13.1	-54.0	20.15	0.31	19.32	0.15
702	UGC 08984	42.0	11.5	35.0	19.96	0.40	18.87	0.14
703	NGC 5473	72.0	53.2	-20.0	18.48	0.06	16.88	0.02

ID	name	a_{last} [arcsec]	b_{last} [arcsec]	PA [deg]	FUV [AB mag]	Δ FUV [AB mag]	NUV [AB mag]	Δ NUV [AB mag]
704	NGC 5454	24.0	16.4	-70.0	20.13	0.27	19.19	0.08
705	NGC 5475	78.0	19.5	-14.0	19.72	0.08	17.80	0.02
706	UGC 09014	48.0	8.7	63.0	20.24	0.08	19.16	0.03
708	NGC 5485	102.0	84.3	-10.0	18.11	0.10	16.63	0.05
709	NGC 5482	18.0	13.5	88.0	20.68	0.41	19.01	0.07
710	NGC 5490	102.0	85.0	5.0	...	...	17.23	0.12
711	UGC 09071	114.0	27.1	37.0	16.69	0.01	16.25	0.01
713	UGC 09080	54.0	8.3	42.0	17.42	0.04	16.96	0.02
714	UGC 09067	48.0	24.0	12.0	16.73	0.04	16.30	0.02
715	NGC 5520	72.0	39.6	66.0	15.55	0.03	15.03	0.01
717	UGC 09110	72.0	26.5	17.0	15.86	0.03	15.51	0.01
718	UGC 09113	72.0	17.1	58.0	17.85	0.12	17.36	0.04
719	NGC 5519	66.0	41.3	75.0	17.54	0.05	16.92	0.02
720	NGC 5522	72.0	15.2	50.0	17.20	0.08	16.39	0.02
721	UGC 09117	72.0	38.1	7.0	16.13	0.04	15.79	0.02
722	UGC 09121	42.0	21.0	-40.0	17.23	0.06	16.80	0.02
723	NGC 5525	30.0	19.3	23.0	19.35	0.19	18.29	0.06
724	NGC 5533	120.0	73.6	30.0	15.93	0.07	15.58	0.02
725	IC 0995	48.0	12.0	-33.0	16.68	0.04	16.29	0.02
726	NGC 5532	54.0	41.5	-55.0	18.57	0.02	17.54	0.01
727	NGC 5546	6.0	5.1	0.0	20.56	0.26	19.16	0.09
728	IC 0994	42.0	19.4	10.0	...	...	18.84	0.15
729	NGC 5557	84.0	70.7	-85.0	17.76	0.03	16.52	0.02
730	NGC 5549	66.0	33.0	-60.0	19.14	0.07	18.21	0.03
731	UGC 09165	66.0	30.5	54.0	18.40	0.01	17.71	0.01
732	NGC 5559	60.0	17.2	67.0	17.71	0.01	17.11	0.01
733	UGC 09182	72.0	17.3	-57.0	16.59	0.05	16.06	0.03
734	NGC 5580	66.0	66.0	0.0	18.92	0.31	17.48	0.11
735	UGC 09199	54.0	8.3	-52.0	18.76	0.14	18.14	0.07
736	NGC 5587	84.0	25.9	-18.0	16.81	0.06	16.22	0.03
737	NGC 5602	54.0	30.8	-14.0	...	...	17.80	0.07
738	NGC 5598	42.0	30.8	50.0	...	...	18.71	0.08
739	NGC 5611	54.0	24.9	63.0	...	...	17.82	0.07
740	NGC 5614	96.0	76.8	0.0	16.78	0.06	15.99	0.03
741	NGC 5616	60.0	25.0	-23.0	17.39	0.06	16.92	0.03
742	NGC 5610	60.0	21.0	-72.0	16.45	0.05	15.98	0.02
743	NGC 5622	66.0	38.8	90.0	16.28	0.04	15.81	0.02
744	NGC 5631	66.0	66.0	0.0	18.68	0.22	16.82	0.06
746	NGC 5623	72.0	49.5	17.0	...	...	17.68	0.09
747	UGC 09262	54.0	8.3	51.0	17.99	0.02	17.55	0.01
749	NGC 5630	84.0	26.7	-82.0	15.15	0.02	14.74	0.01
750	NGC 5635	78.0	37.3	65.0	16.67	0.08	16.17	0.04
752	NGC 5642	18.0	13.0	-50.0	19.58	0.21	18.50	0.04
753	NGC 5656	84.0	66.3	50.0	15.64	0.01	15.07	0.01
754	NGC 5657	84.0	35.4	-17.0	16.66	0.01	16.19	0.01
755	NGC 5659	54.0	13.5	43.0	17.91	0.13	17.08	0.06
756	NGC 5665	90.0	47.2	-35.0	15.22	0.02	14.57	0.01
757	NGC 5675	84.0	30.0	-43.0	17.49	0.06	16.65	0.02
758	NGC 5682	72.0	25.4	-53.0	16.56	0.01	16.07	0.01
759	NGC 5687	102.0	72.2	-75.0	...	...	17.15	0.05
760	NGC 5689	90.0	25.7	85.0	19.01	0.08	17.08	0.01
761	NGC 5684	66.0	57.2	-75.0	...	...	17.78	0.08
762	UGC 09401	48.0	22.4	85.0	17.30	0.10	16.87	0.04

ID	name	a_{last} [arcsec]	b_{last} [arcsec]	PA [deg]	FUV [AB mag]	Δ FUV [AB mag]	NUV [AB mag]	Δ NUV [AB mag]
763	NGC 5714	144.0	18.0	82.0	16.56	0.04	16.12	0.02
773	UGC 09518	6.0	4.8		20.73	0.24	19.50	0.09
774	UGC 09537	102.0	22.1	-40.0	17.15	0.05	16.71	0.02
775	UGC 09542	66.0	20.7	32.0	17.21	0.05	16.76	0.03
776	UGC 09539	42.0	7.6	67.0	...	...	19.07	0.16
777	NGC 5772	90.0	55.7	35.0	16.27	0.04	15.86	0.03
778	NGC 5784	78.0	73.9	0.0	17.55	0.09	16.74	0.04
779	UGC 09598	54.0	21.6	-56.0	17.23	0.05	16.82	0.03
780	NGC 5797	48.0	30.5	-70.0	19.80	0.28	17.34	0.04
781	IC 1079	66.0	38.8	80.0	...	...	18.14	0.11
782	UGC 09629	54.0	19.3	-28.0	19.14	0.20	18.42	0.10
783	UGC 09665	72.0	12.7	-38.0	17.04	0.05	16.55	0.02
784	NGC 5829	60.0	51.4	20.0	15.62	0.03	15.32	0.02
785	UGC 09711	48.0	8.0	-72.0	20.06	0.14	19.33	0.04
786	IC 4534	12.0	8.0	-20.0	21.23	0.60	19.95	0.18
787	NGC 5876	66.0	33.0	50.0	17.63	0.09	16.97	0.04
788	UGC 09759	60.0	12.0	51.0	18.51	0.12	17.86	0.05
789	NGC 5888	42.0	24.0	-22.0	17.63	0.08	16.99	0.02
790	UGC 09777	66.0	39.6	-30.0	16.67	0.04	16.21	0.02
791	NGC 5908	102.0	38.3	-26.0	17.39	0.07	16.54	0.03
792	UGC 09842	54.0	21.0	67.0	17.47	0.07	16.97	0.02
793	UGC 09849	72.0	16.9	82.0	17.02	0.02	16.71	0.01
794	NGC 5928	54.0	39.3	-75.0	19.12	0.25	18.02	0.08
795	NGC 5930	72.0	38.1	-17.0	17.05	0.05	16.16	0.02
796	NGC 5934	18.0	9.0	2.0	19.02	0.11	18.01	0.04
797	UGC 09873	60.0	12.8	-53.0	17.81	0.07	17.50	0.04
799	NGC 5951	144.0	33.0	5.0	15.60	0.02	15.12	0.01
800	UGC 09901	60.0	20.0	-2.0	17.42	0.02	17.01	0.01
801	NGC 5953	60.0	51.4	-11.0	16.69	0.02	15.49	0.01
802	ARP220	54.0	43.2	0.0	18.34	0.19	16.99	0.04
803	NGC 5957	120.0	111.5	0.0	14.96	0.01	14.60	0.01
804	NGC 5971	66.0	24.8	-44.0	17.16	0.04	16.80	0.02
805	UGC 09919	66.0	14.1	-9.0	17.53	0.06	17.02	0.03
806	NGC 5966	24.0	14.7	90.0	19.88	0.18	18.62	0.06
807	IC 4566	54.0	33.8	-15.0	17.71	0.09	17.08	0.04
808	UGC 09937	36.0	7.2	15.0	...	...	19.19	0.12
809	NGC 5987	138.0	42.8	50.0	17.85	0.12	16.82	0.07
810	NGC 5980	66.0	24.3	13.0	16.09	0.04	15.51	0.02
811	UGC 10043	90.0	15.0	-29.0	17.26	0.07	17.00	0.03
812	UGC 10042	66.0	8.8	-11.0	17.85	0.09	17.44	0.05
813	NGC 6004	54.0	48.3	-75.0	15.81	0.03	15.35	0.01
814	UGC 10097	54.0	45.7	-50.0	...	...	17.98	0.04
815	NGC 6020	6.0	4.3	-40.0	21.17	0.44	19.12	0.09
817	IC 1151	102.0	32.6	28.0	15.51	0.02	15.02	0.01
818	UGC 10123	42.0	11.5	57.0	18.23	0.08	17.73	0.03
819	NGC 6027	18.0	9.0	85.0	19.93	0.07	18.44	0.02
820	NGC 6032	54.0	27.0	0.0	17.63	0.15	16.81	0.04
821	NGC 6060	90.0	49.5	-75.0	15.80	0.05	15.30	0.02
822	UGC 10205	36.0	18.0	-45.0	18.82	0.17	17.81	0.05
823	NGC 6063	72.0	33.9	-21.0	16.08	0.03	15.66	0.02
824	IC 1199	54.0	20.8	-23.0	17.13	0.06	16.40	0.03
825	UGC 10257	72.0	15.2	-15.0	16.71	0.04	16.39	0.02
826	NGC 6081	30.0	10.0	-49.0	19.46	0.17	18.57	0.07

ID	name	a_{last} [arcsec]	b_{last} [arcsec]	PA [deg]	FUV [AB mag]	Δ FUV [AB mag]	NUV [AB mag]	Δ NUV [AB mag]
827	UGC 10297	54.0	7.7	1.0	17.35	0.08	16.70	0.02
828	UGC 10331	72.0	12.7	-38.0	16.45	0.03	16.11	0.01
829	NGC 6125	60.0	60.0	0.0	18.39	0.14	17.31	0.05
830	UGC 10337	48.0	16.0	66.0	17.68	0.08	17.30	0.05
831	NGC 6132	48.0	16.0	-53.0	16.72	0.05	16.10	0.02
837	UGC 10384	54.0	12.5	-89.0	17.37	0.07	16.85	0.03
843	UGC 10650	90.0	13.5	23.0	16.18	0.05	15.81	0.03
844	NGC 6278	36.0	21.6	-50.0	19.07	0.26	18.15	0.10
845	UGC 10693	72.0	48.0	-75.0	...	...	18.07	0.10
846	UGC 10695	42.0	32.1	-70.0	20.37	0.70	18.55	0.10
847	UGC 10710	54.0	14.4	-30.0	18.20	0.11	17.47	0.04
848	NGC 6310	90.0	18.0	68.0	17.24	0.06	16.76	0.03
849	NGC 6301	84.0	51.2	-65.0	15.96	0.04	15.57	0.02
850	NGC 6314	48.0	24.0	-5.0	...	...	17.81	0.09
851	NGC 6338	60.0	37.5	14.0	18.83	0.10	18.08	0.03
852	UGC 10796	72.0	54.0	19.0	16.28	0.01	15.97	0.01
853	NGC 6361	66.0	30.8	53.0	17.49	0.01	16.82	0.01
854	UGC 10811	72.0	22.5	-88.0	17.78	0.01	17.34	0.01
855	UGC 10799	48.0	4.4	84.0	19.15	0.20	18.44	0.09
856	IC 1256	54.0	37.1	-83.0	16.54	0.05	15.97	0.02
857	NGC 6394	54.0	16.6	41.0	18.30	0.01	17.61	0.01
858	UGC 10905	54.0	33.2	-10.0	...	...	18.03	0.09
859	NGC 6411	48.0	37.6	69.0	19.64	0.65	17.44	0.08
863	NGC 6497	48.0	24.0	-68.0	17.26	0.06	16.75	0.03
864	NGC 6515	60.0	37.5	10.0	...	...	18.35	0.13
865	UGC 11228	24.0	14.4	0.0	...	...	19.21	0.18
866	UGC 11262	42.0	16.8	48.0	17.65	0.10	17.14	0.05
867	NGC 6762	24.0	6.9	-62.0	20.33	0.39	18.85	0.09
868	MCG-02-51-004	54.0	20.8	-20.0	16.48	0.07	16.10	0.03
869	NGC 6941	90.0	63.0	-65.0	16.00	0.02	15.58	0.02
870	NGC 6945	72.0	40.5	-20.0	19.11	0.22	17.78	0.07
872	UGC 11649	72.0	50.8	85.0	16.51	0.09	16.03	0.08
873	UGC 11680NED01	72.0	46.8	-5.0	17.42	0.14	16.65	0.08
874	NGC 7025	84.0	57.5	33.0	17.61	0.25	16.78	0.11
875	UGC 11694	54.0	33.8	34.0	...	...	17.64	0.07
876	NGC 7047	42.0	24.5	-73.0	16.92	0.03	16.28	0.01
877	UGC 11717	60.0	21.4	35.0	...	...	17.47	0.07
878	MCG-01-54-016	72.0	11.1	30.0	16.80	0.01	16.41	0.01
880	UGC 11792	54.0	3.8	-20.0	19.10	0.28	18.40	0.12
881	NGC 7194	48.0	34.9	20.0	...	...	18.43	0.14
882	NGC 7236	24.0	24.0	0.0	20.47	0.09	19.03	0.02
883	NGC 7237	60.0	33.9	-40.0	19.78	0.09	18.29	0.02
885	UGC 12054	66.0	8.8	46.0	16.76	0.05	16.39	0.03
886	NGC 7311	54.0	27.0	10.0	16.51	0.06	15.85	0.03
887	NGC 7321	72.0	49.5	12.0	16.06	0.04	15.52	0.02
888	UGC 12127	6.0	6.0	0.0	20.37	0.26	19.17	0.11
889	NGC 7364	72.0	42.3	65.0	16.61	0.03	15.93	0.01
890	UGC 12185	66.0	35.2	-30.0	17.36	0.08	16.77	0.04
891	UGC 12224	72.0	65.2	0.0	15.74	0.03	15.35	0.03
892	VV488NED02	90.0	18.0	70.0	17.47	0.08	16.95	0.04
893	NGC 7436B	54.0	54.0	0.0	18.67	0.29	17.79	0.14
894	UGC 12274	54.0	20.8	-40.0	...	...	18.58	0.14
896	NGC 7466	54.0	18.0	26.0	17.56	0.06	16.87	0.03

ID	name	a_{last} [arcsec]	b_{last} [arcsec]	PA [deg]	FUV [AB mag]	Δ FUV [AB mag]	NUV [AB mag]	Δ NUV [AB mag]
897	UGC 12348	54.0	16.2	-42.0	18.52	0.04	17.40	0.01
898	NGC 7489	60.0	31.4	-10.0	15.84	0.09	15.11	0.03
899	NGC 7536	78.0	30.3	56.0	16.24	0.01	15.82	0.01
900	NGC 7550	48.0	41.1	0.0	19.16	0.08	17.59	0.01
901	NGC 7549	120.0	30.0	8.0	16.45	0.02	15.67	0.02
902	NGC 7563	54.0	28.4	-25.0	...	...	18.43	0.12
903	NGC 7562	66.0	45.0	83.0	18.82	0.33	17.25	0.10
904	NGC 7591	84.0	35.4	-35.0	16.61	0.07	15.88	0.03
905	UGC 12494	48.0	17.1	35.0	16.65	0.05	16.24	0.03
906	IC 5309	48.0	22.2	23.0	17.27	0.02	16.74	0.01
907	NGC 7608	60.0	16.0	20.0	18.19	0.04	17.53	0.02
908	NGC 7611	60.0	24.0	-41.0	19.00	0.09	17.65	0.03
909	UGC 12519	54.0	16.6	-22.0	16.80	0.04	16.40	0.02
910	UGC 12518	54.0	8.3	24.0	...	...	19.62	0.11
911	NGC 7619	102.0	93.8	30.0	17.78	0.12	16.36	0.06
912	NGC 7623	42.0	31.5	-5.0	19.77	0.13	18.21	0.04
913	NGC 7625	54.0	47.3	0.0	16.15	0.03	15.29	0.01
914	NGC 7631	66.0	25.7	79.0	16.69	0.02	16.17	0.01
915	NGC 7653	72.0	63.0	0.0	15.62	0.01	15.11	0.02
916	NGC 7671	30.0	17.1	-42.0	19.70	0.27	18.42	0.07
917	NGC 7683	78.0	41.0	-40.0	...	...	17.87	0.14
918	UGC 12633	54.0	36.0	-20.0	18.51	0.06	17.39	0.01
919	NGC 7684	72.0	20.6	21.0	20.08	0.02	18.25	0.01
920	NGC 7691	84.0	64.0	-5.0	15.51	0.03	15.17	0.02
921	UGC 12653	66.0	19.4	-77.0	17.03	0.05	16.46	0.03
922	UGC 12688	60.0	14.1	88.0	16.70	0.06	16.28	0.03
923	NGC 7711	90.0	40.5	80.0	...	...	17.60	0.06
924	NGC 7716	90.0	77.1	35.0	15.27	0.01	14.96	0.01
926	UGC 12723	24.0	8.0	77.0	18.40	0.08	18.16	0.04
927	NGC 7738	72.0	54.0	80.0	17.46	0.03	16.90	0.03
929	UGC 12810	60.0	30.0	52.0	16.63	0.01	16.18	0.01
930	UGC 12816	72.0	38.1	-33.0	16.17	0.03	15.87	0.02
932	NGC 7783NED01	54.0	24.9	-40.0	20.05	0.08	18.53	0.02
933	NGC 7787	78.0	21.7	-76.0	18.22	0.02	17.60	0.01
934	UGC 12857	96.0	21.3	34.0	16.77	0.01	16.34	0.01
935	UGC 12864	72.0	42.3	-70.0	16.28	0.04	15.92	0.02

Table B.1: (1) ID CALIFA identifier; (2) galaxy name; (3) & (4) major and minor axis radii, respectively, for the same common aperture. They correspond to the smaller of the last isophote for which the UV surface photometry can be properly computed in both bands (error < 0.8 mag/arcsec^2); (5) Position Angle that define the shape of the concentrical elliptical apertures used for the photometry (the RA and DEC coordinates that define the center of the galaxy are the ones provided by SDSS DR7); (6) & (8) FUV and NUV aperture magnitudes. The values are expressed in AB mag scale and are computed for the same common aperture. They are corrected for Milky Way attenuation assuming the following expressions between the attenuation in the different bands and the color excess, A(FUV) = 7.9×E(B-V) and A(NUV) = 8.0×E(B-V); (7) & (9) FUV and NUV magnitude errors. The errors in the aperture photometry are obtained after combining the photon noise and sky-subtraction uncertainty. A zero point error (common to all measurements) of 0.1mag commonly adopted for any GALEX measurement is not included in these numbers.

This page was left intentionally blank.

APPENDIX C

Two-dimensional decomposition of SFR in the CALIFA galaxies

In this appendix we provide the compilation of the 2D decomposition analysis of SFR in the CALIFA galaxies as described in Chapter 4.

Left panels in the following figures show the 2D g-band models derived from the multi-component photometric decomposition. Disk, bar, and bulge components are shown from top to bottom, respectively. Units for the flux are given relative to the central surface brightness of the bar component (if the bar is not present the central surface brightness of the disk component is used instead). Central surface brightness and the rest of the parameters needed to create these g-band models are provided in Méndez-Abreu et al. (2017).

Middle panels show the distribution of the continuum-subtracted Hα luminosity in the different stellar galaxy components. To create these Hα maps, the original CALIFA datacubes have been multiplied by the corresponding weight maps in each morphological component, i. e., there is a weighted-datacube for each galaxy component, and then, analyzed spaxel by spaxel.

Finally, the right panels present the integrated spectrum extracted for the weighted-datacube for each galaxy structure (bulge, bar, and disk) is shown in black. Gray-colored vertical ranges correspond to the emission lines and sky lines masked out during the fitting procedure. The red spectrum corresponds to the best fit for the underlying stellar population. The emission-line spectrum originated by the ionized gas is shown in blue. The latest is the one used to measure the Hα and Hβ fluxes associated to each component.

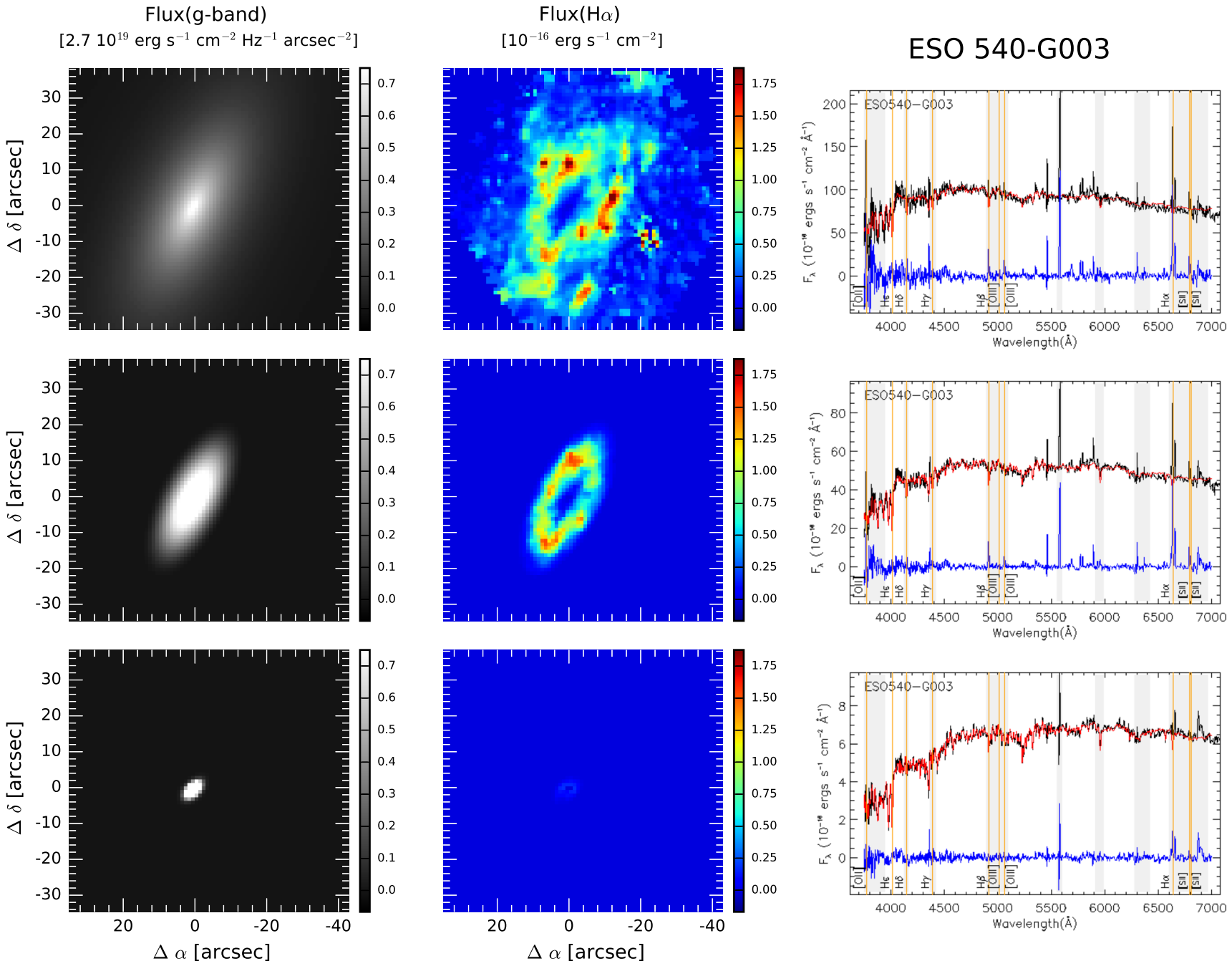
Flux(g-band)
[2.7 10^19 erg s^-1 cm^-2 Hz^-1 arcsec^-2]
Flux(Hα)
[10^-16 erg s^-1 cm^-2]
ESO 540-G003
Δ δ [arcsec]
Δ α [arcsec]
Wavelength(Å)
ESO540−G003

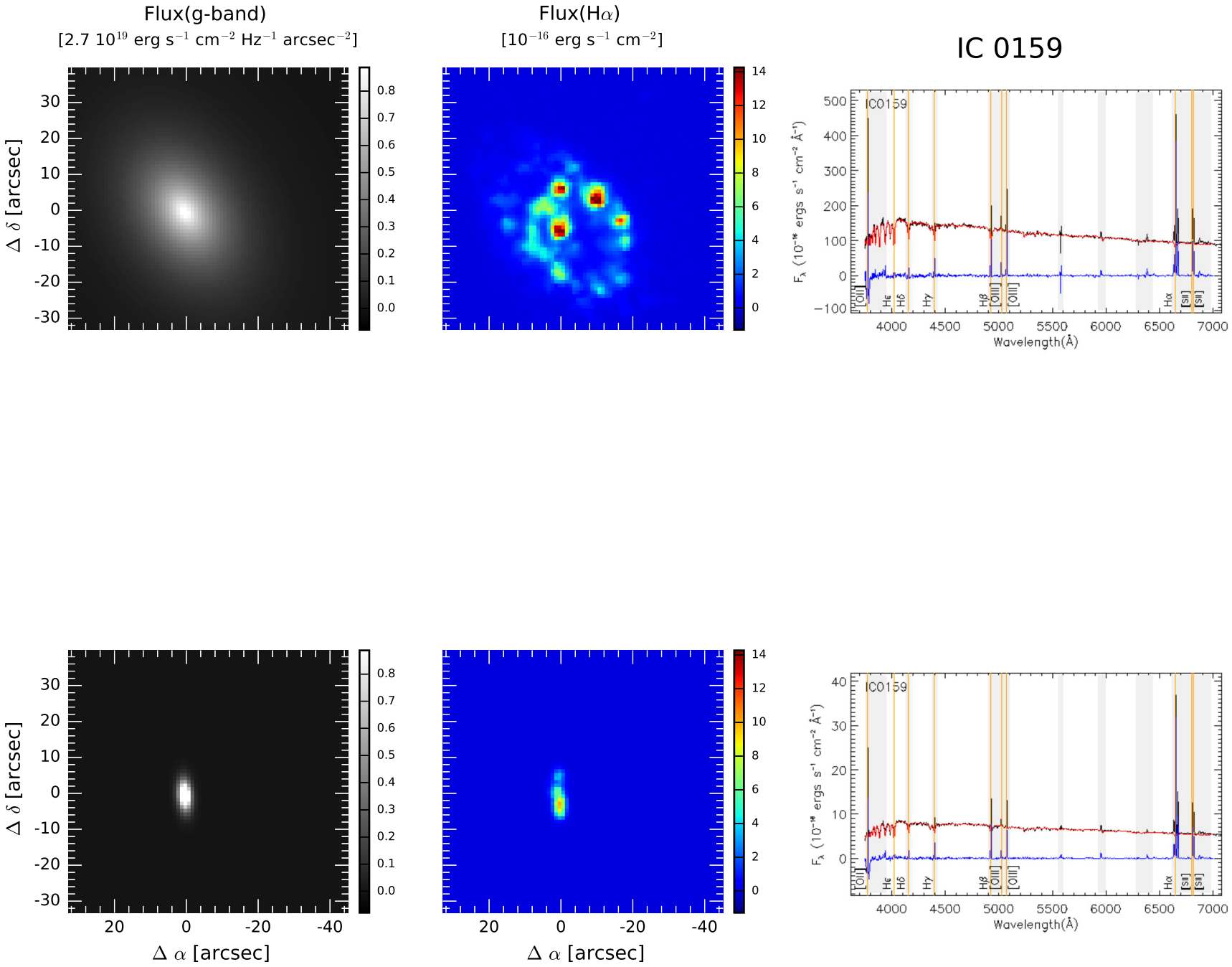
Flux(g-band)
[2.7 10^19 erg s^-1 cm^-2 Hz^-1 arcsec^-2]
Flux(Hα)
[10^-16 erg s^-1 cm^-2]
IC 0159
Δ δ [arcsec]
Δ α [arcsec]
IC0159
Wavelength(Å)
[OII]
Hε
Hδ
Hγ
Hβ
[OIII]
[OIII]
Hα
[SII]
[SII]

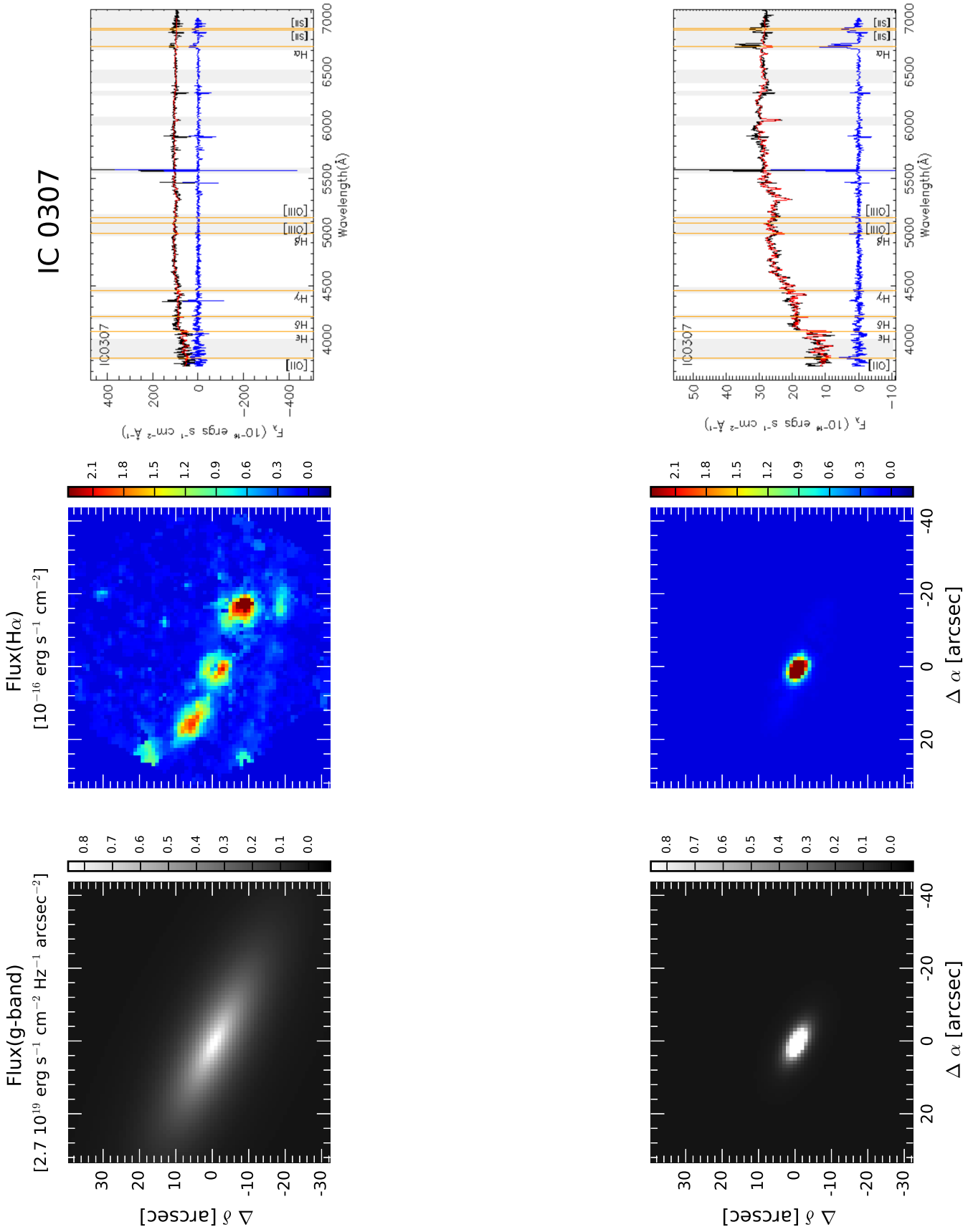
IC 0307
Flux(g-band)
[2.7 10^19 erg s^-1 cm^-2 Hz^-1 arcsec^-2]
Flux(Hα)
[10^-16 erg s^-1 cm^-2]
Δ δ [arcsec]
Δ α [arcsec]
Wavelength(Å)
F_λ (10^-16 ergs s^-1 cm^-2 Å^-1)
[OII]
Hε
Hδ
Hγ
Hβ
[OIII]
[OIII]
[SII]
[SII]
Hα

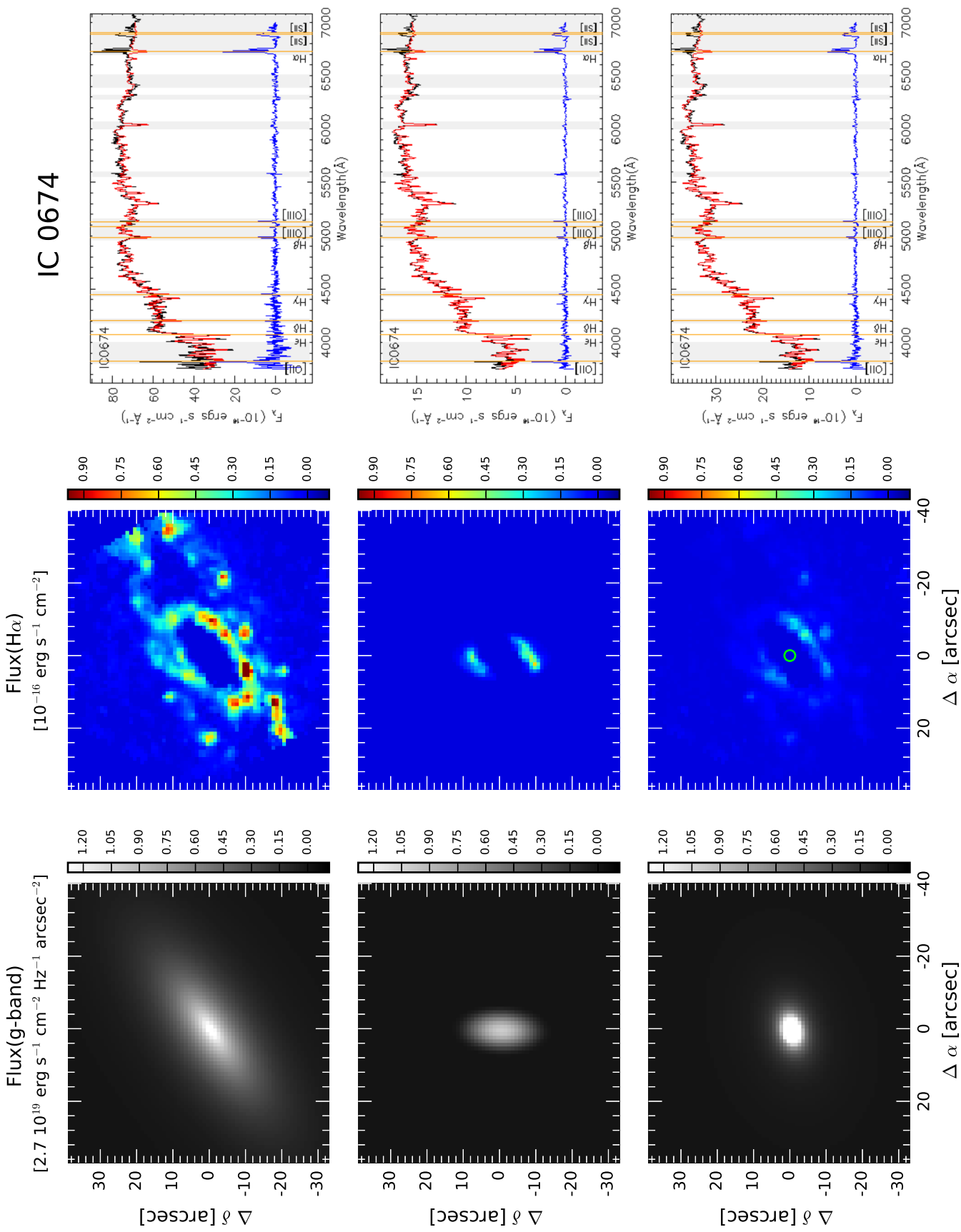
IC 0674
Flux(g-band)
[2.7 10^19 erg s^-1 cm^-2 Hz^-1 arcsec^-2]
Flux(Hα)
[10^-16 erg s^-1 cm^-2]
Δ δ [arcsec]
Δ α [arcsec]
Wavelength(Å)
F_λ (10^-16 ergs s^-1 cm^-2 Å^-1)
IC0674
[OII]
Hε
Hδ
Hγ
Hβ
[OIII]
[OIII]
[SII]
[SII]
Hα

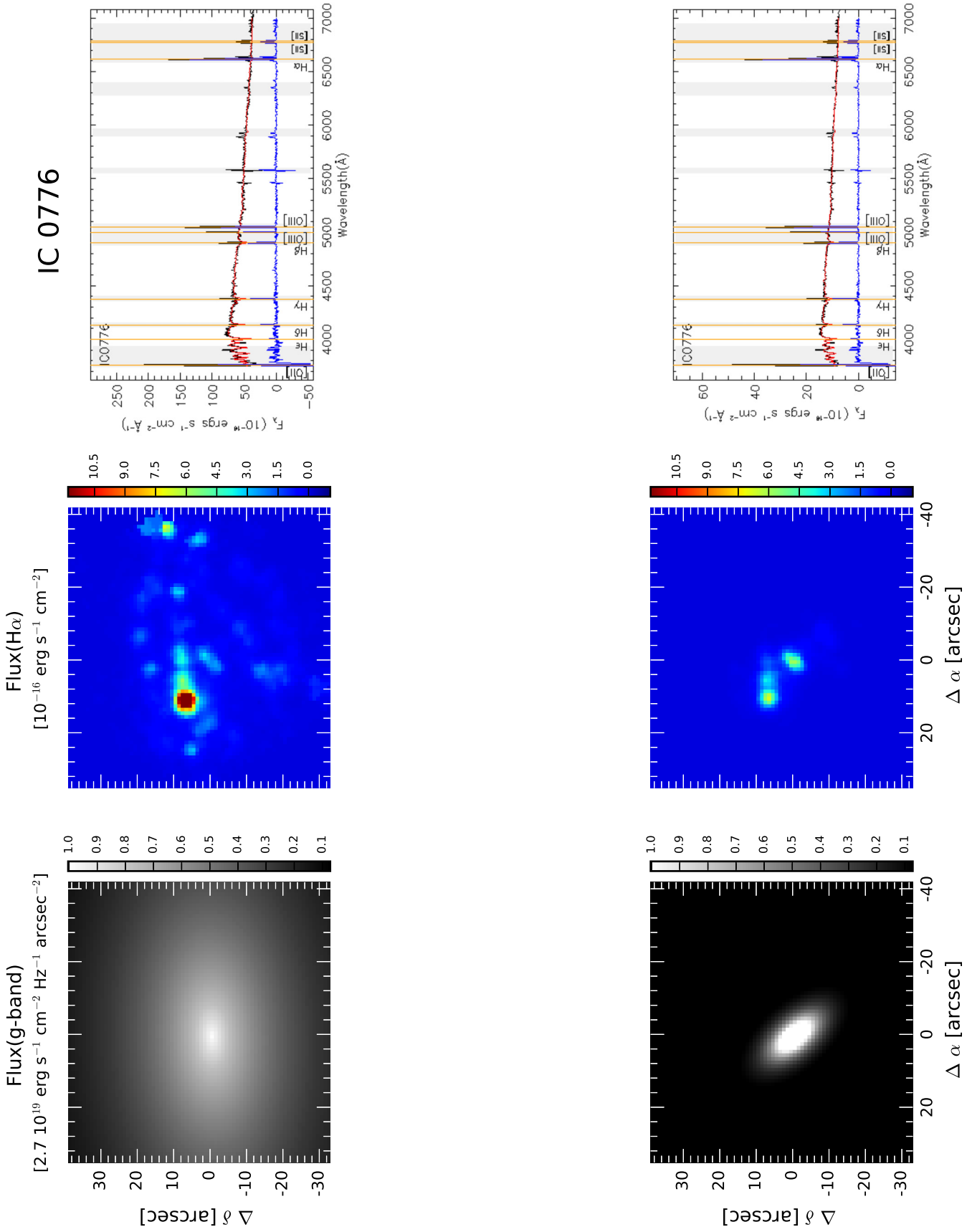
IC 0776
Flux(Hα)
[10^-16 erg s^-1 cm^-2]
Flux(g-band)
[2.7 10^19 erg s^-1 cm^-2 Hz^-1 arcsec^-2]
Δ δ [arcsec]
Δ α [arcsec]
Wavelength(Å)
F_λ (10^-16 ergs s^-1 cm^-2 Å^-1)
[OII]
Hε
Hδ
Hγ
Hβ
[OIII]
[OIII]
[SII]
[SII]
Hα

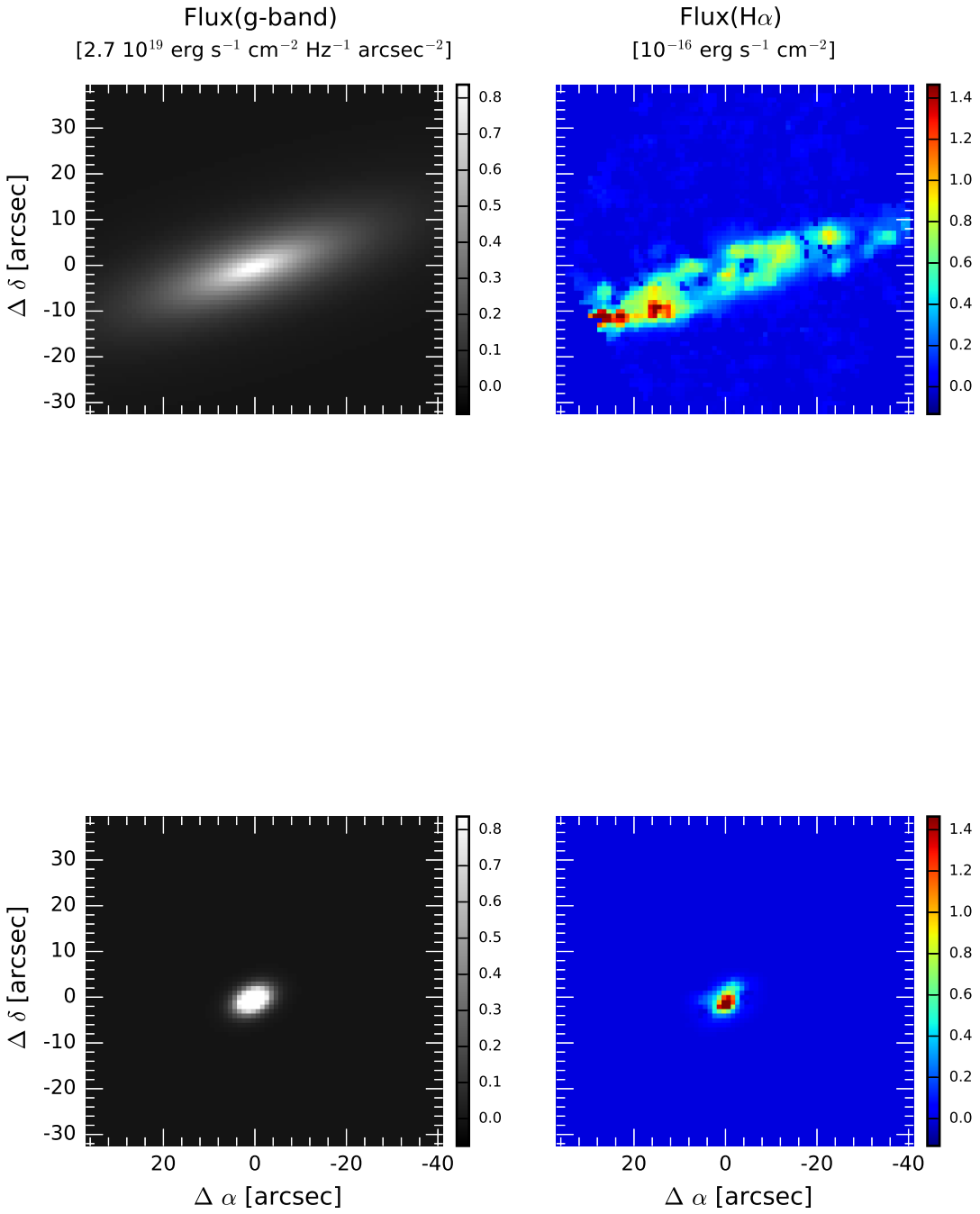
Flux(g-band)
[2.7 10^19 erg s^-1 cm^-2 Hz^-1 arcsec^-2]
Flux(Hα)
[10^-16 erg s^-1 cm^-2]
IC 0944
Δ δ [arcsec]
Δ α [arcsec]
IC0944
Wavelength(Å)
[OII]
Hε
Hδ
Hγ
Hβ
[OIII]
[OIII]
Hα
[SII]
[SII]

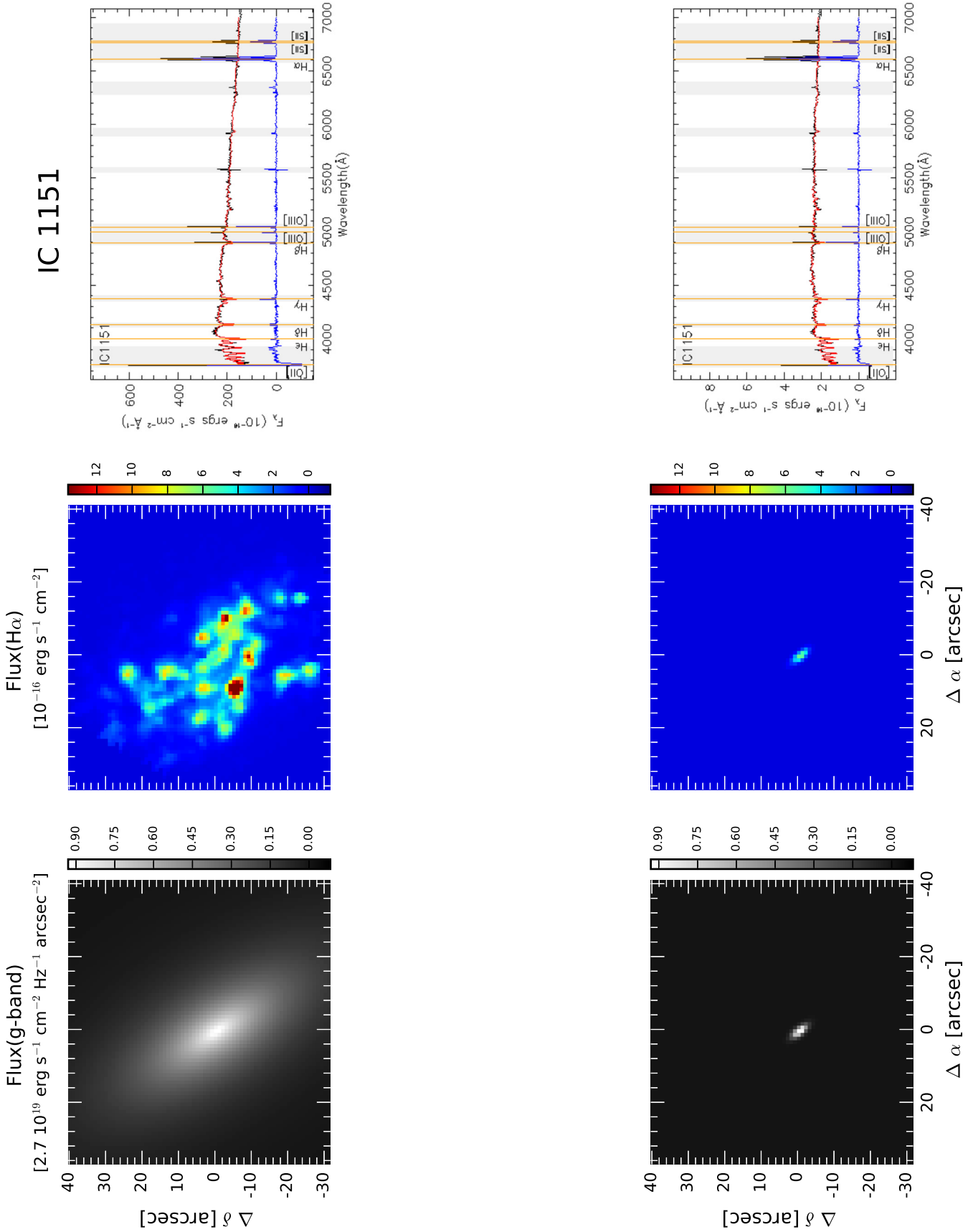
IC 1151
IC1151
[OII]
Hε
Hδ
Hγ
Hβ
[OIII]
[OIII]
Hα
[SII]
[SII]
Wavelength(Å)
Flux(Hα)
[10⁻¹⁶ erg s⁻¹ cm⁻²]
Flux(g-band)
[2.7 10¹⁹ erg s⁻¹ cm⁻² Hz⁻¹ arcsec⁻²]
Δ δ [arcsec]
Δ α [arcsec]

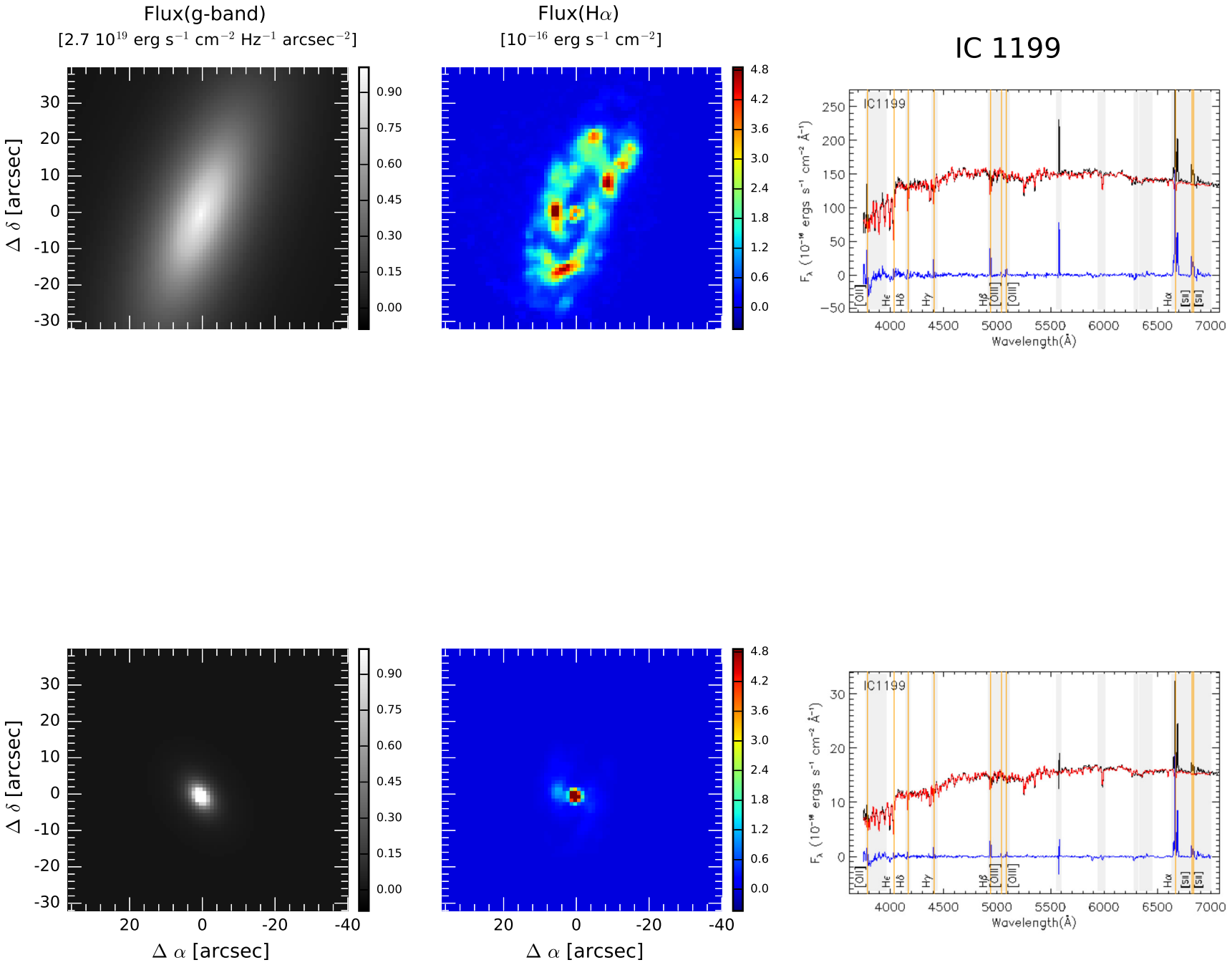
Flux(g-band)
[2.7 10^19 erg s^-1 cm^-2 Hz^-1 arcsec^-2]
Flux(Hα)
[10^-16 erg s^-1 cm^-2]
IC 1199
Δ δ [arcsec]
Δ α [arcsec]
IC1199
Wavelength(Å)
[OII]
Hε
Hδ
Hγ
Hβ
[OIII]
[OIII]
Hα
[SII]
[SII]

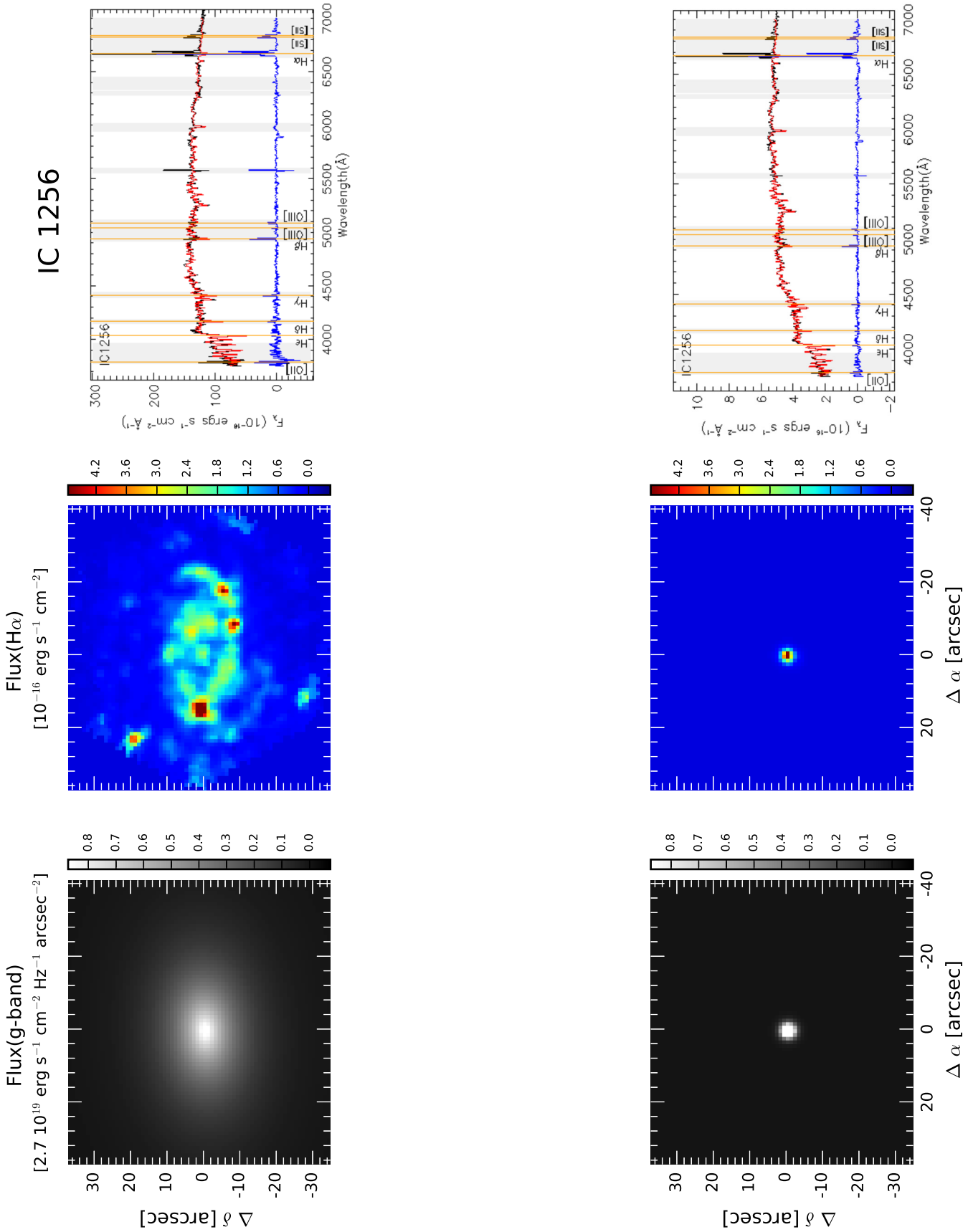
IC 1256
Flux(g-band)
[2.7 10^19 erg s^-1 cm^-2 Hz^-1 arcsec^-2]
Flux(Hα)
[10^-16 erg s^-1 cm^-2]
Δ δ [arcsec]
Δ α [arcsec]
Wavelength(Å)
F_λ (10^-16 ergs s^-1 cm^-2 Å^-1)
IC1256
[OII]
Hε
Hδ
Hγ
Hβ
[OIII]
[OIII]
Hα
[SII]
[SII]

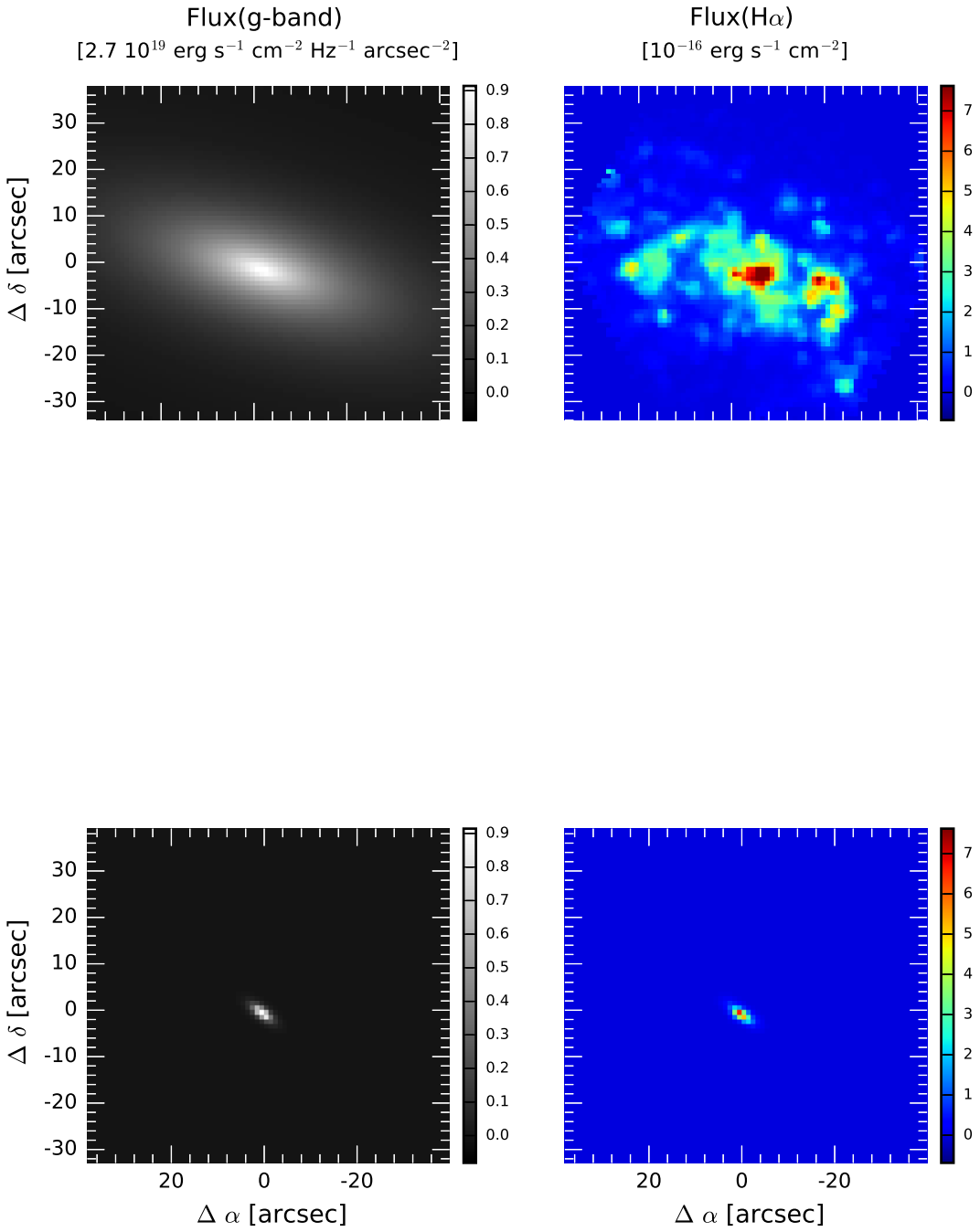
Flux(g-band)
[2.7 10^19 erg s^-1 cm^-2 Hz^-1 arcsec^-2]
Flux(Hα)
[10^-16 erg s^-1 cm^-2]
Δ δ [arcsec]
Δ α [arcsec]

IC 1528

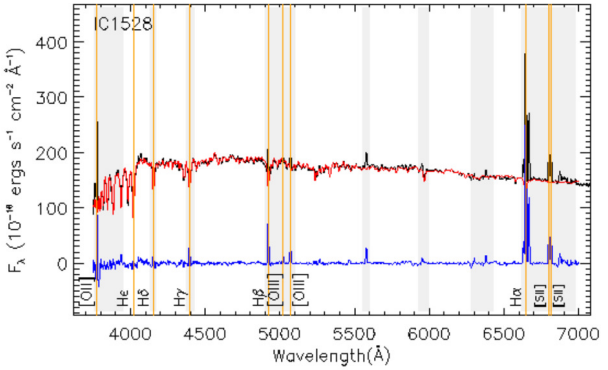
IC1528
Wavelength(Å)

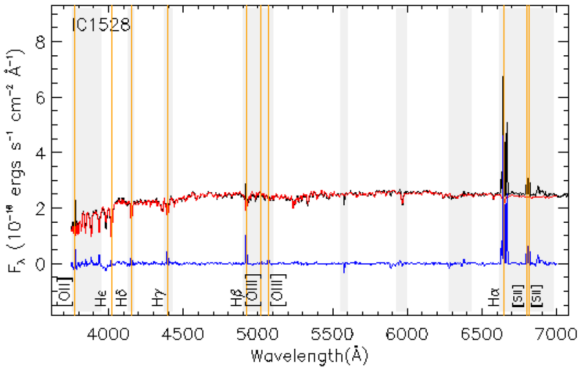
IC1528
Wavelength(Å)

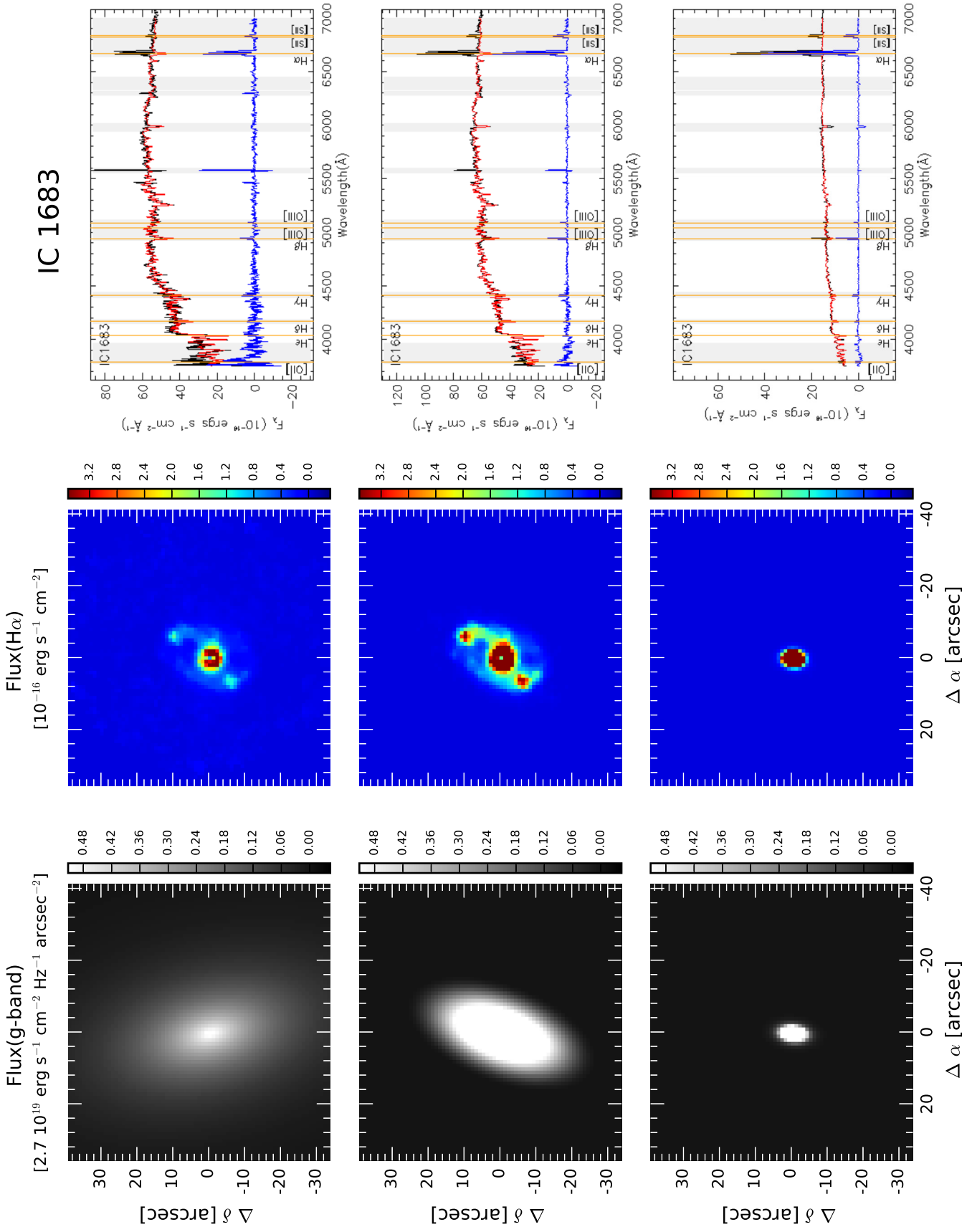
IC 1683
Flux(g-band)
[2.7 10^19 erg s^-1 cm^-2 Hz^-1 arcsec^-2]
Flux(Hα)
[10^-16 erg s^-1 cm^-2]
Δ δ [arcsec]
Δ α [arcsec]
Wavelength(Å)
IC1683
[OII]
Hε
Hδ
Hγ
Hβ
[OIII]
[OIII]
Hα
[SII]
[SII]

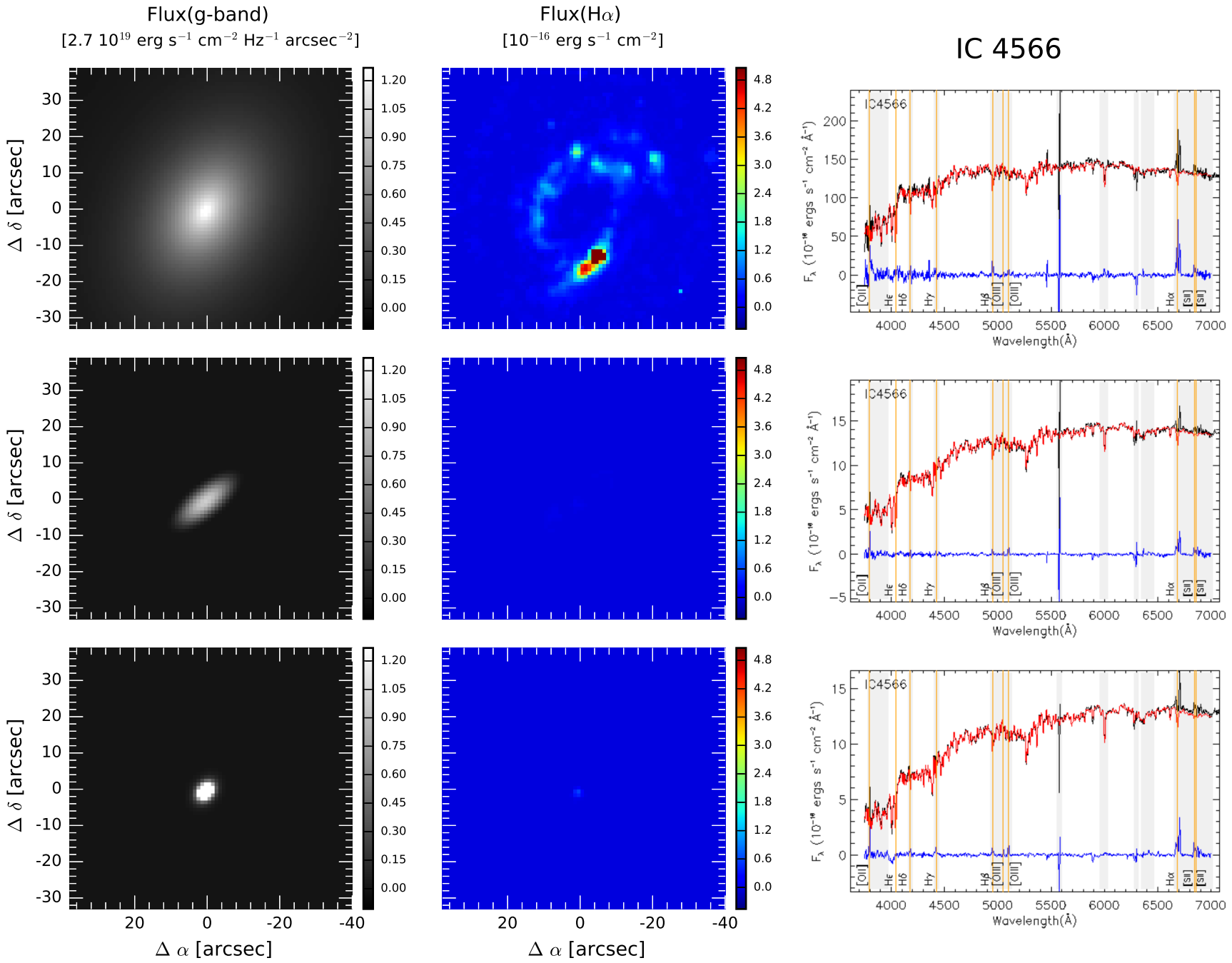
Flux(g-band)
[2.7 10^19 erg s^-1 cm^-2 Hz^-1 arcsec^-2]
Flux(Hα)
[10^-16 erg s^-1 cm^-2]
IC 4566
Δ δ [arcsec]
Δ α [arcsec]
Wavelength(Å)
IC4566
[OII]
Hε
Hδ
Hγ
Hβ
[OIII]
[OIII]
Hα
[SII]
[SII]

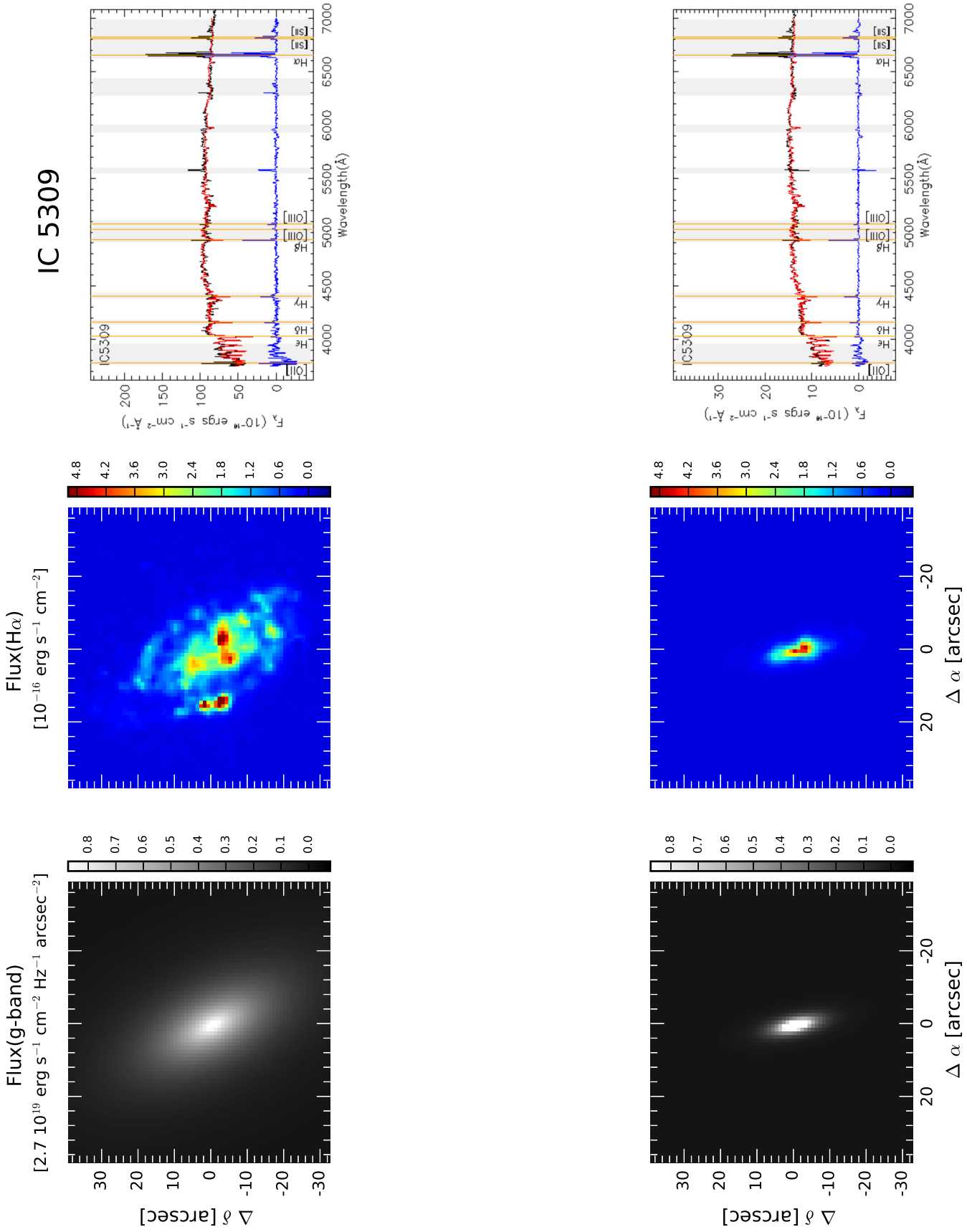
IC 5309
Flux(g-band)
[2.7 10^19 erg s^-1 cm^-2 Hz^-1 arcsec^-2]
Flux(Hα)
[10^-16 erg s^-1 cm^-2]
Δ δ [arcsec]
Δ α [arcsec]
Wavelength(Å)
F_λ (10^-16 ergs s^-1 cm^-2 Å^-1)
IC5309
[OII]
Hε
Hδ
Hγ
[OIII]
Hβ
[OIII]
[SII]
[SII]
Hα

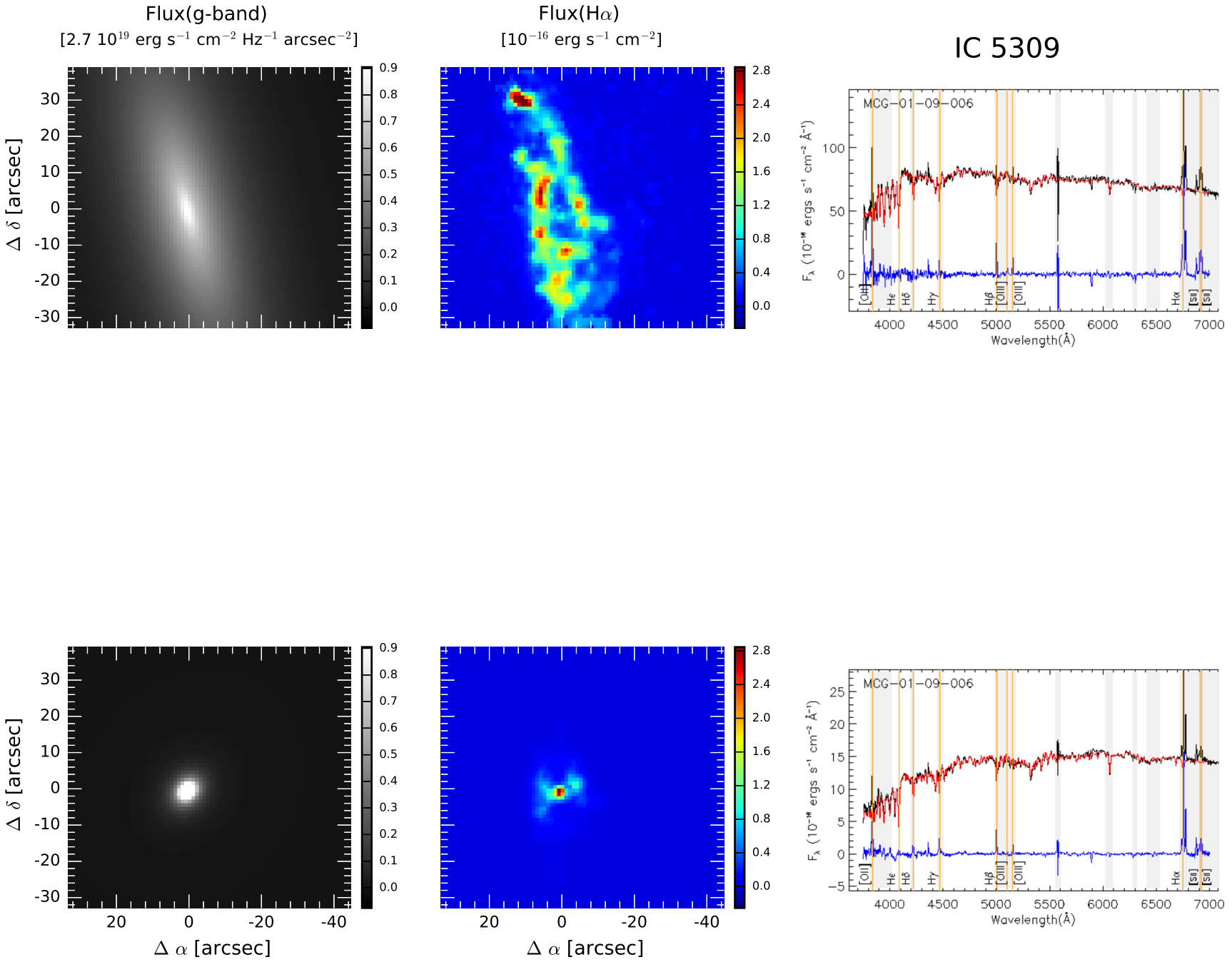
Flux(g-band)
[2.7 10^19 erg s^-1 cm^-2 Hz^-1 arcsec^-2]
Flux(Hα)
[10^-16 erg s^-1 cm^-2]
IC 5309
MCG−01−09−006
Δ δ [arcsec]
Δ α [arcsec]
Wavelength(Å)
[OII]
Hε
Hδ
Hγ
Hβ
[OIII]
[OIII]
Hα
[SII]
[SII]

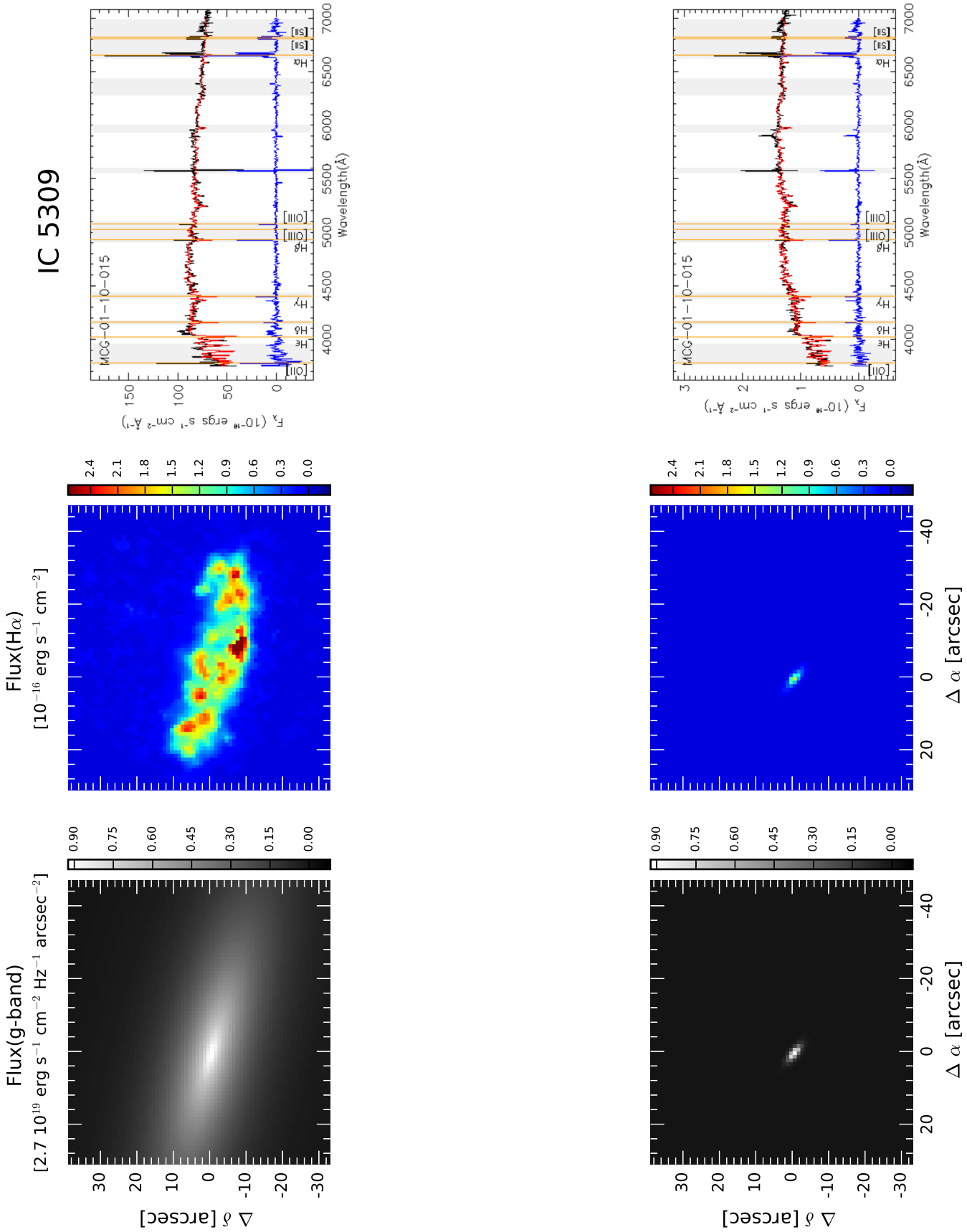
IC 5309
MCG−01−10−015
Wavelength(Å)
Flux(Hα)
[10⁻¹⁶ erg s⁻¹ cm⁻²]
Flux(g-band)
[2.7 10¹⁹ erg s⁻¹ cm⁻² Hz⁻¹ arcsec⁻²]
Δ δ [arcsec]
Δ α [arcsec]

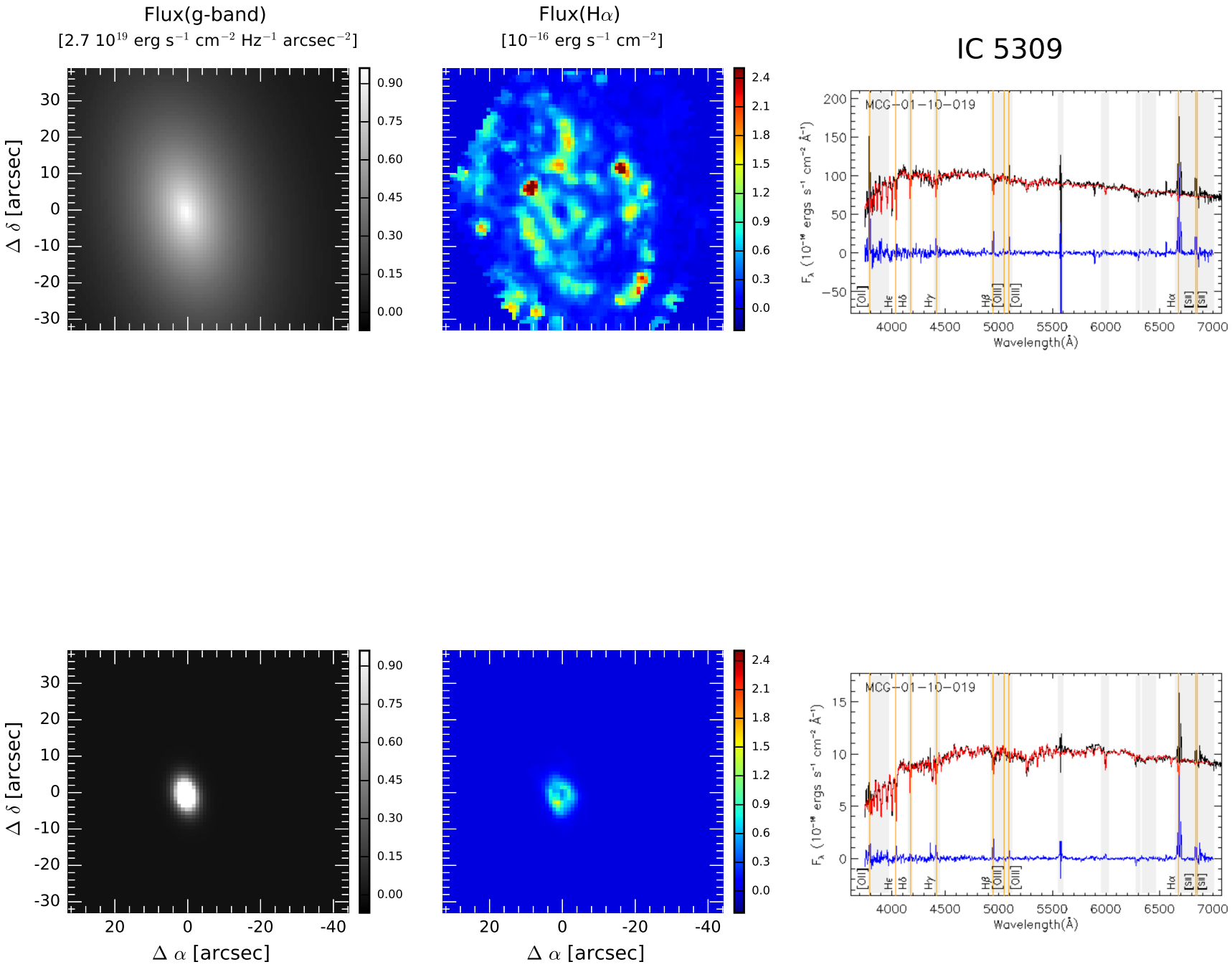
Flux(g-band)
[2.7 10^19 erg s^-1 cm^-2 Hz^-1 arcsec^-2]
Flux(Hα)
[10^-16 erg s^-1 cm^-2]
IC 5309
MCG−01−10−019
Δ δ [arcsec]
Δ α [arcsec]
Wavelength(Å)
[OII]
Hε
Hδ
Hγ
Hβ
[OIII]
[OIII]
Hα
[SII]
[SII]

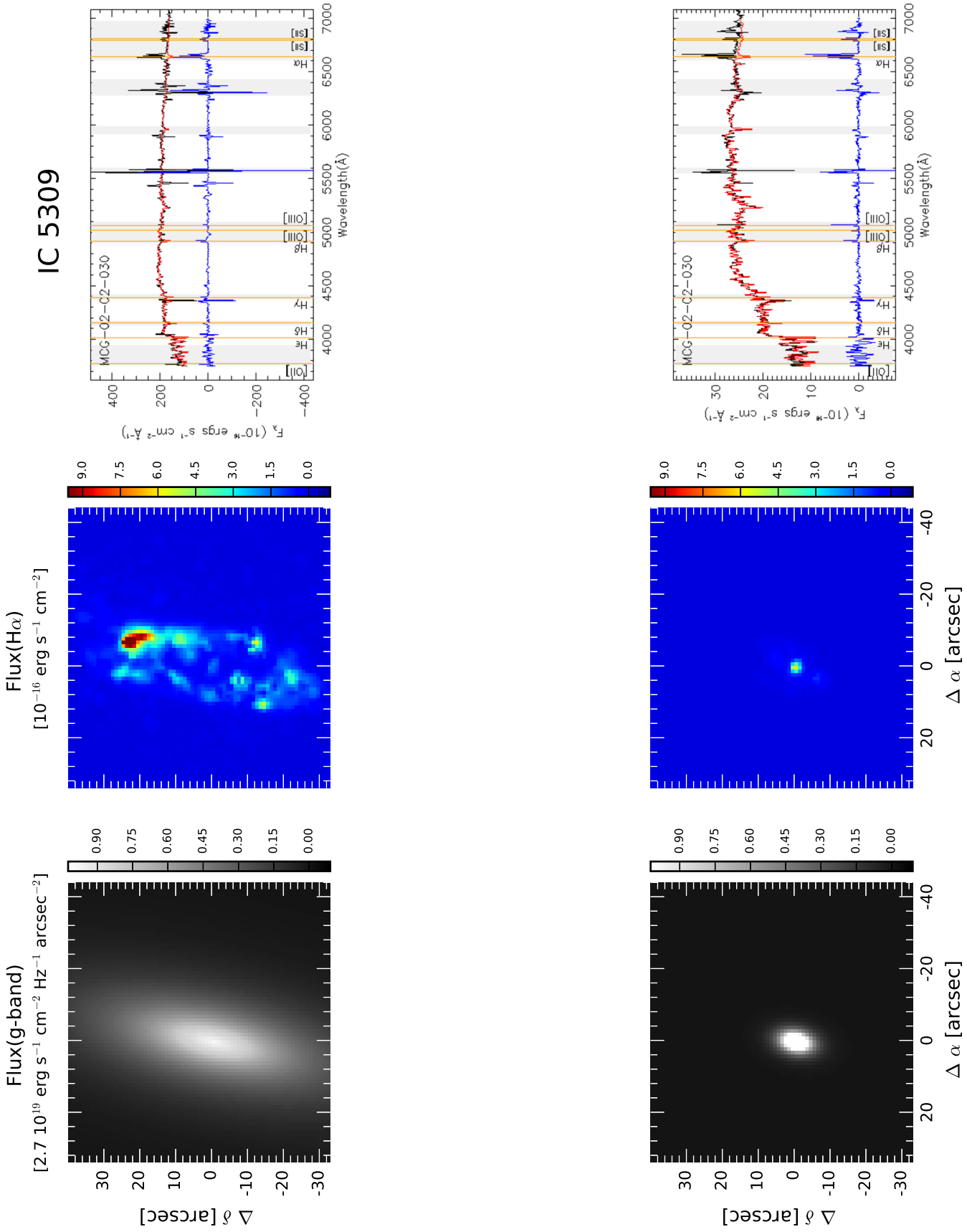
IC 5309
MCG−02−02−030
Wavelength(Å)
Flux(Hα)
[10⁻¹⁶ erg s⁻¹ cm⁻²]
Flux(g-band)
[2.7 10¹⁹ erg s⁻¹ cm⁻² Hz⁻¹ arcsec⁻²]
Δ δ [arcsec]
Δ α [arcsec]

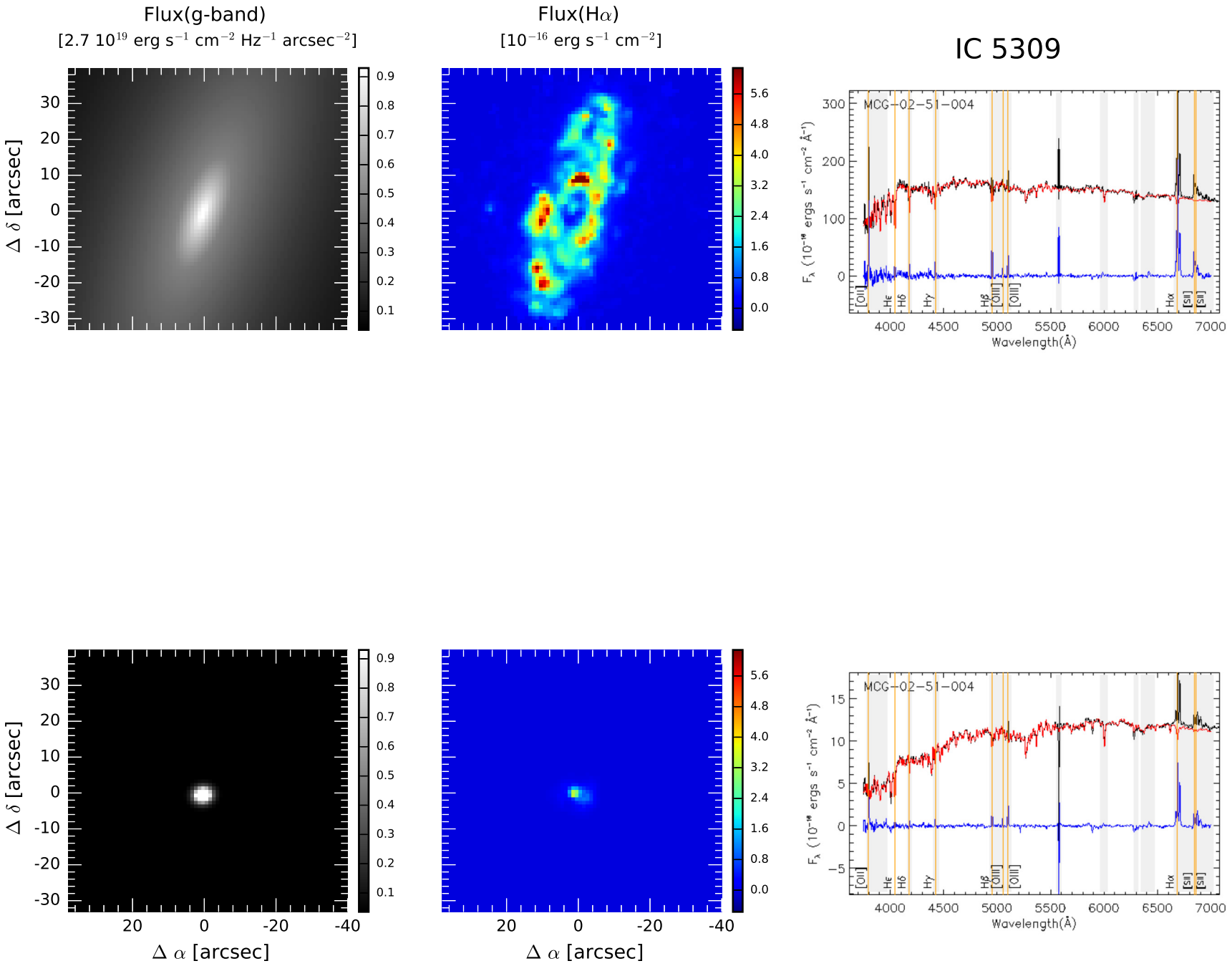
Flux(g-band)
[2.7 10^19 erg s^-1 cm^-2 Hz^-1 arcsec^-2]
Flux(Hα)
[10^-16 erg s^-1 cm^-2]
IC 5309
MCG-02-51-004
MCG-02-51-004
Δ δ [arcsec]
Δ α [arcsec]
Wavelength(Å)
[OII]
Hε
Hδ
Hγ
Hβ
[OIII]
[OIII]
Hα
[SII]
[SII]

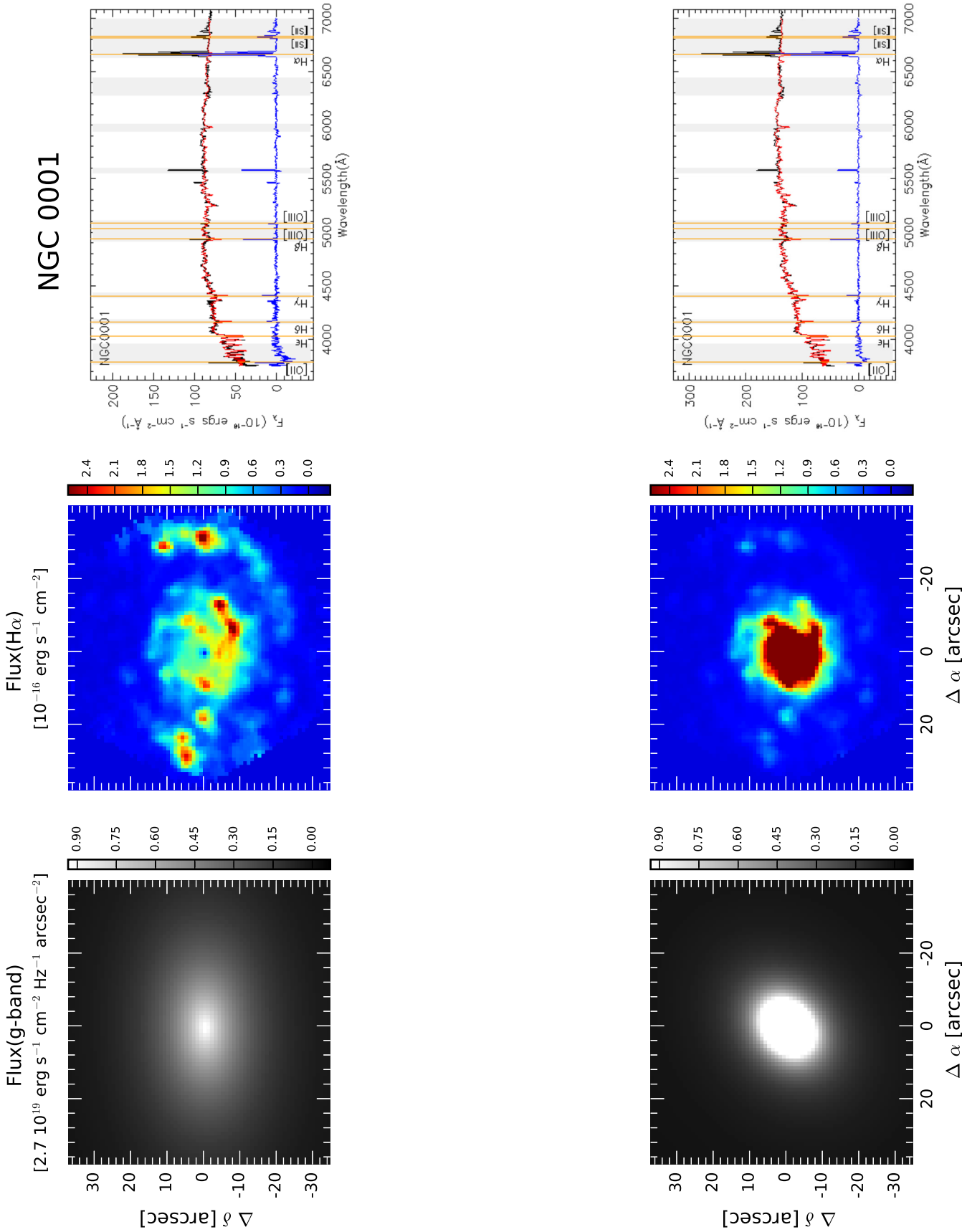
NGC 0001
NGC0001
Wavelength(Å)
[OII]
Hε
Hδ
Hγ
[OIII]
Hβ
[OIII]
[SII]
[SII]
Hα
Flux(Hα)
[10⁻¹⁶ erg s⁻¹ cm⁻²]
Flux(g-band)
[2.7 10¹⁹ erg s⁻¹ cm⁻² Hz⁻¹ arcsec⁻²]
Δ δ [arcsec]
Δ α [arcsec]

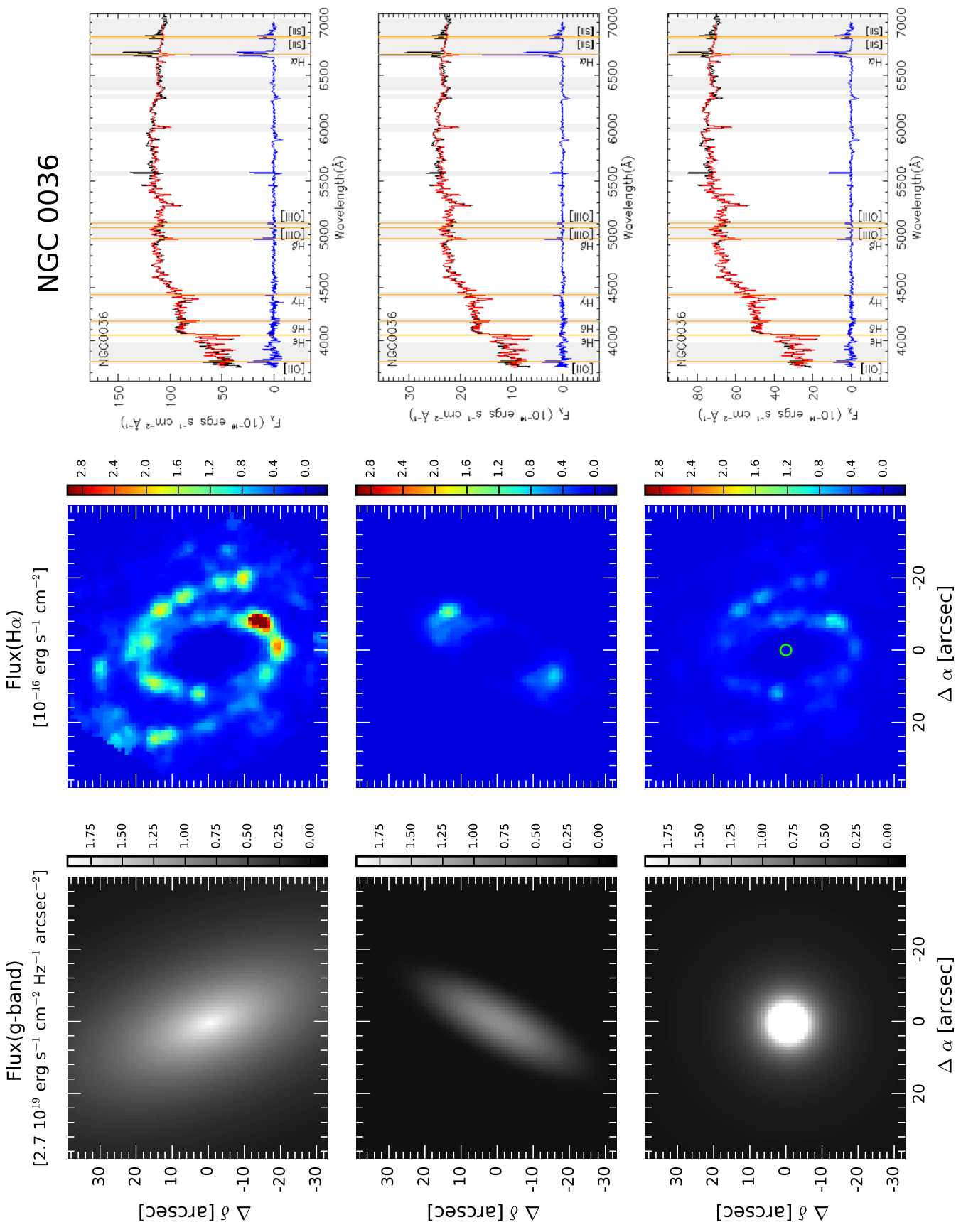
NGC 0036
Flux(g-band)
[2.7 10^19 erg s^-1 cm^-2 Hz^-1 arcsec^-2]
Flux(Hα)
[10^-16 erg s^-1 cm^-2]
Δ δ [arcsec]
Δ α [arcsec]
Wavelength(Å)
NGC0036
[OII]
Hε
Hδ
Hγ
Hβ
[OIII]
[OIII]
[SII]
[SII]
Hα

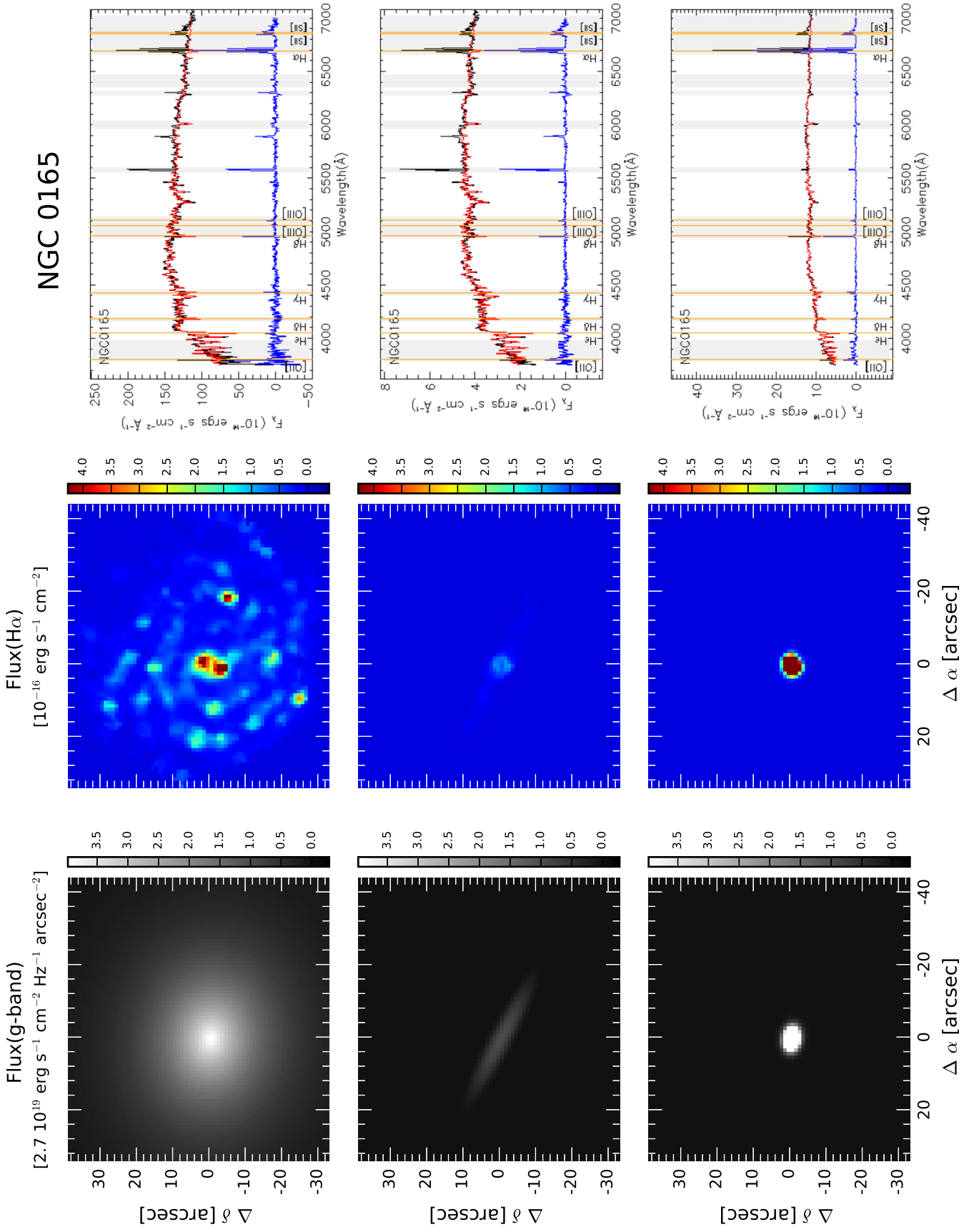
NGC 0165
Flux(g-band)
[2.7 10^19 erg s^-1 cm^-2 Hz^-1 arcsec^-2]
Flux(Hα)
[10^-16 erg s^-1 cm^-2]
Δ δ [arcsec]
Δ α [arcsec]
Wavelength(Å)
NGC0165
[OII]
Hε
Hδ
Hγ
Hβ
[OIII]
[OIII]
[SII]
[SII]
Hα

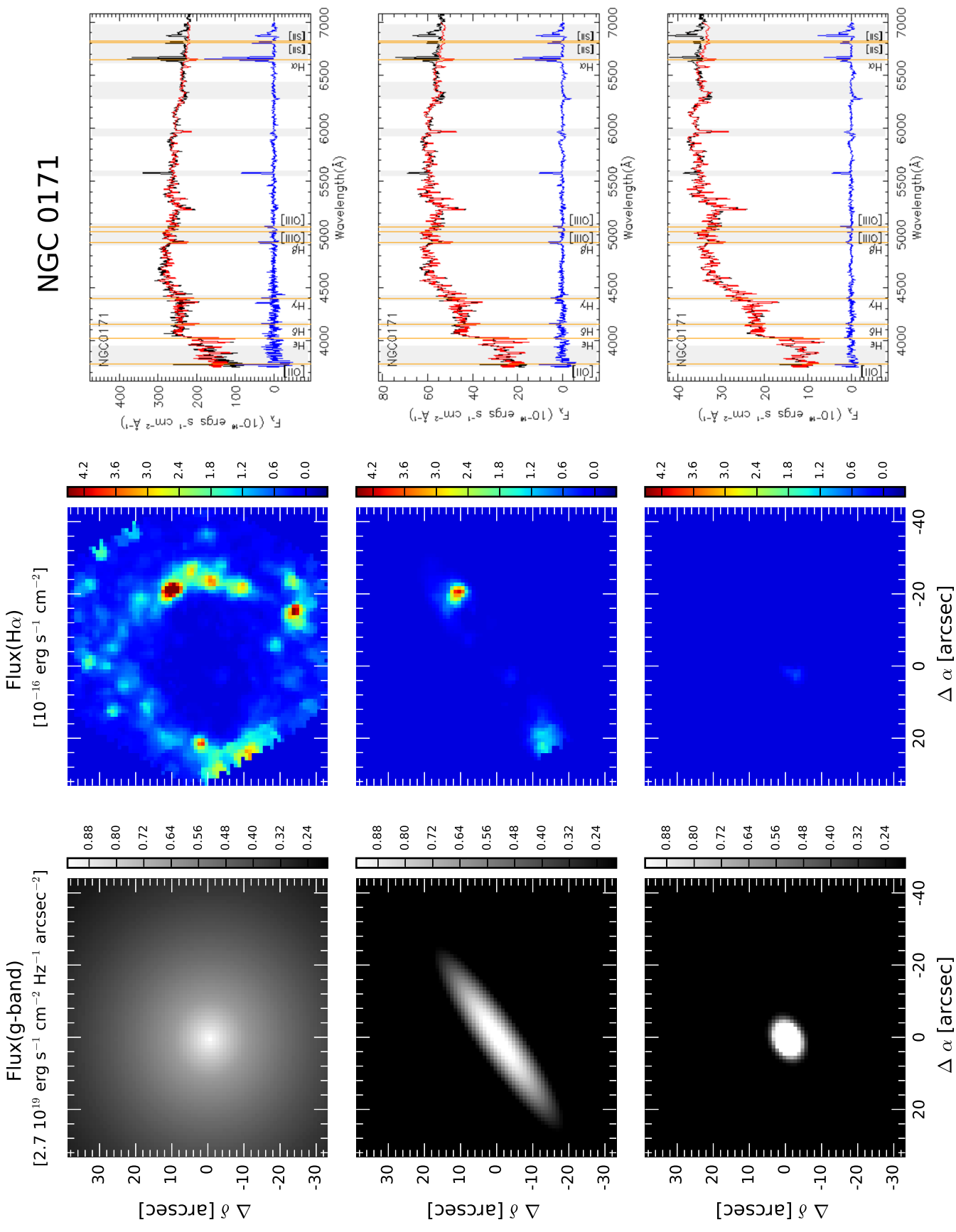
NGC 0171
Flux(g-band)
[2.7 10^19 erg s^-1 cm^-2 Hz^-1 arcsec^-2]
Flux(Hα)
[10^-16 erg s^-1 cm^-2]
Δ δ [arcsec]
Δ α [arcsec]
Wavelength(Å)
NGC0171
[OII]
Hε
Hδ
Hγ
H8
[OIII]
[OIII]
[SII]
[SII]
Hα

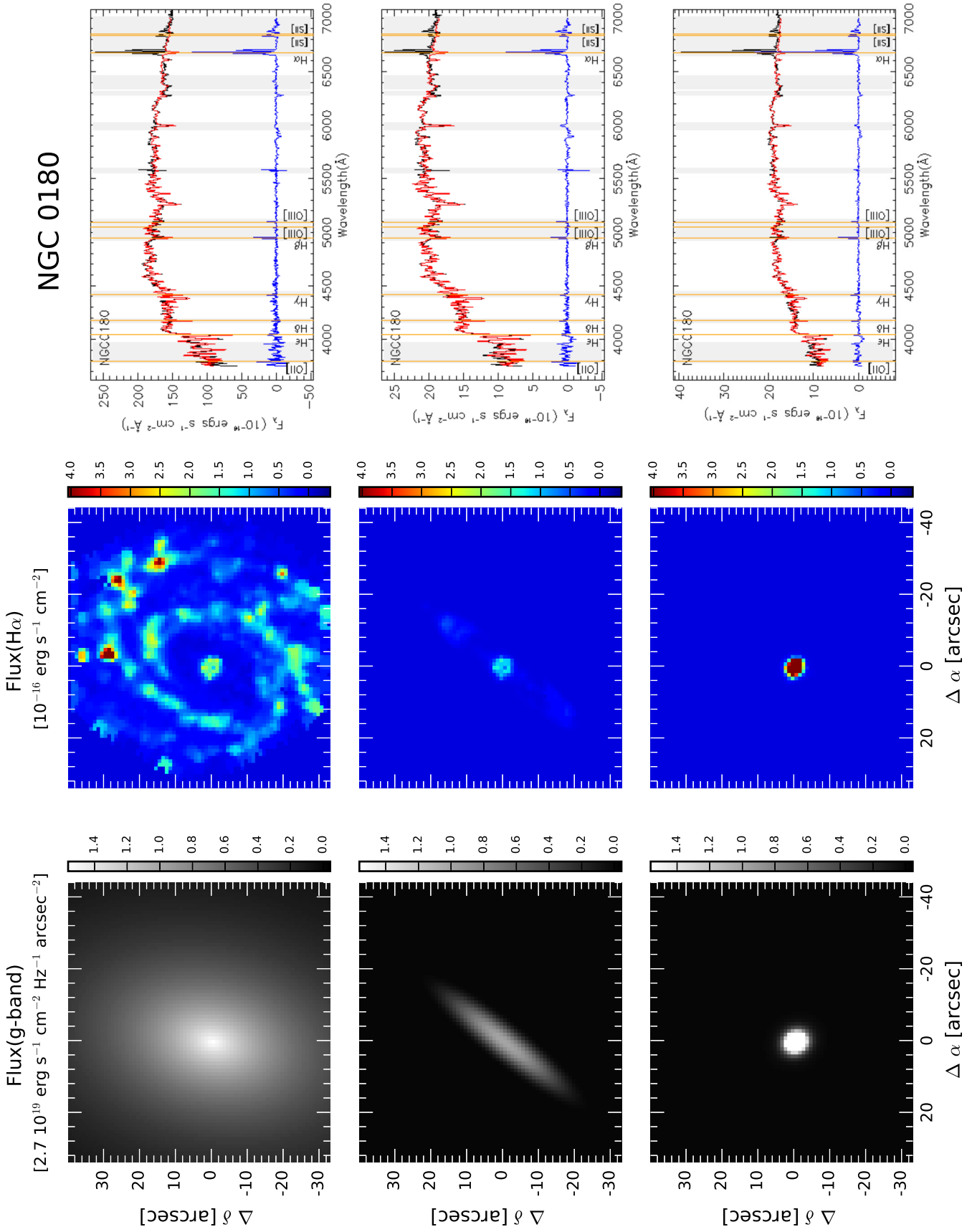
NGC 0180
Flux(g-band)
[2.7 10^19 erg s^-1 cm^-2 Hz^-1 arcsec^-2]
Flux(Hα)
[10^-16 erg s^-1 cm^-2]
Δ δ [arcsec]
Δ α [arcsec]
Wavelength(Å)
F_λ (10^-16 ergs s^-1 cm^-2 Å^-1)
NGC0180
[OII]
Hε
Hδ
Hγ
[OIII]
[OIII]
Hβ
[SII]
[SII]
Hα

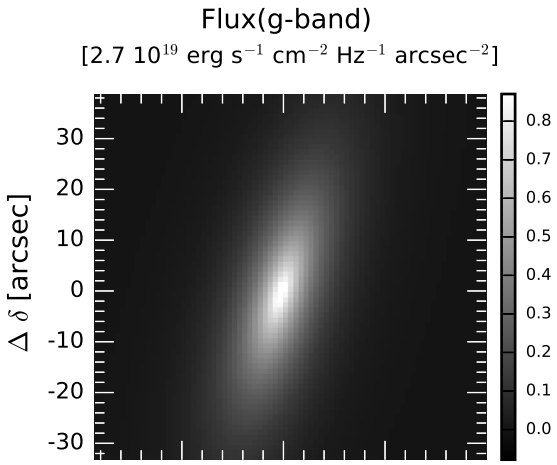
Flux(g-band)
[2.7 10^19 erg s^-1 cm^-2 Hz^-1 arcsec^-2]
Δ δ [arcsec]
30
20
10
0
-10
-20
-30
0.8
0.7
0.6
0.5
0.4
0.3
0.2
0.1
0.0

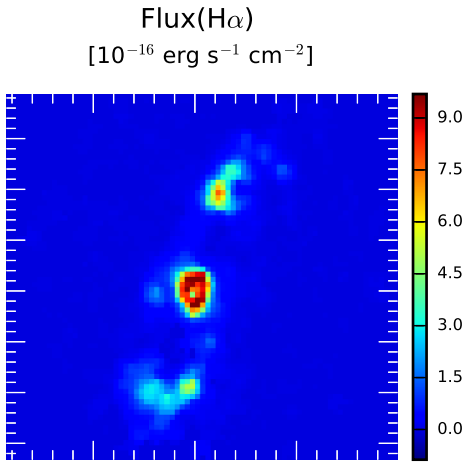
Flux(Hα)
[10^-16 erg s^-1 cm^-2]
9.0
7.5
6.0
4.5
3.0
1.5
0.0

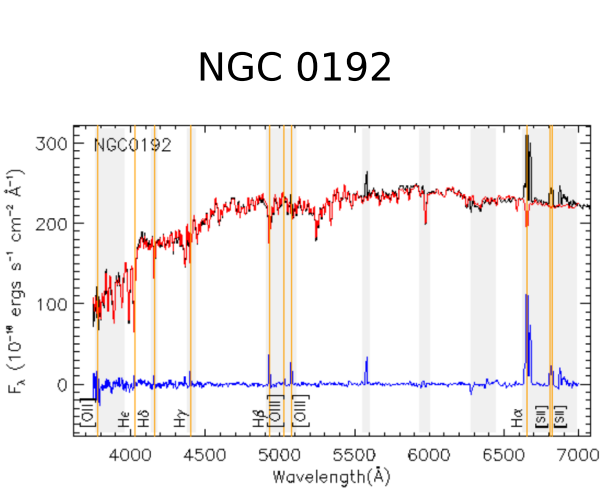
NGC 0192
NGC0192
F_λ (10^-16 ergs s^-1 cm^-2 Å^-1)
Wavelength(Å)
[OII]
Hε
Hδ
Hγ
Hβ
[OIII]
[OIII]
Hα
[SII]
[SII]

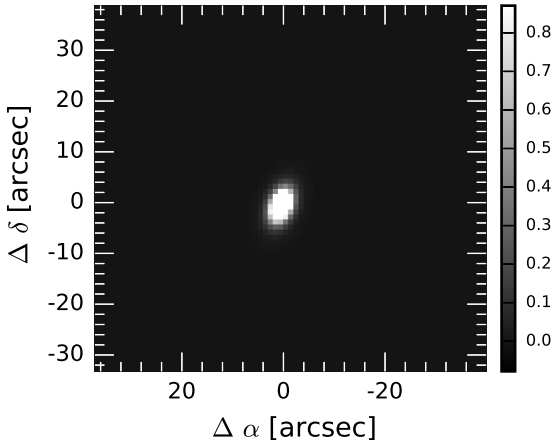
Δ δ [arcsec]
Δ α [arcsec]
30
20
10
0
-10
-20
-30
20
0
-20
0.8
0.7
0.6
0.5
0.4
0.3
0.2
0.1
0.0

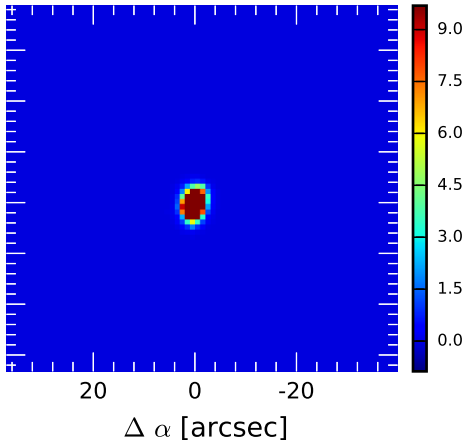
Δ α [arcsec]
20
0
-20
9.0
7.5
6.0
4.5
3.0
1.5
0.0

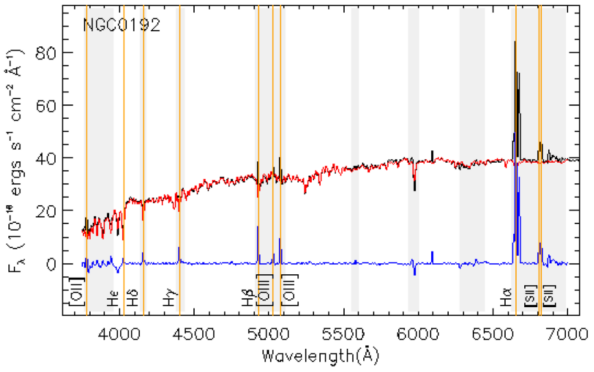
NGC0192
F_λ (10^-16 ergs s^-1 cm^-2 Å^-1)
Wavelength(Å)
[OII]
Hε
Hδ
Hγ
Hβ
[OIII]
[OIII]
Hα
[SII]
[SII]

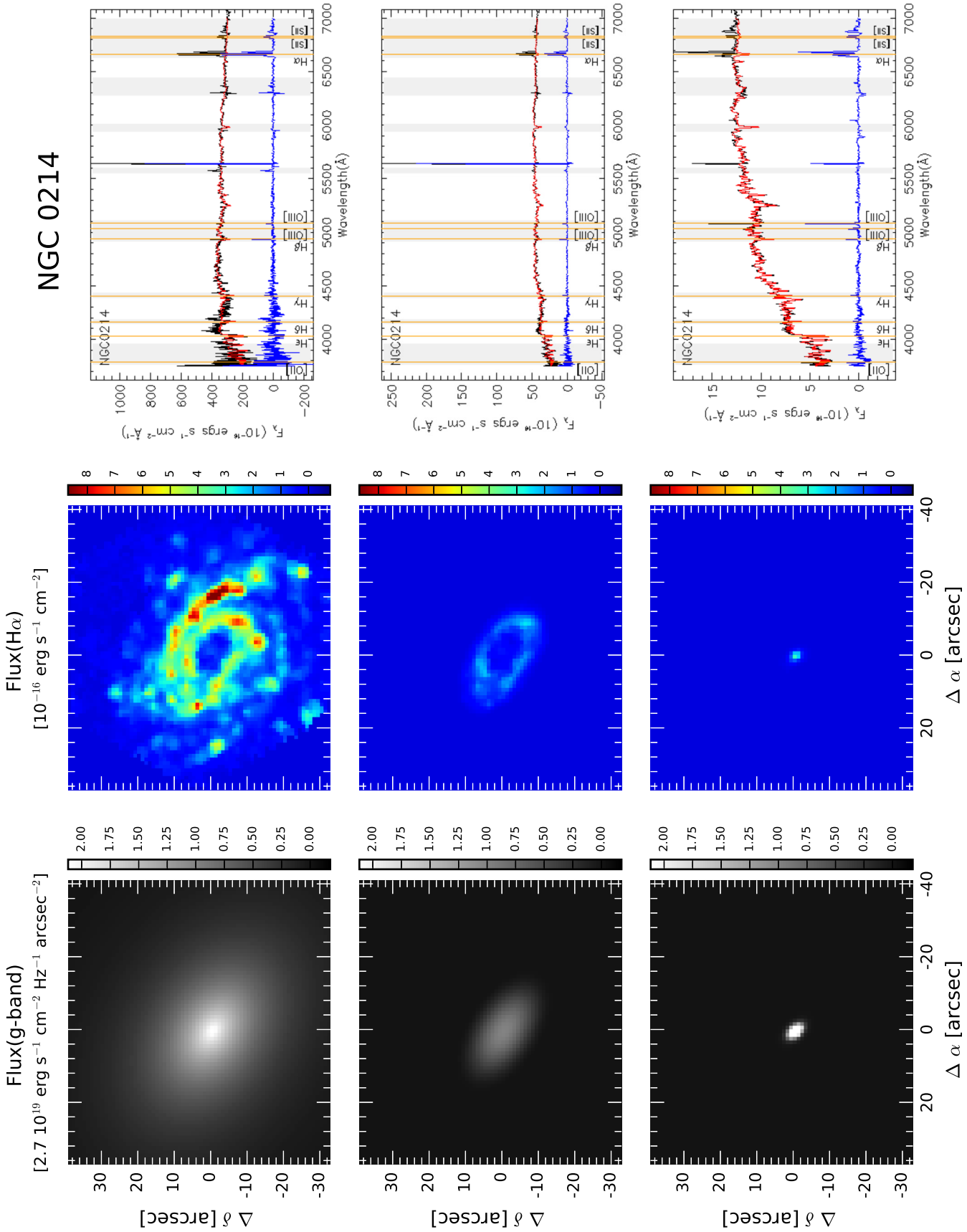
NGC 0214
Flux(g-band)
[2.7 10^19 erg s^-1 cm^-2 Hz^-1 arcsec^-2]
Flux(Hα)
[10^-16 erg s^-1 cm^-2]
Δ δ [arcsec]
Δ α [arcsec]
Wavelength(Å)
F_λ (10^-16 ergs s^-1 cm^-2 Å^-1)
NGC0214
[OII]
Hε
Hδ
Hγ
Hβ
[OIII]
[OIII]
[SII]
[SII]
Hα

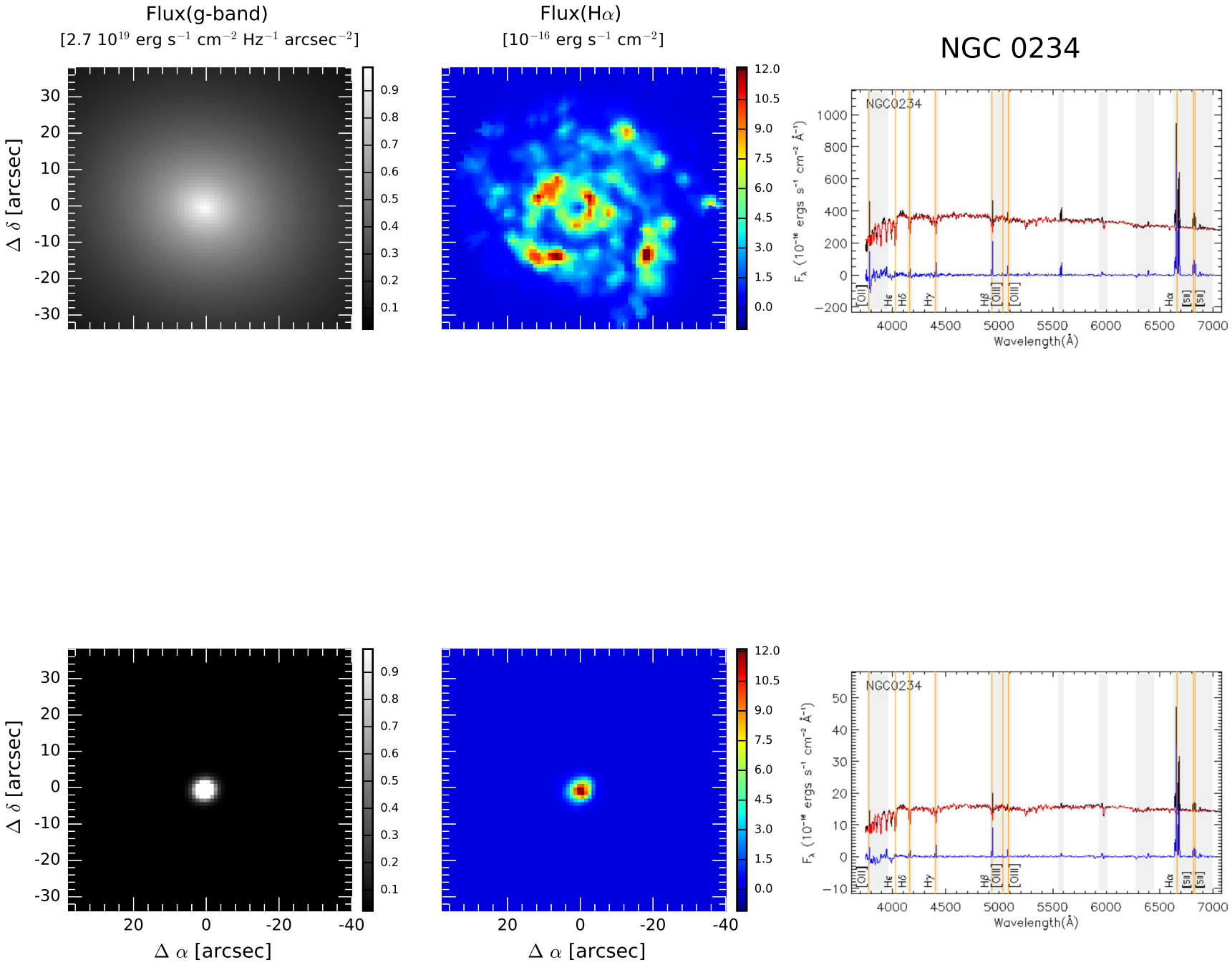
Flux(g-band)
[2.7 10^19 erg s^-1 cm^-2 Hz^-1 arcsec^-2]
Flux(Hα)
[10^-16 erg s^-1 cm^-2]
NGC 0234
Δ δ [arcsec]
Δ α [arcsec]
NGC0234
Wavelength(Å)
[OII]
Hε
Hδ
Hγ
Hβ
[OIII]
[OIII]
Hα
[SII]
[SII]

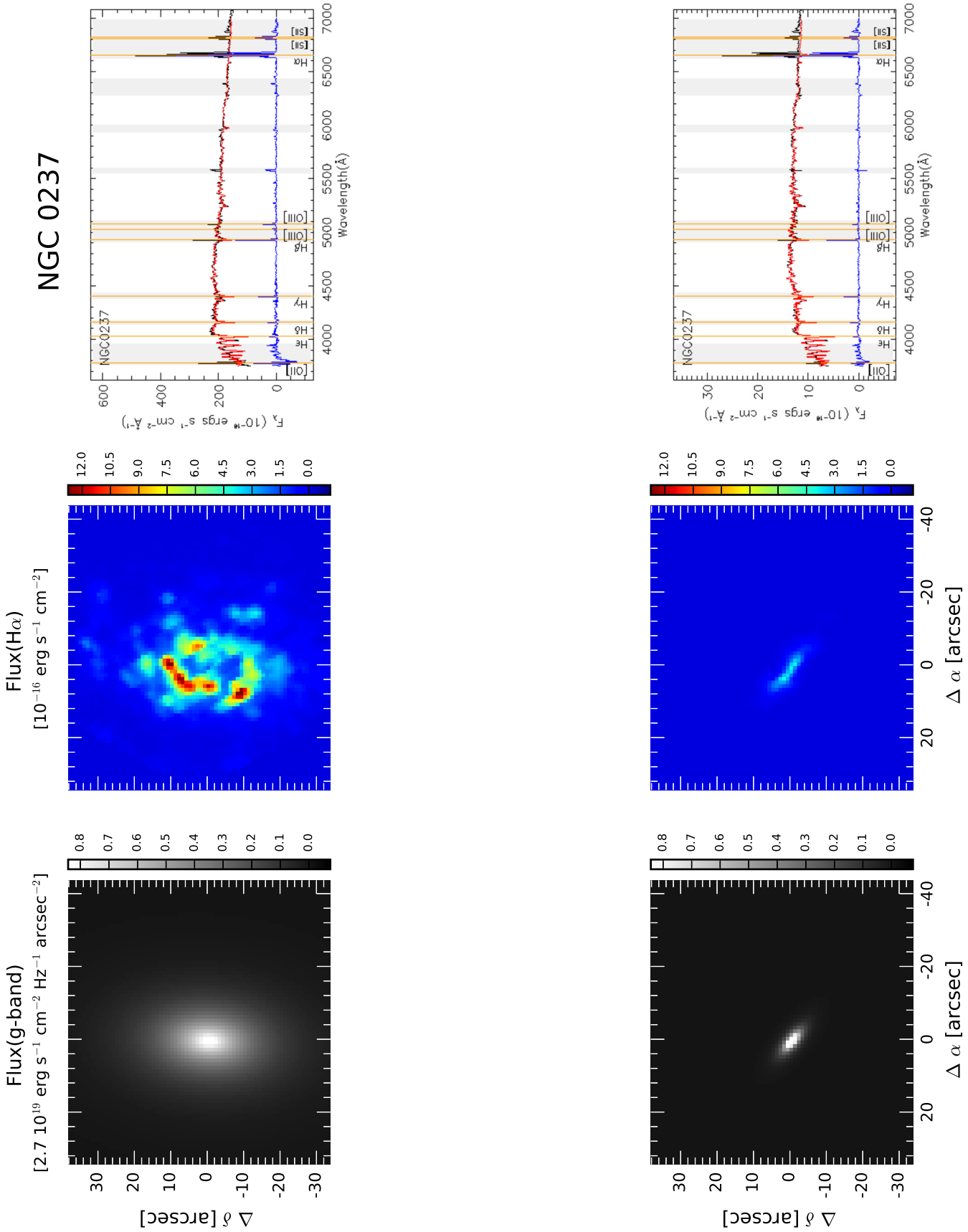
NGC 0237
Flux(g-band)
[2.7 10^19 erg s^-1 cm^-2 Hz^-1 arcsec^-2]
Flux(Hα)
[10^-16 erg s^-1 cm^-2]
Δ δ [arcsec]
Δ α [arcsec]
Wavelength(Å)
F_λ (10^-16 ergs s^-1 cm^-2 Å^-1)
NGC0237
[OII]
Hε
Hδ
Hγ
Hβ
[OIII]
[OIII]
Hα
[SII]
[SII]

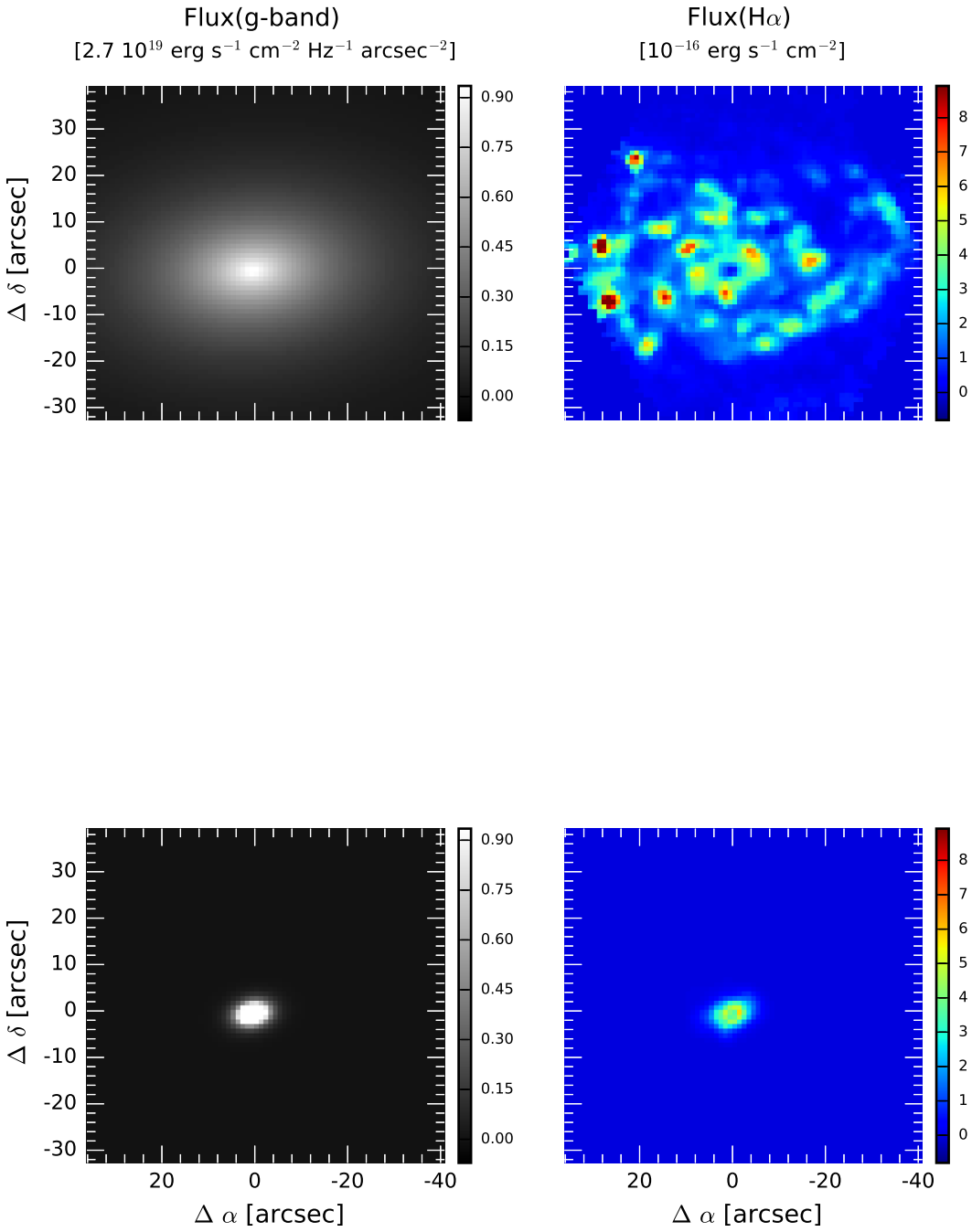
Flux(g-band)
[2.7 10^19 erg s^-1 cm^-2 Hz^-1 arcsec^-2]
Flux(Hα)
[10^-16 erg s^-1 cm^-2]
Δ δ [arcsec]
Δ α [arcsec]

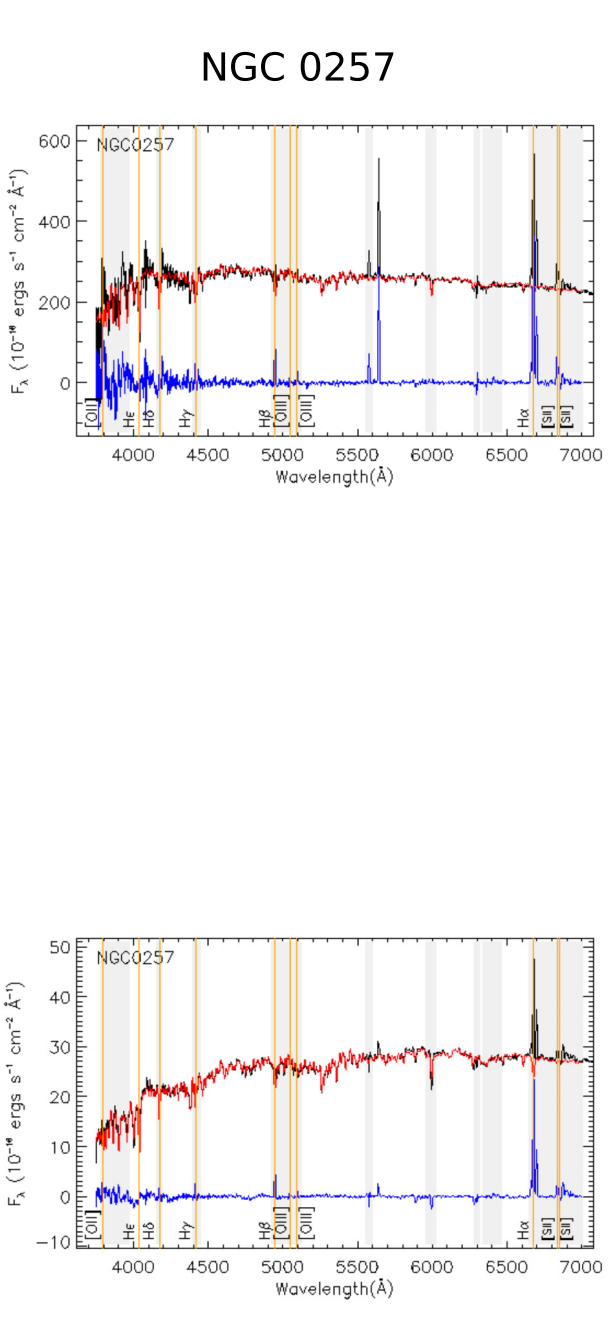
NGC 0257
NGC0257
F_λ (10^-16 ergs s^-1 cm^-2 Å^-1)
Wavelength(Å)
[OII]
Hε
Hδ
Hγ
Hβ
[OIII]
[OIII]
Hα
[SII]
[SII]

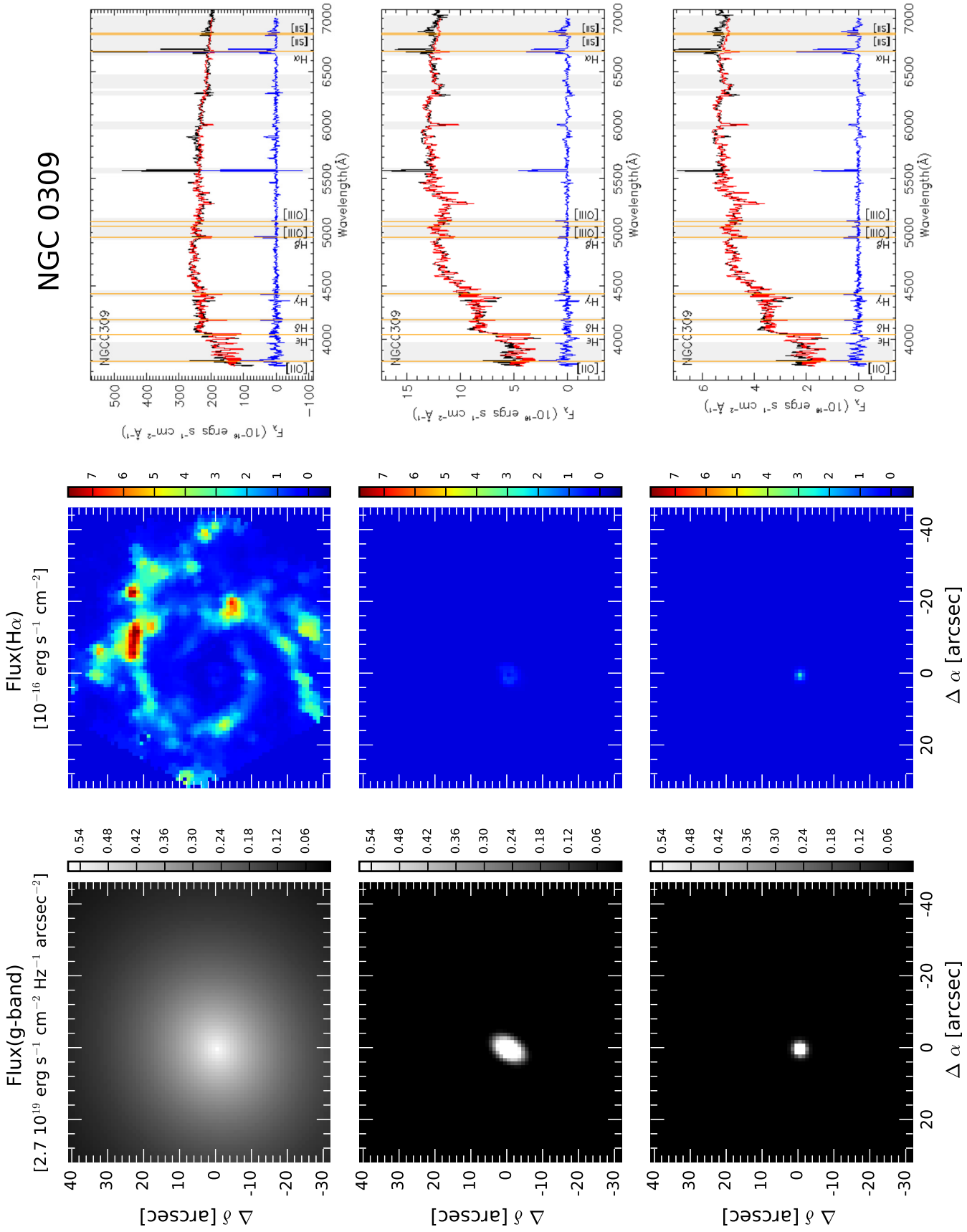
NGC 0309
Flux(g-band)
[2.7 10^19 erg s^-1 cm^-2 Hz^-1 arcsec^-2]
Flux(Hα)
[10^-16 erg s^-1 cm^-2]
Δ δ [arcsec]
Δ α [arcsec]
Wavelength(Å)
F_λ (10^-16 ergs s^-1 cm^-2 Å^-1)
NGC0309
[OII]
HE
Hδ
Hγ
Hβ
[OIII]
[OIII]
[SII]
[SII]
Hα

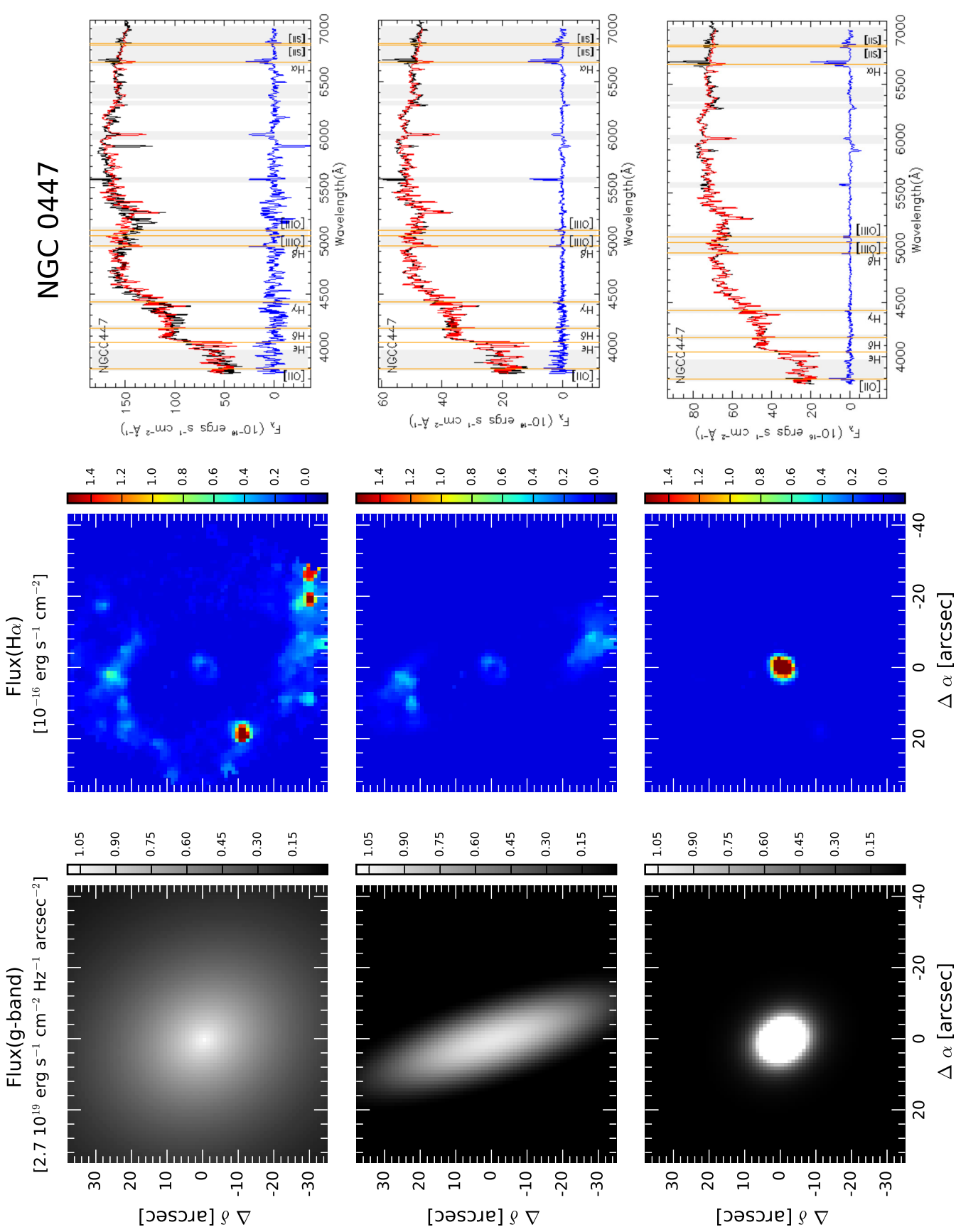
NGC 0447
Flux(g-band)
[2.7 10^19 erg s^-1 cm^-2 Hz^-1 arcsec^-2]
Flux(Hα)
[10^-16 erg s^-1 cm^-2]
Δ δ [arcsec]
Δ α [arcsec]
Wavelength(Å)
NGC0447
[OII]
Hε
Hδ
Hγ
[OIII]
Hβ
[OIII]
[SII]
[SII]
Hα

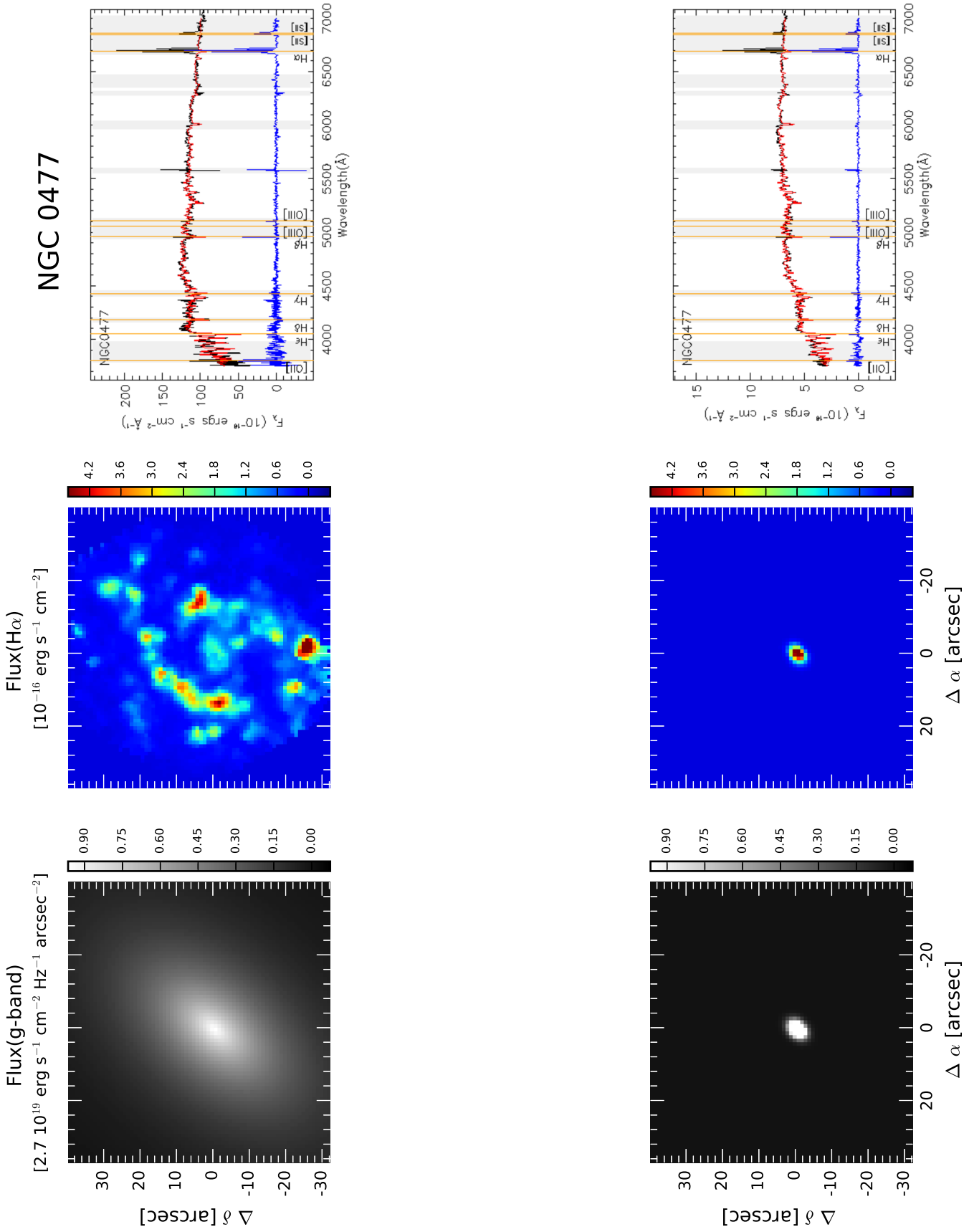
NGC 0477
Flux(g-band)
[2.7 10^19 erg s^-1 cm^-2 Hz^-1 arcsec^-2]
Flux(Hα)
[10^-16 erg s^-1 cm^-2]
Δ δ [arcsec]
Δ α [arcsec]
Wavelength(Å)
F_λ (10^-16 ergs s^-1 cm^-2 Å^-1)
NGC0477
[OII]
Hε
Hδ
Hγ
Hβ
[OIII]
[OIII]
[SII]
[SII]
Hα

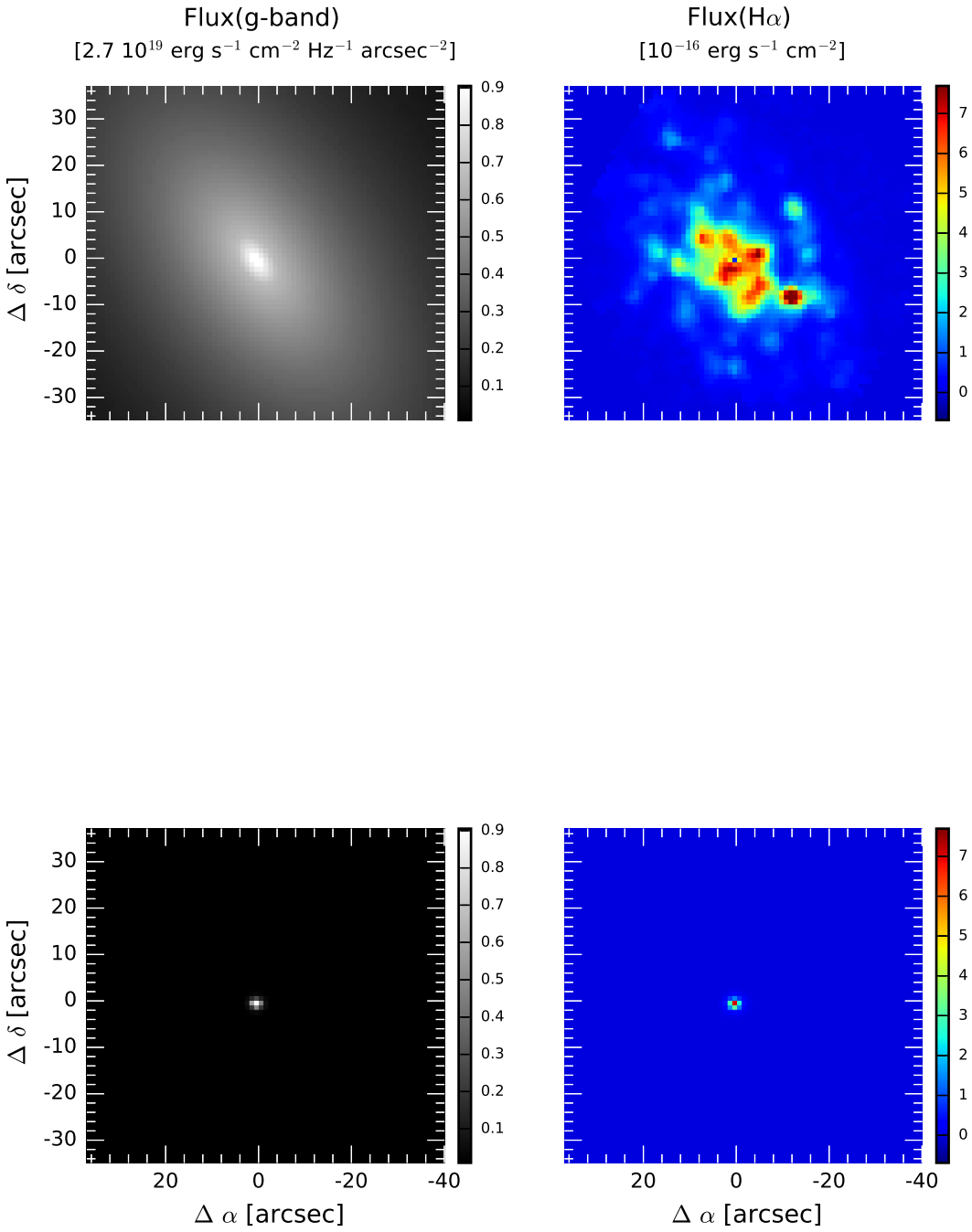
Flux(g-band)
[2.7 10^19 erg s^-1 cm^-2 Hz^-1 arcsec^-2]
Flux(Hα)
[10^-16 erg s^-1 cm^-2]
Δ δ [arcsec]
Δ α [arcsec]

NGC 0496

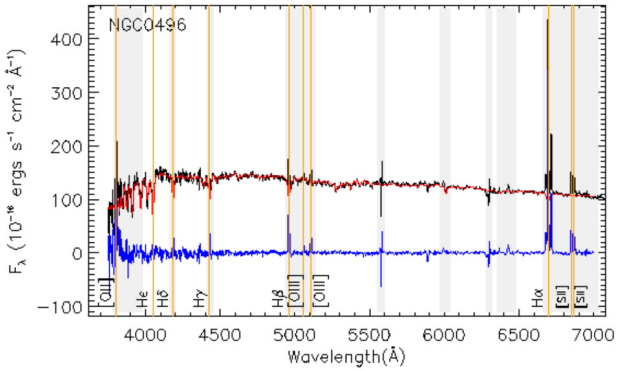
NGC0496
Wavelength(Å)

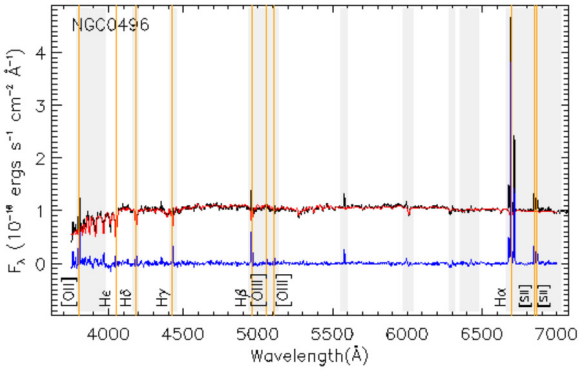
NGC0496
Wavelength(Å)

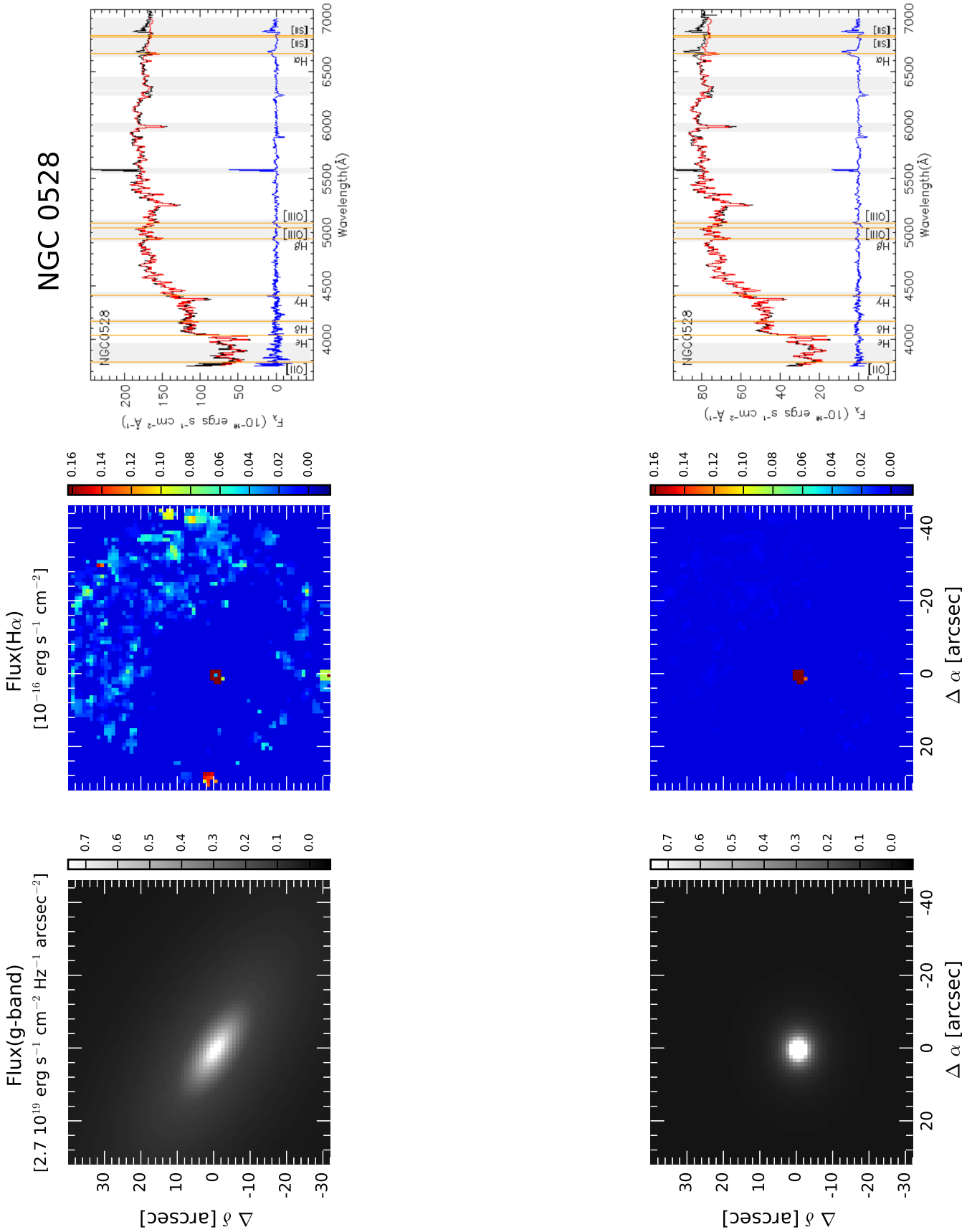
NGC 0528
Flux(g-band)
[2.7 10^19 erg s^-1 cm^-2 Hz^-1 arcsec^-2]
Flux(Hα)
[10^-16 erg s^-1 cm^-2]
Δ δ [arcsec]
Δ α [arcsec]
Wavelength(Å)
F_λ (10^-16 ergs s^-1 cm^-2 Å^-1)
NGC0528
[OII]
Hε
Hδ
Hγ
Hβ
[OIII]
[OIII]
[SII]
[SII]
Hα

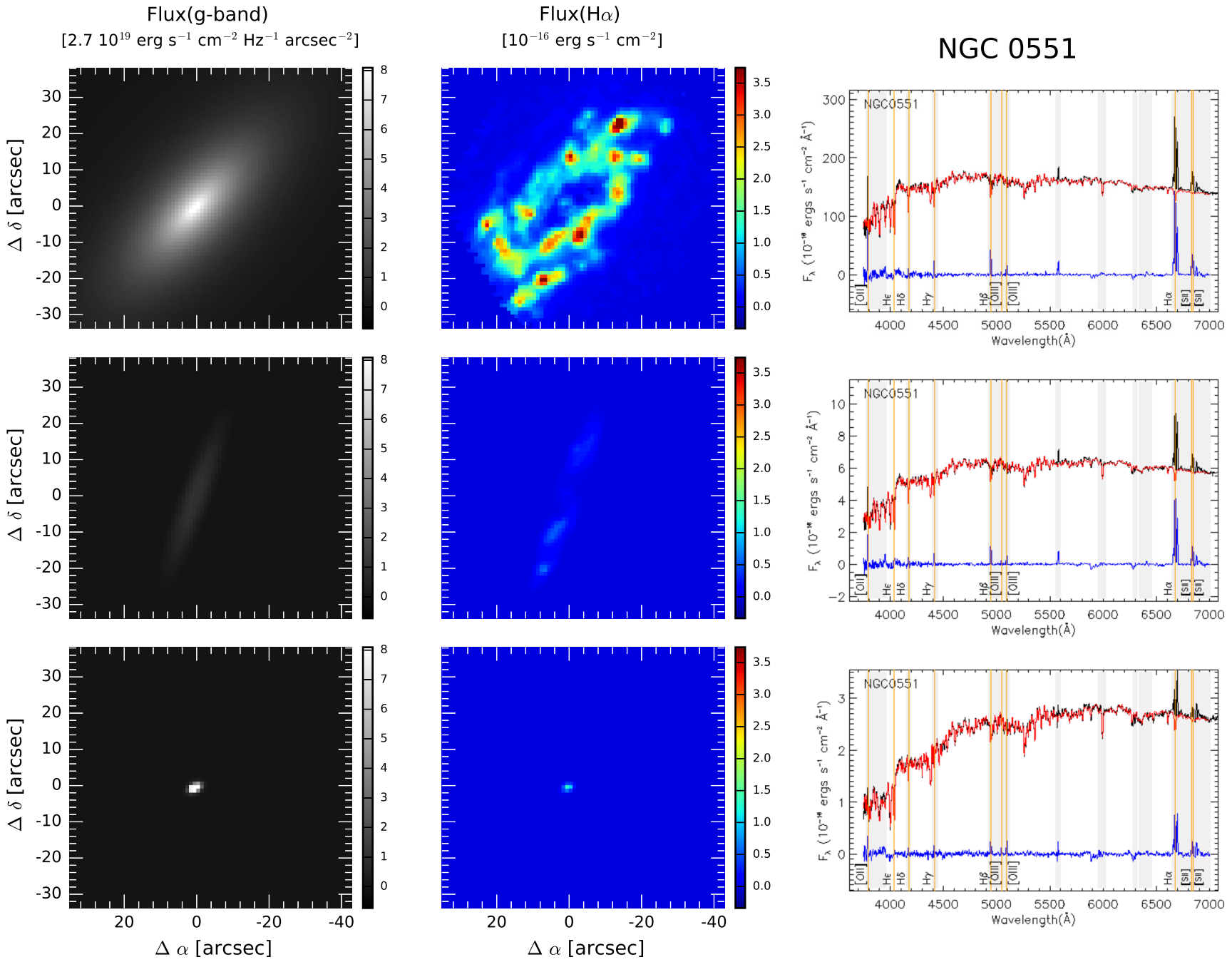
Flux(g-band)
[2.7 10^19 erg s^-1 cm^-2 Hz^-1 arcsec^-2]
Flux(Hα)
[10^-16 erg s^-1 cm^-2]
NGC 0551
Δ δ [arcsec]
Δ α [arcsec]
NGC0551
Wavelength(Å)
[OII]
Hε
Hδ
Hγ
Hβ
[OIII]
[OIII]
Hα
[SII]
[SII]

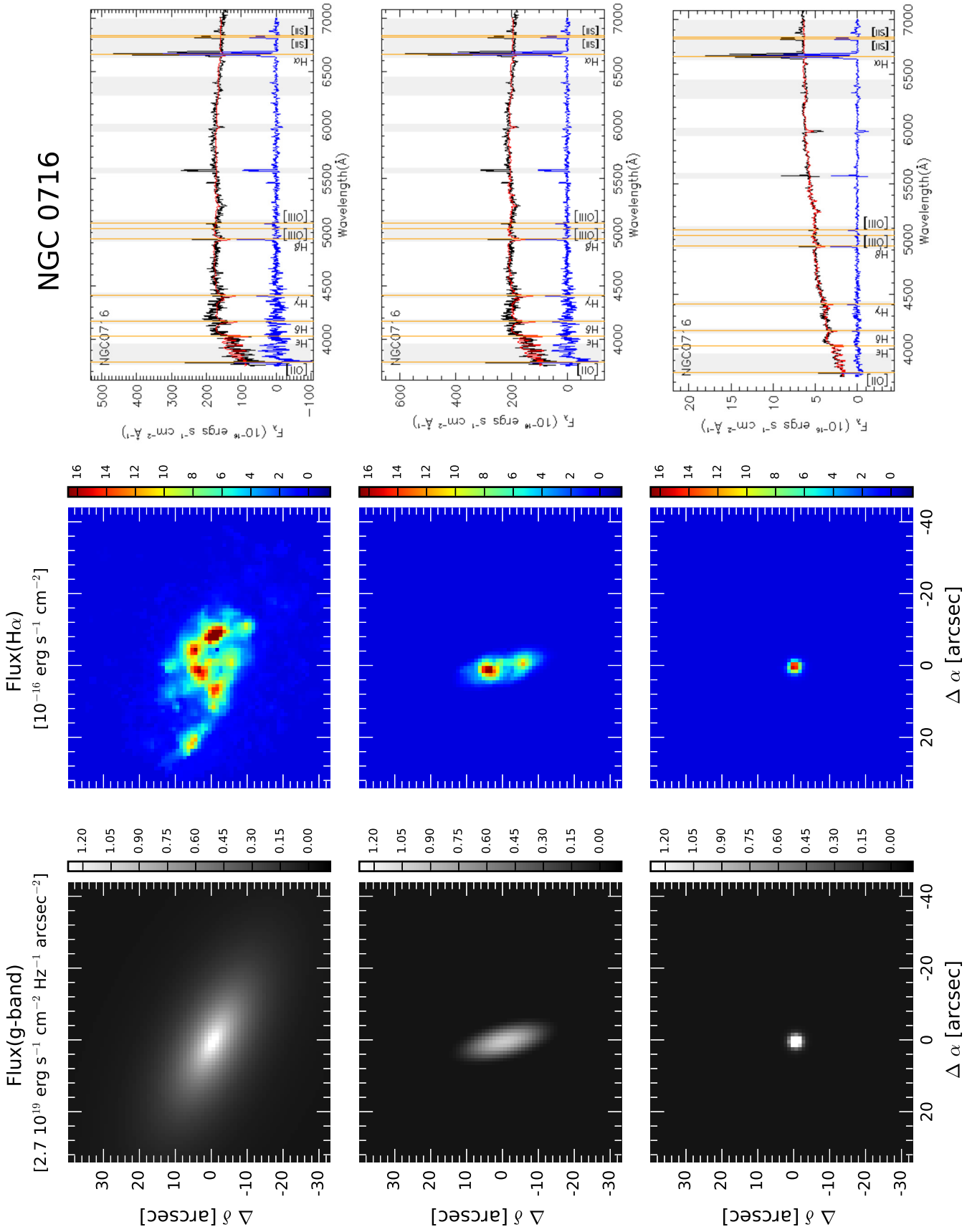
NGC 0716
Flux(g-band)
[2.7 10^19 erg s^-1 cm^-2 Hz^-1 arcsec^-2]
Flux(Hα)
[10^-16 erg s^-1 cm^-2]
Δ δ [arcsec]
Δ α [arcsec]
Wavelength(Å)
F_λ (10^-16 ergs s^-1 cm^-2 Å^-1)
NGC0716
[OII]
[SII]
[SII]
Hα
[OIII]
[OIII]
Hβ
Hγ
Hδ
He
[OII]

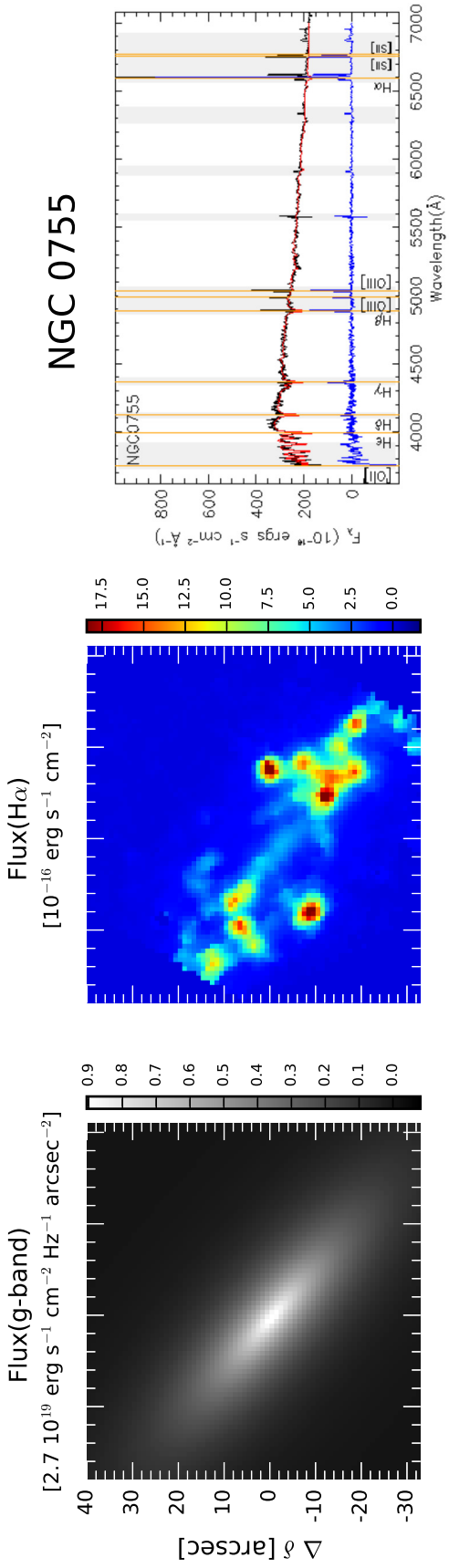
NGC 0755
NGC0755
[OII]
Hε
Hδ
Hγ
Hβ
[OIII]
[OIII]
Hα
[SII]
[SII]
Wavelength(Å)
Flux(Hα)
[10⁻¹⁶ erg s⁻¹ cm⁻²]
Flux(g-band)
[2.7 10¹⁹ erg s⁻¹ cm⁻² Hz⁻¹ arcsec⁻²]
Δ δ [arcsec]

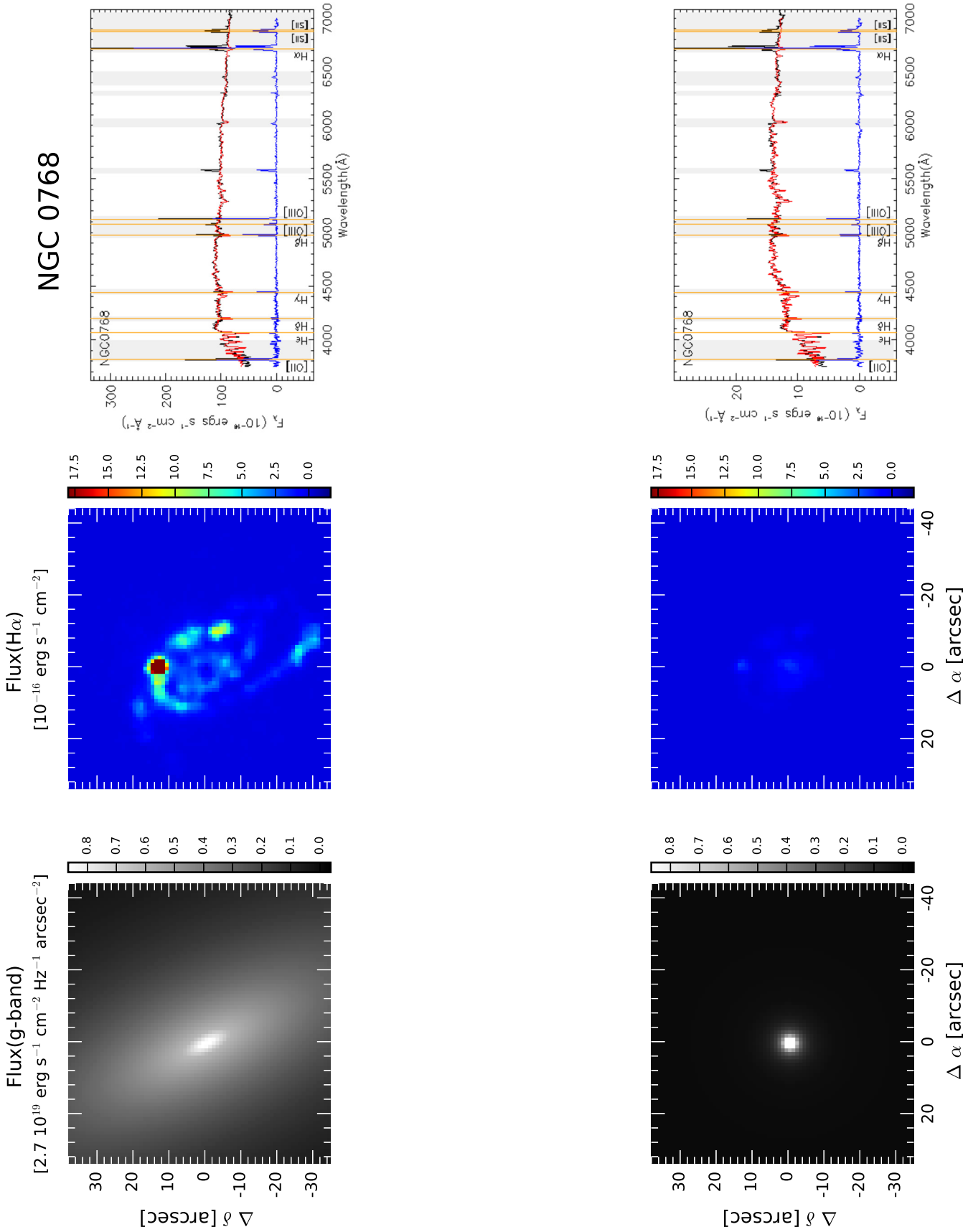
NGC 0768
Flux(Hα)
[10^-16 erg s^-1 cm^-2]
Flux(g-band)
[2.7 10^19 erg s^-1 cm^-2 Hz^-1 arcsec^-2]
Δ δ [arcsec]
Δ α [arcsec]
Wavelength(Å)
NGC0768
[OII]
Hε
Hδ
Hγ
Hβ
[OIII]
[OIII]
Hα
[SII]
[SII]

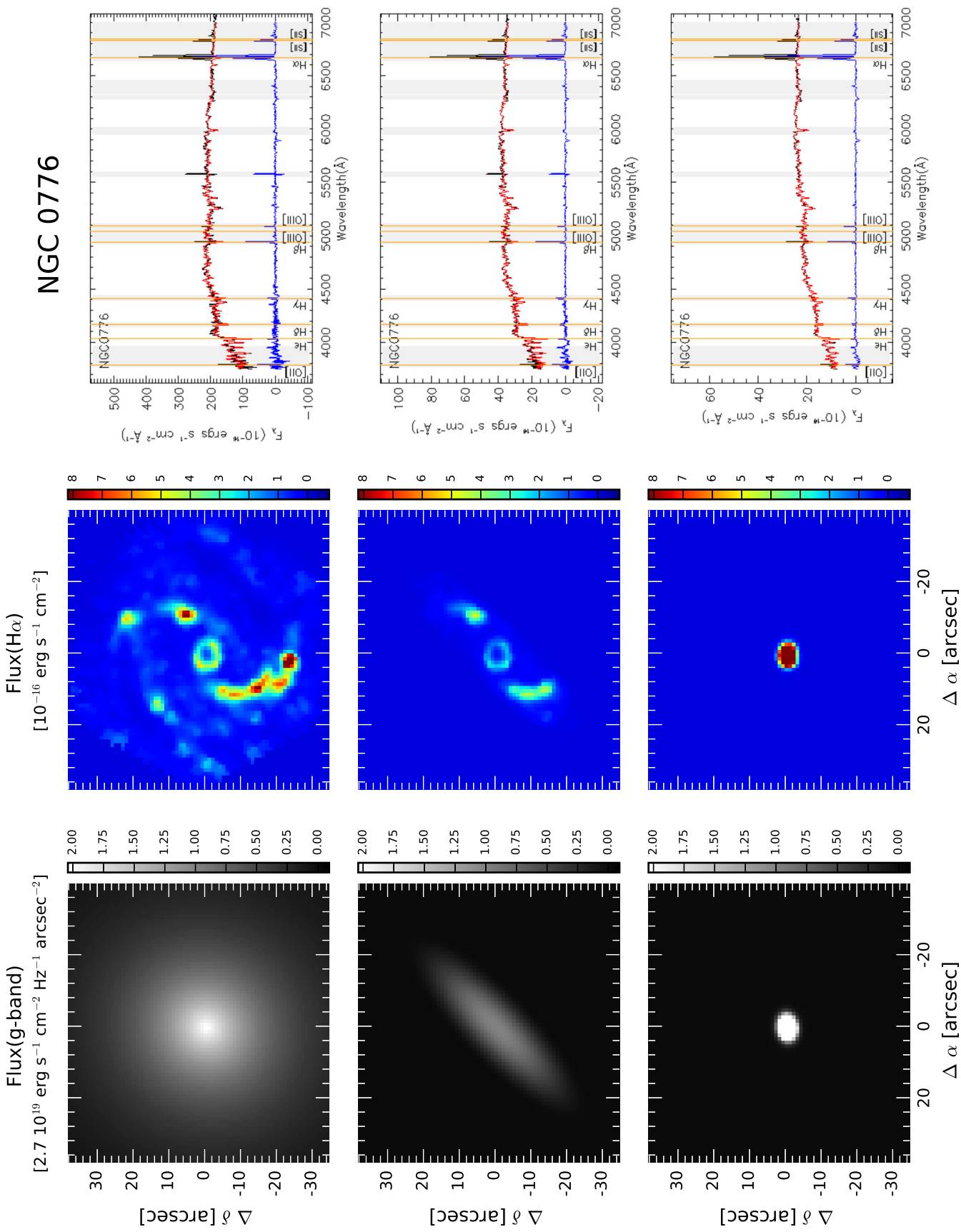
NGC 0776
Flux(g-band)
[2.7 10^19 erg s^-1 cm^-2 Hz^-1 arcsec^-2]
Flux(Hα)
[10^-16 erg s^-1 cm^-2]
Δ δ [arcsec]
Δ α [arcsec]
Wavelength(Å)
NGC0776
[OII]
Hε
Hδ
Hγ
[OIII]
Hβ
[OIII]
[SII]
[SII]
Hα

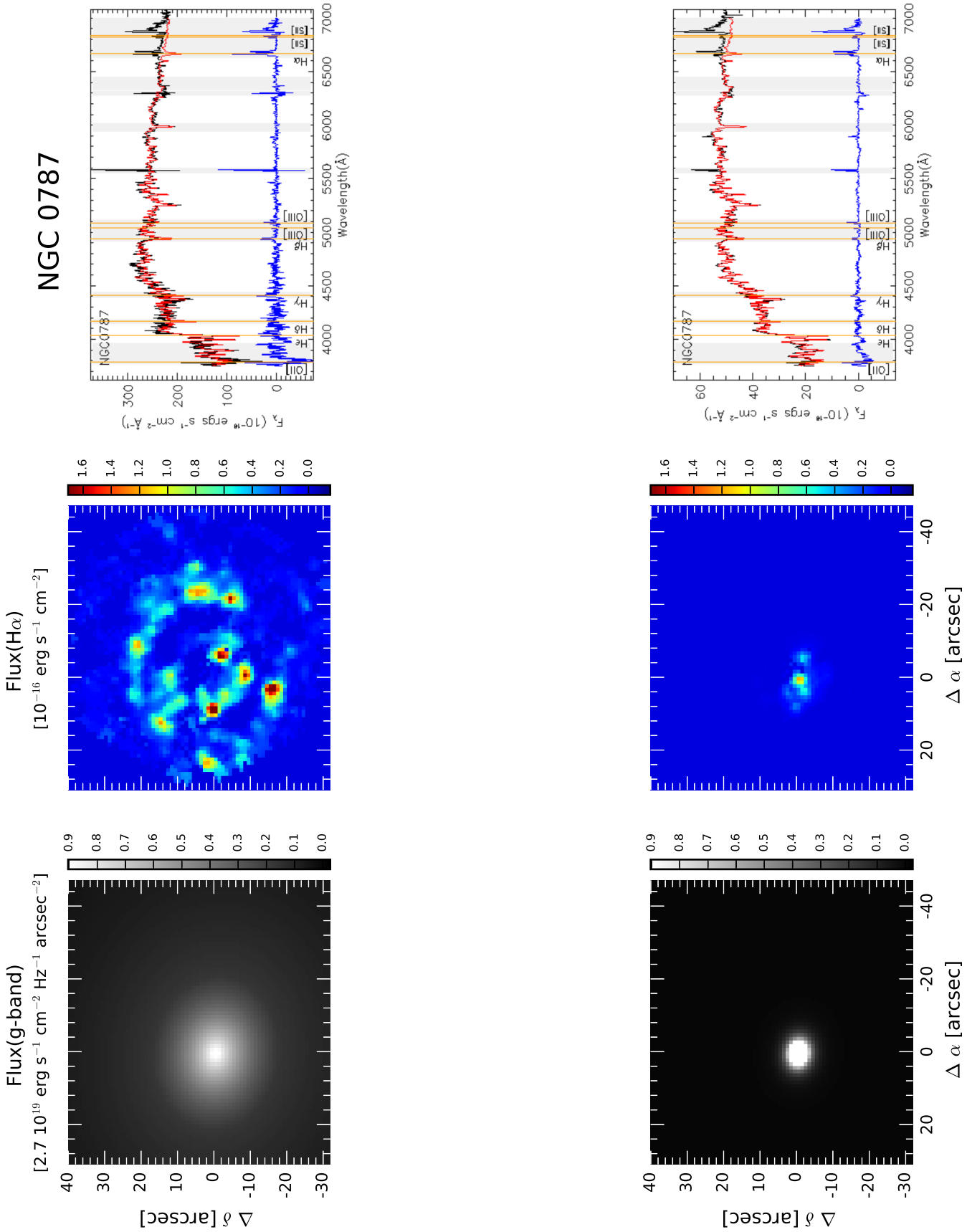
NGC 0787
NGC0787
Wavelength(Å)
[OII]
Hε
Hδ
Hγ
[OIII]
Hβ
Hα
[SII]
Flux(Hα)
[10^-16 erg s^-1 cm^-2]
Flux(g-band)
[2.7 10^19 erg s^-1 cm^-2 Hz^-1 arcsec^-2]
Δ δ [arcsec]
Δ α [arcsec]

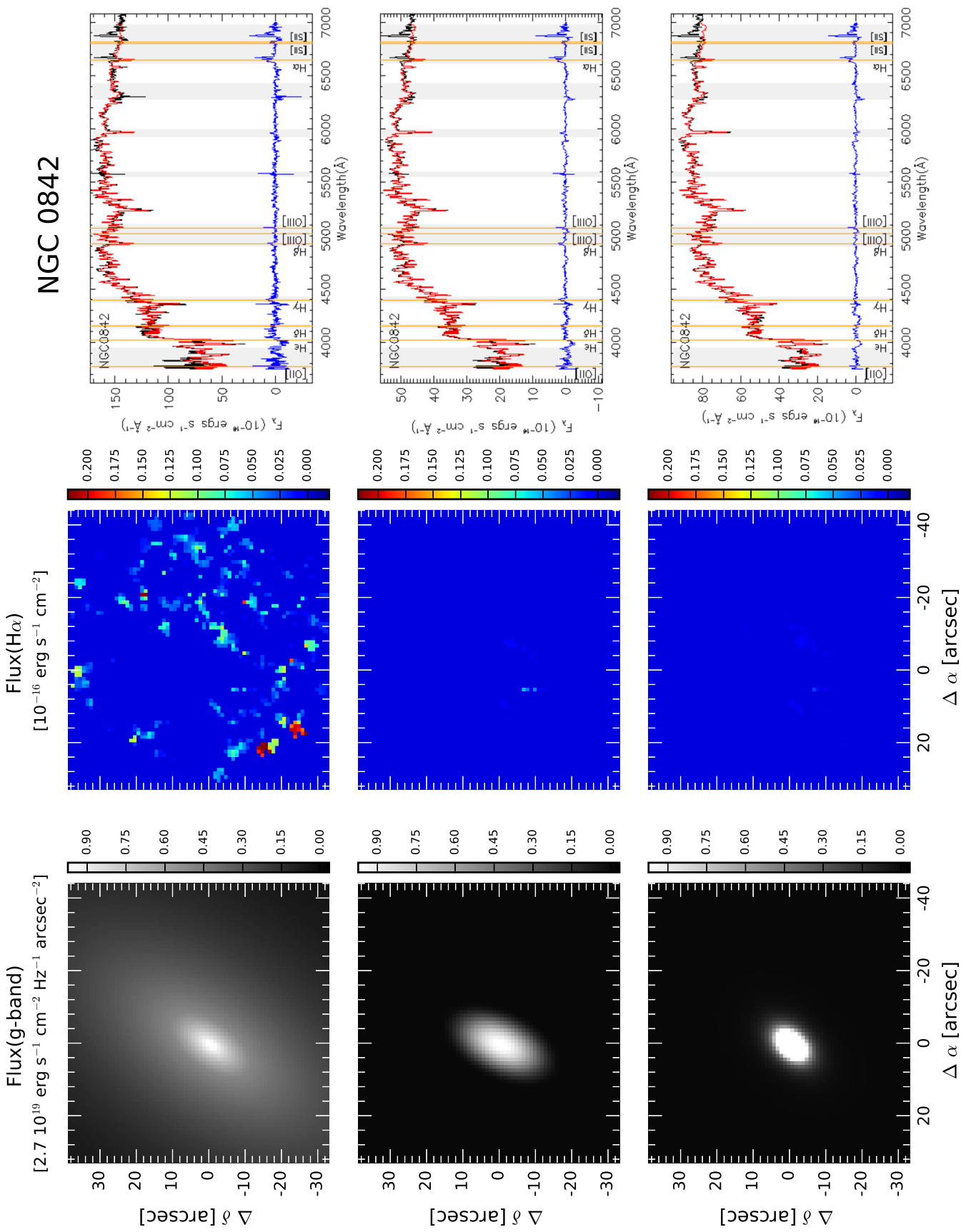
NGC 0842
Flux(g-band)
[2.7 10^19 erg s^-1 cm^-2 Hz^-1 arcsec^-2]
Flux(Hα)
[10^-16 erg s^-1 cm^-2]
Δ δ [arcsec]
Δ α [arcsec]
Wavelength(Å)
NGC0842
[OII]
Hε
Hδ
Hγ
[OIII]
Hβ
[OIII]
Hα
[SII]
[SII]

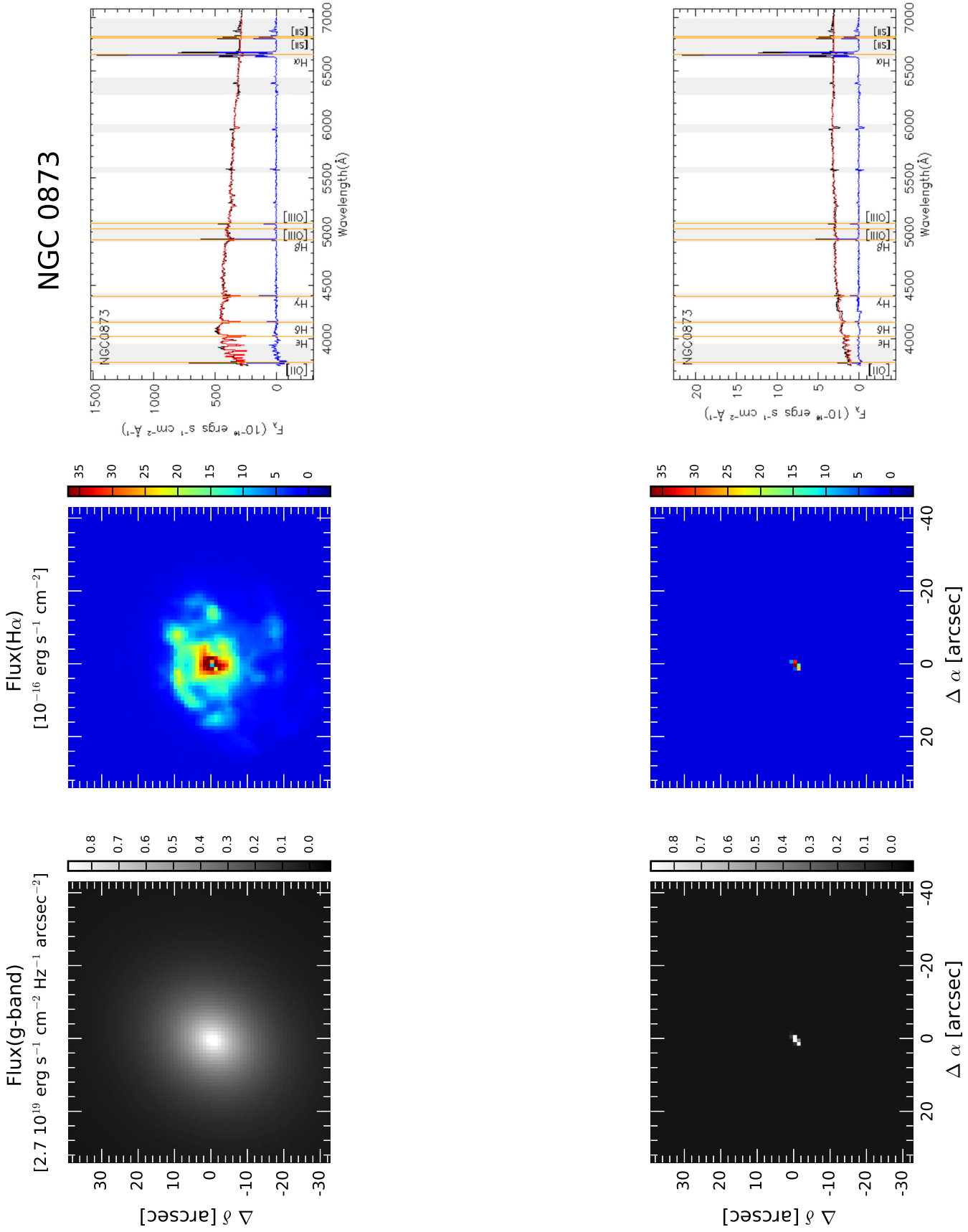
NGC 0873
NGC0873
[OII]
Hε
Hδ
Hγ
H8
[OIII]
[OIII]
[SII]
[SII]
Hα
Wavelength(Å)
F_λ (10^{-16} ergs s^{-1} cm^{-2} Å^{-1})
Flux(Hα)
[10^{-16} erg s^{-1} cm^{-2}]
Flux(g-band)
[2.7 10^{19} erg s^{-1} cm^{-2} Hz^{-1} arcsec^{-2}]
Δ δ [arcsec]
Δ α [arcsec]

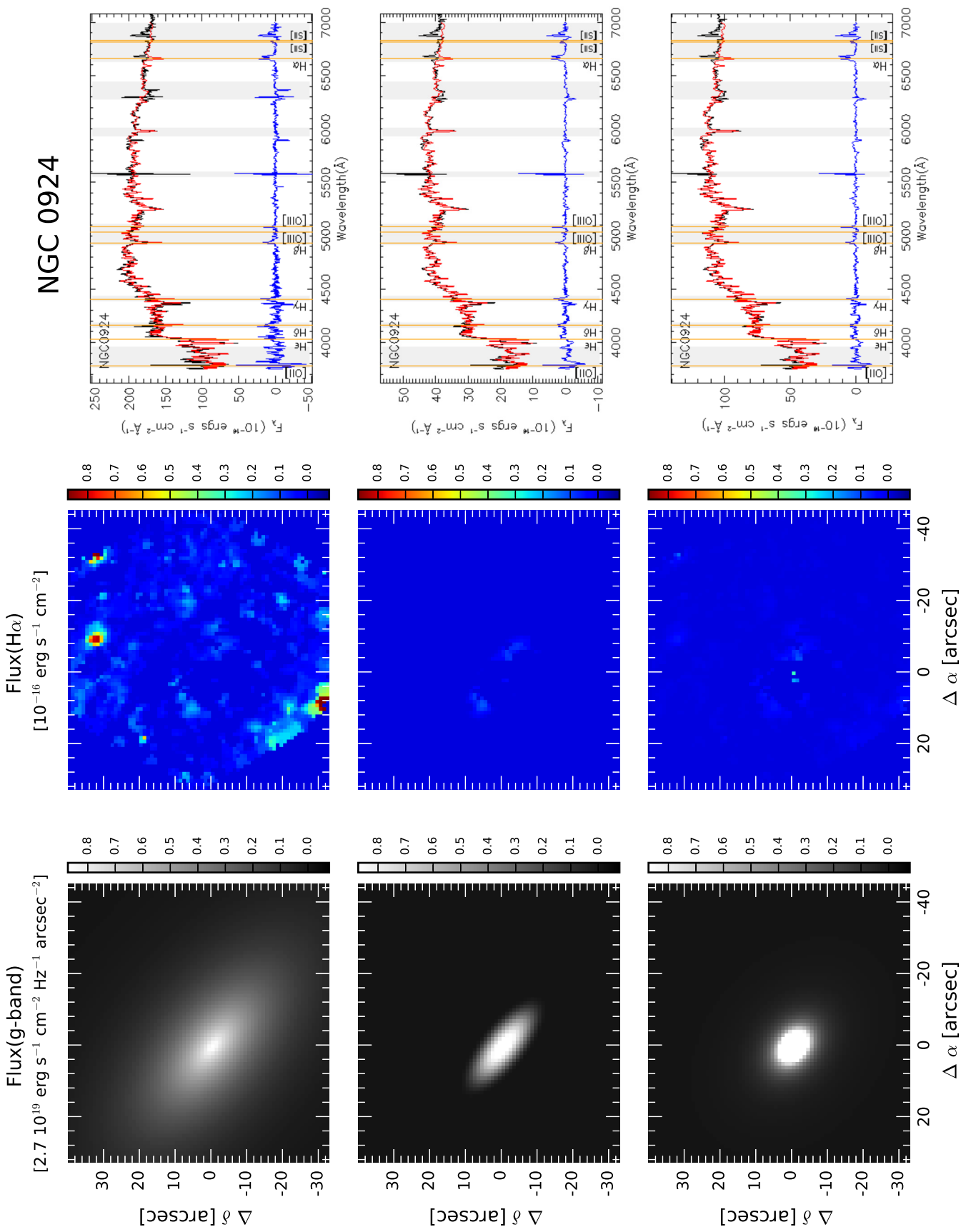
NGC 0924
Flux(g-band)
[2.7 10^19 erg s^-1 cm^-2 Hz^-1 arcsec^-2]
Flux(Hα)
[10^-16 erg s^-1 cm^-2]
Δ δ [arcsec]
Δ α [arcsec]
Wavelength(Å)
NGC0924
[OII]
Hε
Hδ
Hγ
[OIII]
Hβ
[OIII]
Hα
[SII]
[SII]

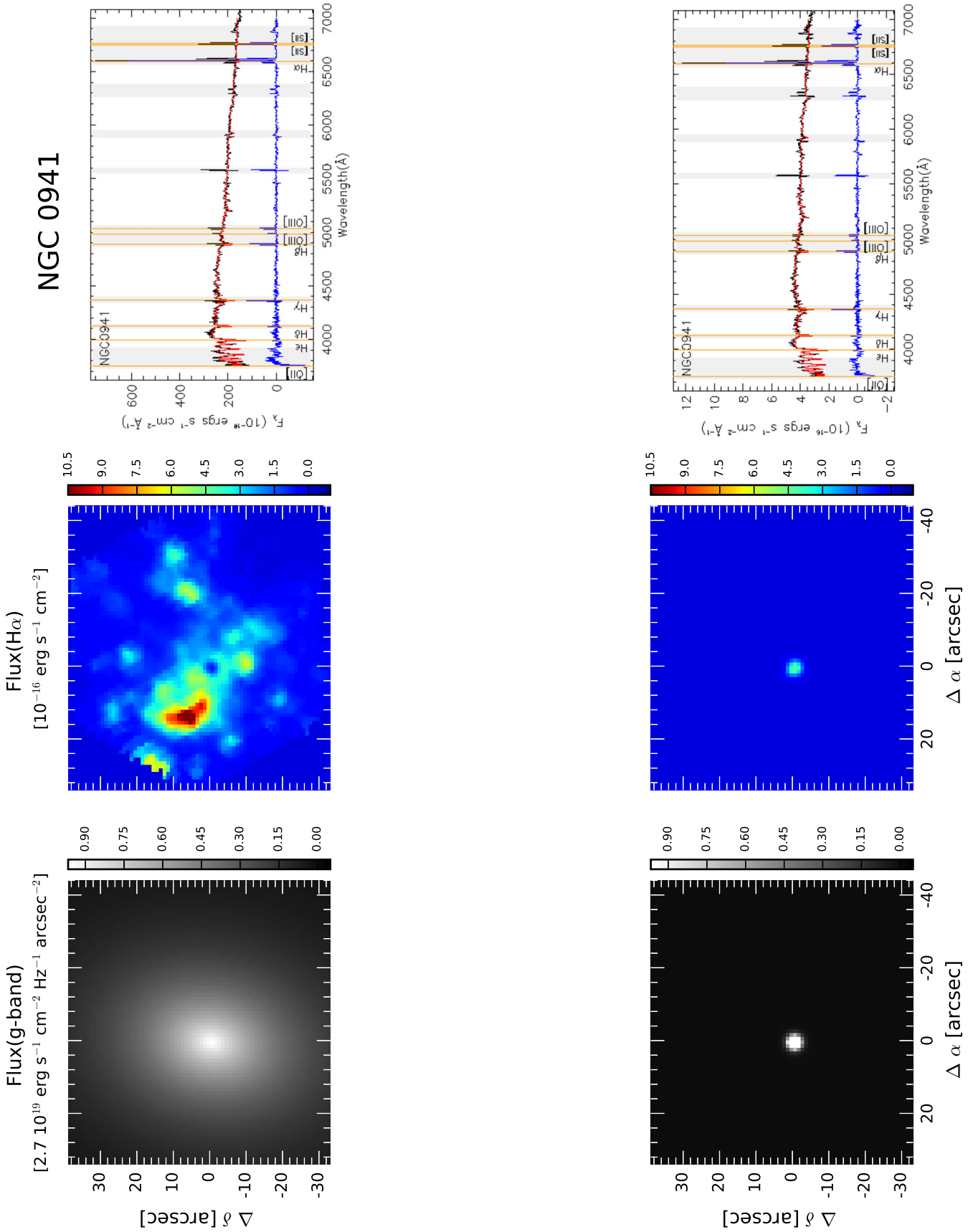
NGC 0941
Flux(Hα)
[10^-16 erg s^-1 cm^-2]
Flux(g-band)
[2.7 10^19 erg s^-1 cm^-2 Hz^-1 arcsec^-2]
Δ δ [arcsec]
Δ α [arcsec]
Wavelength(Å)
NGC0941
[OII]
Hε
Hδ
Hγ
Hβ
[OIII]
[OIII]
Hα
[SII]
[SII]

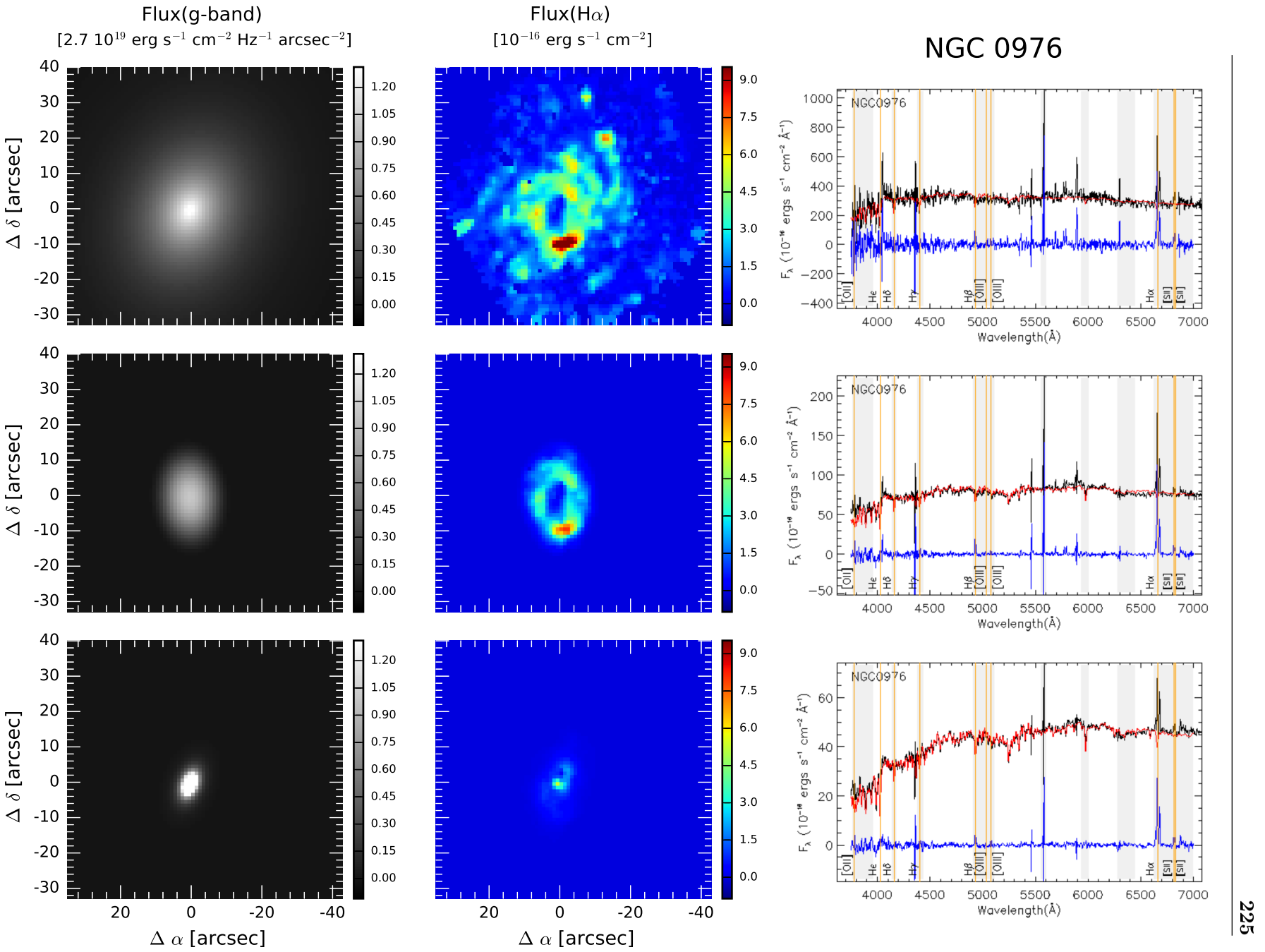
Flux(g-band)
[2.7 10^19 erg s^-1 cm^-2 Hz^-1 arcsec^-2]
Flux(Hα)
[10^-16 erg s^-1 cm^-2]
NGC 0976
Δ δ [arcsec]
Δ α [arcsec]
Wavelength(Å)
NGC0976
[OII]
Hε
Hδ
Hγ
Hβ
[OIII]
[OIII]
Hα
[SII]
[SII]

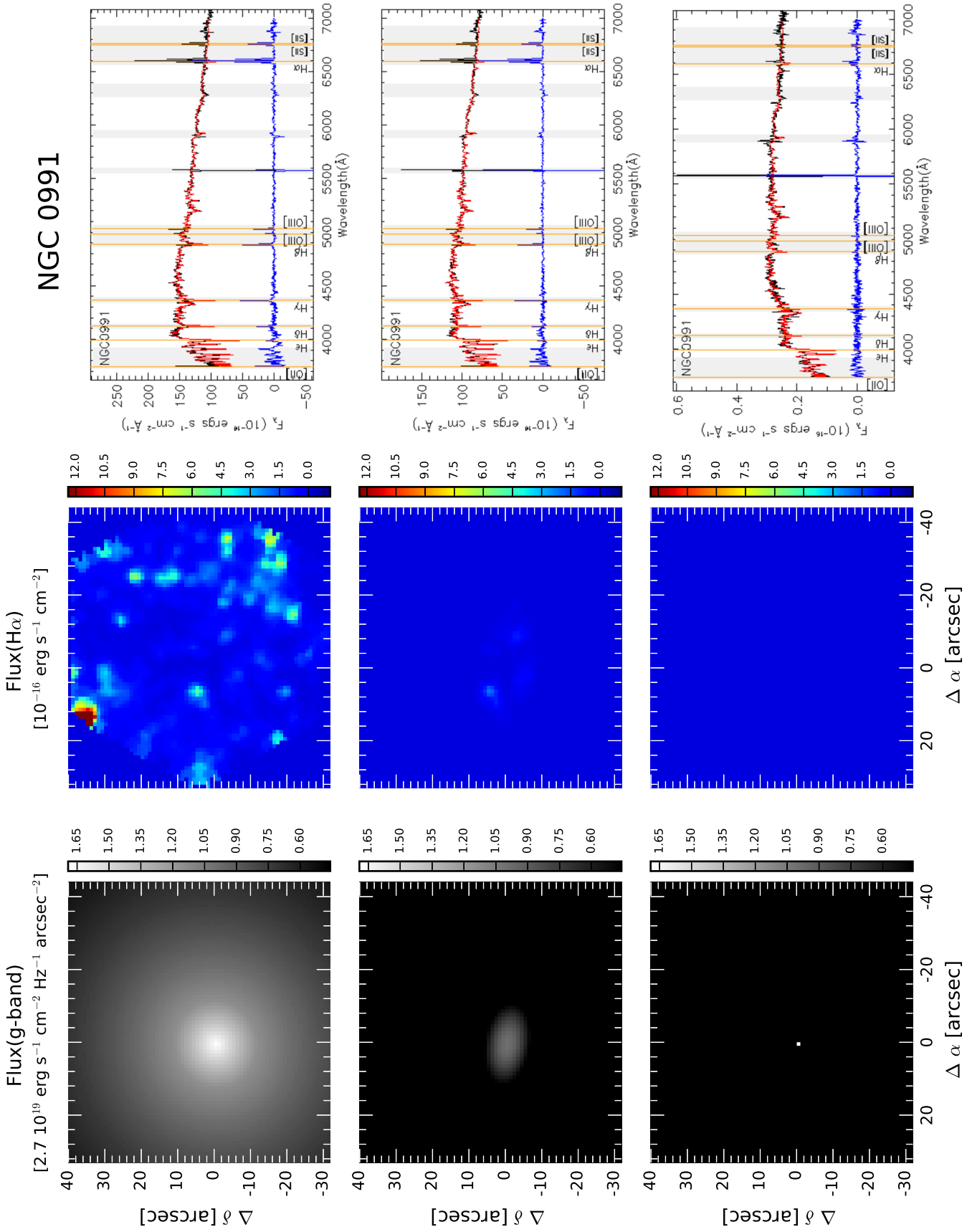
NGC 0991
Flux(g-band)
[2.7 10^19 erg s^-1 cm^-2 Hz^-1 arcsec^-2]
Flux(Hα)
[10^-16 erg s^-1 cm^-2]
Δ δ [arcsec]
Δ α [arcsec]
Wavelength(Å)
NGC0991
[OII]
Hε
Hδ
Hγ
Hβ
[OIII]
[OIII]
Hα
[SII]
[SII]

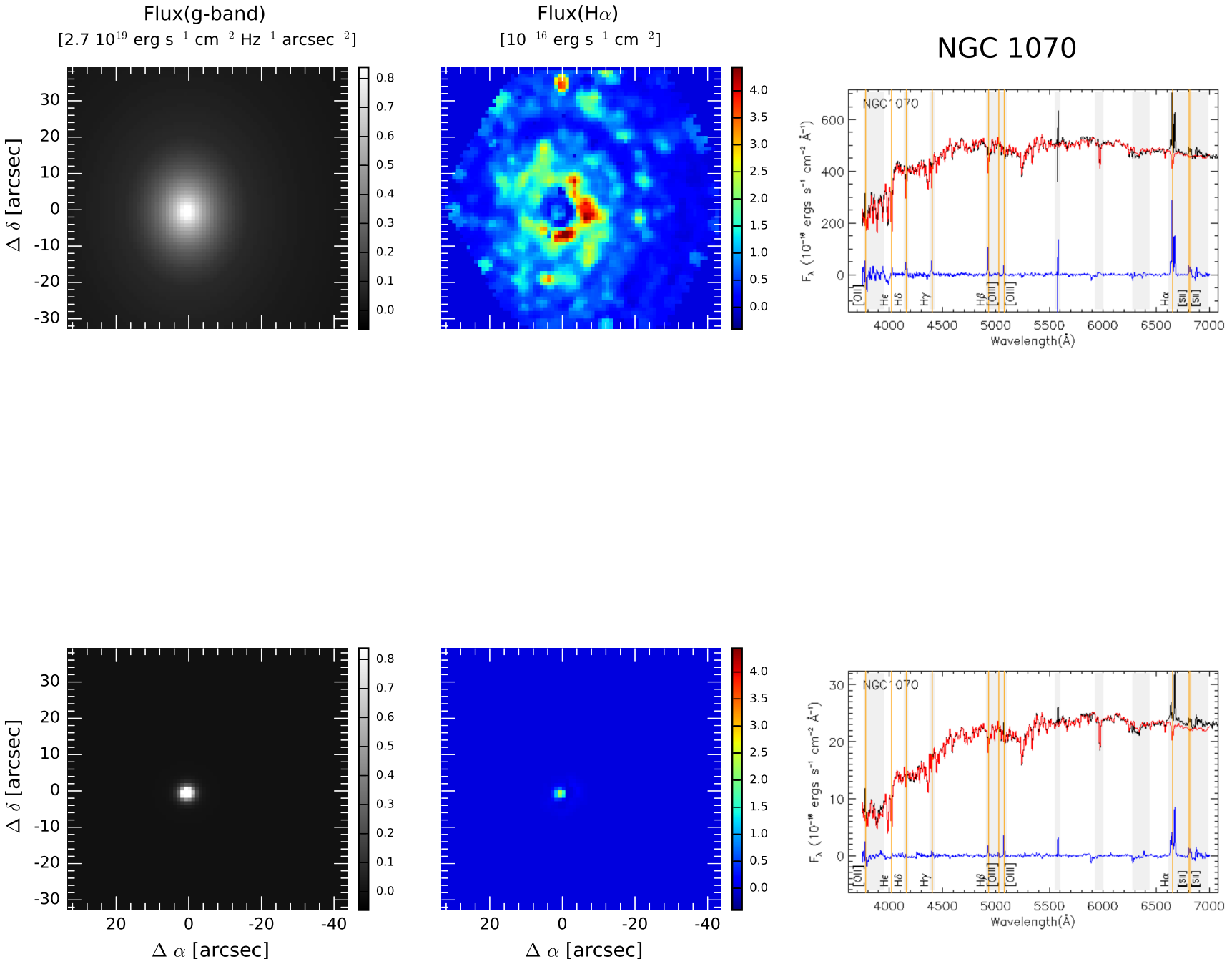
Flux(g-band)
[2.7 10^19 erg s^-1 cm^-2 Hz^-1 arcsec^-2]
Flux(Hα)
[10^-16 erg s^-1 cm^-2]
NGC 1070
Δ δ [arcsec]
Δ α [arcsec]
F_λ (10^-18 ergs s^-1 cm^-2 Å^-1)
Wavelength(Å)
[OII]
Hε
Hδ
Hγ
Hβ
[OIII]
[OIII]
Hα
[SII]
[SII]

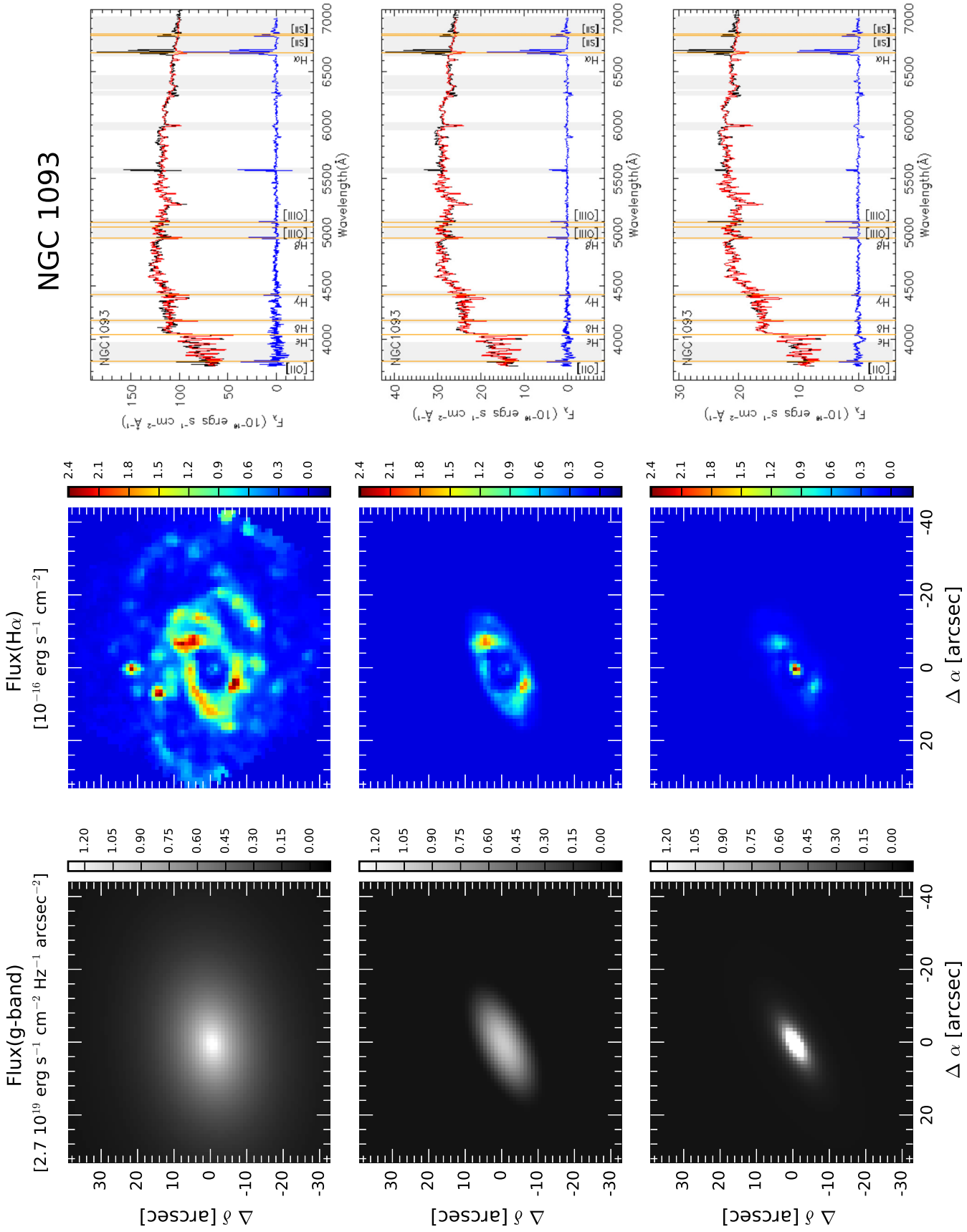
NGC 1093
Flux(g-band)
[2.7 10^19 erg s^-1 cm^-2 Hz^-1 arcsec^-2]
Flux(Hα)
[10^-16 erg s^-1 cm^-2]
Δ δ [arcsec]
Δ α [arcsec]
Wavelength(Å)
NGC1093
[OII]
Hε
Hδ
Hγ
[OIII]
Hβ
[OIII]
[SII]
[SII]
Hα

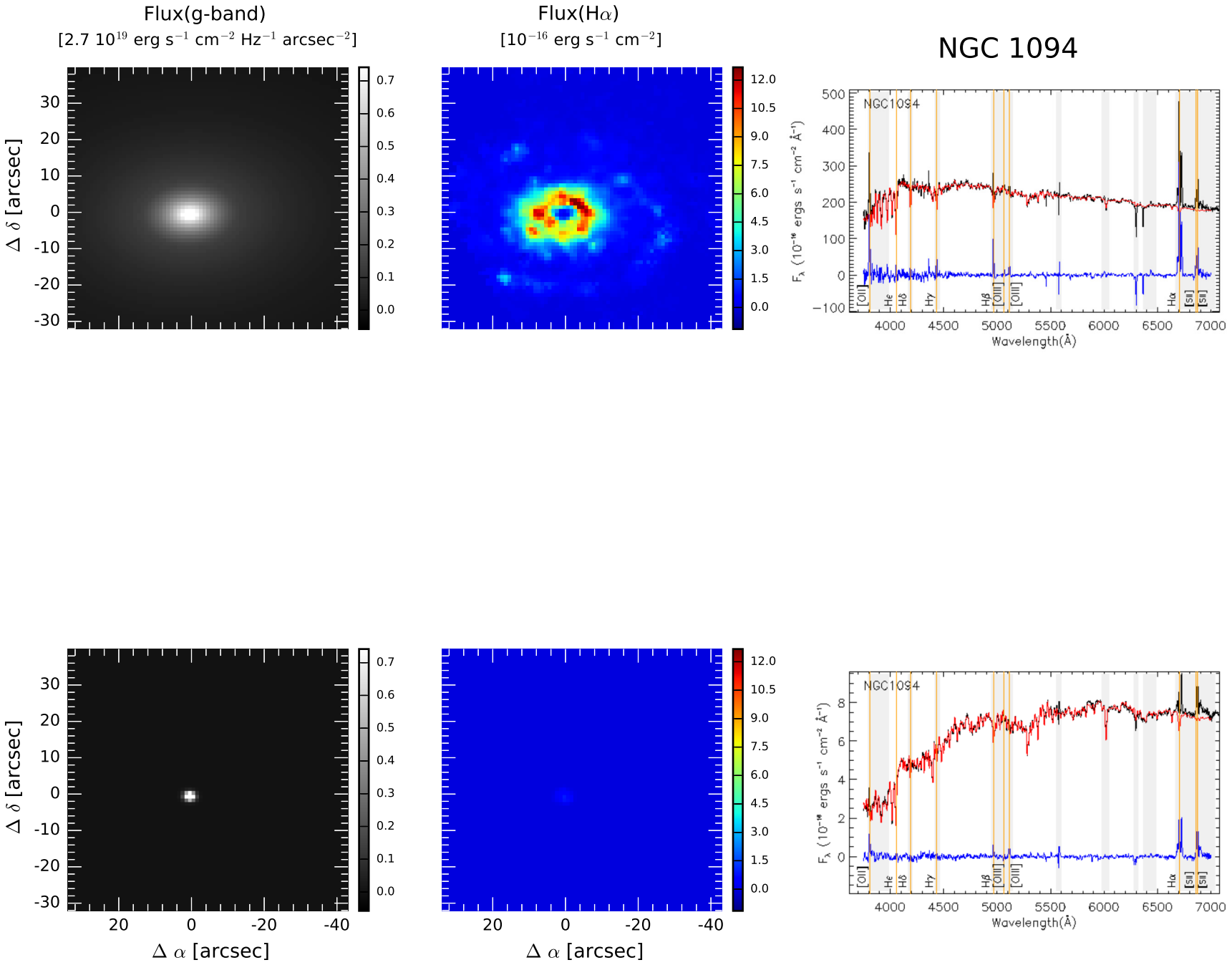
Flux(g-band)
[2.7 10^19 erg s^-1 cm^-2 Hz^-1 arcsec^-2]
Flux(Hα)
[10^-16 erg s^-1 cm^-2]
NGC 1094
Δ δ [arcsec]
Δ α [arcsec]
NGC1094
F_λ (10^-16 ergs s^-1 cm^-2 Å^-1)
Wavelength(Å)
[OII]
Heε
Hδ
Hγ
Hβ
[OIII]
[OIII]
Hα
[SII]
[SII]

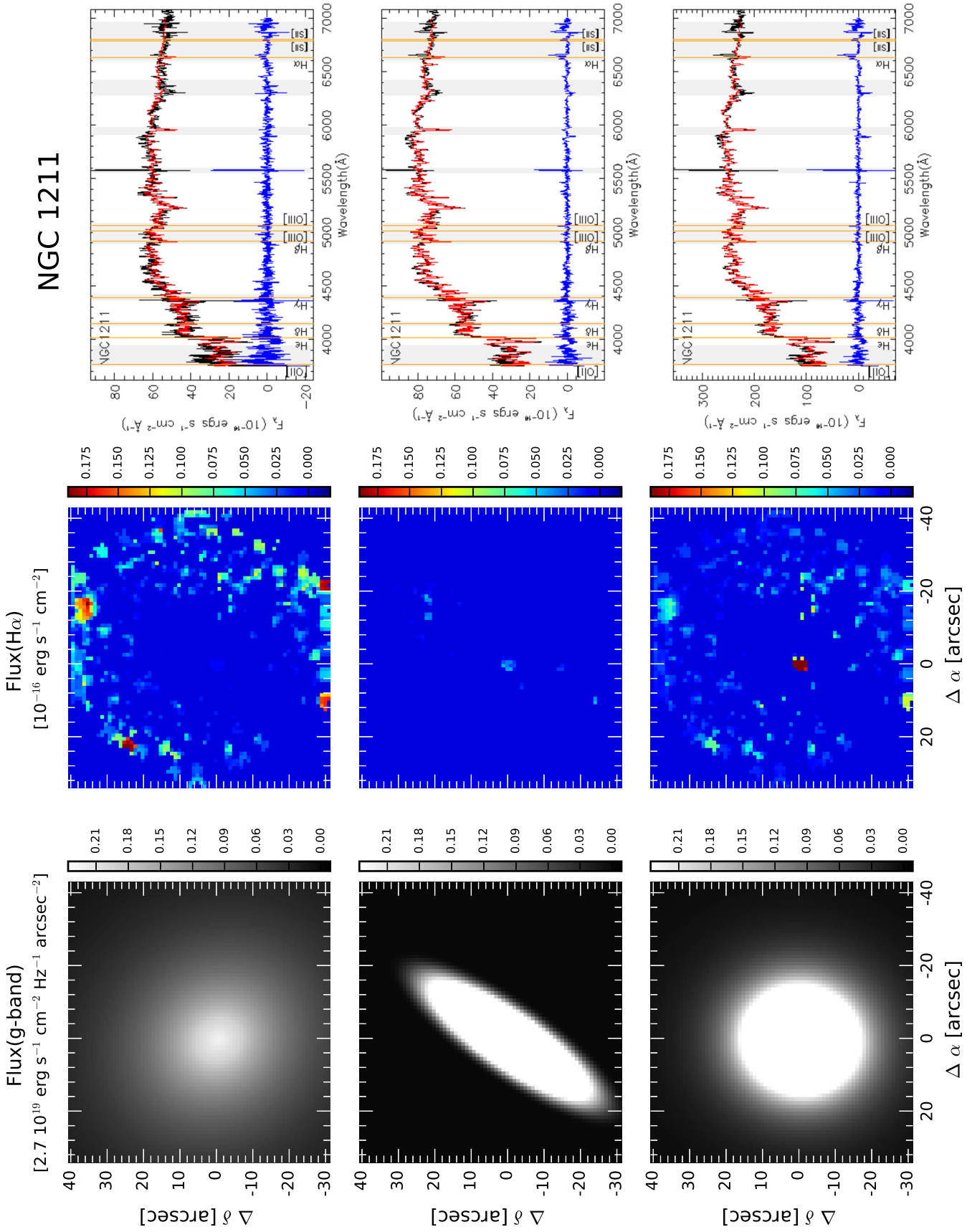
NGC 1211
Flux(g-band)
[2.7 10^19 erg s^-1 cm^-2 Hz^-1 arcsec^-2]
Flux(Hα)
[10^-16 erg s^-1 cm^-2]
Δ δ [arcsec]
Δ α [arcsec]
Wavelength(Å)
F_λ (10^-16 ergs s^-1 cm^-2 Å^-1)
[OII]
Hε
Hδ
Hγ
Hβ
[OIII]
Hα
[SII]

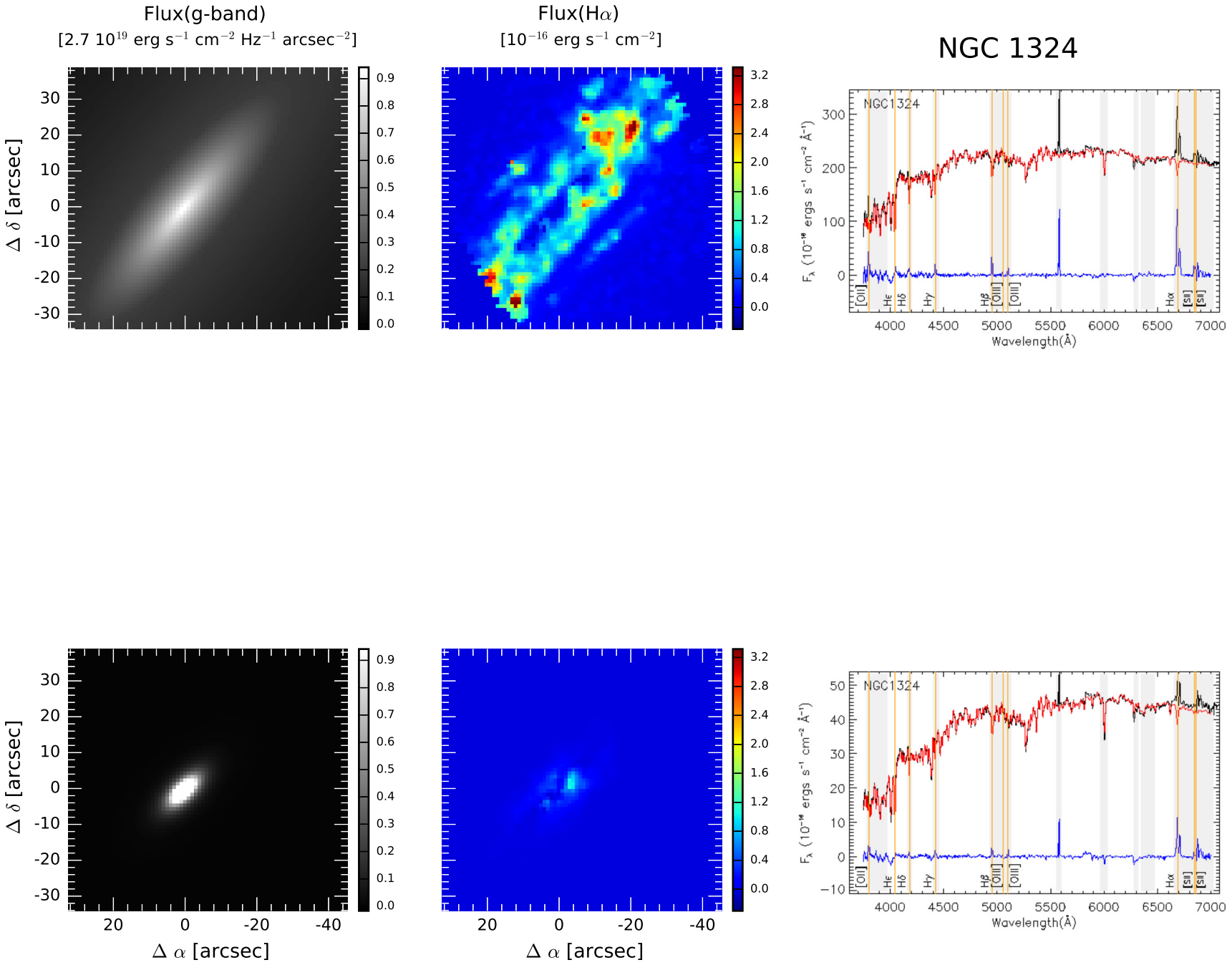
Flux(g-band)
[2.7 10^19 erg s^-1 cm^-2 Hz^-1 arcsec^-2]
Flux(Hα)
[10^-16 erg s^-1 cm^-2]
NGC 1324
Δ δ [arcsec]
Δ α [arcsec]
NGC1324
Wavelength(Å)
[OII]
Hε
Hδ
Hγ
Hβ
[OIII]
[OIII]
Hα
[SII]
[SII]

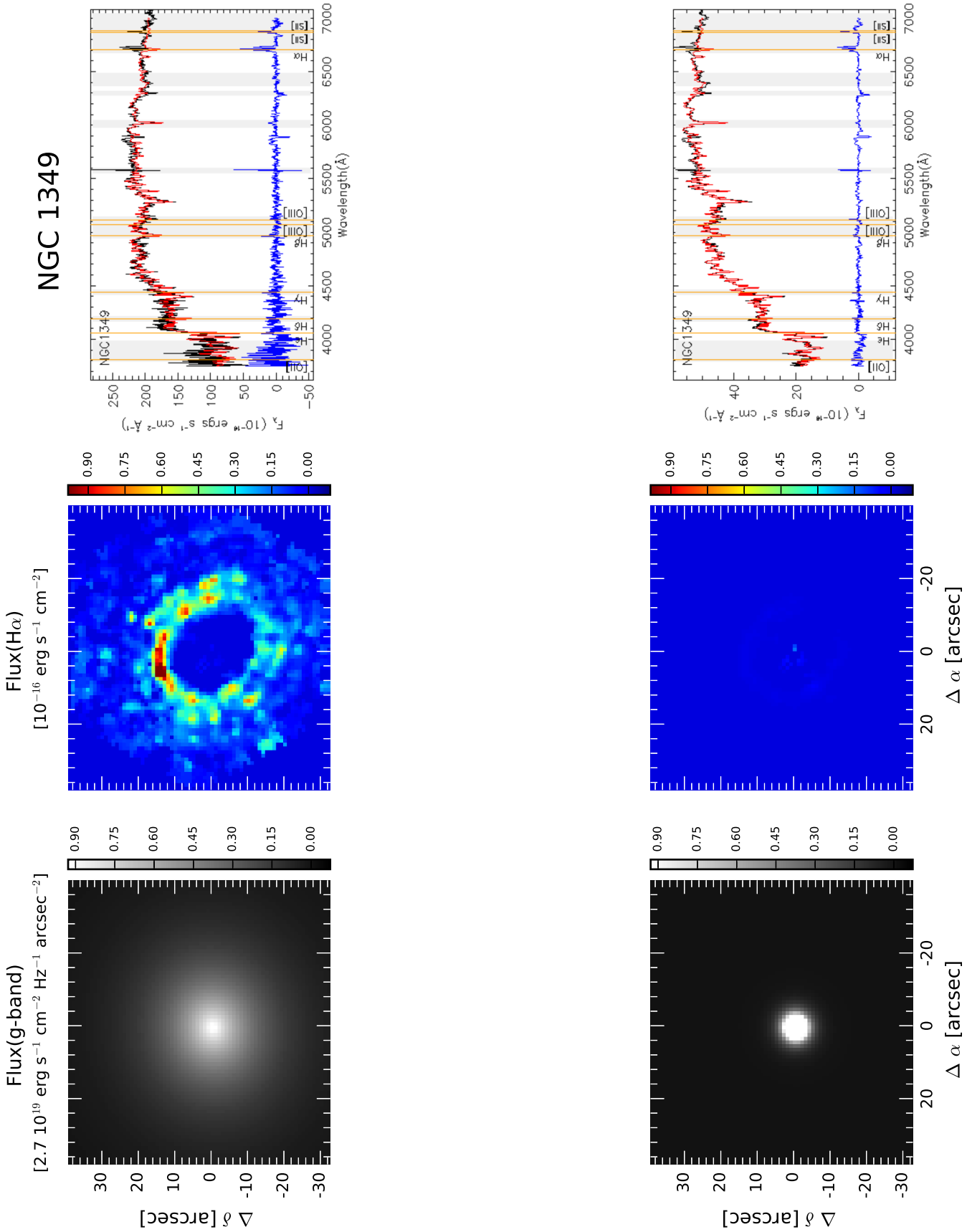
NGC 1349
Flux(g-band)
[2.7 10^19 erg s^-1 cm^-2 Hz^-1 arcsec^-2]
Flux(Hα)
[10^-16 erg s^-1 cm^-2]
Δ δ [arcsec]
Δ α [arcsec]
Wavelength(Å)
F_λ (10^-16 ergs s^-1 cm^-2 Å^-1)
NGC1349
[OII]
Hε
Hδ
Hγ
Hβ
[OIII]
[OIII]
[SII]
[SII]
Hα

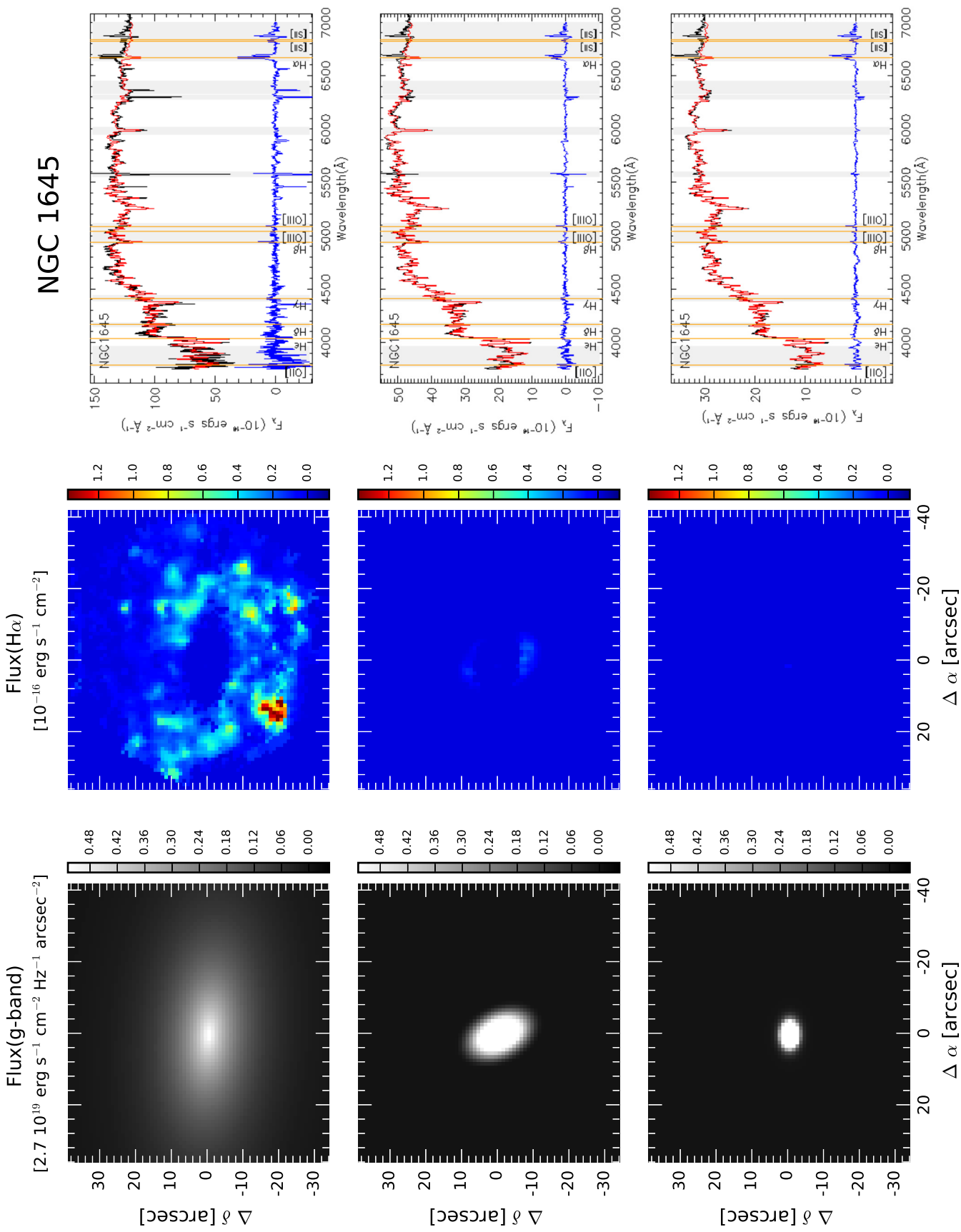
NGC 1645
Flux(g-band)
[2.7 10^19 erg s^-1 cm^-2 Hz^-1 arcsec^-2]
Flux(Hα)
[10^-16 erg s^-1 cm^-2]
Δ δ [arcsec]
Δ α [arcsec]
Wavelength(Å)
NGC1645
[OII]
Hε
Hδ
Hγ
[OIII]
Hβ
[OIII]
[SII]
[SII]
Hα

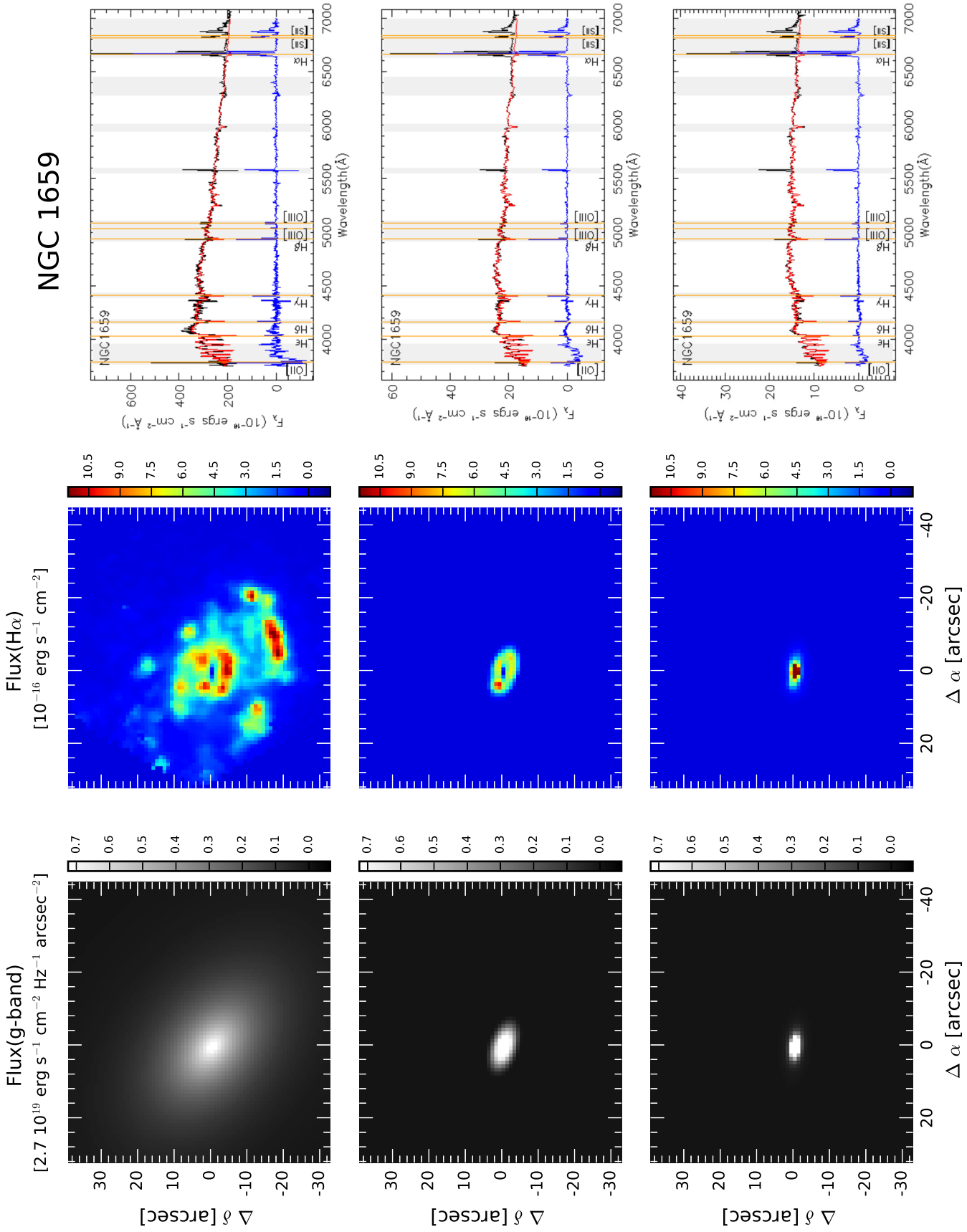
NGC 1659
Flux(g-band)
[2.7 10^19 erg s^-1 cm^-2 Hz^-1 arcsec^-2]
Flux(Hα)
[10^-16 erg s^-1 cm^-2]
Δ δ [arcsec]
Δ α [arcsec]
Wavelength(Å)
F_λ (10^-16 ergs s^-1 cm^-2 Å^-1)
NGC1659
[OII]
Hε
Hδ
Hγ
[OIII]
Hβ
[OIII]
[SII]
[SII]
Hα

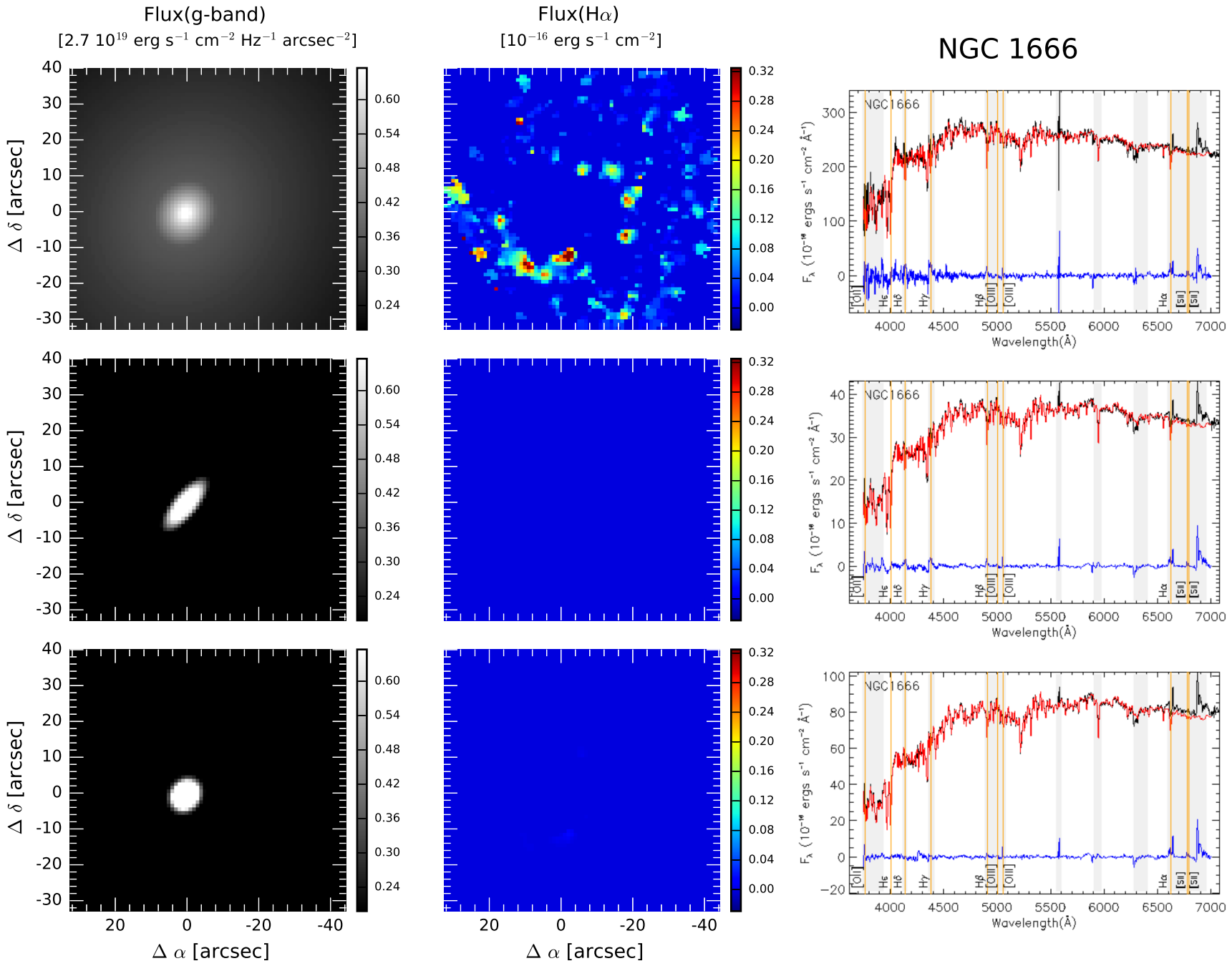
Flux(g-band)
[2.7 10^19 erg s^-1 cm^-2 Hz^-1 arcsec^-2]
Flux(Hα)
[10^-16 erg s^-1 cm^-2]
NGC 1666
Δ δ [arcsec]
Δ α [arcsec]
Wavelength(Å)
NGC1666

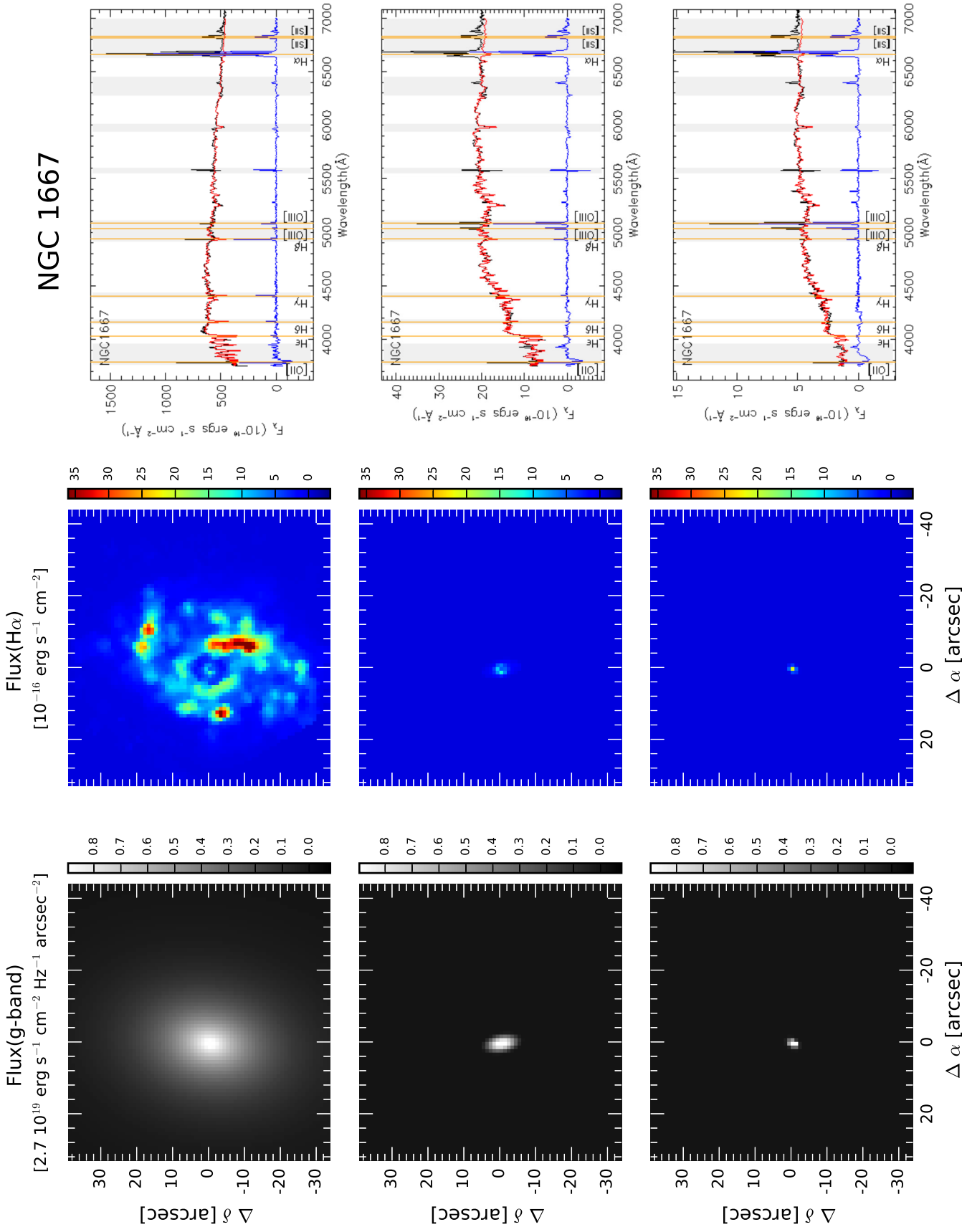
NGC 1667
Flux(g-band)
[2.7 10^19 erg s^-1 cm^-2 Hz^-1 arcsec^-2]
Flux(Hα)
[10^-16 erg s^-1 cm^-2]
Δ δ [arcsec]
Δ α [arcsec]
Wavelength(Å)
F_λ (10^-16 ergs s^-1 cm^-2 Å^-1)
NGC1667
[OII]
Hε
Hδ
Hγ
Hβ
[OIII]
[OIII]
[SII]
[SII]
Hα

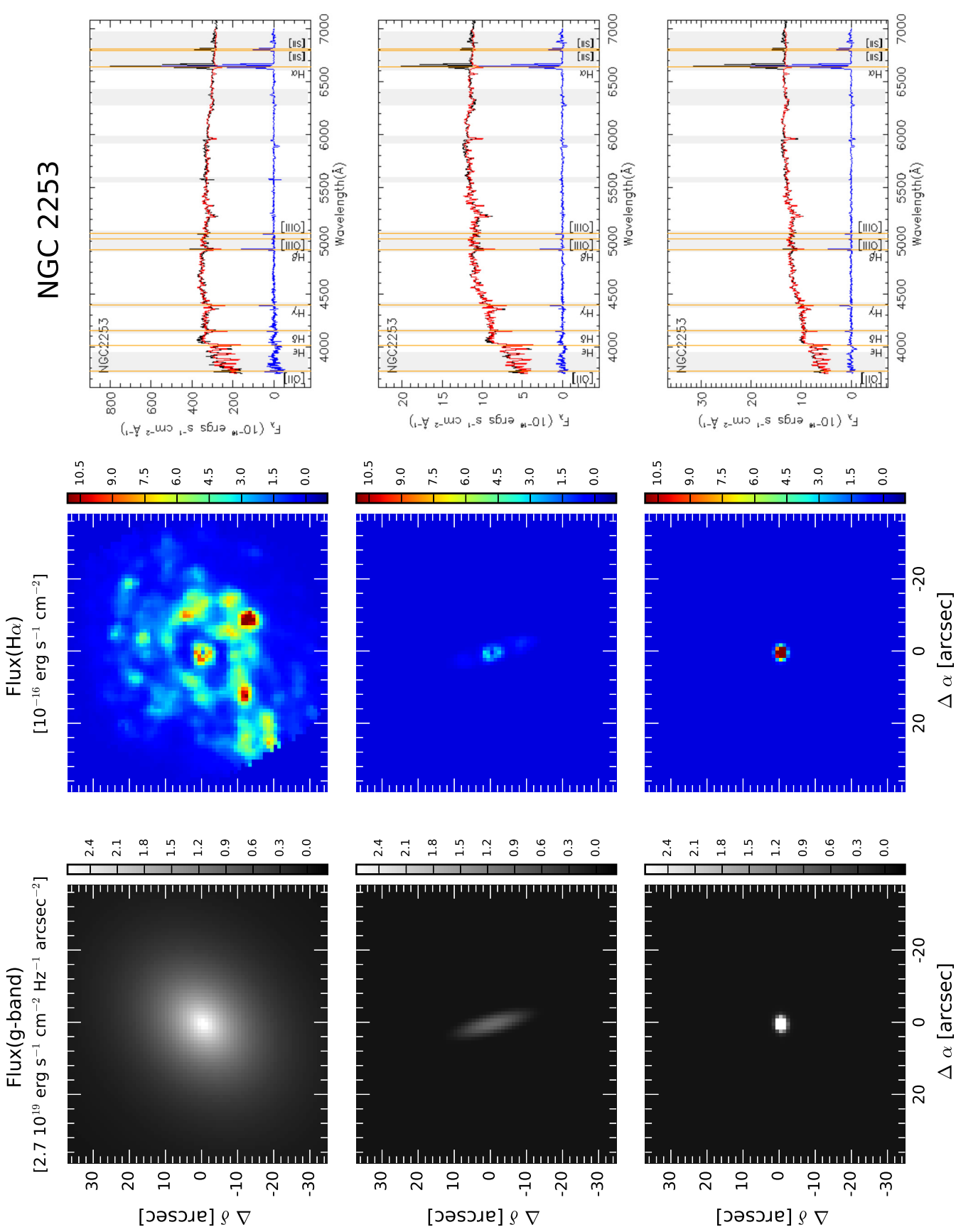
NGC 2253
Flux(g-band)
[2.7 10^19 erg s^-1 cm^-2 Hz^-1 arcsec^-2]
Flux(Hα)
[10^-16 erg s^-1 cm^-2]
Δ δ [arcsec]
Δ α [arcsec]
Wavelength(Å)
NGC2253
[OII]
Hε
Hδ
Hγ
[OIII]
Hβ
[OIII]
Hα
[SII]
[SII]

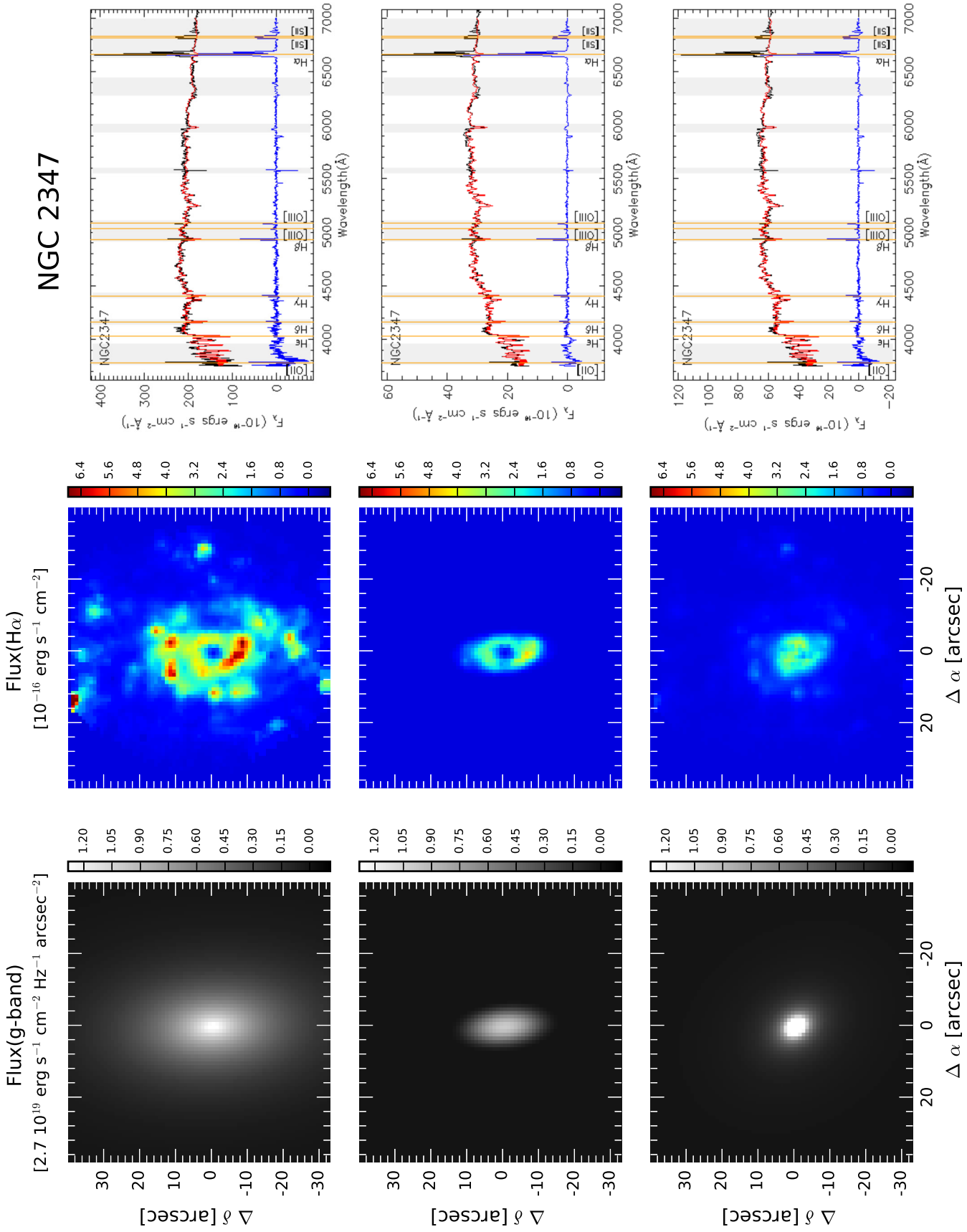
NGC 2347
Flux(g-band)
[2.7 10^19 erg s^-1 cm^-2 Hz^-1 arcsec^-2]
Flux(Hα)
[10^-16 erg s^-1 cm^-2]
Δ δ [arcsec]
Δ α [arcsec]
Wavelength(Å)
NGC2347
[OII]
Hε
Hδ
Hγ
[OIII]
Hβ
[OIII]
Hα
[SII]
[SII]

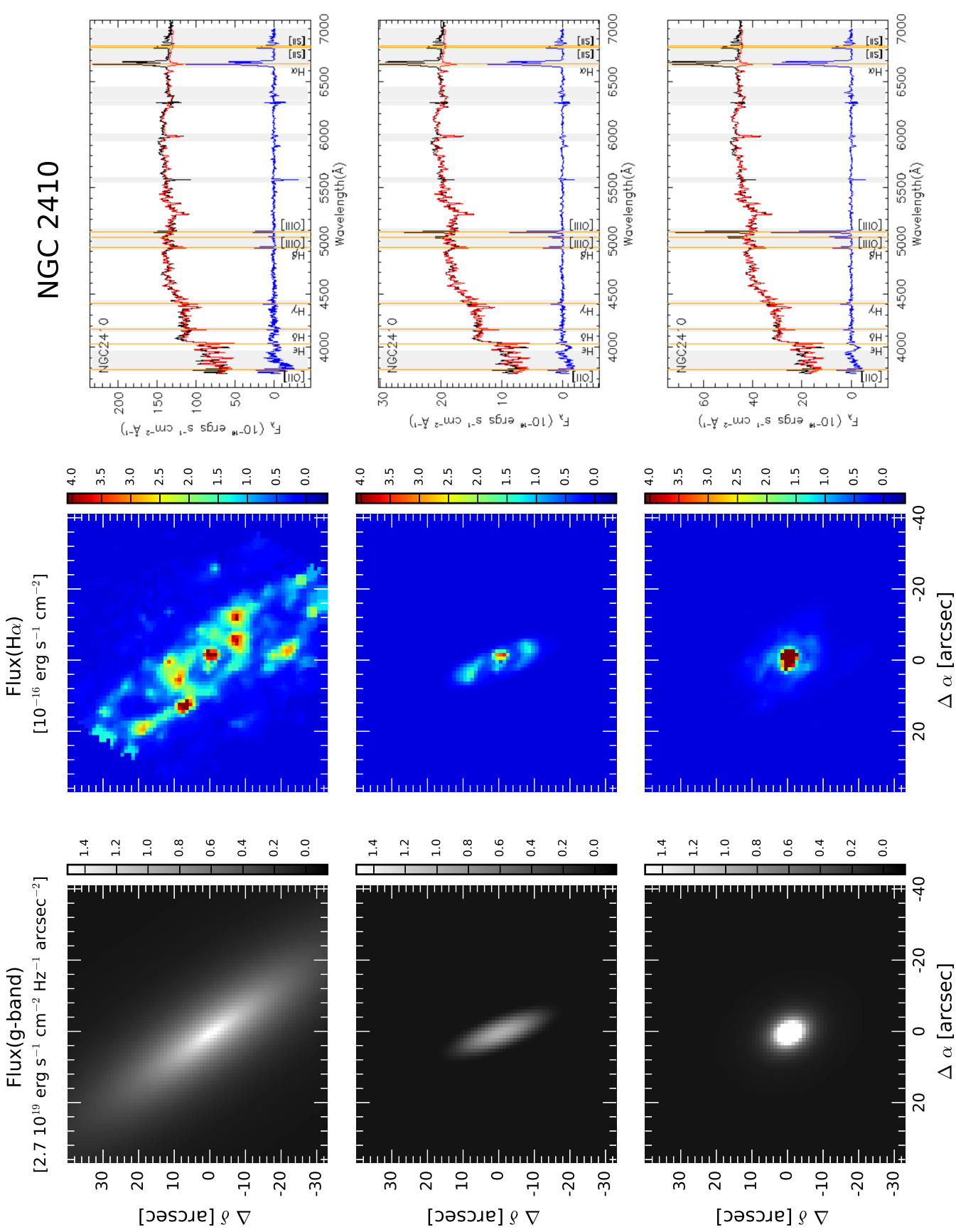
NGC 2410
Flux(g-band)
[2.7 10^19 erg s^-1 cm^-2 Hz^-1 arcsec^-2]
Flux(Hα)
[10^-16 erg s^-1 cm^-2]
Δ δ [arcsec]
Δ α [arcsec]
Wavelength(Å)
F_λ (10^-16 ergs s^-1 cm^-2 Å^-1)
NGC24-0
[OII]
Hε
Hδ
Hγ
[OIII]
Hβ
[OIII]
Hα
[SII]
[SII]

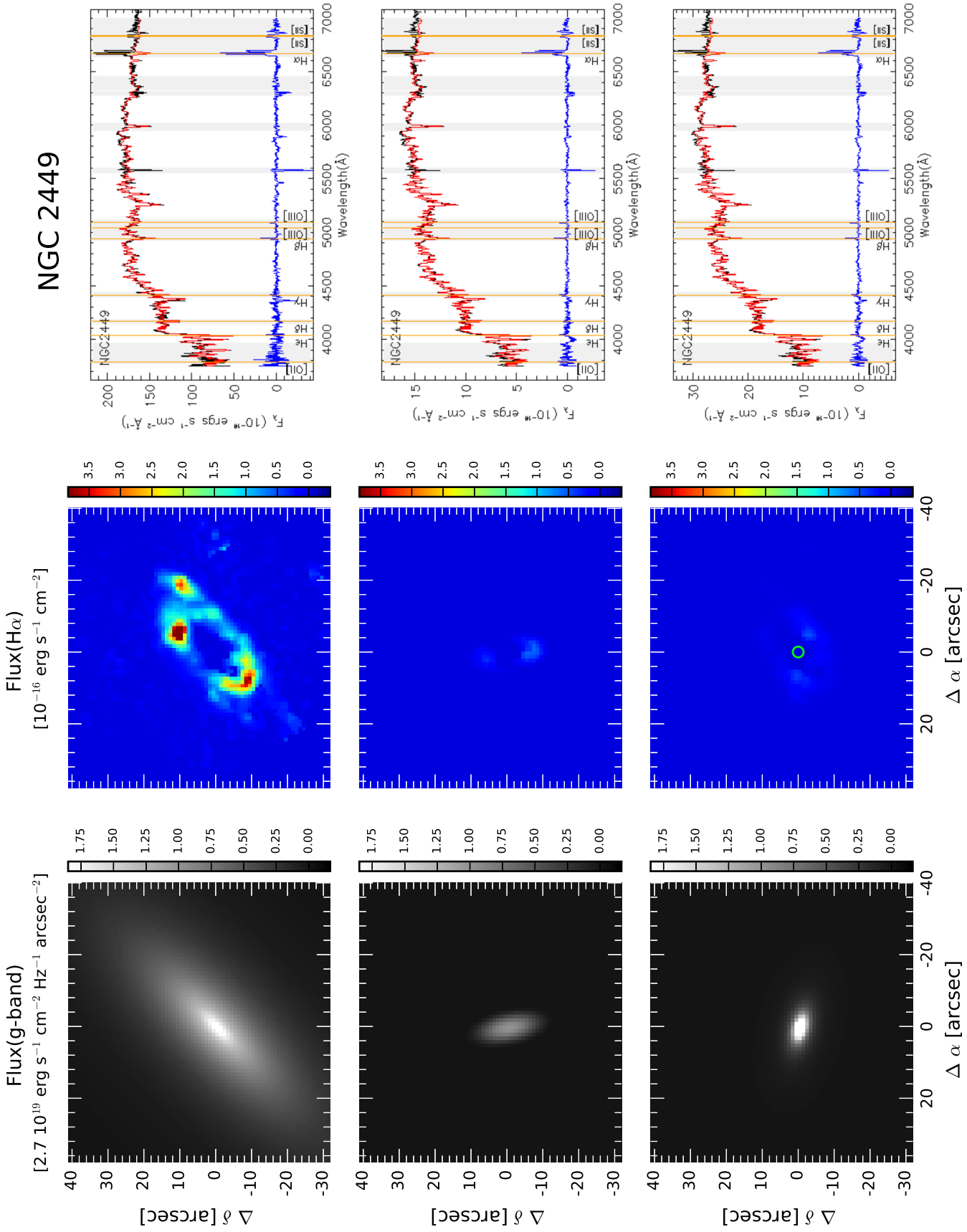
NGC 2449
Flux(g-band)
[2.7 10^19 erg s^-1 cm^-2 Hz^-1 arcsec^-2]
Flux(Hα)
[10^-16 erg s^-1 cm^-2]
Δ δ [arcsec]
Δ α [arcsec]
Wavelength(Å)
F_λ (10^-16 ergs s^-1 cm^-2 Å^-1)
NGC2449
[OII]
Hε
Hδ
Hγ
[OIII]
Hβ
[OIII]
Hα
[SII]
[SII]

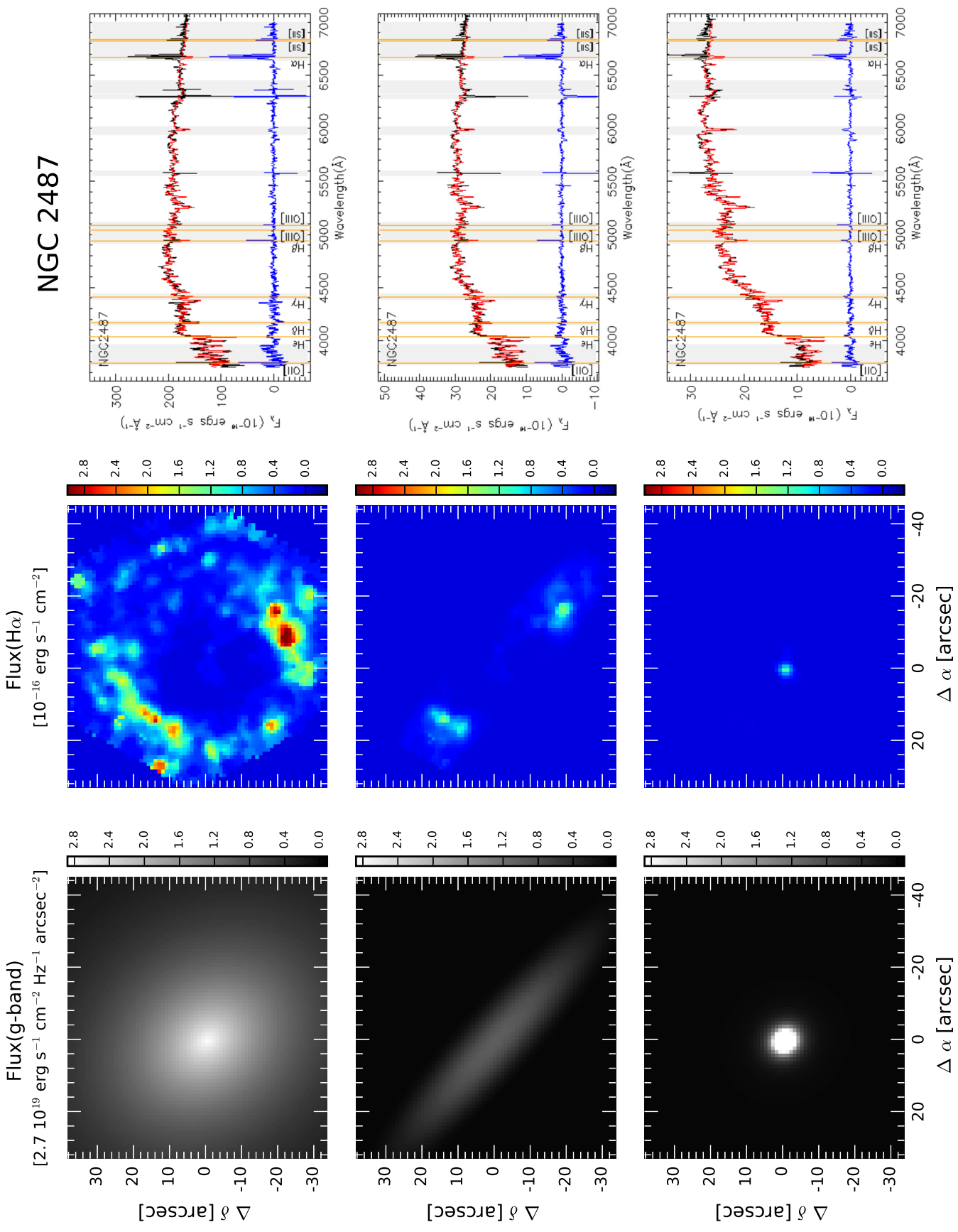
NGC 2487
Flux(g-band)
[2.7 10^19 erg s^-1 cm^-2 Hz^-1 arcsec^-2]
Flux(Hα)
[10^-16 erg s^-1 cm^-2]
Δ δ [arcsec]
Δ α [arcsec]
Wavelength(Å)
NGC2487
[OII]
Hε
Hδ
Hγ
Hβ
[OIII]
[OIII]
[SII]
[SII]
Hα

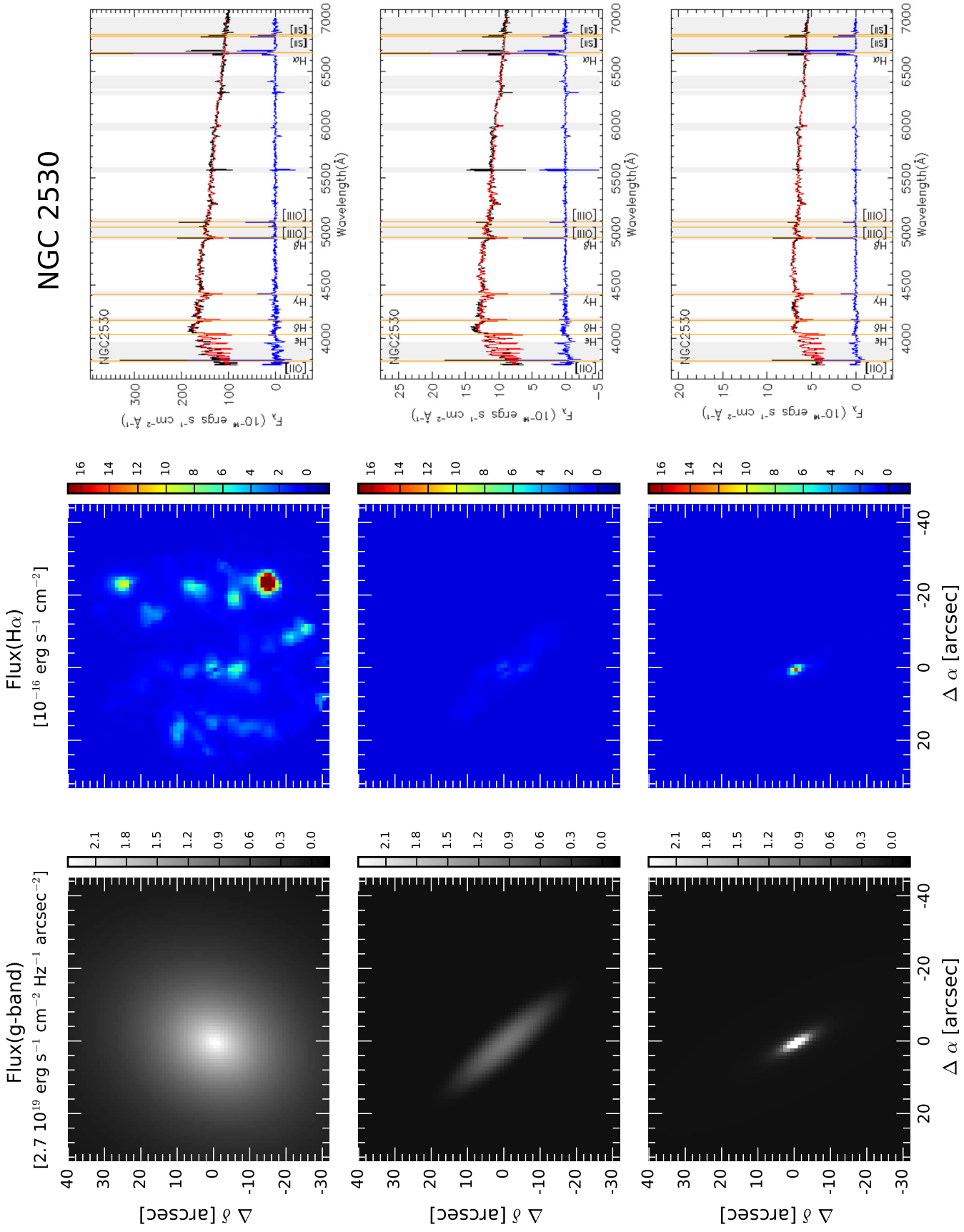
NGC 2530
Flux(g-band)
[2.7 10^19 erg s^-1 cm^-2 Hz^-1 arcsec^-2]
Flux(Hα)
[10^-16 erg s^-1 cm^-2]
Δ δ [arcsec]
Δ α [arcsec]
Wavelength(Å)
NGC2530
[OII]
HE
Hδ
Hγ
[OIII]
Hβ
[OIII]
Hα
[SII]
[SII]

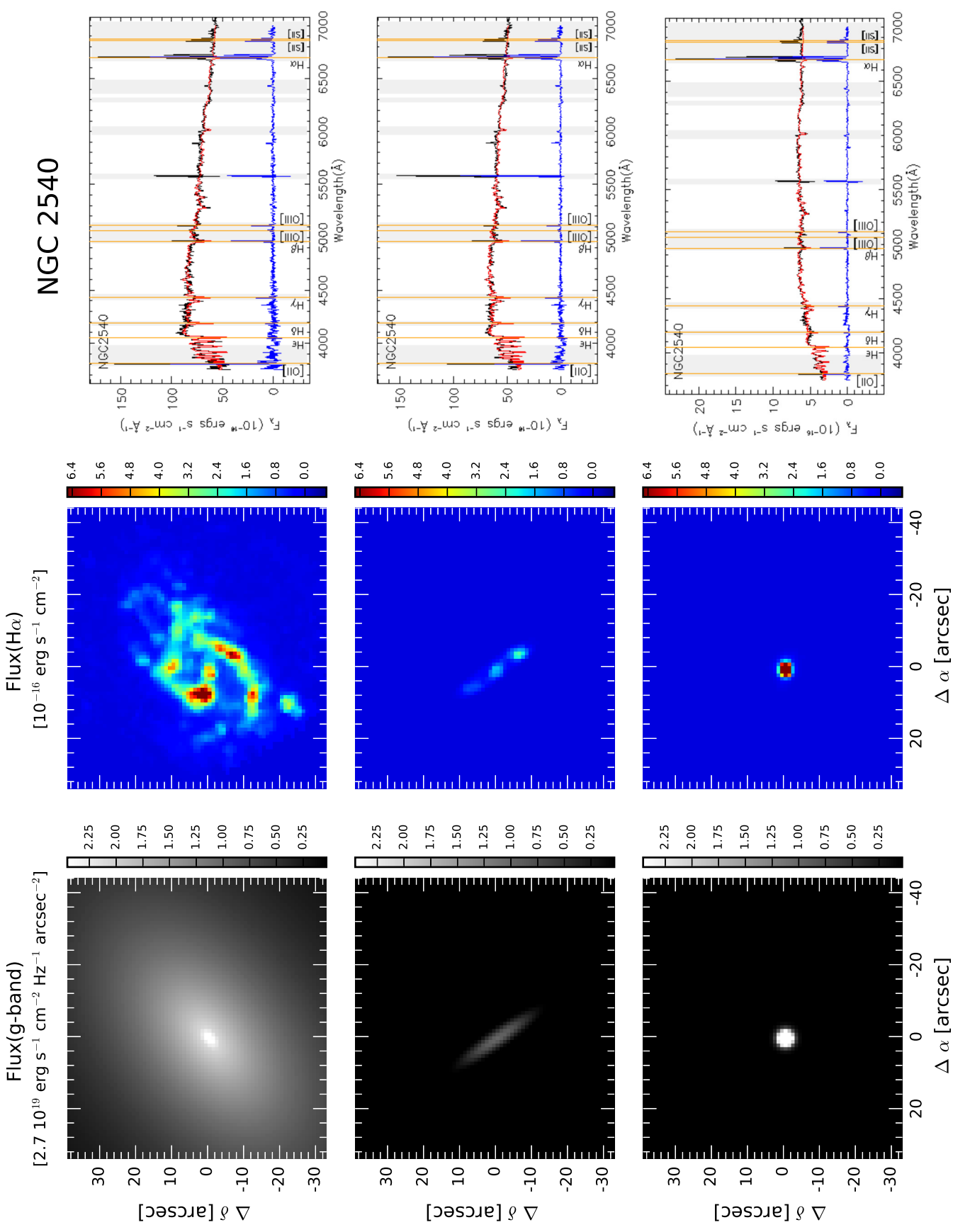
NGC 2540
Flux(g-band)
[2.7 10^19 erg s^-1 cm^-2 Hz^-1 arcsec^-2]
Flux(Hα)
[10^-16 erg s^-1 cm^-2]
Δ δ [arcsec]
Δ α [arcsec]
Wavelength(Å)
NGC2540
[OII]
Hε
Hδ
Hγ
Hβ
[OIII]
[OIII]
[SII]
[SII]
Hα

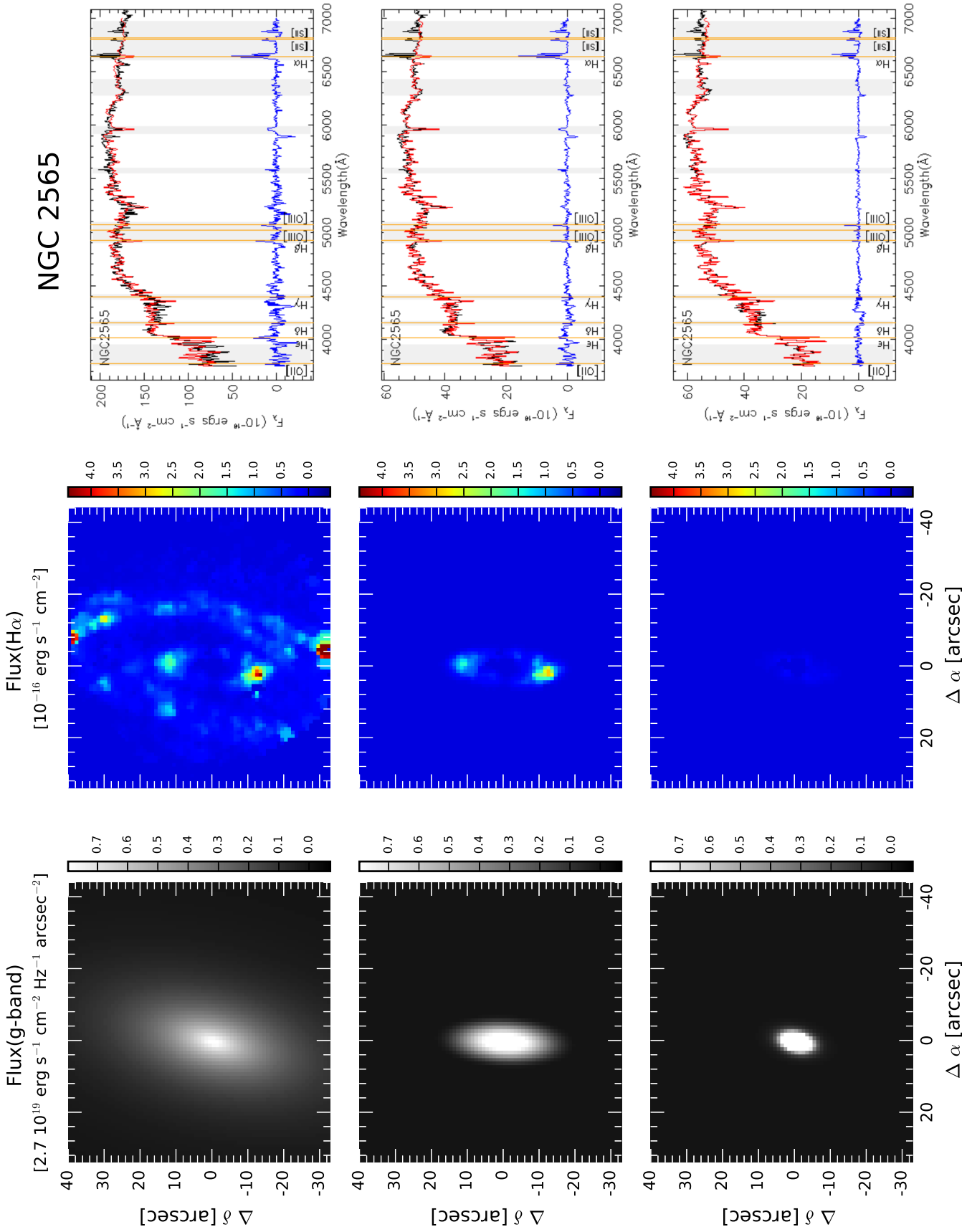
NGC 2565
Flux(g-band)
[2.7 10^19 erg s^-1 cm^-2 Hz^-1 arcsec^-2]
Flux(Hα)
[10^-16 erg s^-1 cm^-2]
Δ δ [arcsec]
Δ α [arcsec]
Wavelength(Å)
F_λ (10^-16 ergs s^-1 cm^-2 Å^-1)
NGC2565
[OII]
Hε
Hδ
Hγ
Hβ
[OIII]
[OIII]
Hα
[SII]
[SII]

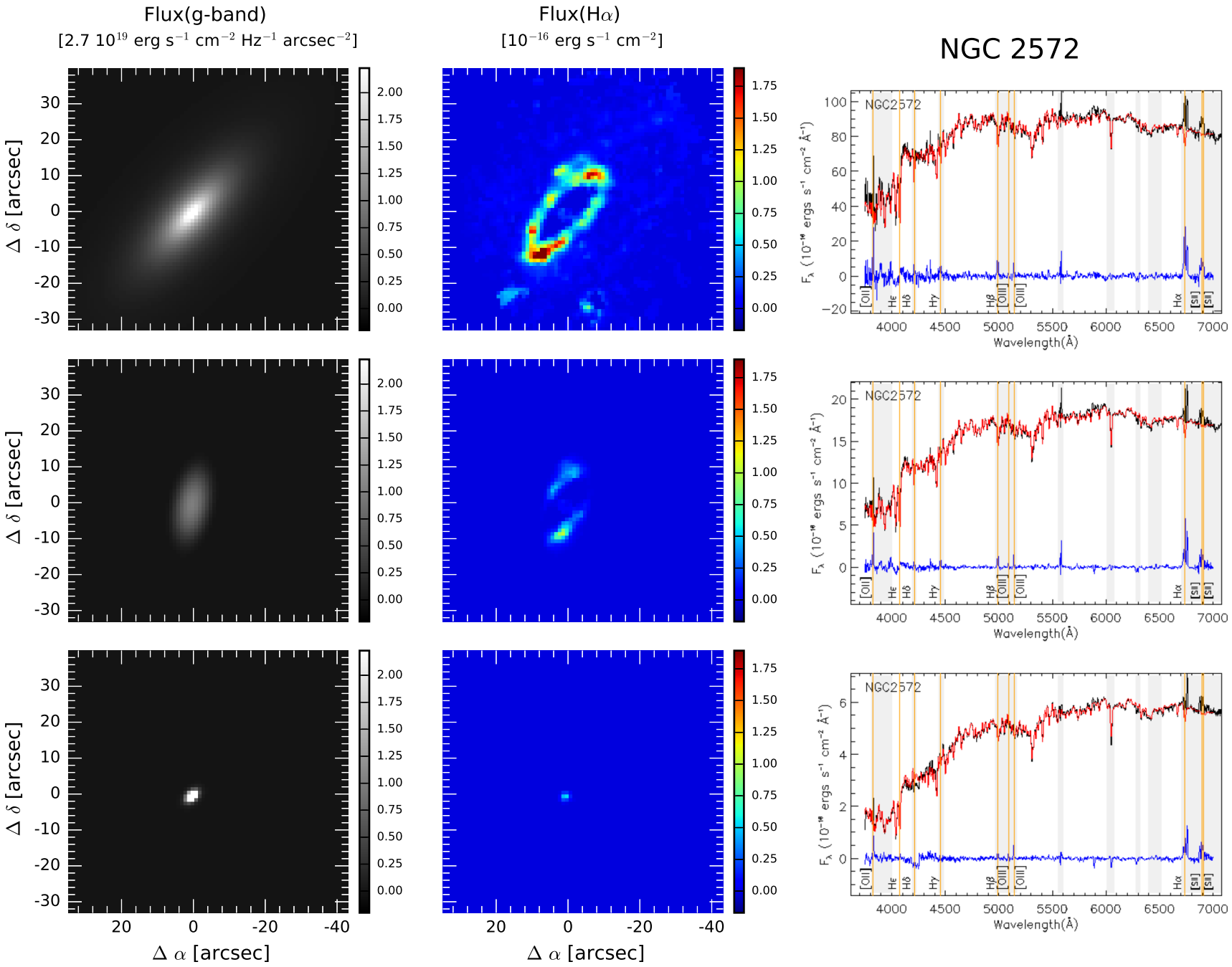
Flux(g-band)
[2.7 10^19 erg s^-1 cm^-2 Hz^-1 arcsec^-2]
Flux(Hα)
[10^-16 erg s^-1 cm^-2]
NGC 2572
Δ δ [arcsec]
Δ α [arcsec]
Wavelength(Å)
NGC2572
[OII]
Hε
Hδ
Hγ
Hβ
[OIII]
[OIII]
Hα
[SII]
[SII]

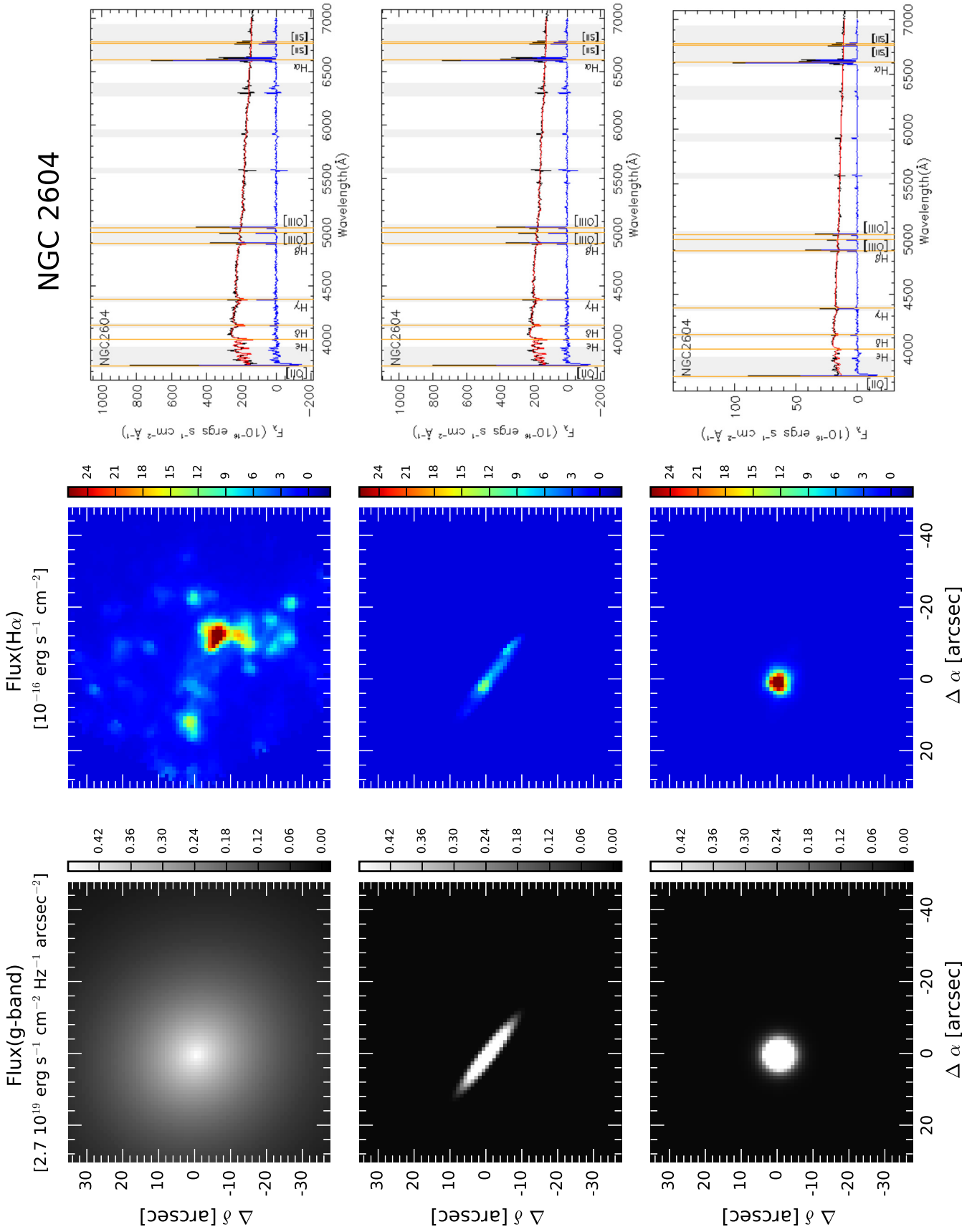
NGC 2604
Flux(g-band)
[2.7 10^19 erg s^-1 cm^-2 Hz^-1 arcsec^-2]
Flux(Hα)
[10^-16 erg s^-1 cm^-2]
Δ δ [arcsec]
Δ α [arcsec]
Wavelength(Å)
F_λ (10^-16 ergs s^-1 cm^-2 Å^-1)
NGC2604
[OII]
Hε
Hδ
Hγ
Hβ
[OIII]
[OIII]
Hα
[SII]
[SII]

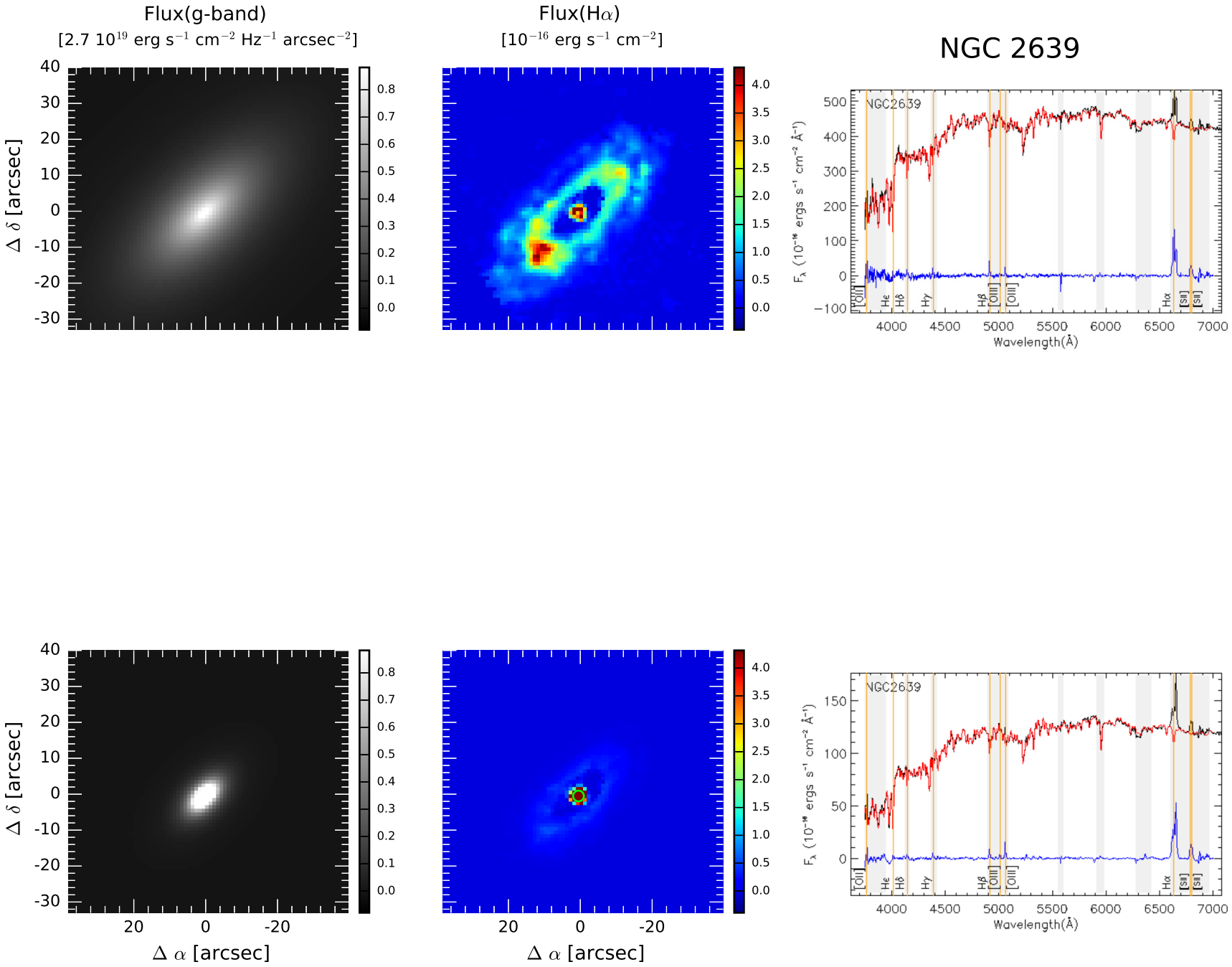
Flux(g-band)
[2.7 10^19 erg s^-1 cm^-2 Hz^-1 arcsec^-2]
Flux(Hα)
[10^-16 erg s^-1 cm^-2]
NGC 2639
Δ δ [arcsec]
Δ α [arcsec]
F_λ (10^-16 ergs s^-1 cm^-2 Å^-1)
Wavelength(Å)
NGC2639
[OII]
Hε
Hδ
Hγ
Hβ
[OIII]
[OIII]
Hα
[SII]
[SII]

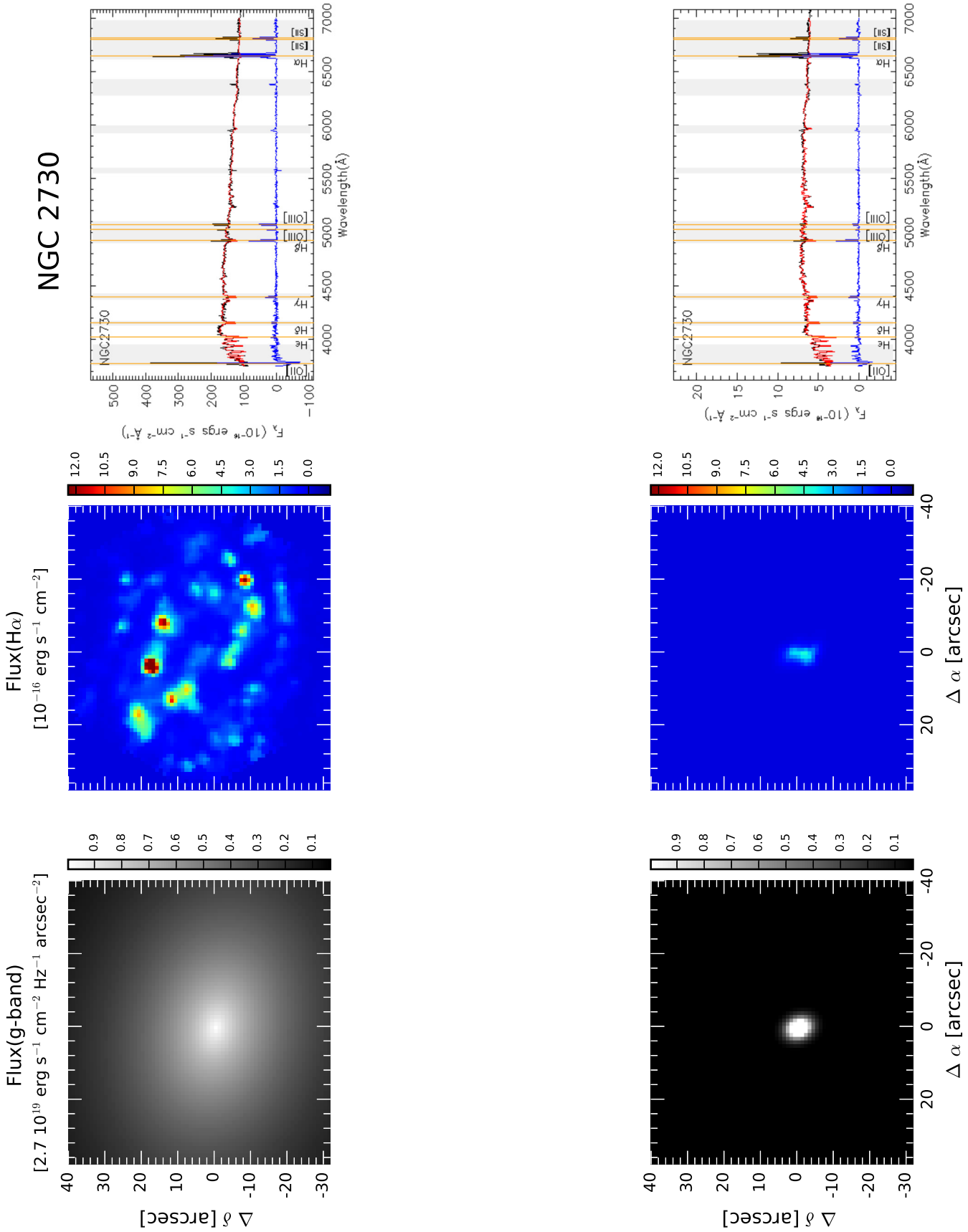
NGC 2730
Flux(g-band)
[2.7 10^19 erg s^-1 cm^-2 Hz^-1 arcsec^-2]
Flux(Hα)
[10^-16 erg s^-1 cm^-2]
Δ δ [arcsec]
Δ α [arcsec]
Wavelength(Å)
F_λ (10^-16 ergs s^-1 cm^-2 Å^-1)
NGC2730
[OII]
Hε
Hδ
Hγ
[OIII]
Hβ
[OIII]
[SII]
[SII]
Hα

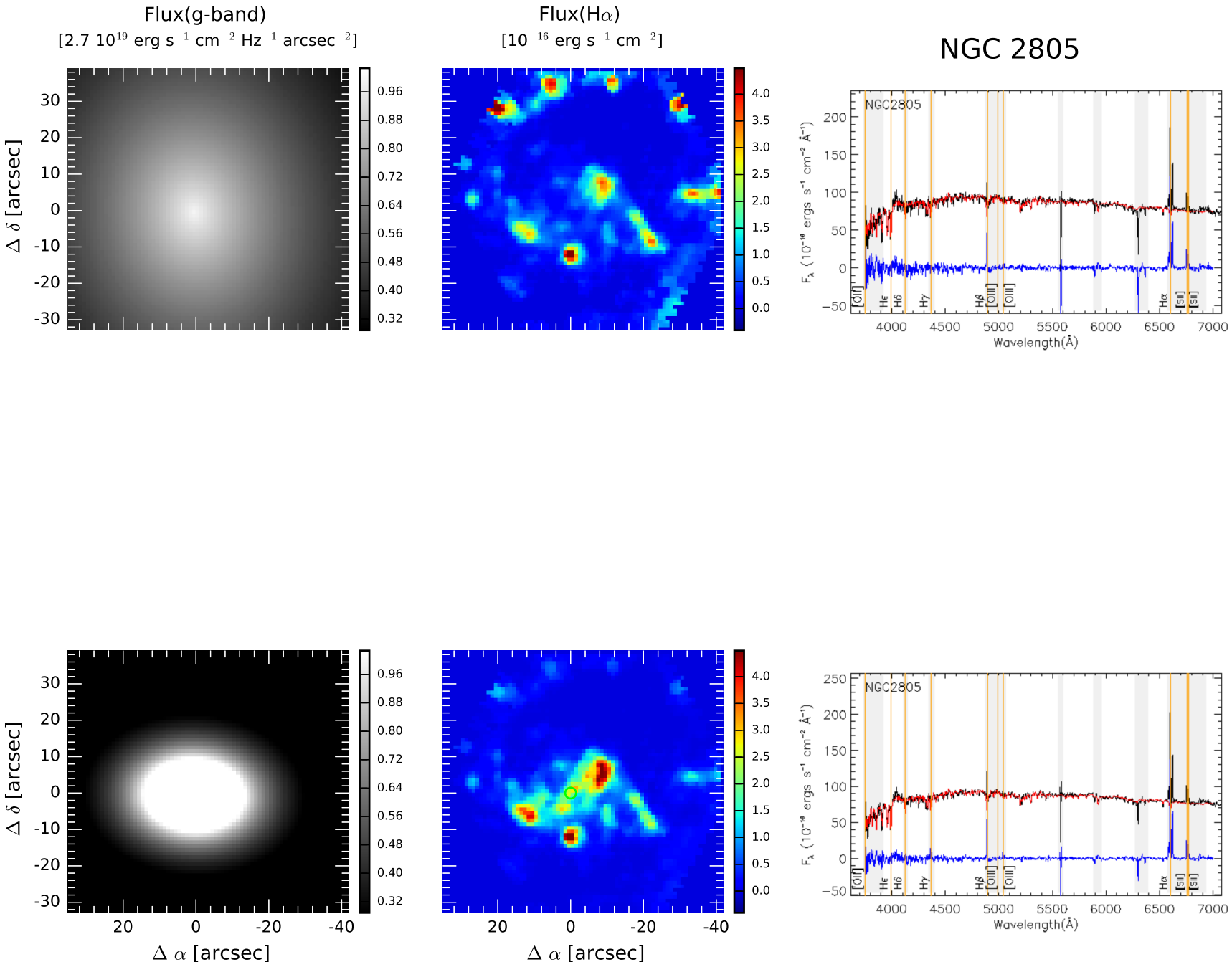
Flux(g-band)
[2.7 10^19 erg s^-1 cm^-2 Hz^-1 arcsec^-2]
Flux(Hα)
[10^-16 erg s^-1 cm^-2]
NGC 2805
Δ δ [arcsec]
Δ α [arcsec]
Wavelength(Å)
NGC2805

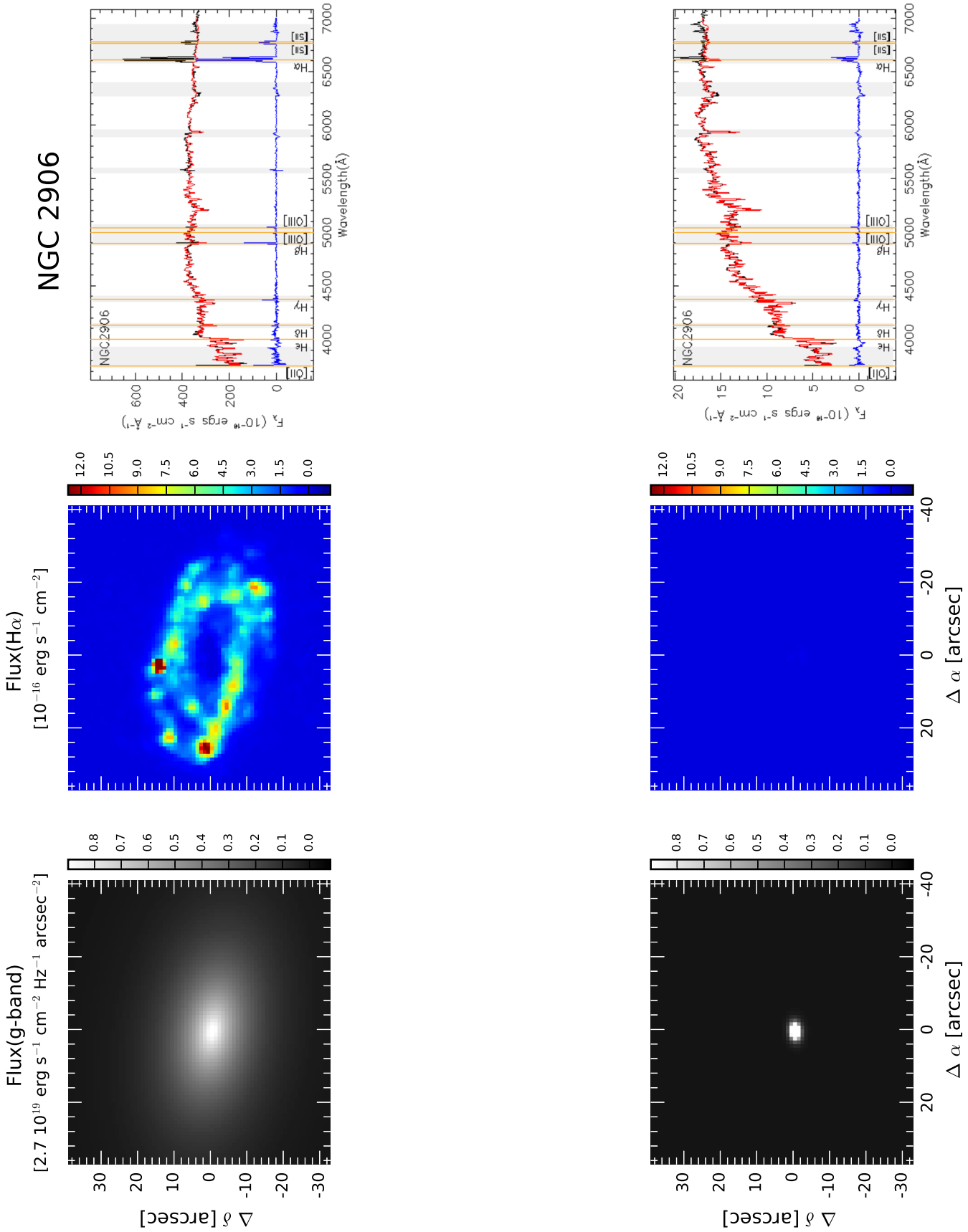
NGC 2906
NGC2906
Wavelength(Å)
Flux(Hα)
[10⁻¹⁶ erg s⁻¹ cm⁻²]
Flux(g-band)
[2.7 10¹⁹ erg s⁻¹ cm⁻² Hz⁻¹ arcsec⁻²]
Δ δ [arcsec]
Δ α [arcsec]

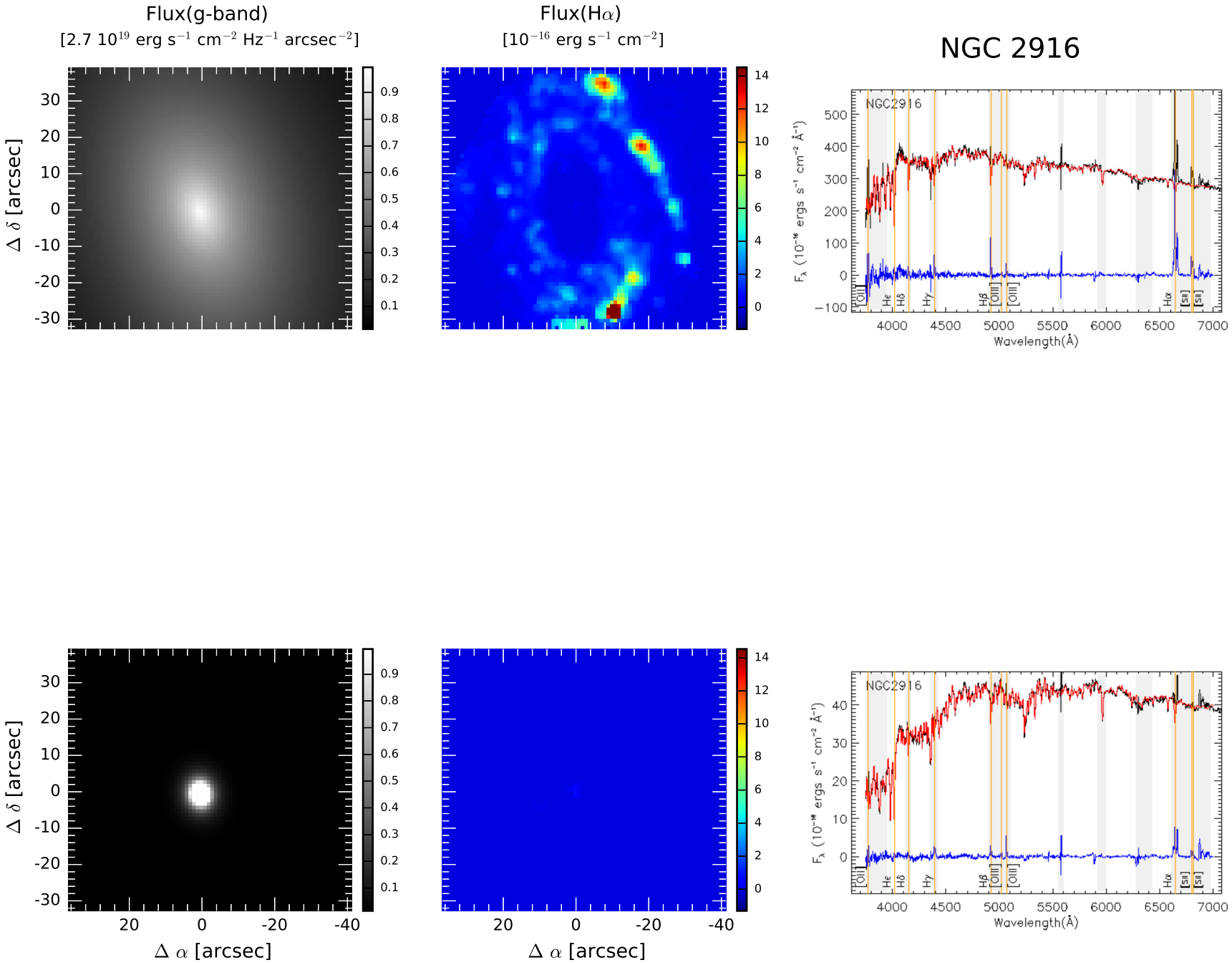
Flux(g-band)
[2.7 10^19 erg s^-1 cm^-2 Hz^-1 arcsec^-2]
Flux(Hα)
[10^-16 erg s^-1 cm^-2]
NGC 2916
Δ δ [arcsec]
Δ α [arcsec]
NGC2916
Wavelength(Å)
[OII]
Hε
Hδ
Hγ
Hβ
[OIII]
[OIII]
Hα
[SII]
[SII]

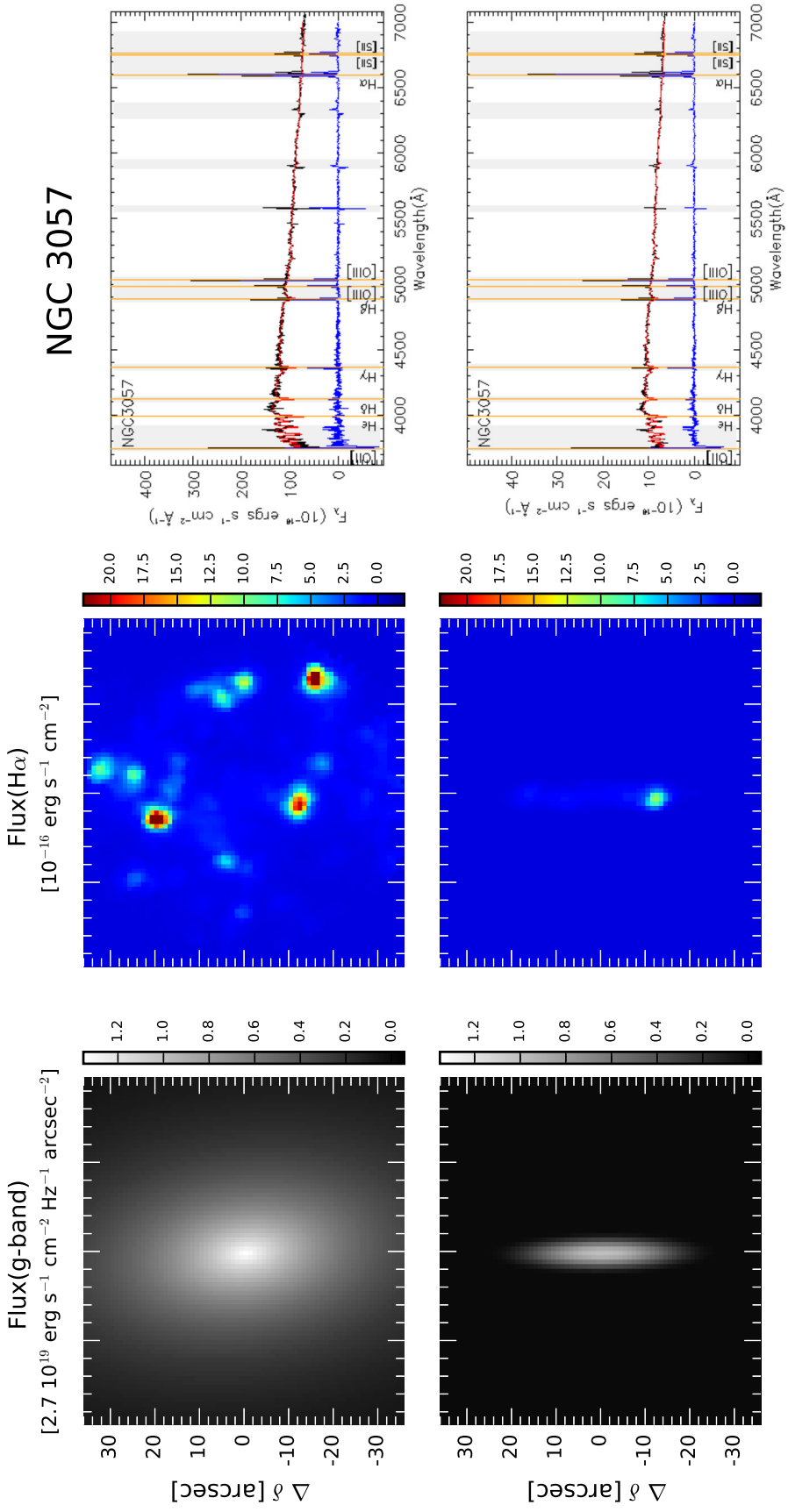
NGC 3057
Flux(g-band)
[2.7 10^19 erg s^-1 cm^-2 Hz^-1 arcsec^-2]
Flux(Hα)
[10^-16 erg s^-1 cm^-2]
Δ δ [arcsec]
Δ α [arcsec]
Wavelength(Å)
NGC3057
[OII]
Hε
Hδ
Hγ
Hβ
[OIII]
[OIII]
[SII]
[SII]
Hα

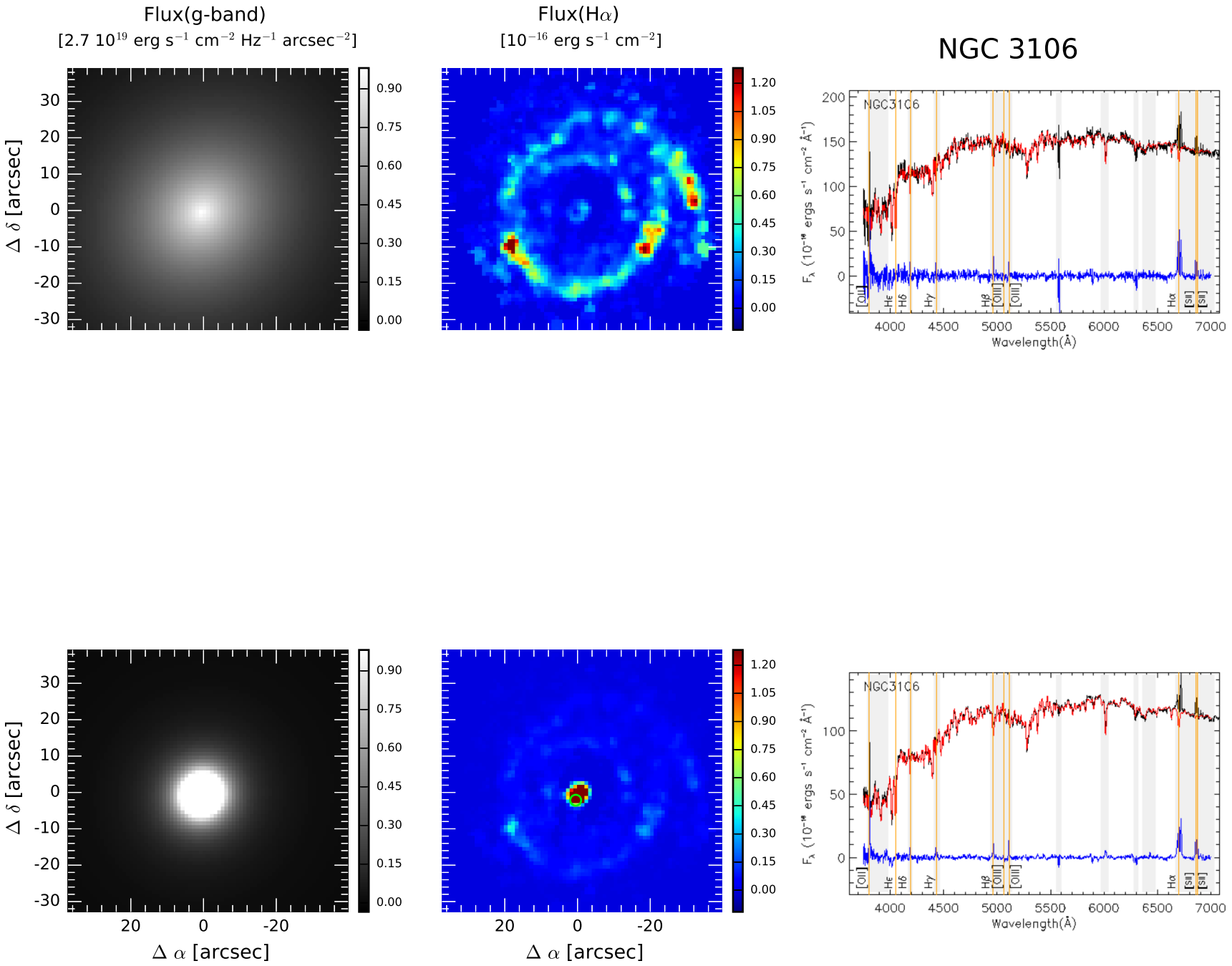
Flux(g-band)
[2.7 10^19 erg s^-1 cm^-2 Hz^-1 arcsec^-2]
Flux(Hα)
[10^-16 erg s^-1 cm^-2]
NGC 3106
Δ δ [arcsec]
Δ α [arcsec]
NGC3106
Wavelength(Å)
[OII]
Hε
Hδ
Hγ
Hβ
[OIII]
[OIII]
Hα
[SII]
[SII]

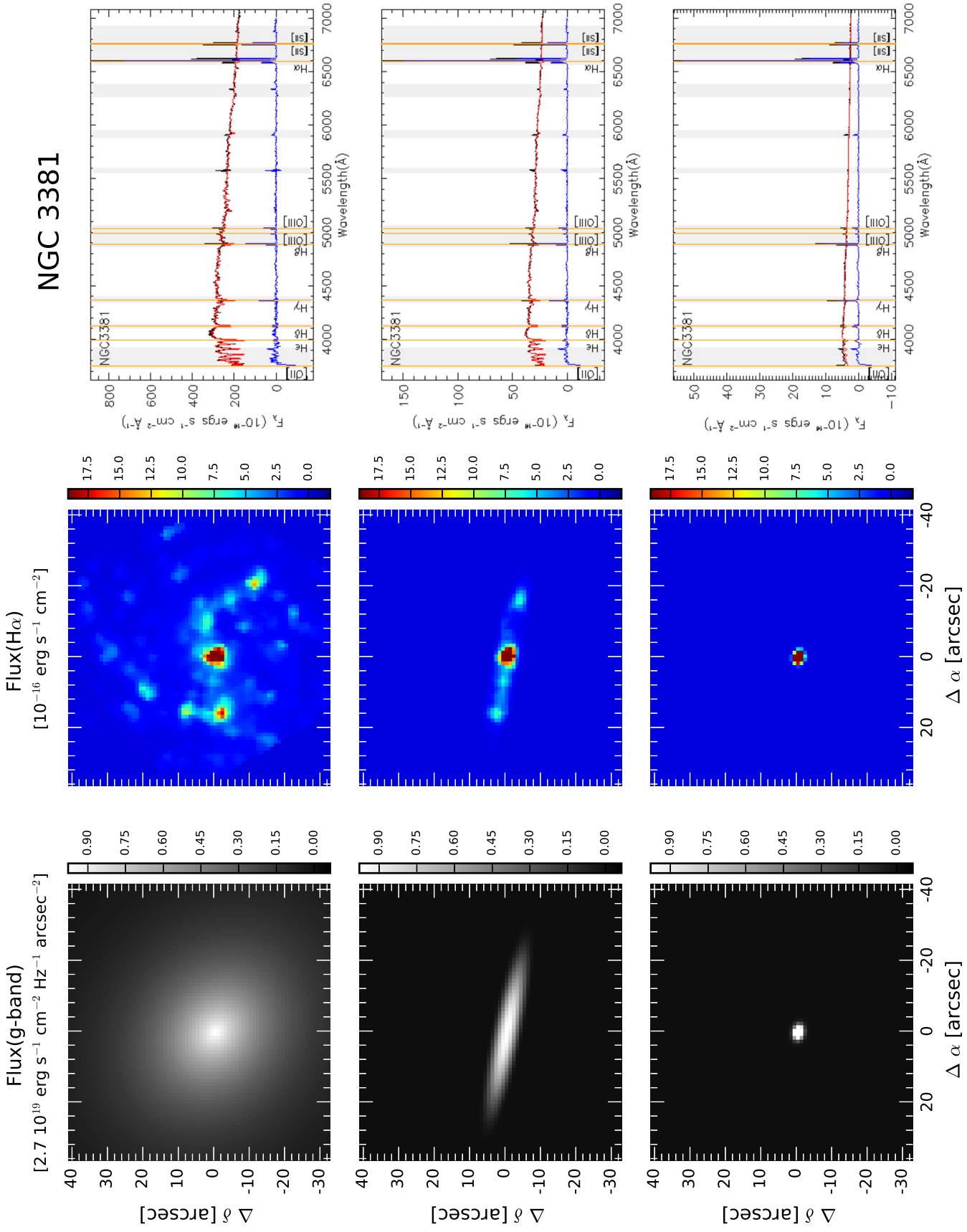
NGC 3381
Flux(g-band)
[2.7 10^19 erg s^-1 cm^-2 Hz^-1 arcsec^-2]
Flux(Hα)
[10^-16 erg s^-1 cm^-2]
Δ δ [arcsec]
Δ α [arcsec]
Wavelength(Å)
NGC3381
[OII]
Hε
Hδ
Hγ
Hβ
[OIII]
[OIII]
[SII]
[SII]
Hα

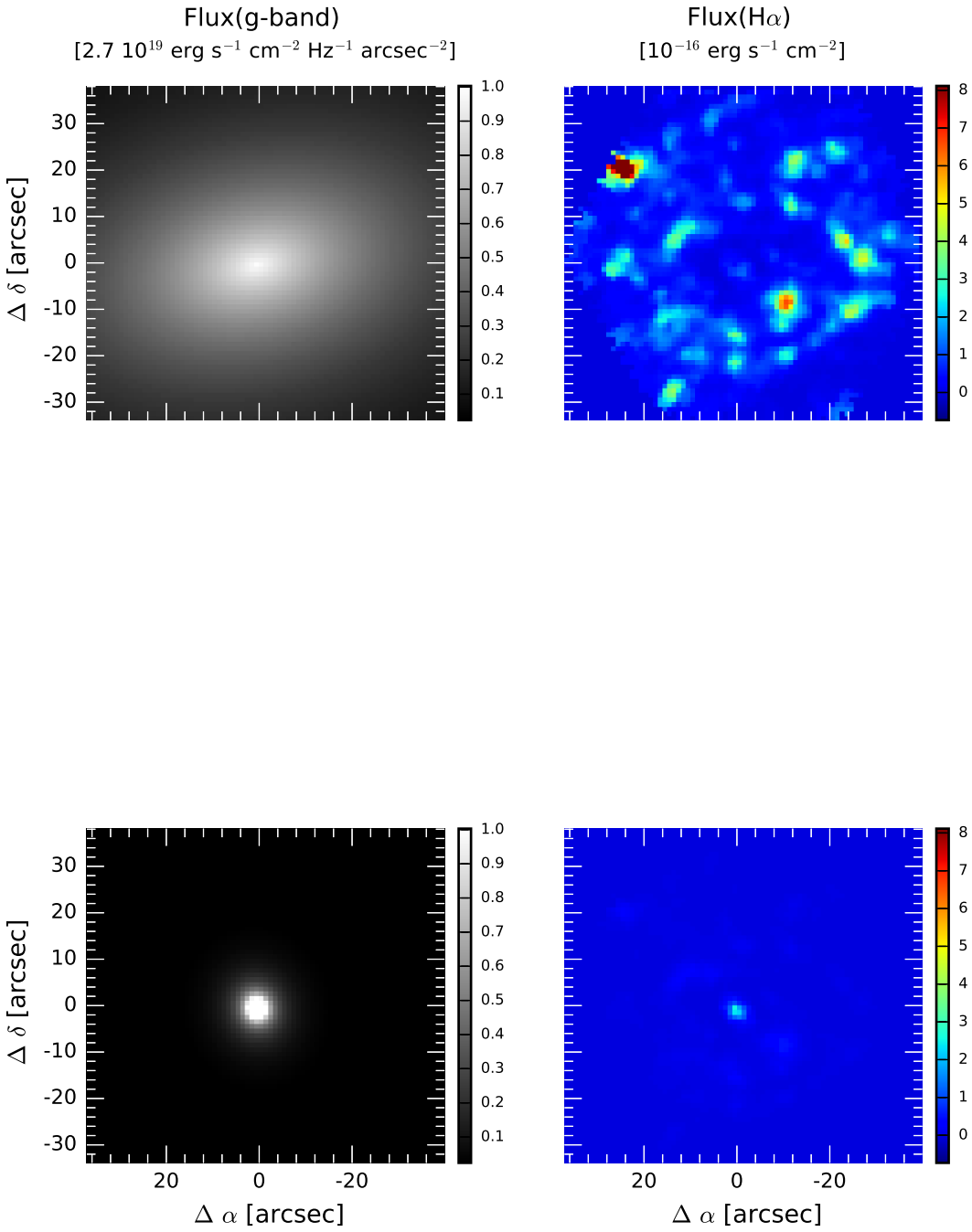
Flux(g-band)
[2.7 10^19 erg s^-1 cm^-2 Hz^-1 arcsec^-2]
Flux(Hα)
[10^-16 erg s^-1 cm^-2]
Δ δ [arcsec]
Δ α [arcsec]

NGC 3614

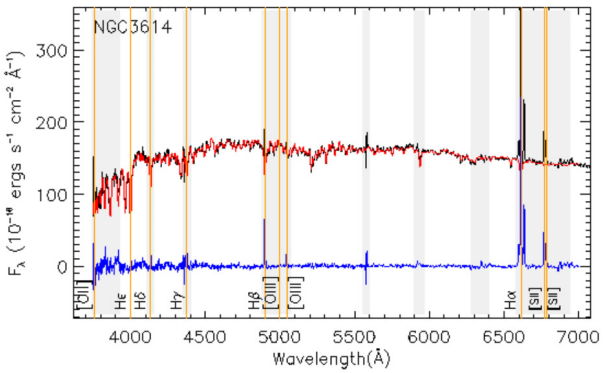
NGC3614
Wavelength(Å)

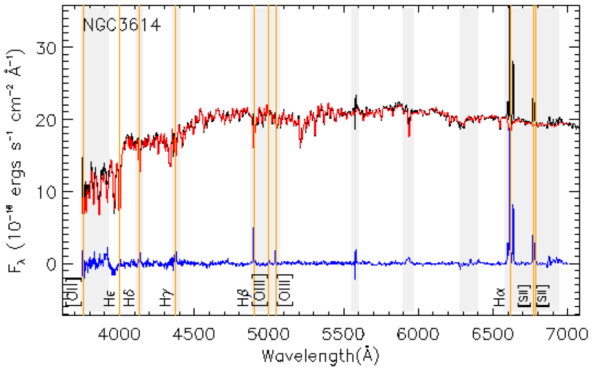
NGC3614
Wavelength(Å)

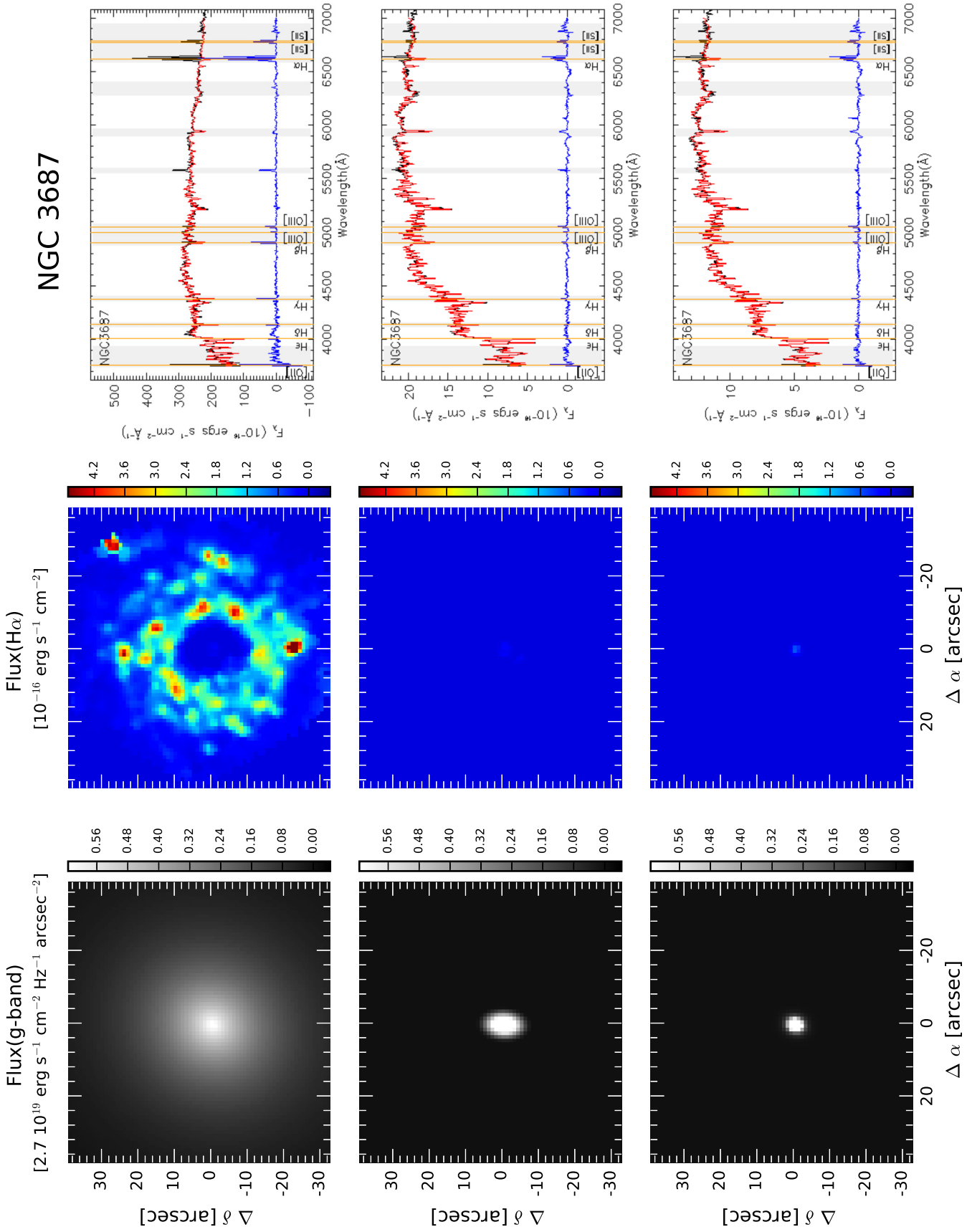
NGC 3687
Flux(g-band)
[2.7 10^19 erg s^-1 cm^-2 Hz^-1 arcsec^-2]
Flux(Hα)
[10^-16 erg s^-1 cm^-2]
Δ δ [arcsec]
Δ α [arcsec]
F_λ (10^-16 ergs s^-1 cm^-2 Å^-1)
Wavelength(Å)
NGC3687
[OII]
Hε
Hδ
Hγ
Hβ
[OIII]
[OIII]
Hα
[SII]
[SII]

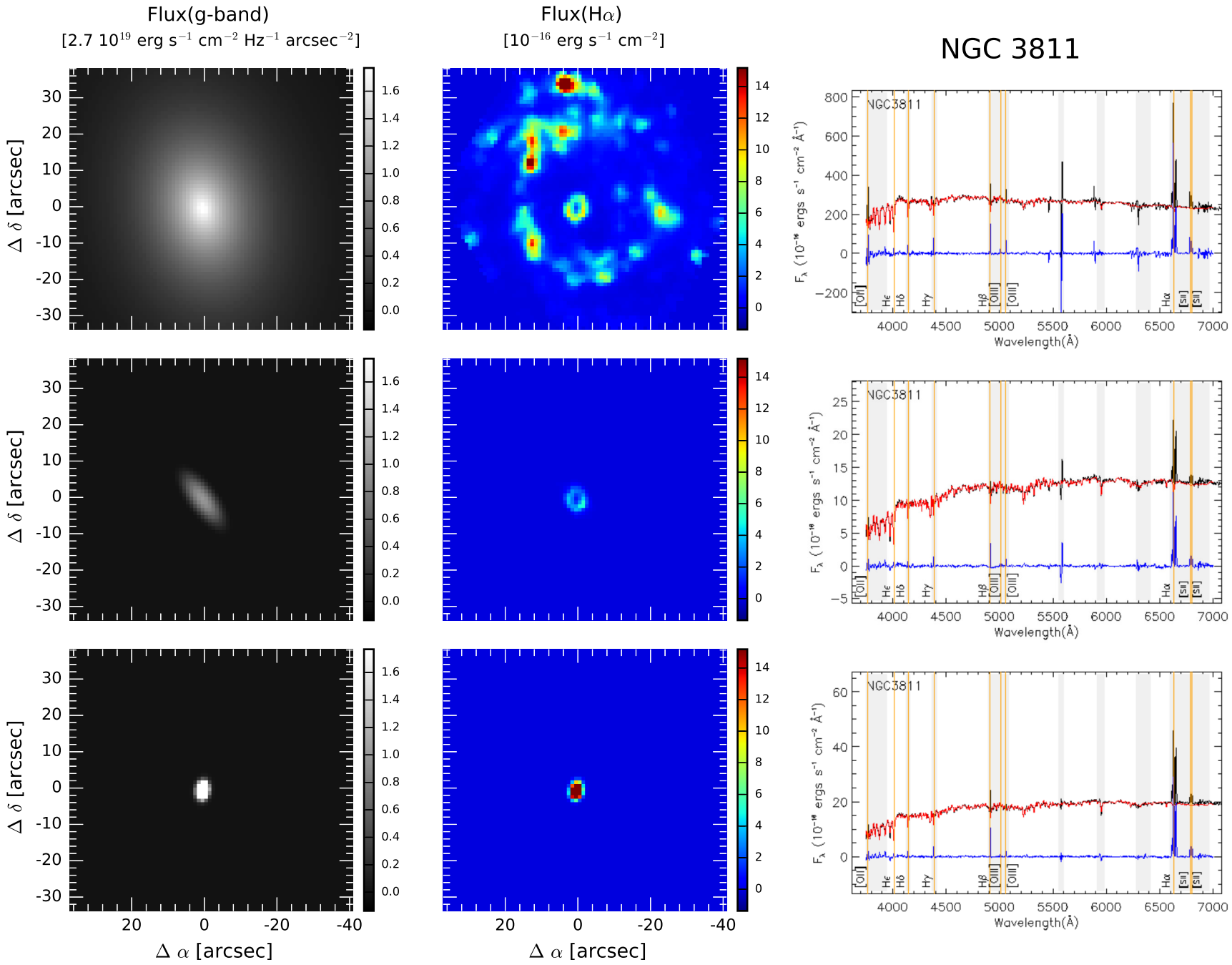
Flux(g-band)
[2.7 10^19 erg s^-1 cm^-2 Hz^-1 arcsec^-2]
Flux(Hα)
[10^-16 erg s^-1 cm^-2]
NGC 3811
Δ δ [arcsec]
Δ α [arcsec]
Wavelength(Å)
NGC3811
[OII]
Hε
Hδ
Hγ
Hβ
[OIII]
[OIII]
Hα
[SII]
[SII]

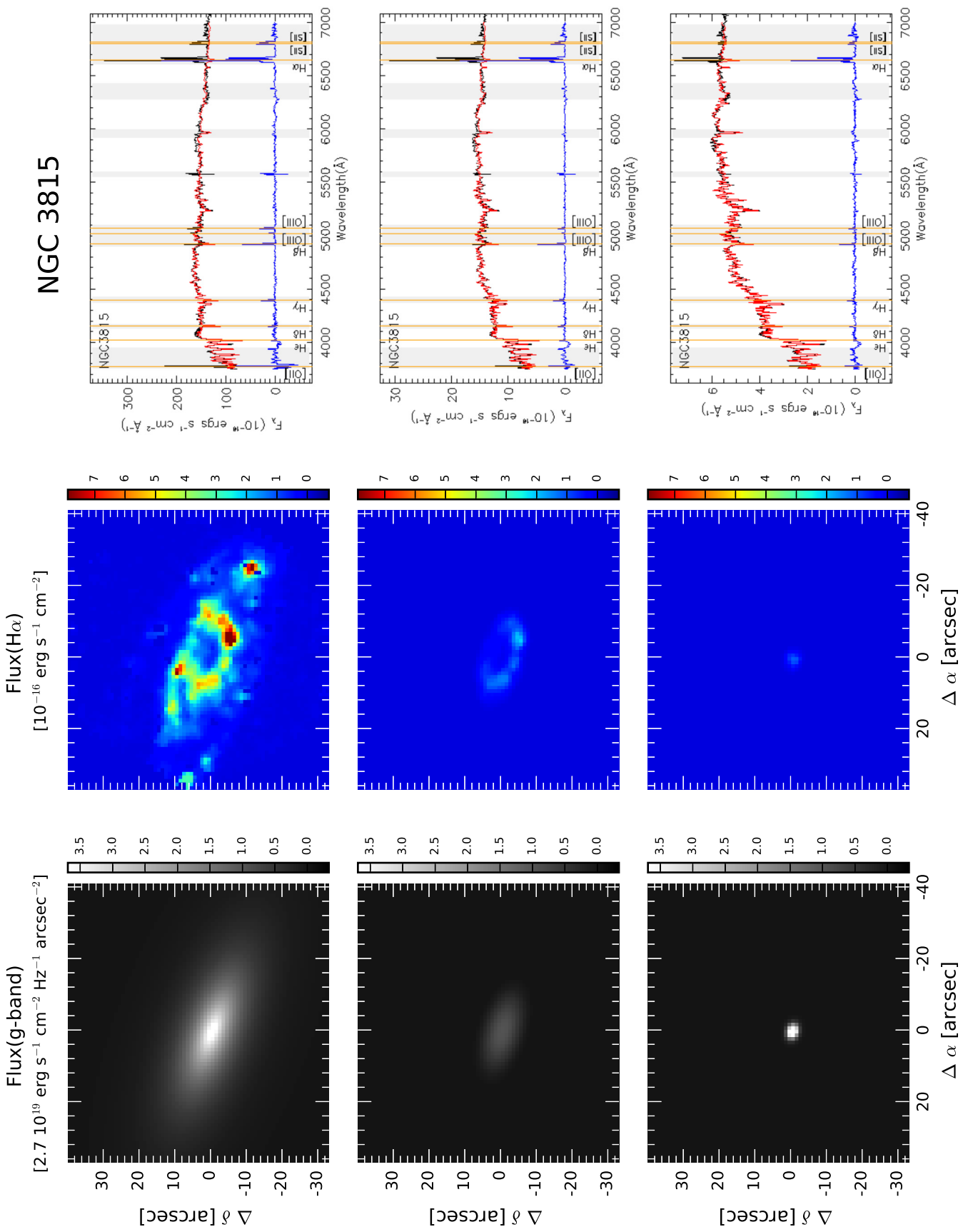
NGC 3815
Flux(g-band)
[2.7 10^19 erg s^-1 cm^-2 Hz^-1 arcsec^-2]
Flux(Hα)
[10^-16 erg s^-1 cm^-2]
Δ δ [arcsec]
Δ α [arcsec]
Wavelength(Å)
NGC3815
[OII]
Hε
Hδ
Hγ
Hβ
[OIII]
Hα
[SII]

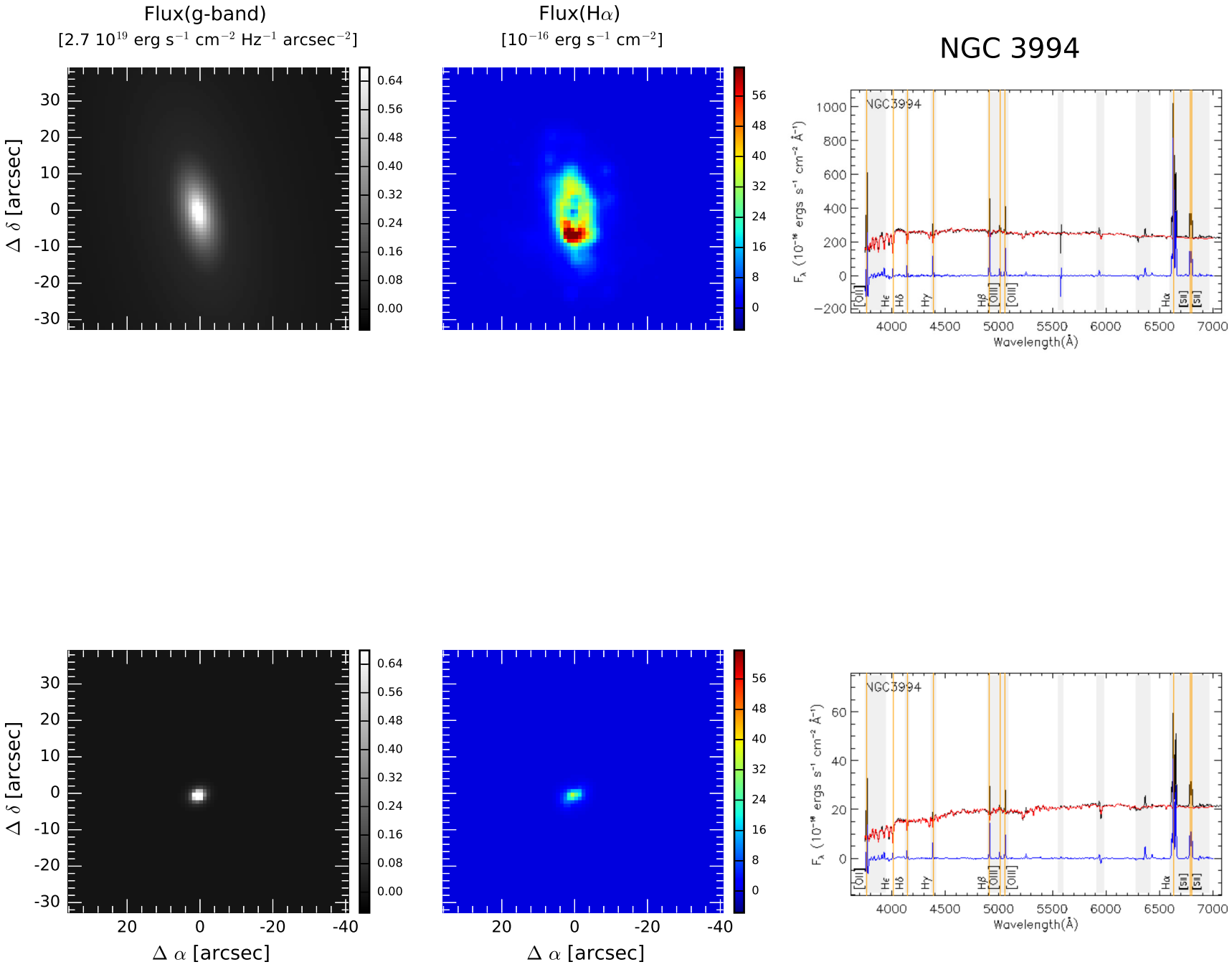
Flux(g-band)
[2.7 10^19 erg s^-1 cm^-2 Hz^-1 arcsec^-2]
Flux(Hα)
[10^-16 erg s^-1 cm^-2]
NGC 3994
Δ δ [arcsec]
Δ α [arcsec]
NGC3994
Wavelength(Å)
Hε
Hδ
Hγ
Hβ
Hα

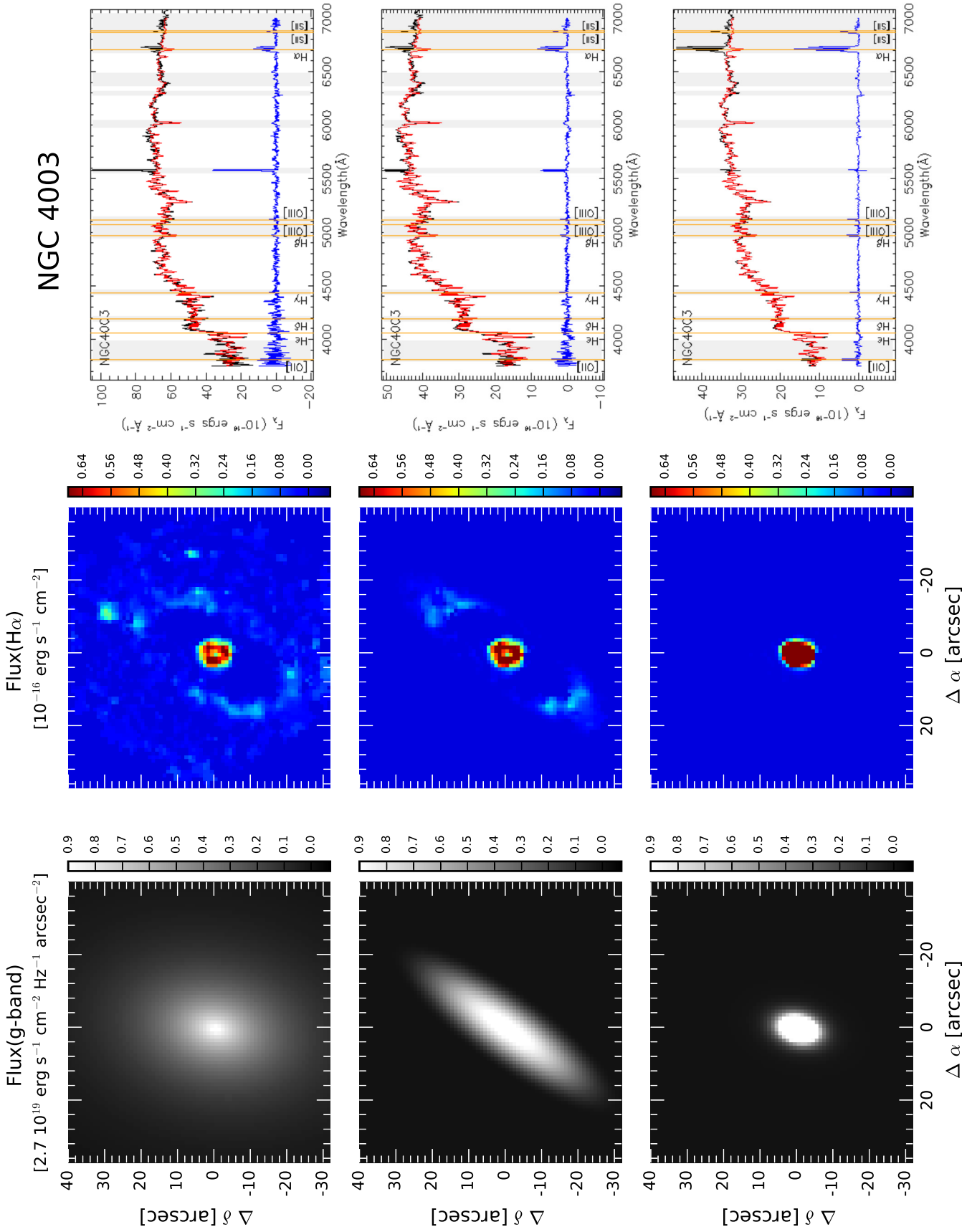
NGC 4003
Flux(g-band)
[2.7 10^19 erg s^-1 cm^-2 Hz^-1 arcsec^-2]
Flux(Hα)
[10^-16 erg s^-1 cm^-2]
Δ δ [arcsec]
Δ α [arcsec]
Wavelength(Å)
NGC4003
[OII]
Hε
Hδ
Hγ
Hβ
[OIII]
[OIII]
[SII]
[SII]
Hα

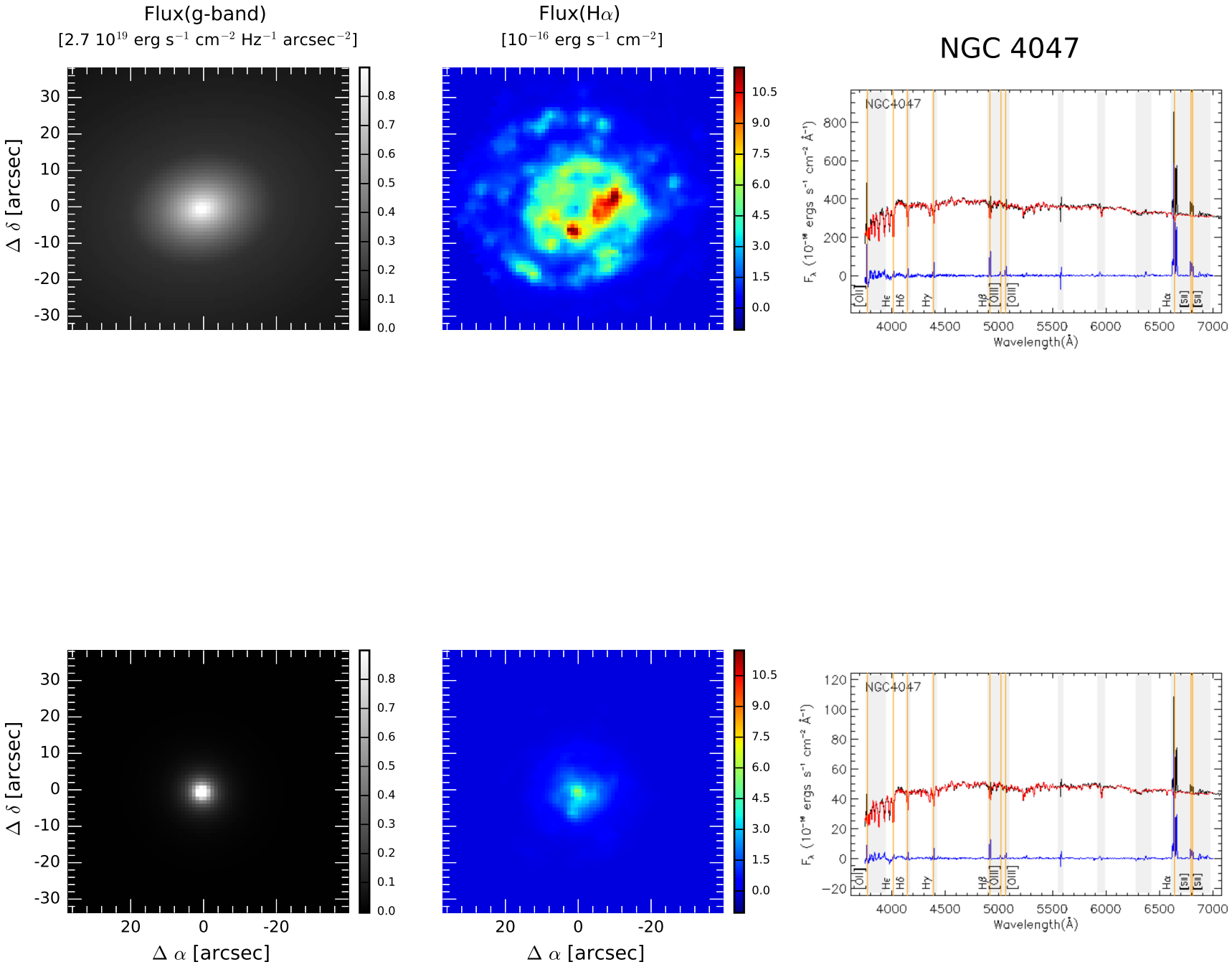
Flux(g-band)
[2.7 10^19 erg s^-1 cm^-2 Hz^-1 arcsec^-2]
Flux(Hα)
[10^-16 erg s^-1 cm^-2]
NGC 4047
Δ δ [arcsec]
Δ α [arcsec]
NGC4047
Wavelength(Å)
[OII]
Hε
Hδ
Hγ
Hβ
[OIII]
[OIII]
Hα
[SII]
[SII]

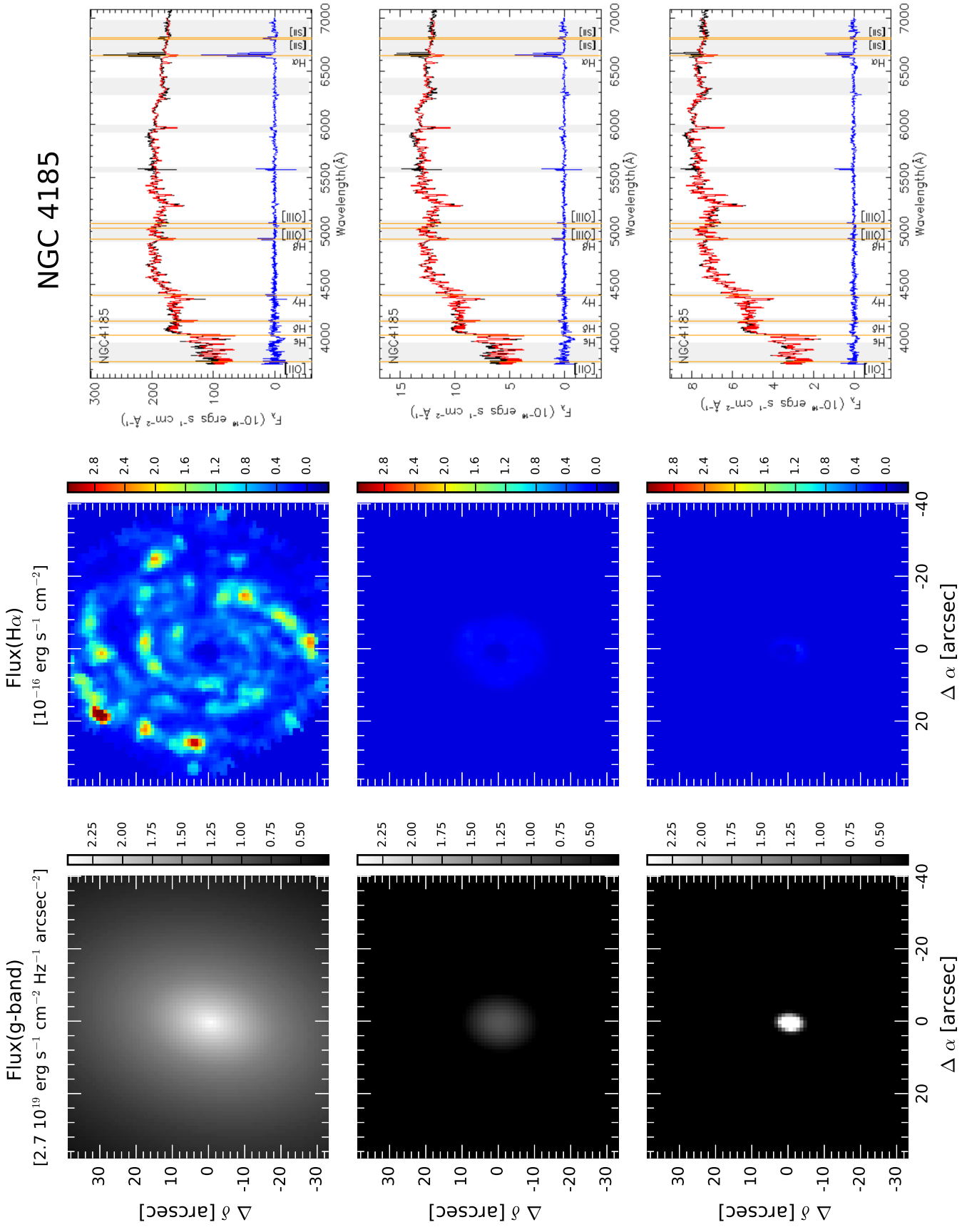
NGC 4185
Flux(g-band)
[2.7 10^19 erg s^-1 cm^-2 Hz^-1 arcsec^-2]
Flux(Hα)
[10^-16 erg s^-1 cm^-2]
Δ δ [arcsec]
Δ α [arcsec]
Wavelength(Å)
F_λ (10^-16 ergs s^-1 cm^-2 Å^-1)
NGC4185
[OII]
Hε
Hδ
Hγ
[OIII]
Hβ
[OIII]
Hα
[SII]
[SII]

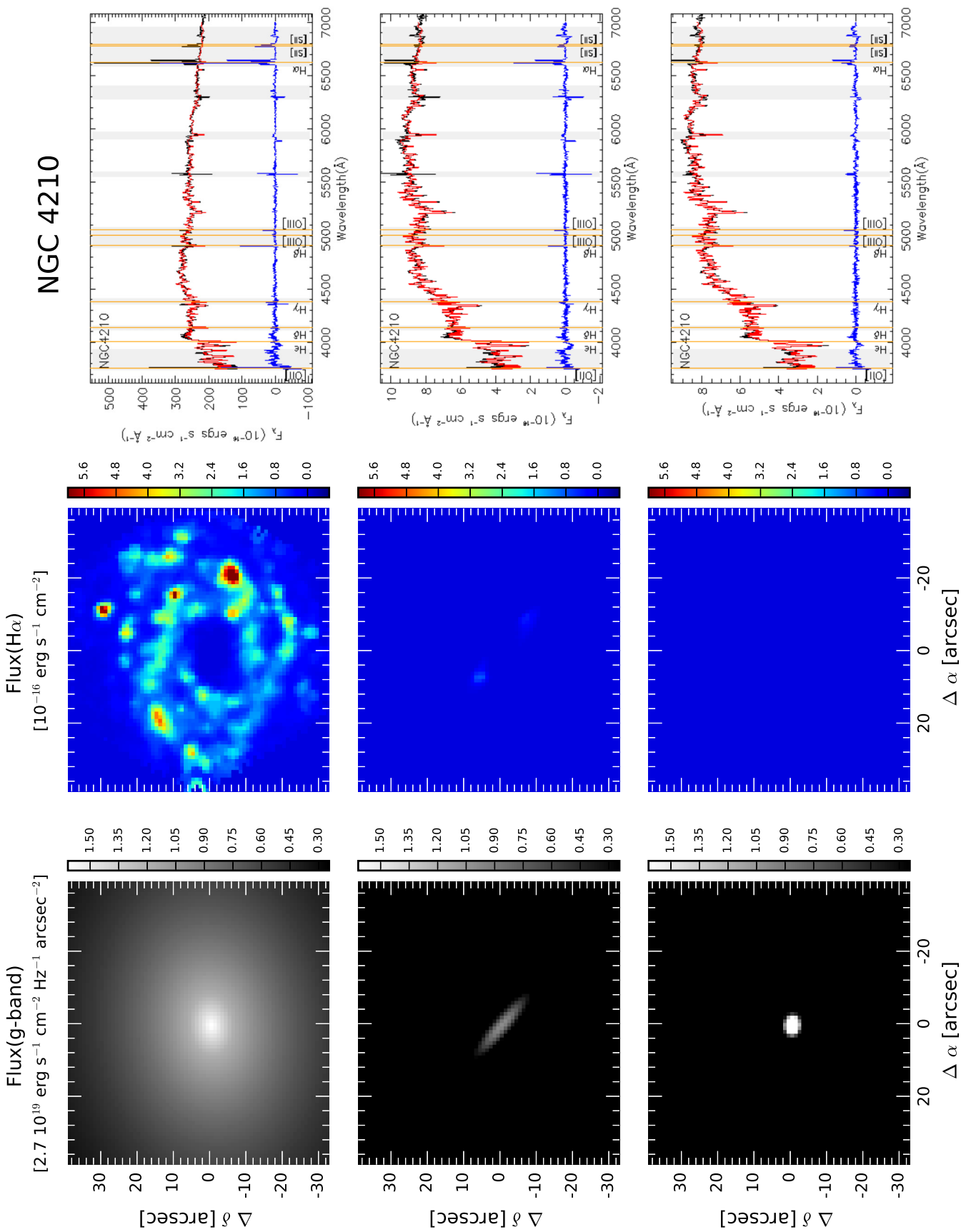
NGC 4210
Flux(g-band)
[2.7 10^19 erg s^-1 cm^-2 Hz^-1 arcsec^-2]
Flux(Hα)
[10^-16 erg s^-1 cm^-2]
Δ δ [arcsec]
Δ α [arcsec]
Wavelength(Å)
NGC4210
[OII]
Hε
Hδ
Hγ
Hβ
[OIII]
[OIII]
Hα
[SII]
[SII]

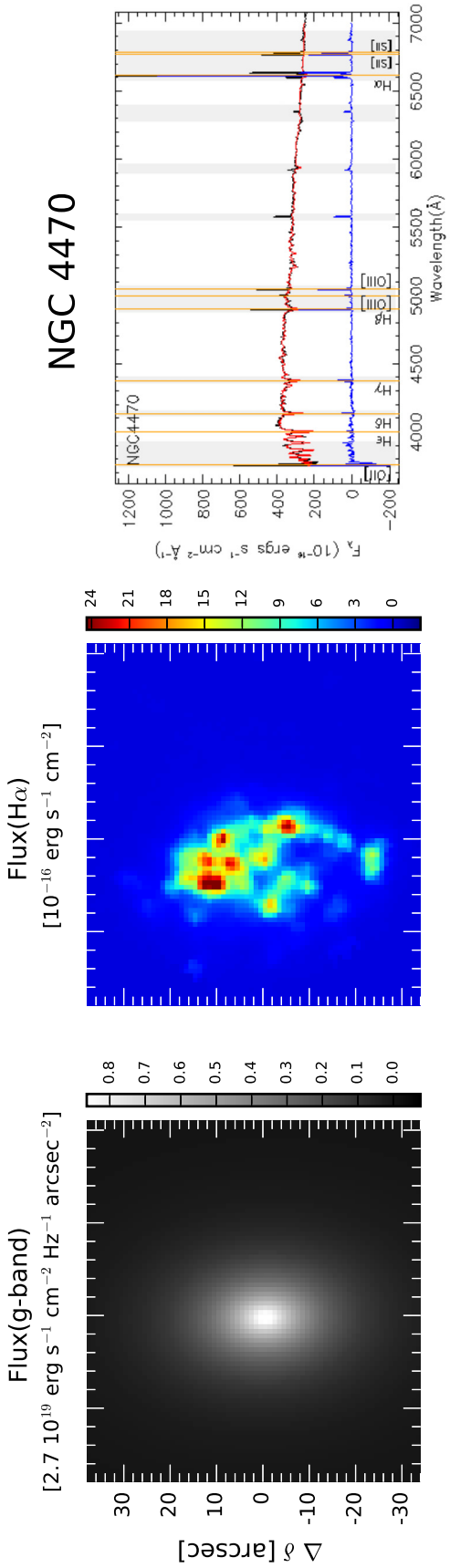
NGC 4470
NGC4470
[OII]
Hε
Hδ
Hγ
Hβ
[OIII]
[OIII]
[SII]
[SII]
Hα
Wavelength(Å)
Flux(Hα)
[10⁻¹⁶ erg s⁻¹ cm⁻²]
Flux(g-band)
[2.7 10¹⁹ erg s⁻¹ cm⁻² Hz⁻¹ arcsec⁻²]
Δ δ [arcsec]

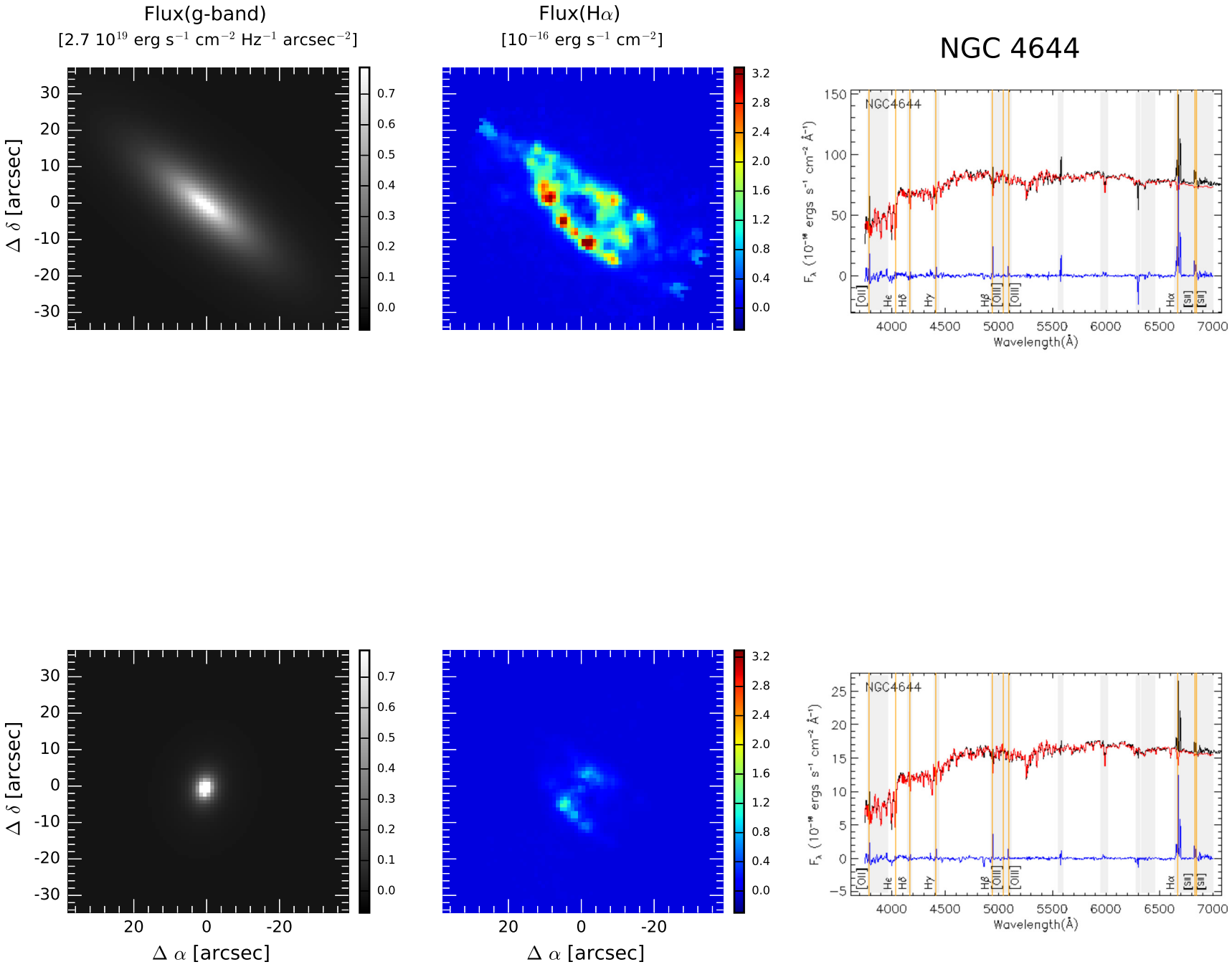
Flux(g-band)
[2.7 10^19 erg s^-1 cm^-2 Hz^-1 arcsec^-2]
Flux(Hα)
[10^-16 erg s^-1 cm^-2]
NGC 4644
Δ δ [arcsec]
Δ α [arcsec]
NGC4644
Wavelength(Å)
[OII]
Hε
Hδ
Hγ
Hβ
[OIII]
[OIII]
Hα
[SII]
[SII]

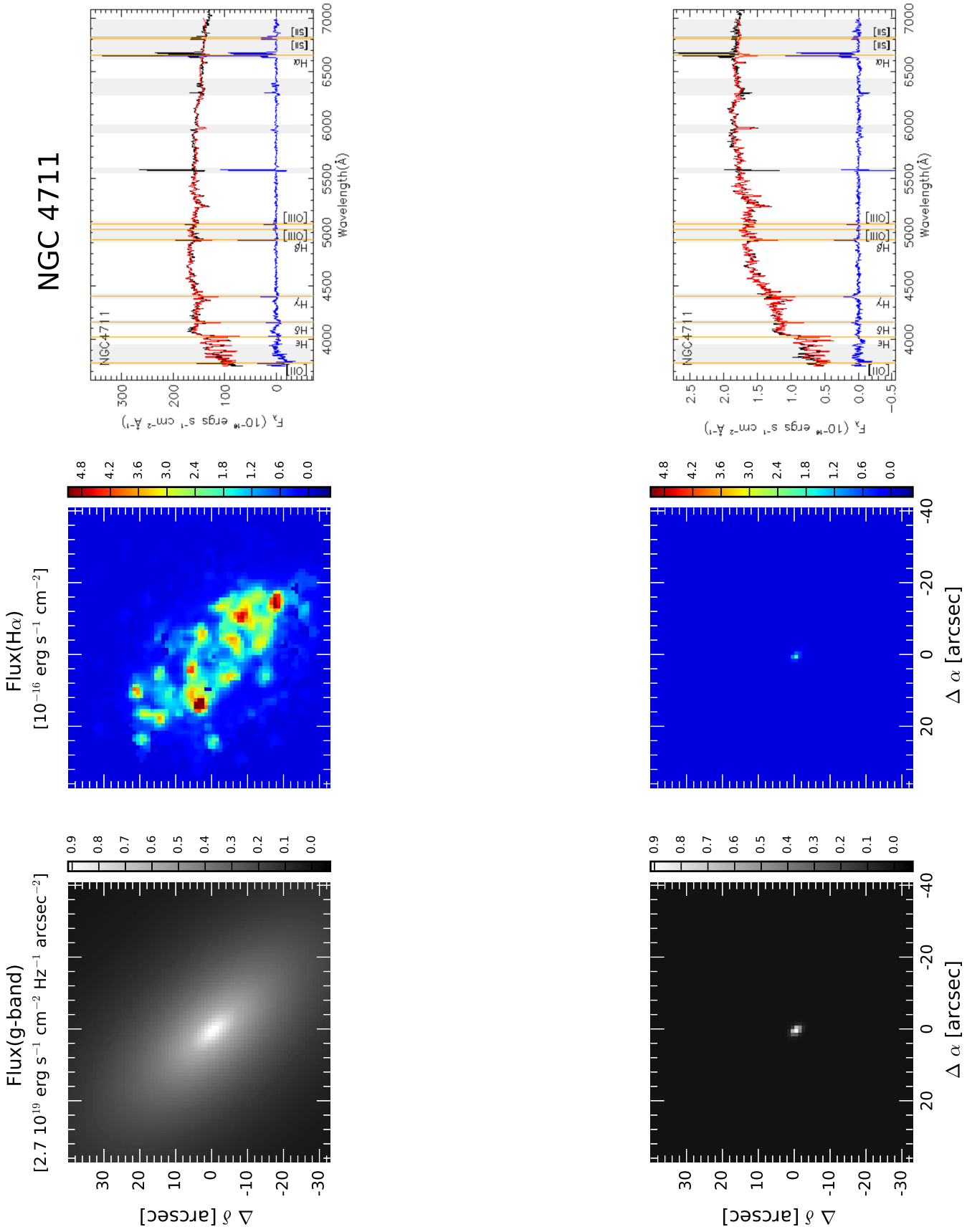
NGC 4711
Flux(g-band)
[2.7 10^19 erg s^-1 cm^-2 Hz^-1 arcsec^-2]
Flux(Hα)
[10^-16 erg s^-1 cm^-2]
Δ δ [arcsec]
Δ α [arcsec]
Wavelength(Å)
F_λ (10^-16 ergs s^-1 cm^-2 Å^-1)
NGC4711
[OII]
Hε
Hδ
Hγ
[OIII]
Hβ
[OIII]
Hα
[SII]
[SII]

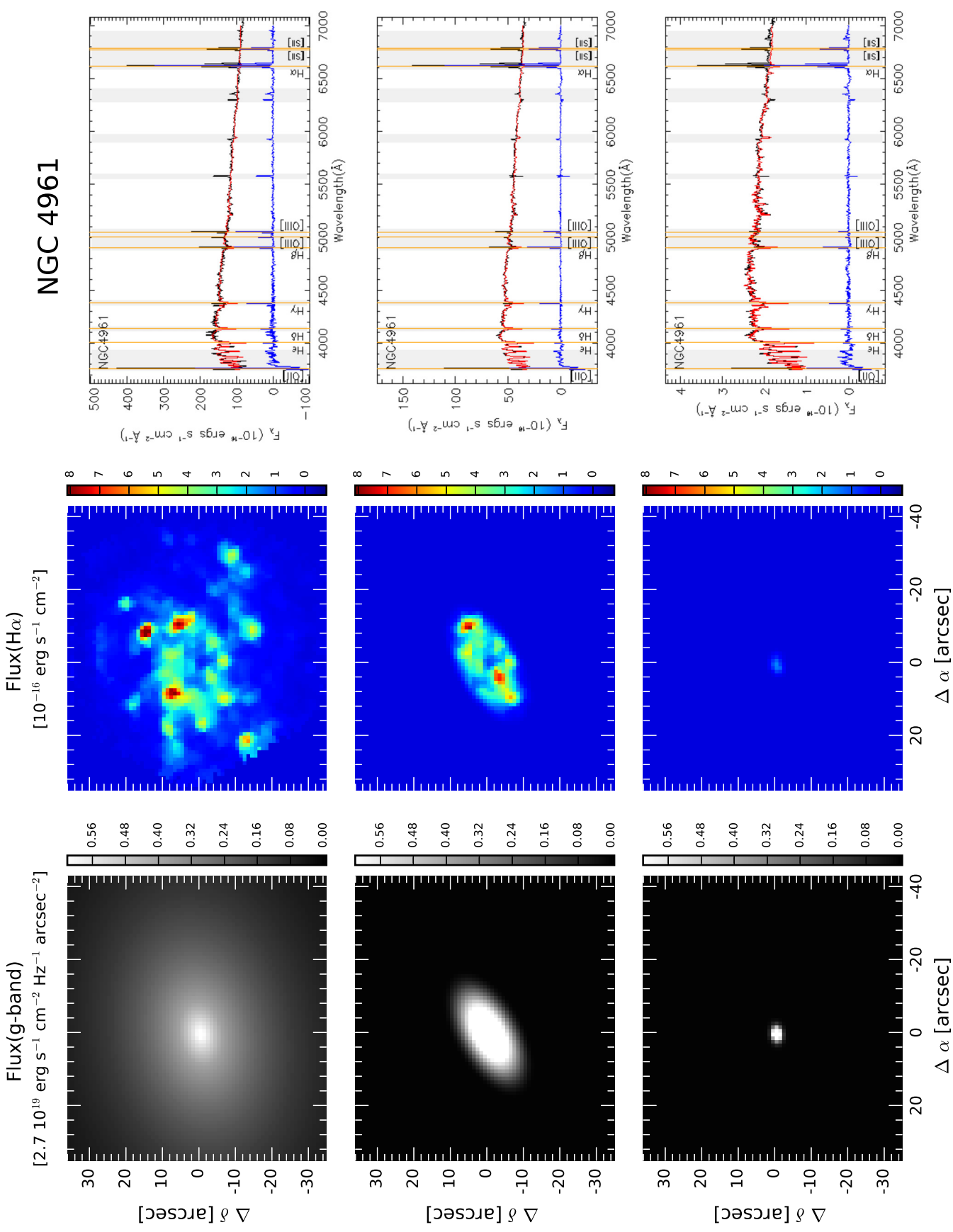
NGC 4961
Flux(g-band)
[2.7 10^19 erg s^-1 cm^-2 Hz^-1 arcsec^-2]
Flux(Hα)
[10^-16 erg s^-1 cm^-2]
Δ δ [arcsec]
Δ α [arcsec]
F_λ (10^-16 ergs s^-1 cm^-2 Å^-1)
Wavelength(Å)
NGC4961
[OII]
Hε
Hδ
Hγ
Hβ
[OIII]
[OIII]
Hα
[SII]
[SII]

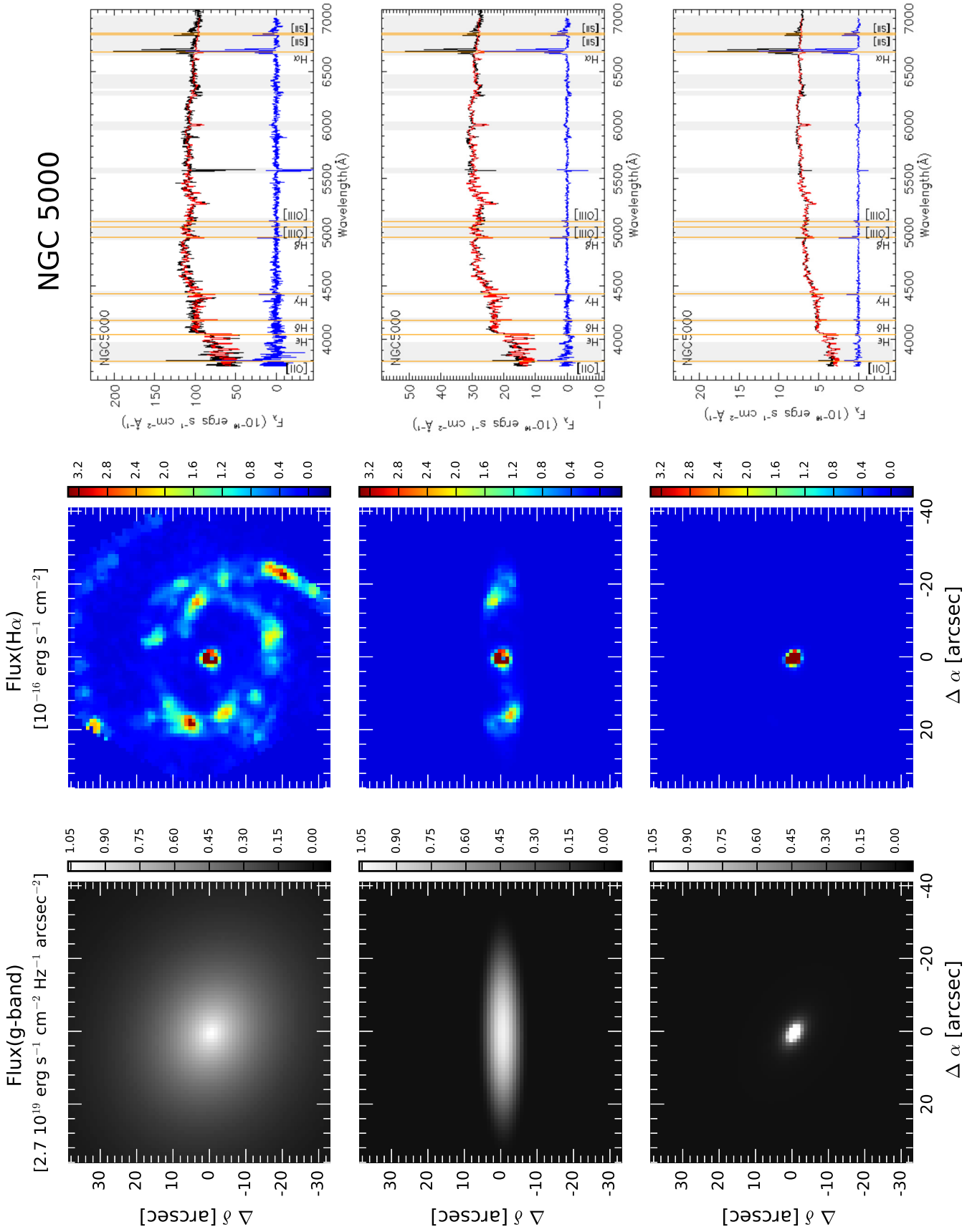
NGC 5000
Flux(g-band)
[2.7 10^19 erg s^-1 cm^-2 Hz^-1 arcsec^-2]
Flux(Hα)
[10^-16 erg s^-1 cm^-2]
Δ δ [arcsec]
Δ α [arcsec]
Wavelength(Å)
NGC5000
[OII]
Hε
Hδ
Hγ
Hβ
[OIII]
[OIII]
[SII]
[SII]
Hα

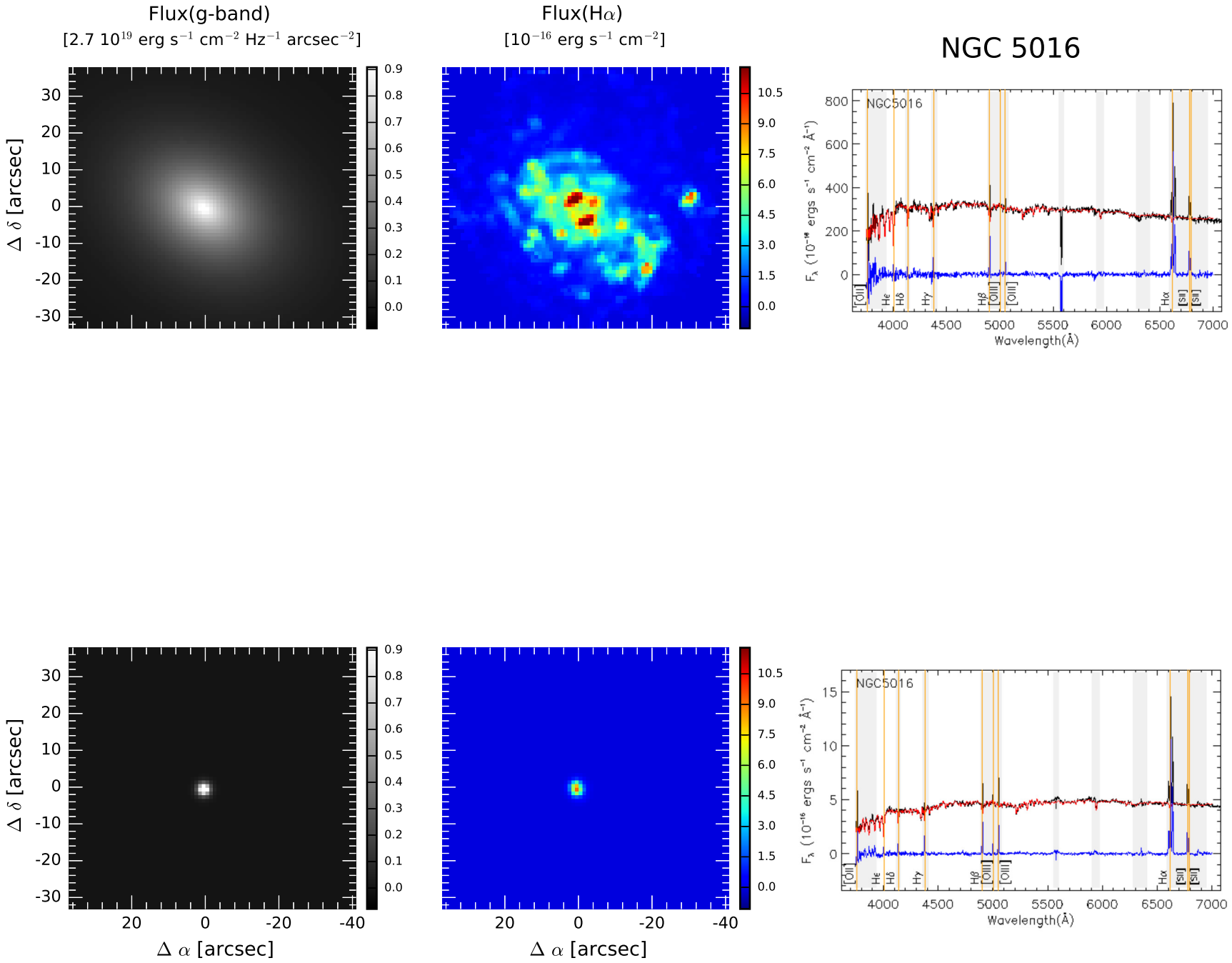
Flux(g-band)
[2.7 10^19 erg s^-1 cm^-2 Hz^-1 arcsec^-2]
Flux(Hα)
[10^-16 erg s^-1 cm^-2]
NGC 5016
Δ δ [arcsec]
Δ α [arcsec]
NGC5016
Wavelength(Å)
[OII]
Hε
Hδ
Hγ
Hβ
[OIII]
[OIII]
Hα
[SII]
[SII]

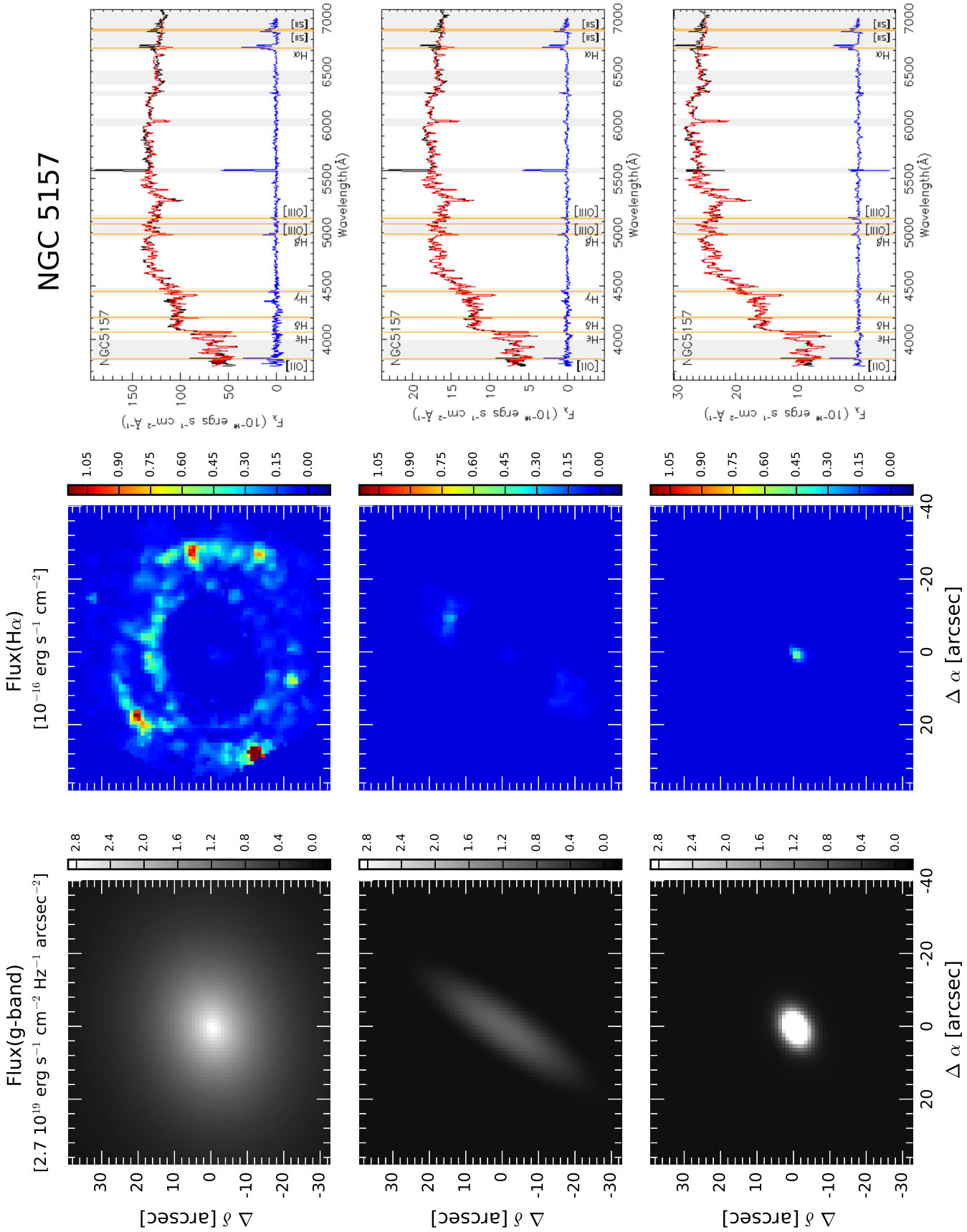
NGC 5157
Flux(g-band)
[2.7 10^19 erg s^-1 cm^-2 Hz^-1 arcsec^-2]
Flux(Hα)
[10^-16 erg s^-1 cm^-2]
Δ δ [arcsec]
Δ α [arcsec]
Wavelength(Å)
F_λ (10^-16 ergs s^-1 cm^-2 Å^-1)
NGC5157
[OII]
Hε
Hδ
Hγ
Hβ
[OIII]
[OIII]
[SII]
[SII]
Hα

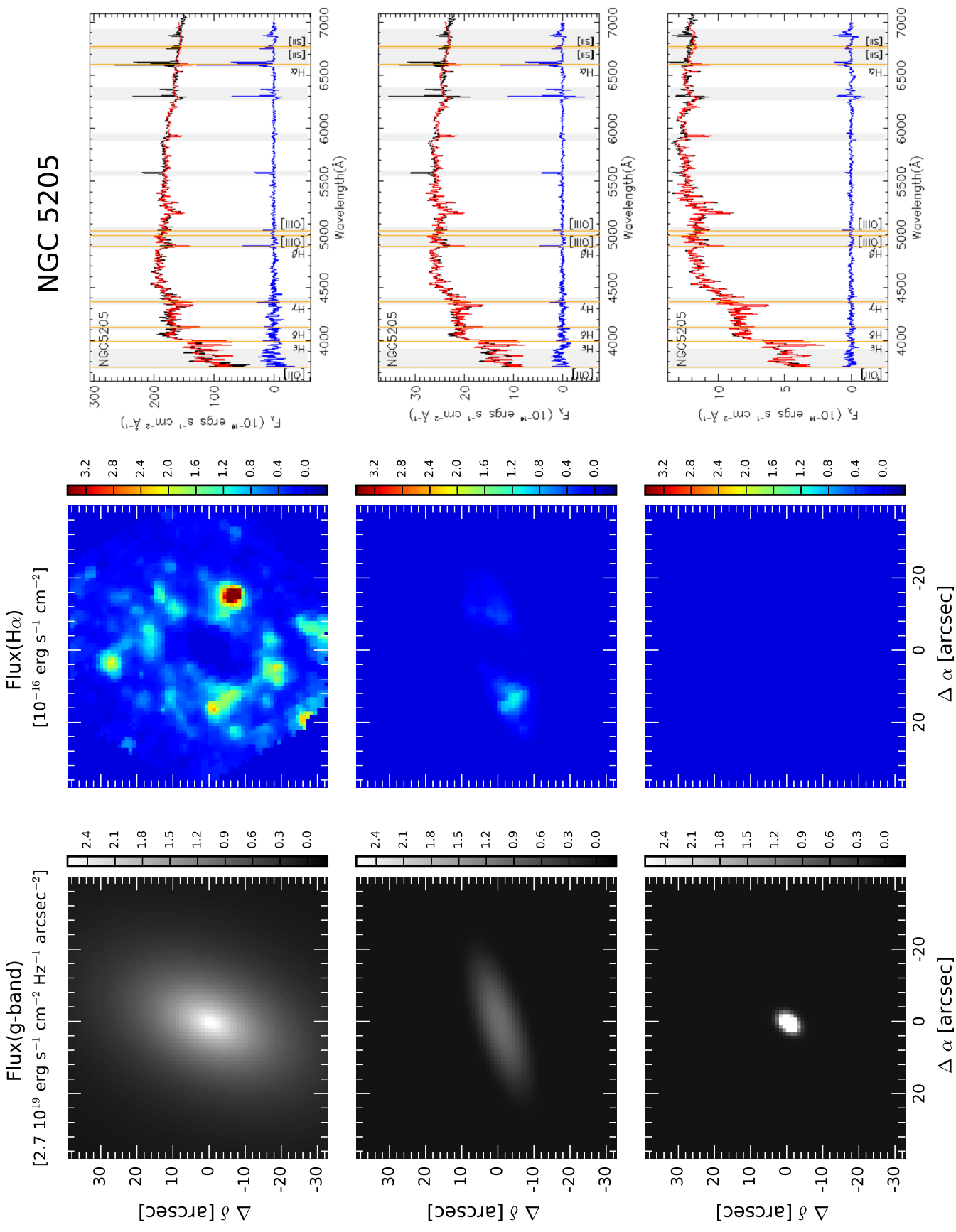
NGC 5205
Flux(g-band)
[2.7 10^19 erg s^-1 cm^-2 Hz^-1 arcsec^-2]
Flux(Hα)
[10^-16 erg s^-1 cm^-2]
Δ δ [arcsec]
Δ α [arcsec]
Wavelength(Å)
NGC5205
[OII]
Hε
Hδ
Hγ
Hβ
[OIII]
Hα
[SII]

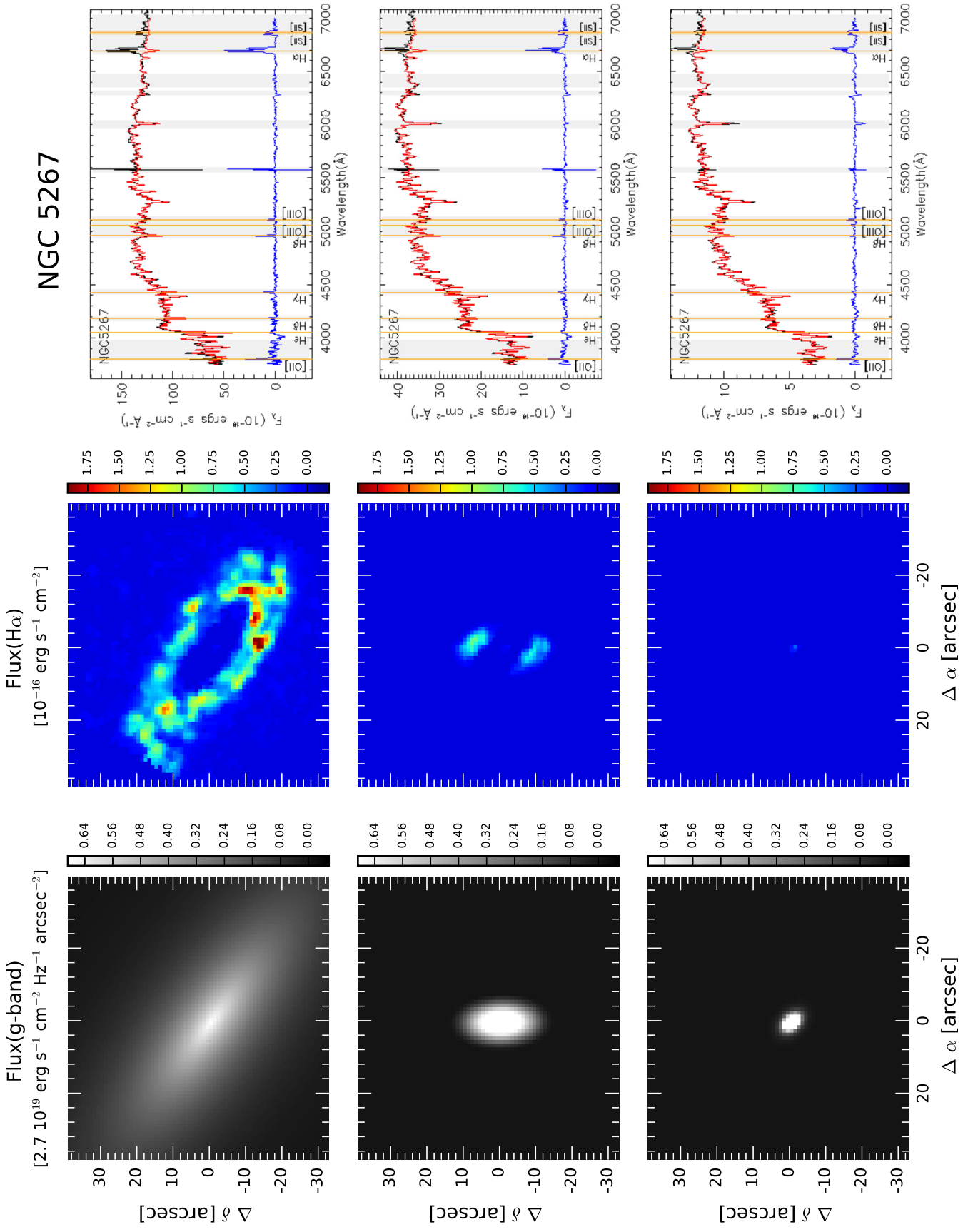
NGC 5267
Flux(g-band)
[2.7 10^19 erg s^-1 cm^-2 Hz^-1 arcsec^-2]
Flux(Hα)
[10^-16 erg s^-1 cm^-2]
Δ δ [arcsec]
Δ α [arcsec]
Wavelength(Å)
NGC5267
[OII]
Hε
Hδ
Hγ
Hβ
[OIII]
[OIII]
[SII]
[SII]
Hα

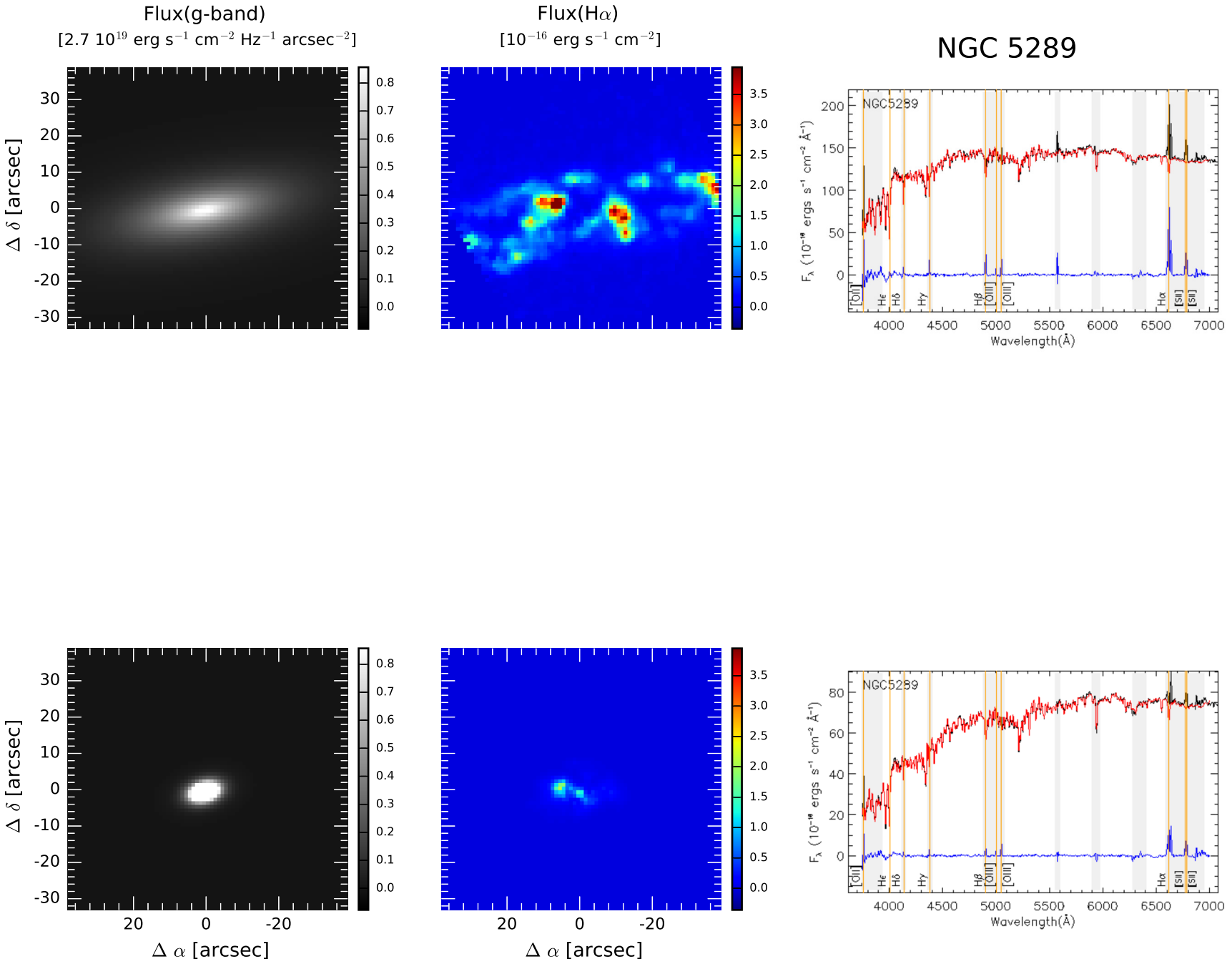
Flux(g-band)
[2.7 10^19 erg s^-1 cm^-2 Hz^-1 arcsec^-2]
Flux(Hα)
[10^-16 erg s^-1 cm^-2]
NGC 5289
Δ δ [arcsec]
Δ α [arcsec]
NGC5289
Wavelength(Å)
[OII]
Hε
Hδ
Hγ
Hβ
[OIII]
[OIII]
Hα
[SII]
[SII]

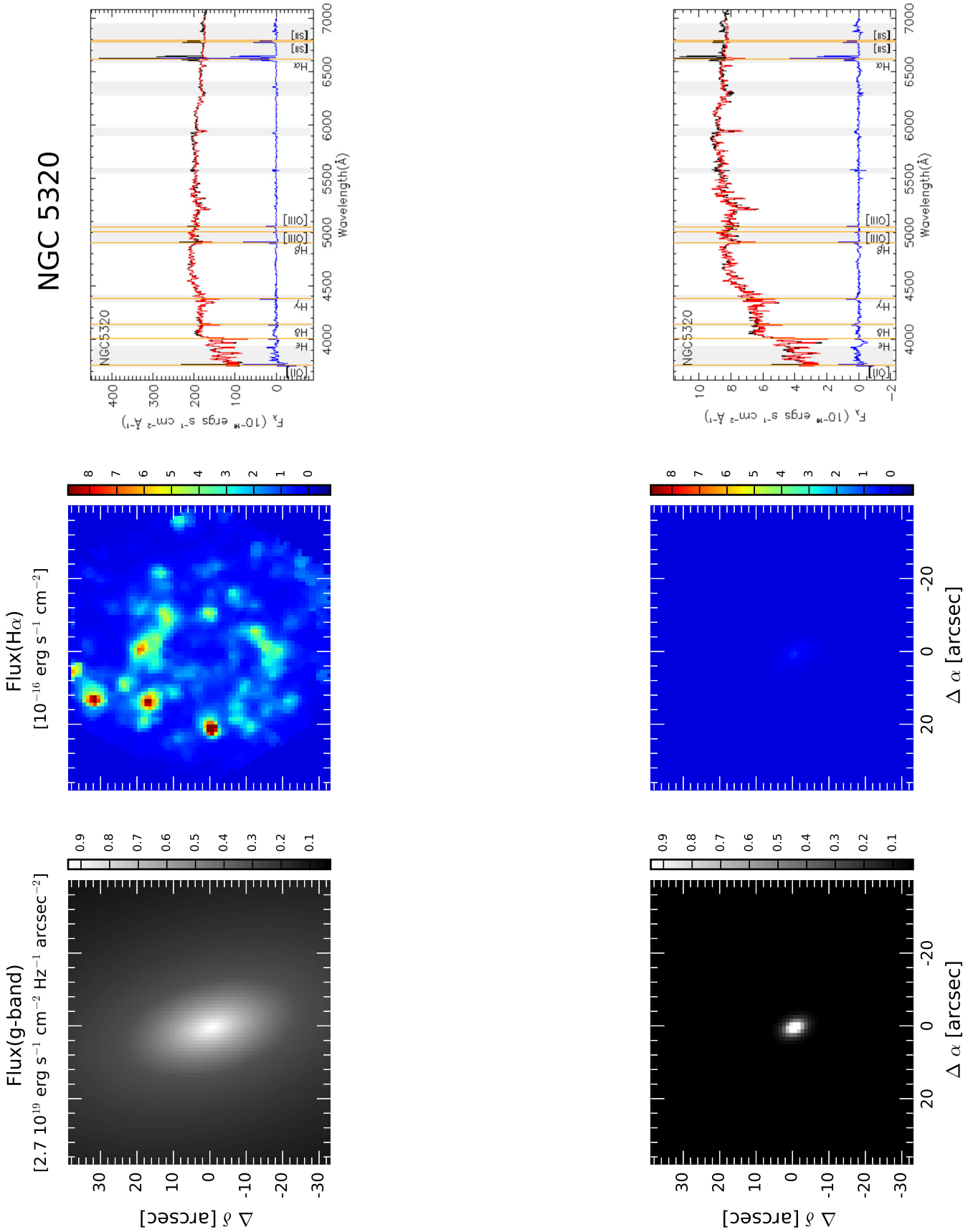
NGC 5320
NGC5320
[OII]
Hε
Hδ
Hγ
Hβ
[OIII]
[OIII]
Hα
[SII]
[SII]
Wavelength(Å)
Flux(Hα)
[10⁻¹⁶ erg s⁻¹ cm⁻²]
Flux(g-band)
[2.7 10¹⁹ erg s⁻¹ cm⁻² Hz⁻¹ arcsec⁻²]
Δ δ [arcsec]
Δ α [arcsec]

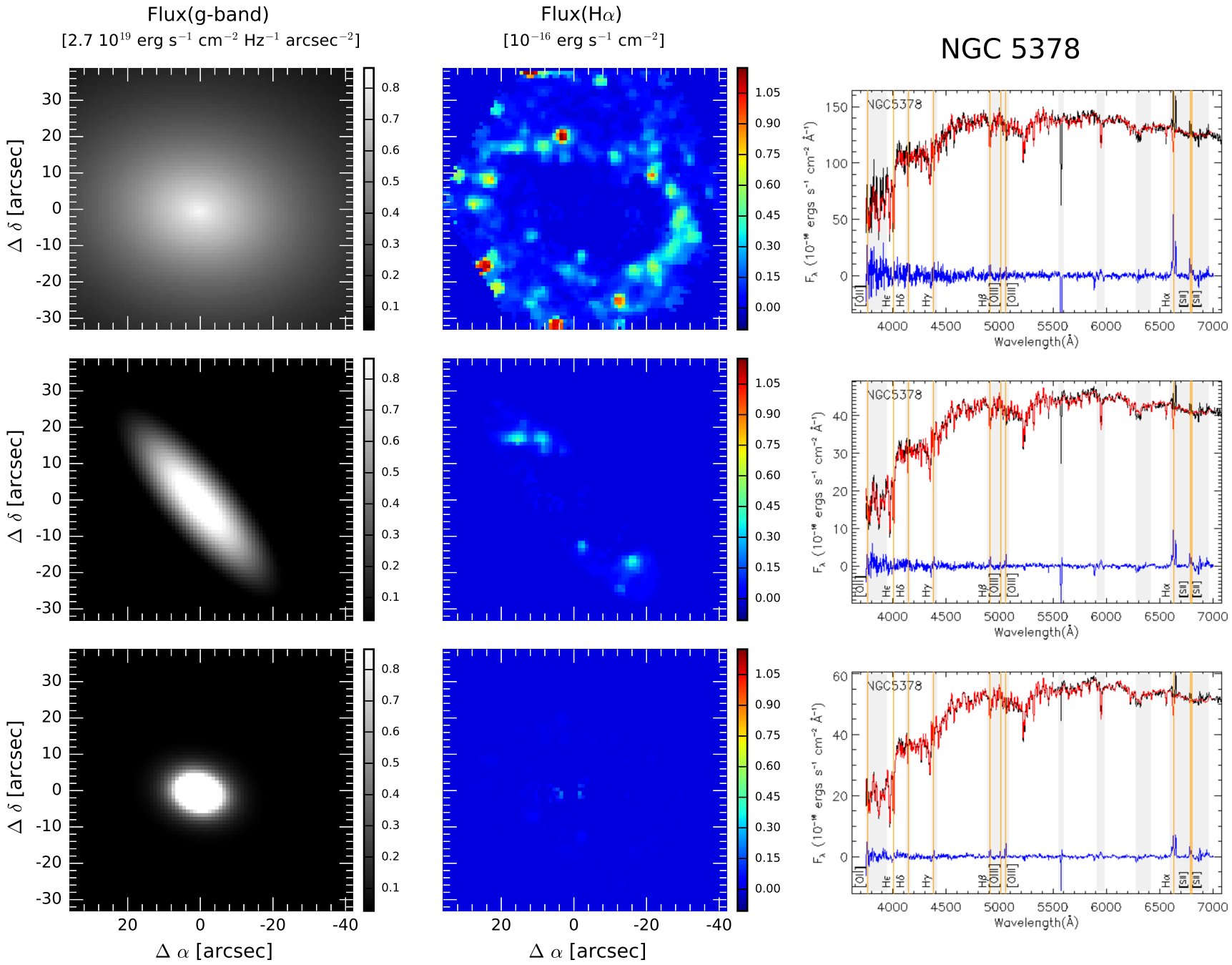
Flux(g-band)
[2.7 10^19 erg s^-1 cm^-2 Hz^-1 arcsec^-2]
Flux(Hα)
[10^-16 erg s^-1 cm^-2]
NGC 5378
Δ δ [arcsec]
Δ α [arcsec]
Wavelength(Å)
NGC5378

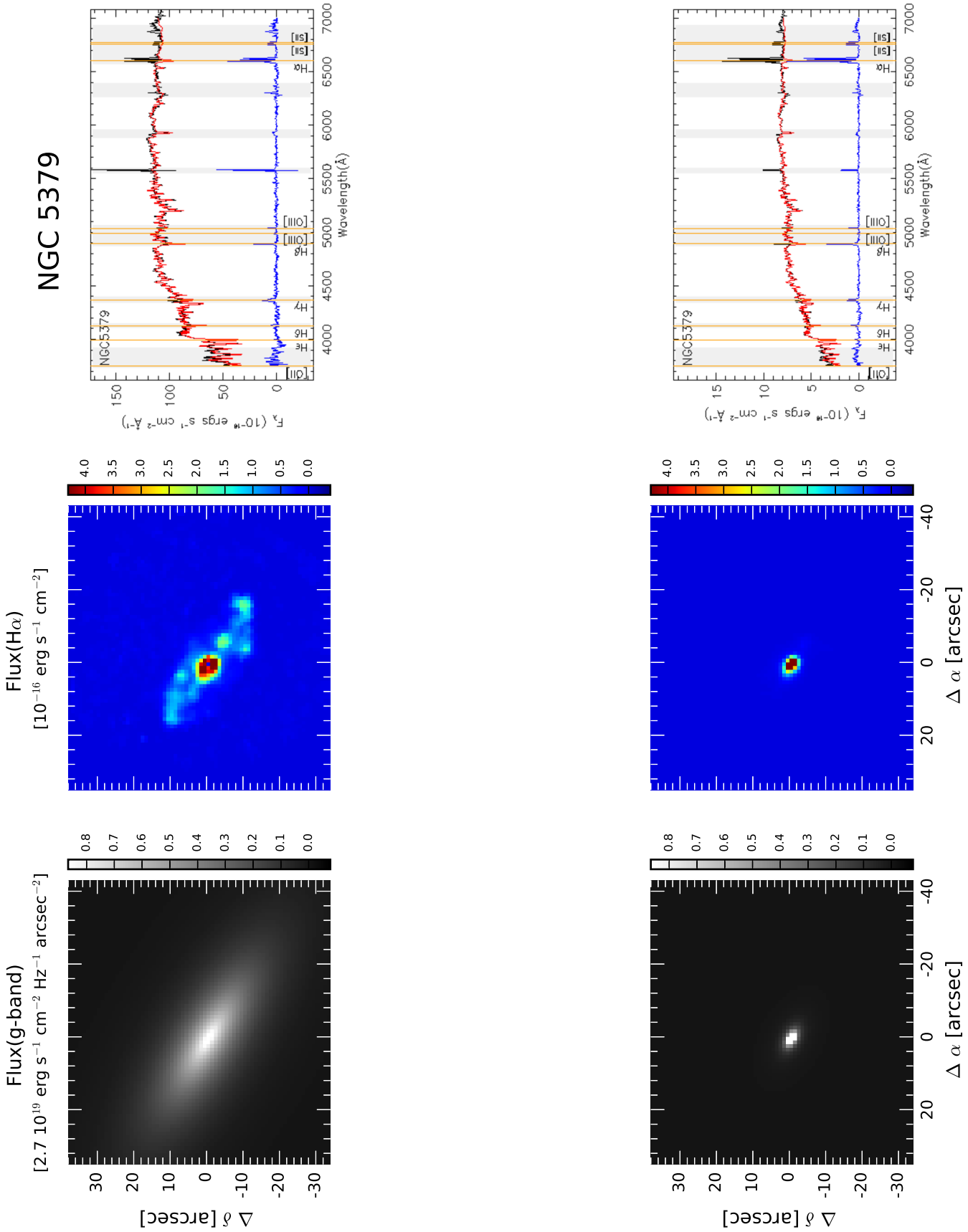
NGC 5379
Flux(g-band)
[2.7 10^19 erg s^-1 cm^-2 Hz^-1 arcsec^-2]
Flux(Hα)
[10^-16 erg s^-1 cm^-2]
Δ δ [arcsec]
Δ α [arcsec]
Wavelength(Å)
F_λ (10^-16 ergs s^-1 cm^-2 Å^-1)
NGC5379
[OII]
Hε
Hδ
Hγ
Hβ
[OIII]
[OIII]
[SII]
[SII]
Hα

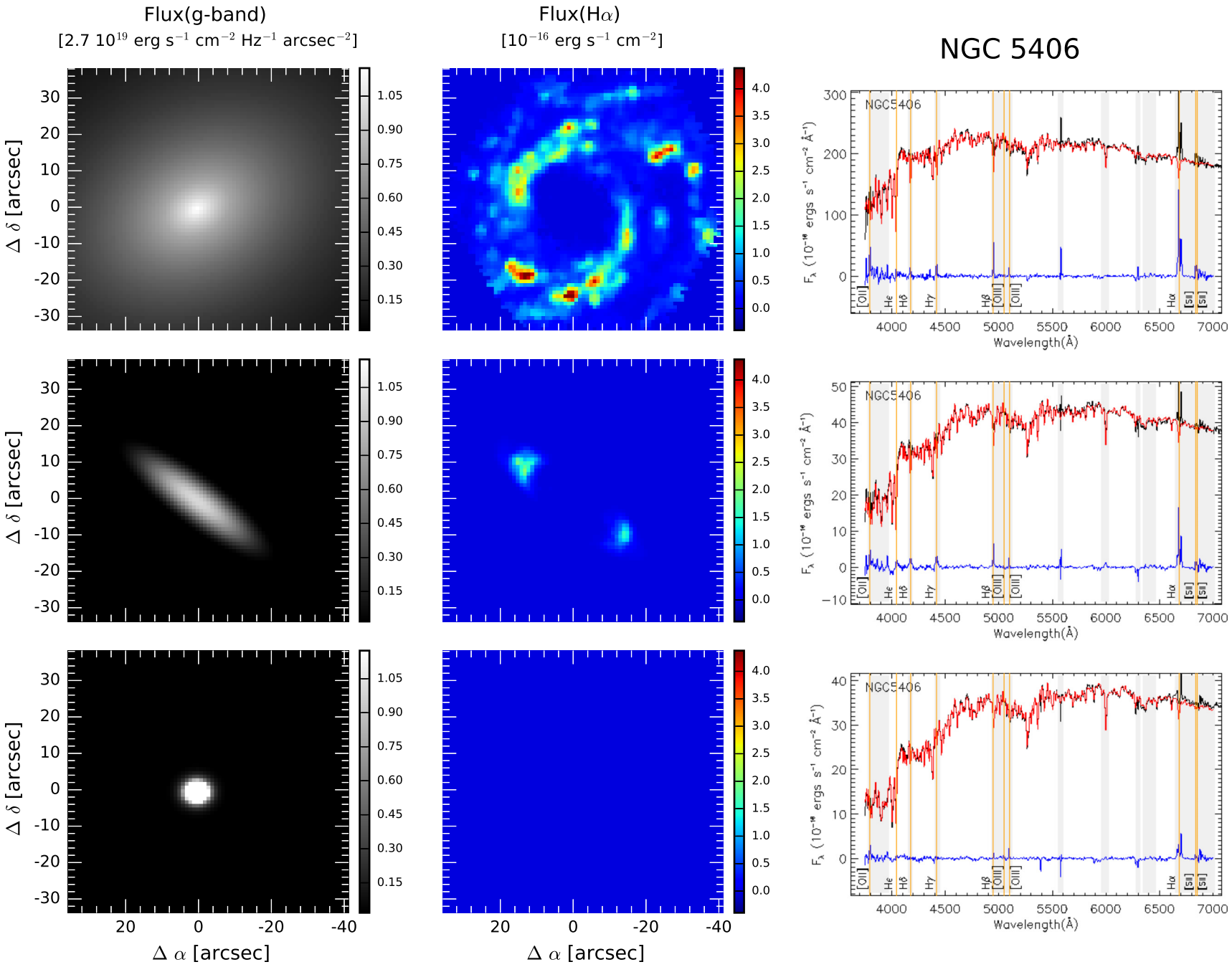
Flux(g-band)
[2.7 10^19 erg s^-1 cm^-2 Hz^-1 arcsec^-2]
Flux(Hα)
[10^-16 erg s^-1 cm^-2]
NGC 5406
Δ δ [arcsec]
Δ α [arcsec]
Wavelength(Å)
NGC5406
[OII]
Hε
Hδ
Hγ
Hβ
[OIII]
[OIII]
Hα
[SII]
[SII]

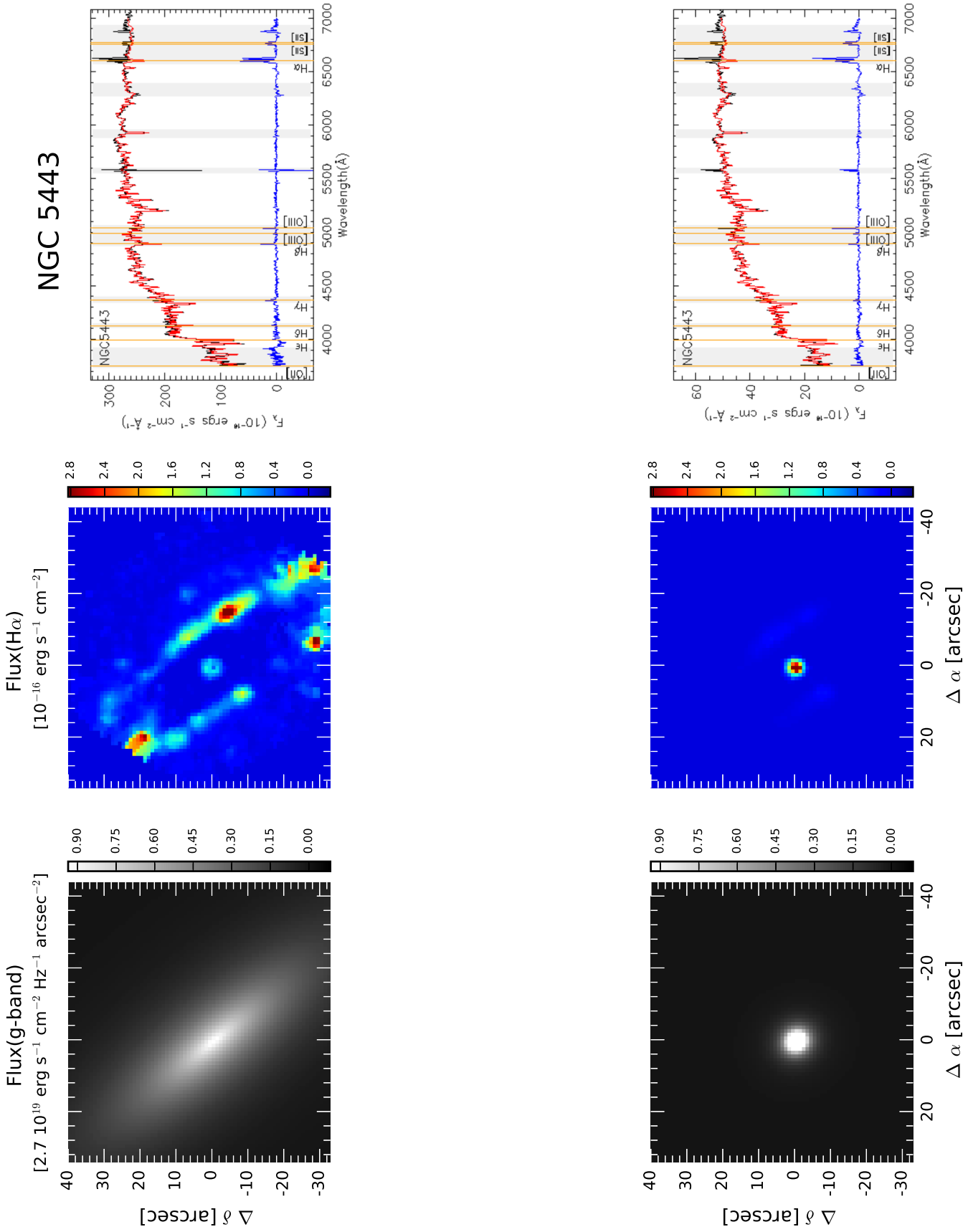
NGC 5443
Flux(g-band)
[2.7 10^19 erg s^-1 cm^-2 Hz^-1 arcsec^-2]
Flux(Hα)
[10^-16 erg s^-1 cm^-2]
Δ δ [arcsec]
Δ α [arcsec]
Wavelength(Å)
NGC5443
[OII]
Hε
Hδ
Hγ
Hβ
[OIII]
[OIII]
Hα
[SII]
[SII]

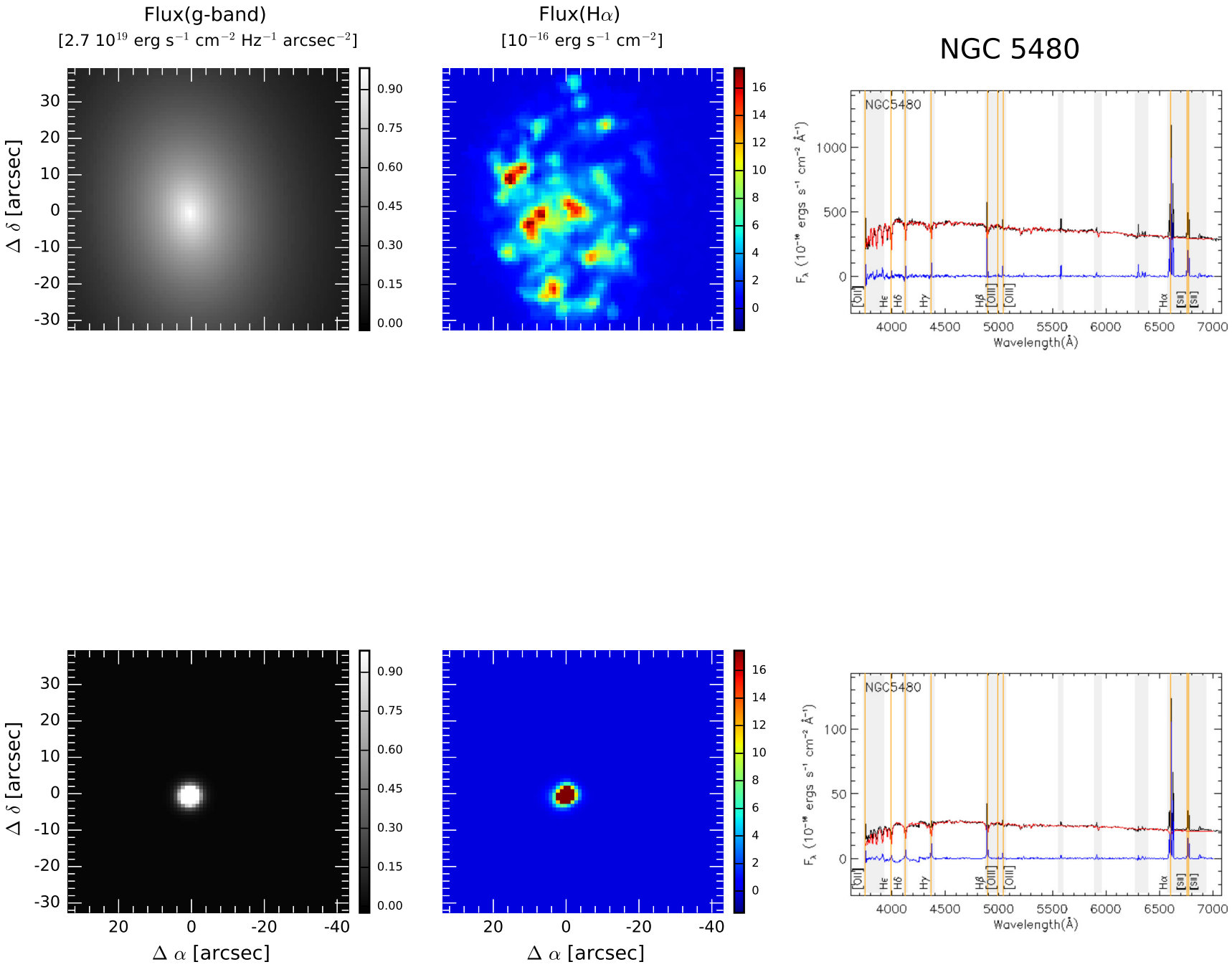
Flux(g-band)
[2.7 10^19 erg s^-1 cm^-2 Hz^-1 arcsec^-2]
Flux(Hα)
[10^-16 erg s^-1 cm^-2]
NGC 5480
Δ δ [arcsec]
Δ α [arcsec]
NGC5480
Wavelength(Å)
[OII]
Hε
Hδ
Hγ
Hβ
[OIII]
[OIII]
Hα
[SII]
[SII]

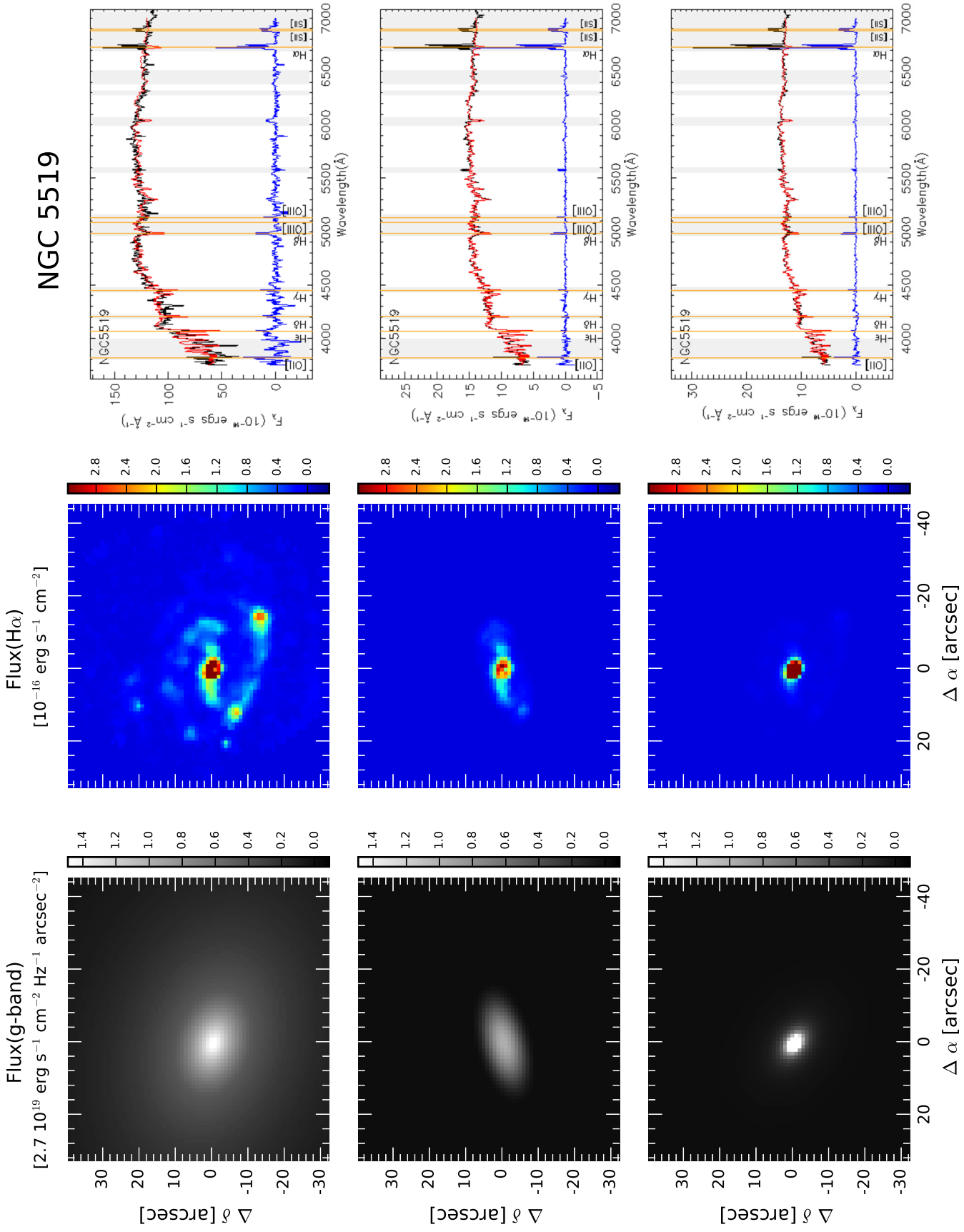
NGC 5519
Flux(g-band)
[2.7 10^19 erg s^-1 cm^-2 Hz^-1 arcsec^-2]
Flux(Hα)
[10^-16 erg s^-1 cm^-2]
Δ δ [arcsec]
Δ α [arcsec]
Wavelength(Å)
F_λ (10^-16 ergs s^-1 cm^-2 Å^-1)
NGC5519
[OII]
Hε
Hδ
Hγ
[OIII]
Hβ
[SII]
Hα

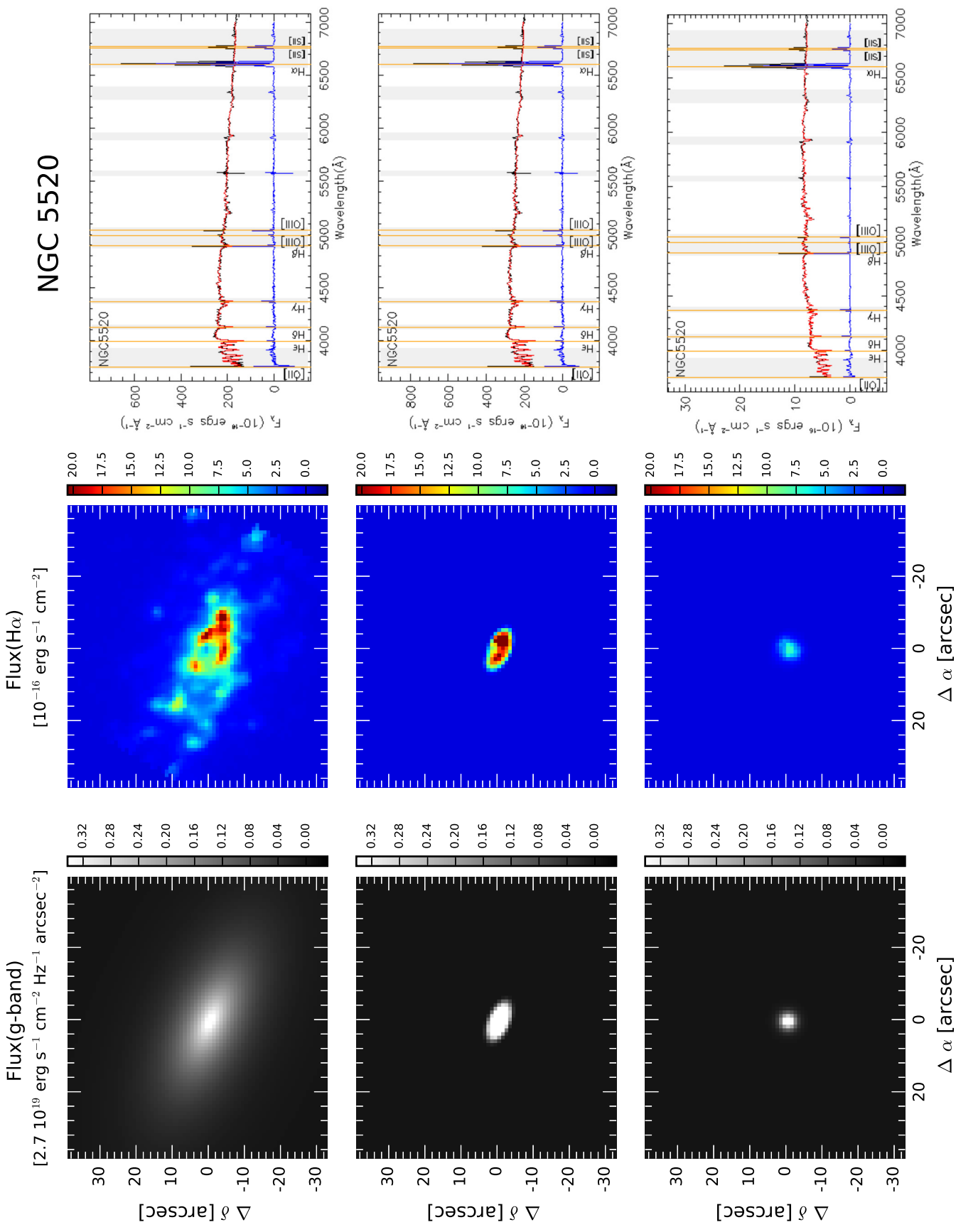
NGC 5520
Flux(g-band)
[2.7 10^19 erg s^-1 cm^-2 Hz^-1 arcsec^-2]
Flux(Hα)
[10^-16 erg s^-1 cm^-2]
Δ δ [arcsec]
Δ α [arcsec]
F_λ (10^-16 ergs s^-1 cm^-2 Å^-1)
Wavelength(Å)
NGC5520
[OII]
Hε
Hδ
Hγ
Hβ
[OIII]
[OIII]
[SII]
[SII]
Hα

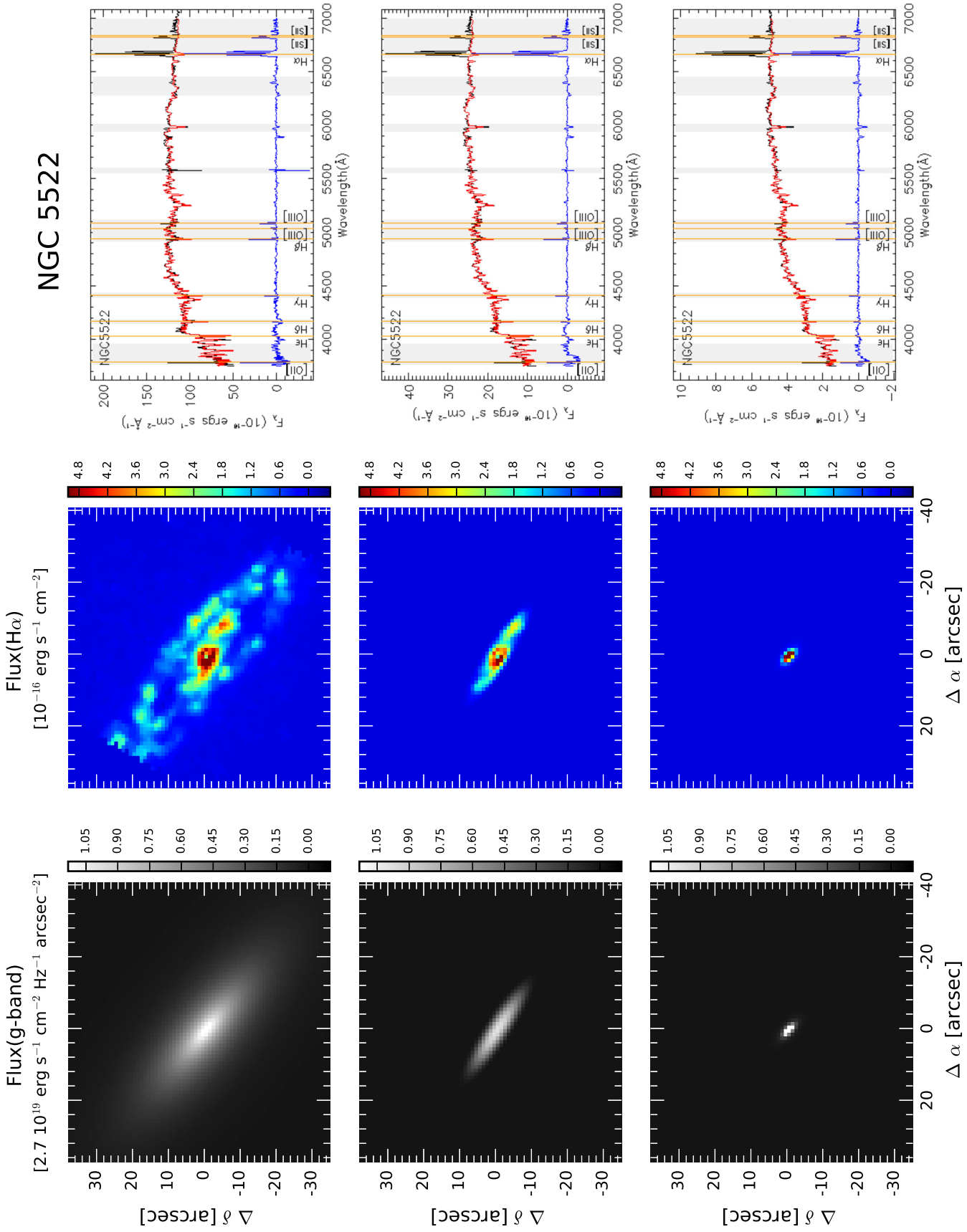
NGC 5522
Flux(Hα)
[10^-16 erg s^-1 cm^-2]
Flux(g-band)
[2.7 10^19 erg s^-1 cm^-2 Hz^-1 arcsec^-2]
Δ α [arcsec]
Δ δ [arcsec]
Wavelength(Å)
NGC5522
[OII]
Hε
Hδ
Hγ
Hβ
[OIII]
[OIII]
Hα
[SII]
[SII]

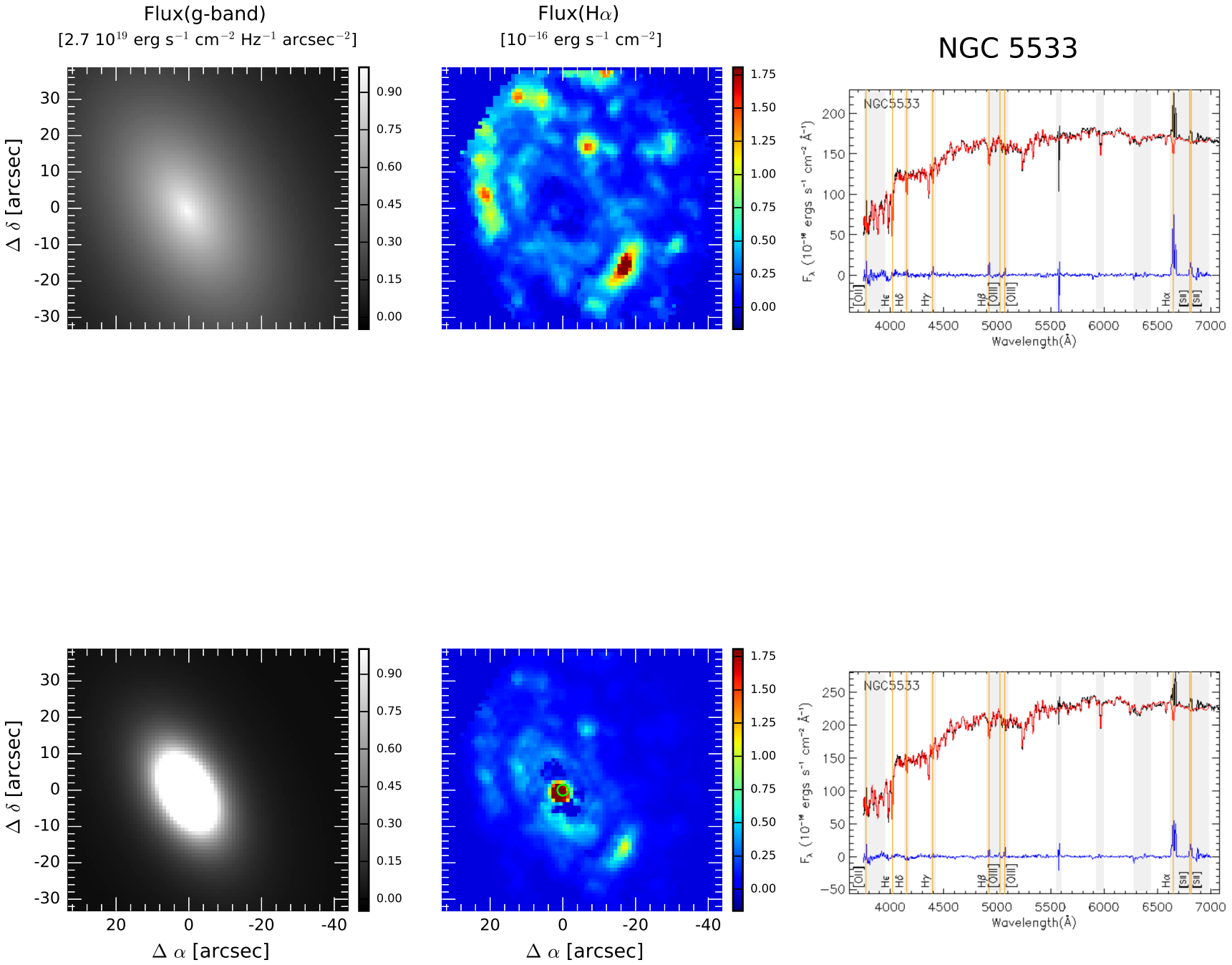
Flux(g-band)
[2.7 10^19 erg s^-1 cm^-2 Hz^-1 arcsec^-2]
Flux(Hα)
[10^-16 erg s^-1 cm^-2]
NGC 5533
Δ δ [arcsec]
Δ α [arcsec]
NGC5533
Wavelength(Å)
[OII]
Hε
Hδ
Hγ
Hβ
[OIII]
[OIII]
Hα
[SII]
[SII]

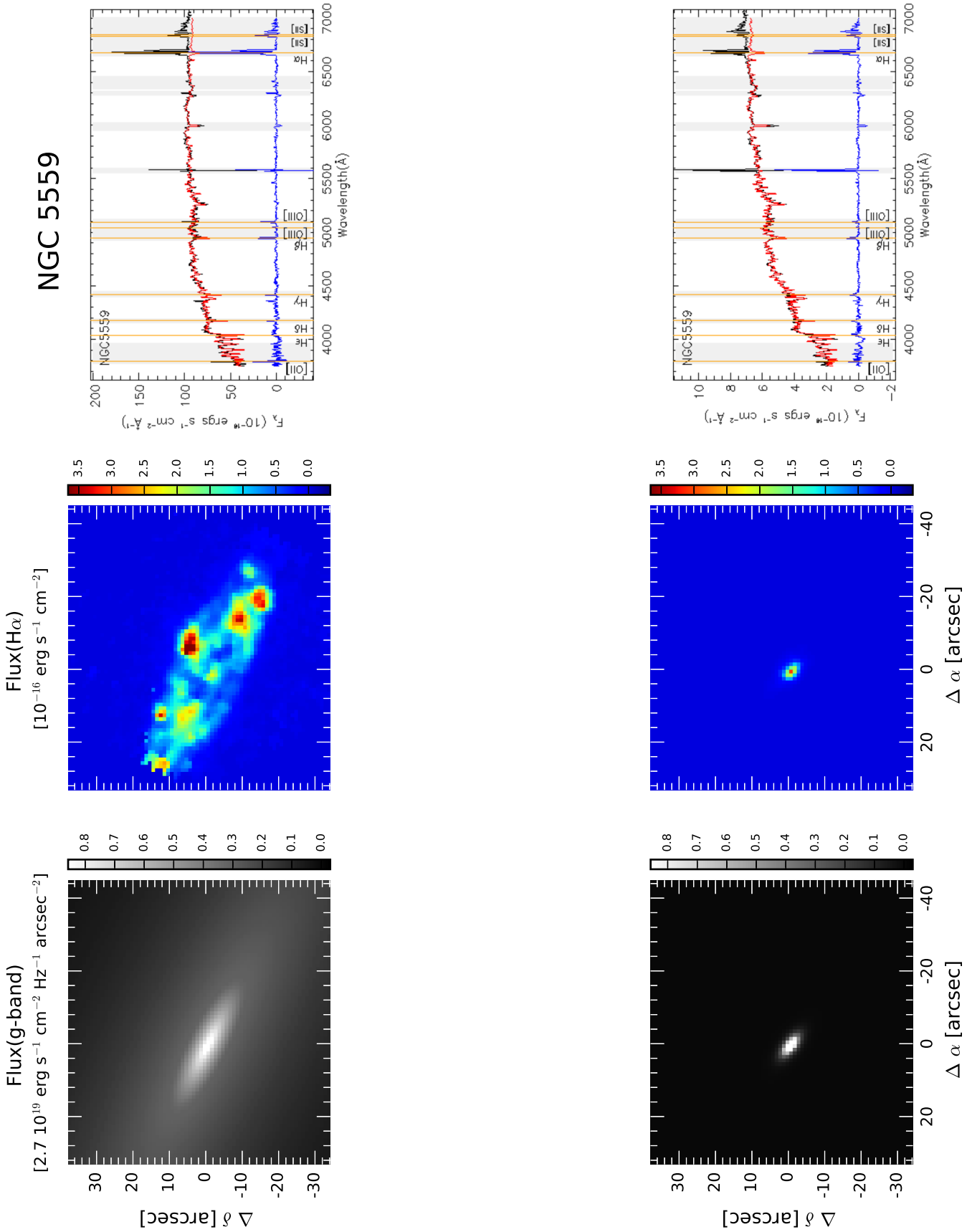
NGC 5559
Flux(g-band)
[2.7 10^19 erg s^-1 cm^-2 Hz^-1 arcsec^-2]
Flux(Hα)
[10^-16 erg s^-1 cm^-2]
Δ δ [arcsec]
Δ α [arcsec]
Wavelength(Å)
F_λ (10^-16 ergs s^-1 cm^-2 Å^-1)
NGC5559
[OII]
Hε
Hδ
Hγ
[OIII]
Hβ
[SII]
Hα

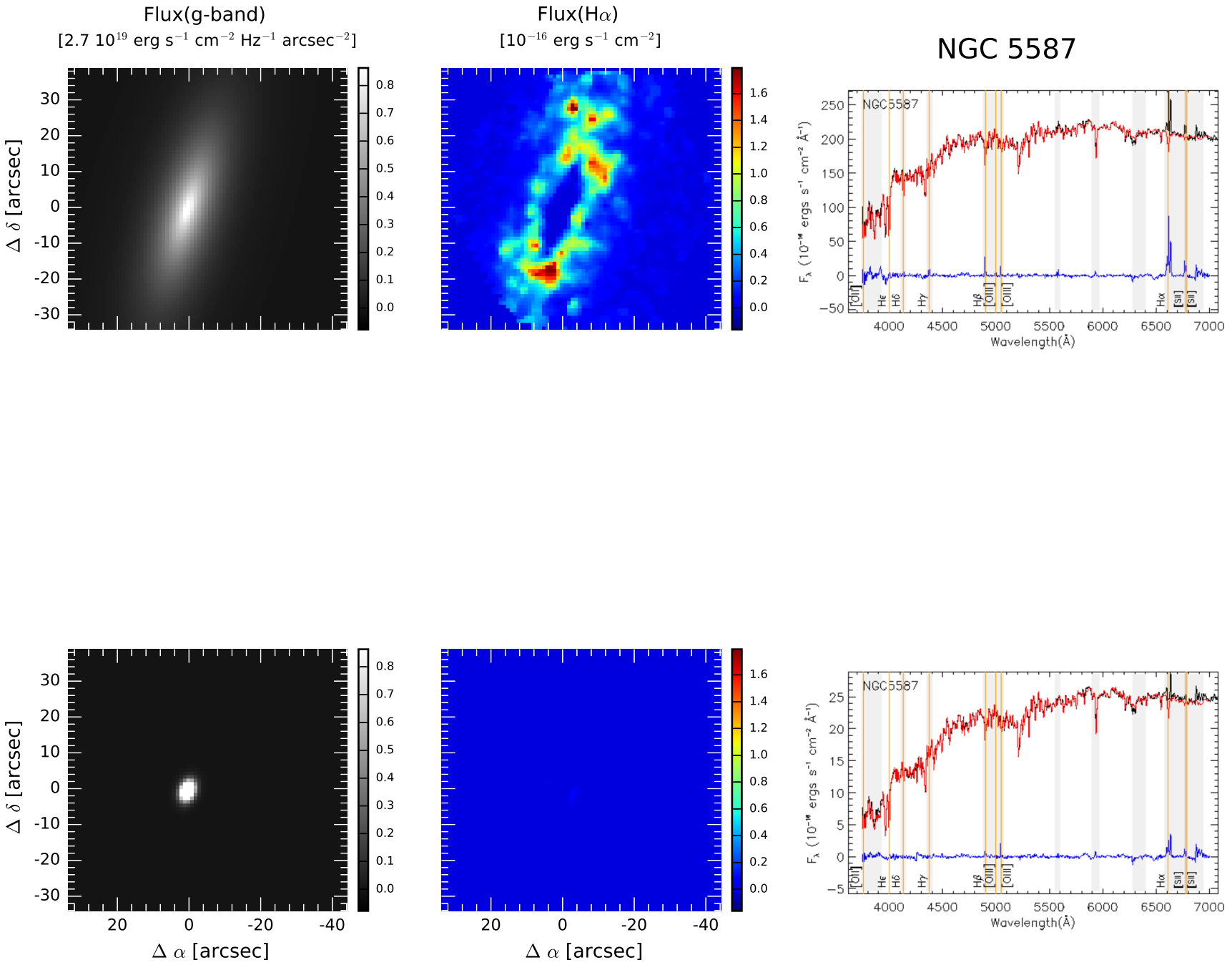
Flux(g-band)
[2.7 10^19 erg s^-1 cm^-2 Hz^-1 arcsec^-2]
Flux(Hα)
[10^-16 erg s^-1 cm^-2]
NGC 5587
Δ δ [arcsec]
Δ α [arcsec]
F_λ (10^-16 ergs s^-1 cm^-2 Å^-1)
Wavelength(Å)
NGC5587
[OIII]
Hε
Hδ
Hγ
Hβ
[OIII]
[OIII]
Hα
[SII]
[SII]

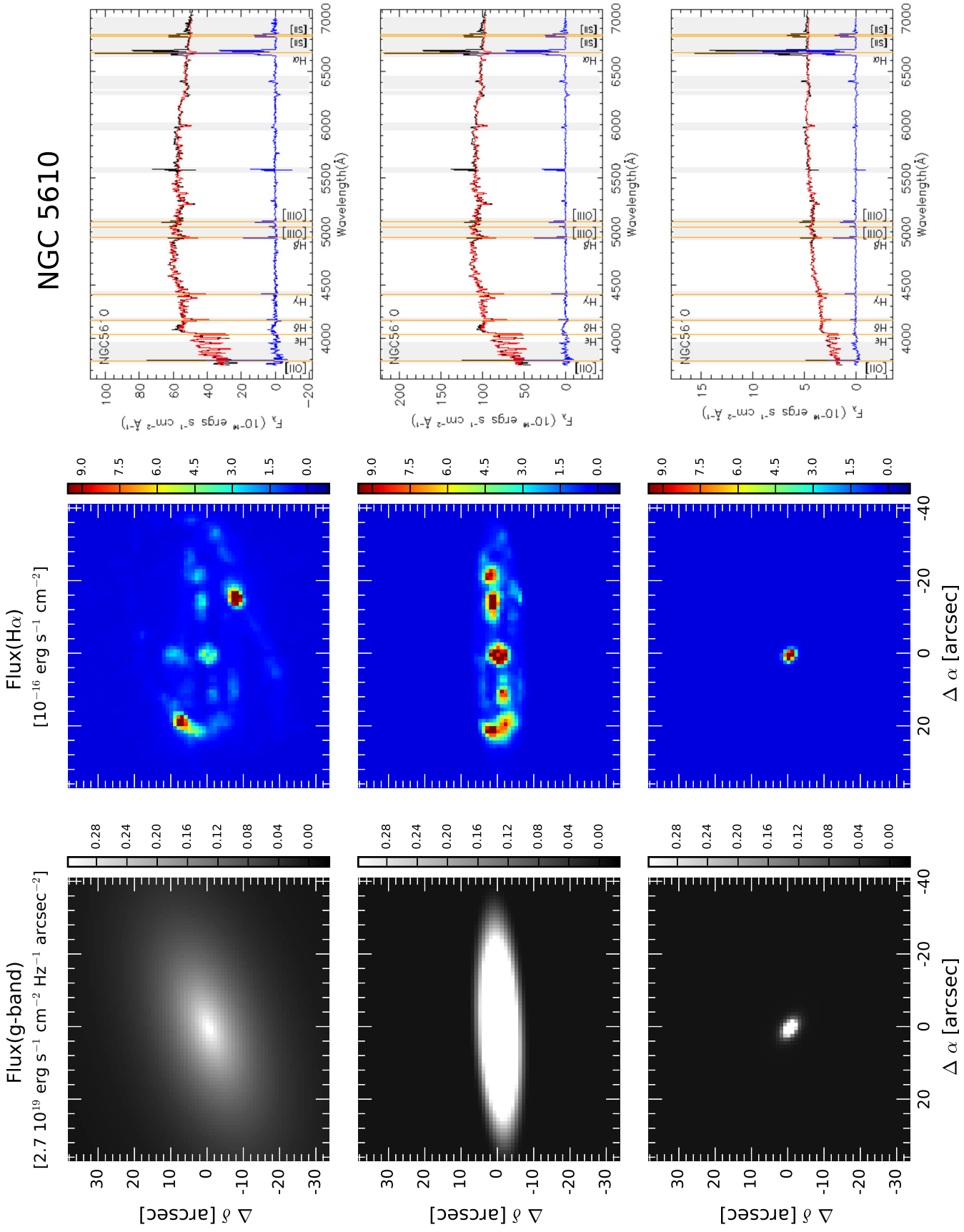
NGC 5610
Flux(g-band)
[2.7 10^19 erg s^-1 cm^-2 Hz^-1 arcsec^-2]
Flux(Hα)
[10^-16 erg s^-1 cm^-2]
Δ δ [arcsec]
Δ α [arcsec]
Wavelength(Å)
[OII]
Hε
Hδ
Hγ
Hβ
[OIII]
Hα
[SII]

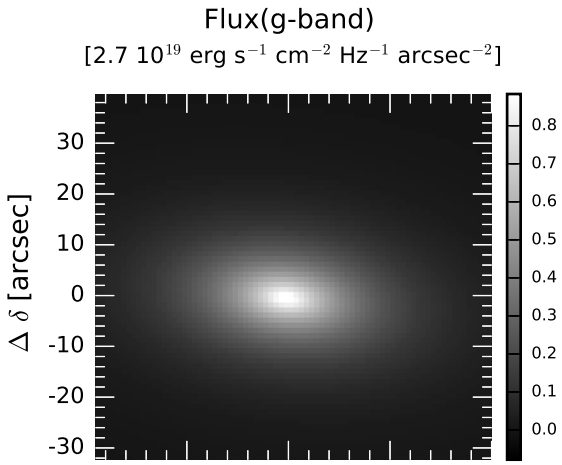
Flux(g-band)
[2.7 10^19 erg s^-1 cm^-2 Hz^-1 arcsec^-2]
Δ δ [arcsec]
30
20
10
0
-10
-20
-30
0.8
0.7
0.6
0.5
0.4
0.3
0.2
0.1
0.0

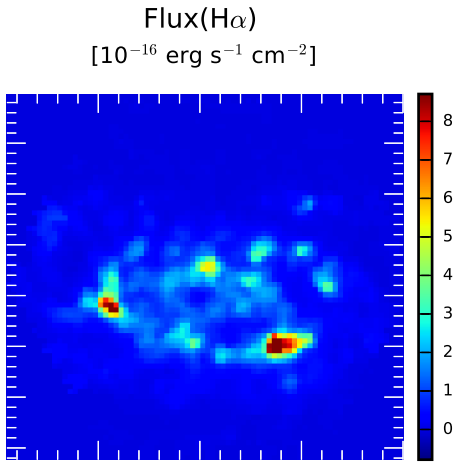
Flux(Hα)
[10^-16 erg s^-1 cm^-2]
8
7
6
5
4
3
2
1
0

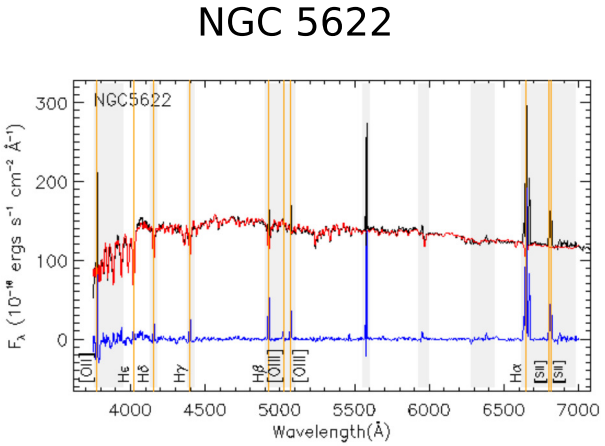
NGC 5622
NGC5622
F_λ (10^-16 ergs s^-1 cm^-2 Å^-1)
300
200
100
0
[OII]
Hε
Hδ
Hγ
Hβ
[OIII]
[OIII]
Hα
[SII]
[SII]
4000
4500
5000
5500
6000
6500
7000
Wavelength(Å)

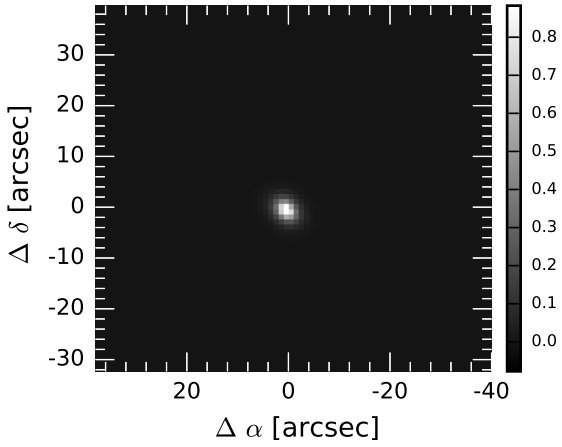
Δ δ [arcsec]
30
20
10
0
-10
-20
-30
0.8
0.7
0.6
0.5
0.4
0.3
0.2
0.1
0.0
20
0
-20
-40
Δ α [arcsec]

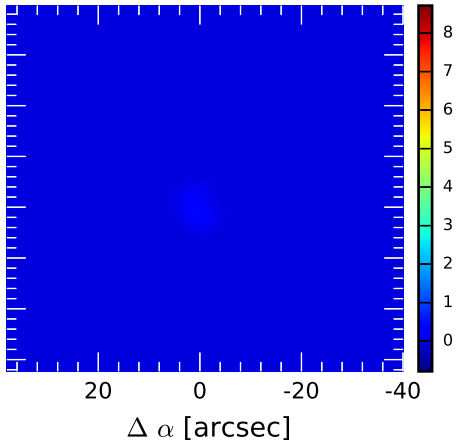
8
7
6
5
4
3
2
1
0
20
0
-20
-40
Δ α [arcsec]

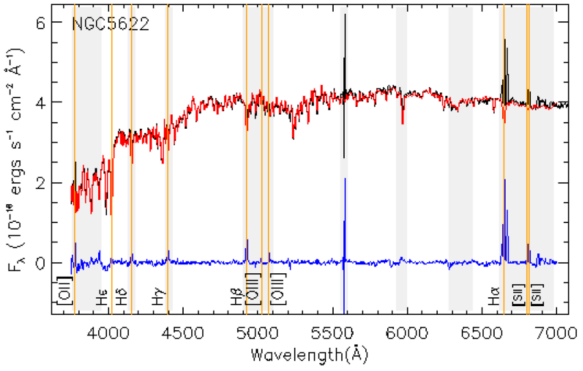
NGC5622
F_λ (10^-16 ergs s^-1 cm^-2 Å^-1)
6
4
2
0
[OII]
Hε
Hδ
Hγ
Hβ
[OIII]
[OIII]
Hα
[SII]
[SII]
4000
4500
5000
5500
6000
6500
7000
Wavelength(Å)

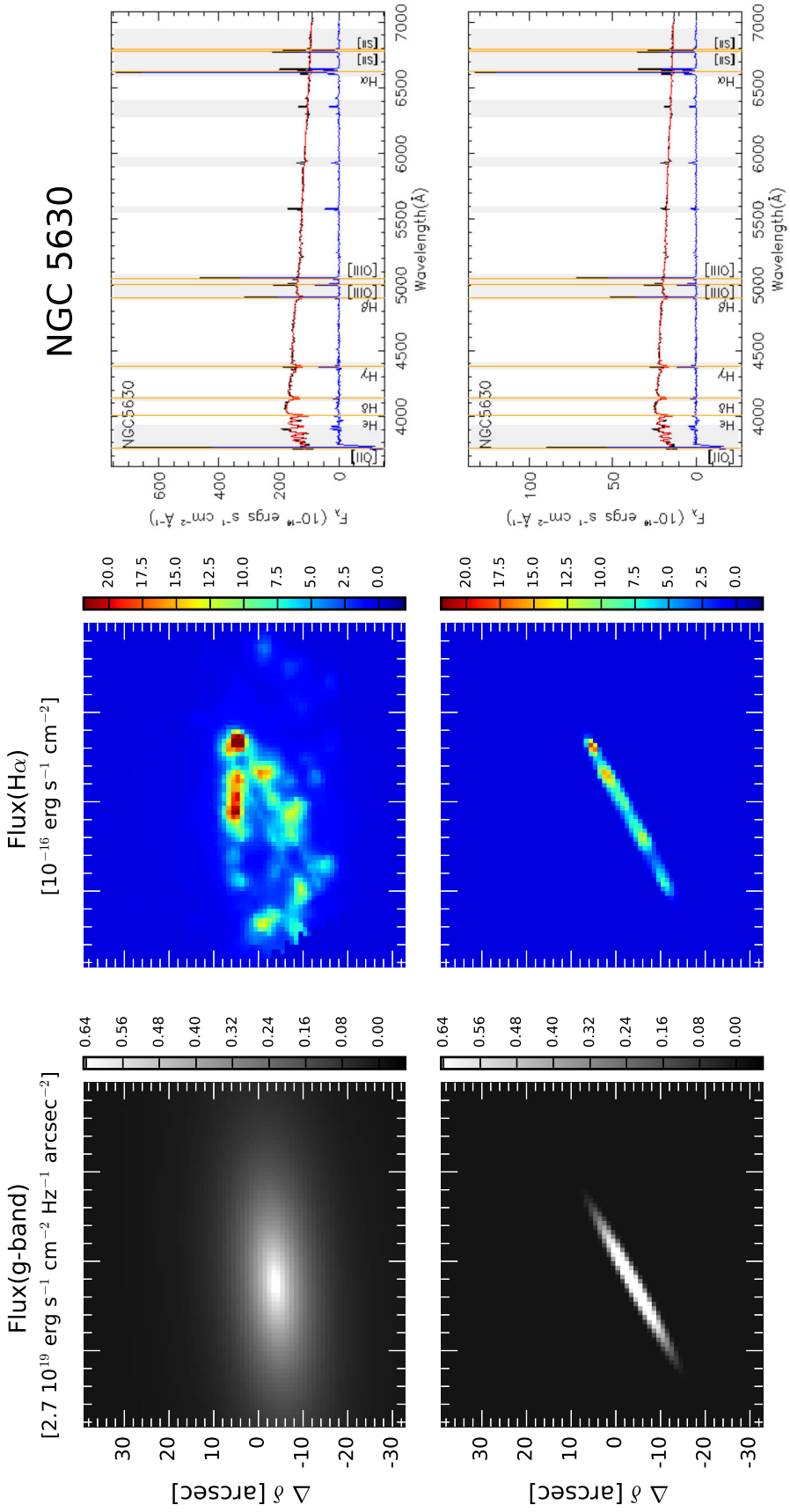
NGC 5630
NGC5630
Wavelength(Å)
Flux(Hα)
[10^-16 erg s^-1 cm^-2]
Flux(g-band)
[2.7 10^19 erg s^-1 cm^-2 Hz^-1 arcsec^-2]
Δ δ [arcsec]

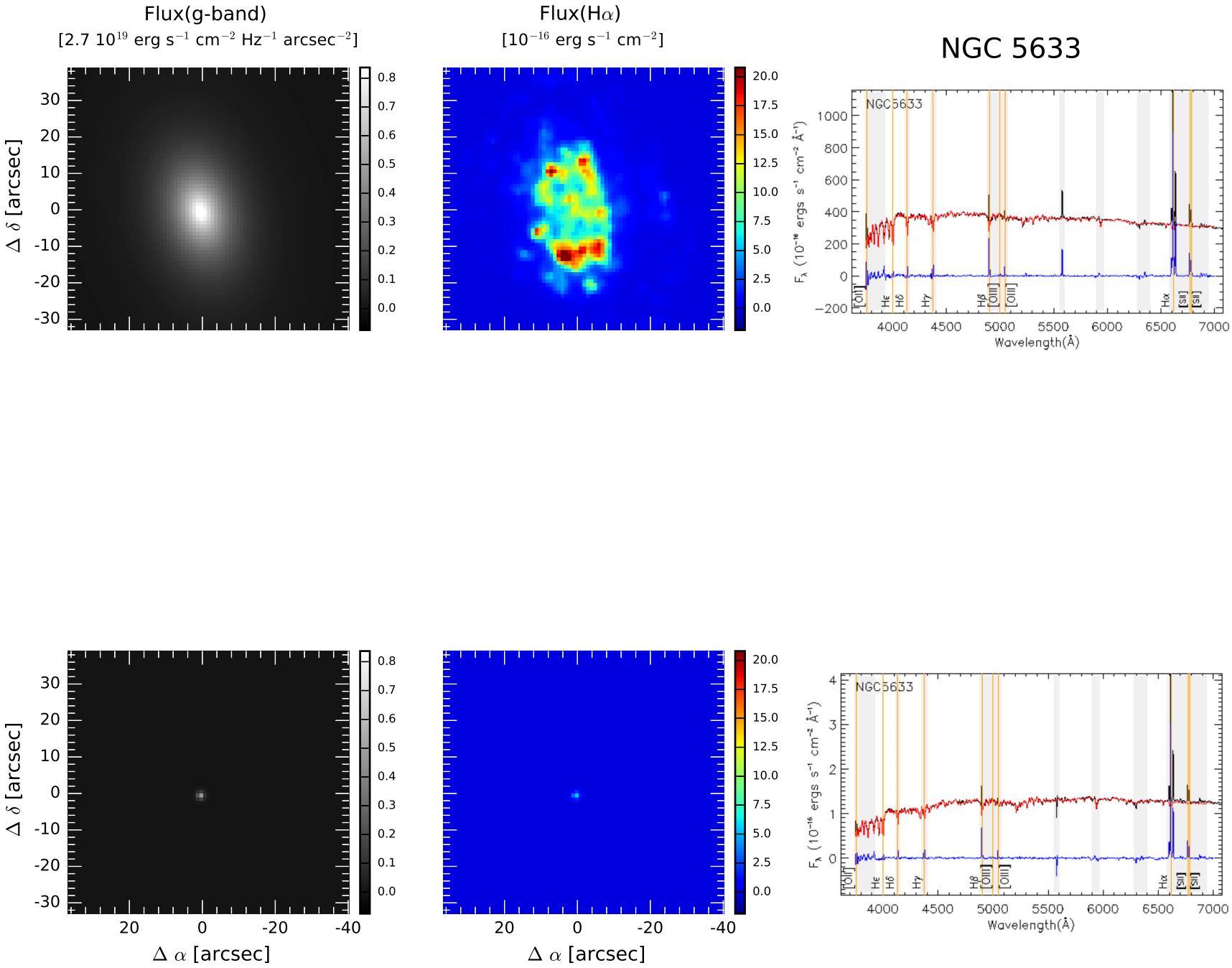
Flux(g-band)
[2.7 10^19 erg s^-1 cm^-2 Hz^-1 arcsec^-2]
Flux(Hα)
[10^-16 erg s^-1 cm^-2]
NGC 5633
Δ δ [arcsec]
Δ α [arcsec]
F_λ (10^-16 ergs s^-1 cm^-2 Å^-1)
Wavelength(Å)
[OII]
Hε
Hδ
Hγ
Hβ
[OIII]
[OIII]
Hα
[SII]
[SII]

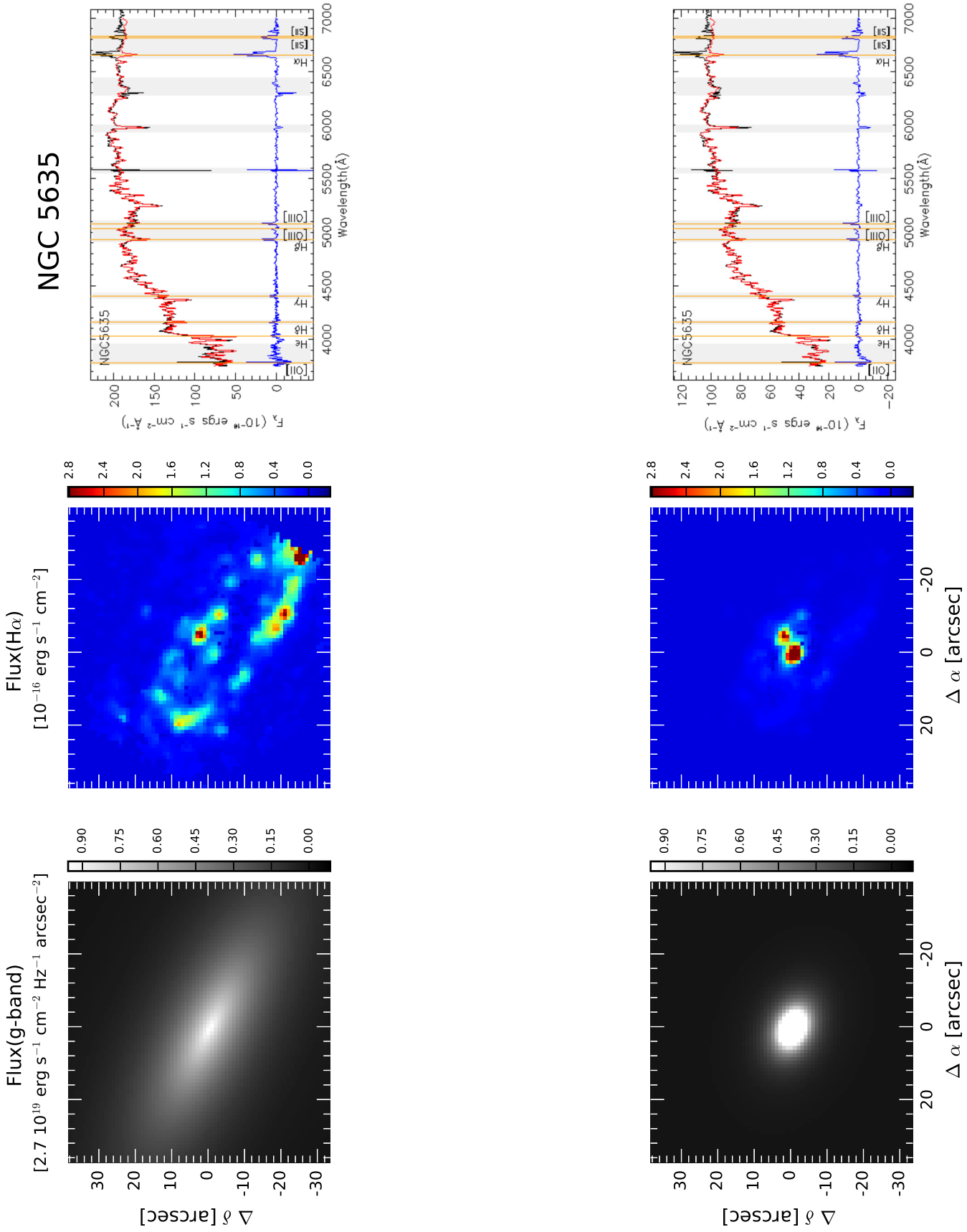
NGC 5635
Flux(g-band)
[2.7 10^19 erg s^-1 cm^-2 Hz^-1 arcsec^-2]
Flux(Hα)
[10^-16 erg s^-1 cm^-2]
Δ δ [arcsec]
Δ α [arcsec]
Wavelength(Å)
NGC5635
[OII]
Hε
Hδ
Hγ
Hβ
[OIII]
[OIII]
Hα
[SII]
[SII]

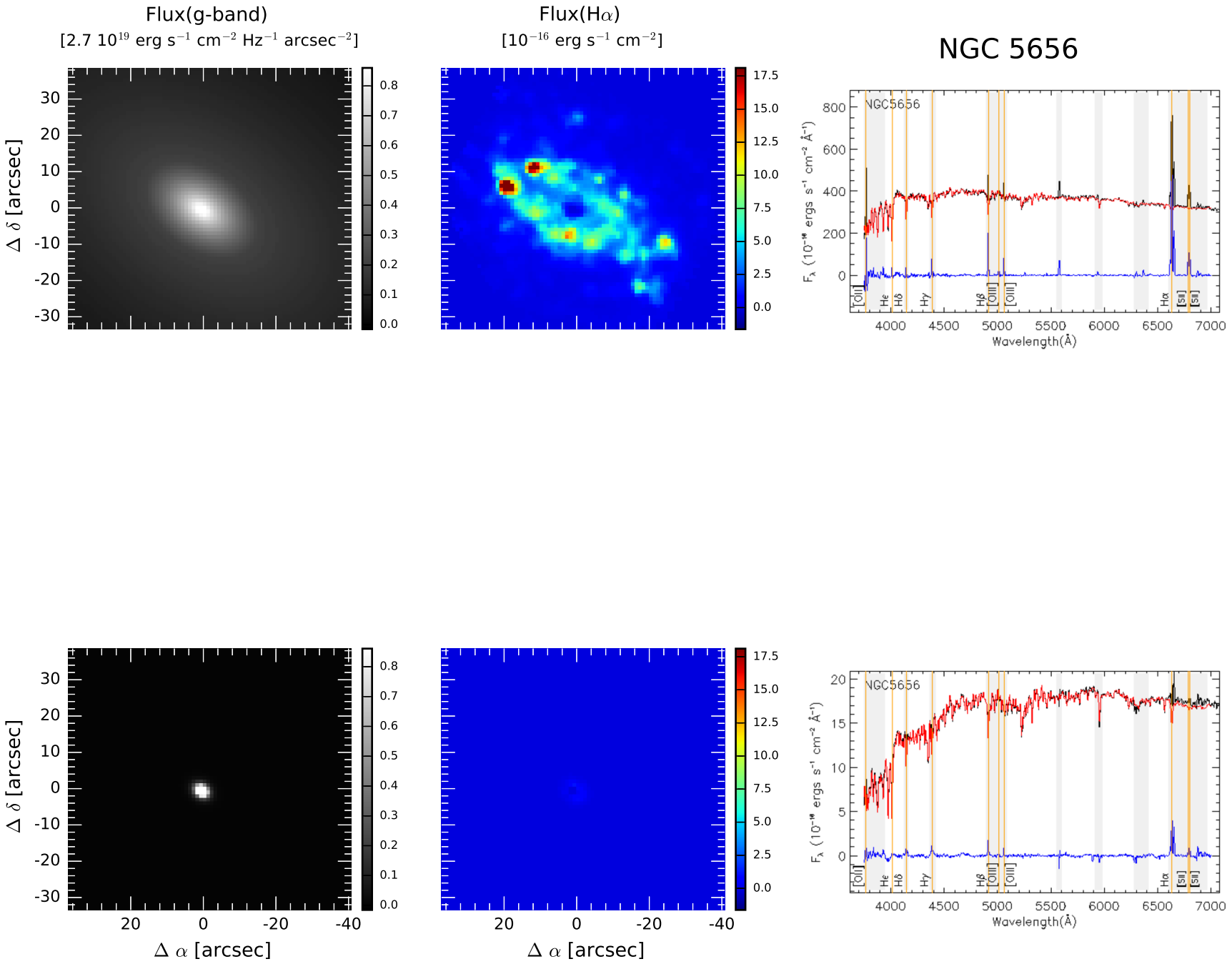
Flux(g-band)
[2.7 10^19 erg s^-1 cm^-2 Hz^-1 arcsec^-2]
Flux(Hα)
[10^-16 erg s^-1 cm^-2]
NGC 5656
Δ δ [arcsec]
Δ α [arcsec]
NGC5656
Wavelength(Å)
[OII]
Hε
Hδ
Hγ
Hβ
[OIII]
[OIII]
Hα
[SII]
[SII]

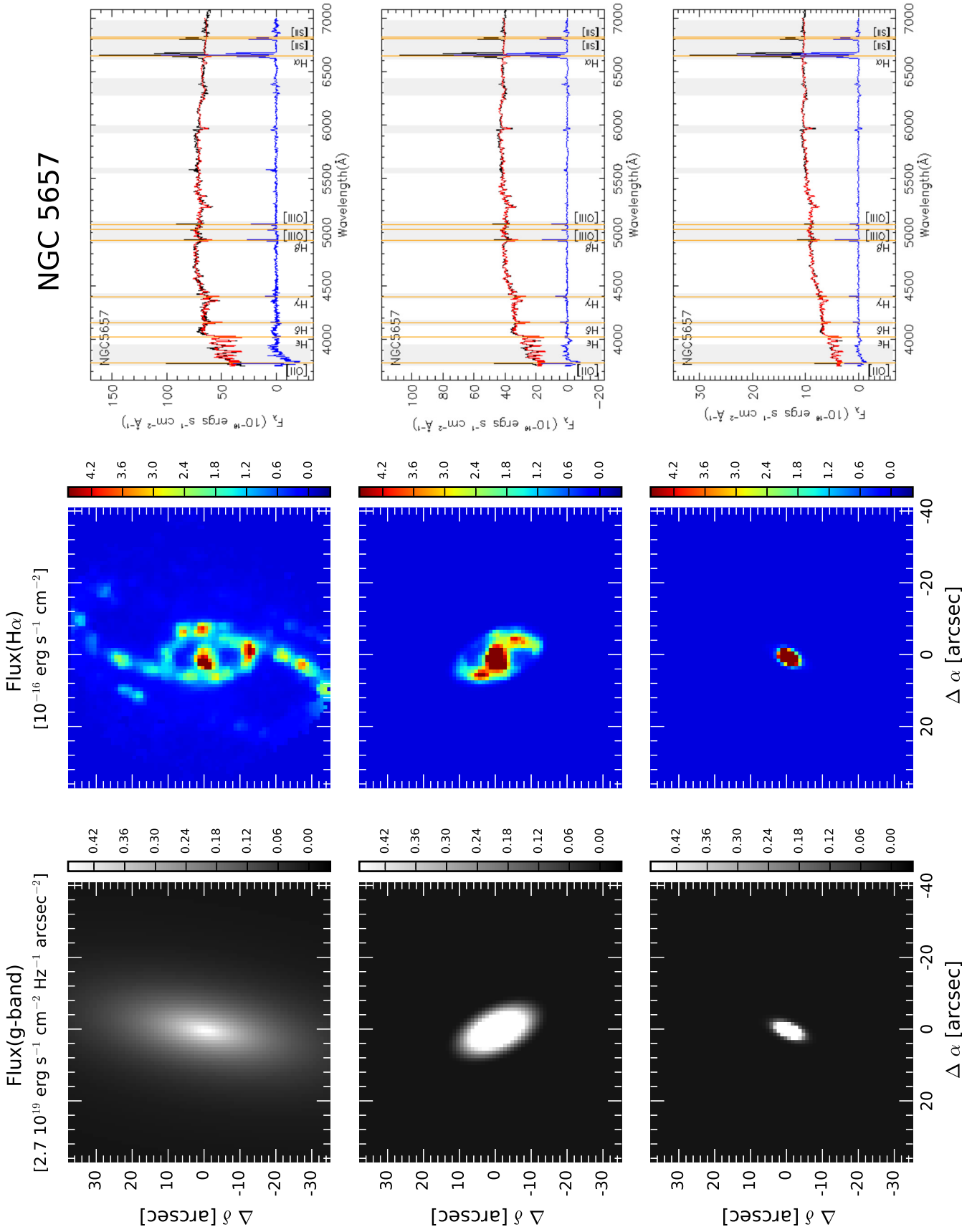
NGC 5657
Flux(g-band)
[2.7 10^19 erg s^-1 cm^-2 Hz^-1 arcsec^-2]
Flux(Hα)
[10^-16 erg s^-1 cm^-2]
Δ δ [arcsec]
Δ α [arcsec]
Wavelength(Å)
NGC5657
[OII]
Hε
Hδ
Hγ
H8
[OIII]
[OIII]
[OIII]
Hα
[SII]
[SII]

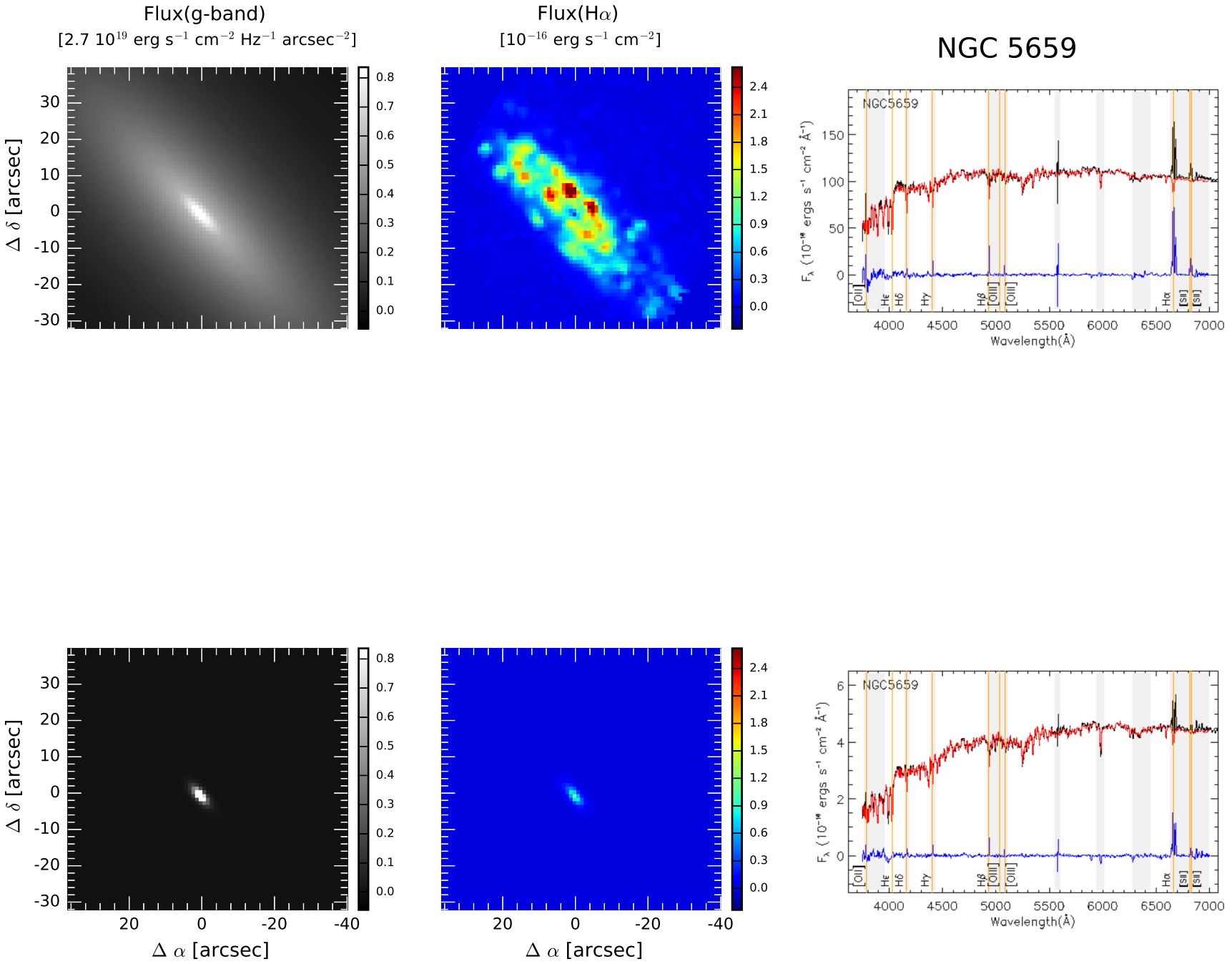
Flux(g-band)
[2.7 10^19 erg s^-1 cm^-2 Hz^-1 arcsec^-2]
Flux(Hα)
[10^-16 erg s^-1 cm^-2]
NGC 5659
Δ δ [arcsec]
Δ α [arcsec]
NGC5659
Wavelength(Å)
[OII]
Hε
Hδ
Hγ
Hβ
[OIII]
[OIII]
Hα
[SII]
[SII]

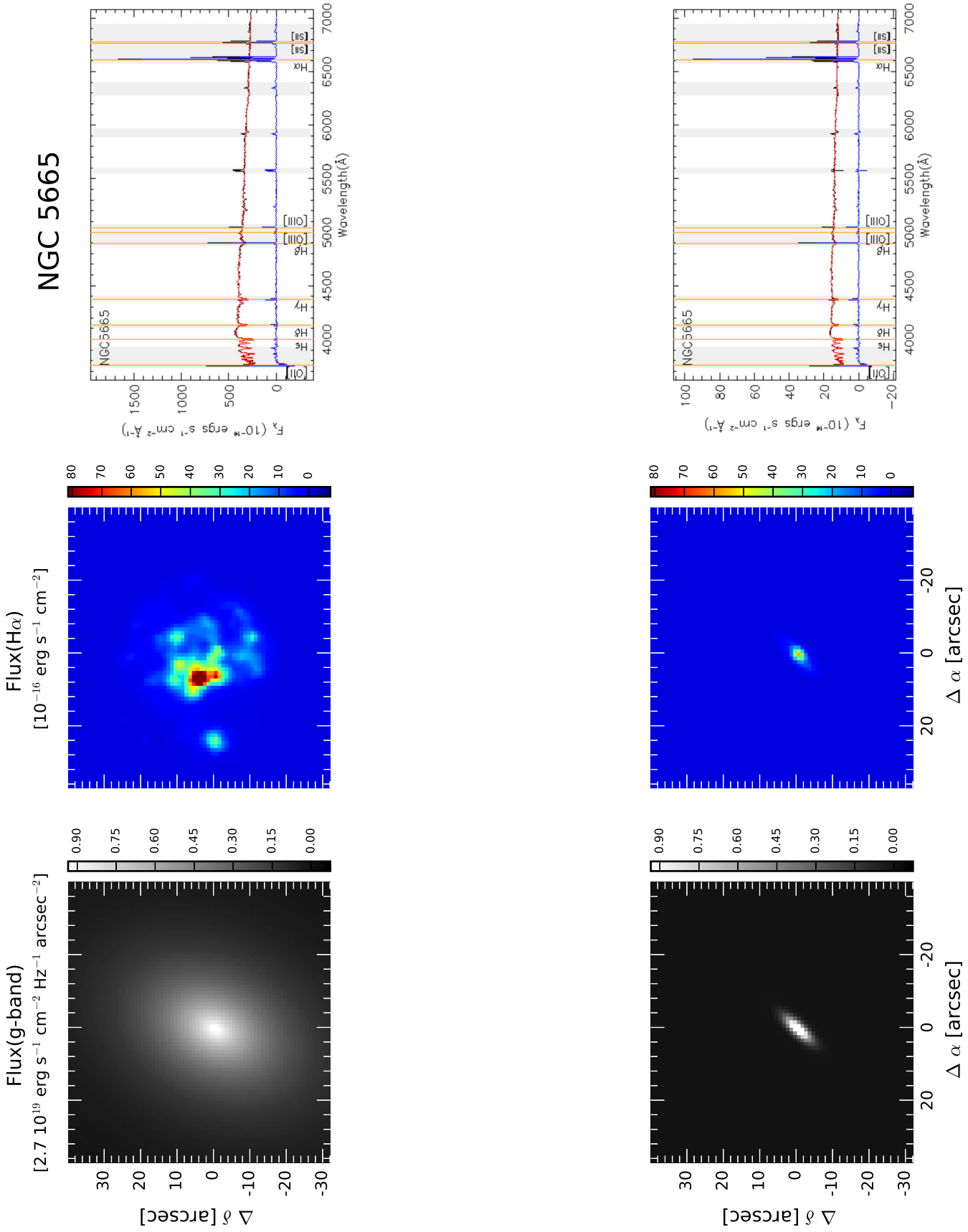
NGC 5665
Flux(g-band)
[2.7 10^19 erg s^-1 cm^-2 Hz^-1 arcsec^-2]
Flux(Hα)
[10^-16 erg s^-1 cm^-2]
Δ δ [arcsec]
Δ α [arcsec]
Wavelength(Å)
NGC5665
[OII]
Hε
Hδ
Hγ
Hβ
[OIII]
[OIII]
Hα
[SII]
[SII]

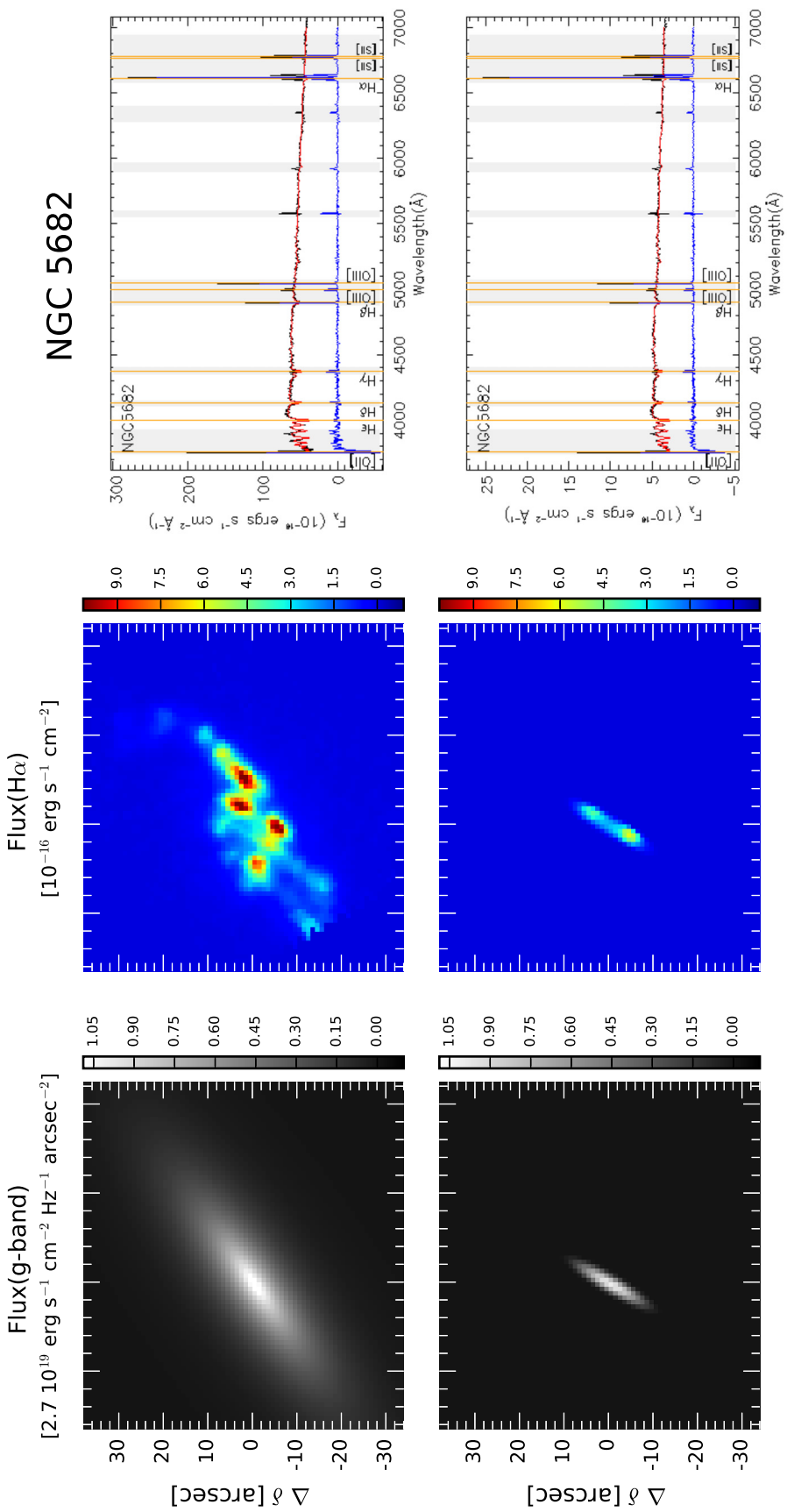
NGC 5682
Flux(g-band)
[2.7 10^19 erg s^-1 cm^-2 Hz^-1 arcsec^-2]
Flux(Hα)
[10^-16 erg s^-1 cm^-2]
Δ δ [arcsec]
Wavelength(Å)
NGC5682
[OII]
Hε
Hδ
Hγ
Hβ
[OIII]
Hα
[SII]

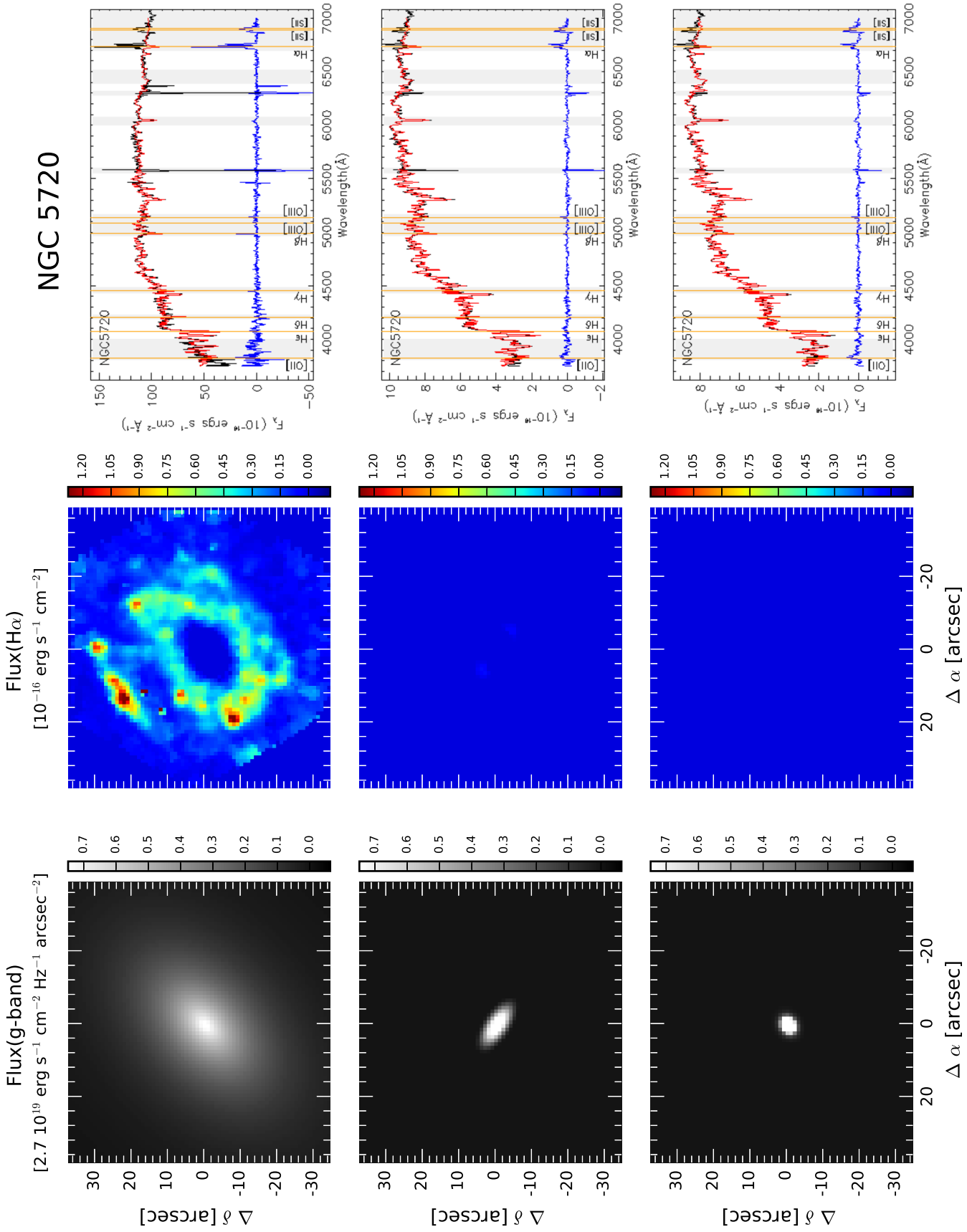
NGC 5720
Flux(g-band)
[2.7 10^19 erg s^-1 cm^-2 Hz^-1 arcsec^-2]
Flux(Hα)
[10^-16 erg s^-1 cm^-2]
Δ δ [arcsec]
Δ α [arcsec]
Wavelength(Å)
NGC5720
[OII]
Hε
Hδ
Hγ
Hβ
[OIII]
[OIII]
[SII]
[SII]
Hα

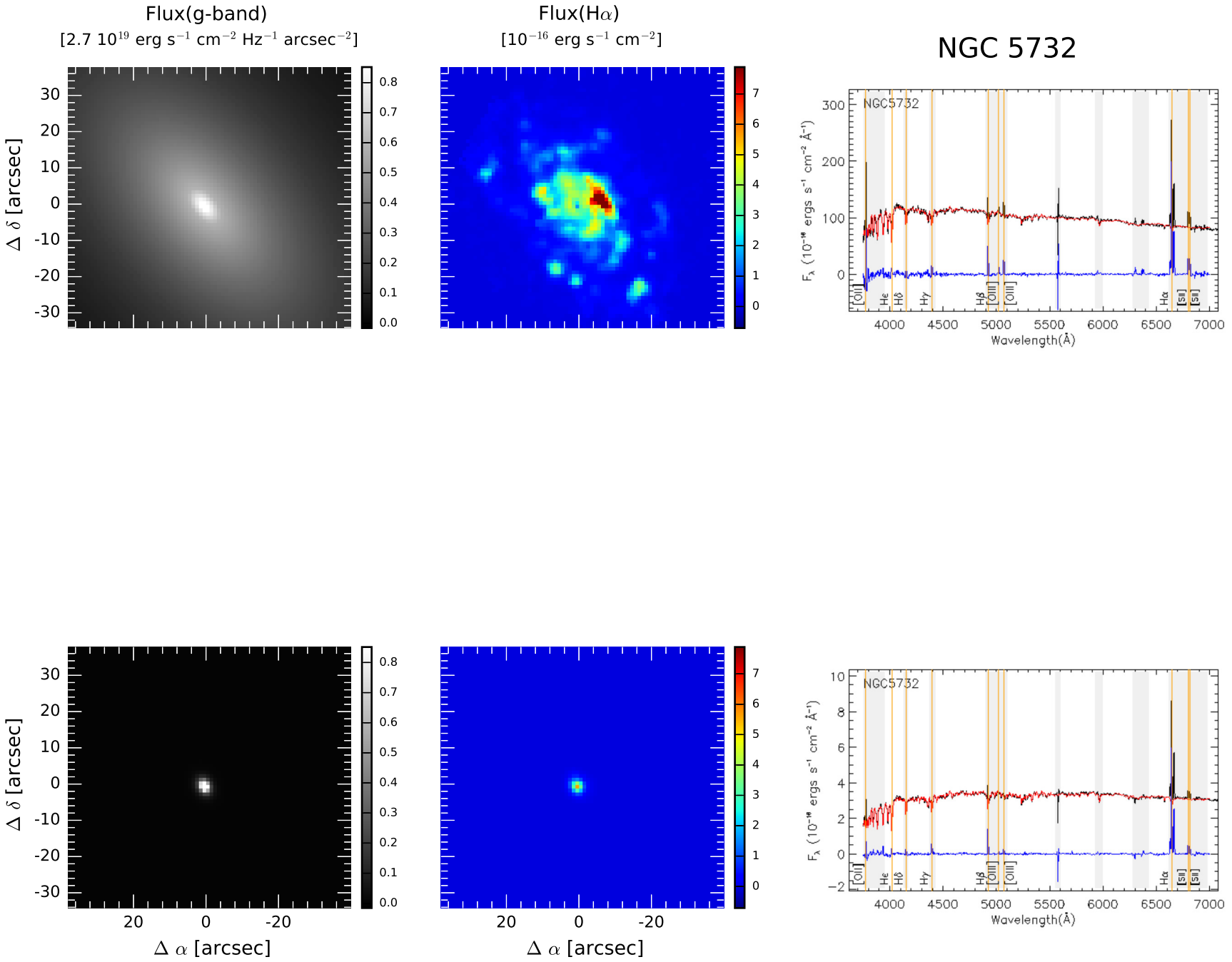
Flux(g-band)
[2.7 10^19 erg s^-1 cm^-2 Hz^-1 arcsec^-2]
Flux(Hα)
[10^-16 erg s^-1 cm^-2]
NGC 5732
Δ δ [arcsec]
Δ α [arcsec]
NGC5732
Wavelength(Å)
[OII]
Hε
Hδ
Hγ
Hβ
[OIII]
[OIII]
Hα
[SII]
[SII]

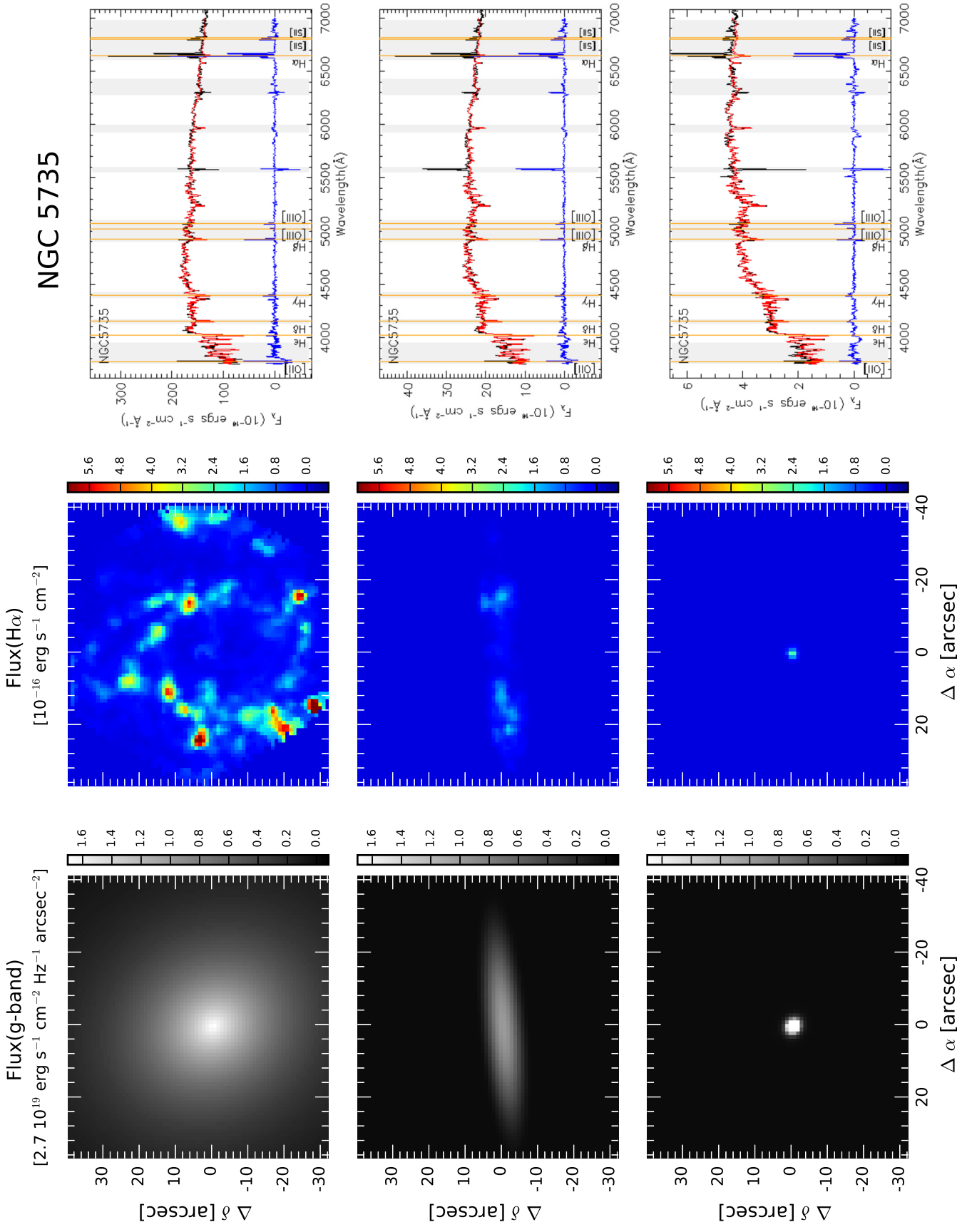
NGC 5735
Flux(g-band)
[2.7 10^19 erg s^-1 cm^-2 Hz^-1 arcsec^-2]
Flux(Hα)
[10^-16 erg s^-1 cm^-2]
Δ δ [arcsec]
Δ α [arcsec]
Wavelength(Å)
NGC5735
[OII]
Hε
Hδ
Hγ
Hβ
[OIII]
[OIII]
Hα
[SII]
[SII]

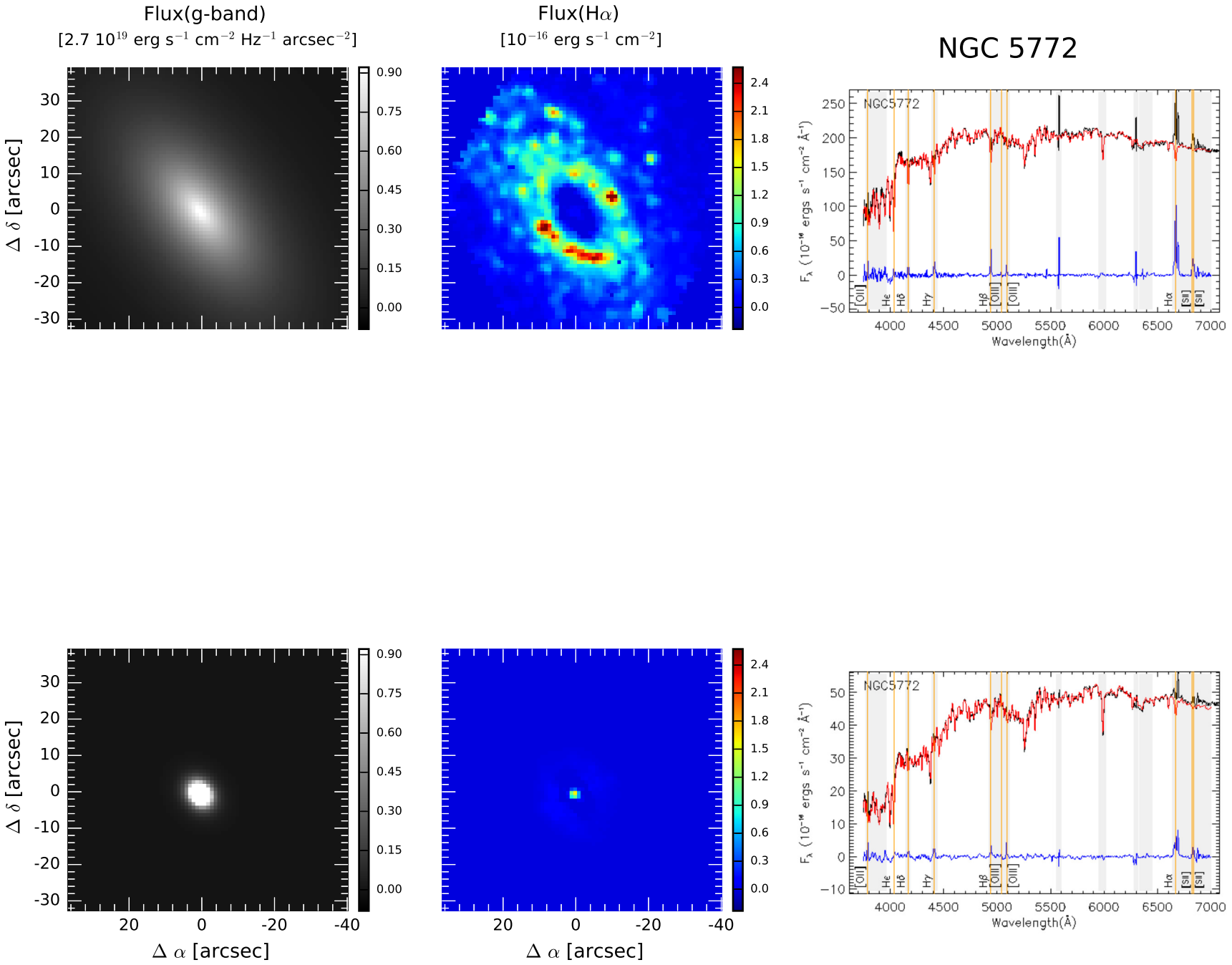
Flux(g-band)
[2.7 10^19 erg s^-1 cm^-2 Hz^-1 arcsec^-2]
Flux(Hα)
[10^-16 erg s^-1 cm^-2]
NGC 5772
Δ δ [arcsec]
Δ α [arcsec]
NGC5772
Wavelength(Å)
[OII]
Hε
Hδ
Hγ
Hβ
[OIII]
[OIII]
Hα
[SII]
[SII]

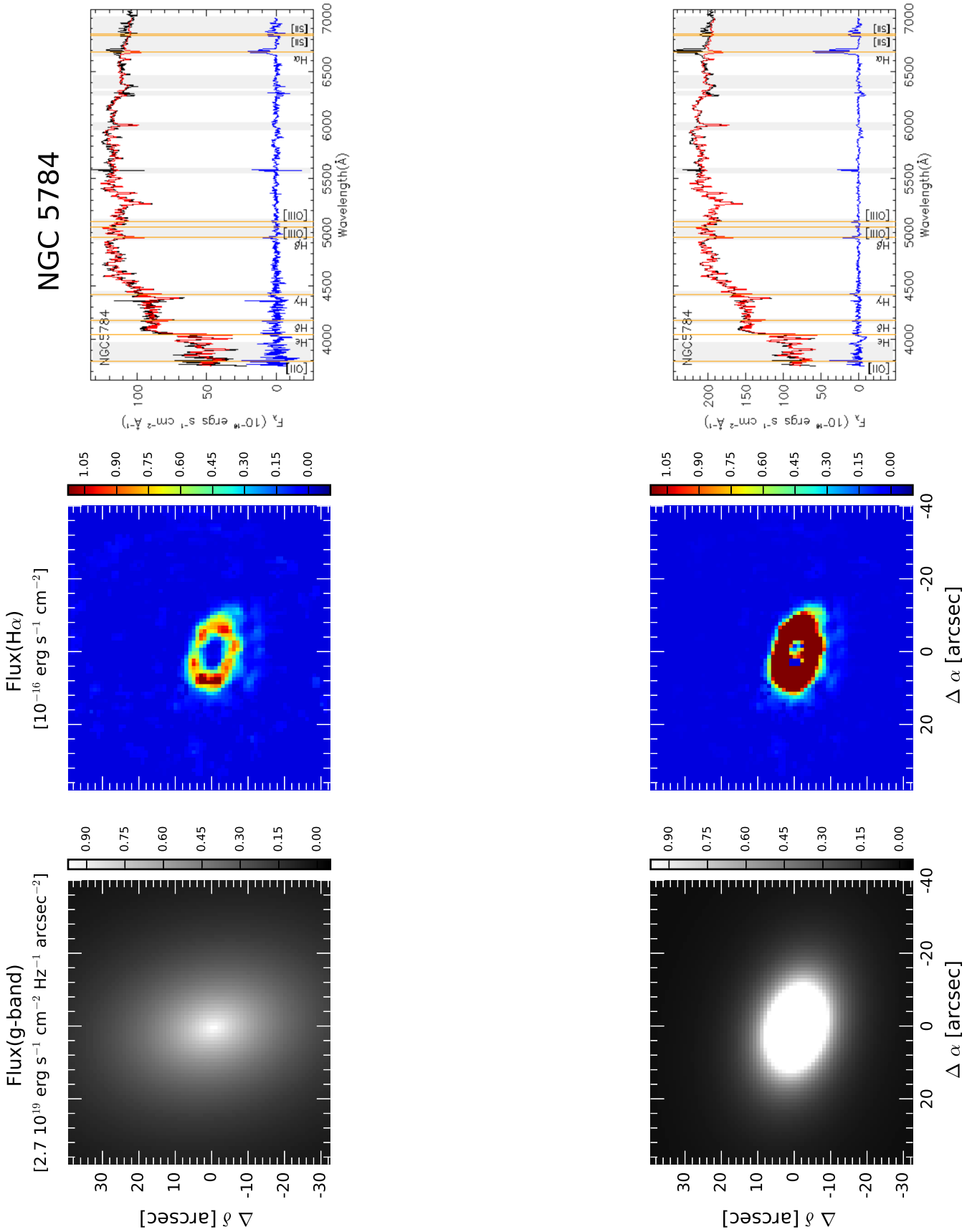
NGC 5784
Flux(g-band)
[2.7 10^19 erg s^-1 cm^-2 Hz^-1 arcsec^-2]
Flux(Hα)
[10^-16 erg s^-1 cm^-2]
Δ δ [arcsec]
Δ α [arcsec]
Wavelength(Å)
F_λ (10^-16 ergs s^-1 cm^-2 Å^-1)
NGC5784
[OII]
Hε
Hδ
Hγ
[OIII]
Hβ
[OIII]
[SII]
[SII]
Hα

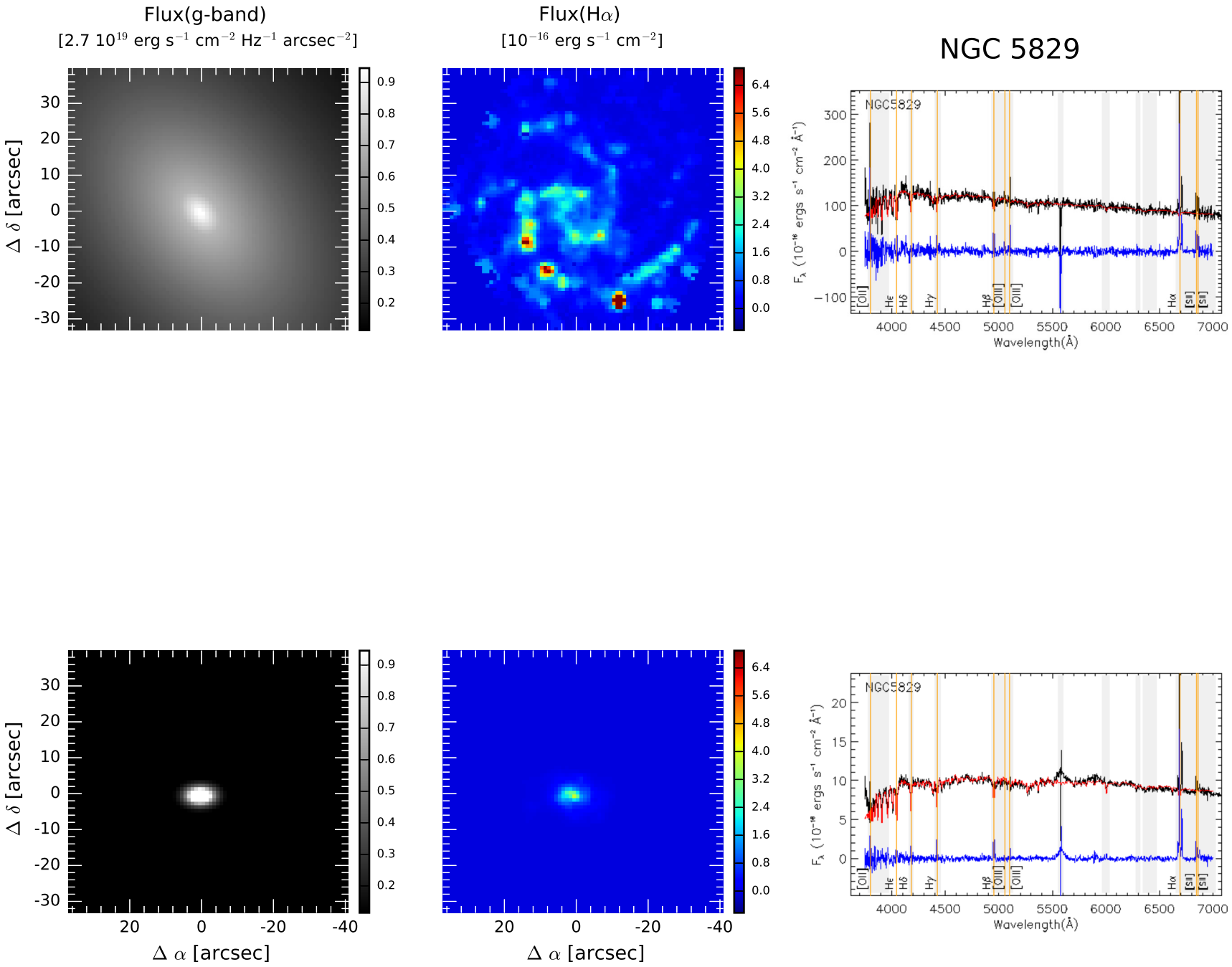
Flux(g-band)
[2.7 10^19 erg s^-1 cm^-2 Hz^-1 arcsec^-2]
Flux(Hα)
[10^-16 erg s^-1 cm^-2]
NGC 5829
Δ δ [arcsec]
Δ α [arcsec]
NGC5829
Wavelength(Å)
[OII]
Hε
Hδ
Hγ
Hβ
[OIII]
Hα
[SII]

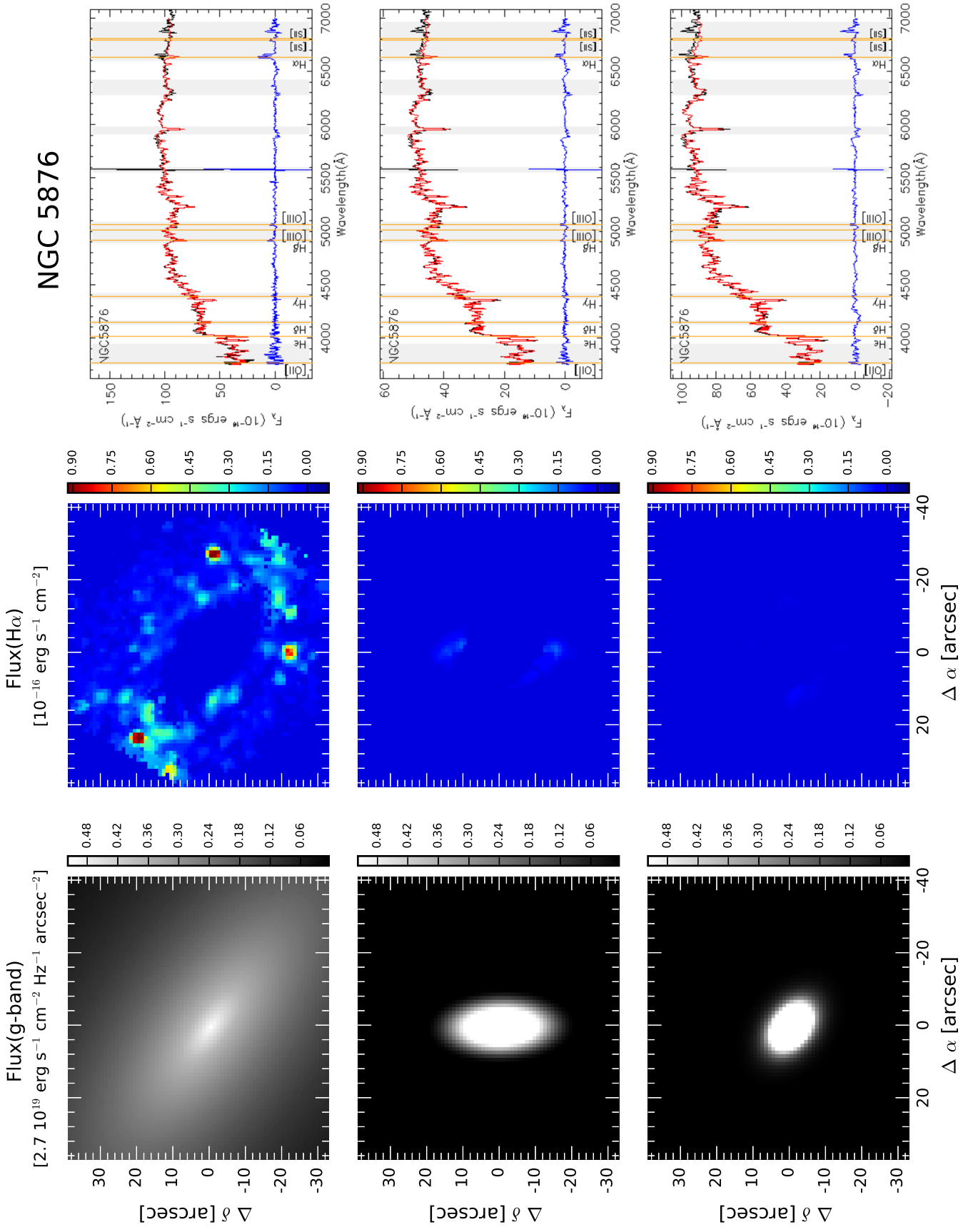
NGC 5876
Flux(g-band)
[2.7 10^19 erg s^-1 cm^-2 Hz^-1 arcsec^-2]
Flux(Hα)
[10^-16 erg s^-1 cm^-2]
Δ δ [arcsec]
Δ α [arcsec]
Wavelength(Å)
VGC5876
[OII]
Hε
Hδ
Hγ
Hβ
[OIII]
Hα
[SII]

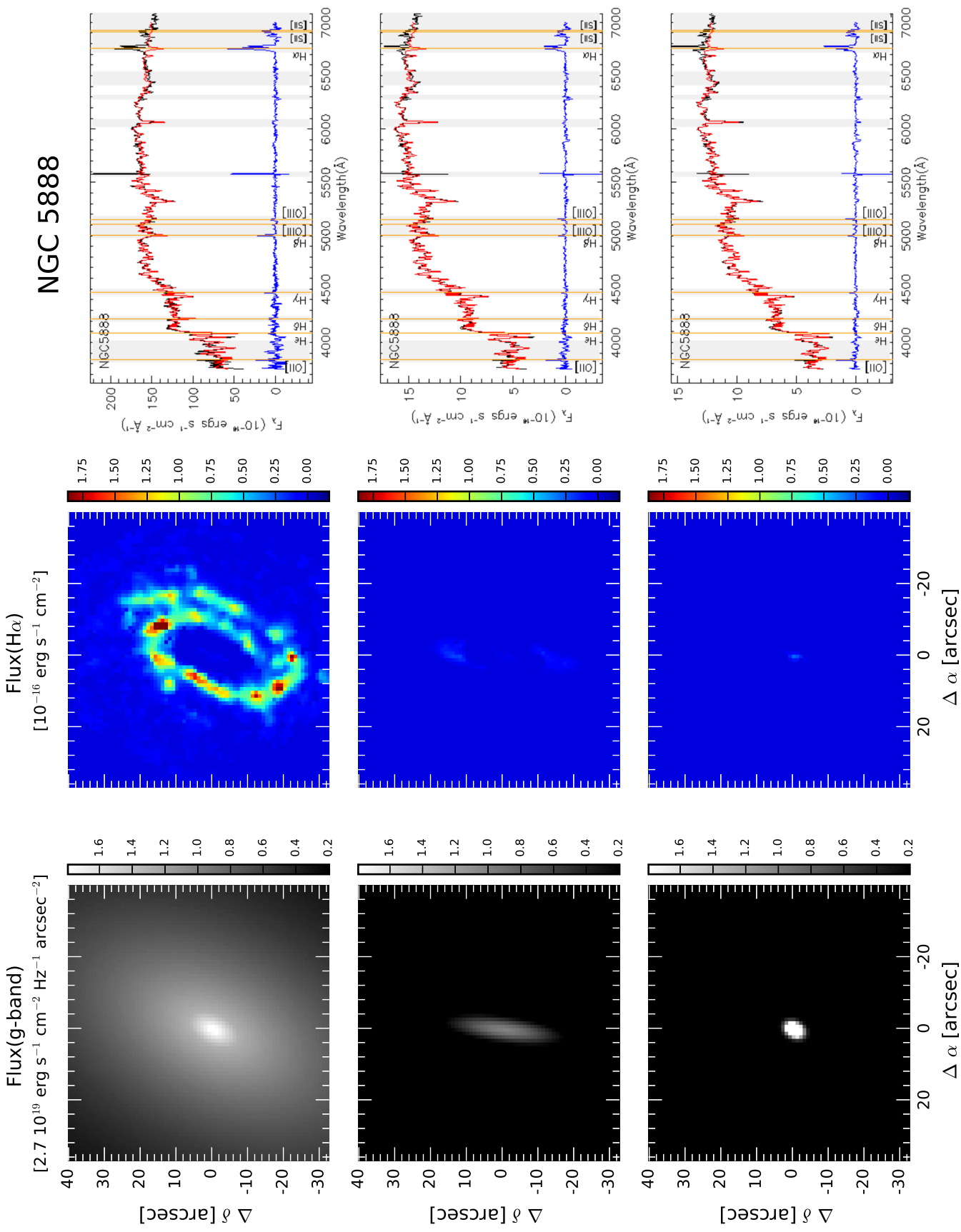
NGC 5888
Flux(g-band)
[2.7 10^19 erg s^-1 cm^-2 Hz^-1 arcsec^-2]
Flux(Hα)
[10^-16 erg s^-1 cm^-2]
Δ δ [arcsec]
Δ α [arcsec]
Wavelength(Å)
NGC5888
[OII]
Hε
Hδ
Hγ
Hβ
[OIII]
[OIII]
Hα
[SII]
[SII]

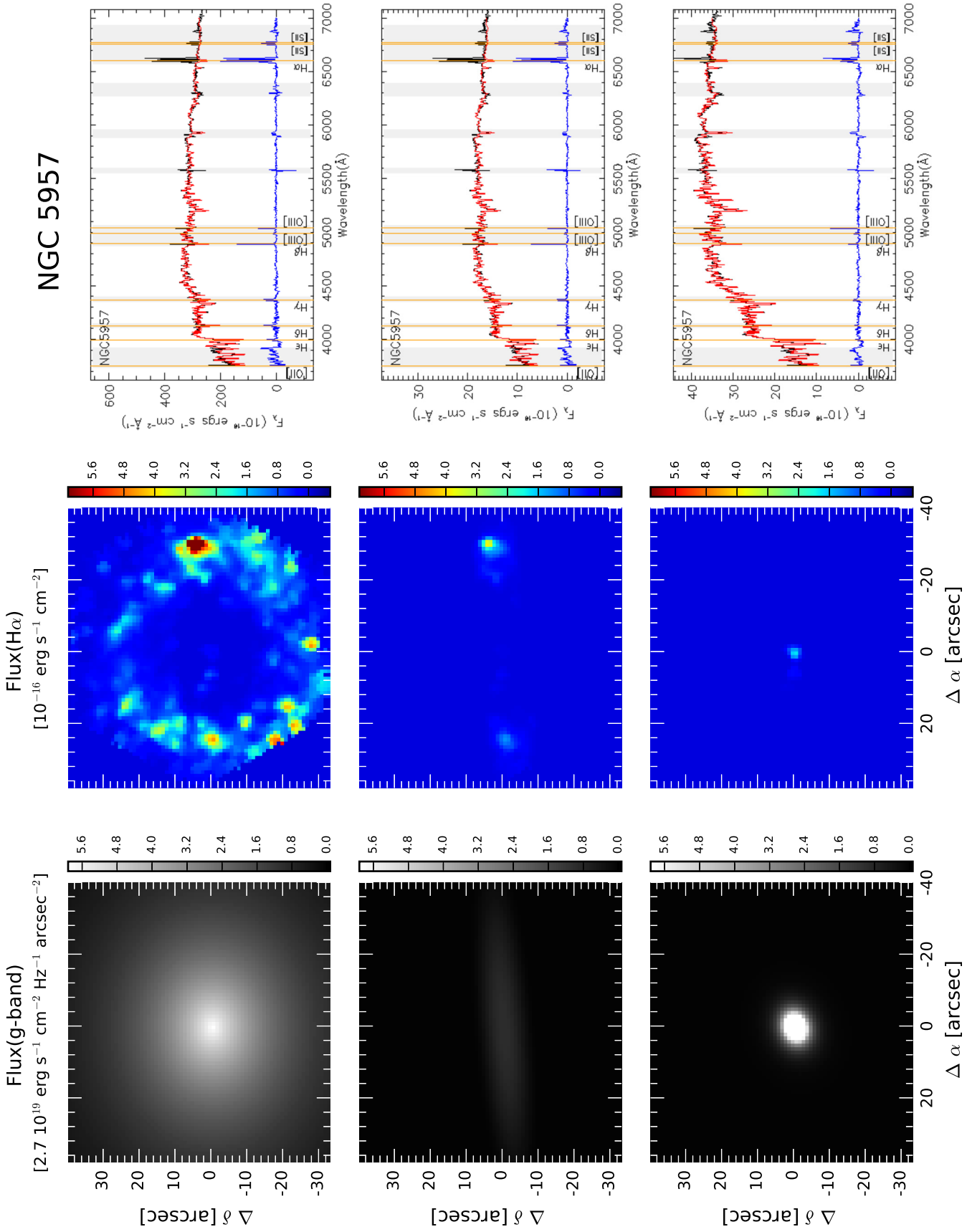
NGC 5957
Flux(g-band)
[2.7 10^19 erg s^-1 cm^-2 Hz^-1 arcsec^-2]
Flux(Hα)
[10^-16 erg s^-1 cm^-2]
Δ δ [arcsec]
Δ α [arcsec]
Wavelength(Å)
NGC5957
[OII]
Hε
Hδ
Hγ
Hβ
[OIII]
[OIII]
[SII]
[SII]
Hα

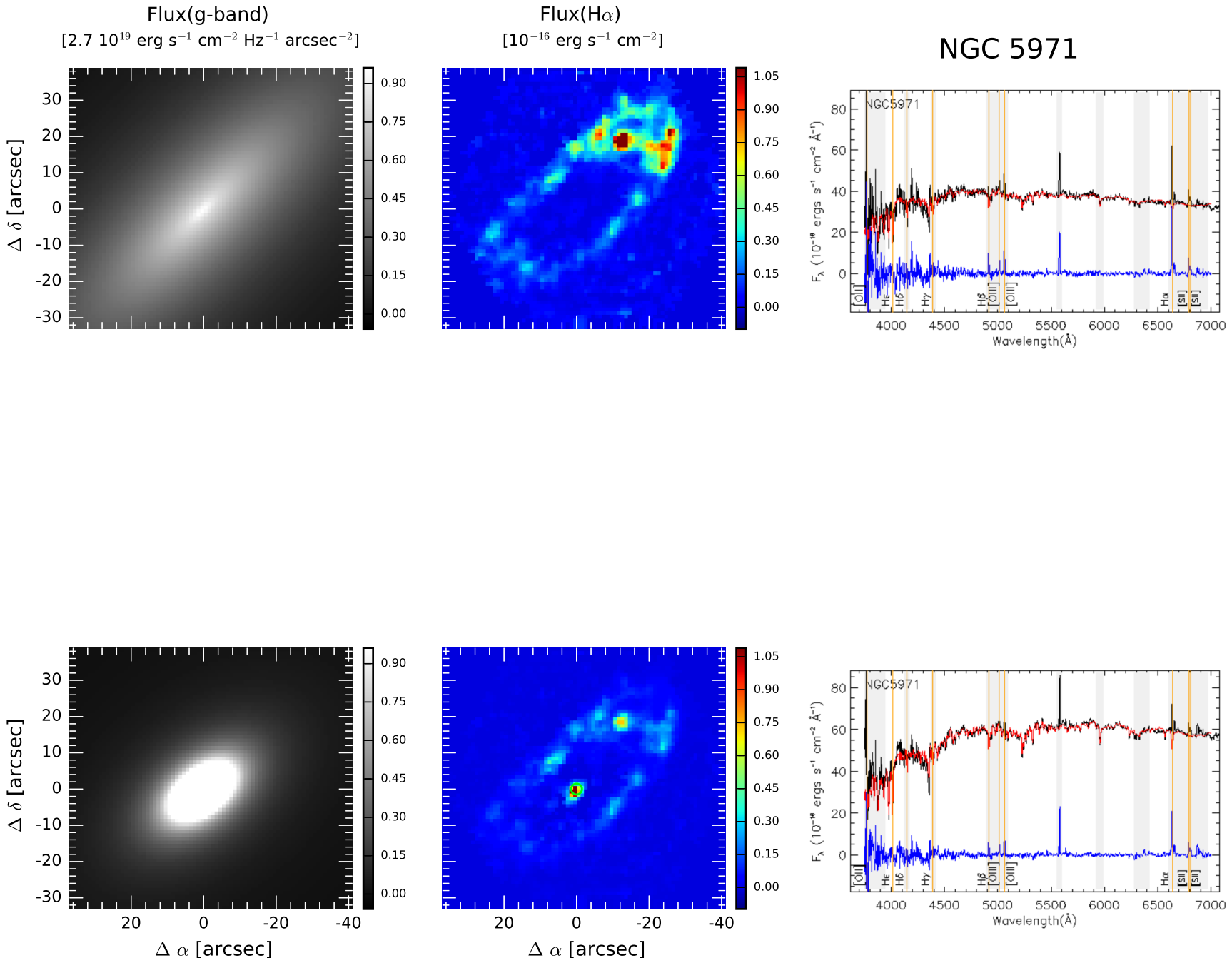
Flux(g-band)
[2.7 10^19 erg s^-1 cm^-2 Hz^-1 arcsec^-2]
Flux(Hα)
[10^-16 erg s^-1 cm^-2]
NGC 5971
Δ δ [arcsec]
Δ α [arcsec]
Wavelength(Å)
NGC5971
[OII]
Hε
Hδ
Hγ
Hβ
[OIII]
[OIII]
Hα
[SII]
[SII]

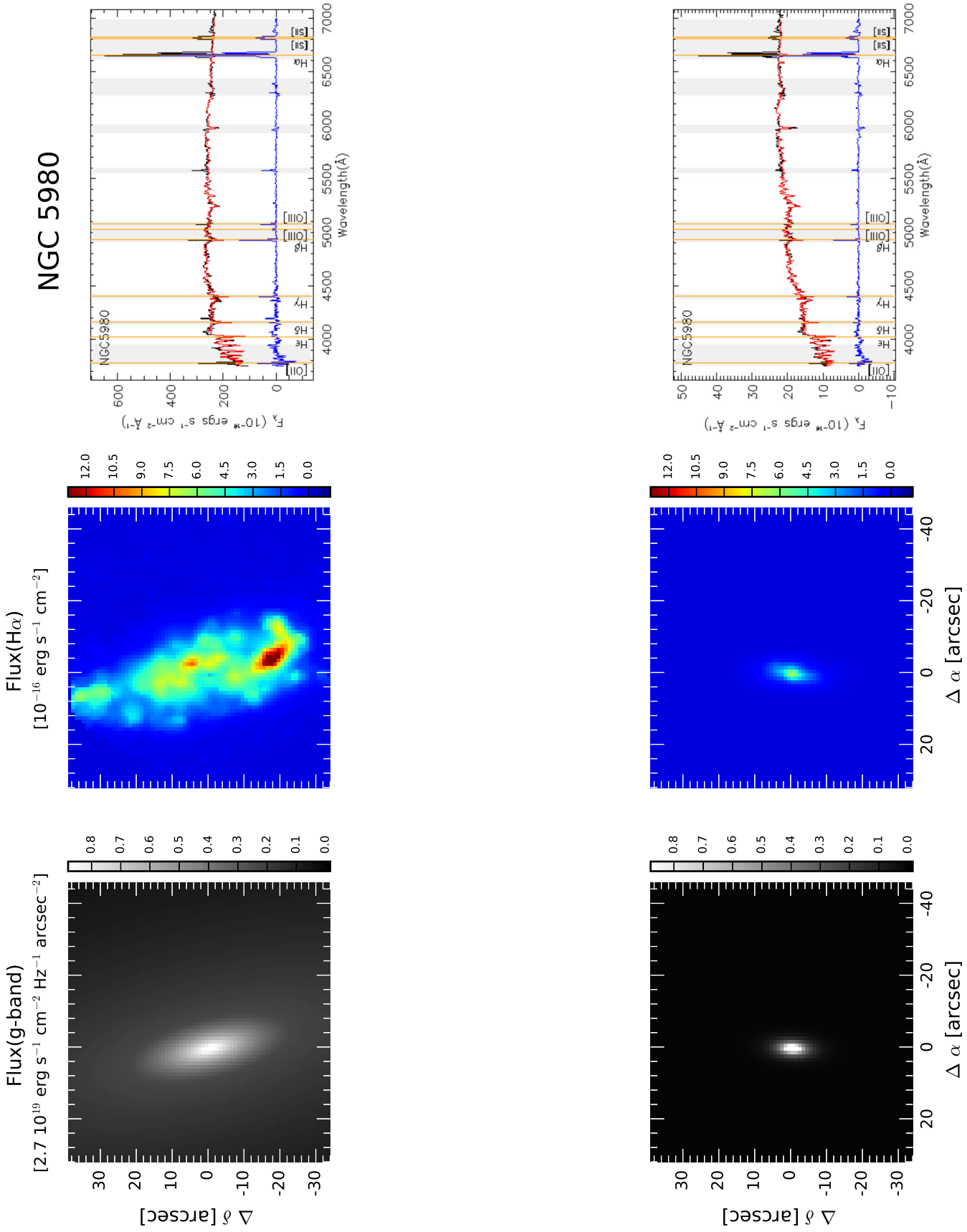
NGC 5980
Flux(Hα)
[10^-16 erg s^-1 cm^-2]
Flux(g-band)
[2.7 10^19 erg s^-1 cm^-2 Hz^-1 arcsec^-2]
Δ δ [arcsec]
Δ α [arcsec]
Wavelength(Å)
NGC5980
[OII]
Hε
Hδ
Hγ
[OIII]
Hβ
[OIII]
Hα
[SII]
[SII]

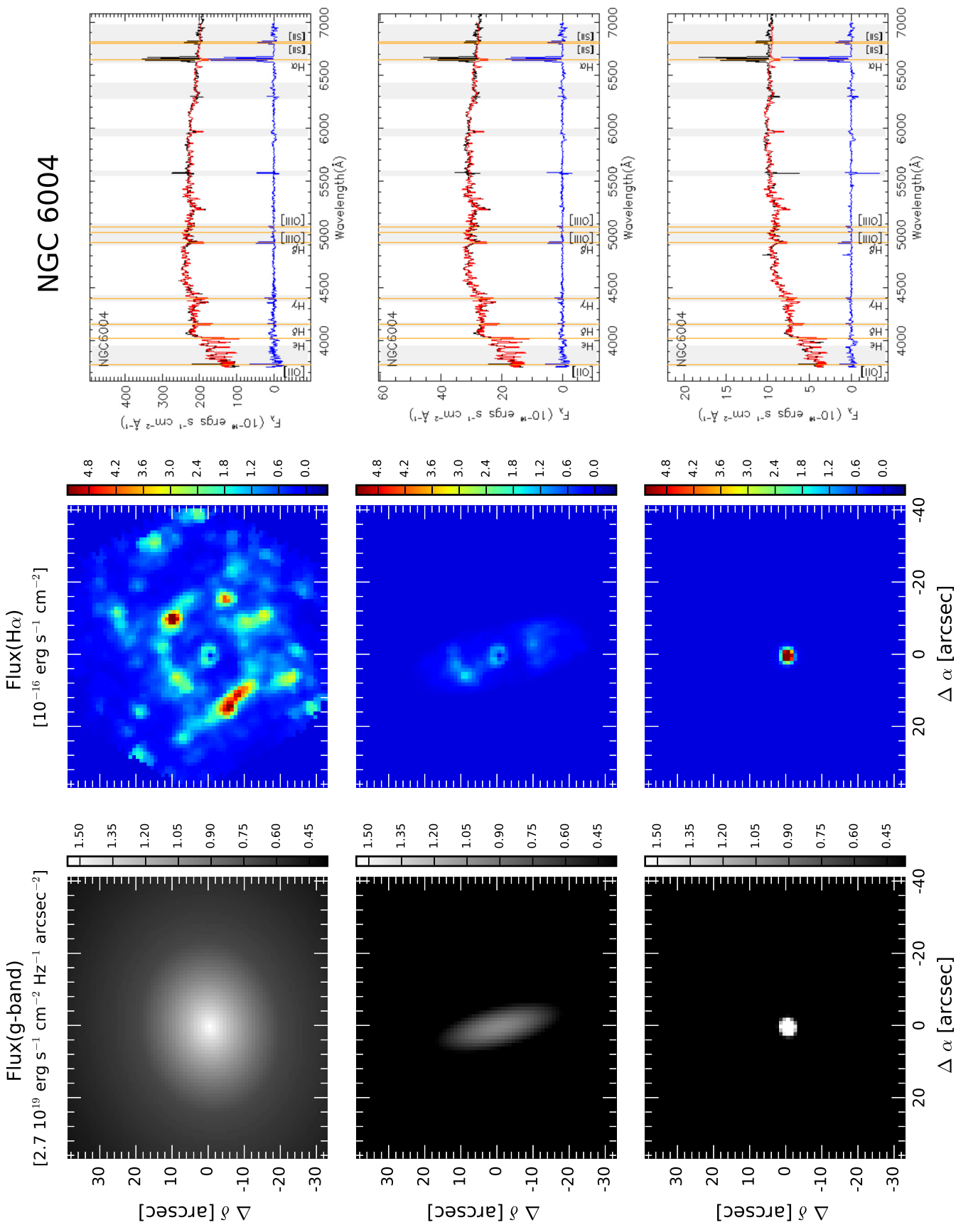
NGC 6004
Flux(g-band)
[2.7 10^19 erg s^-1 cm^-2 Hz^-1 arcsec^-2]
Flux(Hα)
[10^-16 erg s^-1 cm^-2]
Δ δ [arcsec]
Δ α [arcsec]
Wavelength(Å)
NGC6004
[OII]
Hε
Hδ
Hγ
Hβ
[OIII]
[OIII]
[SII]
[SII]
Hα

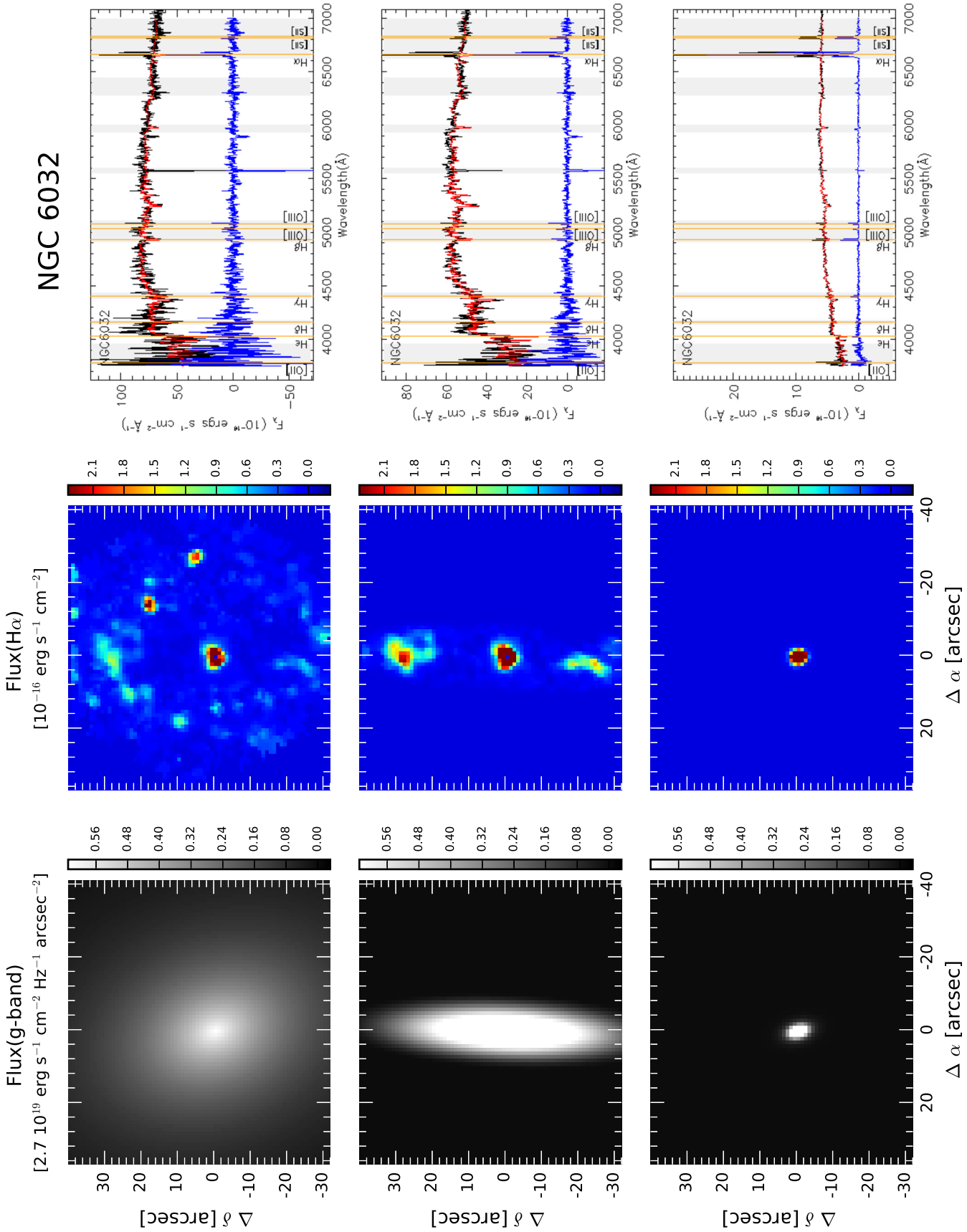
NGC 6032
Flux(g-band)
[2.7 10^19 erg s^-1 cm^-2 Hz^-1 arcsec^-2]
Flux(Hα)
[10^-16 erg s^-1 cm^-2]
Δ δ [arcsec]
Δ α [arcsec]
Wavelength(Å)
F_λ (10^-16 ergs s^-1 cm^-2 Å^-1)
NGC6032
[OII]
Hε
Hδ
Hγ
[OIII]
Hβ
[OIII]
Hα
[SII]
[SII]

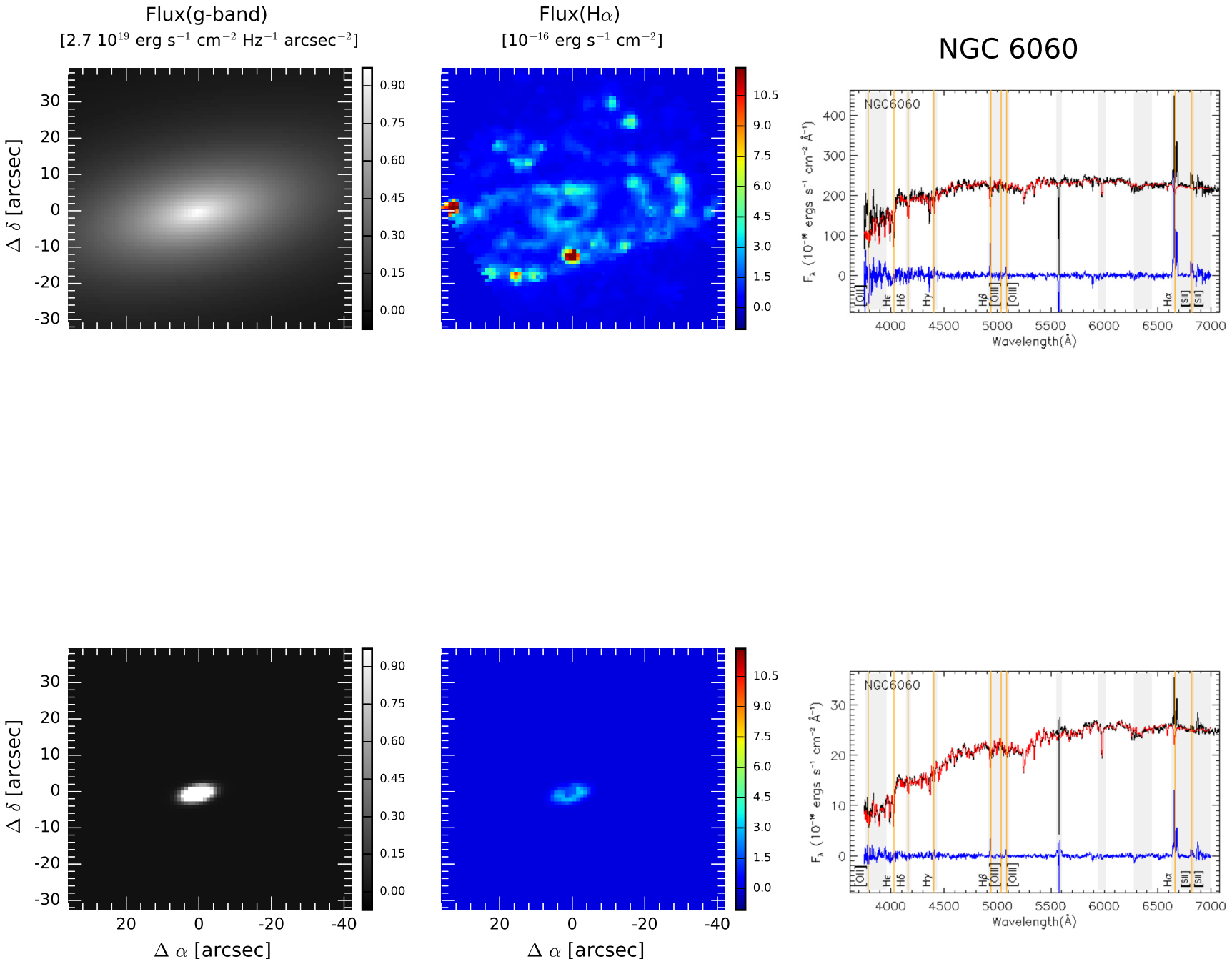
Flux(g-band)
[2.7 10^19 erg s^-1 cm^-2 Hz^-1 arcsec^-2]
Flux(Hα)
[10^-16 erg s^-1 cm^-2]
NGC 6060
Δ δ [arcsec]
Δ α [arcsec]
NGC6060
Wavelength(Å)
[OII]
Hε
Hδ
Hγ
Hβ
[OIII]
[OIII]
Hα
[SII]
[SII]

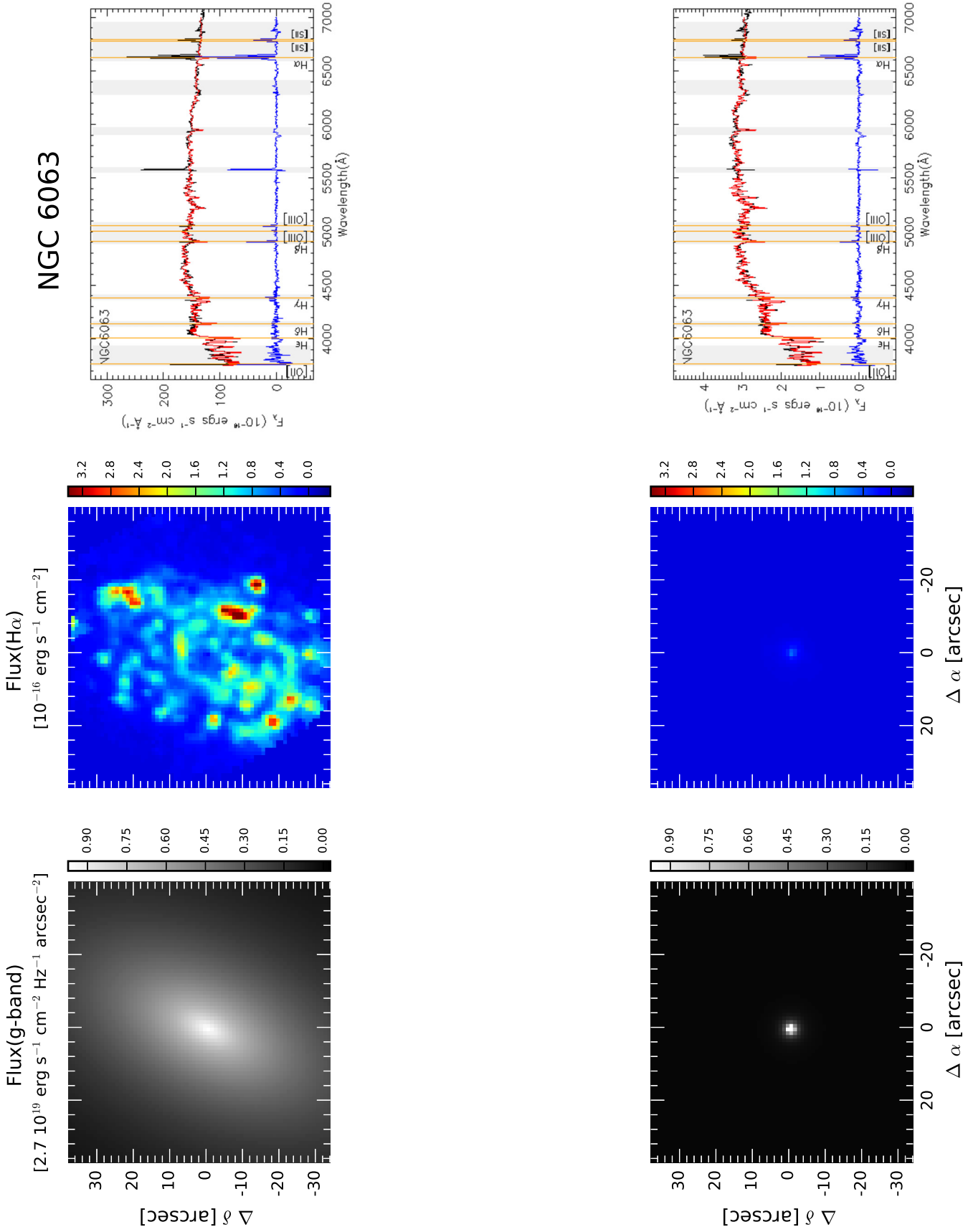
NGC 6063
Flux(g-band)
[2.7 10^19 erg s^-1 cm^-2 Hz^-1 arcsec^-2]
Flux(Hα)
[10^-16 erg s^-1 cm^-2]
Δ δ [arcsec]
Δ α [arcsec]
Wavelength(Å)
F_λ (10^-16 ergs s^-1 cm^-2 Å^-1)
NGC6063
[OII]
Hε
Hδ
Hγ
Hβ
[OIII]
[OIII]
[SII]
[SII]
Hα

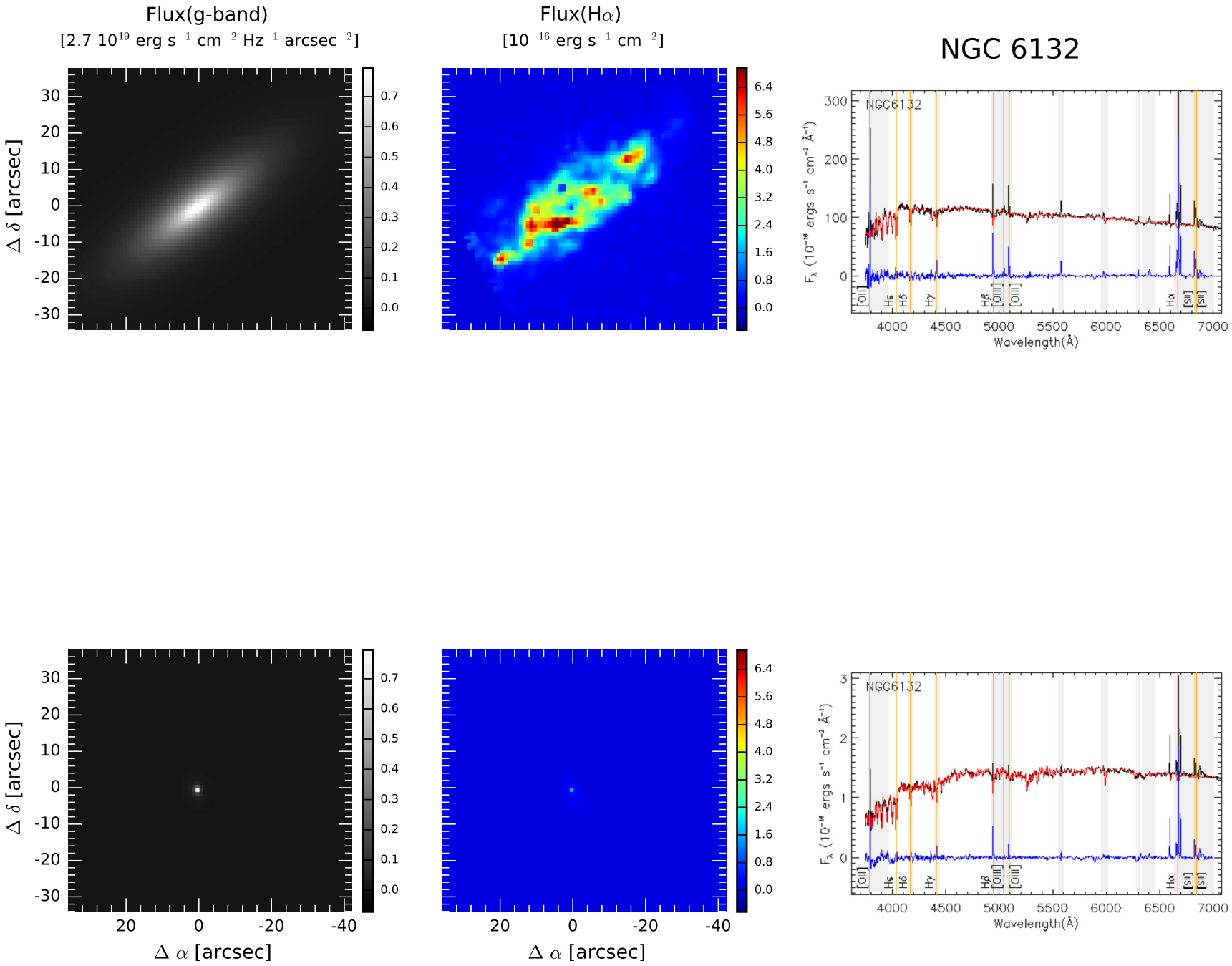
Flux(g-band)
[2.7 10^19 erg s^-1 cm^-2 Hz^-1 arcsec^-2]
Flux(Hα)
[10^-16 erg s^-1 cm^-2]
NGC 6132
Δ δ [arcsec]
Δ α [arcsec]
NGC6132
Wavelength(Å)
[OII]
Hε
Hδ
Hγ
Hβ
[OIII]
[OIII]
Hα
[SII]
[SII]

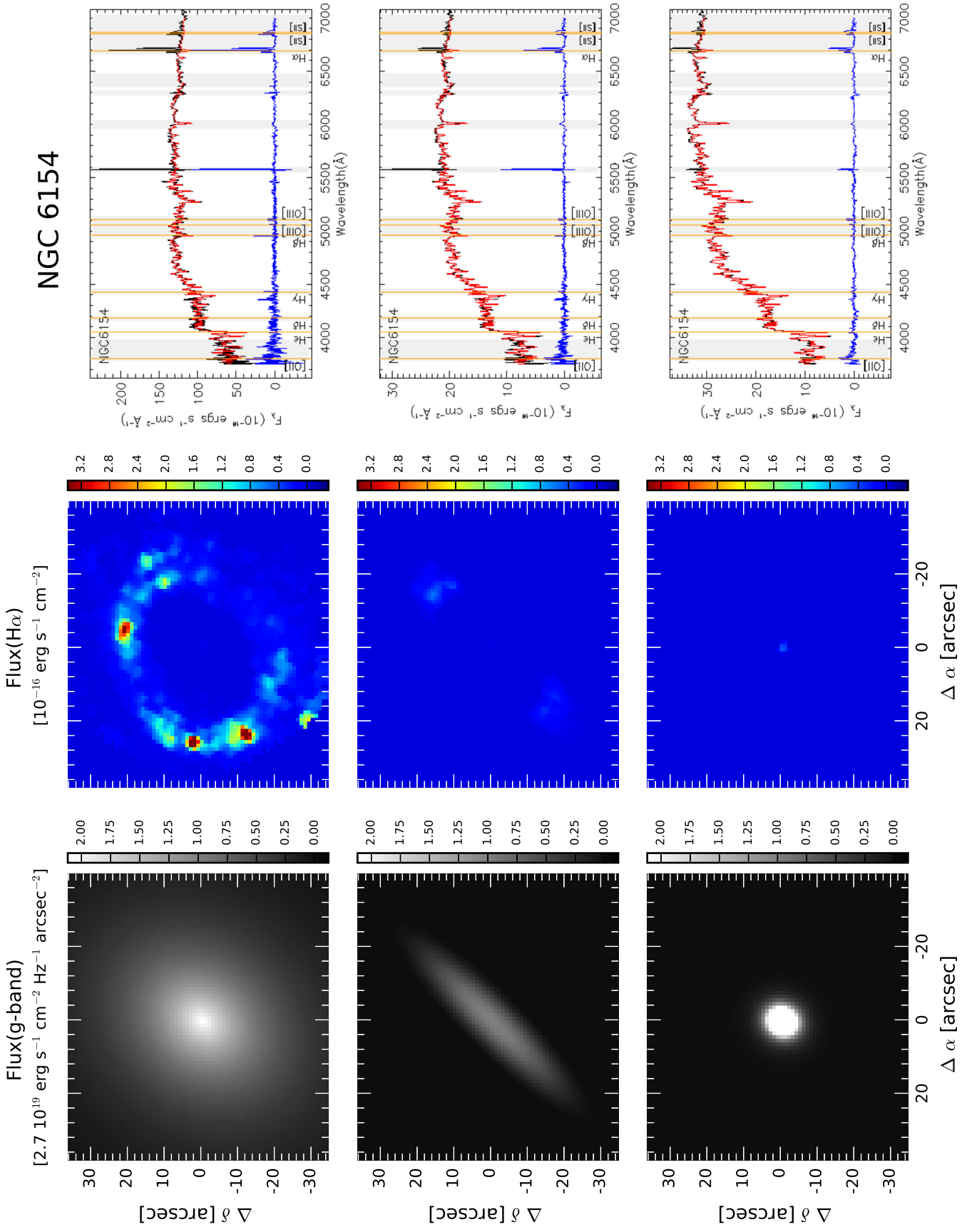
NGC 6154
Flux(g-band)
[2.7 10^19 erg s^-1 cm^-2 Hz^-1 arcsec^-2]
Flux(Hα)
[10^-16 erg s^-1 cm^-2]
Δ δ [arcsec]
Δ α [arcsec]
Wavelength(Å)
NGC6154
[OII]
Hε
Hδ
Hγ
Hβ
[OIII]
[OIII]
[SII]
[SII]
Hα

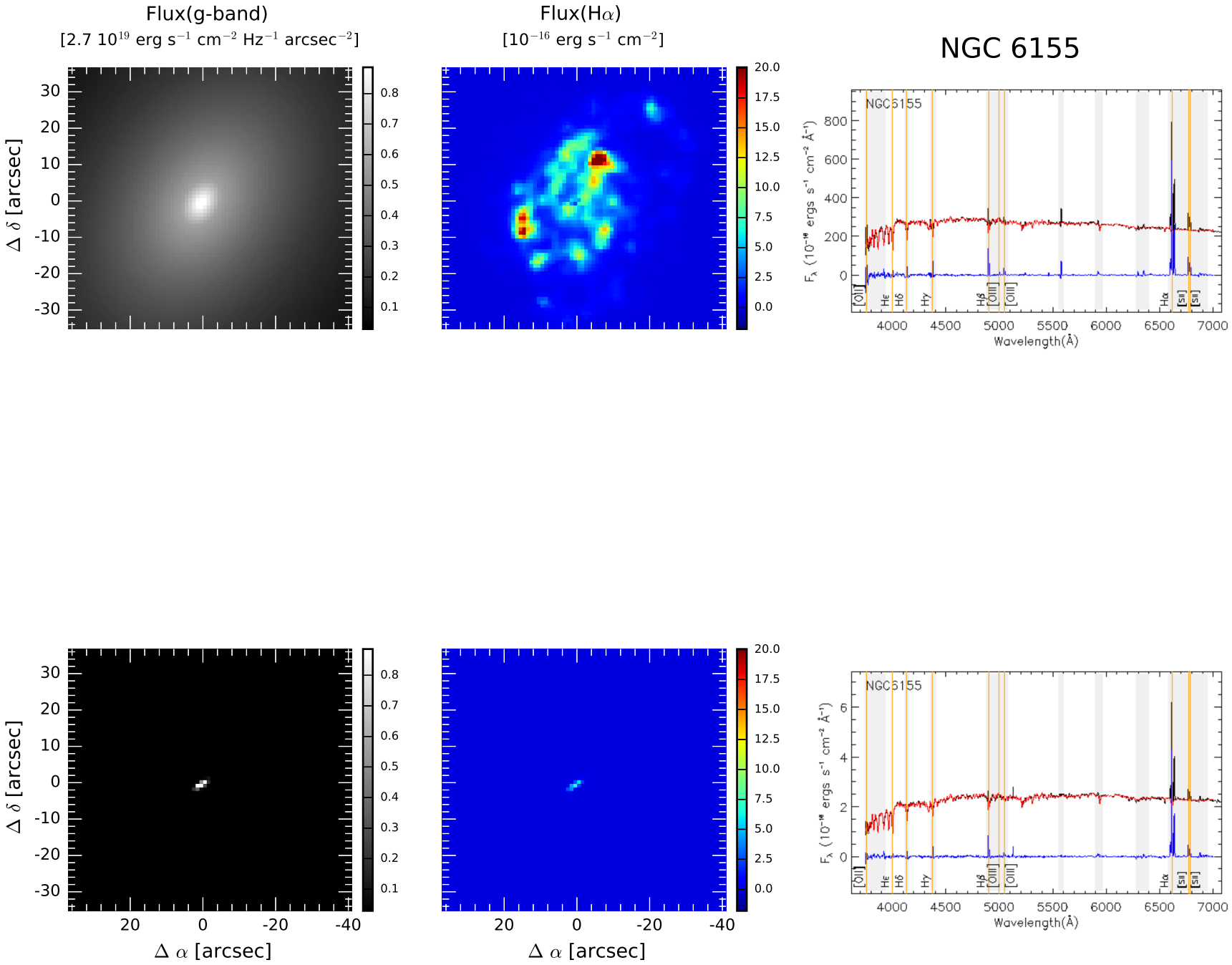
Flux(g-band)
[2.7 10^19 erg s^-1 cm^-2 Hz^-1 arcsec^-2]
Flux(Hα)
[10^-16 erg s^-1 cm^-2]
NGC 6155
Δ δ [arcsec]
Δ α [arcsec]
NGC6155
Wavelength(Å)
[OII]
Hε
Hδ
Hγ
Hβ
[OIII]
[OIII]
Hα
[SII]
[SII]

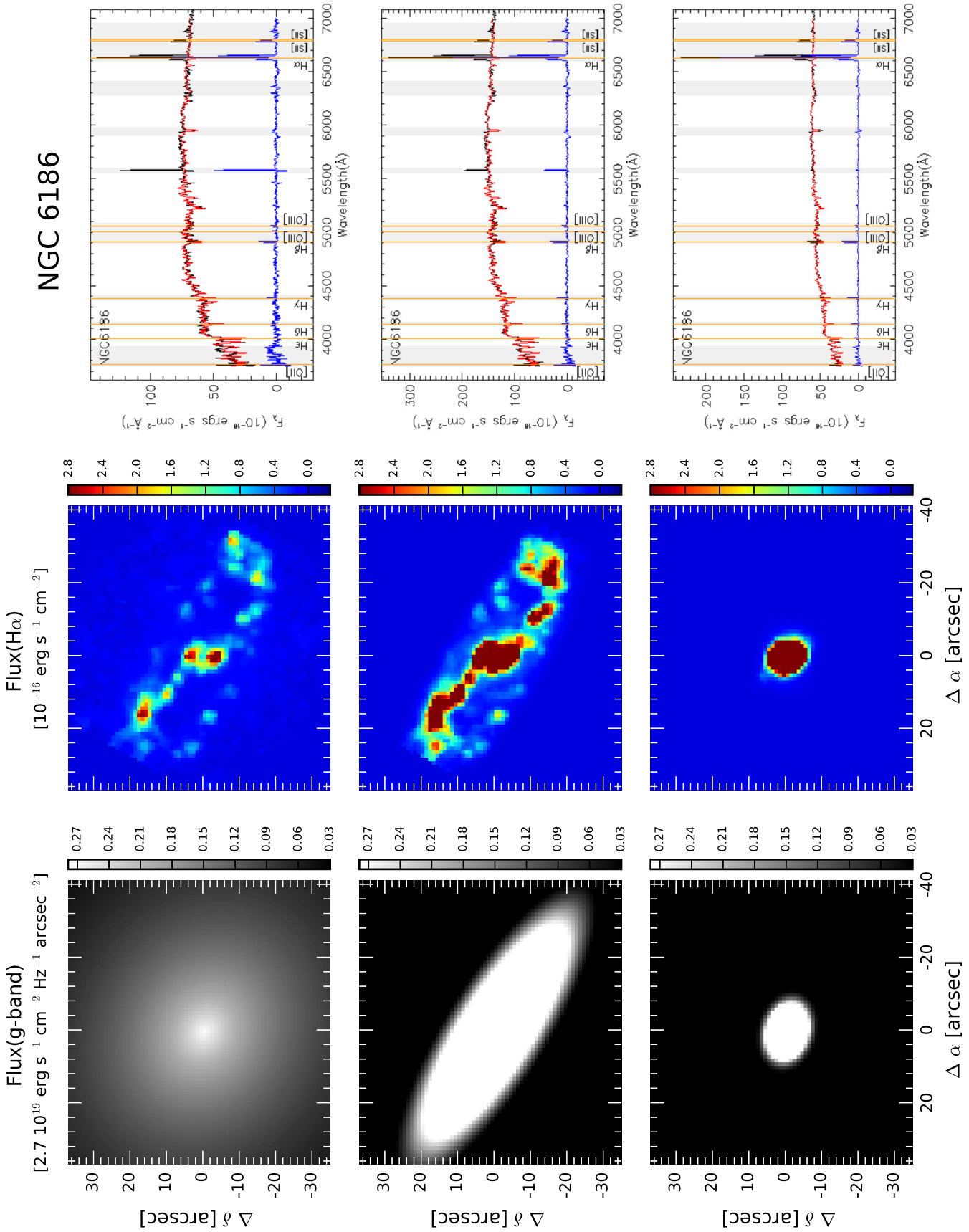
NGC 6186
Flux(g-band)
[2.7 10^19 erg s^-1 cm^-2 Hz^-1 arcsec^-2]
Flux(Hα)
[10^-16 erg s^-1 cm^-2]
Δ δ [arcsec]
Δ α [arcsec]
Wavelength(Å)
F_λ (10^-16 ergs s^-1 cm^-2 Å^-1)
[OII]
Hε
Hδ
Hγ
[OIII]
Hβ
Hα
[SII]

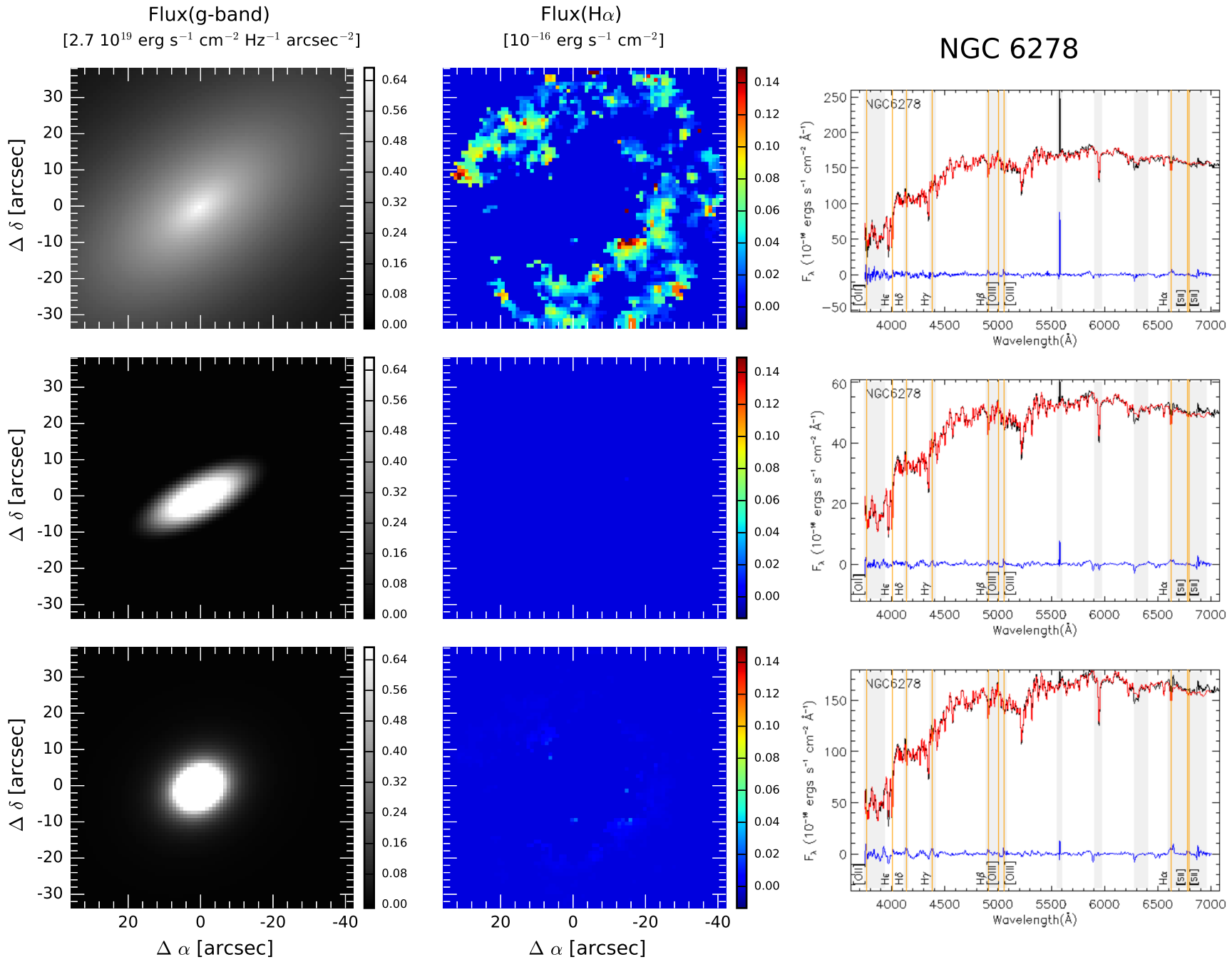
Flux(g-band)
[2.7 10^19 erg s^-1 cm^-2 Hz^-1 arcsec^-2]
Flux(Hα)
[10^-16 erg s^-1 cm^-2]
NGC 6278
Δ δ [arcsec]
Δ α [arcsec]
Wavelength(Å)
NGC6278
[OII]
Hε
Hδ
Hγ
Hβ
[OIII]
[OIII]
Hα
[SII]
[SII]

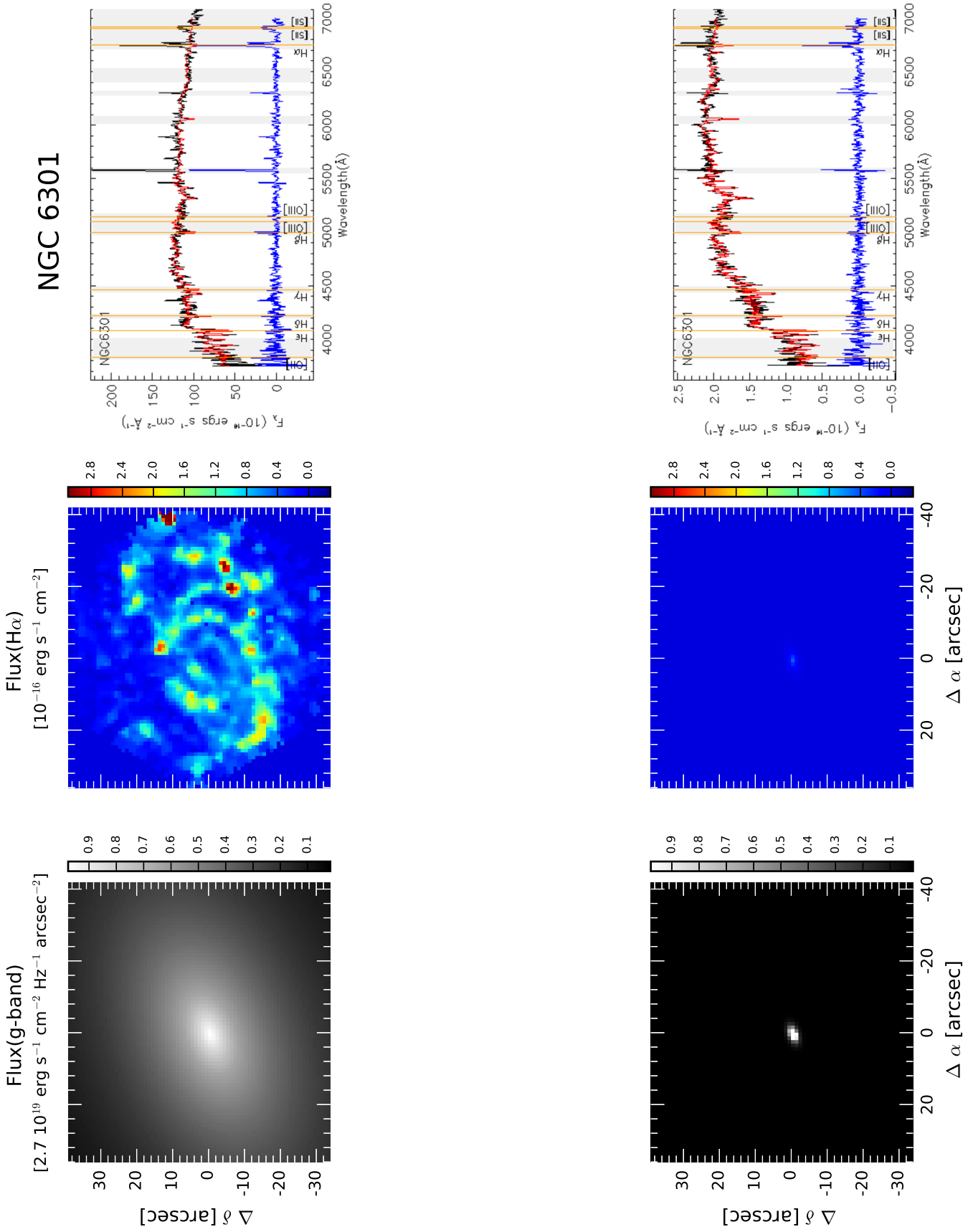
NGC 6301
Flux(Hα)
[10^-16 erg s^-1 cm^-2]
Flux(g-band)
[2.7 10^19 erg s^-1 cm^-2 Hz^-1 arcsec^-2]
Δ δ [arcsec]
Δ α [arcsec]
Wavelength(Å)
NGC6301
[OII]
Hε
Hδ
Hγ
Hβ
[OIII]
[OIII]
Hα
[SII]
[SII]

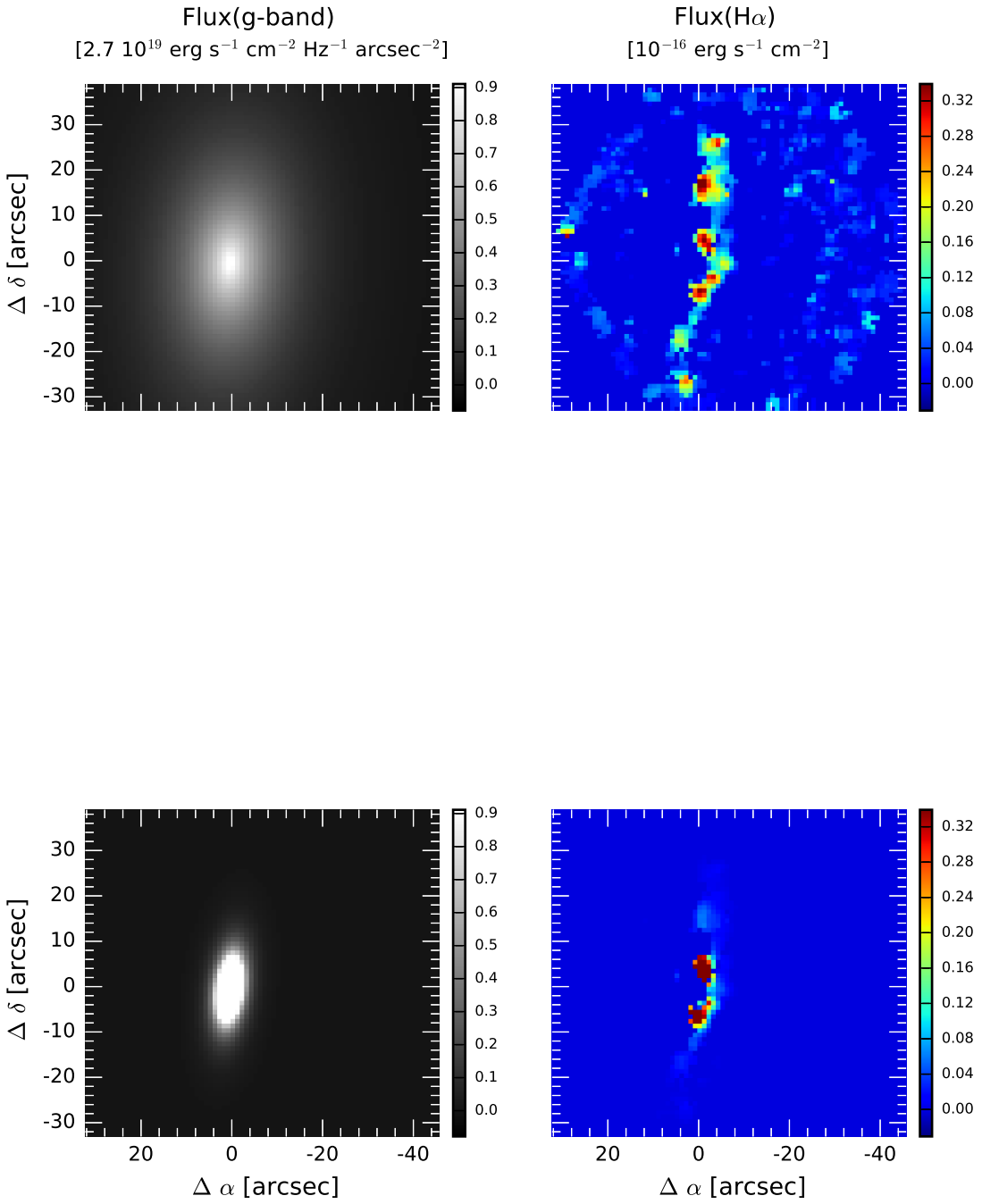
Flux(g-band)
[2.7 10^19 erg s^-1 cm^-2 Hz^-1 arcsec^-2]
Flux(Hα)
[10^-16 erg s^-1 cm^-2]
NGC 6314
Δ δ [arcsec]
Δ α [arcsec]
NGC6314
Wavelength(Å)
[OII]
Hε
Hδ
Hγ
Hβ
[OIII]
[OIII]
Hα
[SII]
[SII]

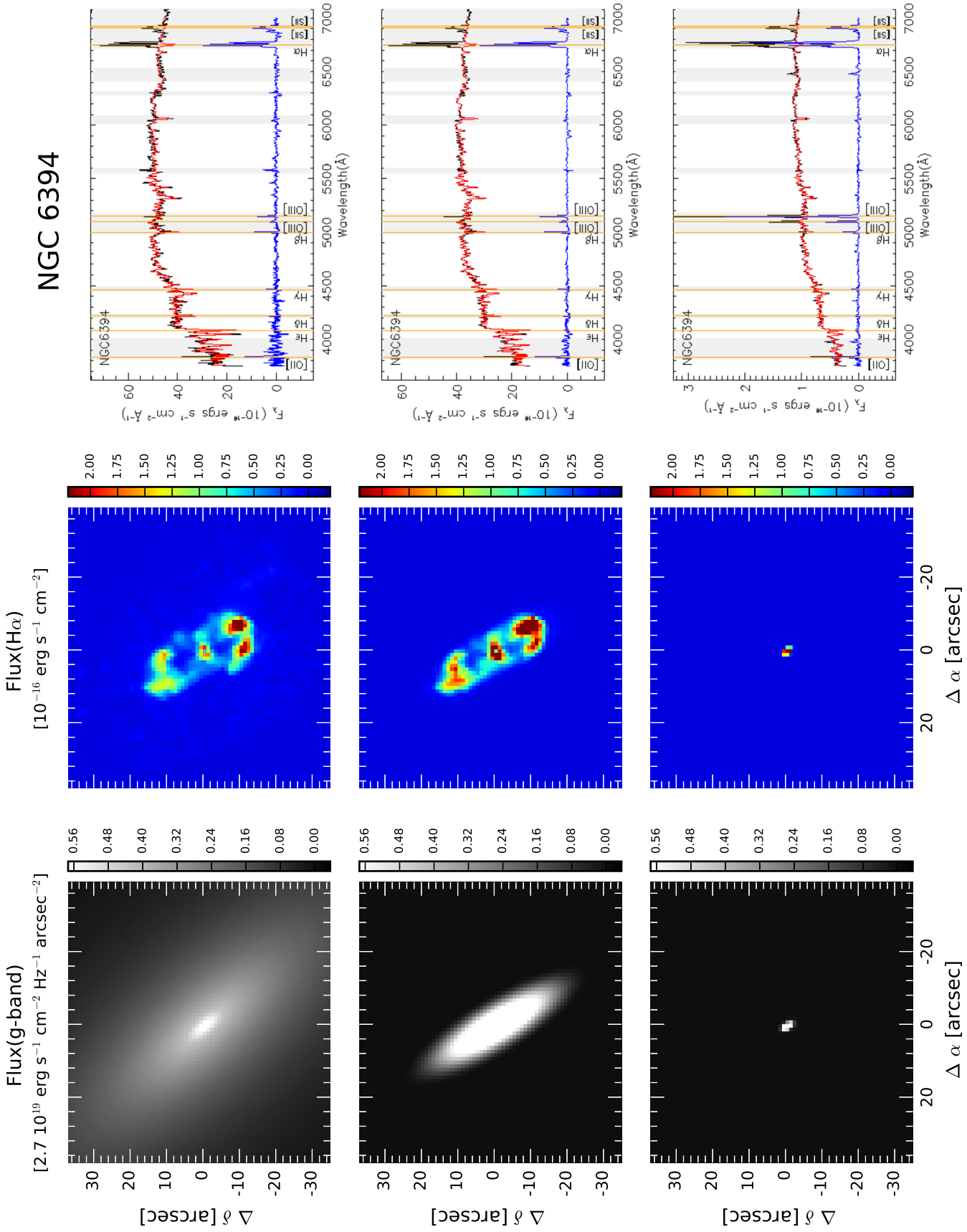
NGC 6394
Flux(g-band)
[2.7 10^19 erg s^-1 cm^-2 Hz^-1 arcsec^-2]
Flux(Hα)
[10^-16 erg s^-1 cm^-2]
Δ δ [arcsec]
Δ α [arcsec]
Wavelength(Å)
F_λ (10^-16 ergs s^-1 cm^-2 Å^-1)
NGC6394
[OII]
Hε
Hδ
Hγ
Hβ
[OIII]
[OIII]
[SII]
[SII]
Hα

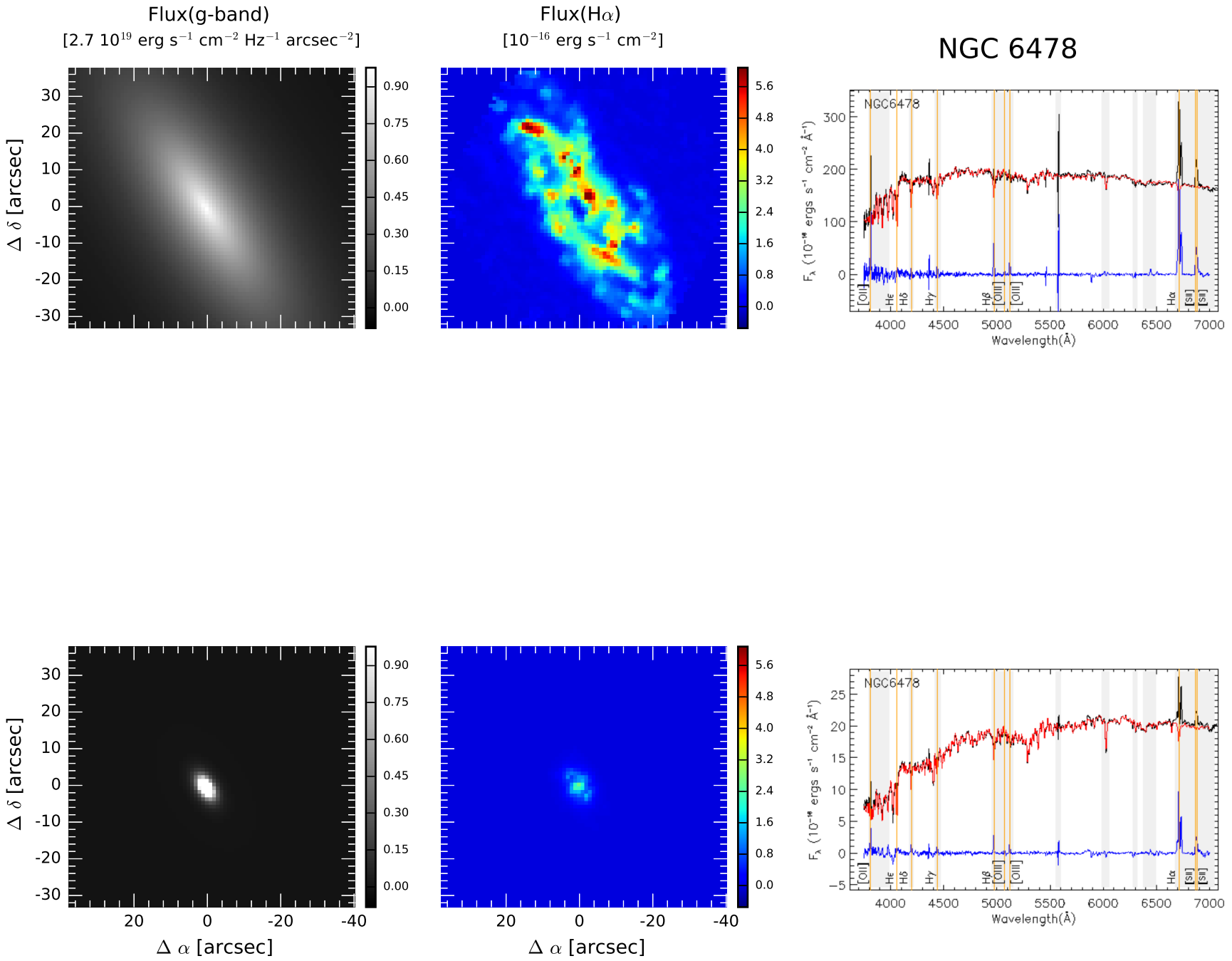
Flux(g-band)
[2.7 10^19 erg s^-1 cm^-2 Hz^-1 arcsec^-2]
Flux(Hα)
[10^-16 erg s^-1 cm^-2]
NGC 6478
Δ δ [arcsec]
Δ α [arcsec]
NGC6478
Wavelength(Å)
[OII]
Hε
Hδ
Hγ
Hβ
[OIII]
[OIII]
Hα
[SII]
[SII]

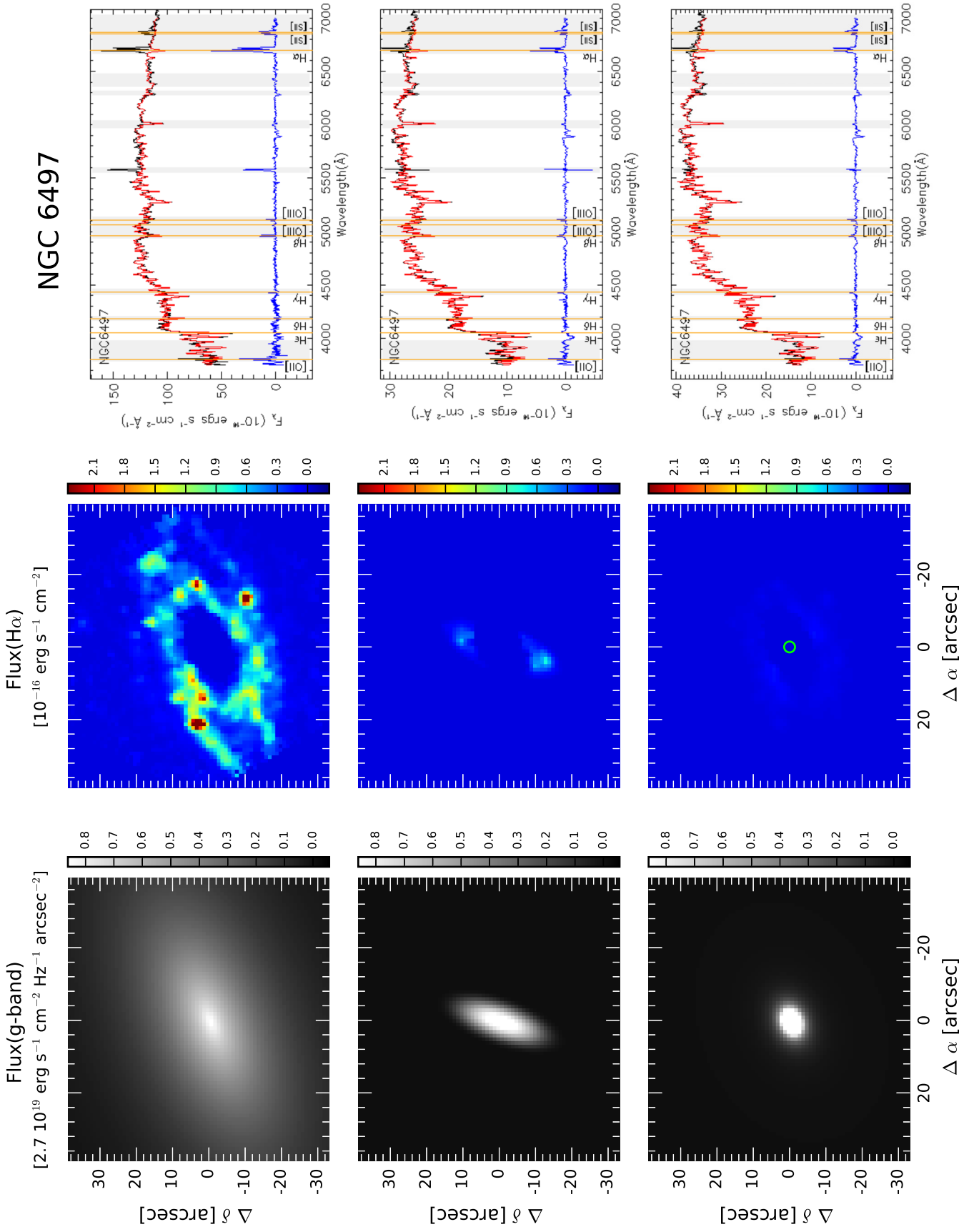
NGC 6497
Flux(g-band)
[2.7 10^19 erg s^-1 cm^-2 Hz^-1 arcsec^-2]
Flux(Hα)
[10^-16 erg s^-1 cm^-2]
Δ δ [arcsec]
Δ α [arcsec]
Wavelength(Å)
F_λ (10^-16 ergs s^-1 cm^-2 Å^-1)
NGC6497
[OII]
[SII]
[SII]
Hα
[OIII]
[OIII]
Hβ
Hγ
Hδ
Hε
[OII]

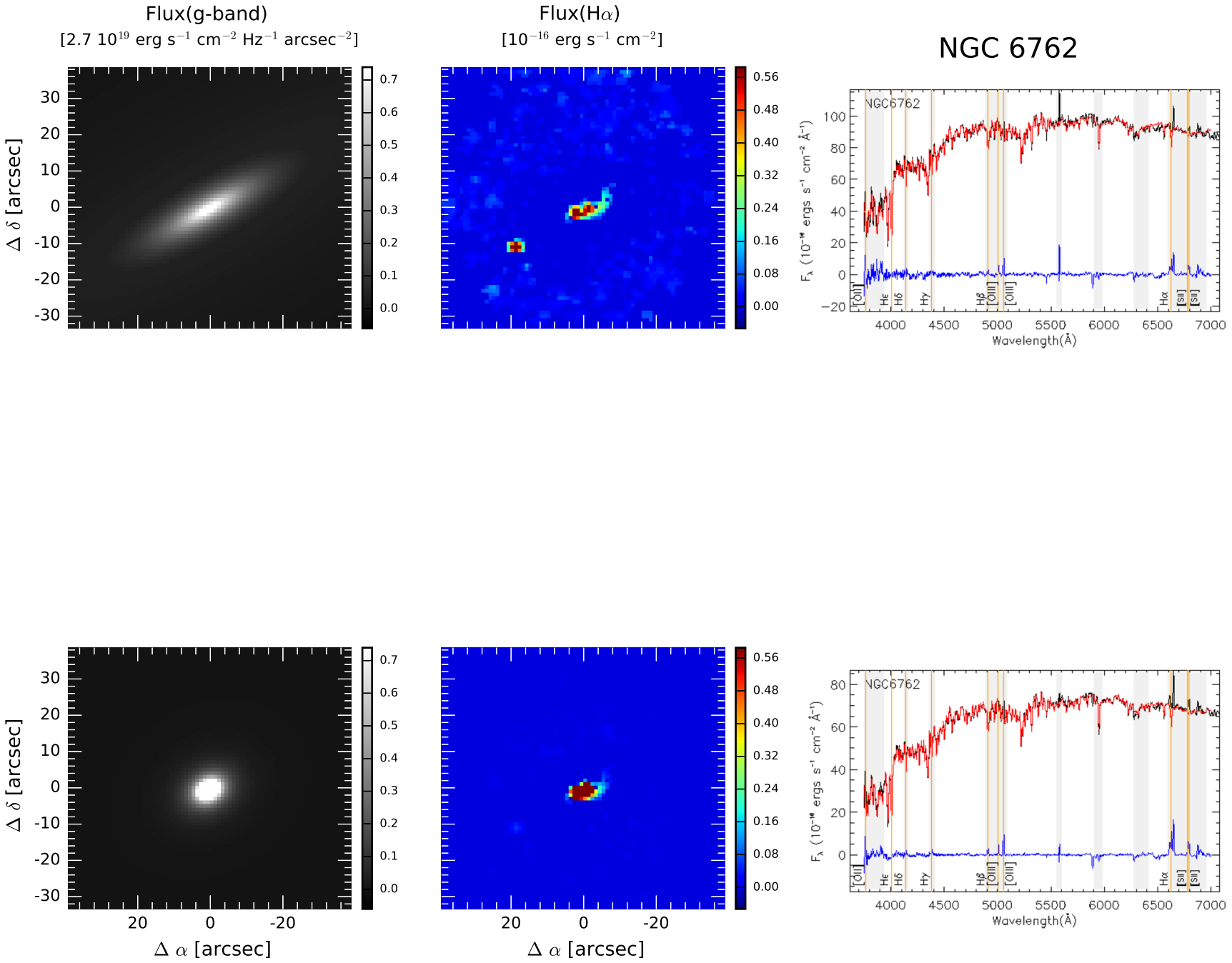
Flux(g-band)
[2.7 10^19 erg s^-1 cm^-2 Hz^-1 arcsec^-2]
Flux(Hα)
[10^-16 erg s^-1 cm^-2]
NGC 6762
Δ δ [arcsec]
Δ α [arcsec]
NGC6762
Wavelength(Å)
[OII]
Hε
H6
Hγ
Hβ
[OIII]
[OIII]
Hα
[SII]
[SII]

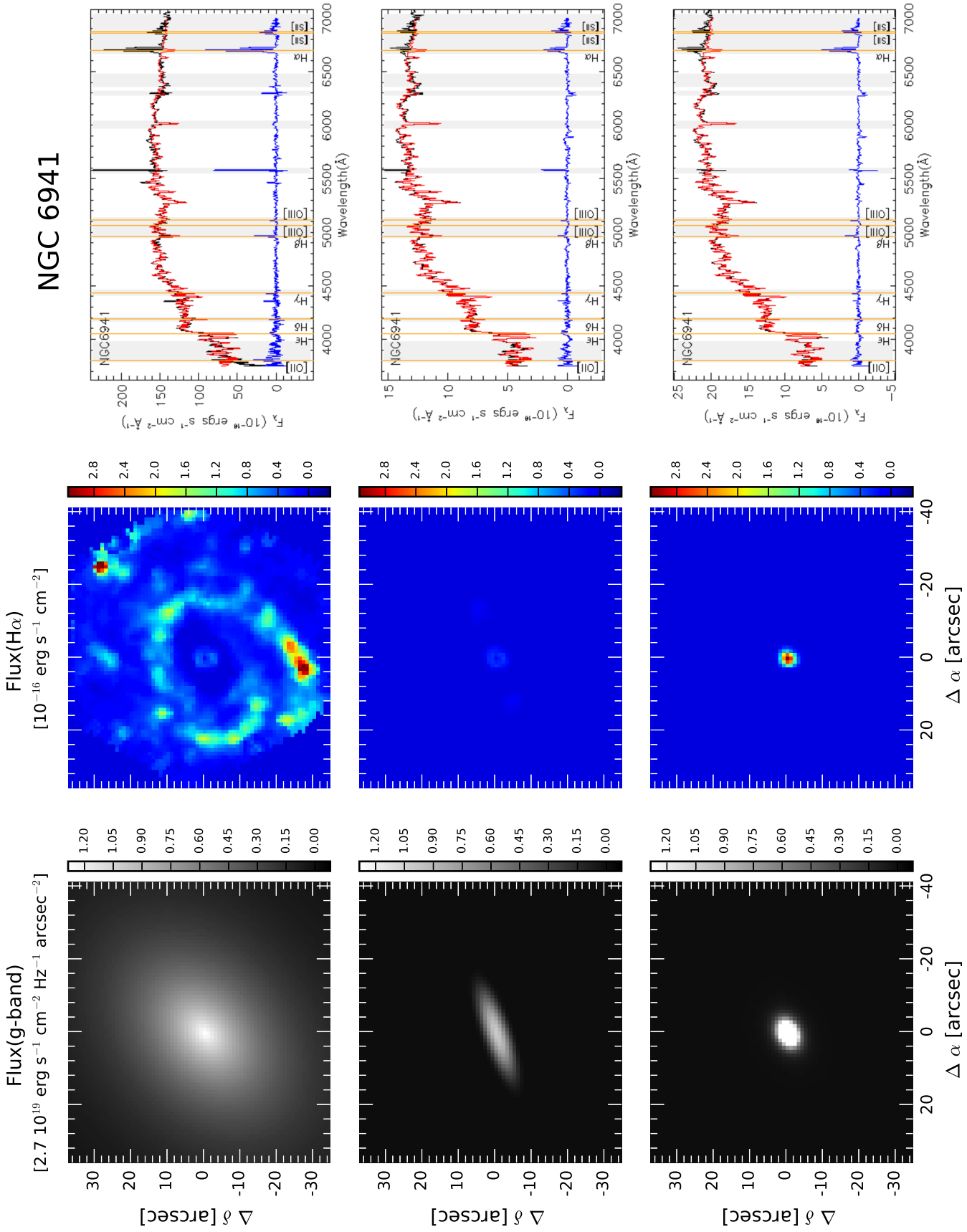
NGC 6941
Flux(Hα)
[10^-16 erg s^-1 cm^-2]
Flux(g-band)
[2.7 10^19 erg s^-1 cm^-2 Hz^-1 arcsec^-2]
Δ α [arcsec]
Δ δ [arcsec]
Wavelength(Å)
NGC6941
[OII]
Hε
Hδ
Hγ
Hβ
[OIII]
[OIII]
[SII]
[SII]
Hα

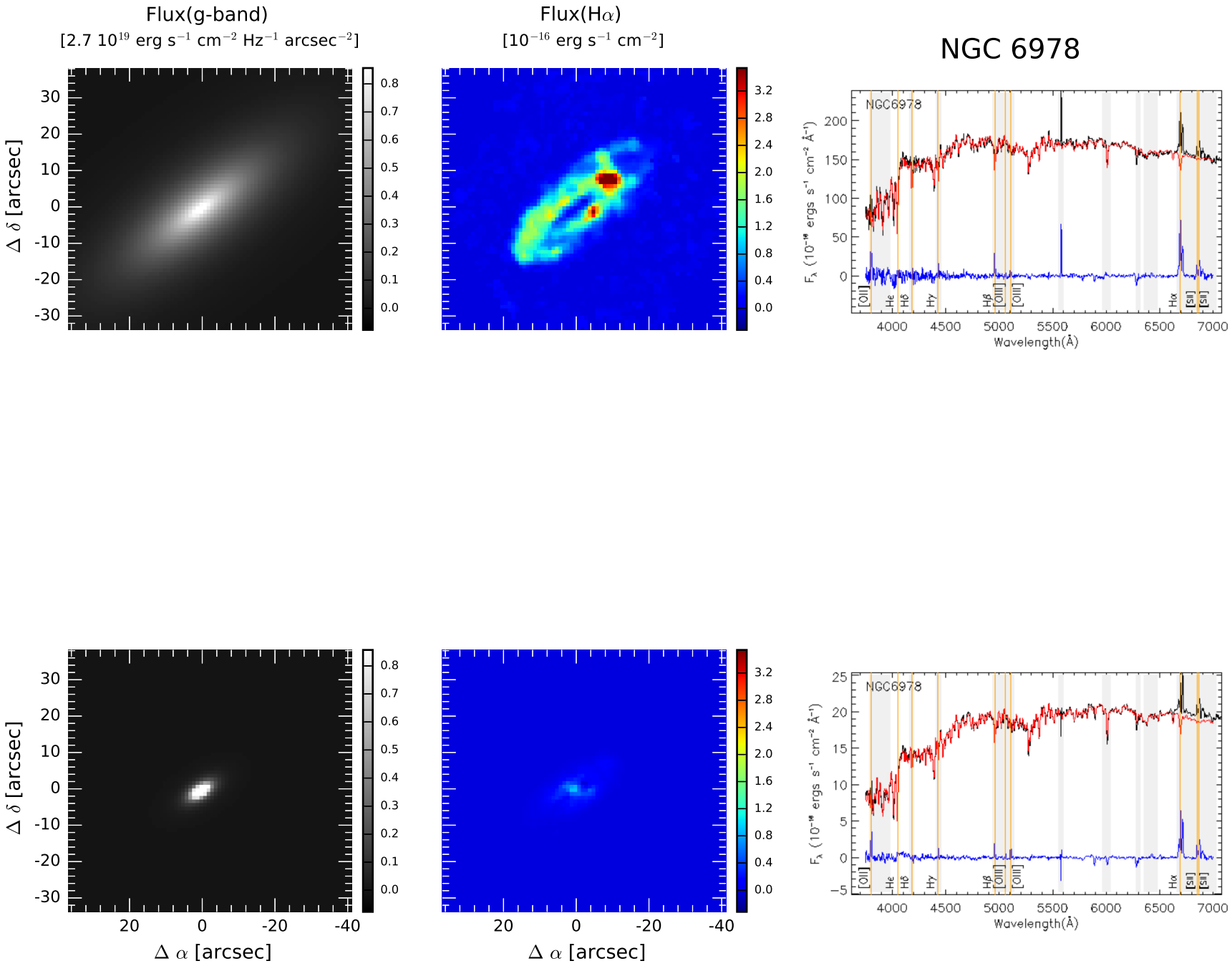
Flux(g-band)
[2.7 10^19 erg s^-1 cm^-2 Hz^-1 arcsec^-2]
Flux(Hα)
[10^-16 erg s^-1 cm^-2]
NGC 6978
Δ δ [arcsec]
Δ α [arcsec]
NGC6978
Wavelength(Å)
[OII]
Hε
Hδ
Hγ
Hβ
[OIII]
[OIII]
Hα
[SII]
[SII]

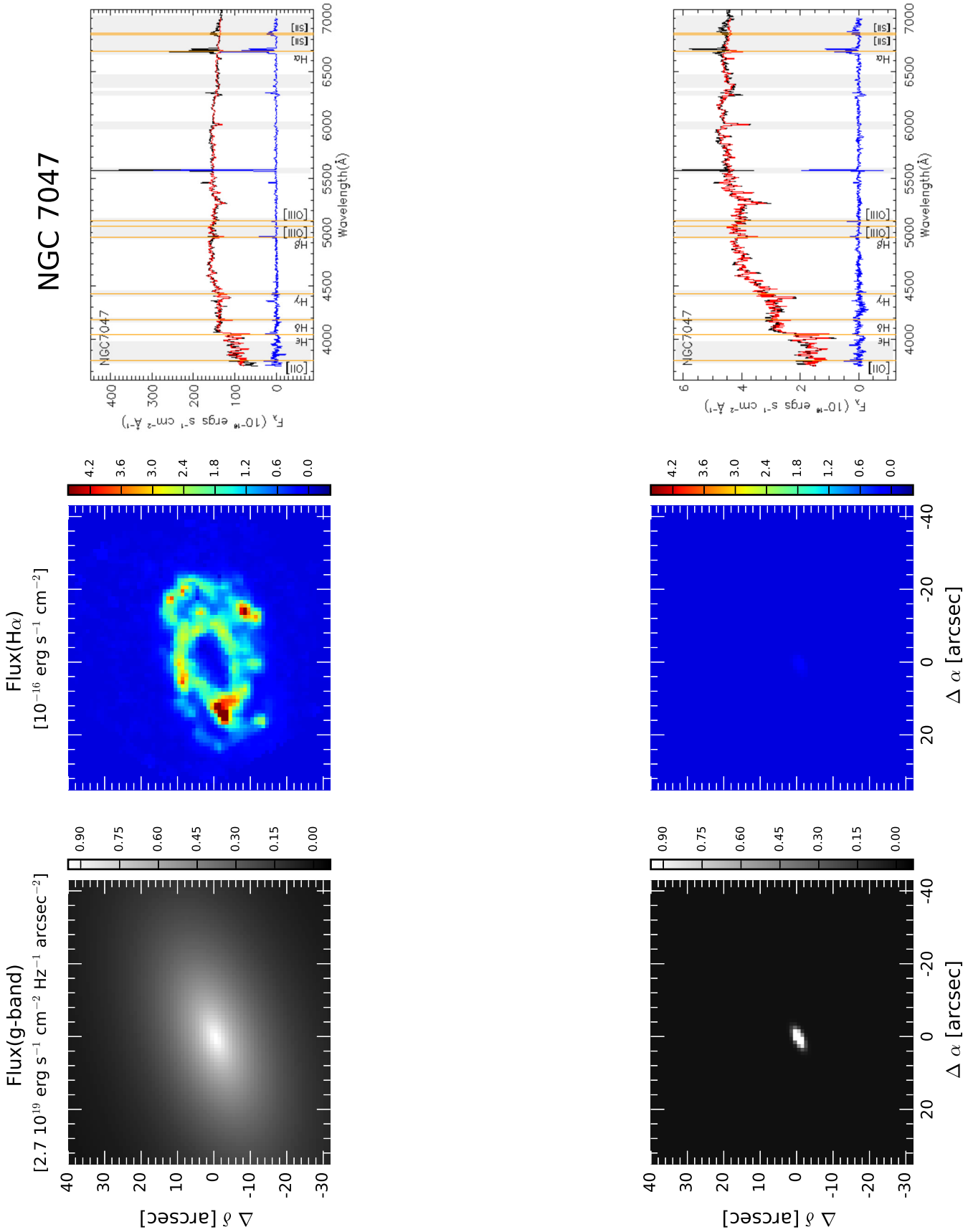
NGC 7047
Flux(g-band)
[2.7 10^19 erg s^-1 cm^-2 Hz^-1 arcsec^-2]
Flux(Hα)
[10^-16 erg s^-1 cm^-2]
Δ δ [arcsec]
Δ α [arcsec]
Wavelength(Å)
F_λ (10^-16 ergs s^-1 cm^-2 Å^-1)
NGC7047
[OII]
Hε
Hδ
Hγ
Hβ
[OIII]
[OIII]
[SII]
[SII]
Hα

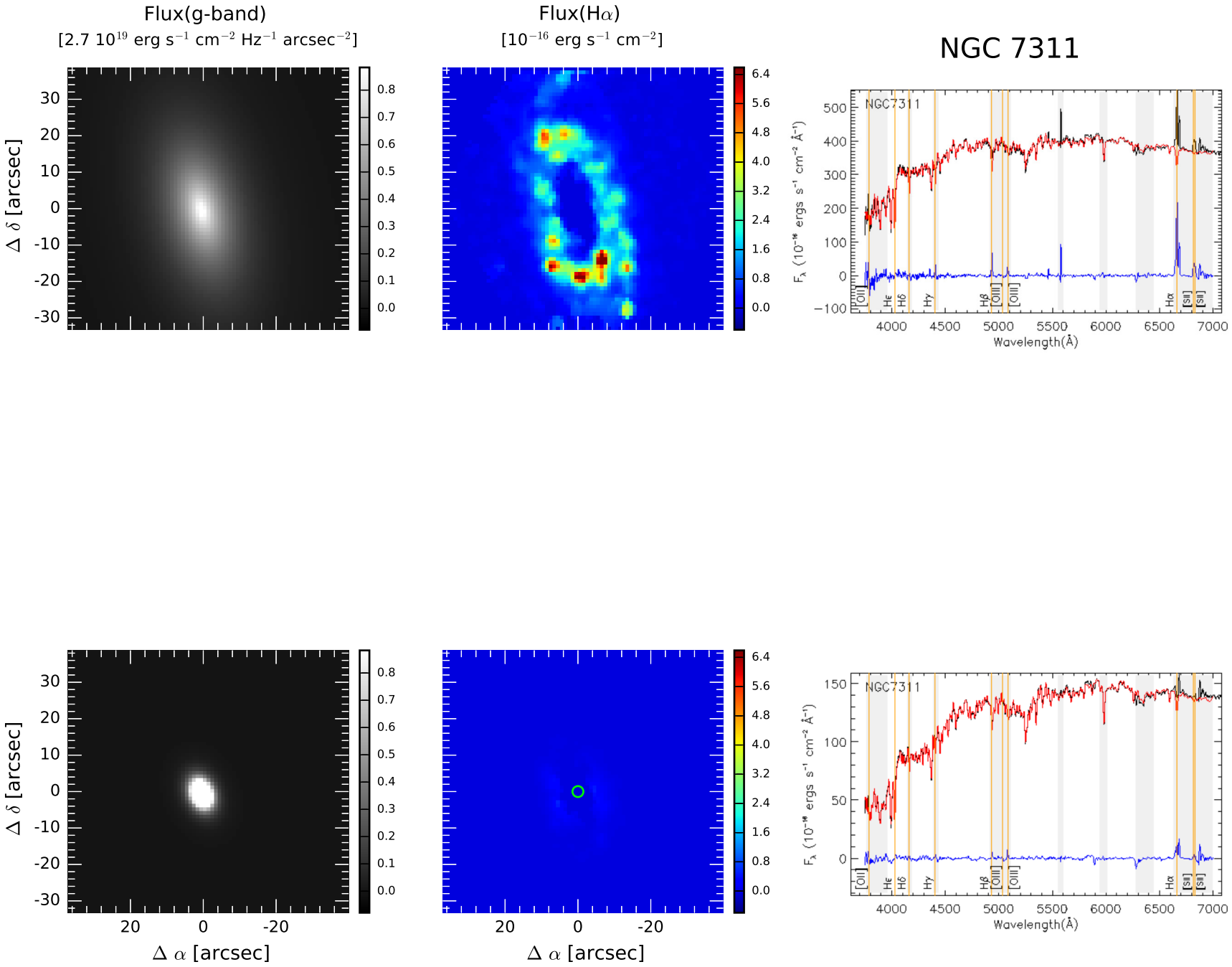
Flux(g-band)
[2.7 10^19 erg s^-1 cm^-2 Hz^-1 arcsec^-2]
Flux(Hα)
[10^-16 erg s^-1 cm^-2]
NGC 7311
Δ δ [arcsec]
Δ α [arcsec]
NGC7311
Wavelength(Å)
[OII]
Hε
Hδ
Hγ
Hβ
[OIII]
[OIII]
Hα
[SII]
[SII]

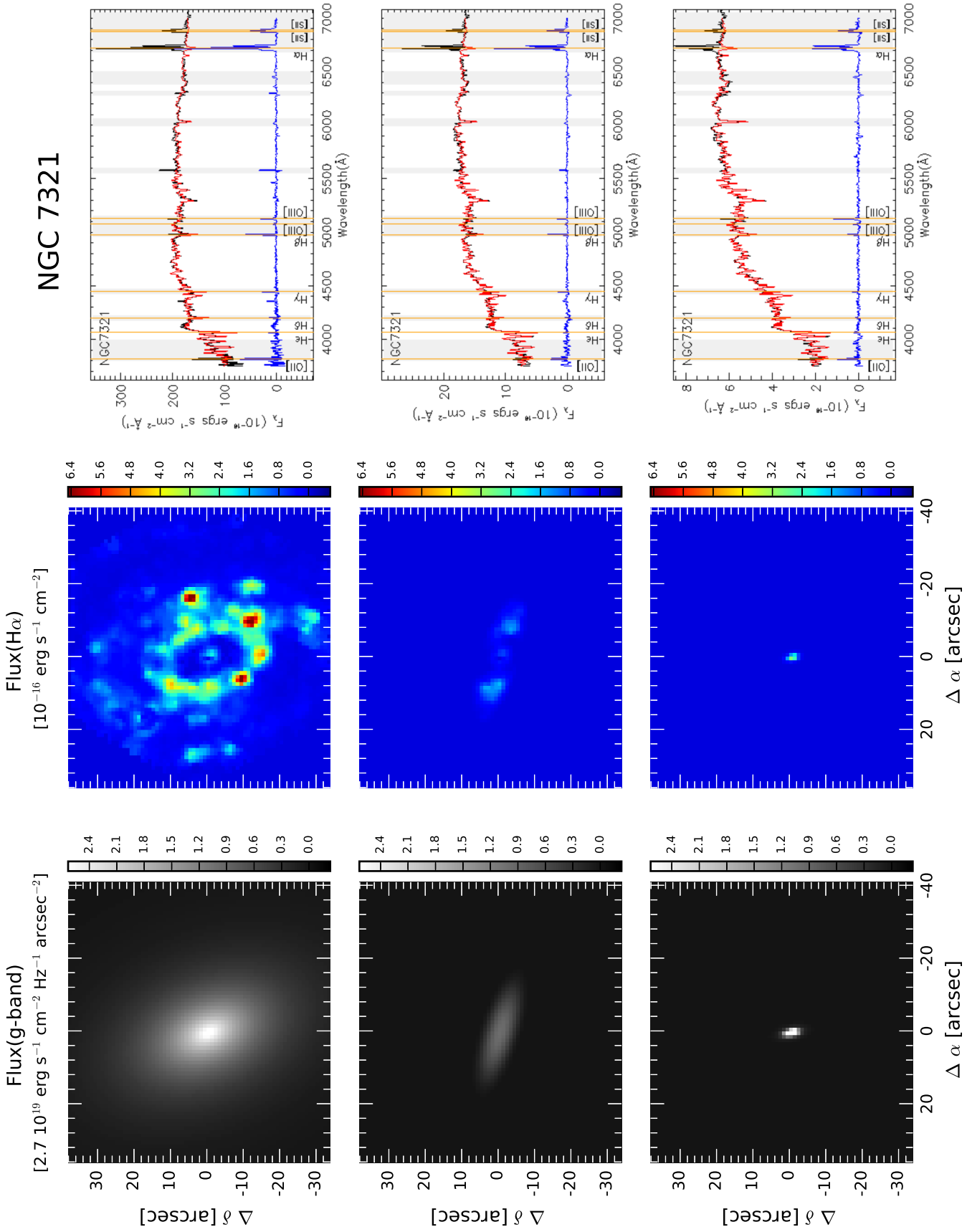
NGC 7321
Flux(g-band)
[2.7 10^19 erg s^-1 cm^-2 Hz^-1 arcsec^-2]
Flux(Hα)
[10^-16 erg s^-1 cm^-2]
Δ δ [arcsec]
Δ α [arcsec]
Wavelength(Å)
F_λ (10^-16 ergs s^-1 cm^-2 Å^-1)
[OII]
Hε
Hδ
Hγ
Hβ
[OIII]
Hα
[SII]

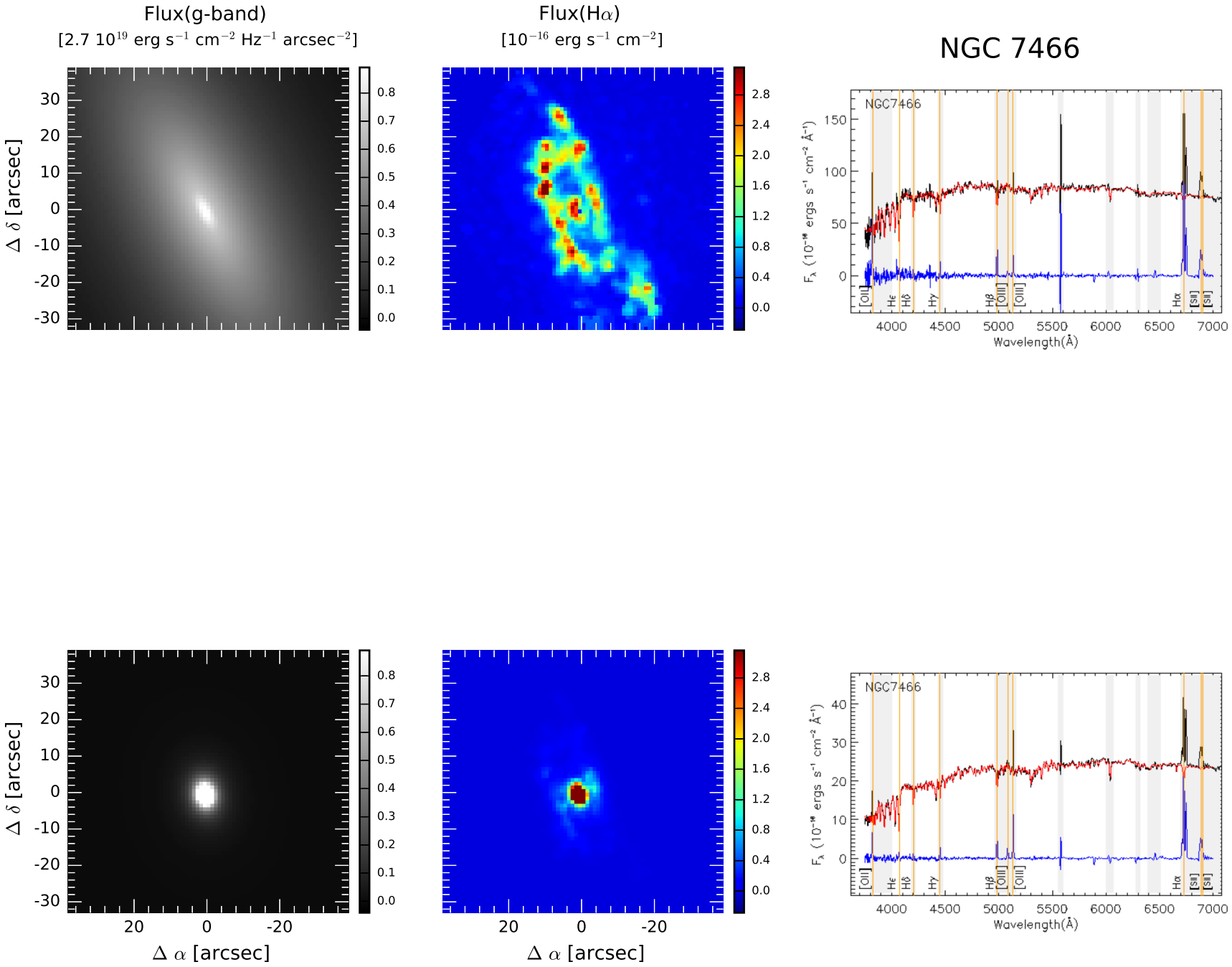
Flux(g-band)
[2.7 10^19 erg s^-1 cm^-2 Hz^-1 arcsec^-2]
Flux(Hα)
[10^-16 erg s^-1 cm^-2]
NGC 7466
NGC7466
Δ δ [arcsec]
Δ α [arcsec]
Wavelength(Å)
[OII]
Hε
Hδ
Hγ
Hβ
[OIII]
[OIII]
Hα
[SII]
[SII]

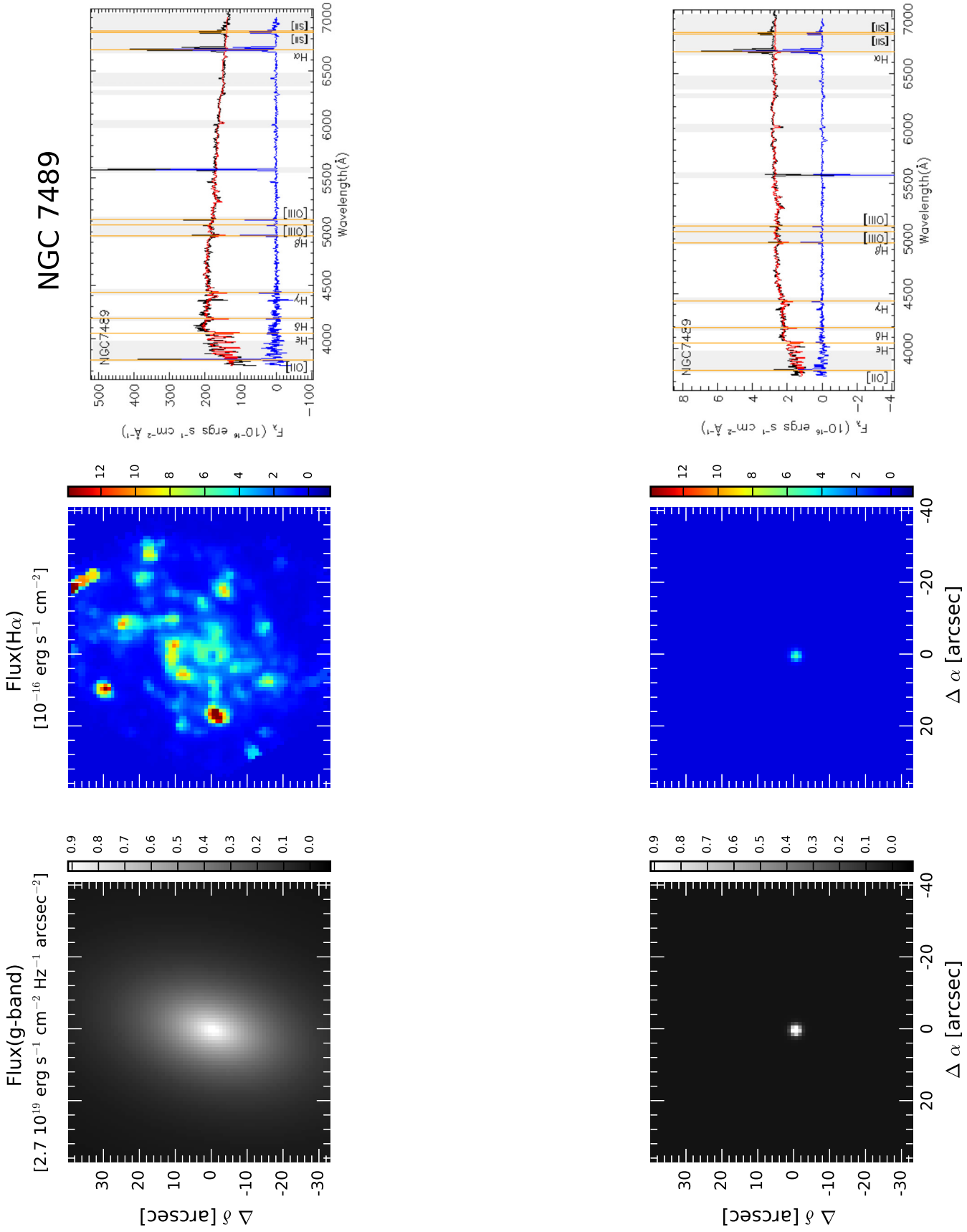
NGC 7489
Flux(g-band)
[2.7 10^19 erg s^-1 cm^-2 Hz^-1 arcsec^-2]
Flux(Hα)
[10^-16 erg s^-1 cm^-2]
Δ δ [arcsec]
Δ α [arcsec]
Wavelength(Å)
F_λ (10^-16 ergs s^-1 cm^-2 Å^-1)
NGC7489
[OII]
Hε
Hδ
Hγ
Hβ
[OIII]
[OIII]
[SII]
[SII]
Hα

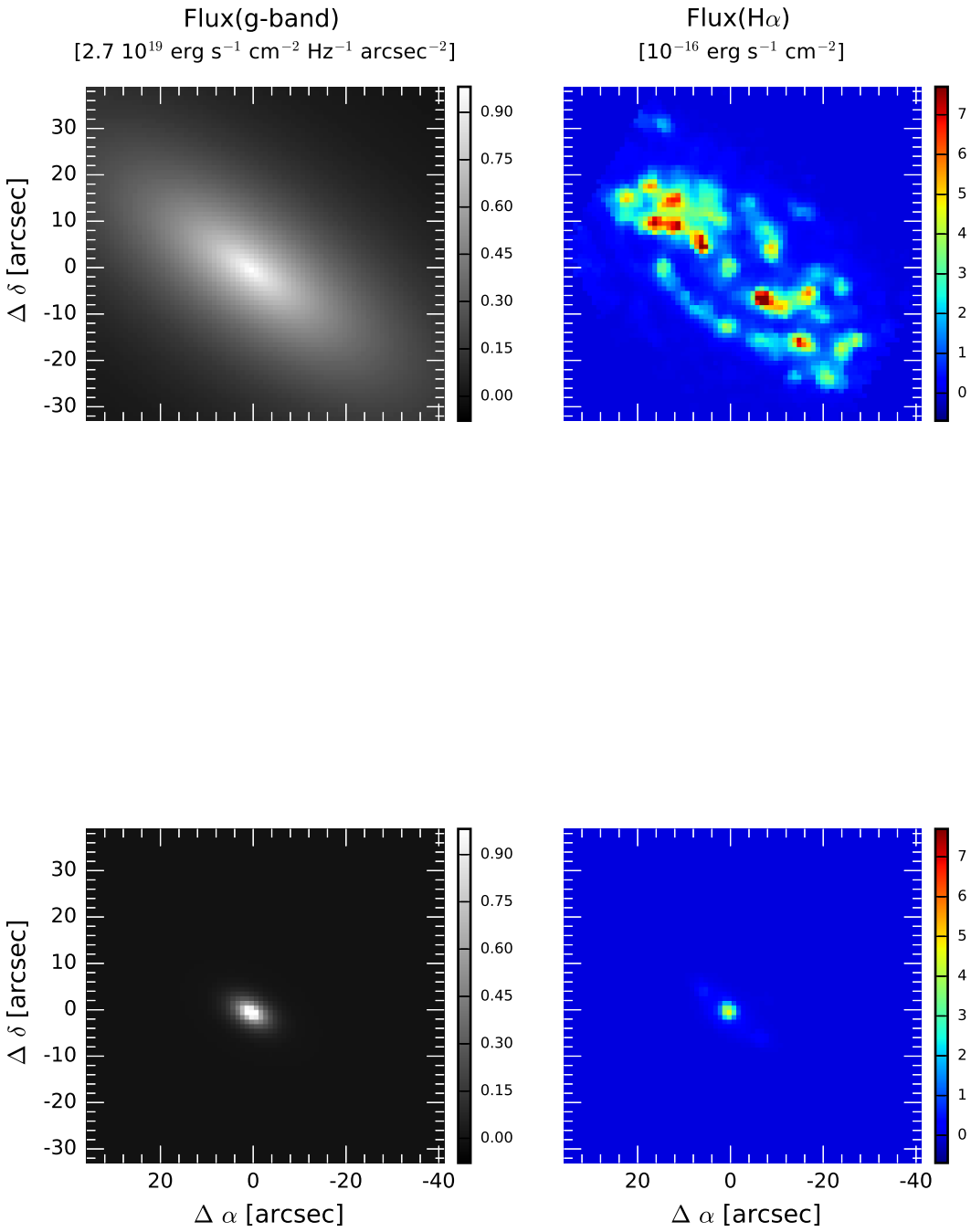
Flux(g-band)
[2.7 10^19 erg s^-1 cm^-2 Hz^-1 arcsec^-2]
Flux(Hα)
[10^-16 erg s^-1 cm^-2]
Δ δ [arcsec]
Δ α [arcsec]

NGC 7536

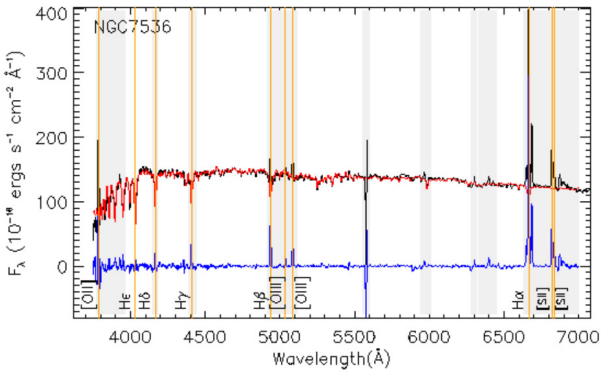
NGC7536
Wavelength(Å)
[OII]
Hε
Hδ
Hγ
Hβ
[OIII]
[OIII]
Hα
[SII]
[SII]

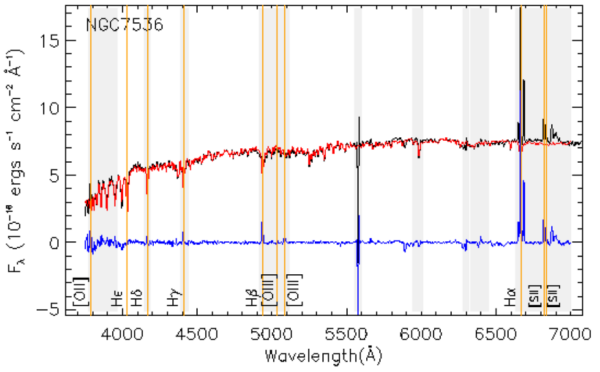
NGC7536
Wavelength(Å)
[OII]
Hε
Hδ
Hγ
Hβ
[OIII]
[OIII]
Hα
[SII]
[SII]

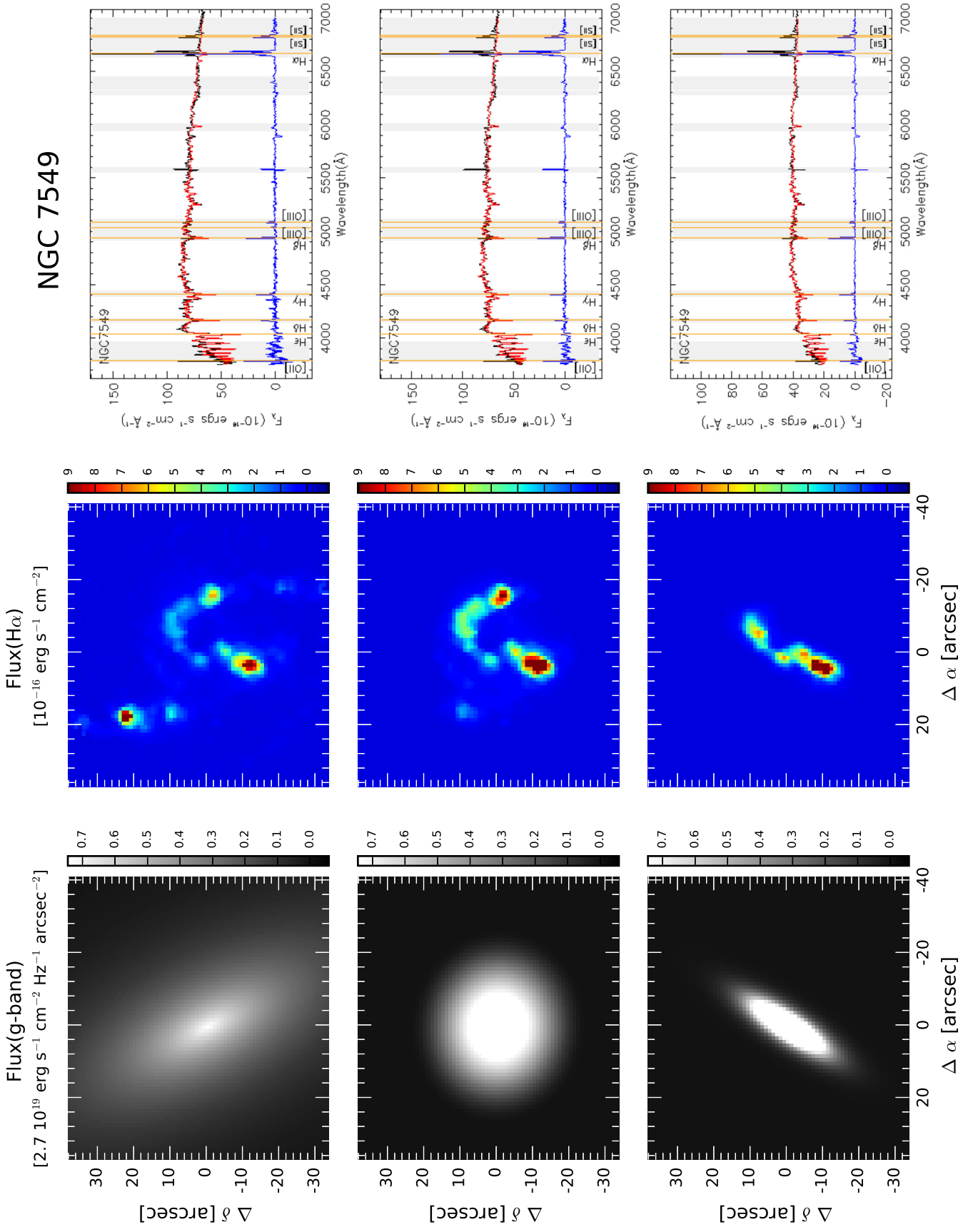
NGC 7549
Flux(g-band)
[2.7 10^19 erg s^-1 cm^-2 Hz^-1 arcsec^-2]
Flux(Hα)
[10^-16 erg s^-1 cm^-2]
Δ δ [arcsec]
Δ α [arcsec]
Wavelength(Å)
F_λ (10^-16 ergs s^-1 cm^-2 Å^-1)
NGC7549
[OII]
Hε
Hδ
Hγ
Hβ
[OIII]
[OIII]
Hα
[SII]
[SII]

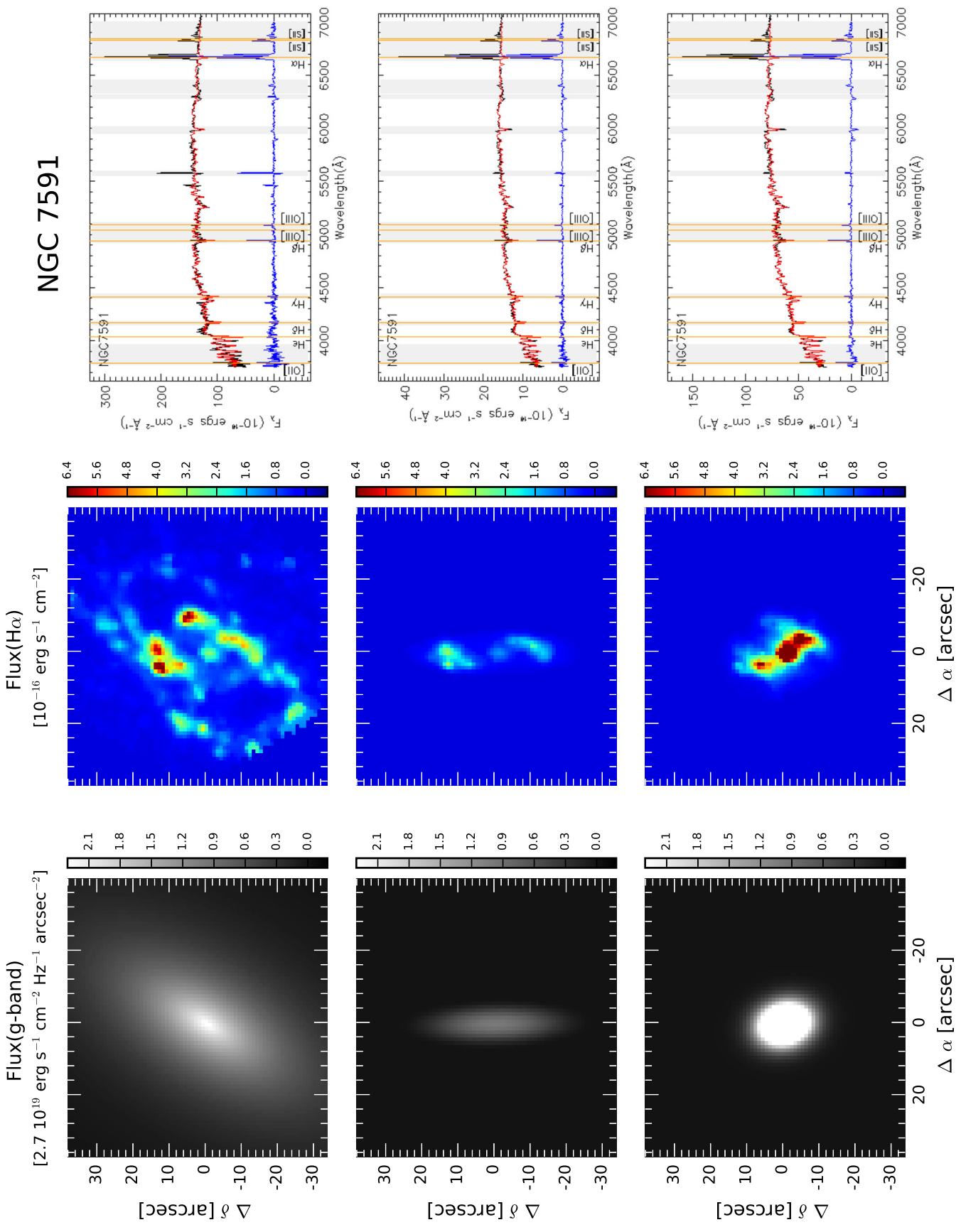
NGC 7591
Flux(g-band)
[2.7 10^19 erg s^-1 cm^-2 Hz^-1 arcsec^-2]
Flux(Hα)
[10^-16 erg s^-1 cm^-2]
Δ δ [arcsec]
Δ α [arcsec]
Wavelength(Å)
NGC7591
[OII]
Hε
Hδ
Hγ
Hβ
[OIII]
[OIII]
Hα
[SII]
[SII]

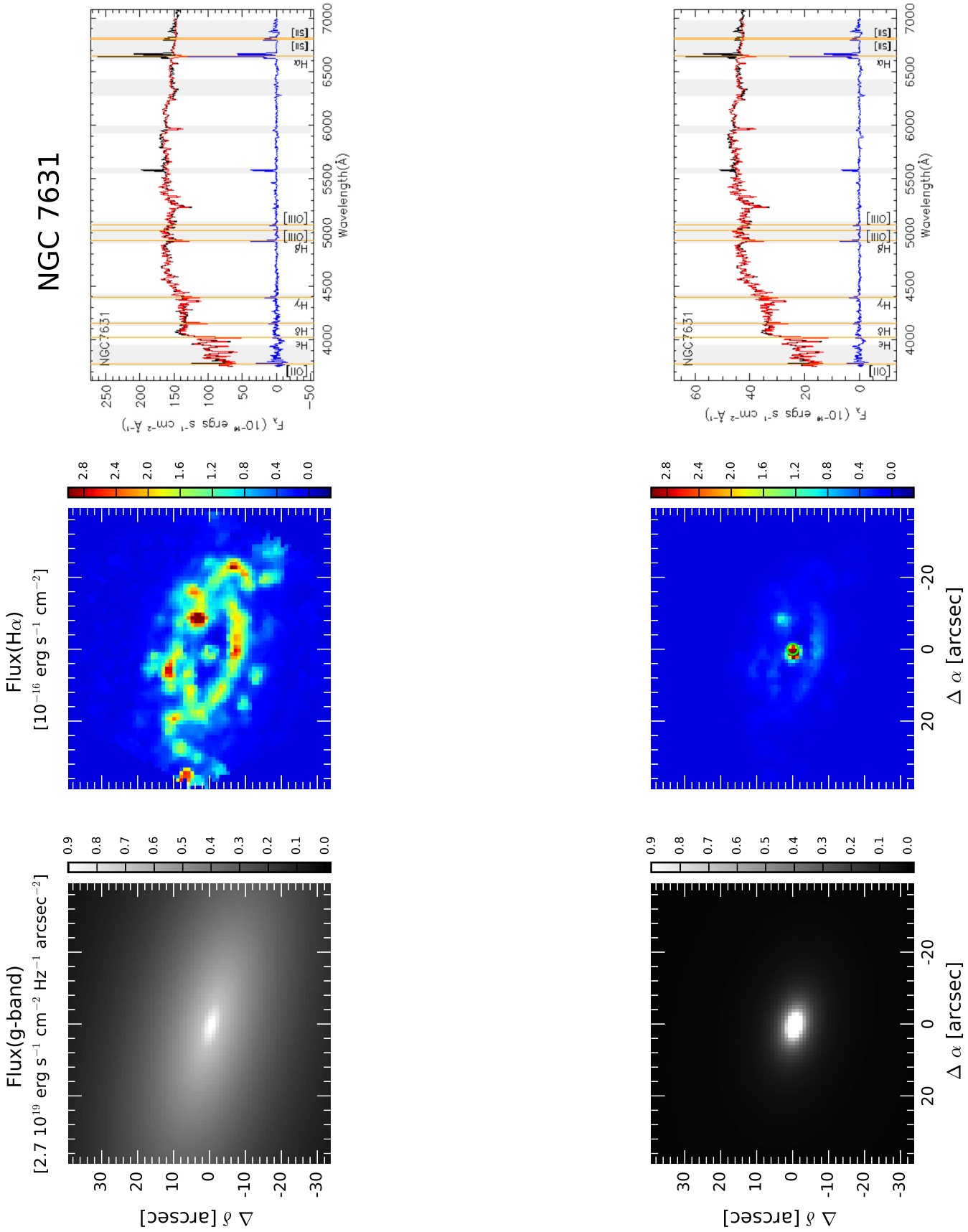
NGC 7631
Flux(g-band)
[2.7 10^19 erg s^-1 cm^-2 Hz^-1 arcsec^-2]
Flux(Hα)
[10^-16 erg s^-1 cm^-2]
Δ δ [arcsec]
Δ α [arcsec]
Wavelength(Å)
NGC7631
[OII]
Hε
Hδ
Hγ
[OIII]
Hβ
[OIII]
[SII]
[SII]
Hα

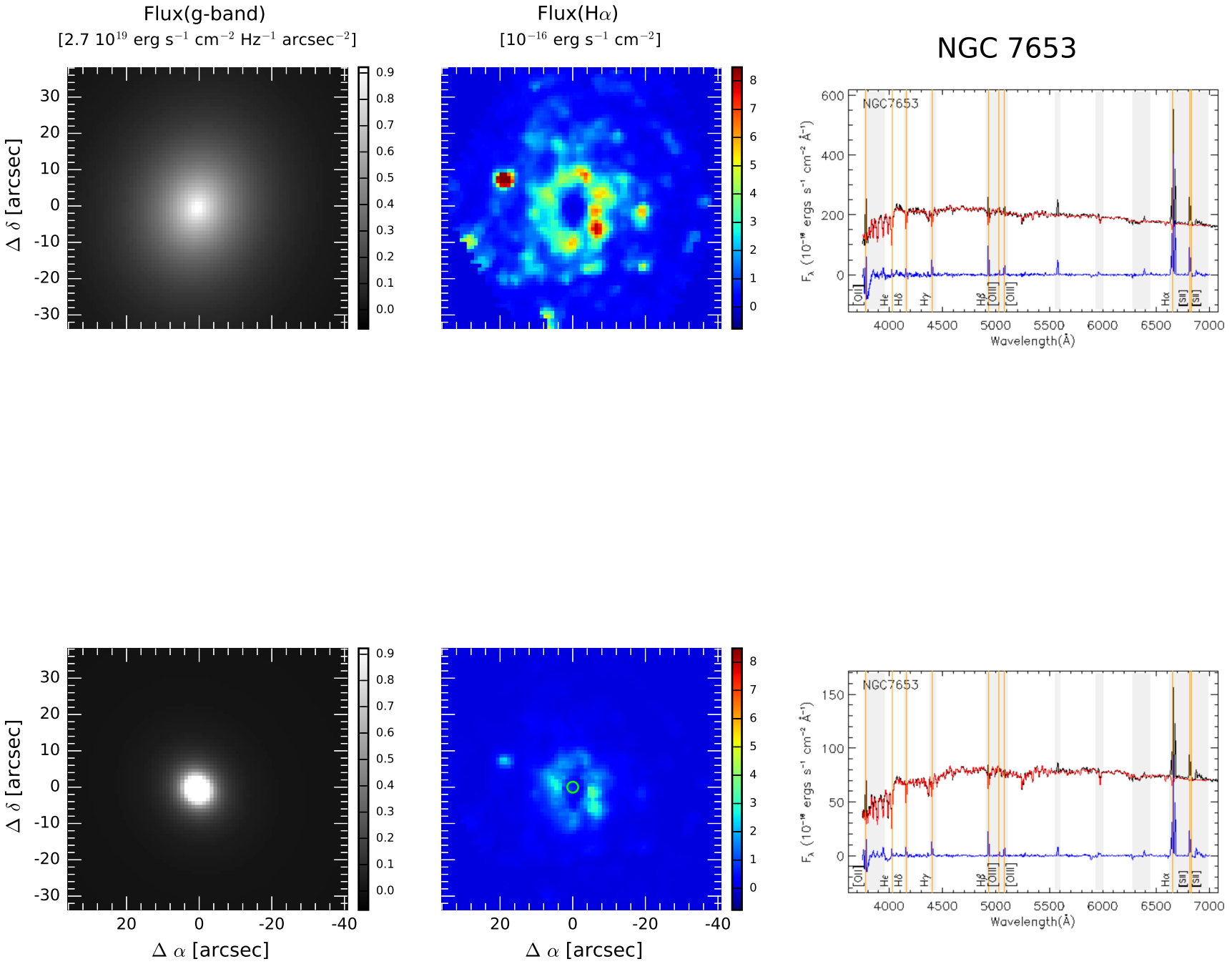
Flux(g-band)
[2.7 10^19 erg s^-1 cm^-2 Hz^-1 arcsec^-2]
Flux(Hα)
[10^-16 erg s^-1 cm^-2]
NGC 7653
Δ δ [arcsec]
Δ α [arcsec]
NGC7653
F_λ (10^-16 ergs s^-1 cm^-2 Å^-1)
Wavelength(Å)
[OII]
Hε
Hδ
Hγ
Hβ
[OIII]
[OIII]
Hα
[SII]
[SII]

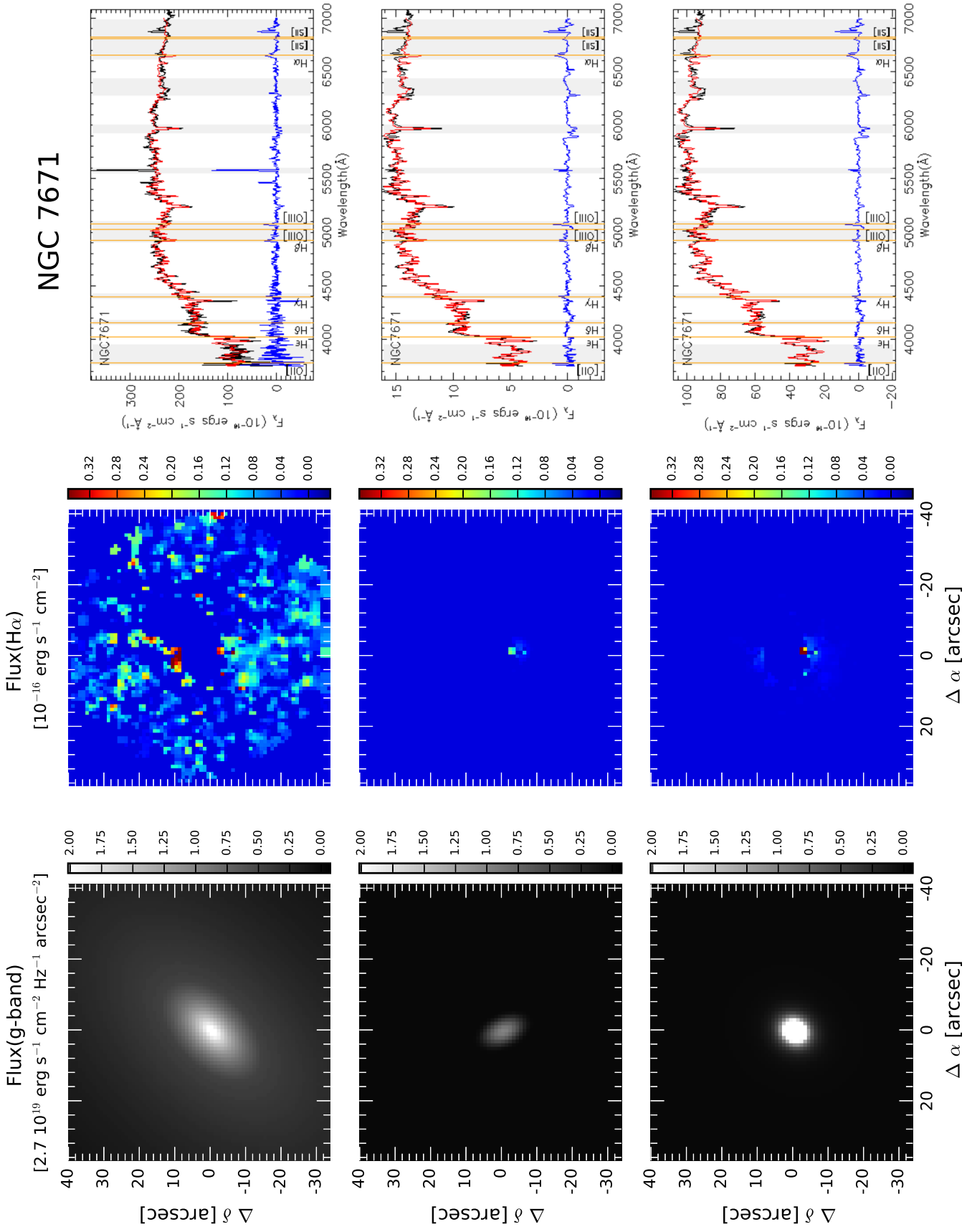
NGC 7671
Flux(g-band)
[2.7 10^19 erg s^-1 cm^-2 Hz^-1 arcsec^-2]
Flux(Hα)
[10^-16 erg s^-1 cm^-2]
Δ δ [arcsec]
Δ α [arcsec]
Wavelength(Å)
NGC7671
[OII]
Hε
Hδ
Hγ
[OIII]
Hβ
[OIII]
Hα
[SII]
[SII]

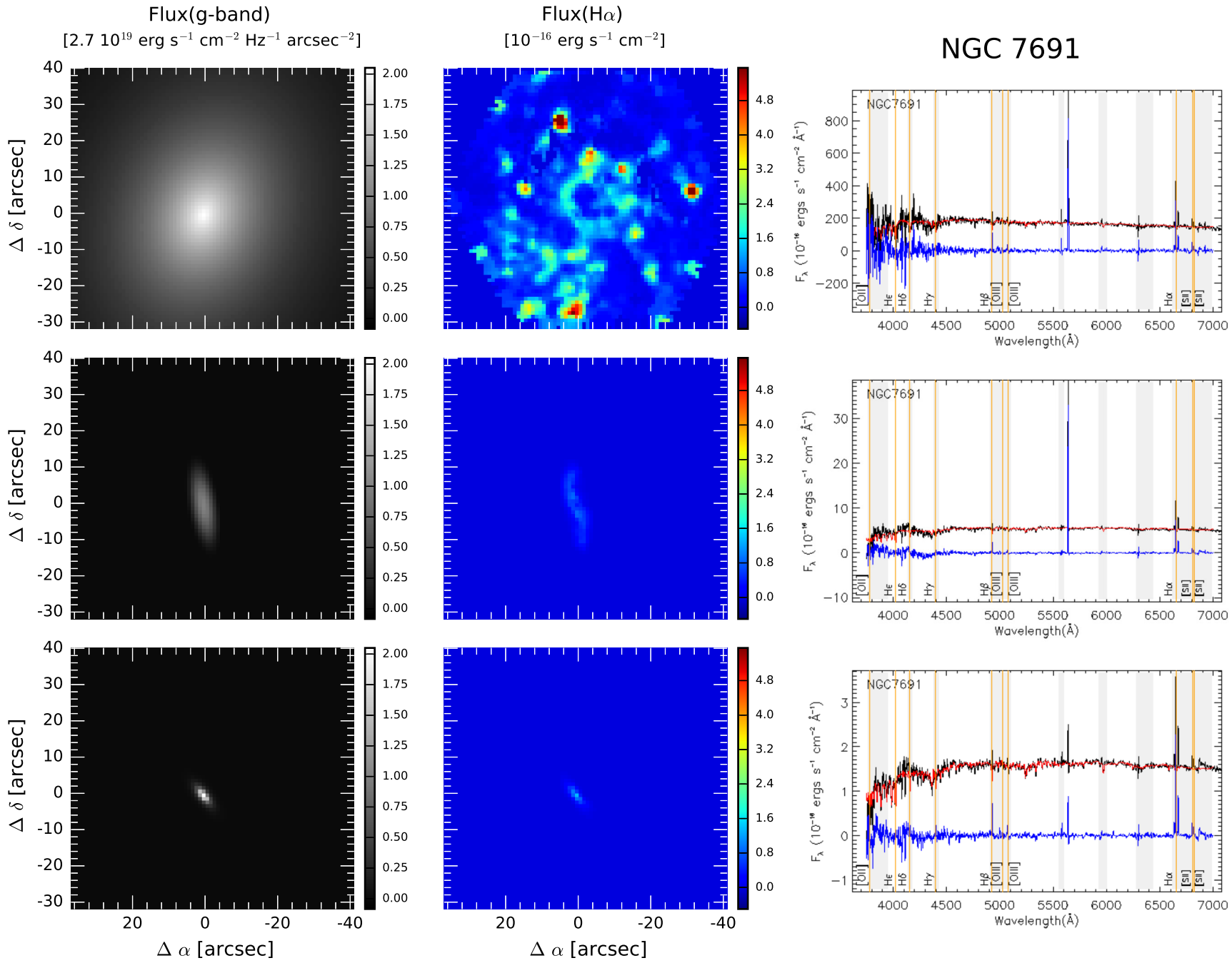
Flux(g-band)
[2.7 10^19 erg s^-1 cm^-2 Hz^-1 arcsec^-2]
Flux(Hα)
[10^-16 erg s^-1 cm^-2]
NGC 7691
Δ δ [arcsec]
Δ α [arcsec]
Wavelength(Å)
NGC7691
[OII]
Hε
Hδ
Hγ
Hβ
[OIII]
[OIII]
Hα
[SII]
[SII]

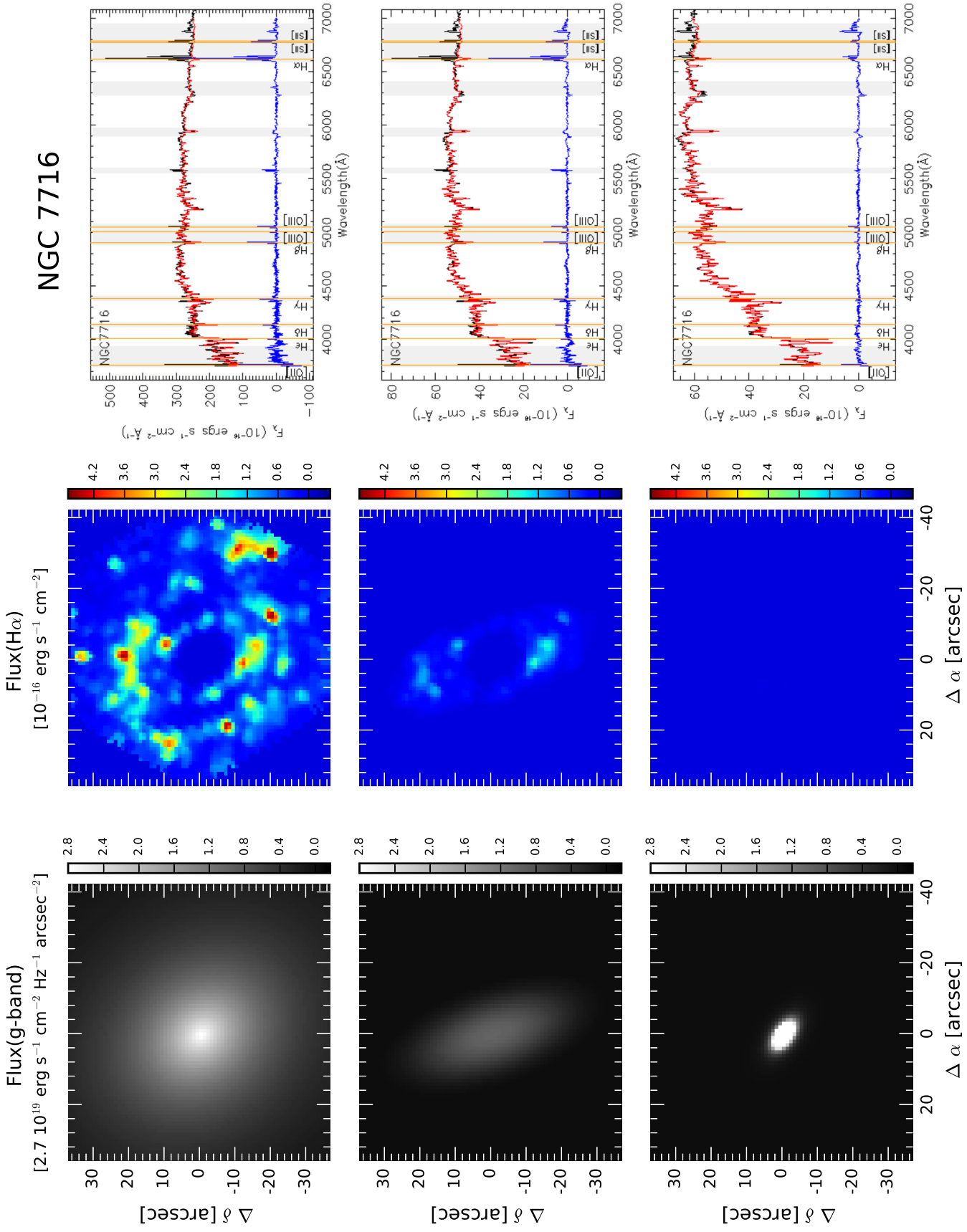
NGC 7716
Flux(g-band)
[2.7 10^19 erg s^-1 cm^-2 Hz^-1 arcsec^-2]
Flux(Hα)
[10^-16 erg s^-1 cm^-2]
Δ δ [arcsec]
Δ α [arcsec]
Wavelength(Å)
F_λ (10^-16 ergs s^-1 cm^-2 Å^-1)
NGC7716
[OII]
Hε
Hδ
Hγ
H8
[OIII]
[OIII]
[SII]
[SII]
Hα

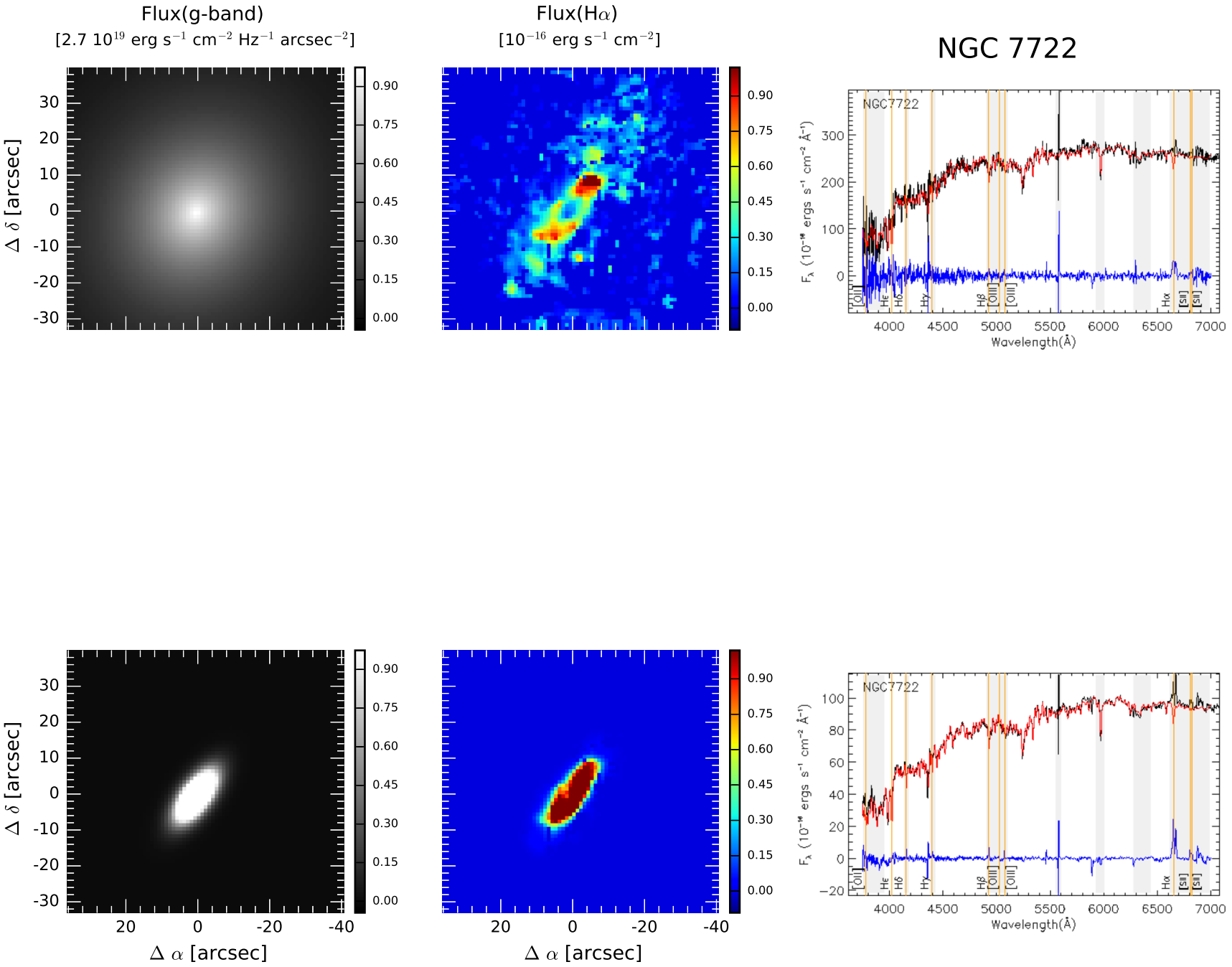
Flux(g-band)
[2.7 10^19 erg s^-1 cm^-2 Hz^-1 arcsec^-2]
Flux(Hα)
[10^-16 erg s^-1 cm^-2]
NGC 7722
Δ δ [arcsec]
Δ α [arcsec]
Wavelength(Å)
NGC7722
[OII]
Hε
Hδ
Hγ
Hβ
[OIII]
[OIII]
Hα
[SII]
[SII]

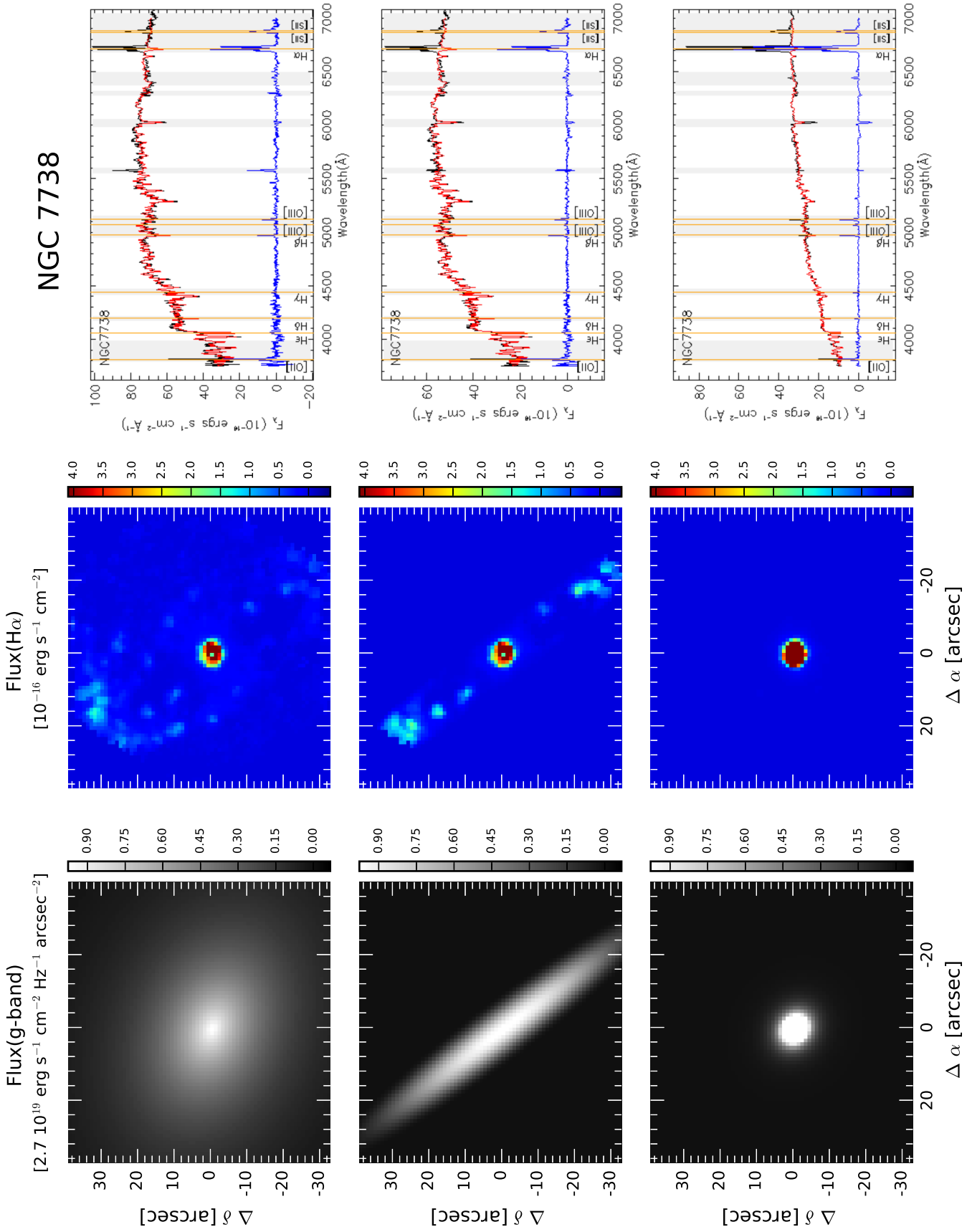
NGC 7738
Flux(g-band)
[2.7 10^19 erg s^-1 cm^-2 Hz^-1 arcsec^-2]
Flux(Hα)
[10^-16 erg s^-1 cm^-2]
Δ δ [arcsec]
Δ α [arcsec]
Wavelength(Å)
F_λ (10^-16 ergs s^-1 cm^-2 Å^-1)
NGC7738
[OII]
Hε
Hδ
Hγ
Hβ
[OIII]
[OIII]
[SII]
[SII]
Hα

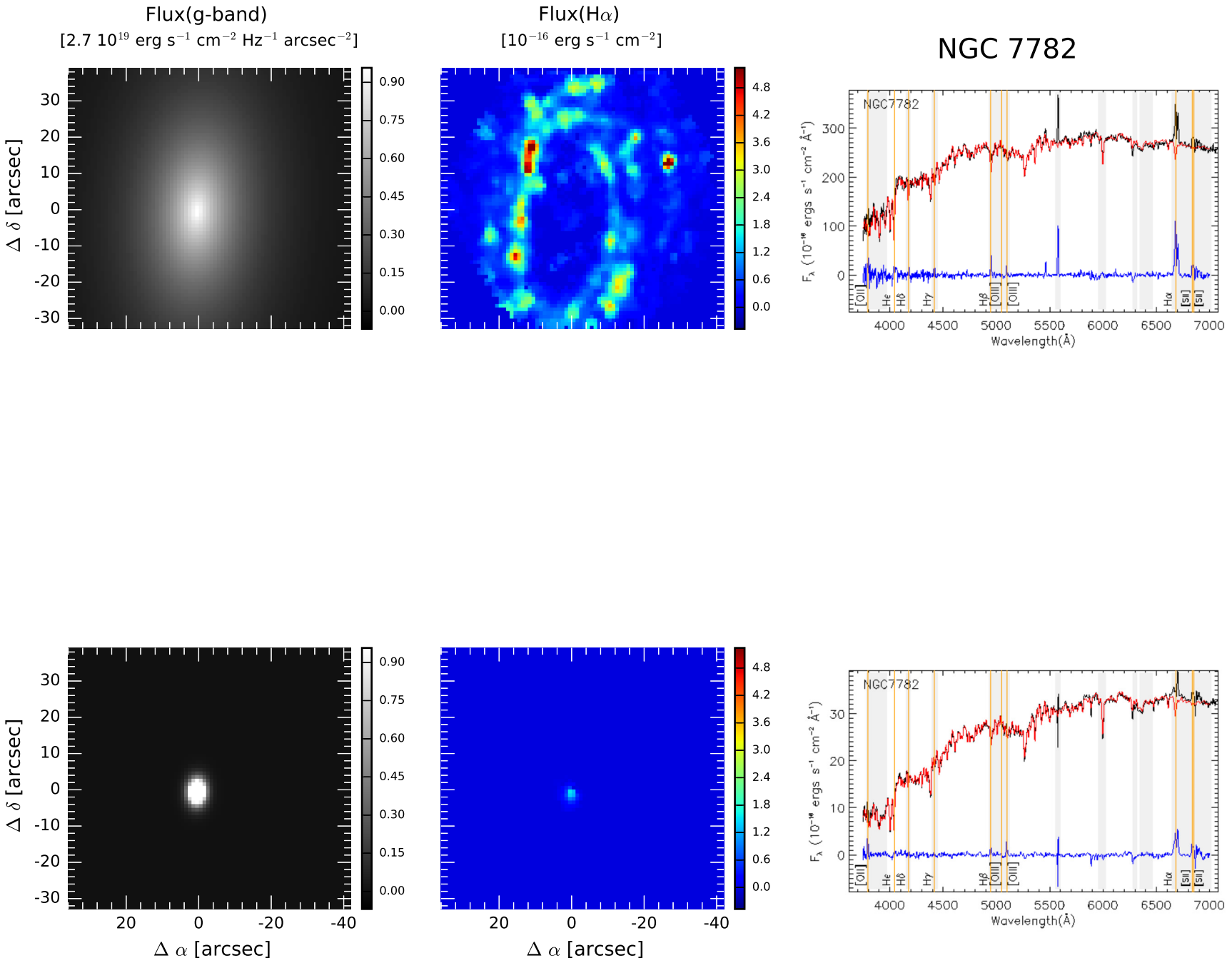
Flux(g-band)
[2.7 10^19 erg s^-1 cm^-2 Hz^-1 arcsec^-2]
Flux(Hα)
[10^-16 erg s^-1 cm^-2]
NGC 7782
Δ δ [arcsec]
Δ α [arcsec]
NGC7782
Wavelength(Å)
[OII]
Heε
Hδ
Hγ
Hβ
[OIII]
[OIII]
Hα
[SII]
[SII]

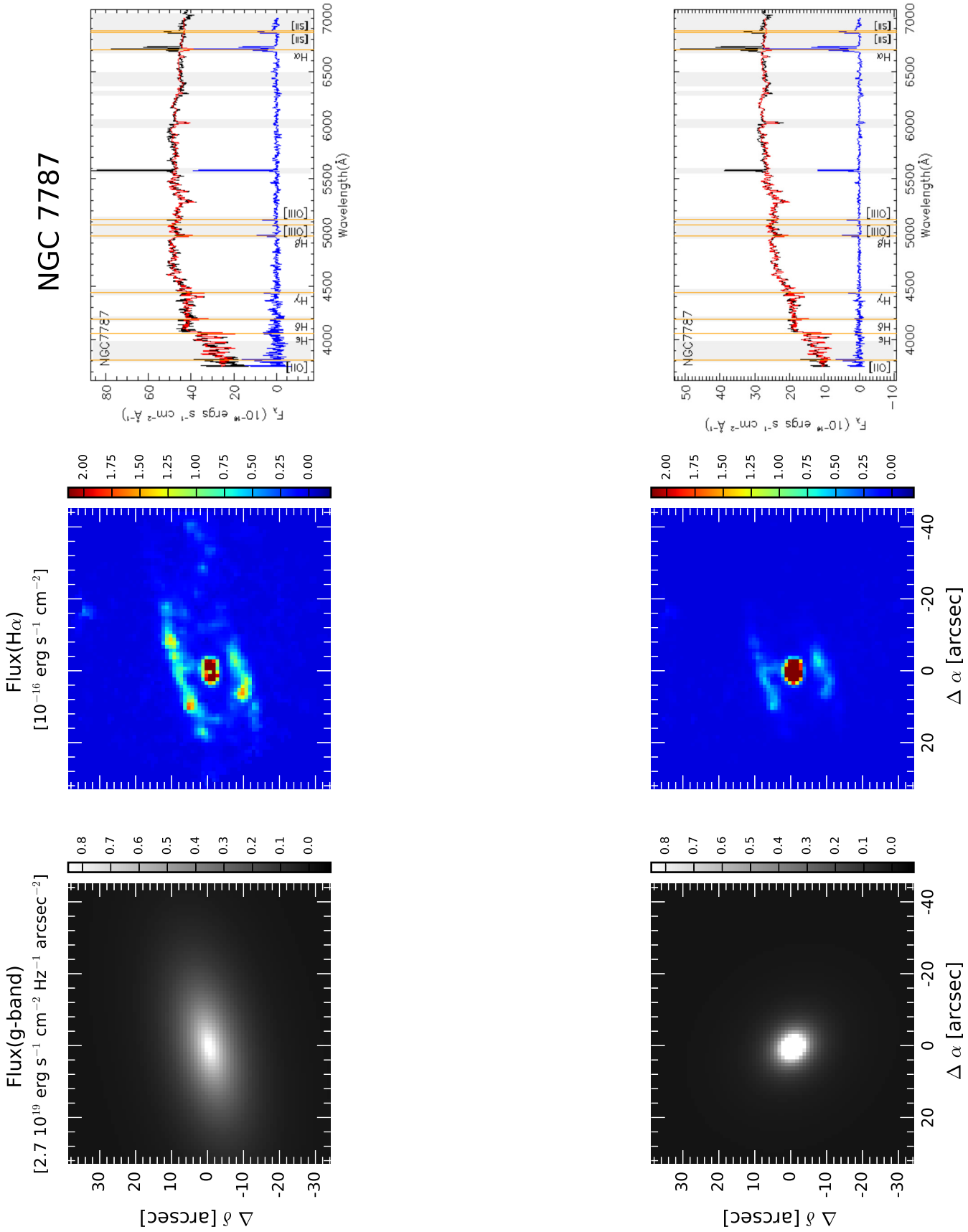
NGC 7787
Flux(g-band)
[2.7 10^19 erg s^-1 cm^-2 Hz^-1 arcsec^-2]
Flux(Hα)
[10^-16 erg s^-1 cm^-2]
Δ δ [arcsec]
Δ α [arcsec]
F_λ (10^-16 ergs s^-1 cm^-2 Å^-1)
Wavelength(Å)
NGC7787
[OII]
Hε
Hδ
Hγ
Hβ
[OIII]
[OIII]
Hα
[SII]
[SII]

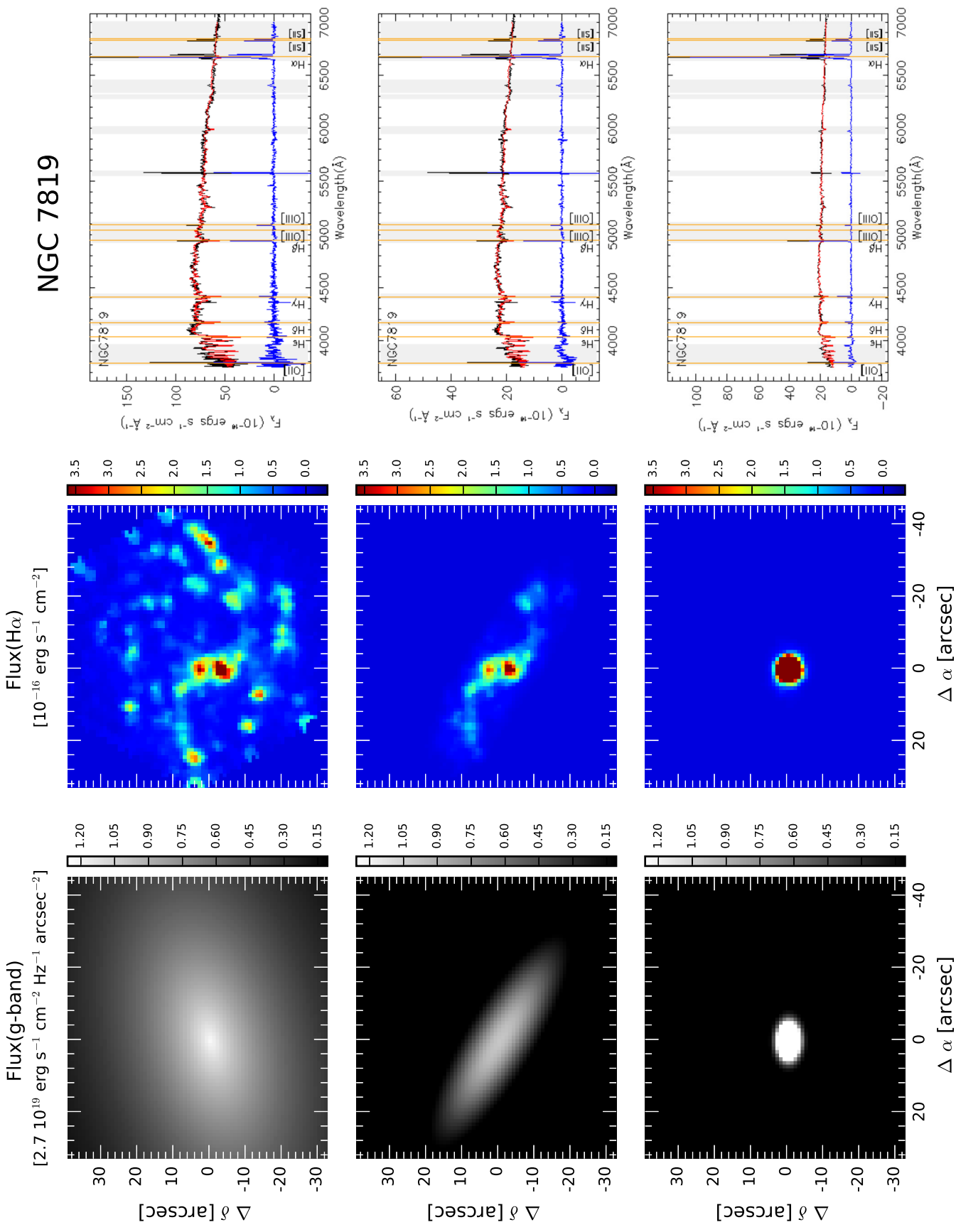
NGC 7819
Flux(g-band)
[2.7 10^19 erg s^-1 cm^-2 Hz^-1 arcsec^-2]
Flux(Hα)
[10^-16 erg s^-1 cm^-2]
Δ δ [arcsec]
Δ α [arcsec]
Wavelength(Å)
F_λ (10^-16 ergs s^-1 cm^-2 Å^-1)
NGC7819
[OII]
Hε
Hδ
Hγ
Hβ
[OIII]
[OIII]
Hα
[SII]
[SII]

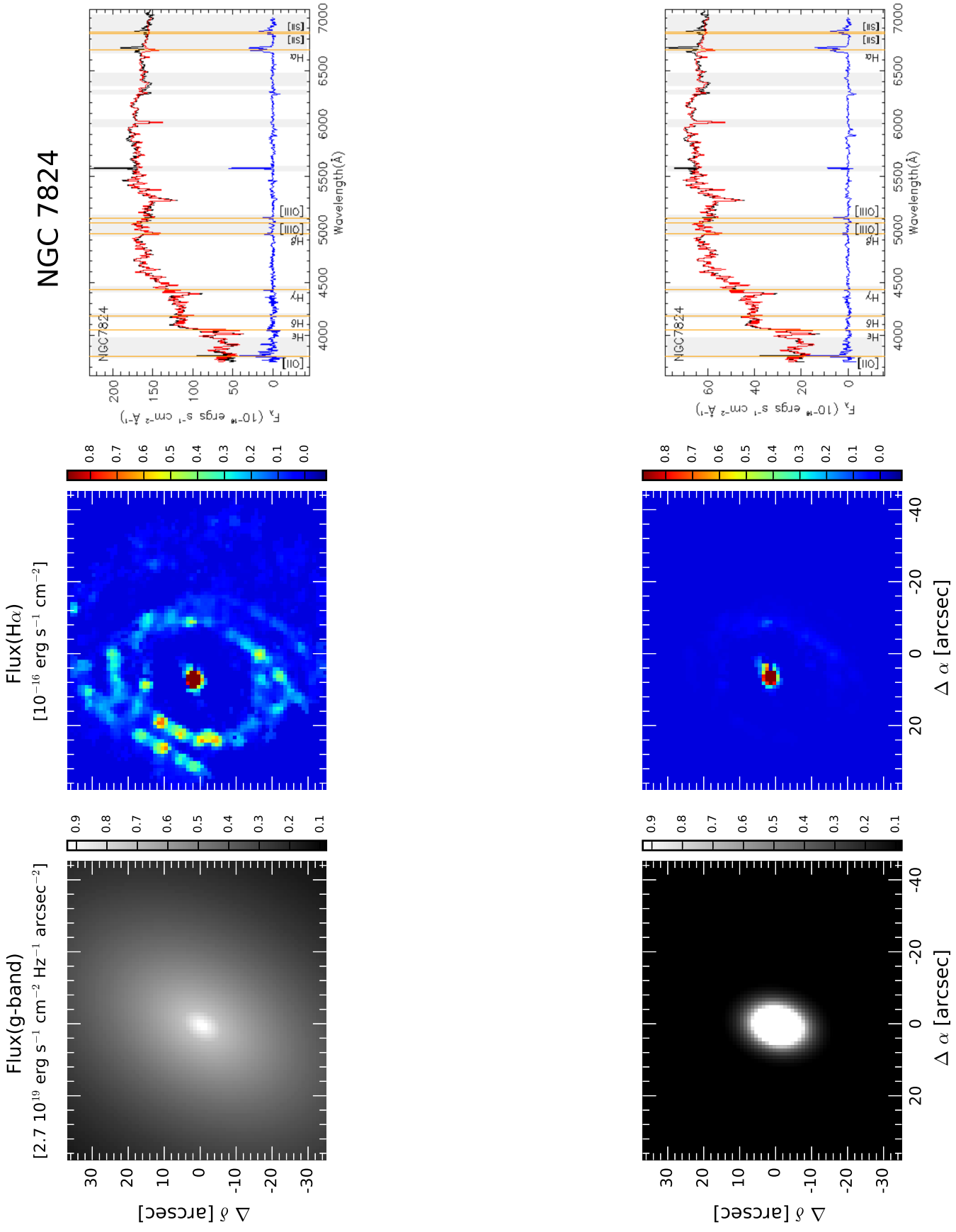
NGC 7824
Flux(Hα)
[10^-16 erg s^-1 cm^-2]
Flux(g-band)
[2.7 10^19 erg s^-1 cm^-2 Hz^-1 arcsec^-2]
Δ δ [arcsec]
Δ α [arcsec]
Wavelength(Å)
NGC7824
[OII]
Hε
Hδ
Hγ
Hβ
[OIII]
[OIII]
[SII]
[SII]
Hα

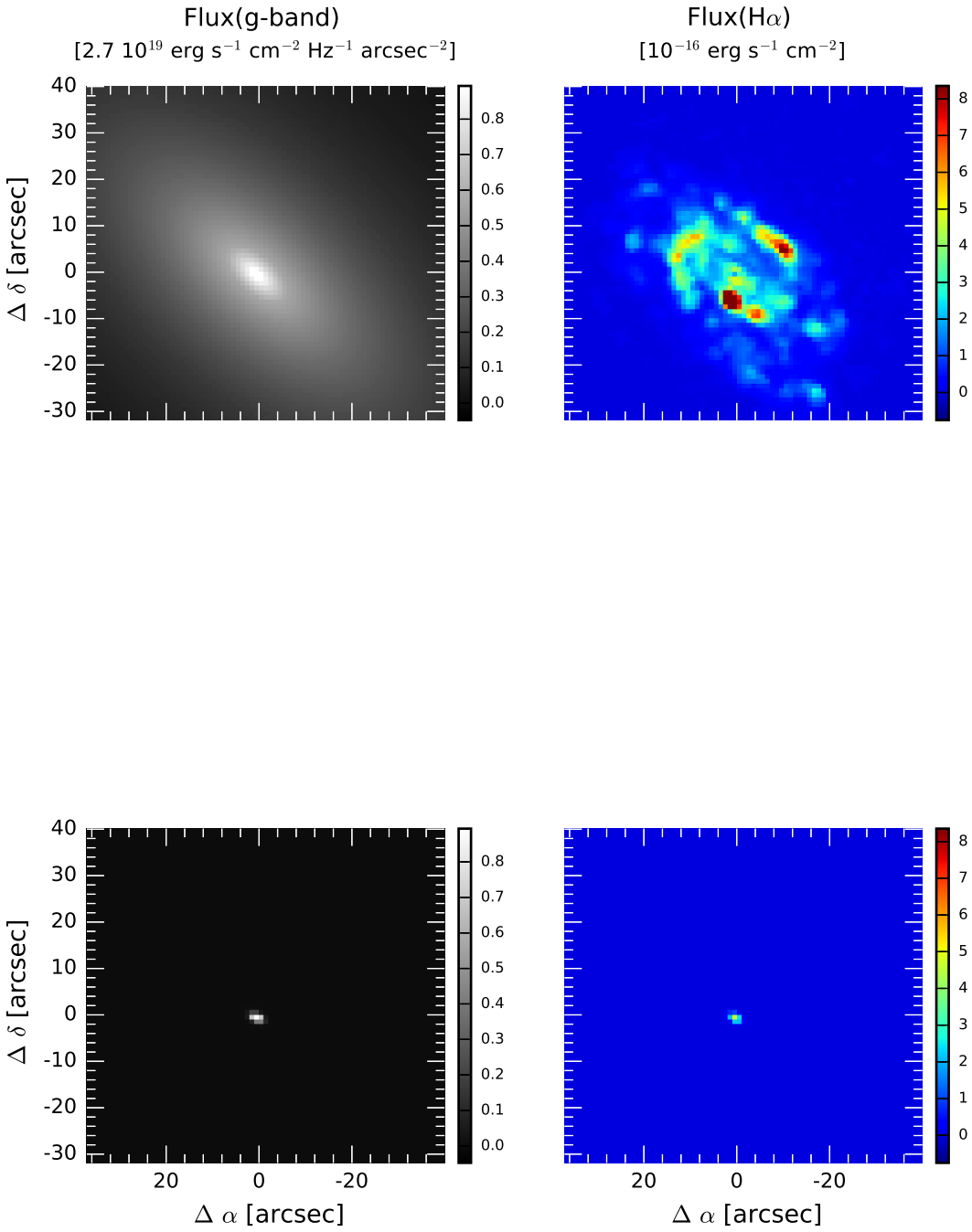
Flux(g-band)
[2.7 10^19 erg s^-1 cm^-2 Hz^-1 arcsec^-2]
Flux(Hα)
[10^-16 erg s^-1 cm^-2]
Δ δ [arcsec]
Δ α [arcsec]

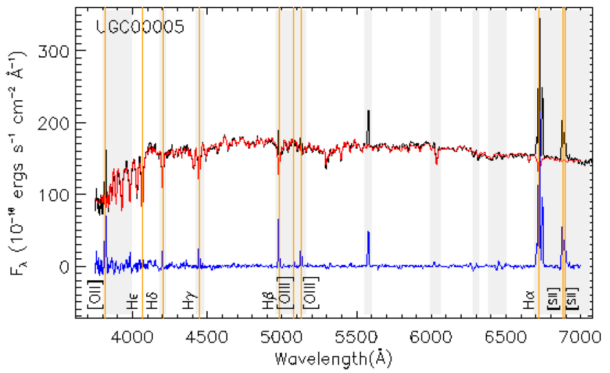
UGC 00005
UGC00005
Wavelength(Å)
[OII]
Hε
Hδ
Hγ
Hβ
[OIII]
[OIII]
Hα
[SII]
[SII]

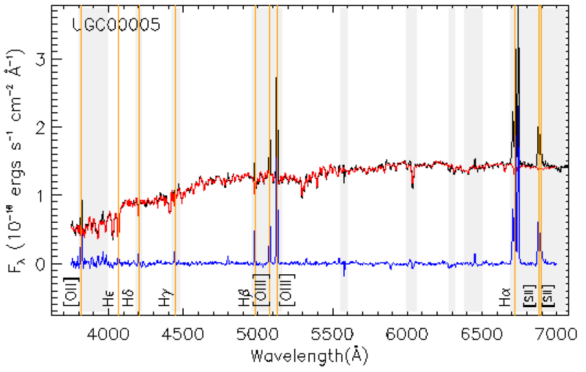
UGC00005
Wavelength(Å)

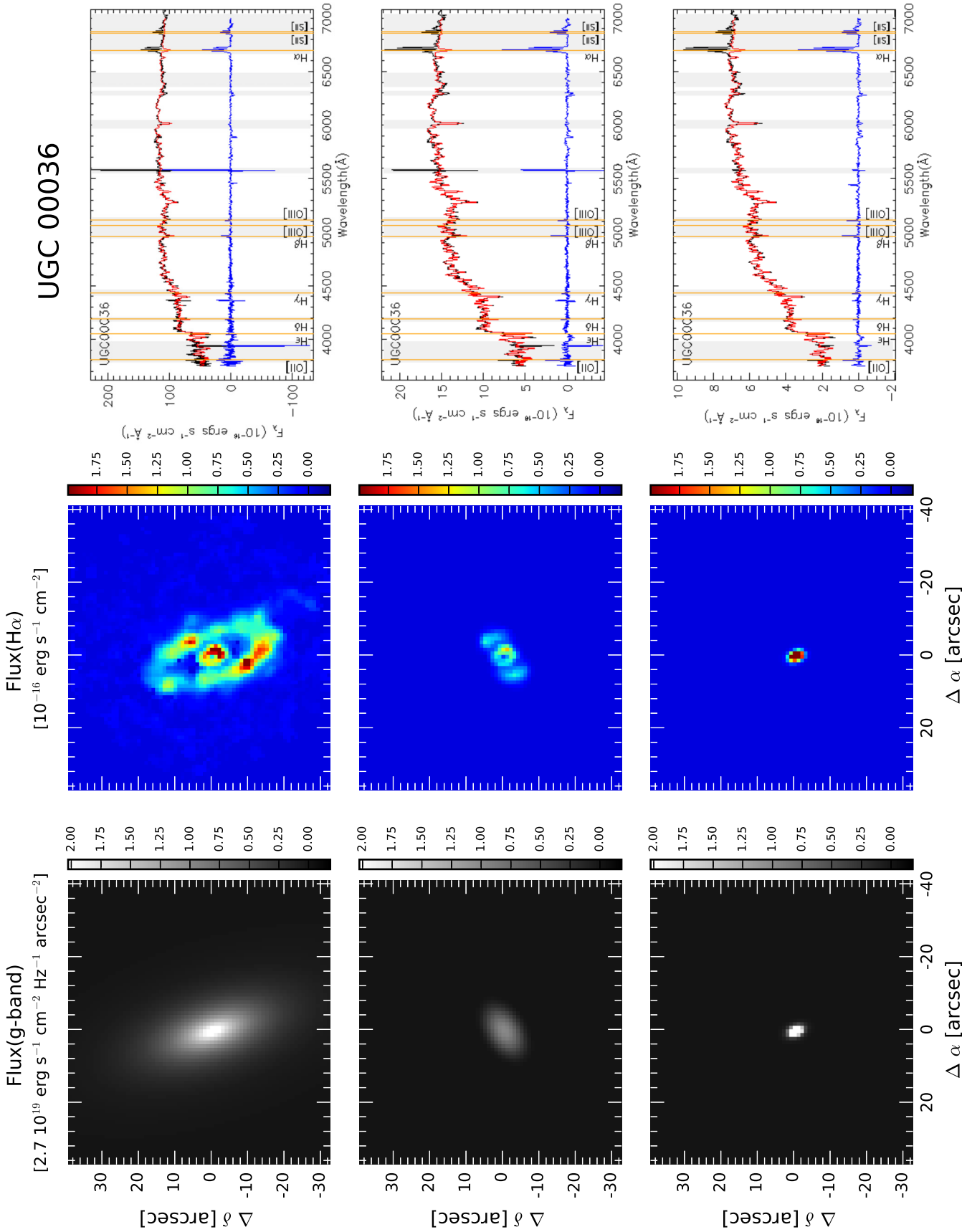
UGC 00036
Flux(g-band)
[2.7 10^19 erg s^-1 cm^-2 Hz^-1 arcsec^-2]
Flux(Hα)
[10^-16 erg s^-1 cm^-2]
Δ δ [arcsec]
Δ α [arcsec]
Wavelength(Å)
F_λ (10^-16 ergs s^-1 cm^-2 Å^-1)
UGC00036
[OII]
HE
Hδ
Hγ
Hβ
[OIII]
[OIII]
[SII]
[SII]
Hα

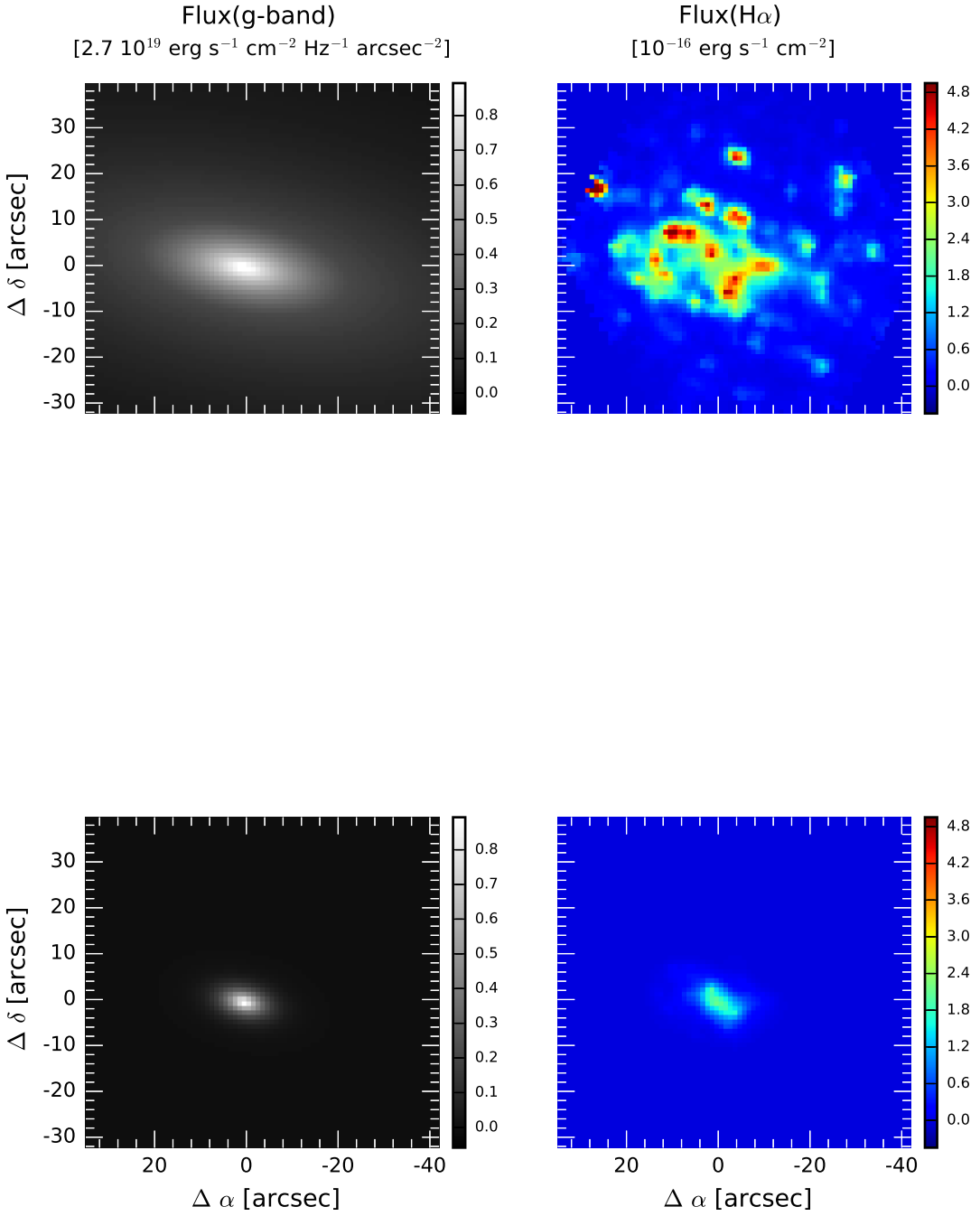
Flux(g-band)
[2.7 10^19 erg s^-1 cm^-2 Hz^-1 arcsec^-2]
Flux(Hα)
[10^-16 erg s^-1 cm^-2]
UGC 00139
Δ δ [arcsec]
Δ α [arcsec]
Wavelength(Å)
UGC00139
[OII]
Hε
Hδ
Hγ
Hβ
[OIII]
[OIII]
Hα
[SII]
[SII]

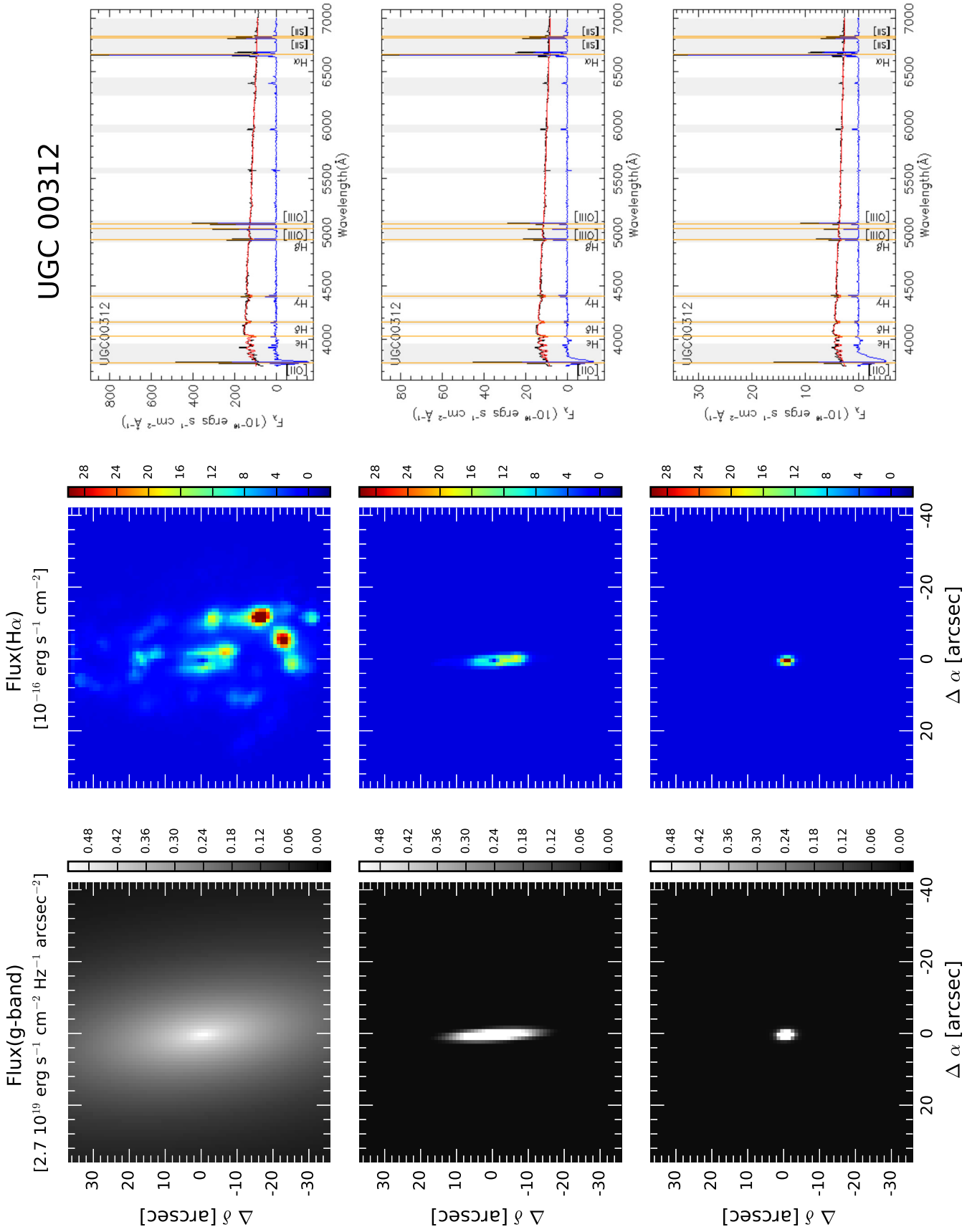
UGC 00312
Flux(g-band)
[2.7 10^19 erg s^-1 cm^-2 Hz^-1 arcsec^-2]
Flux(Hα)
[10^-16 erg s^-1 cm^-2]
Δ δ [arcsec]
Δ α [arcsec]
Wavelength(Å)
UGC00312
[OII]
Hε
Hδ
Hγ
Hβ
[OIII]
[OIII]
Hα
[SII]
[SII]

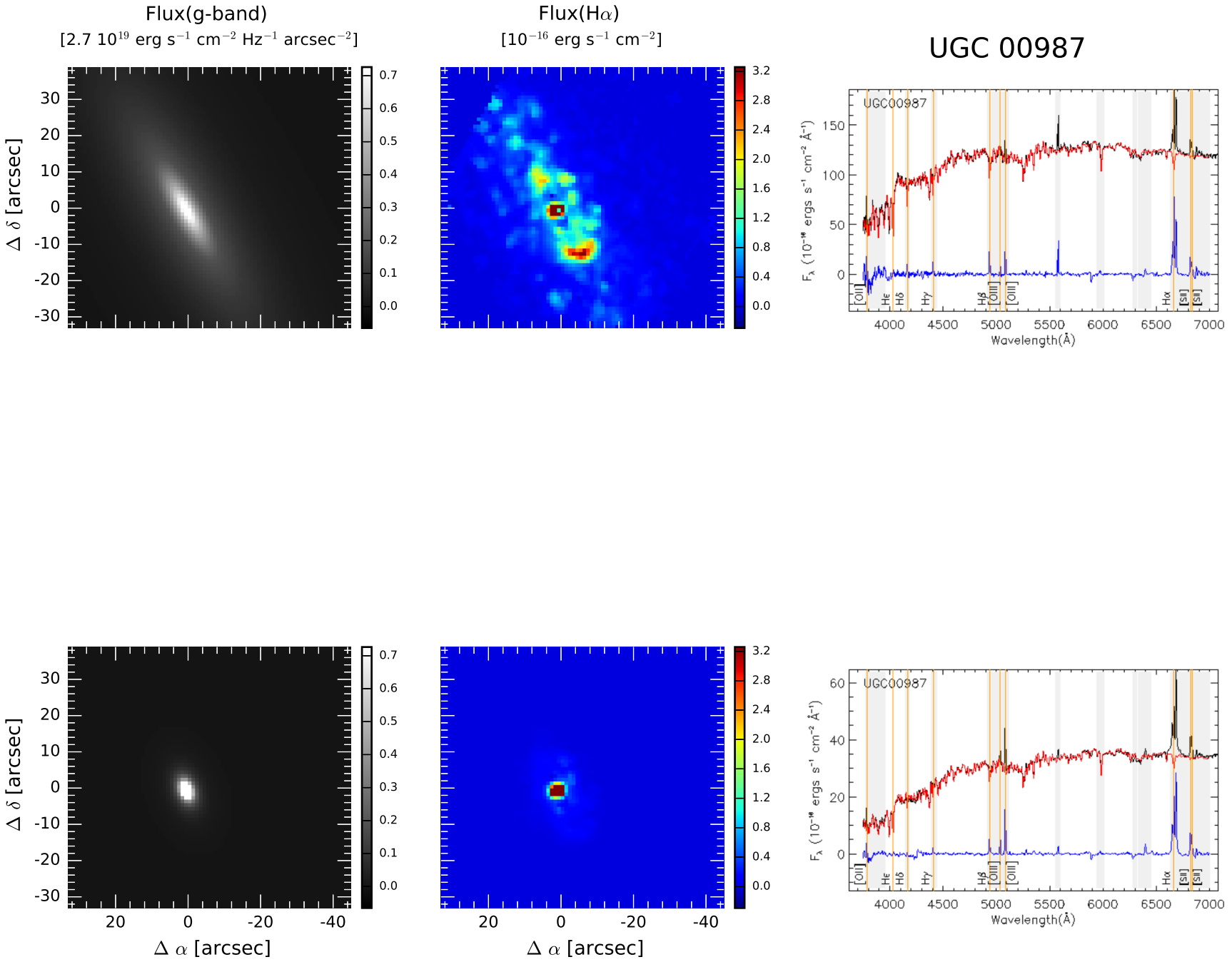
Flux(g-band)
[2.7 10^19 erg s^-1 cm^-2 Hz^-1 arcsec^-2]
Flux(Hα)
[10^-16 erg s^-1 cm^-2]
UGC 00987
Δ δ [arcsec]
Δ α [arcsec]
UGC00987
F_λ (10^-18 ergs s^-1 cm^-2 Å^-1)
Wavelength(Å)
[OII]
Hε
Hδ
Hγ
Hβ
[OIII]
[OIII]
Hα
[SII]
[SII]

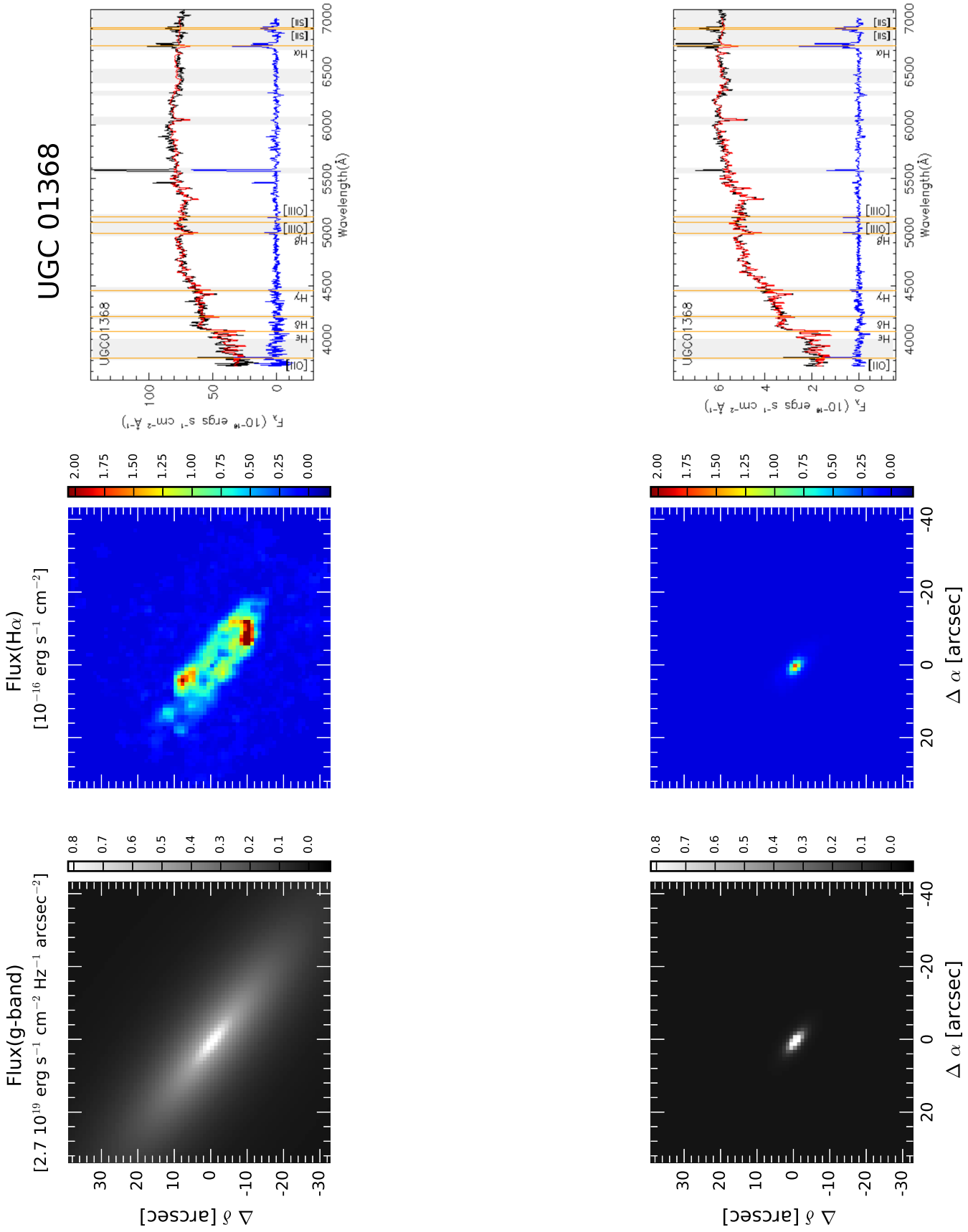
UGC 01368
Flux(g-band)
[2.7 10^19 erg s^-1 cm^-2 Hz^-1 arcsec^-2]
Flux(Hα)
[10^-16 erg s^-1 cm^-2]
Δ δ [arcsec]
Δ α [arcsec]
F_λ (10^-16 ergs s^-1 cm^-2 Å^-1)
Wavelength(Å)
UGC01368
[OII]
Hε
Hδ
Hγ
Hβ
[OIII]
[OIII]
Hα
[SII]
[SII]

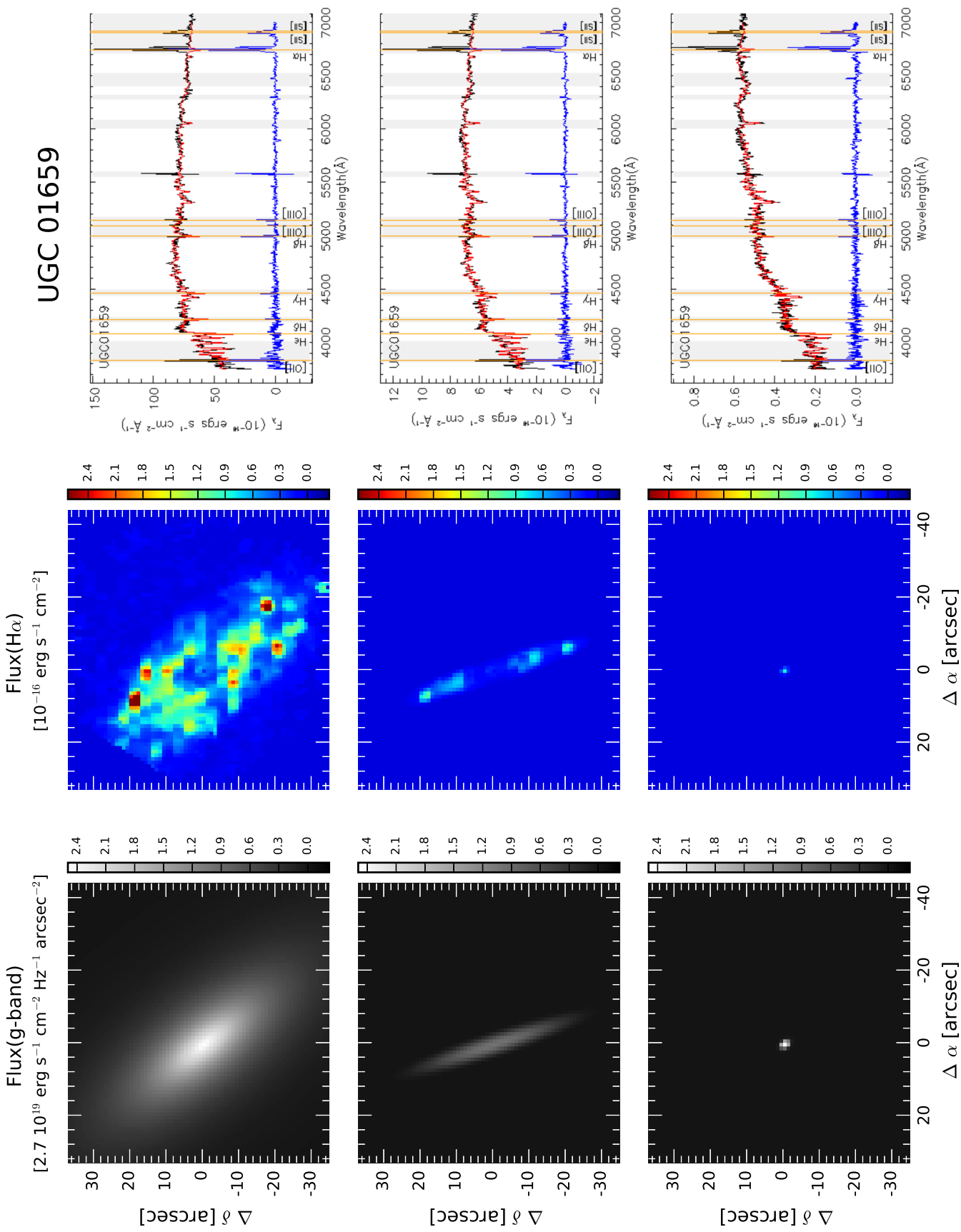
UGC 01659
Flux(g-band)
[2.7 10^19 erg s^-1 cm^-2 Hz^-1 arcsec^-2]
Flux(Hα)
[10^-16 erg s^-1 cm^-2]
Δ δ [arcsec]
Δ α [arcsec]
Wavelength(Å)
UGC01659
[OII]
Hε
Hδ
Hγ
Hβ
[OIII]
[OIII]
[SII]
[SII]
Hα

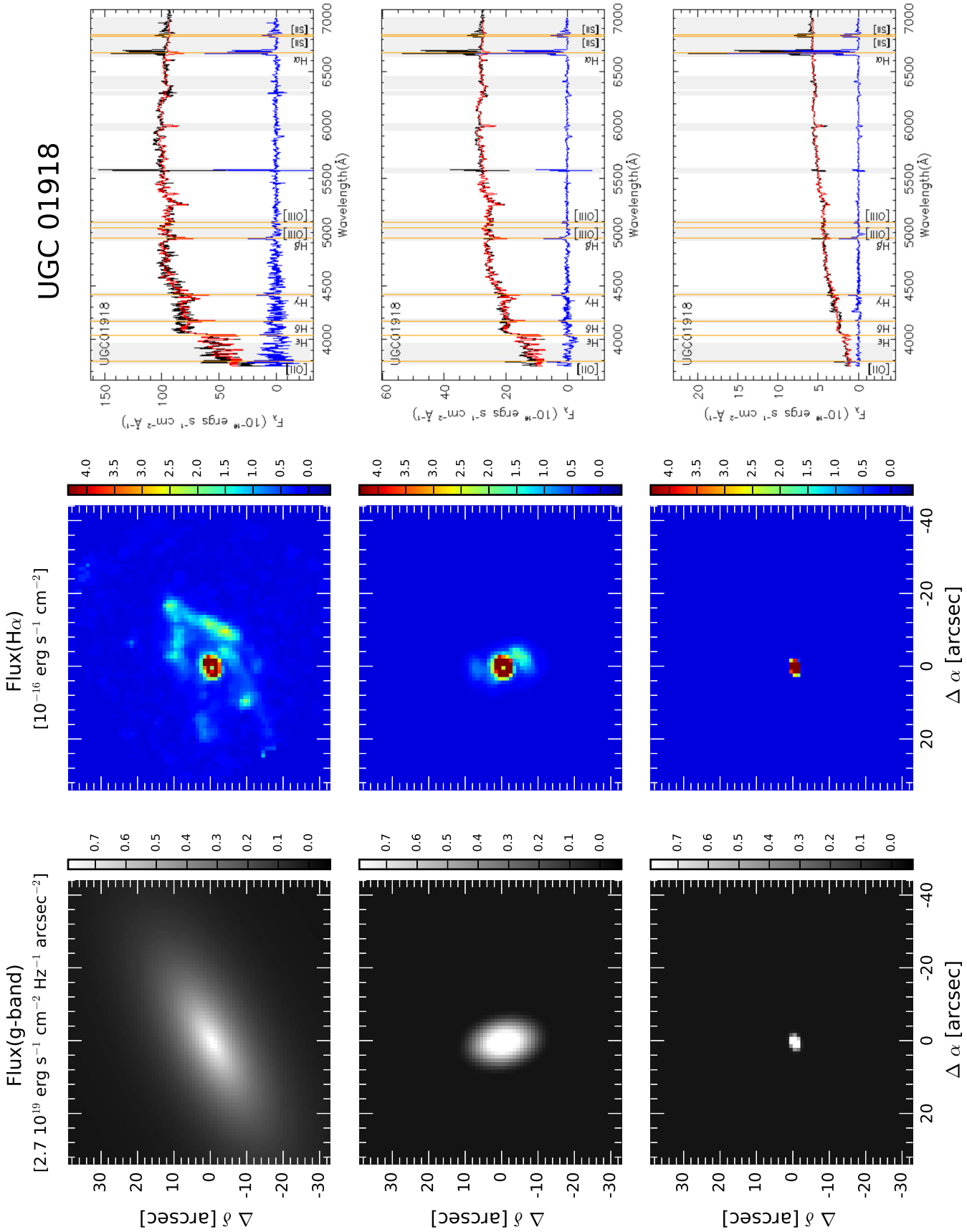
UGC 01918
Flux(g-band)
[2.7 10^19 erg s^-1 cm^-2 Hz^-1 arcsec^-2]
Flux(Hα)
[10^-16 erg s^-1 cm^-2]
Δ δ [arcsec]
Δ α [arcsec]
Wavelength(Å)
UGC01918
[OII]
Hε
Hδ
Hγ
Hβ
[OIII]
[OIII]
Hα
[SII]
[SII]

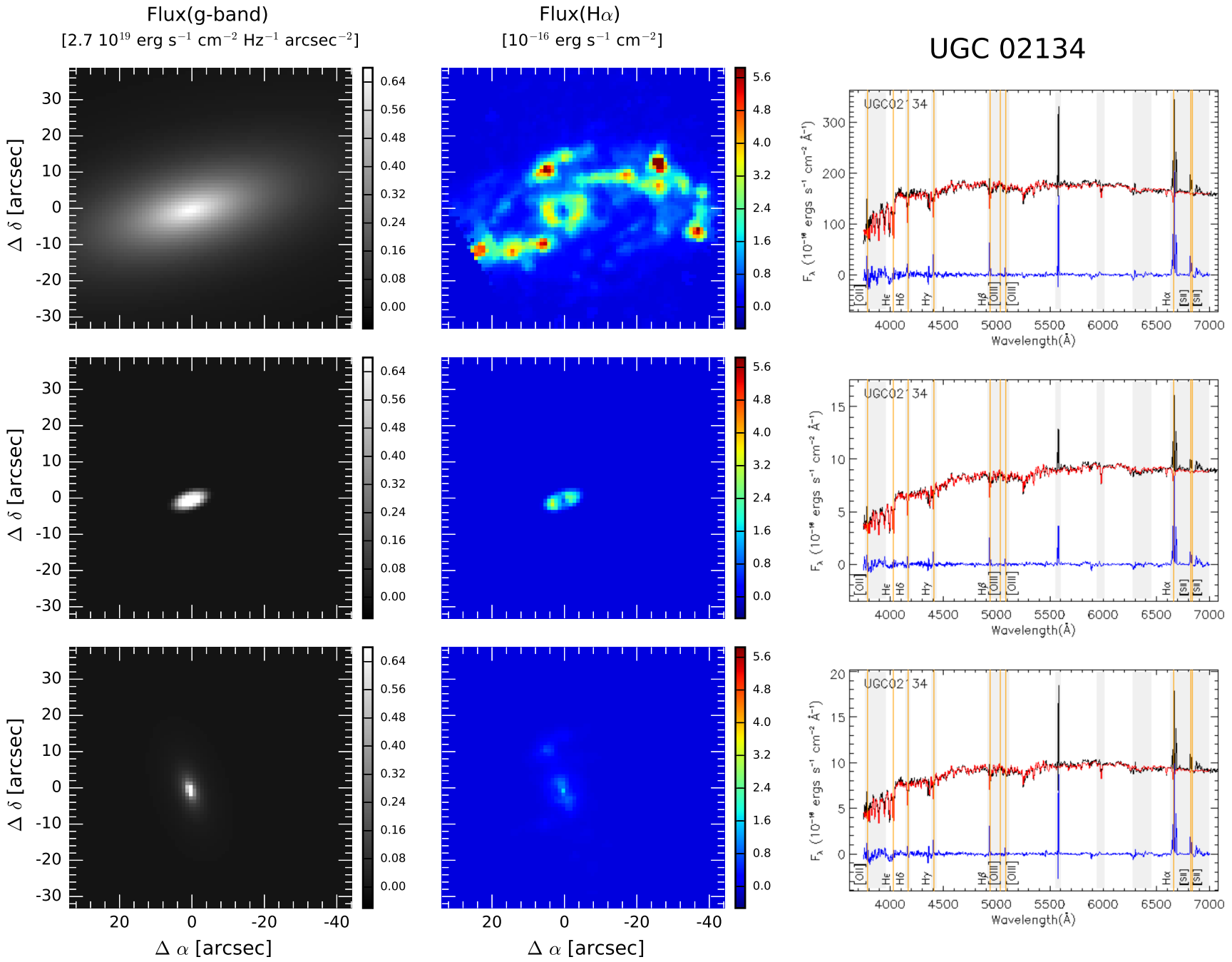
Flux(g-band)
[2.7 10^19 erg s^-1 cm^-2 Hz^-1 arcsec^-2]
Flux(Hα)
[10^-16 erg s^-1 cm^-2]
UGC 02134
Δ δ [arcsec]
Δ α [arcsec]
Wavelength(Å)
UGC02 34
[OII]
Hε
Hδ
Hγ
Hβ
[OIII]
[OIII]
Hα
[SII]
[SII]

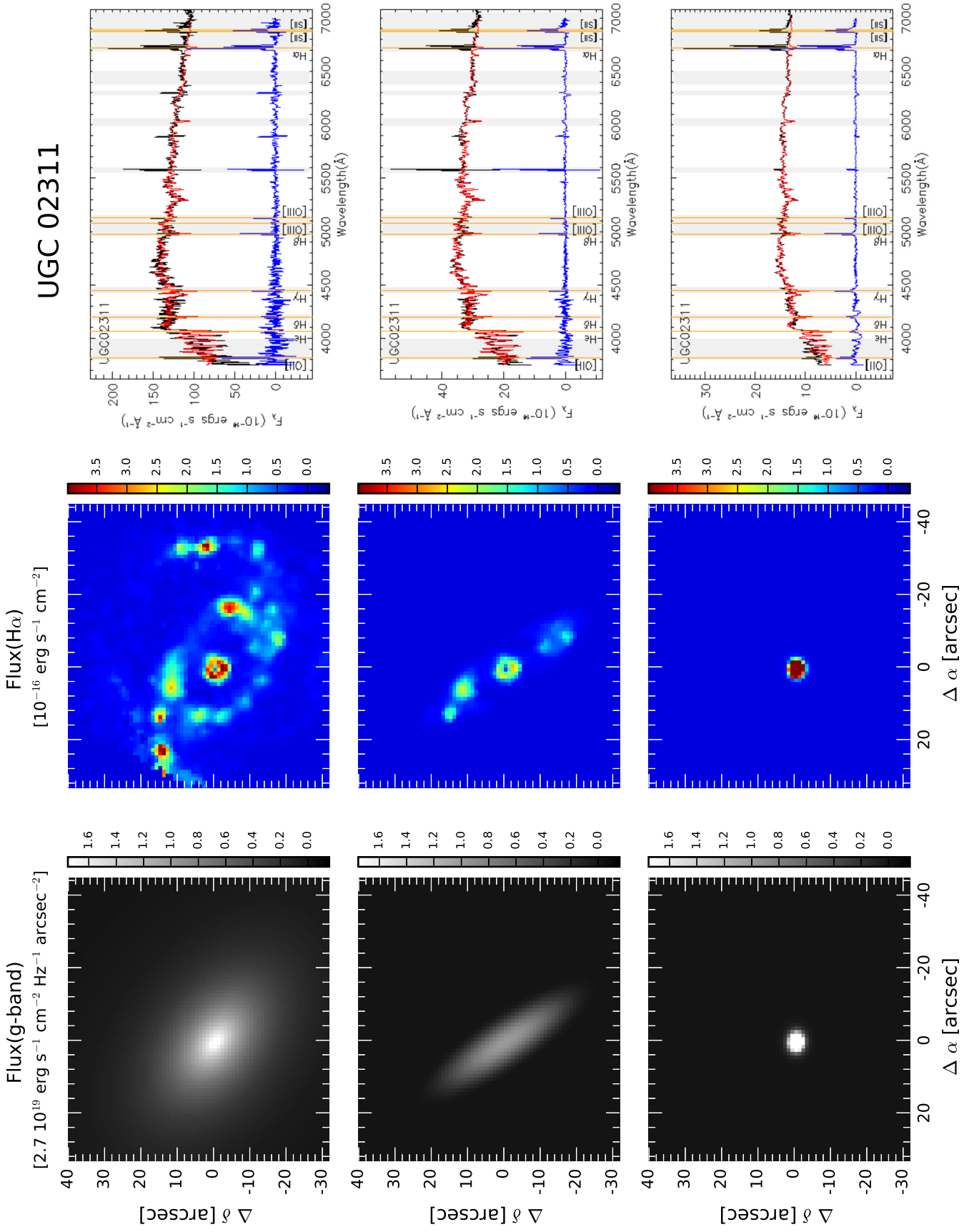
UGC 02311
Flux(g-band)
[2.7 10^19 erg s^-1 cm^-2 Hz^-1 arcsec^-2]
Flux(Hα)
[10^-16 erg s^-1 cm^-2]
Δ δ [arcsec]
Δ α [arcsec]
Wavelength(Å)
F_λ (10^-16 ergs s^-1 cm^-2 Å^-1)
[OII]
Hε
Hδ
Hγ
Hβ
[OIII]
[OIII]
[SII]
[SII]
Hα

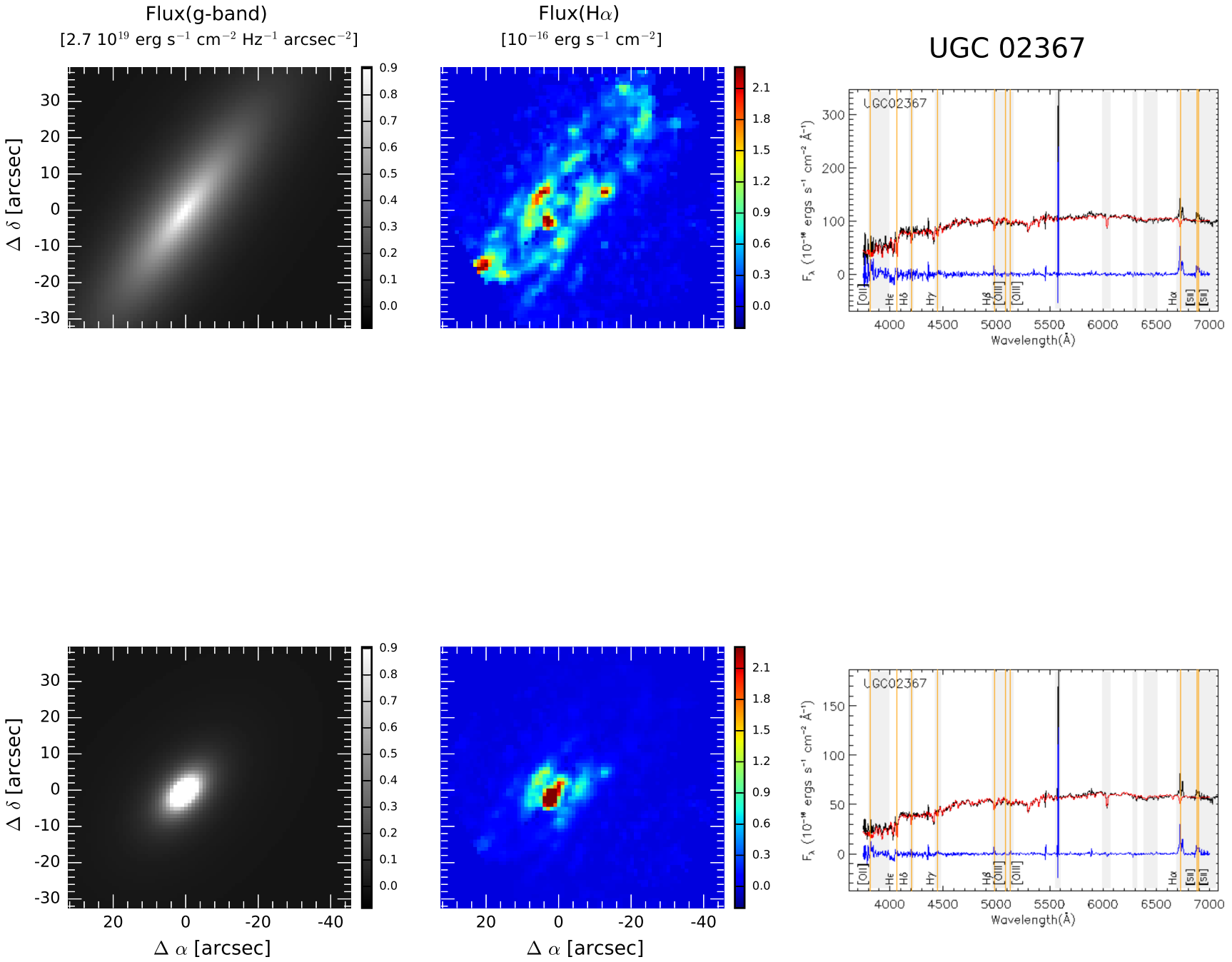
Flux(g-band)
[2.7 10^19 erg s^-1 cm^-2 Hz^-1 arcsec^-2]
Flux(Hα)
[10^-16 erg s^-1 cm^-2]
UGC 02367
Δ δ [arcsec]
Δ α [arcsec]
UGC02367
F_λ (10^-16 ergs s^-1 cm^-2 Å^-1)
Wavelength(Å)
[OII]
Hε
Hδ
Hγ
Hβ
[OIII]
[OIII]
Hα
[SII]
[SII]

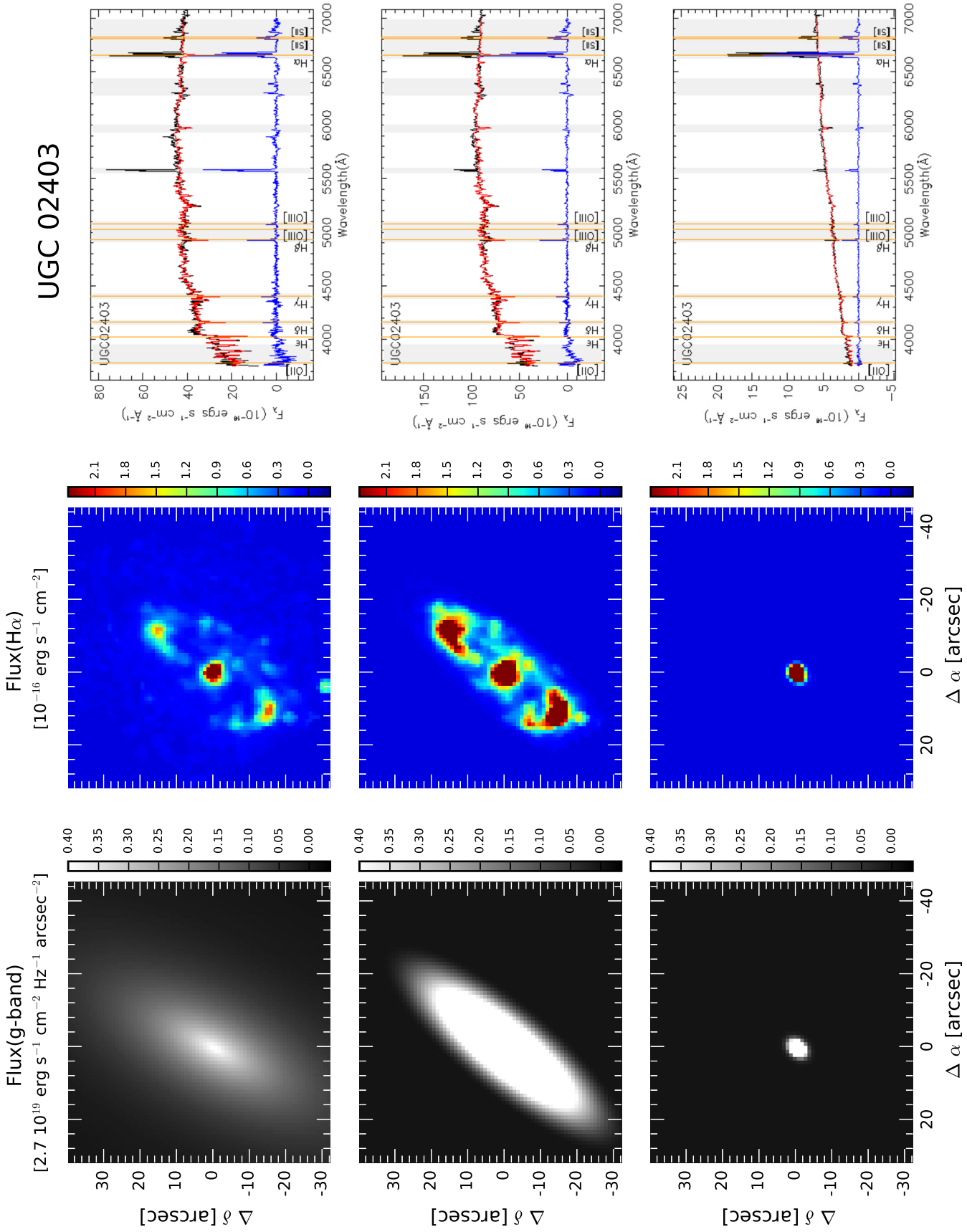
UGC 02403
Flux(g-band)
[2.7 10^19 erg s^-1 cm^-2 Hz^-1 arcsec^-2]
Flux(Hα)
[10^-16 erg s^-1 cm^-2]
Δ δ [arcsec]
Δ α [arcsec]
Wavelength(Å)
F_λ (10^-16 ergs s^-1 cm^-2 Å^-1)
UGC02403
[OII]
Hε
Hδ
Hγ
[OIII]
Hβ
[OIII]
[SII]
[SII]
Hα

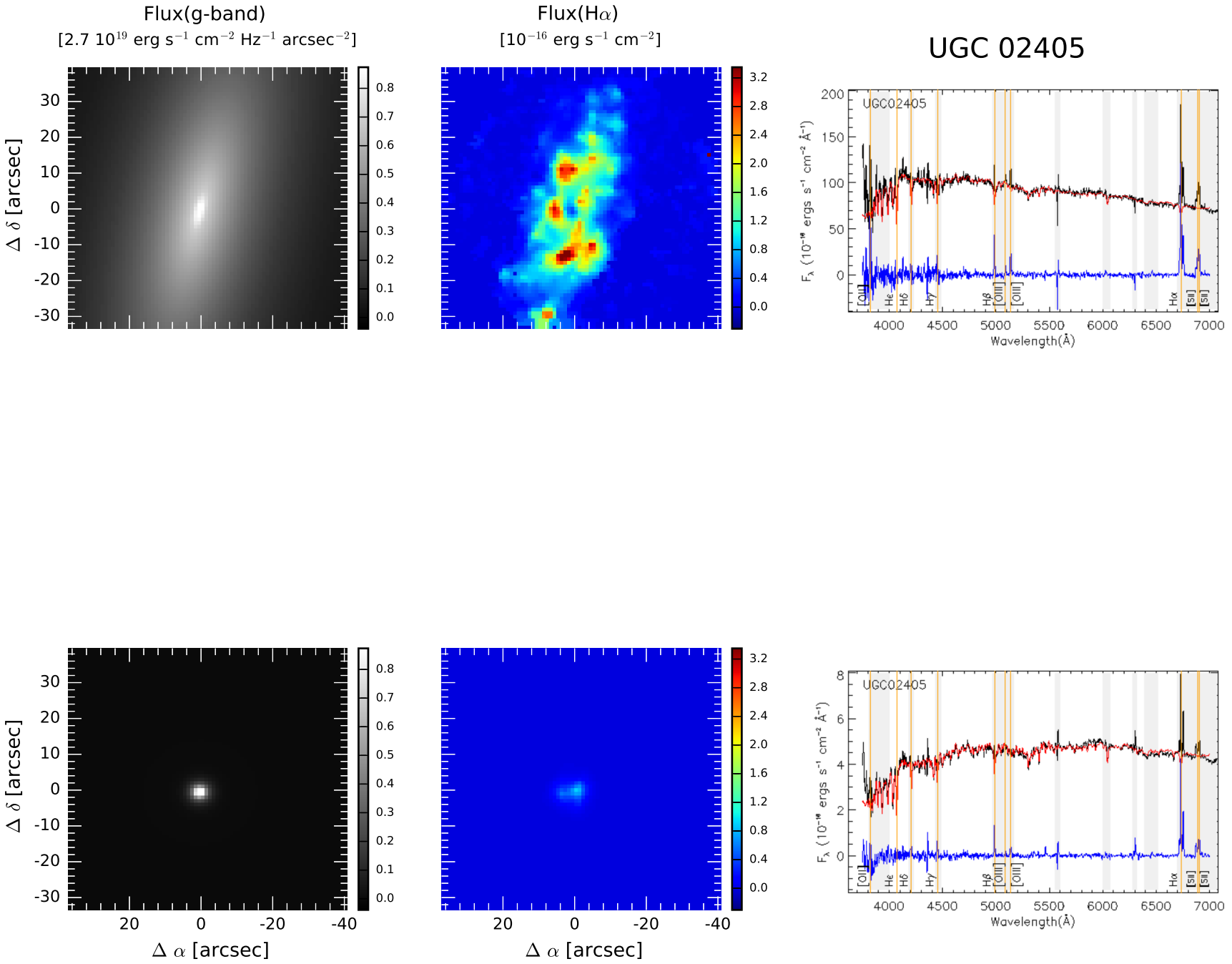
Flux(g-band)
[2.7 10^19 erg s^-1 cm^-2 Hz^-1 arcsec^-2]
Flux(Hα)
[10^-16 erg s^-1 cm^-2]
UGC 02405
Δ δ [arcsec]
Δ α [arcsec]
UGC02405
Wavelength(Å)
[OII]
Hε
Hδ
Hγ
Hβ
[OIII]
[OIII]
Hα
[SII]
[SII]

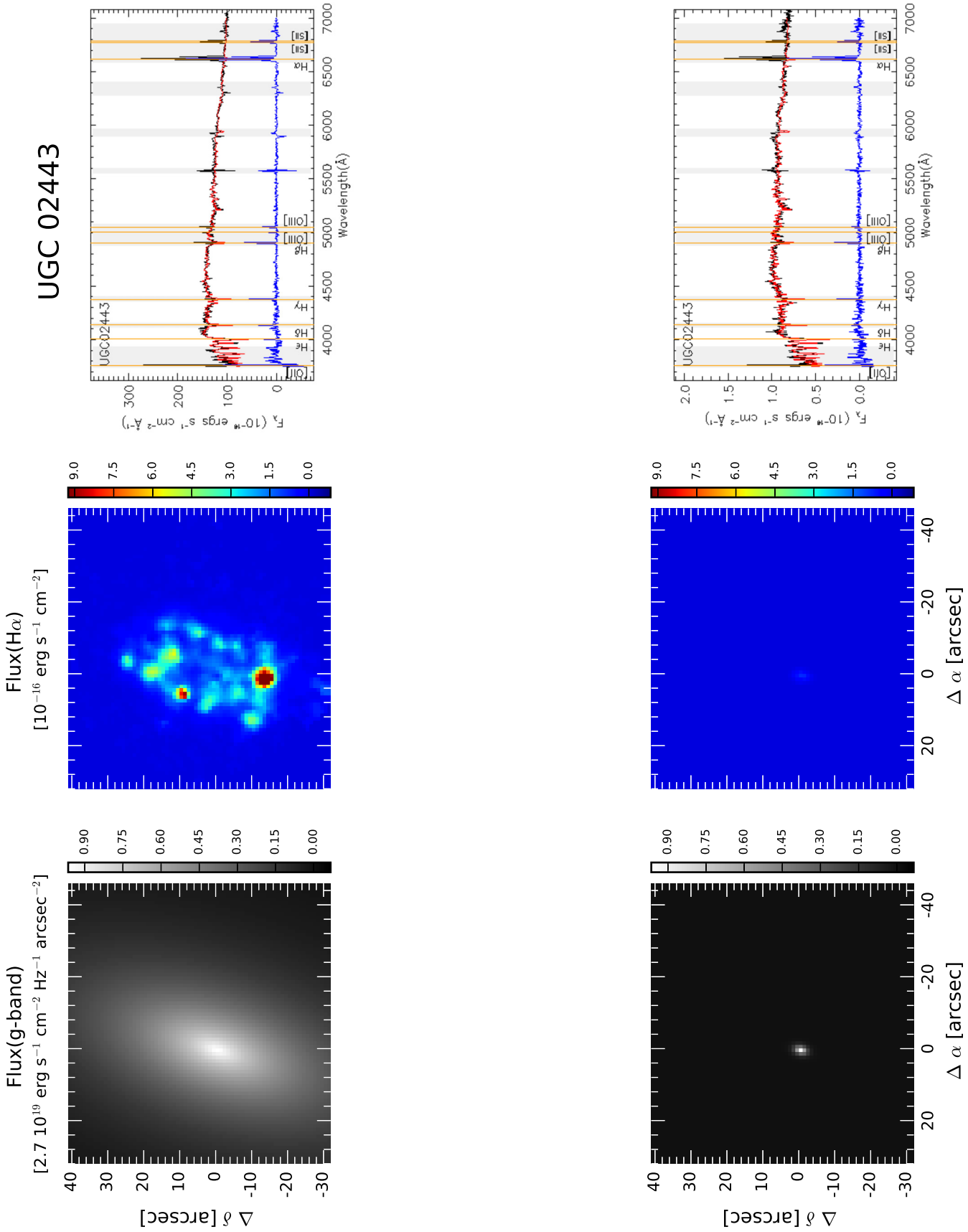
UGC 02443
Flux(g-band)
[2.7 10^19 erg s^-1 cm^-2 Hz^-1 arcsec^-2]
Flux(Hα)
[10^-16 erg s^-1 cm^-2]
Δ δ [arcsec]
Δ α [arcsec]
Wavelength(Å)
F_λ (10^-16 ergs s^-1 cm^-2 Å^-1)
UGC02443
[OII]
Hε
Hδ
Hγ
Hβ
[OIII]
[OIII]
Hα
[SII]
[SII]

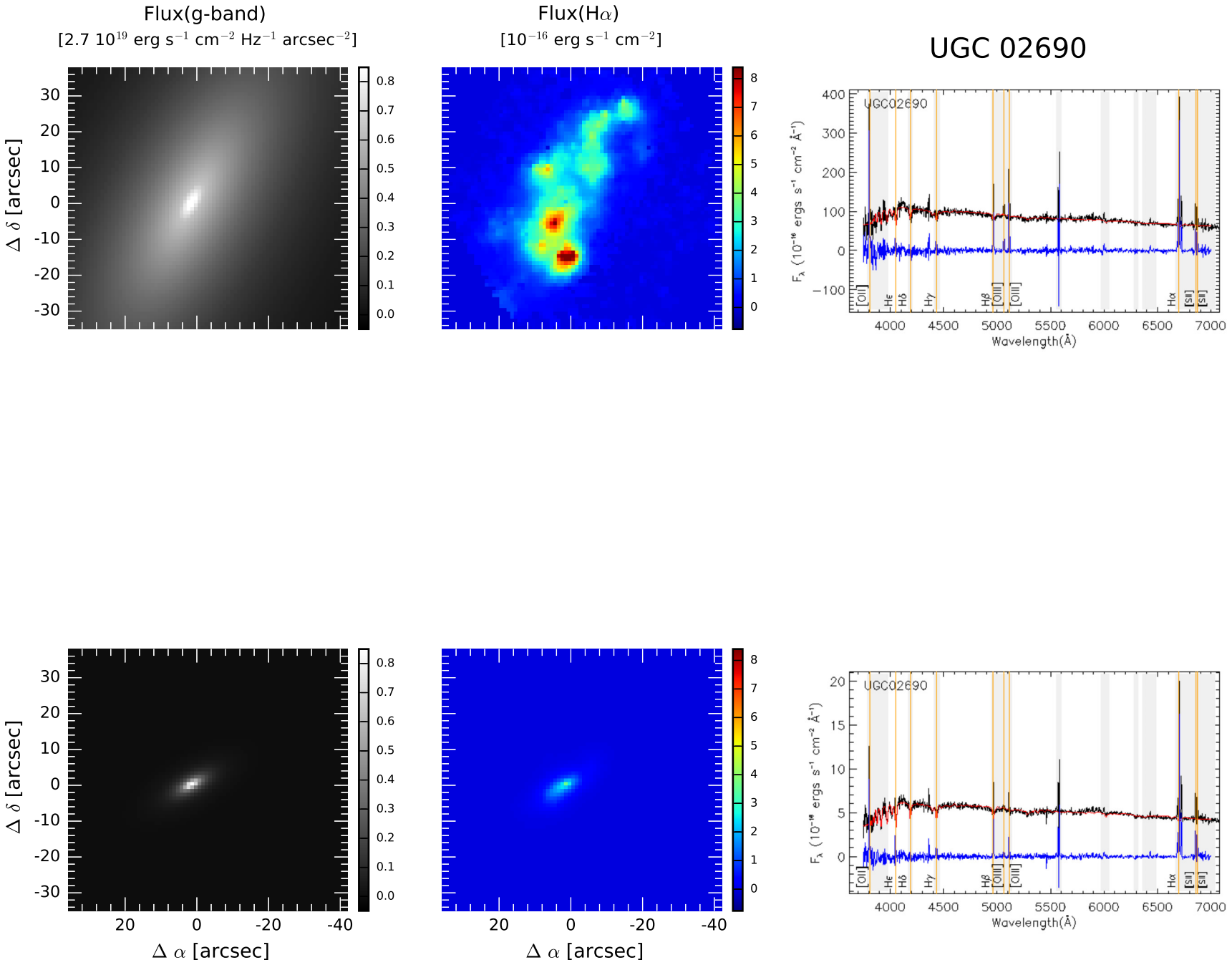
Flux(g-band)
[2.7 10^19 erg s^-1 cm^-2 Hz^-1 arcsec^-2]
Flux(Hα)
[10^-16 erg s^-1 cm^-2]
UGC 02690
Δ δ [arcsec]
Δ α [arcsec]
UGC02690
Wavelength(Å)
[OII]
Hε
Hδ
Hγ
Hβ
[OIII]
[OIII]
Hα
[SII]
[SII]

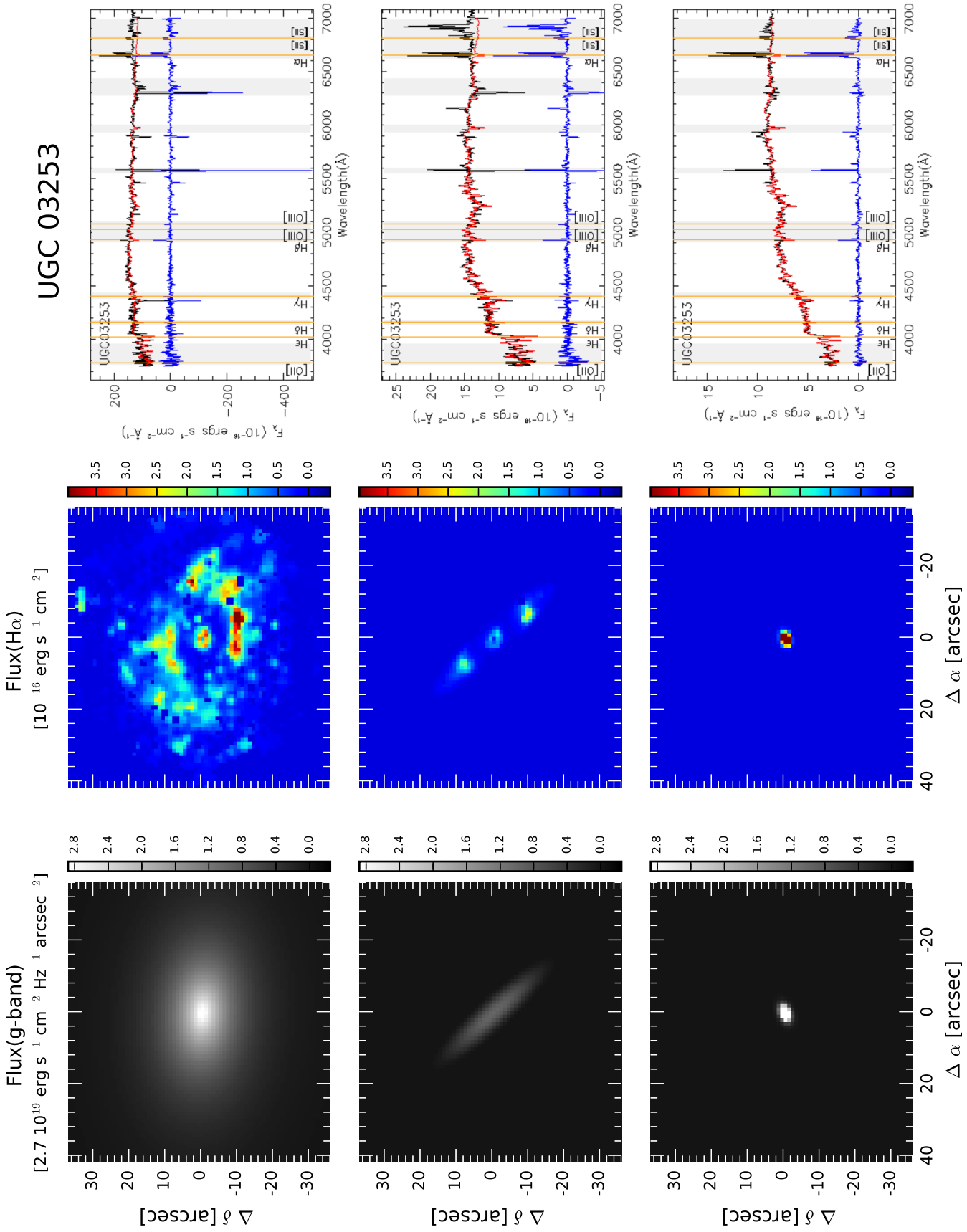
UGC 03253
Flux(g-band)
[2.7 10^19 erg s^-1 cm^-2 Hz^-1 arcsec^-2]
Flux(Hα)
[10^-16 erg s^-1 cm^-2]
Δ δ [arcsec]
Δ α [arcsec]
Wavelength(Å)
F_λ (10^-16 ergs s^-1 cm^-2 Å^-1)
UGC03253
[OII]
Hε
Hδ
Hγ
[OIII]
Hβ
[OIII]
[SII]
[SII]
Hα

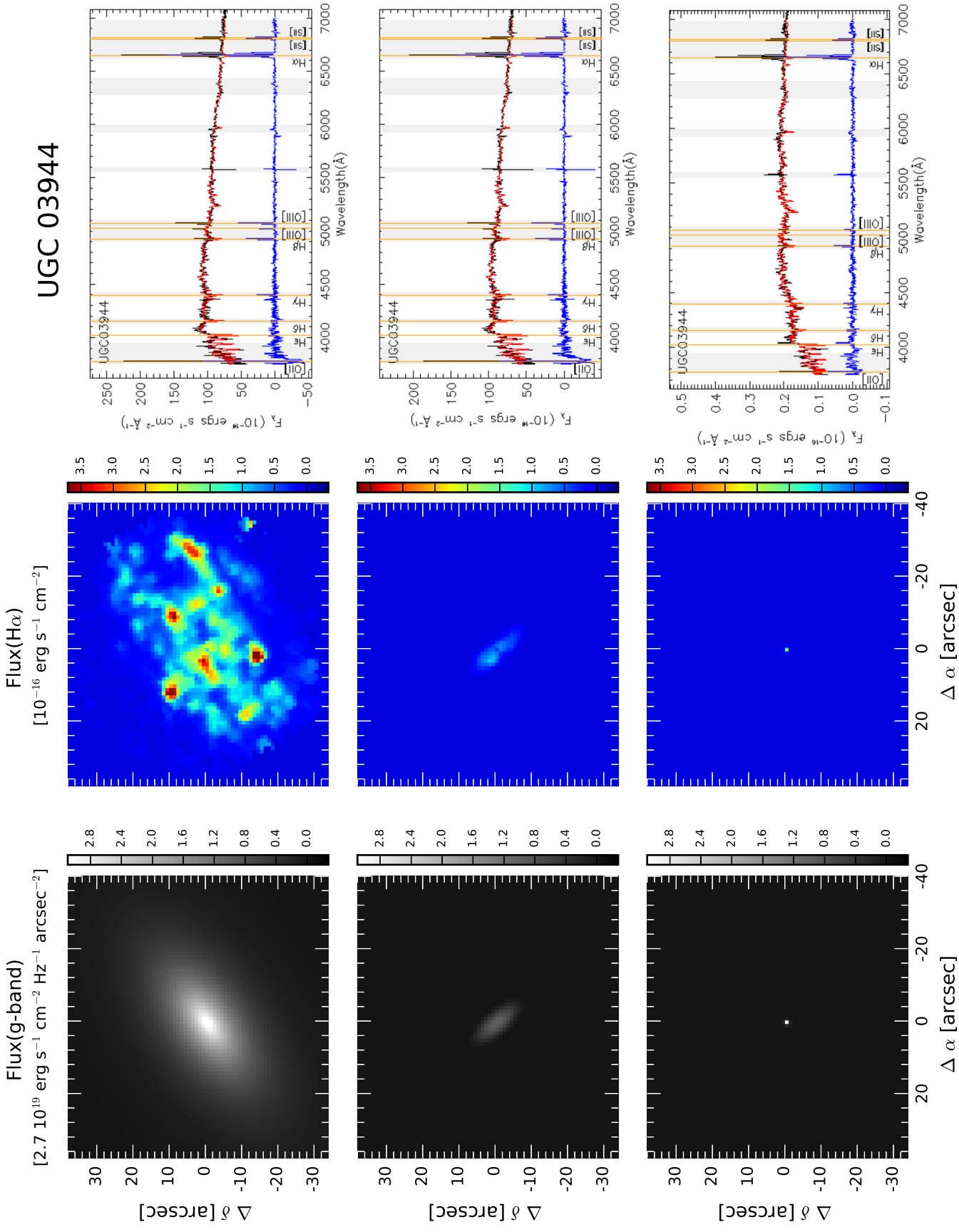
UGC 03944
Flux(g-band)
[2.7 10^19 erg s^-1 cm^-2 Hz^-1 arcsec^-2]
Flux(Hα)
[10^-16 erg s^-1 cm^-2]
Δ δ [arcsec]
Δ α [arcsec]
Wavelength(Å)
UGC03944
[OII]
Hε
Hδ
Hγ
Hβ
[OIII]
[OIII]
[OIII]
Hα
[SII]
[SII]

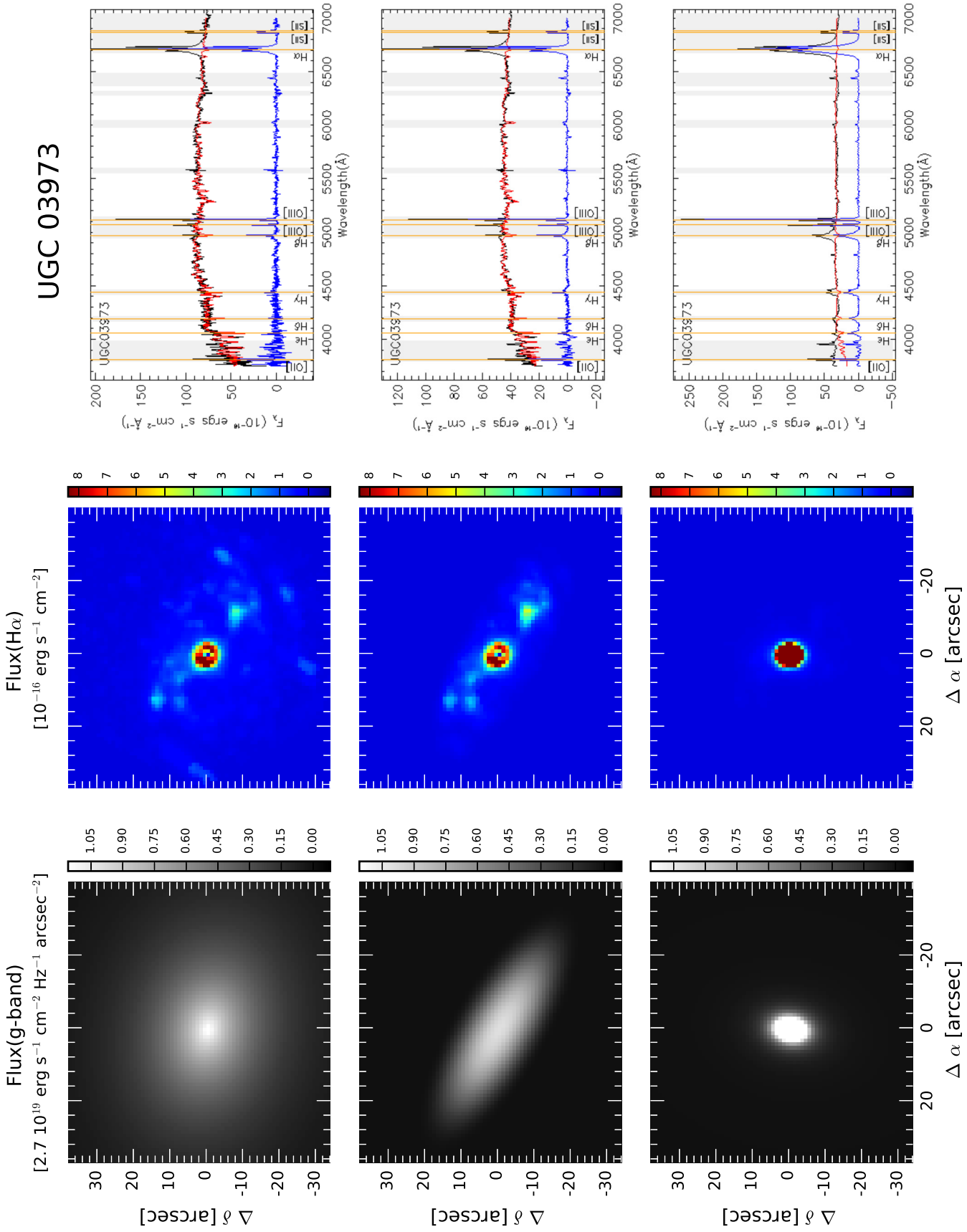
UGC 03973
Flux(g-band)
[2.7 10^19 erg s^-1 cm^-2 Hz^-1 arcsec^-2]
Flux(Hα)
[10^-16 erg s^-1 cm^-2]
Δ δ [arcsec]
Δ α [arcsec]
Wavelength(Å)
F_λ (10^-16 ergs s^-1 cm^-2 Å^-1)
UGC03973
[OII]
Hε
Hδ
Hγ
Hβ
[OIII]
[OIII]
[SII]
[SII]
Hα

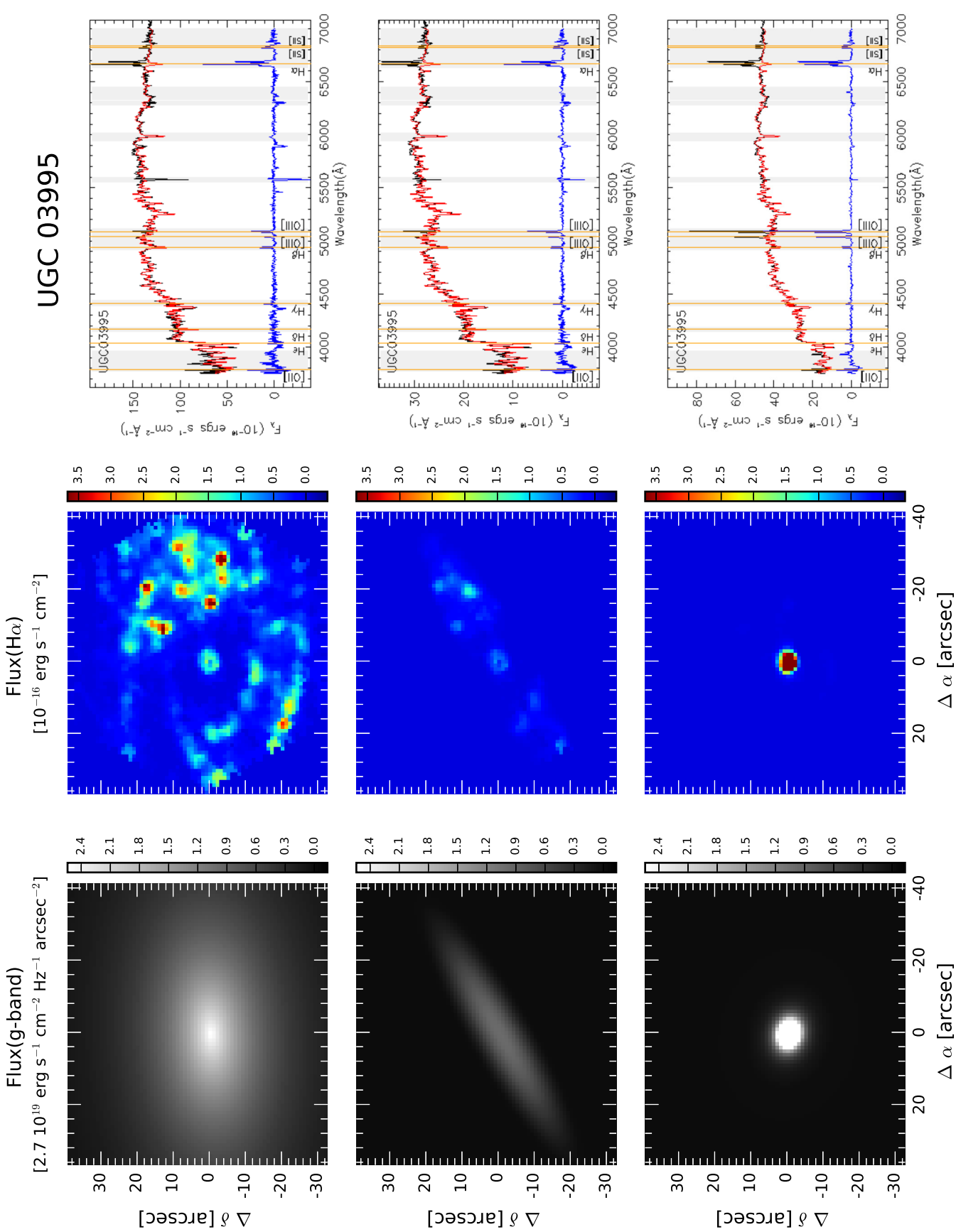
UGC 03995
Flux(g-band)
[2.7 10^19 erg s^-1 cm^-2 Hz^-1 arcsec^-2]
Flux(Hα)
[10^-16 erg s^-1 cm^-2]
Δ δ [arcsec]
Δ α [arcsec]
Wavelength(Å)
F_λ (10^-16 ergs s^-1 cm^-2 Å^-1)
UGC03995
[OII]
Hε
Hδ
Hγ
[OIII]
Hβ
[OIII]
Hα
[SII]
[SII]

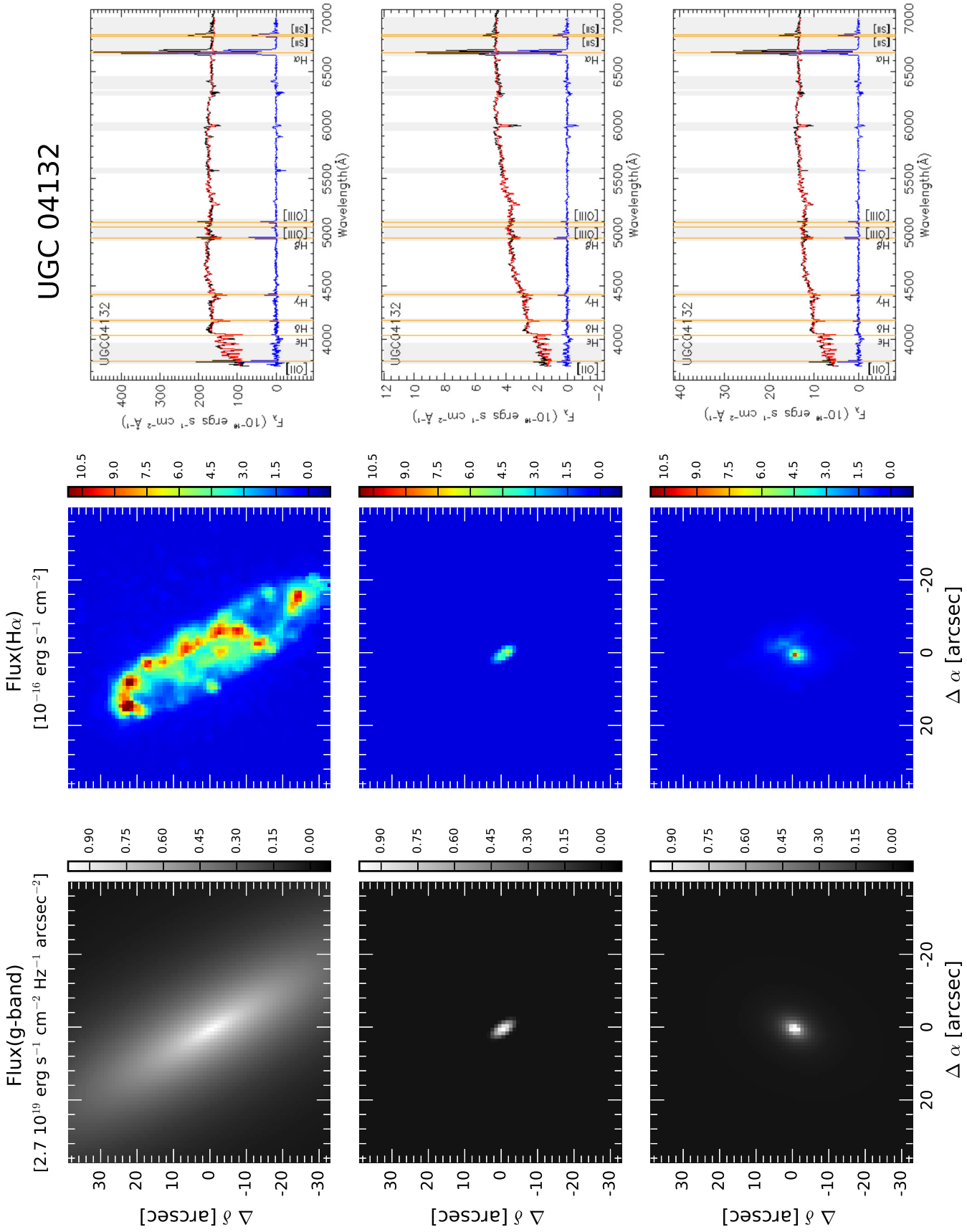
UGC 04132
Flux(g-band)
[2.7 10^19 erg s^-1 cm^-2 Hz^-1 arcsec^-2]
Flux(Hα)
[10^-16 erg s^-1 cm^-2]
Δ δ [arcsec]
Δ α [arcsec]
Wavelength(Å)
UGC04132
[OII]
Hε
Hδ
Hγ
[OIII]
Hβ
[SII]
Hα

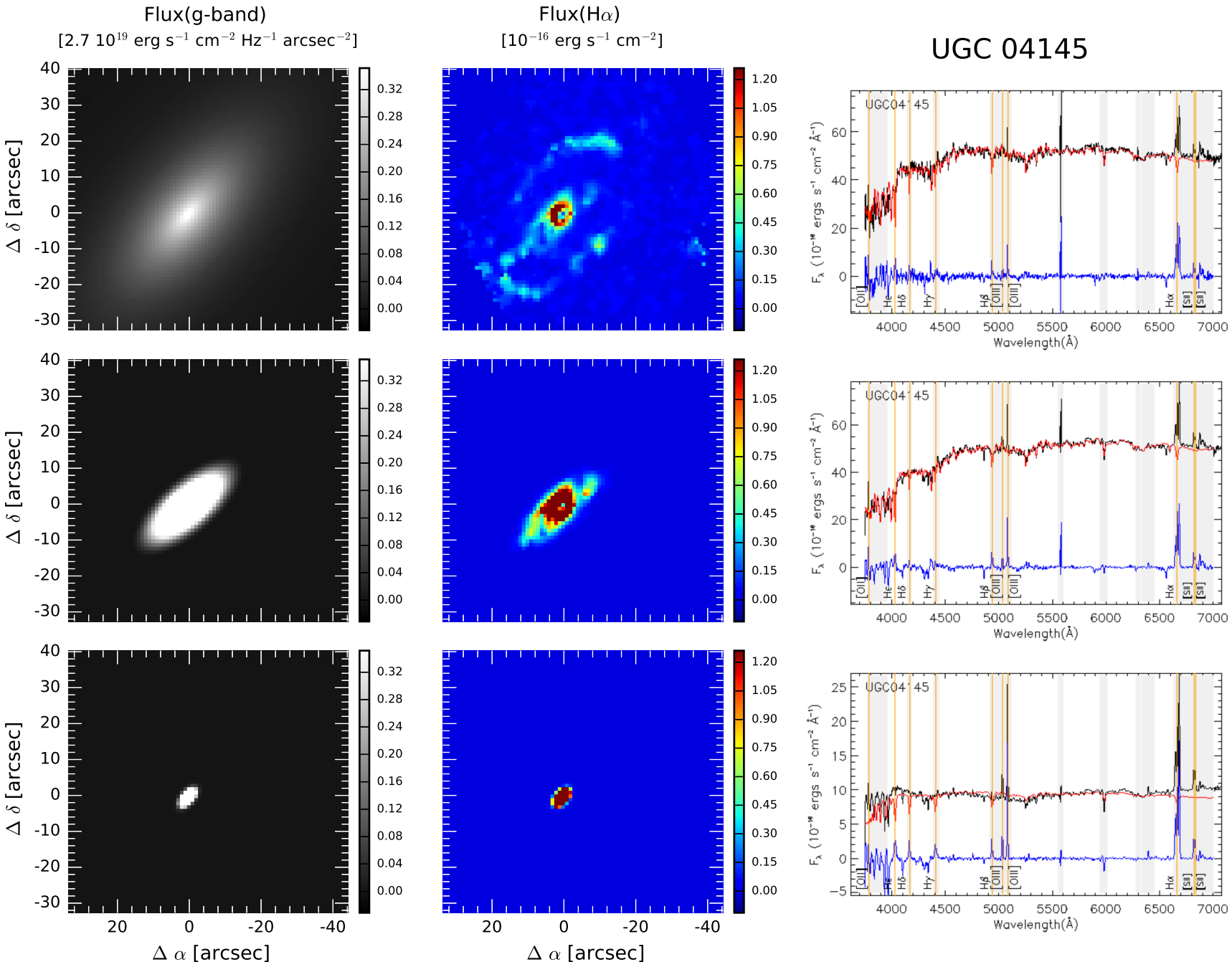
Flux(g-band)
[2.7 10^19 erg s^-1 cm^-2 Hz^-1 arcsec^-2]
Flux(Hα)
[10^-16 erg s^-1 cm^-2]
UGC 04145
Δ δ [arcsec]
Δ α [arcsec]
Wavelength(Å)
UGC04145
[OII]
Hε
Hδ
Hγ
Hβ
[OIII]
[OIII]
Hα
[SII]
[SII]

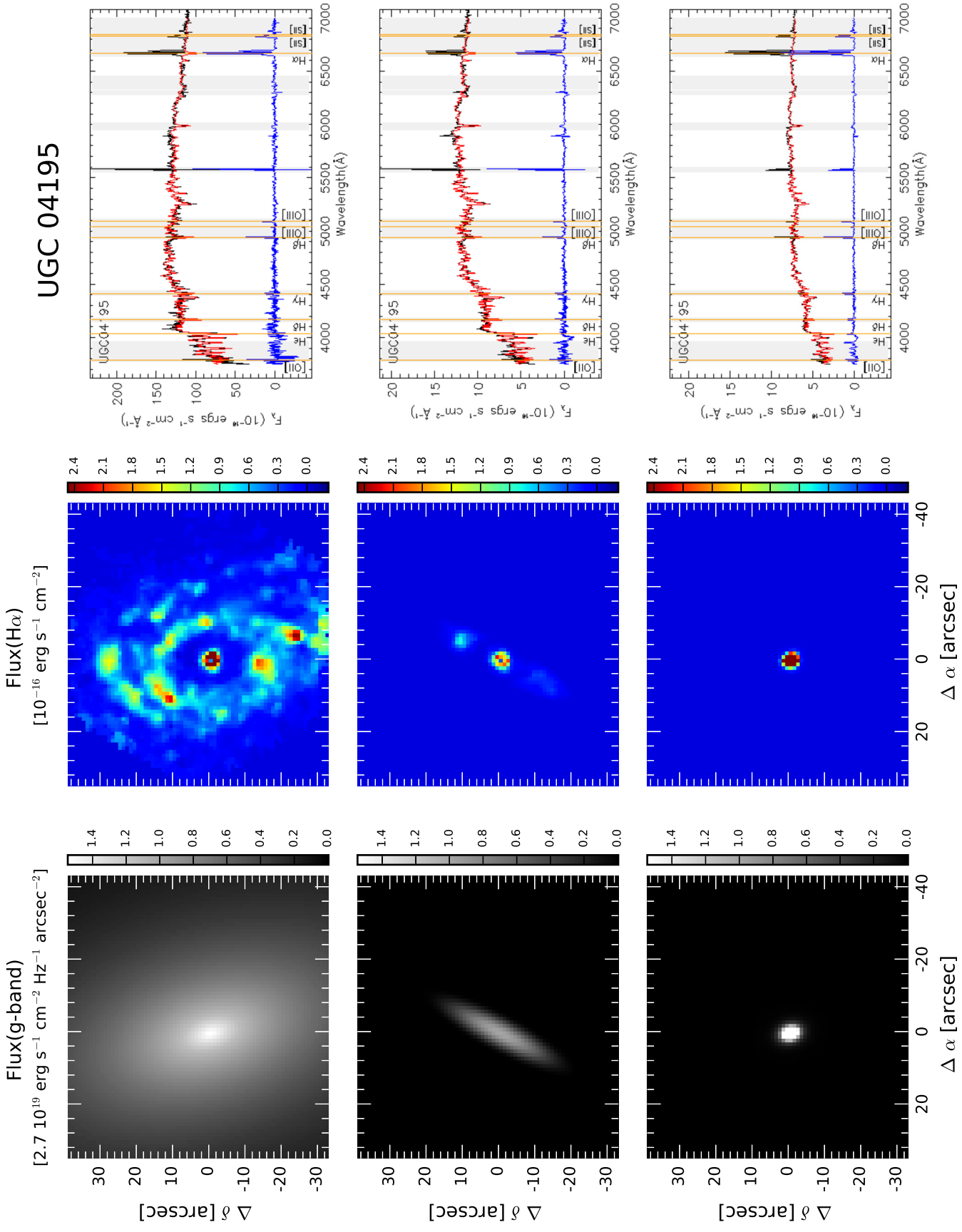
UGC 04195
Flux(g-band)
[2.7 10^19 erg s^-1 cm^-2 Hz^-1 arcsec^-2]
Flux(Hα)
[10^-16 erg s^-1 cm^-2]
Δ δ [arcsec]
Δ α [arcsec]
Wavelength(Å)
F_λ (10^-16 ergs s^-1 cm^-2 Å^-1)
UGC04195
[OII]
Hε
Hδ
Hγ
Hβ
[OIII]
[OIII]
[SII]
[SII]
Hα

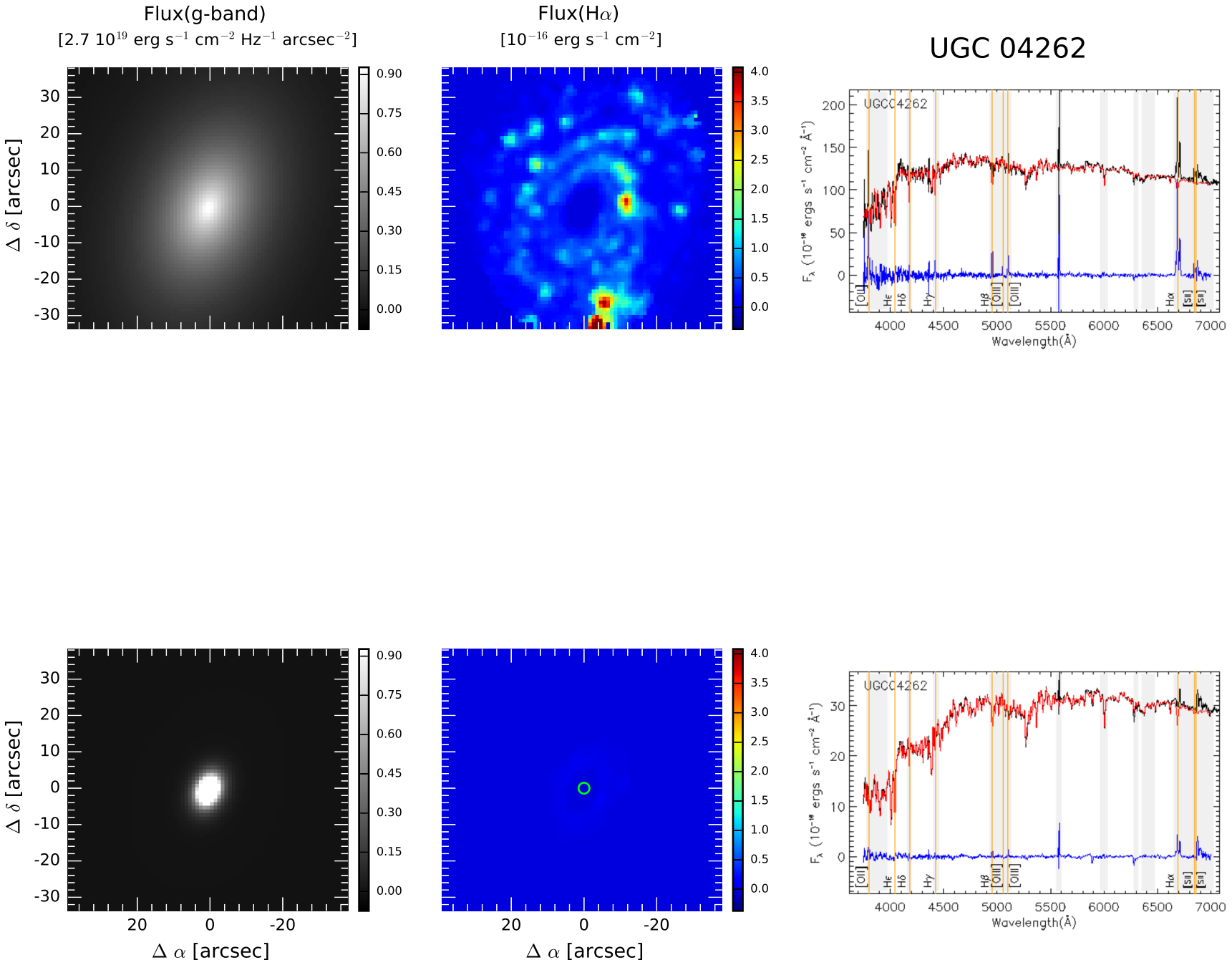
Flux(g-band)
[2.7 10^19 erg s^-1 cm^-2 Hz^-1 arcsec^-2]
Flux(Hα)
[10^-16 erg s^-1 cm^-2]
UGC 04262
Δ δ [arcsec]
Δ α [arcsec]
UGCC4262
Wavelength(Å)
[OII]
Hε
Hδ
Hγ
Hβ
[OIII]
[OIII]
Hα
[SII]
[SII]

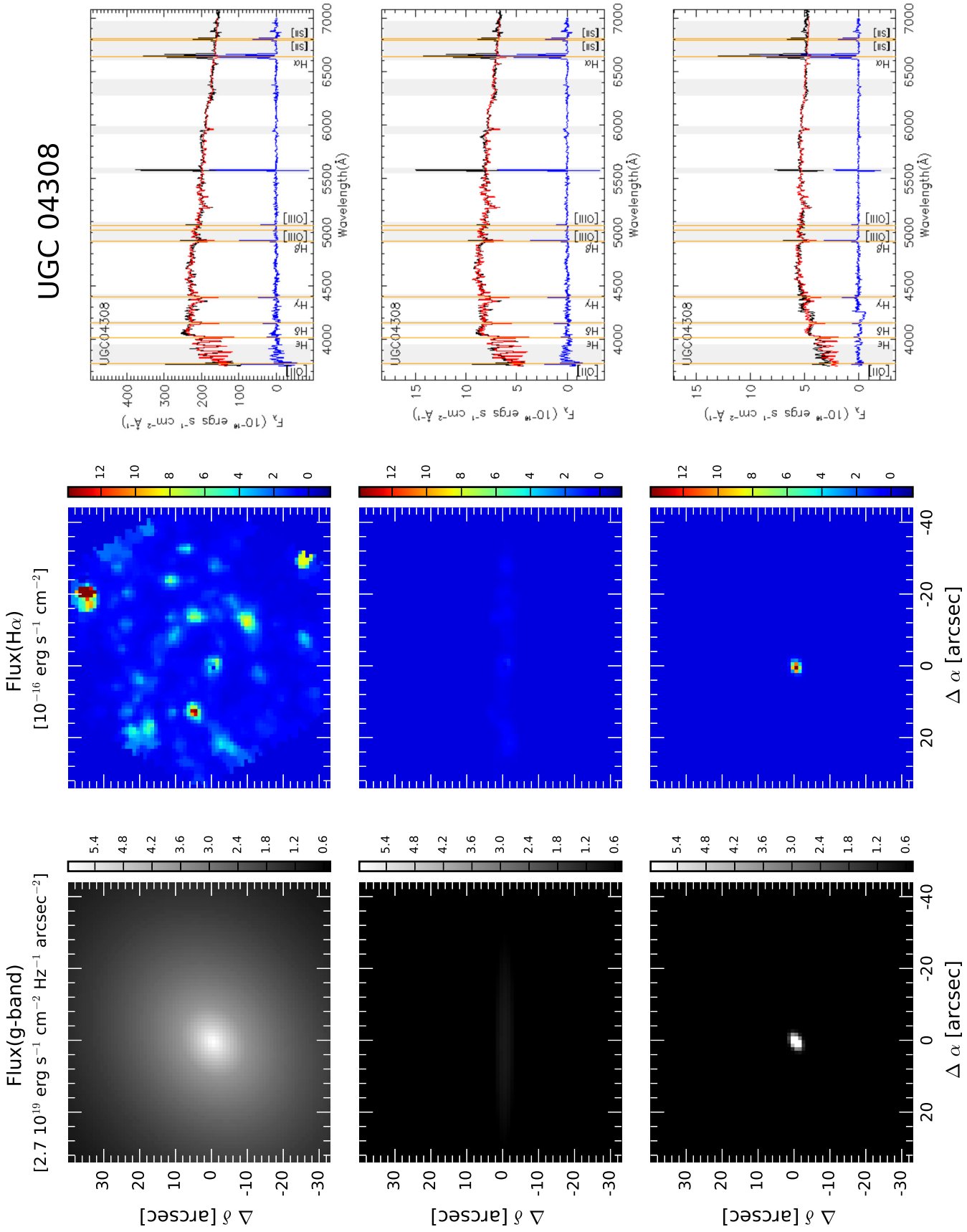
UGC 04308
Flux(g-band)
[2.7 10^19 erg s^-1 cm^-2 Hz^-1 arcsec^-2]
Flux(Hα)
[10^-16 erg s^-1 cm^-2]
Δ δ [arcsec]
Δ α [arcsec]
Wavelength(Å)
UGC04308
[OII]
Hε
Hδ
Hγ
[OIII]
Hβ
[OIII]
[OIII]
Hα
[SII]
[SII]

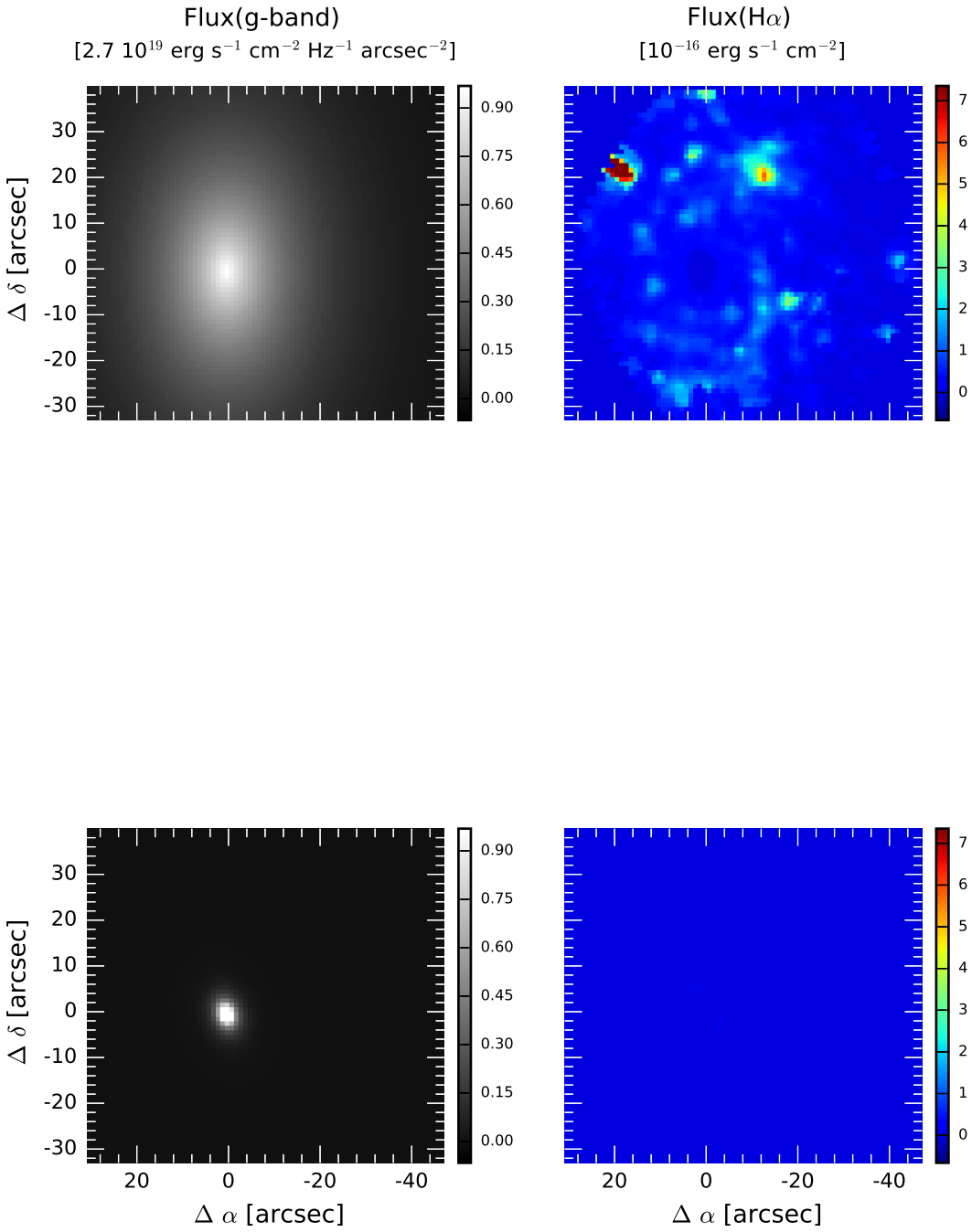
Flux(g-band)
[2.7 10^19 erg s^-1 cm^-2 Hz^-1 arcsec^-2]
Flux(Hα)
[10^-16 erg s^-1 cm^-2]
Δ δ [arcsec]
Δ α [arcsec]

UGC 04375

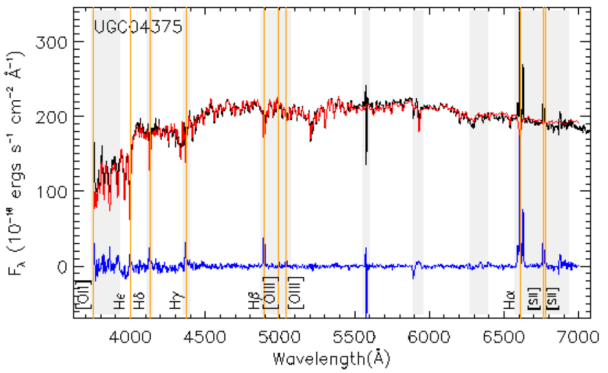
UGC04375
Wavelength(Å)

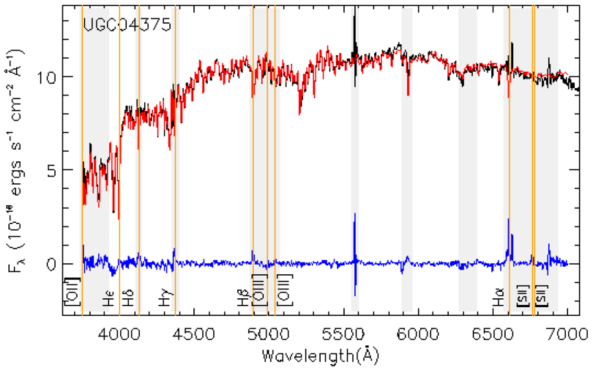
UGC04375
Wavelength(Å)

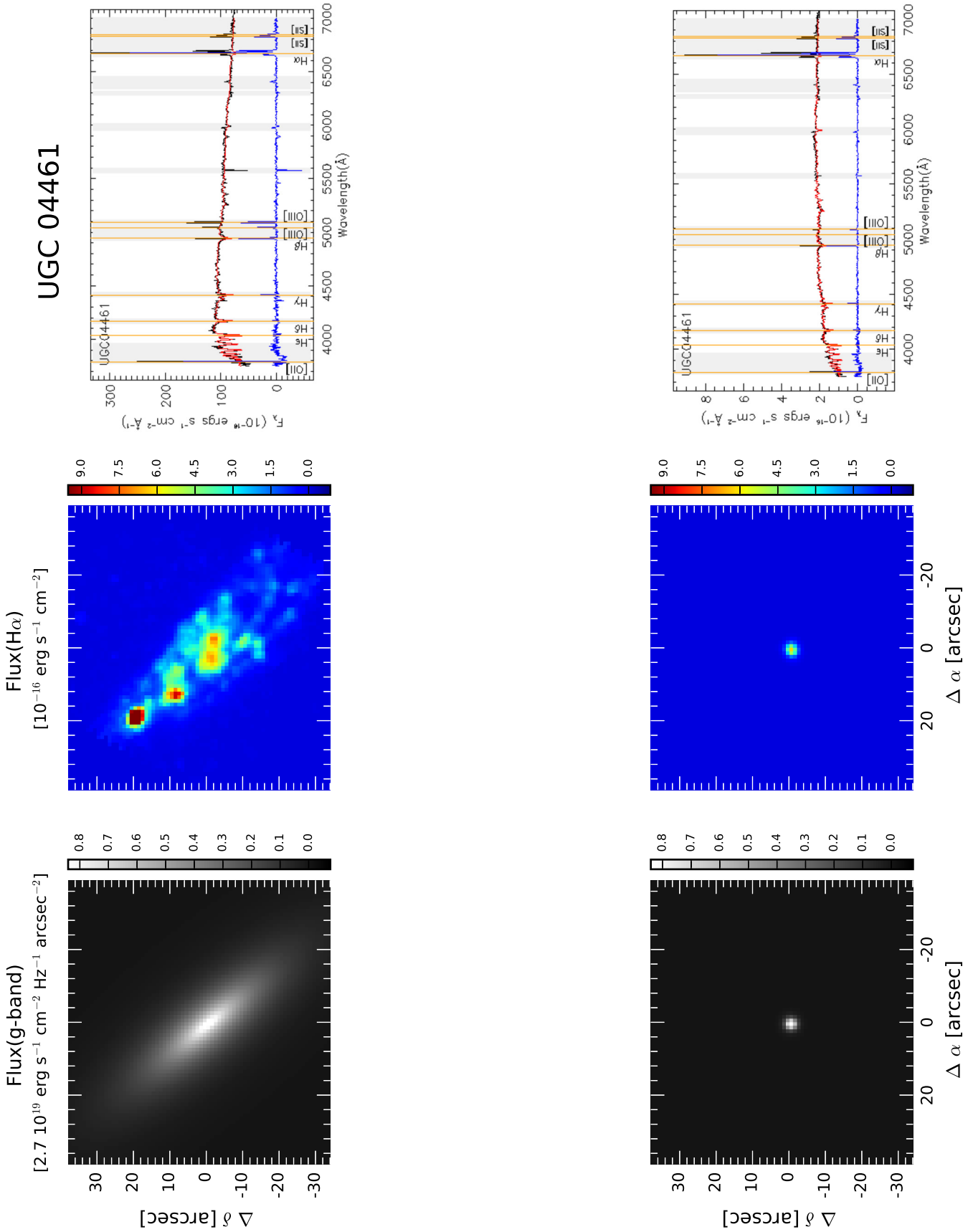
UGC 04461
Flux(Hα)
[10^-16 erg s^-1 cm^-2]
Flux(g-band)
[2.7 10^19 erg s^-1 cm^-2 Hz^-1 arcsec^-2]
Δ δ [arcsec]
Δ α [arcsec]
Wavelength(Å)
F_λ (10^-16 ergs s^-1 cm^-2 Å^-1)
UGC04461
[SII]
Hα
[OIII]
Hβ
Hγ
Hδ
Hε
[OII]

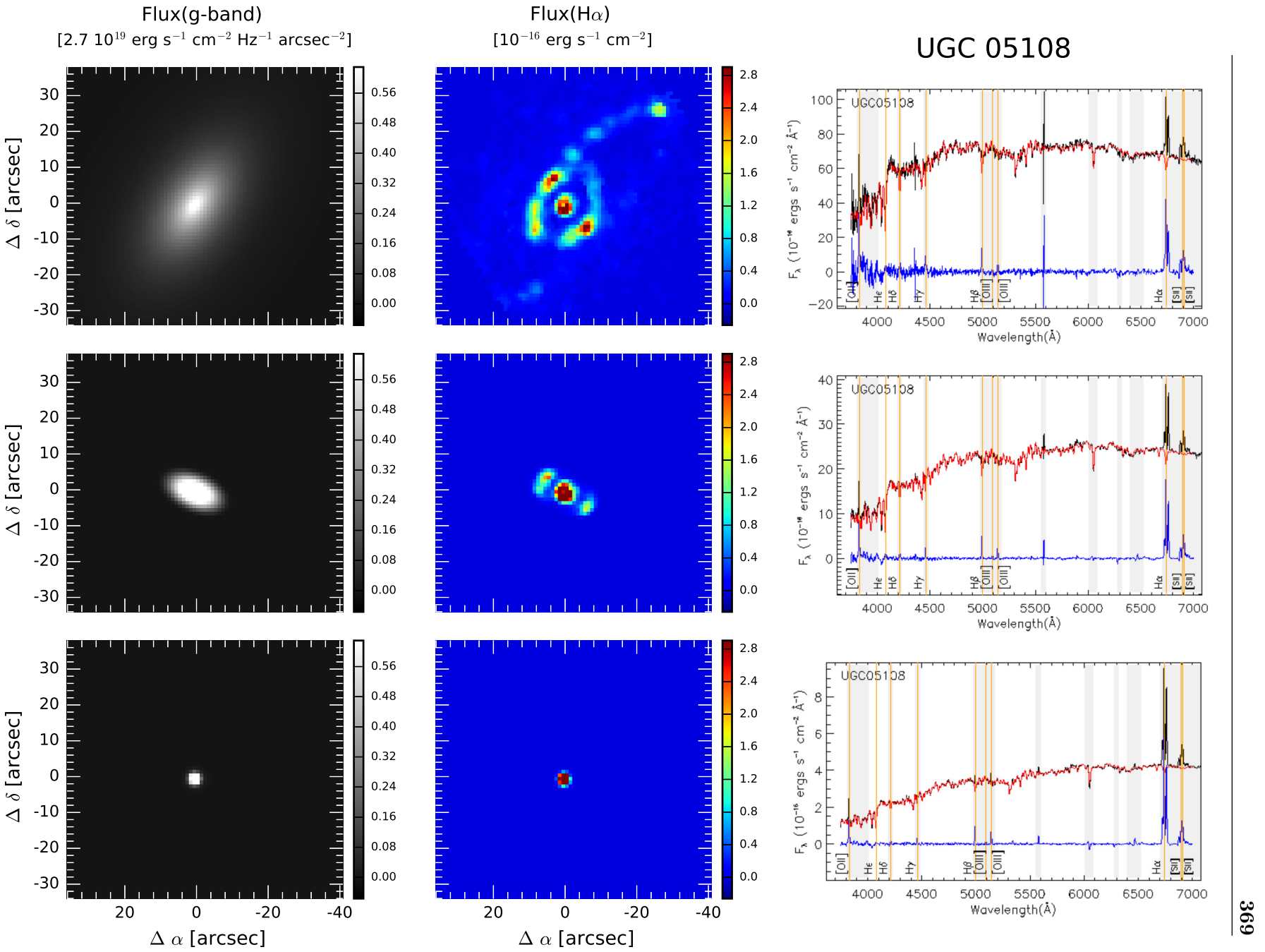
Flux(g-band)
[2.7 10^19 erg s^-1 cm^-2 Hz^-1 arcsec^-2]
Flux(Hα)
[10^-16 erg s^-1 cm^-2]
UGC 05108
Δ δ [arcsec]
Δ α [arcsec]
Wavelength(Å)
UGC05108
[OII]
Hε
Hδ
Hγ
Hβ
[OIII]
[OIII]
Hα
[SII]
[SII]

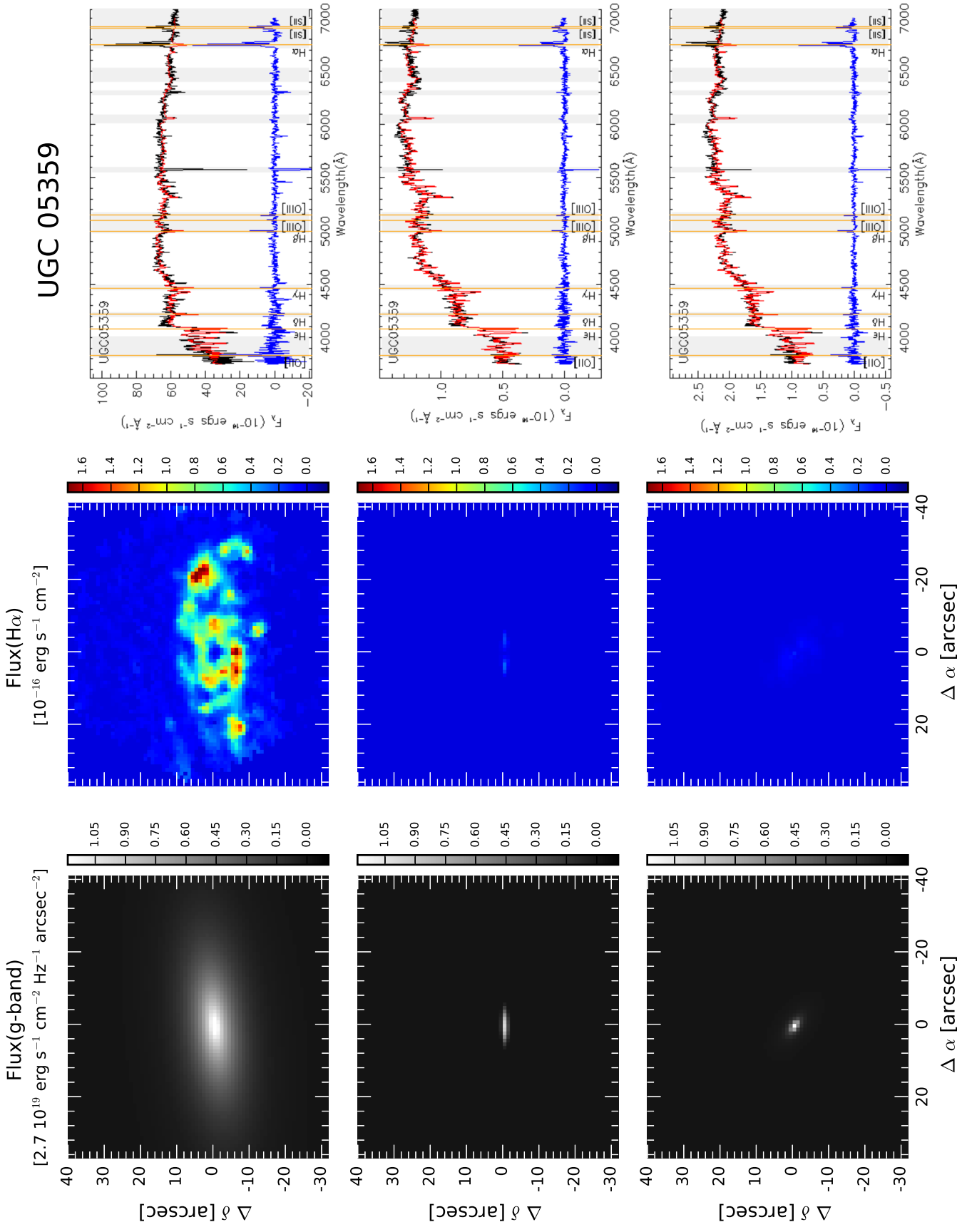
UGC 05359
Flux(g-band)
[2.7 10^19 erg s^-1 cm^-2 Hz^-1 arcsec^-2]
Flux(Hα)
[10^-16 erg s^-1 cm^-2]
Δ δ [arcsec]
Δ α [arcsec]
Wavelength(Å)
F_λ (10^-16 ergs s^-1 cm^-2 Å^-1)
UGC05359
[OII]
Hε
Hδ
Hγ
Hβ
[OIII]
[OIII]
Hα
[SII]
[SII]

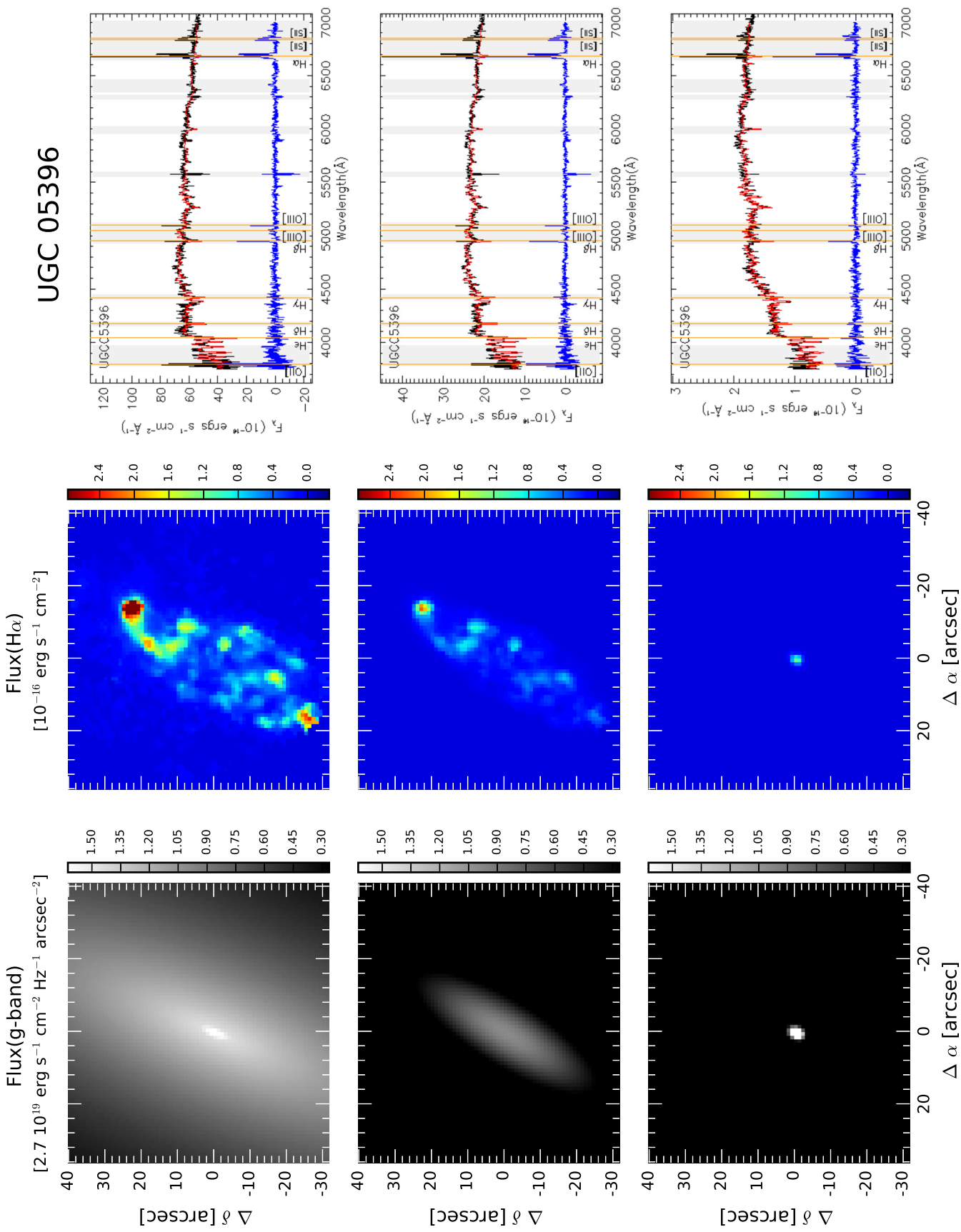
UGC 05396
Flux(g-band)
[2.7 10^19 erg s^-1 cm^-2 Hz^-1 arcsec^-2]
Flux(Hα)
[10^-16 erg s^-1 cm^-2]
Δ δ [arcsec]
Δ α [arcsec]
Wavelength(Å)
UGC05396
[OII]
Hε
Hδ
Hγ
Hβ
[OIII]
[OIII]
[SII]
[SII]
Hα

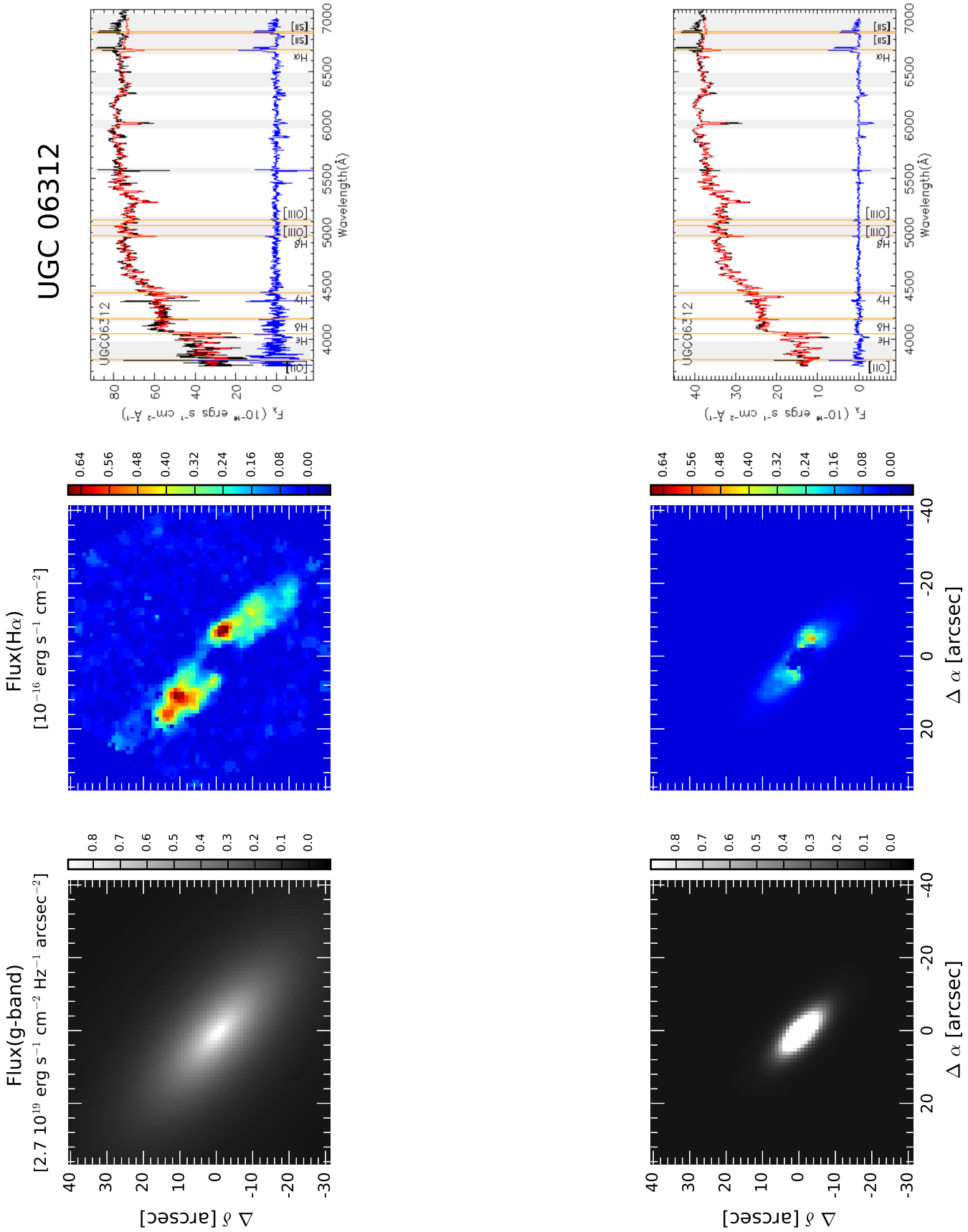
UGC 06312
Flux(g-band)
[2.7 10^19 erg s^-1 cm^-2 Hz^-1 arcsec^-2]
Flux(Hα)
[10^-16 erg s^-1 cm^-2]
Δ δ [arcsec]
Δ α [arcsec]
Wavelength(Å)
F_λ (10^-16 ergs s^-1 cm^-2 Å^-1)
UGC06312
[OII]
Hε
Hδ
Hγ
Hβ
[OIII]
[OIII]
[SII]
[SII]
Hα

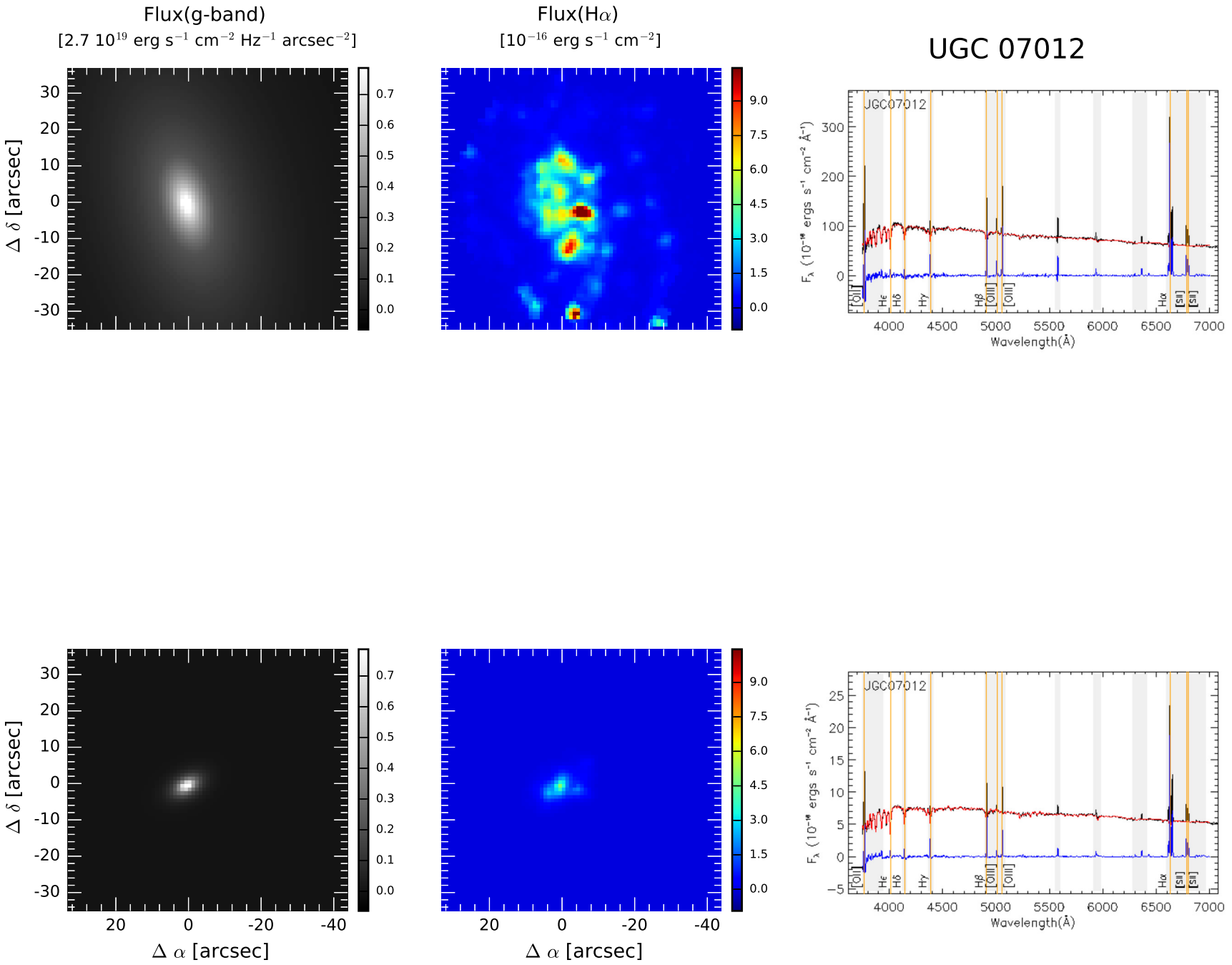
Flux(g-band)
[2.7 10^19 erg s^-1 cm^-2 Hz^-1 arcsec^-2]
Flux(Hα)
[10^-16 erg s^-1 cm^-2]
UGC 07012
Δ δ [arcsec]
Δ α [arcsec]
JGC07012
Wavelength(Å)
[OII]
Hε
Hδ
Hγ
Hβ
[OIII]
[OIII]
Hα
[SII]
[SII]

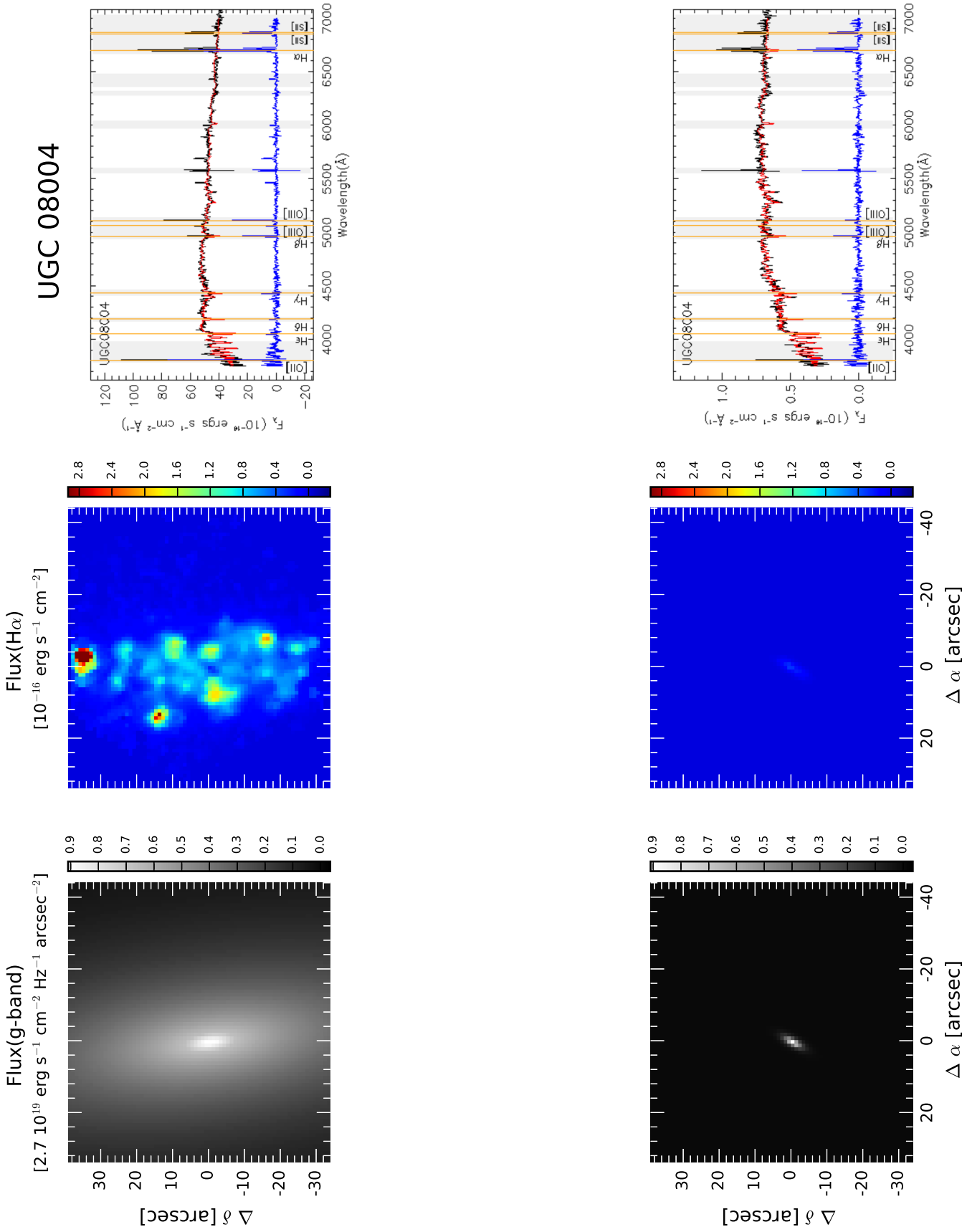
UGC 08004
UGC08004
Wavelength(Å)
Flux(Hα)
[10^-16 erg s^-1 cm^-2]
Flux(g-band)
[2.7 10^19 erg s^-1 cm^-2 Hz^-1 arcsec^-2]
Δ δ [arcsec]
Δ α [arcsec]

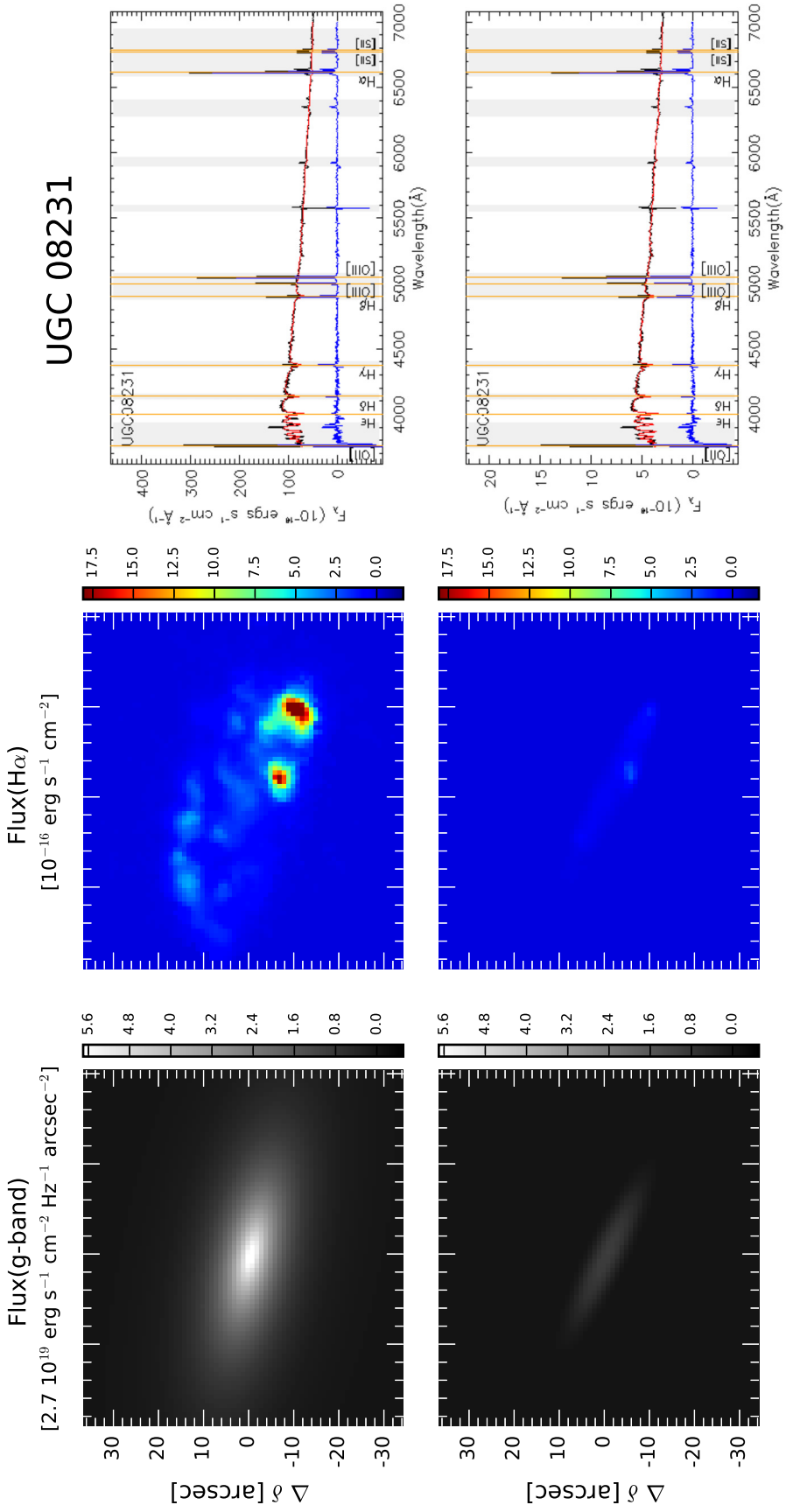
UGC 08231
Flux(g-band)
[2.7 10^19 erg s^-1 cm^-2 Hz^-1 arcsec^-2]
Flux(Hα)
[10^-16 erg s^-1 cm^-2]
Δ δ [arcsec]
Δ α [arcsec]
Wavelength(Å)
F_λ (10^-16 ergs s^-1 cm^-2 Å^-1)
UGC08231
[OII]
Hε
Hδ
Hγ
Hβ
[OIII]
[OIII]
Hα
[SII]
[SII]

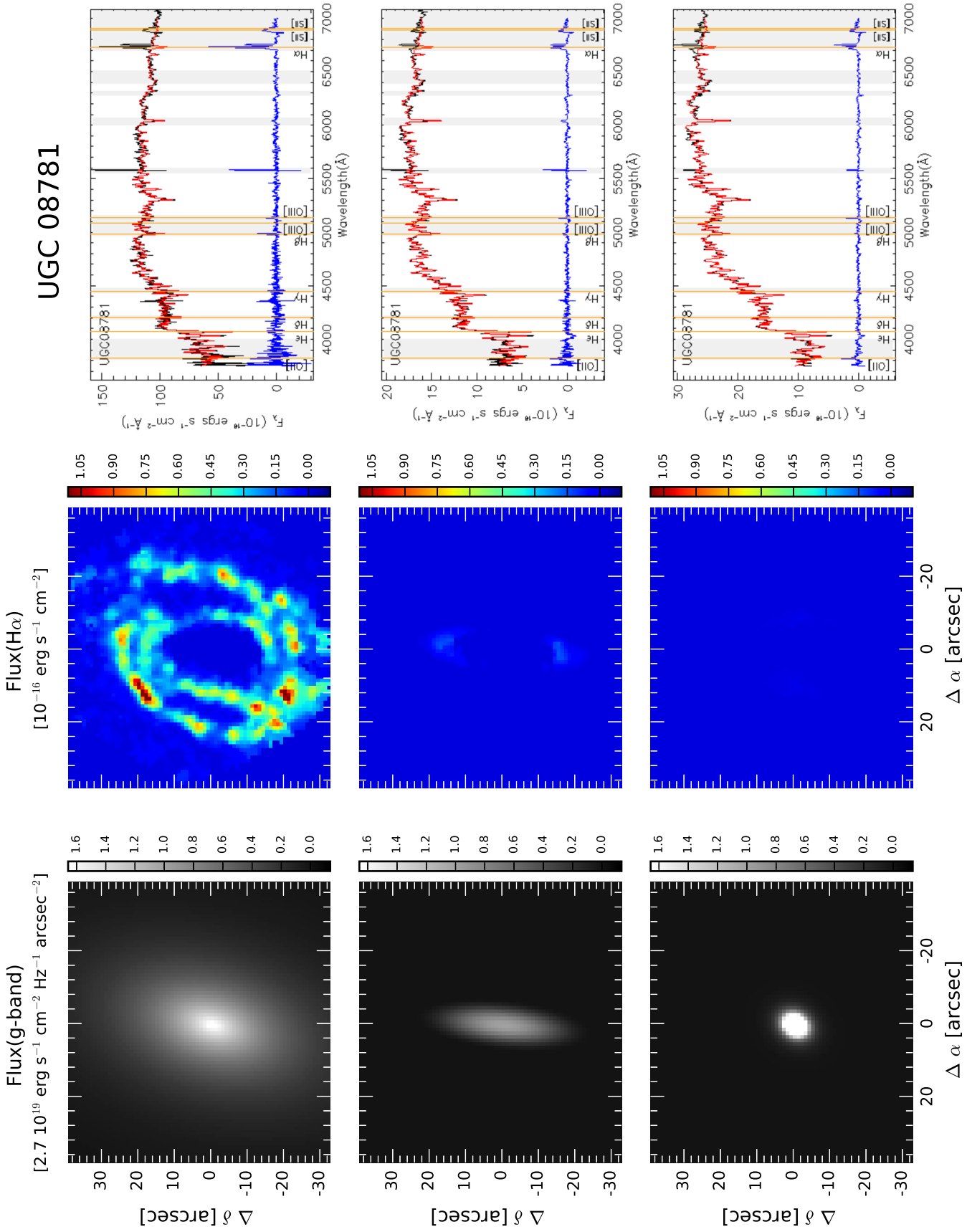
UGC 08781
Flux(g-band)
[2.7 10^19 erg s^-1 cm^-2 Hz^-1 arcsec^-2]
Flux(Hα)
[10^-16 erg s^-1 cm^-2]
Δ δ [arcsec]
Δ α [arcsec]
Wavelength(Å)
UGC08781
[OII]
Hε
Hδ
Hγ
Hβ
[OIII]
[OIII]
[SII]
[SII]
Hα

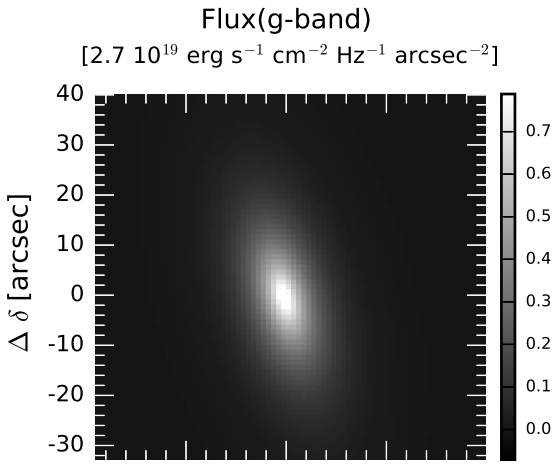
Flux(g-band)
[2.7 10^19 erg s^-1 cm^-2 Hz^-1 arcsec^-2]
Δ δ [arcsec]
40
30
20
10
0
-10
-20
-30
0.7
0.6
0.5
0.4
0.3
0.2
0.1
0.0

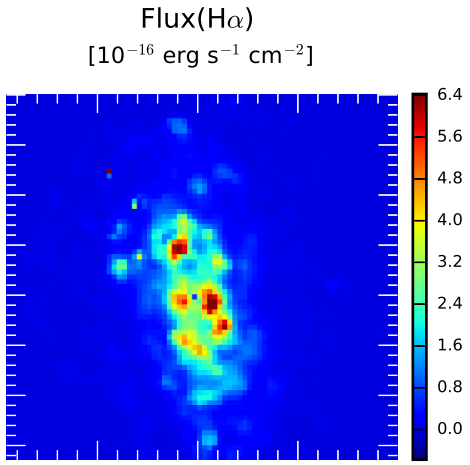
Flux(Hα)
[10^-16 erg s^-1 cm^-2]
6.4
5.6
4.8
4.0
3.2
2.4
1.6
0.8
0.0

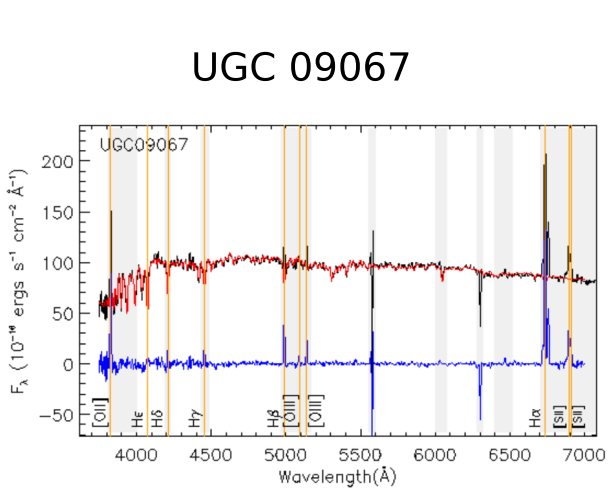
UGC 09067
UGC09067
F_λ (10^-16 ergs s^-1 cm^-2 Å^-1)
Wavelength(Å)
[OII]
Hε
Hδ
Hγ
Hβ
[OIII]
[OIII]
Hα
[SII]
[SII]

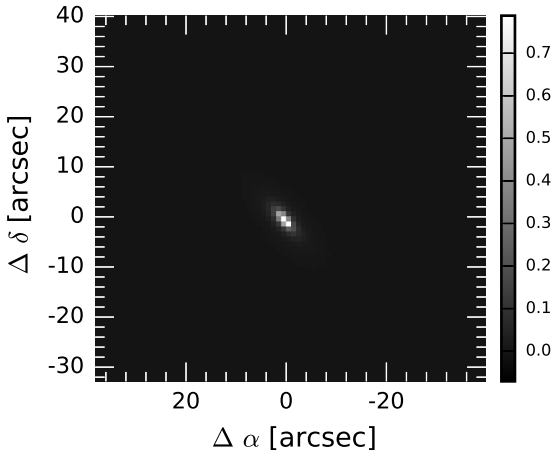
Δ δ [arcsec]
Δ α [arcsec]
40
30
20
10
0
-10
-20
-30
20
0
-20
0.7
0.6
0.5
0.4
0.3
0.2
0.1
0.0

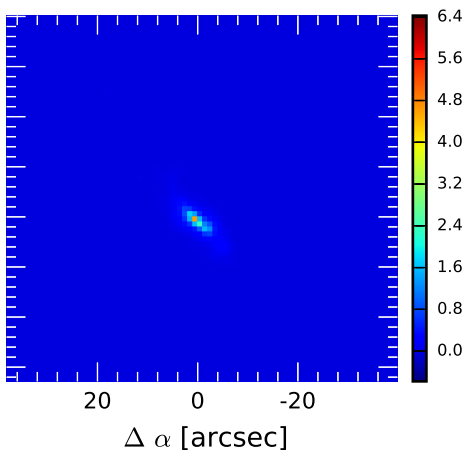
Δ α [arcsec]
20
0
-20
6.4
5.6
4.8
4.0
3.2
2.4
1.6
0.8
0.0

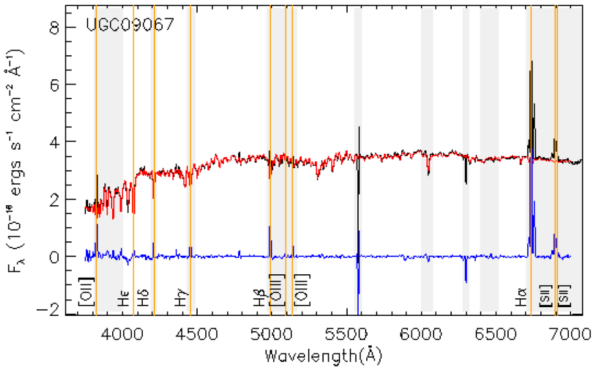
UGC09067
F_λ (10^-16 ergs s^-1 cm^-2 Å^-1)
Wavelength(Å)
[OII]
Hε
Hδ
Hγ
Hβ
[OIII]
[OIII]
Hα
[SII]
[SII]

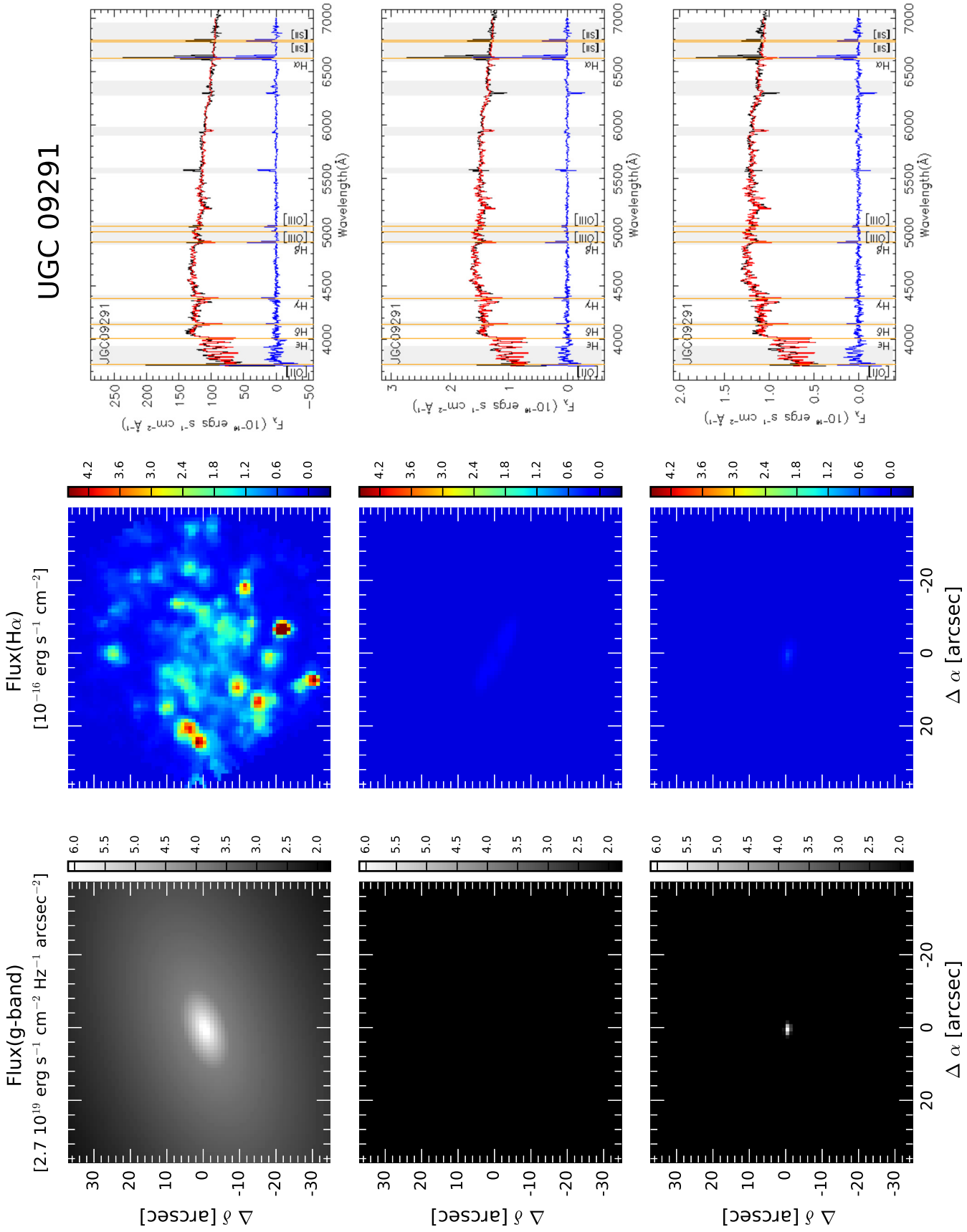
UGC 09291
Flux(g-band)
[2.7 10^19 erg s^-1 cm^-2 Hz^-1 arcsec^-2]
Flux(Hα)
[10^-16 erg s^-1 cm^-2]
Δ δ [arcsec]
Δ α [arcsec]
Wavelength(Å)
JGC09291
[OII]
Hε
Hδ
Hγ
Hβ
[OIII]
[OIII]
Hα
[SII]
[SII]

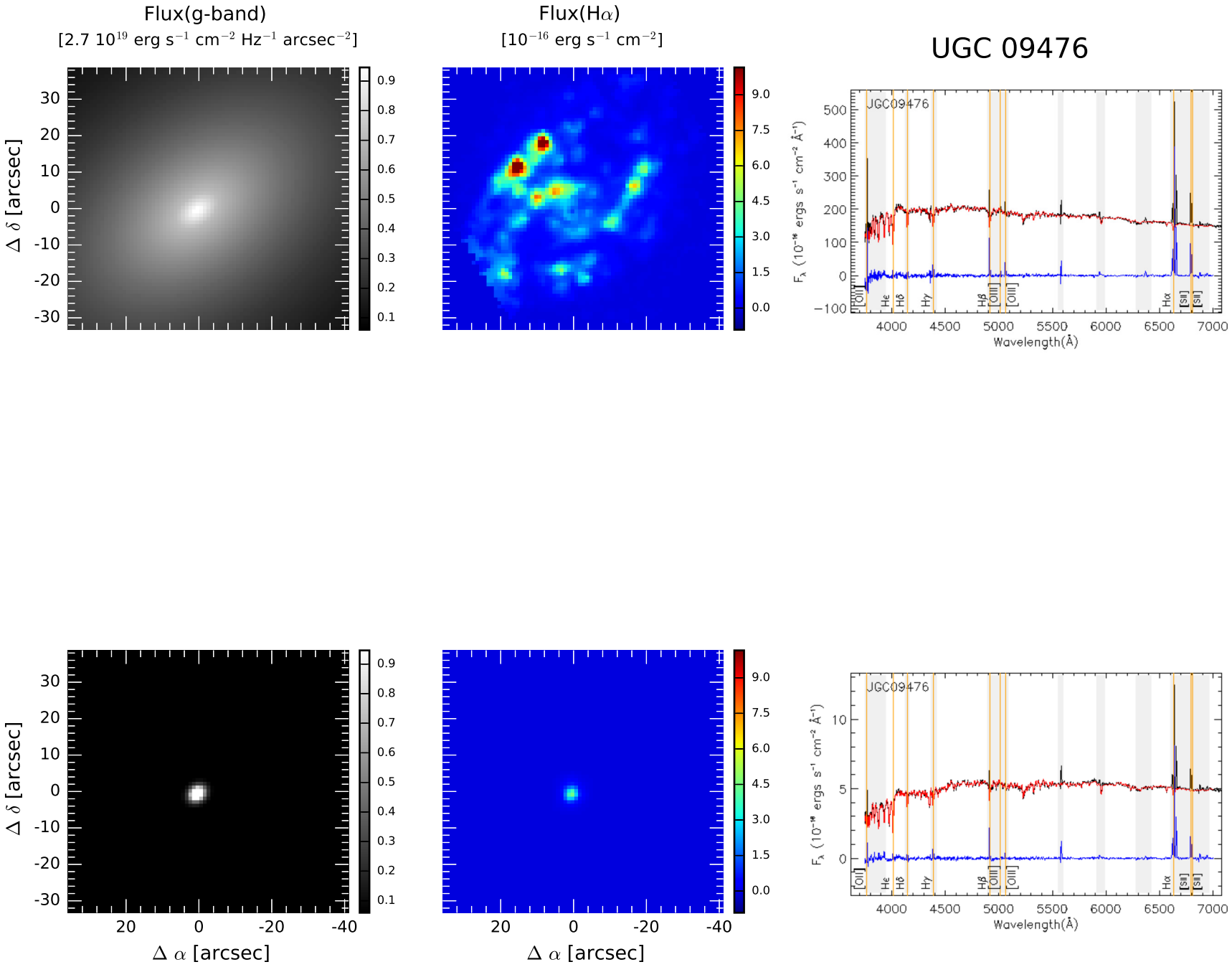
Flux(g-band)
[2.7 10^19 erg s^-1 cm^-2 Hz^-1 arcsec^-2]
Flux(Hα)
[10^-16 erg s^-1 cm^-2]
UGC 09476
Δ δ [arcsec]
Δ α [arcsec]
JGC09476
Wavelength(Å)
[OII]
Hε
Hδ
Hγ
Hβ
[OIII]
[OIII]
Hα
[SII]
[SII]

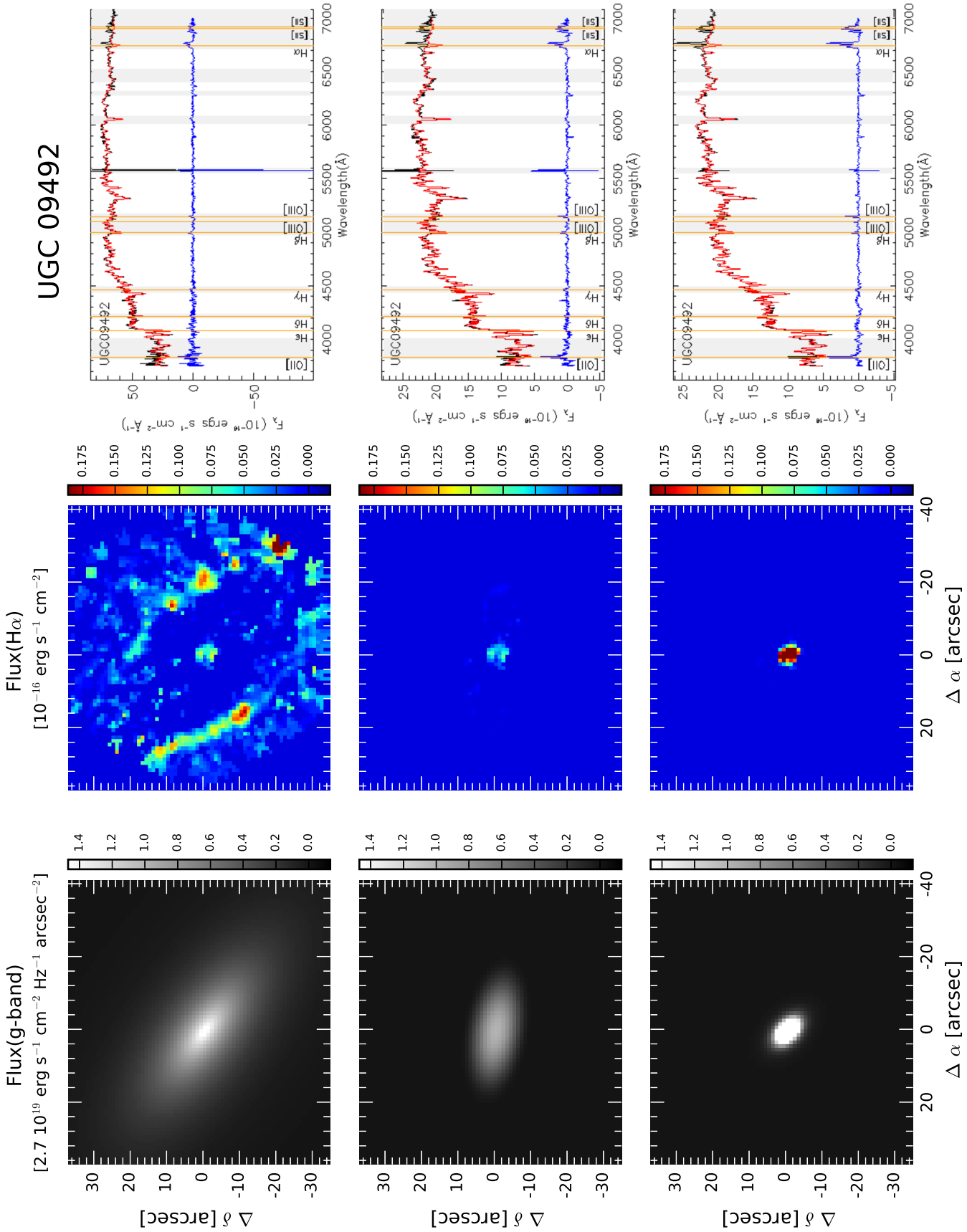
UGC 09492
Flux(g-band)
[2.7 10^19 erg s^-1 cm^-2 Hz^-1 arcsec^-2]
Flux(Hα)
[10^-16 erg s^-1 cm^-2]
Δ δ [arcsec]
Δ α [arcsec]
Wavelength(Å)
F_λ (10^-16 ergs s^-1 cm^-2 Å^-1)
UGC09492
[OII]
Hε
Hδ
Hγ
Hβ
[OIII]
[OIII]
Hα
[SII]
[SII]

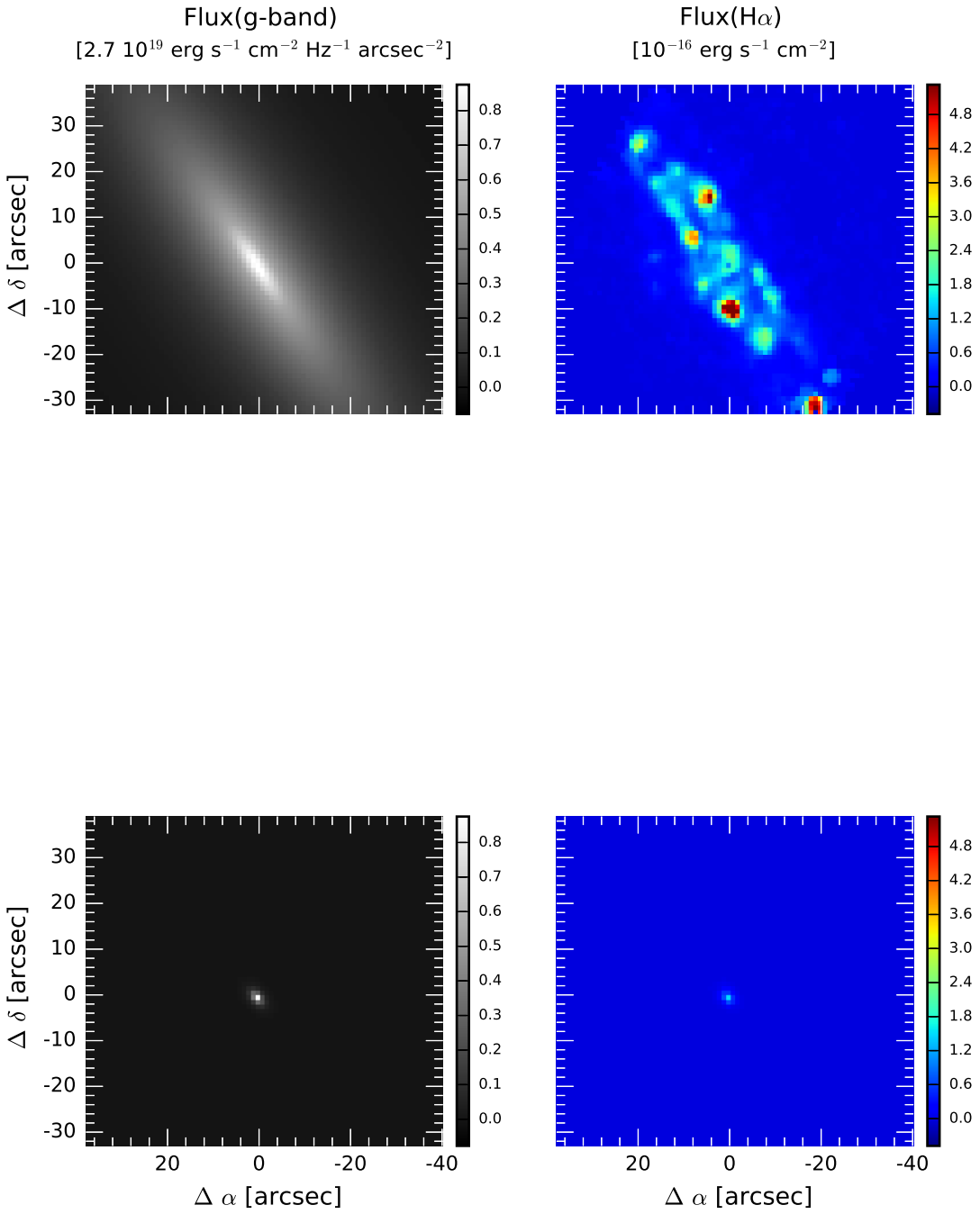
Flux(g-band)
[2.7 10^19 erg s^-1 cm^-2 Hz^-1 arcsec^-2]
Flux(Hα)
[10^-16 erg s^-1 cm^-2]
Δ δ [arcsec]
Δ α [arcsec]

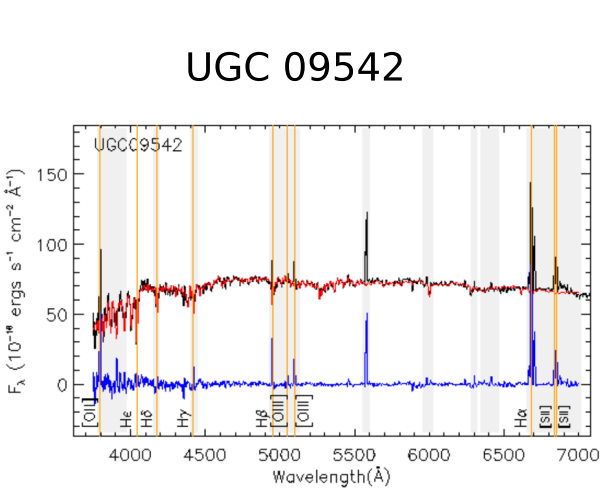
UGC 09542
UGC09542
Wavelength(Å)

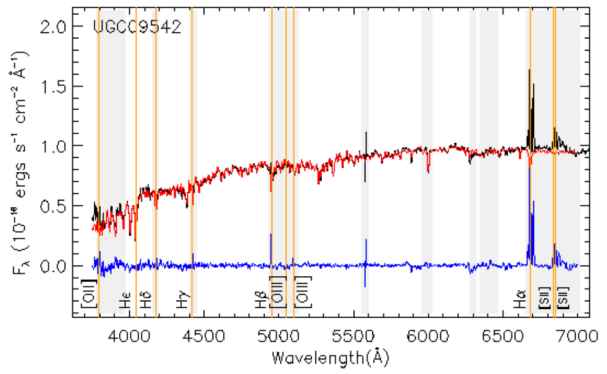
UGC09542
Wavelength(Å)

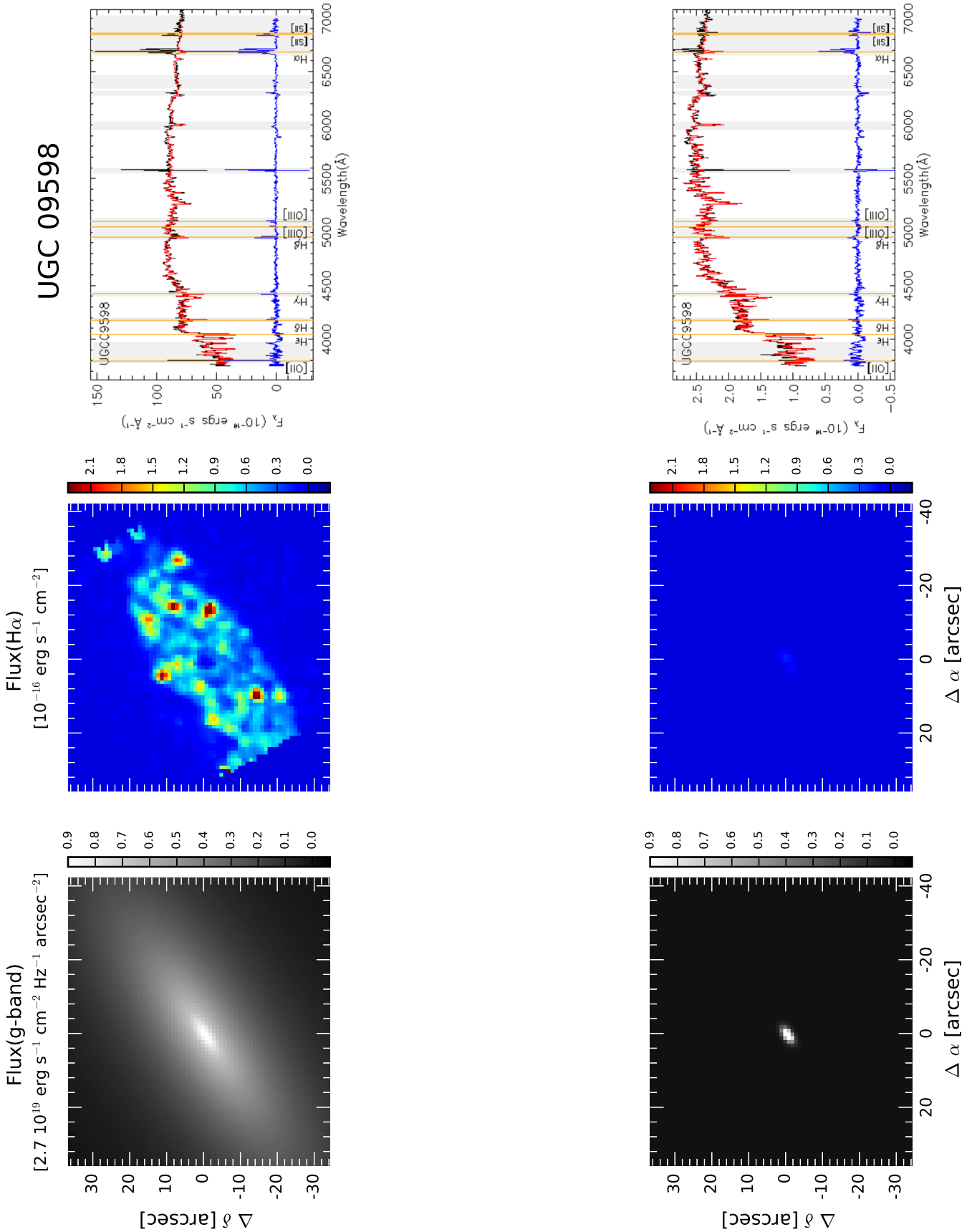
UGC 09598
Flux(g-band)
[2.7 10^19 erg s^-1 cm^-2 Hz^-1 arcsec^-2]
Flux(Hα)
[10^-16 erg s^-1 cm^-2]
Δ δ [arcsec]
Δ α [arcsec]
Wavelength(Å)
F_λ (10^-16 ergs s^-1 cm^-2 Å^-1)
UGC09598
[OII]
Hε
Hδ
Hγ
[OIII]
Hβ
[SII]
Hα

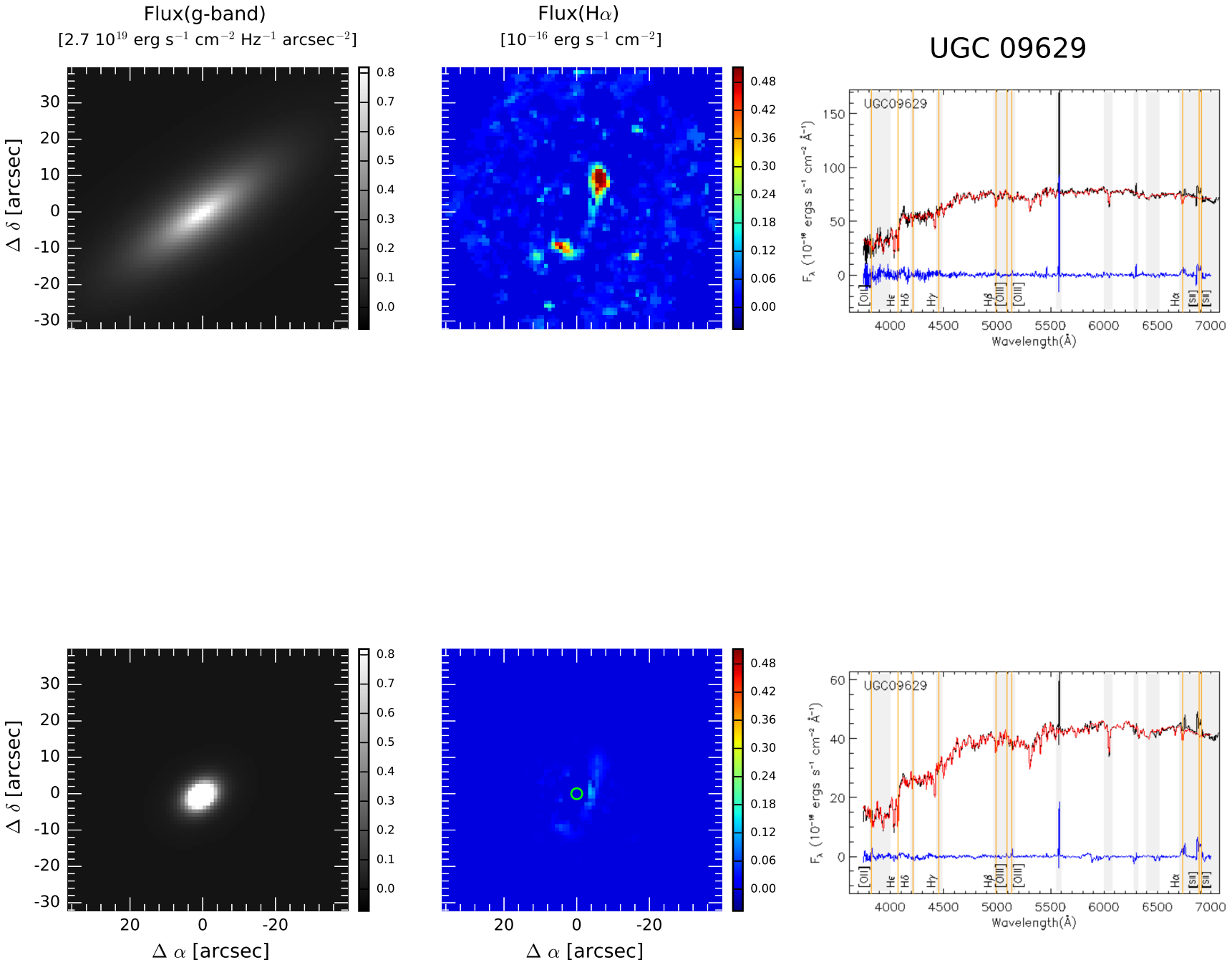
Flux(g-band)
[2.7 10^19 erg s^-1 cm^-2 Hz^-1 arcsec^-2]
Flux(Hα)
[10^-16 erg s^-1 cm^-2]
UGC 09629
Δ δ [arcsec]
Δ α [arcsec]
UGC09629
Wavelength(Å)
[OII]
Hε
Hδ
Hγ
Hβ
[OIII]
[OIII]
Hα
[SII]
[SII]

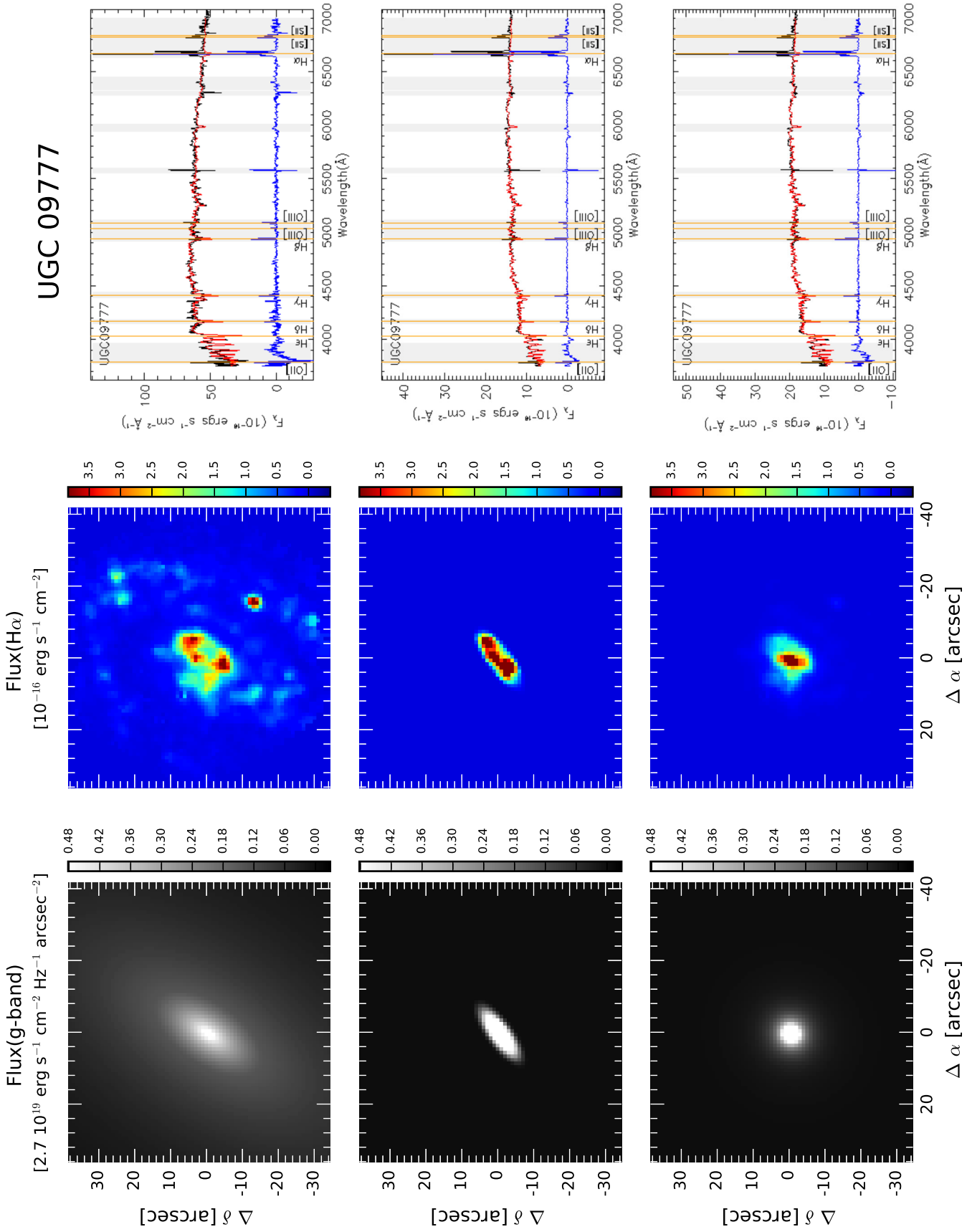
UGC 09777
Flux(g-band)
[2.7 10^19 erg s^-1 cm^-2 Hz^-1 arcsec^-2]
Flux(Hα)
[10^-16 erg s^-1 cm^-2]
Δ δ [arcsec]
Δ α [arcsec]
Wavelength(Å)
F_λ (10^-16 ergs s^-1 cm^-2 Å^-1)
UGC09777
[OII]
Hε
Hδ
Hγ
[OIII]
Hβ
[OIII]
Hα
[SII]
[SII]

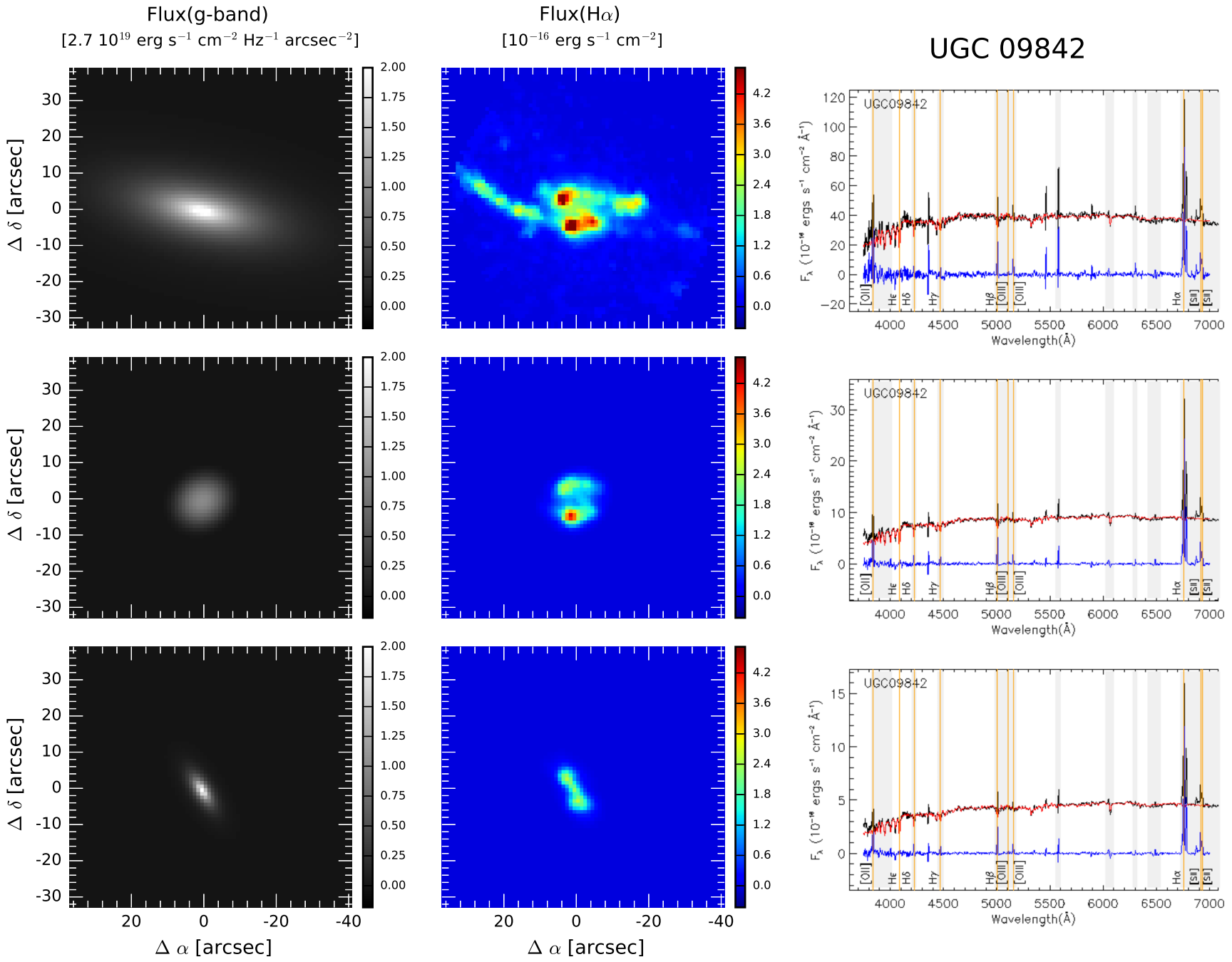
Flux(g-band)
[2.7 10^19 erg s^-1 cm^-2 Hz^-1 arcsec^-2]
Flux(Hα)
[10^-16 erg s^-1 cm^-2]
UGC 09842
Δ δ [arcsec]
Δ α [arcsec]
Wavelength(Å)
UGC09842
[OII]
Hε
Hδ
Hγ
Hβ
[OIII]
[OIII]
Hα
[SII]
[SII]

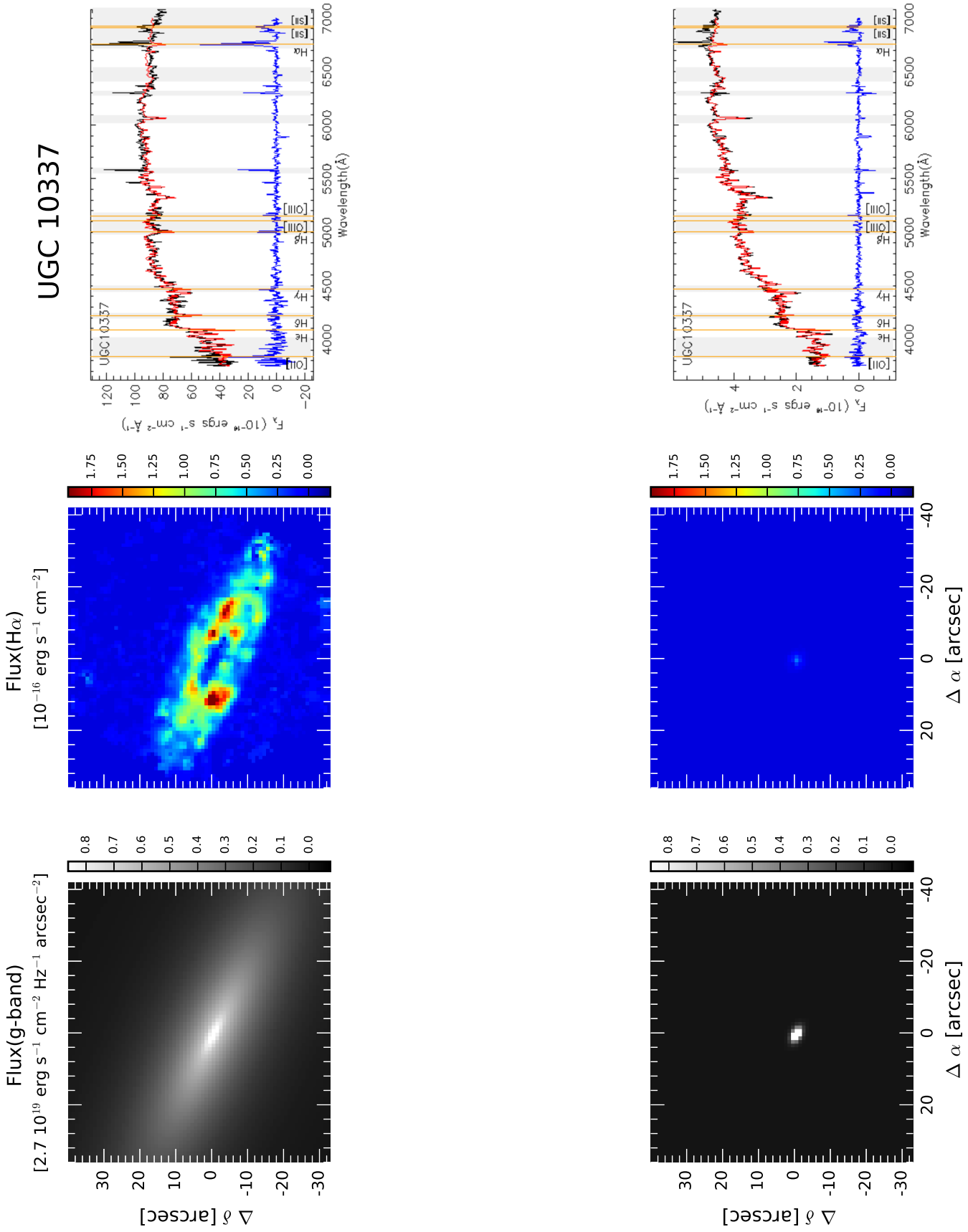
UGC 10337
Flux(g-band)
[2.7 10^19 erg s^-1 cm^-2 Hz^-1 arcsec^-2]
Flux(Hα)
[10^-16 erg s^-1 cm^-2]
Δ δ [arcsec]
Δ α [arcsec]
Wavelength(Å)
F_λ (10^-16 ergs s^-1 cm^-2 Å^-1)
UGC10337
[OII]
Hε
Hδ
Hγ
Hβ
[OIII]
[OIII]
Hα
[SII]
[SII]

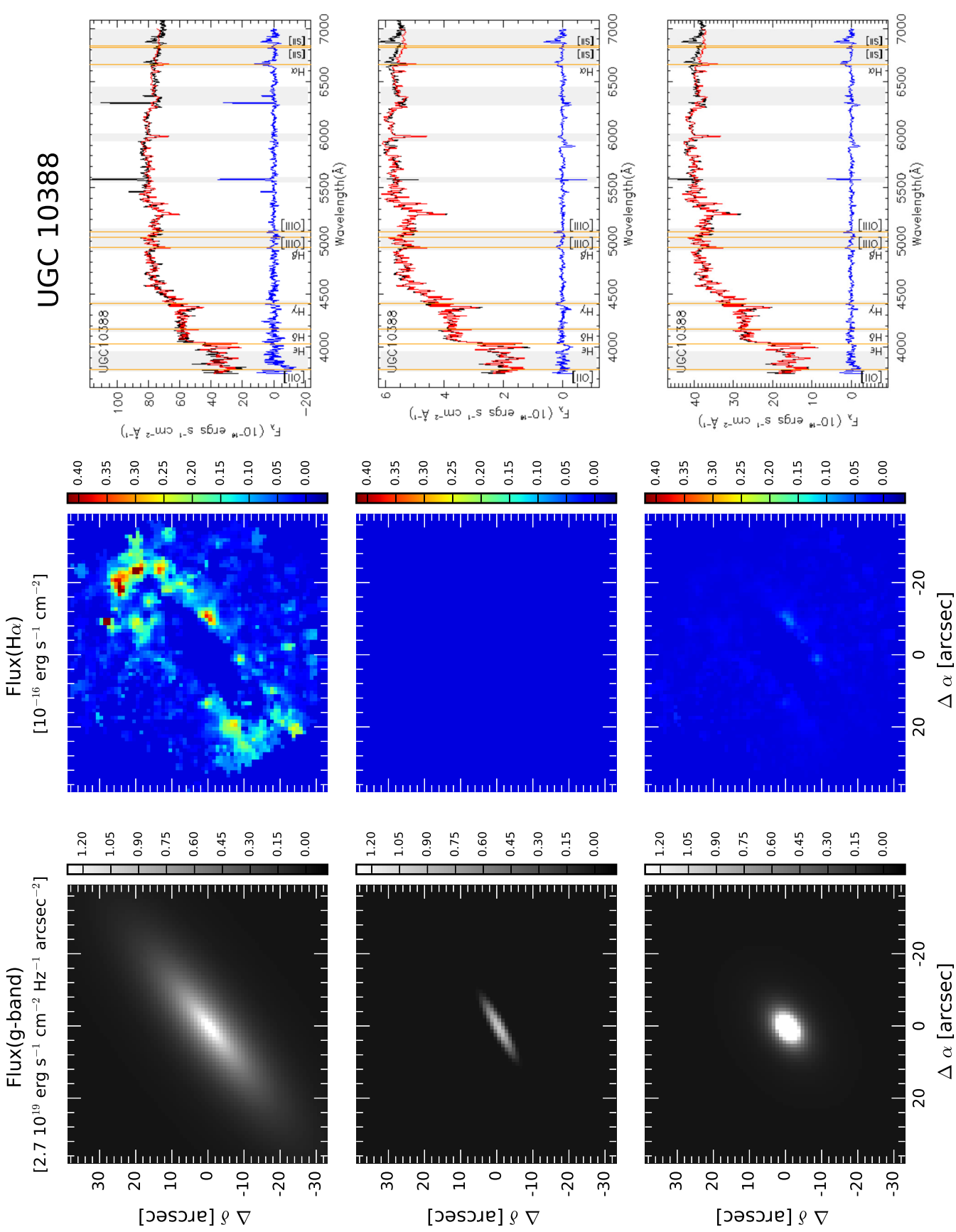
UGC 10388
Flux(g-band)
[2.7 10^19 erg s^-1 cm^-2 Hz^-1 arcsec^-2]
Flux(Hα)
[10^-16 erg s^-1 cm^-2]
Δ δ [arcsec]
Δ α [arcsec]
Wavelength(Å)
UGC10388
[OII]
Hε
Hδ
Hγ
[OIII]
Hβ
[OIII]
Hα
[SII]
[SII]

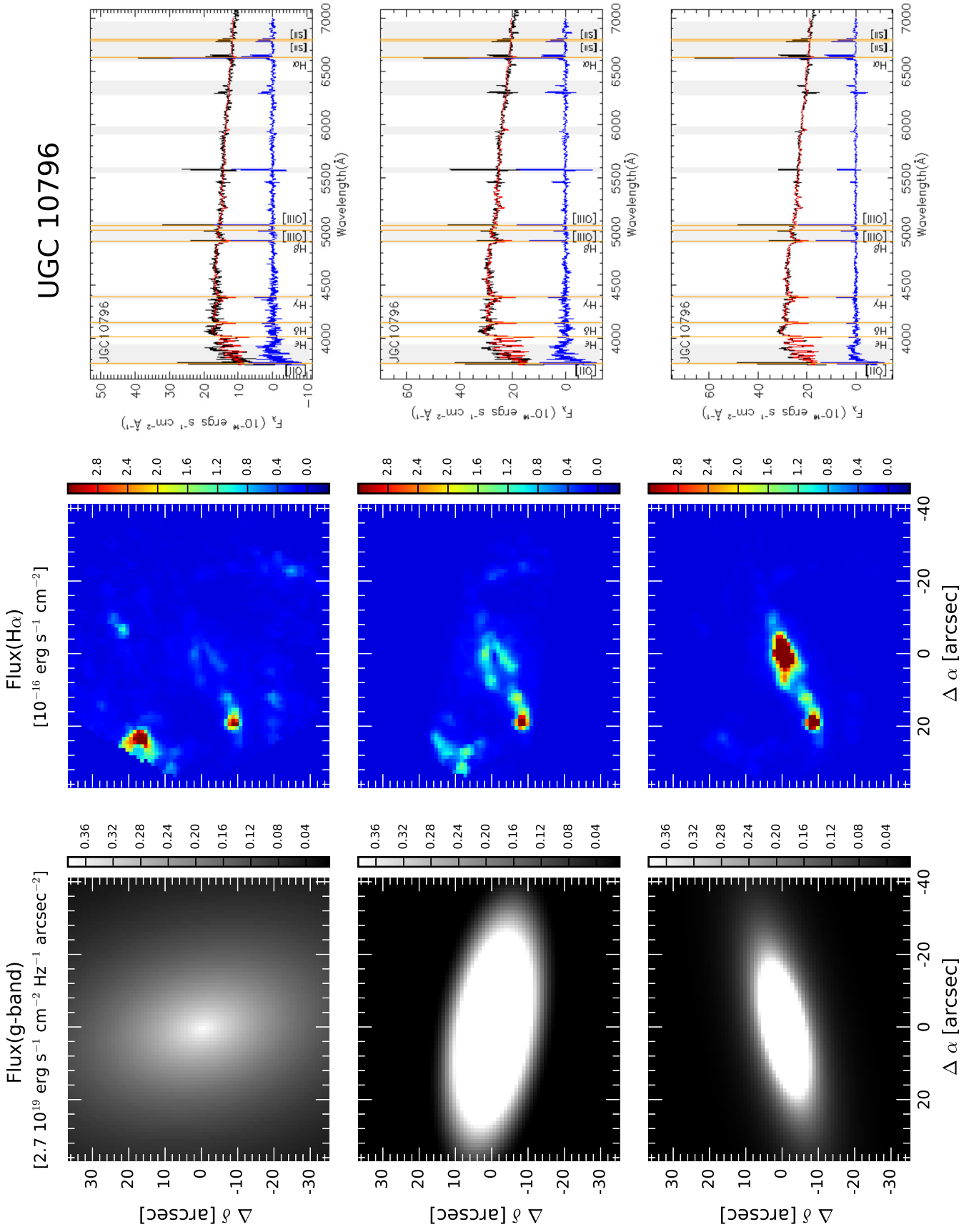
UGC 10796
Flux(g-band)
[2.7 10^19 erg s^-1 cm^-2 Hz^-1 arcsec^-2]
Flux(Hα)
[10^-16 erg s^-1 cm^-2]
Δ δ [arcsec]
Δ α [arcsec]
Wavelength(Å)
JGC10796
[OII]
Hε
Hδ
Hγ
Hβ
[OIII]
Hα
[SII]

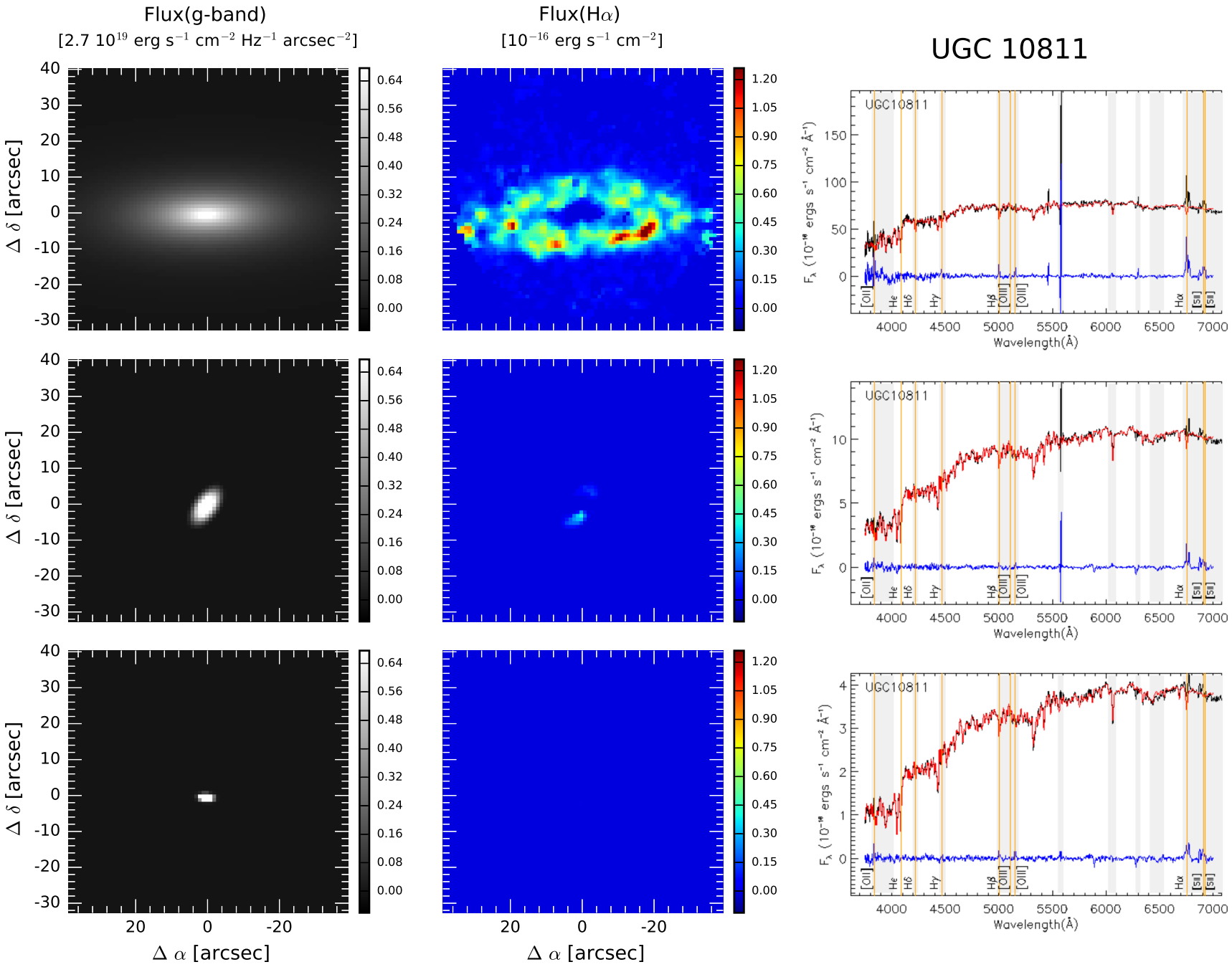
Flux(g-band)
[2.7 10^19 erg s^-1 cm^-2 Hz^-1 arcsec^-2]
Flux(Hα)
[10^-16 erg s^-1 cm^-2]
UGC 10811
Δ δ [arcsec]
Δ α [arcsec]
Wavelength(Å)
UGC10811
[OII]
Hε
Hδ
Hγ
Hβ
[OIII]
[OIII]
Hα
[SII]
[SII]

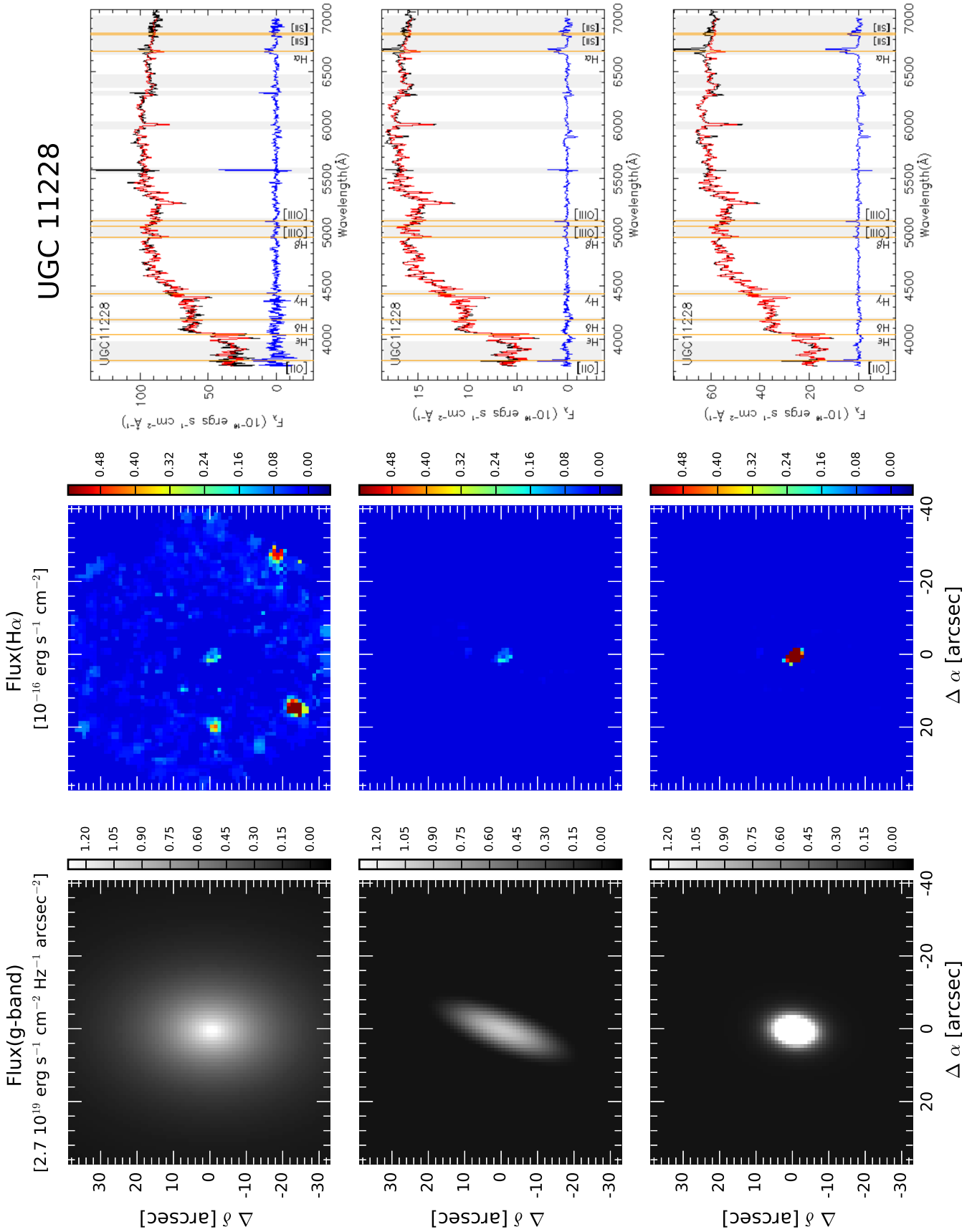
UGC 11228
Flux(g-band)
[2.7 10^19 erg s^-1 cm^-2 Hz^-1 arcsec^-2]
Flux(Hα)
[10^-16 erg s^-1 cm^-2]
Δ δ [arcsec]
Δ α [arcsec]
Wavelength(Å)
UGC11228
[OII]
Hε
Hδ
Hγ
Hβ
[OIII]
[OIII]
[SII]
[SII]
Hα

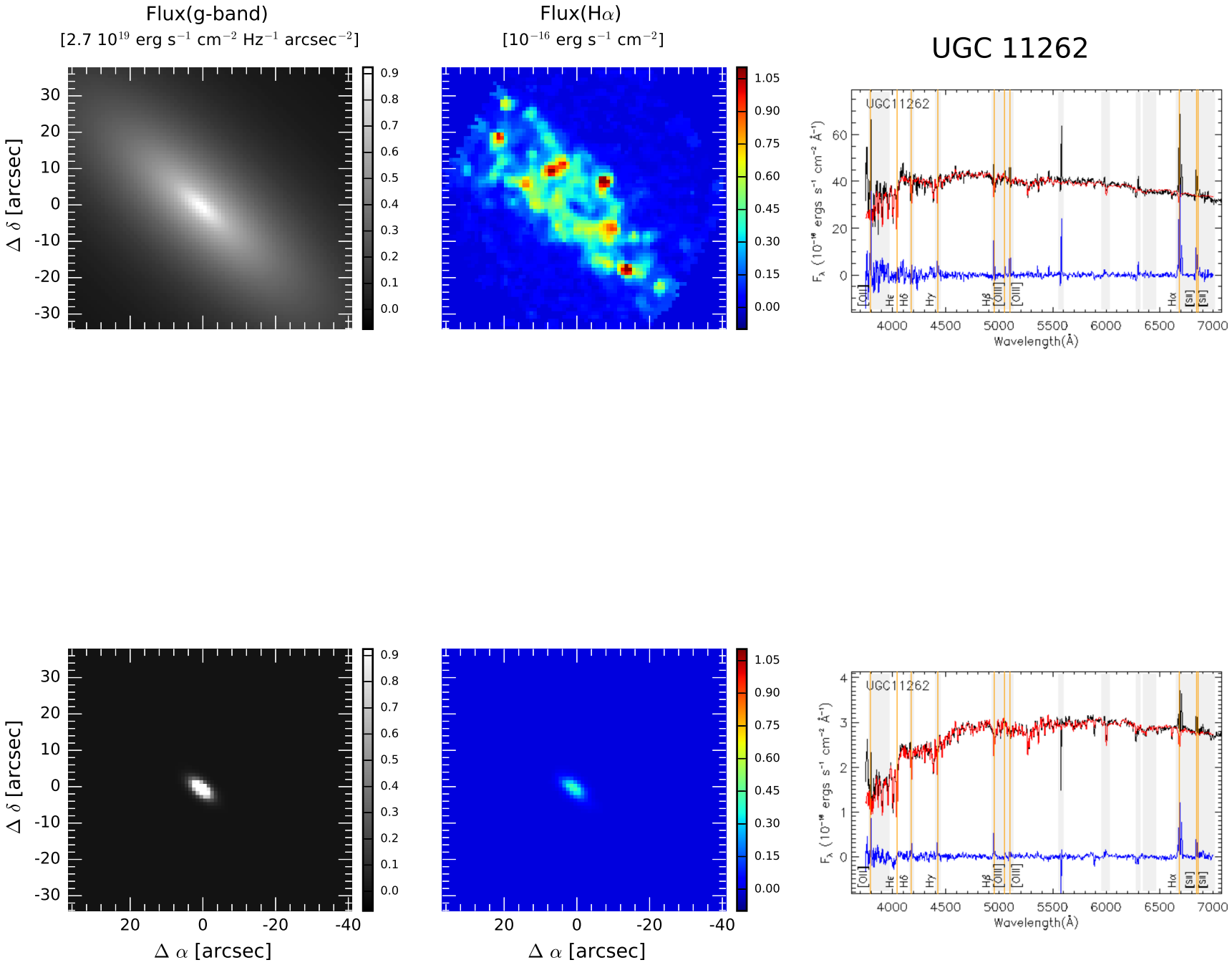
Flux(g-band)
[2.7 10^19 erg s^-1 cm^-2 Hz^-1 arcsec^-2]
Flux(Hα)
[10^-16 erg s^-1 cm^-2]
UGC 11262
Δ δ [arcsec]
Δ α [arcsec]
UGC11262
Wavelength(Å)
[OII]
Hε
Hδ
Hγ
Hβ
[OIII]
[OIII]
Hα
[SII]
[SII]

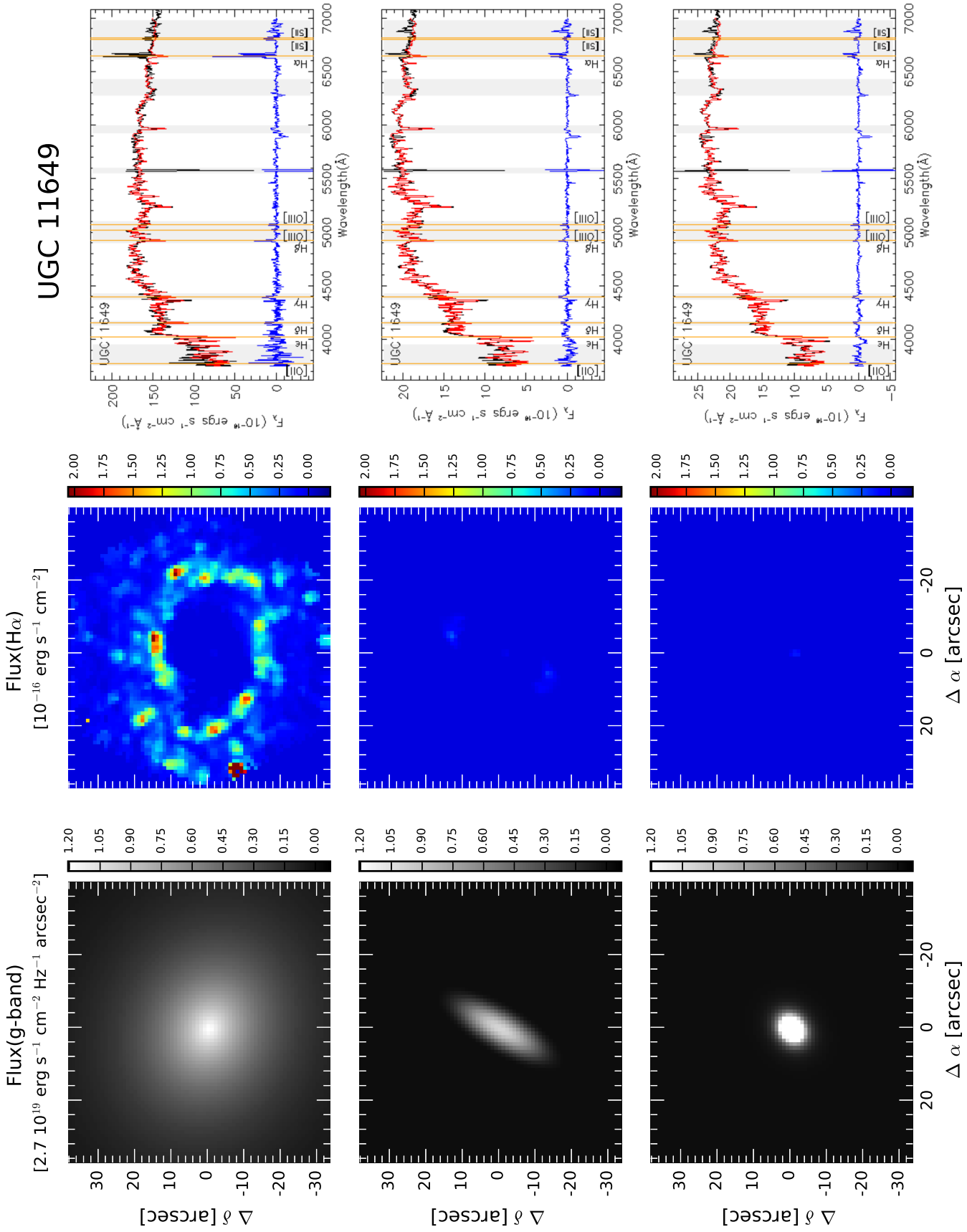
UGC 11649
Flux(g-band)
[2.7 10^19 erg s^-1 cm^-2 Hz^-1 arcsec^-2]
Flux(Hα)
[10^-16 erg s^-1 cm^-2]
Δ δ [arcsec]
Δ α [arcsec]
Wavelength(Å)
F_λ (10^-16 ergs s^-1 cm^-2 Å^-1)
UGC 1649
[OII]
Hε
Hδ
Hγ
[OIII]
Hβ
[OIII]
[SII]
[SII]
Hα

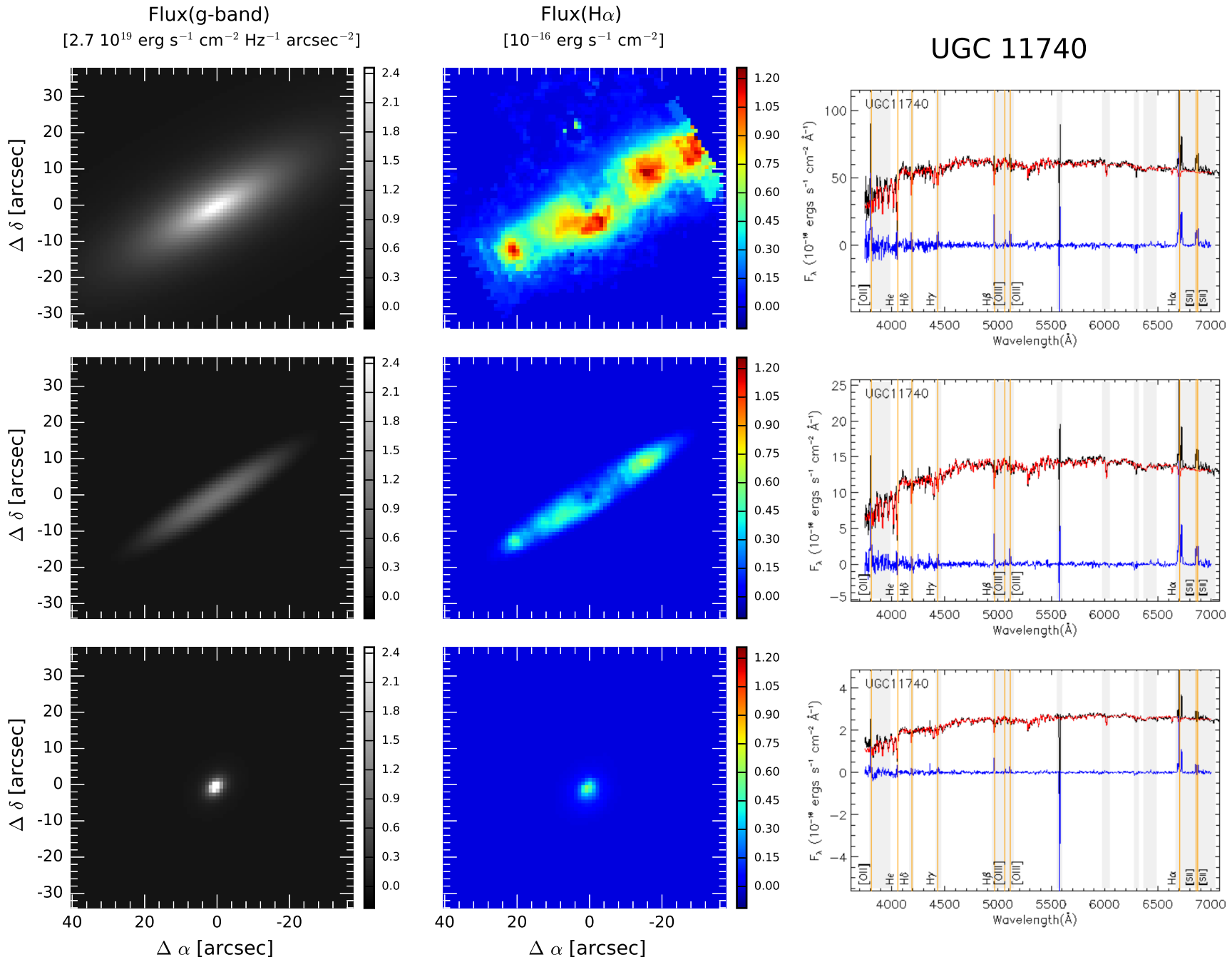
Flux(g-band)
[2.7 10^19 erg s^-1 cm^-2 Hz^-1 arcsec^-2]
Flux(Hα)
[10^-16 erg s^-1 cm^-2]
UGC 11740
Δ δ [arcsec]
Δ α [arcsec]
Wavelength(Å)
UGC11740
[OII]
Hε
Hδ
Hγ
Hβ
[OIII]
[OIII]
Hα
[SII]
[SII]

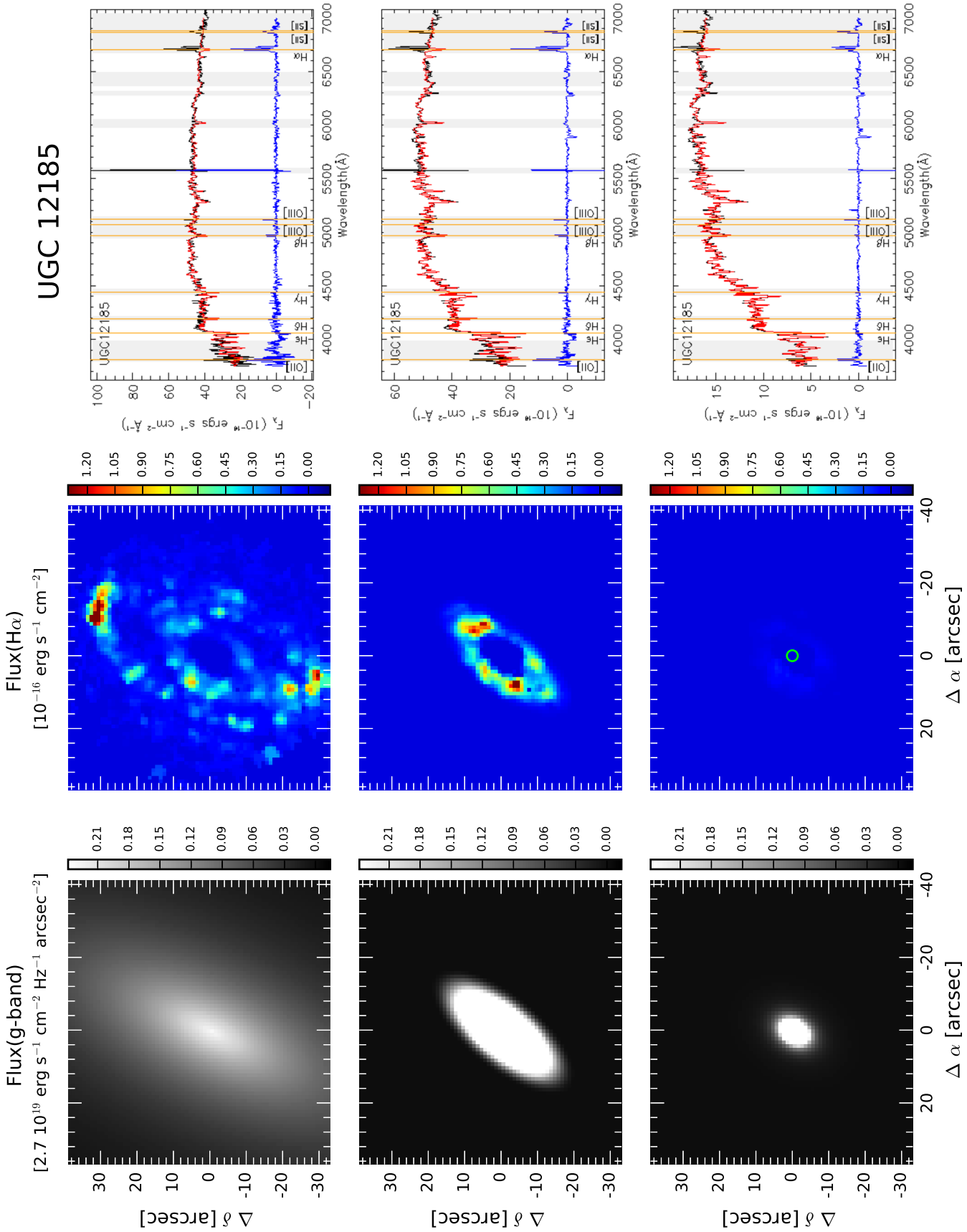
UGC 12185
Flux(g-band)
[2.7 10^19 erg s^-1 cm^-2 Hz^-1 arcsec^-2]
Flux(Hα)
[10^-16 erg s^-1 cm^-2]
Δ δ [arcsec]
Δ α [arcsec]
Wavelength(Å)
F_λ (10^-16 ergs s^-1 cm^-2 Å^-1)
UGC12185
[OII]
Hε
Hδ
Hγ
H8
[OIII]
[OIII]
[SII]
[SII]
Hα

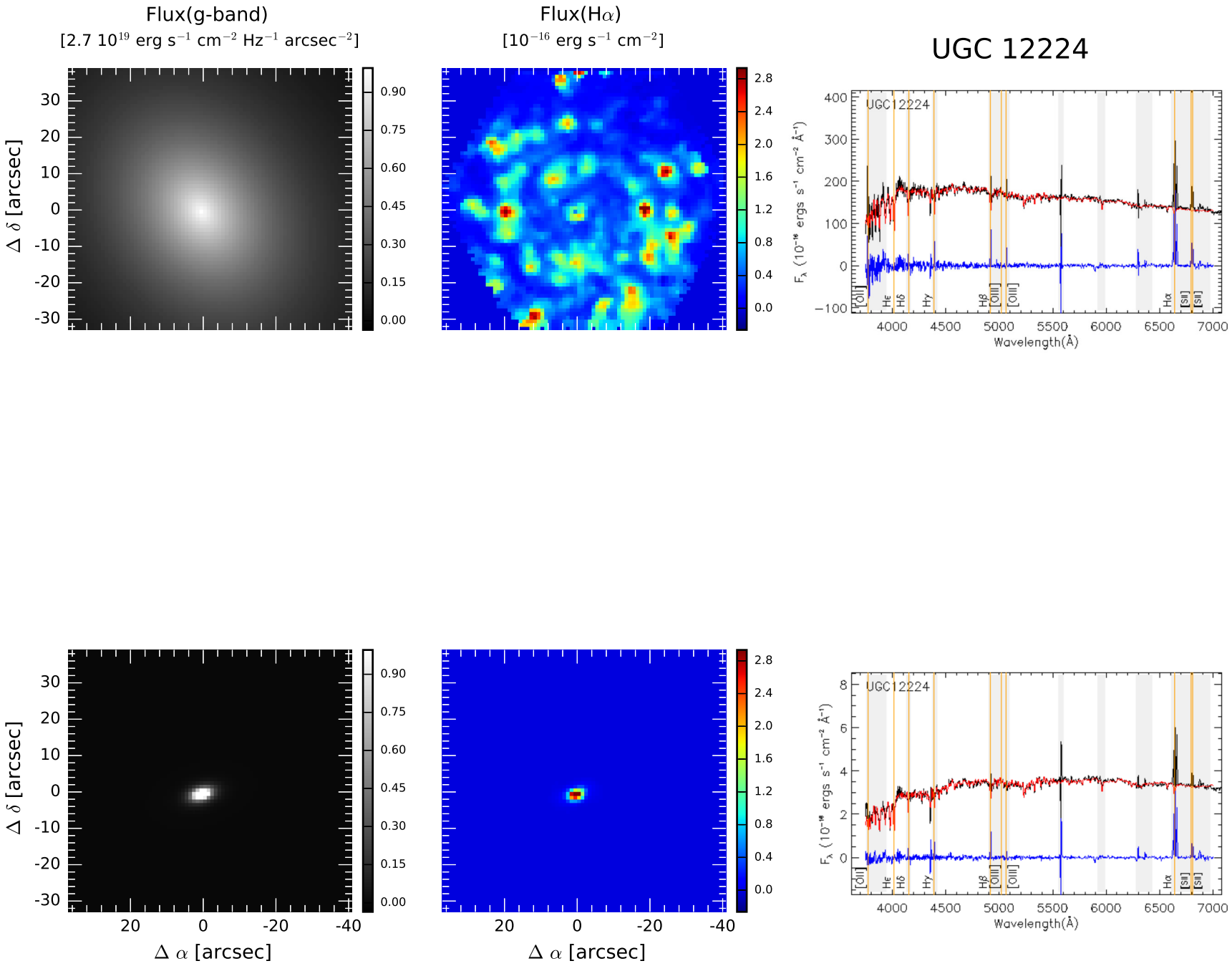
Flux(g-band)
[2.7 10^19 erg s^-1 cm^-2 Hz^-1 arcsec^-2]
Flux(Hα)
[10^-16 erg s^-1 cm^-2]
UGC 12224
Δ δ [arcsec]
Δ α [arcsec]
F_λ (10^-16 ergs s^-1 cm^-2 Å^-1)
Wavelength(Å)
UGC12224
[OII]
Hε
Hδ
Hγ
Hβ
[OIII]
[OIII]
Hα
[SII]
[SII]

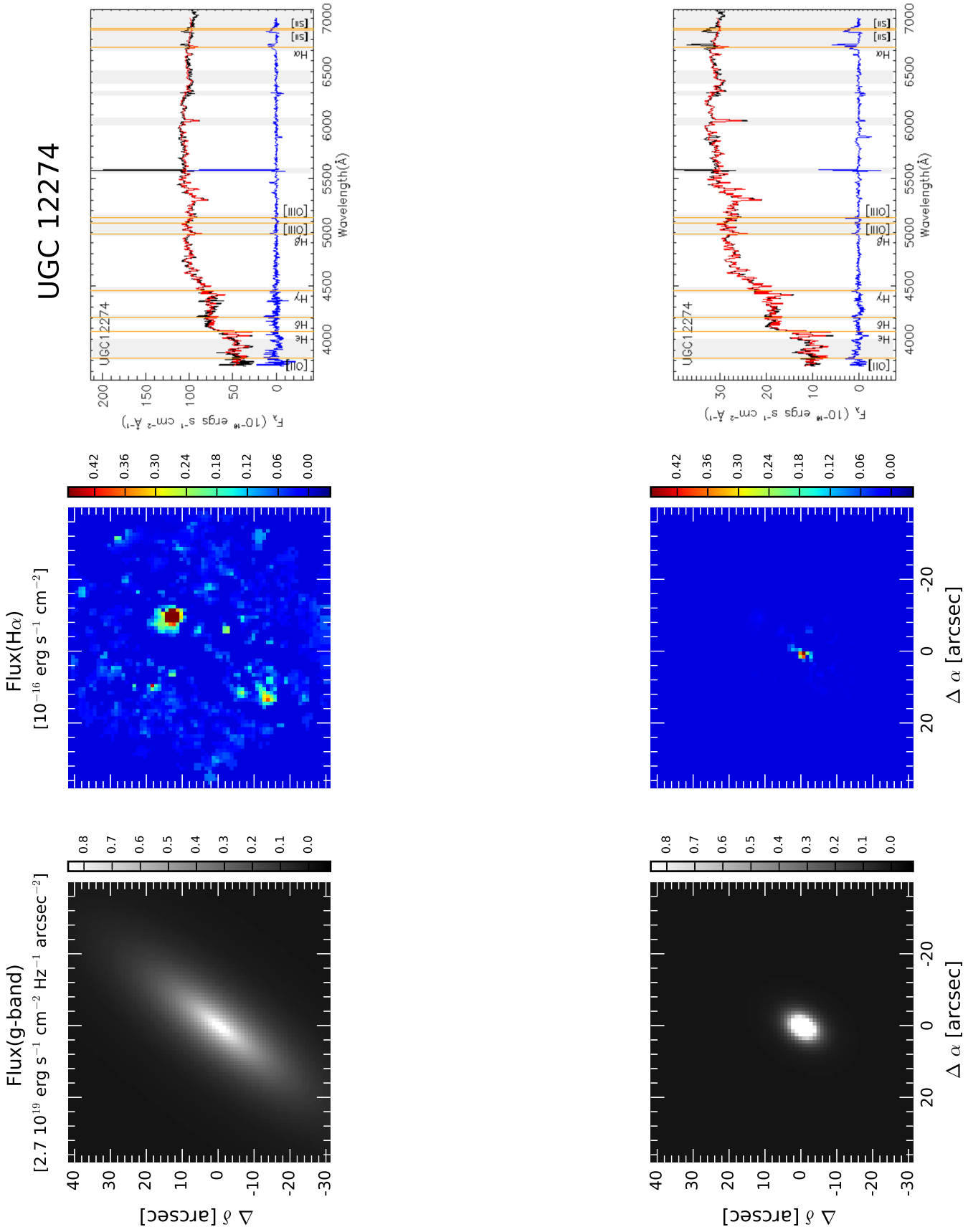
UGC 12274
Flux(g-band)
[2.7 10^19 erg s^-1 cm^-2 Hz^-1 arcsec^-2]
Flux(Hα)
[10^-16 erg s^-1 cm^-2]
Δ δ [arcsec]
Δ α [arcsec]
Wavelength(Å)
F_λ (10^-16 ergs s^-1 cm^-2 Å^-1)
UGC12274
[OII]
Hε
Hδ
Hγ
Hβ
[OIII]
[OIII]
Hα
[SII]
[SII]

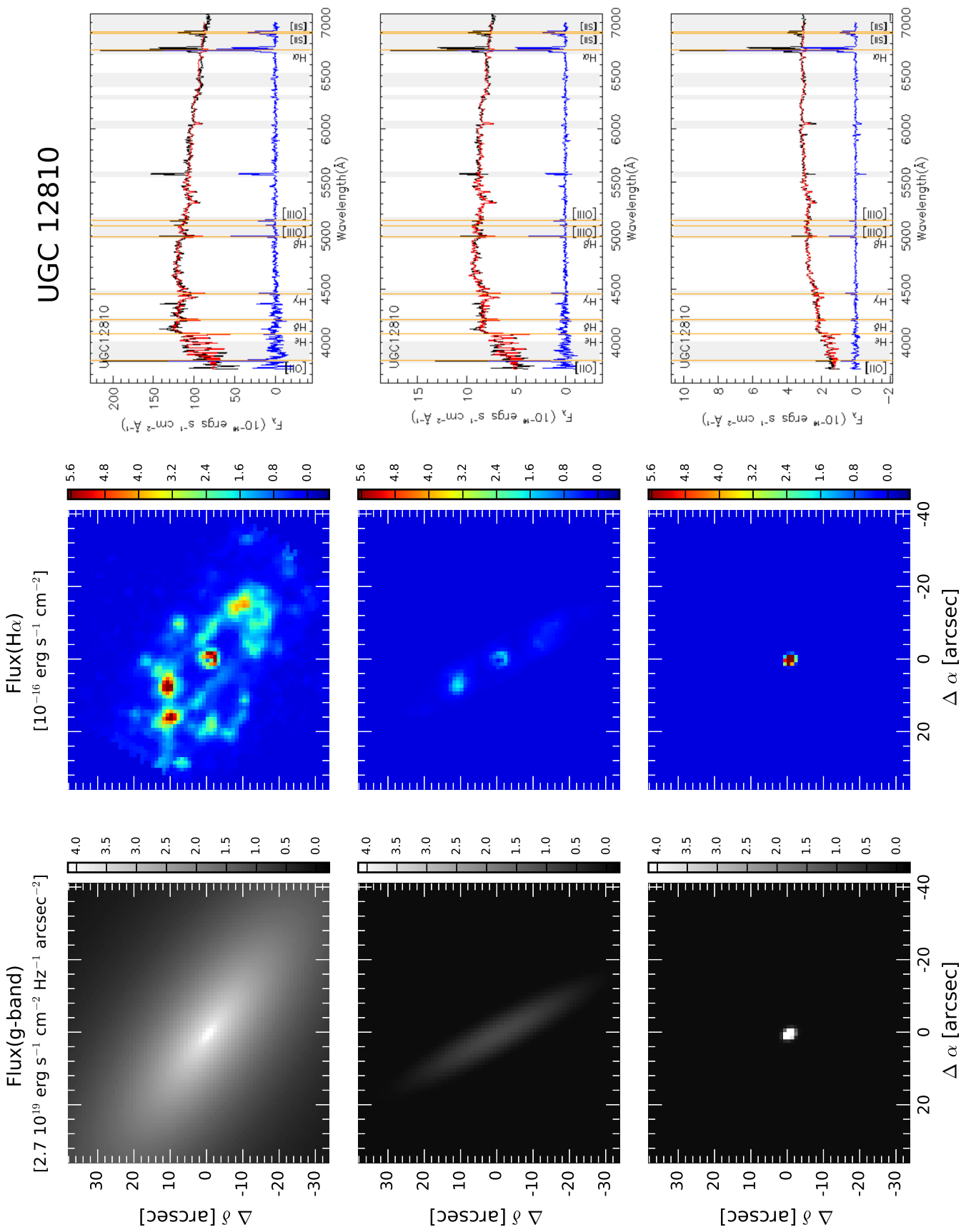
UGC 12810
Flux(g-band)
[2.7 10^19 erg s^-1 cm^-2 Hz^-1 arcsec^-2]
Flux(Hα)
[10^-16 erg s^-1 cm^-2]
Δ δ [arcsec]
Δ α [arcsec]
Wavelength(Å)
UGC12810
[OII]
Hδ
Hε
Hγ
Hβ
[OIII]
[OIII]
[SII]
[SII]
Hα

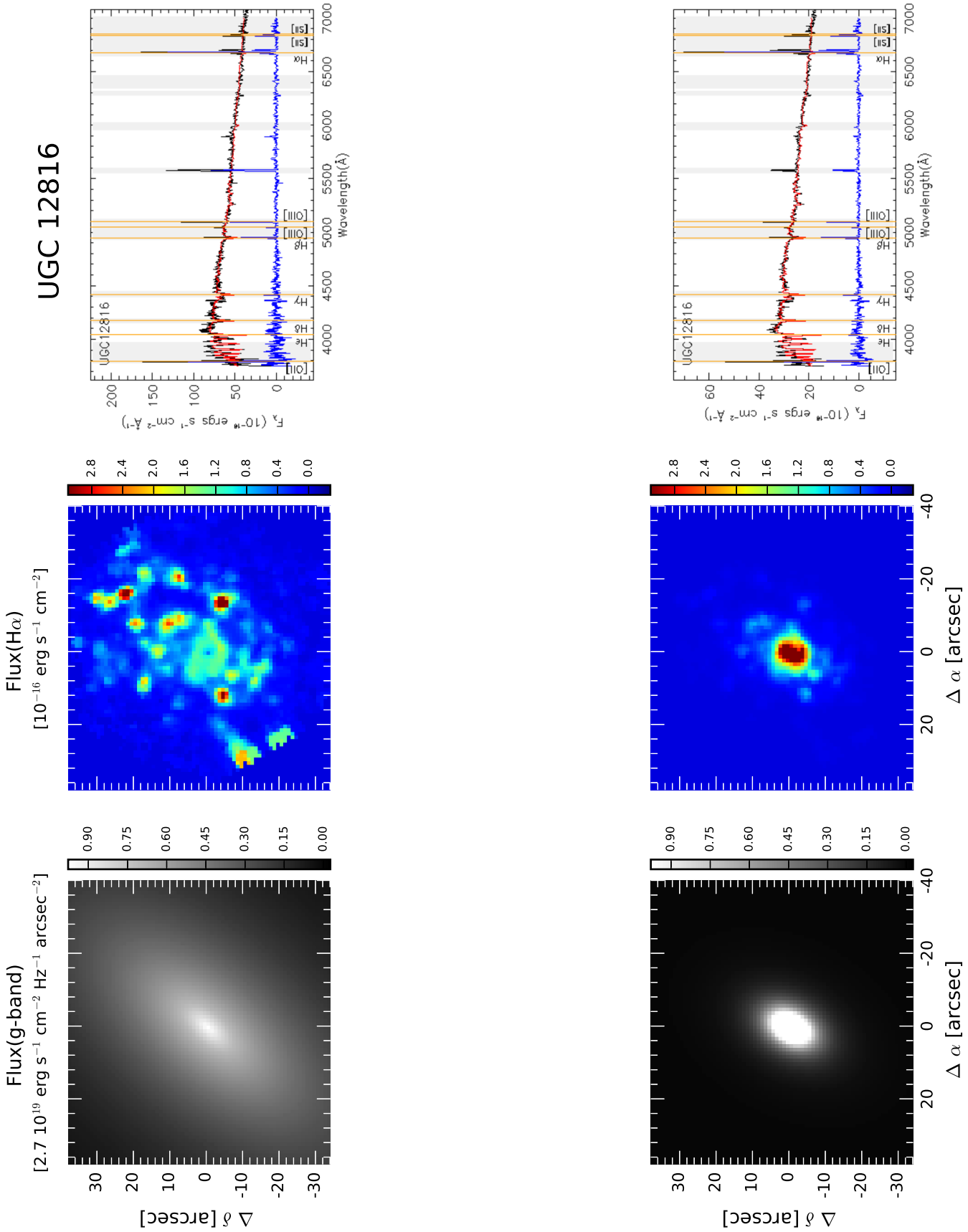
UGC 12816
Flux(g-band)
[2.7 10^19 erg s^-1 cm^-2 Hz^-1 arcsec^-2]
Flux(Hα)
[10^-16 erg s^-1 cm^-2]
Δ δ [arcsec]
Δ α [arcsec]
Wavelength(Å)
F_λ (10^-16 ergs s^-1 cm^-2 Å^-1)
UGC12816
[OII]
Hε
Hδ
Hγ
[OIII]
Hβ
[OIII]
[SII]
[SII]
Hα

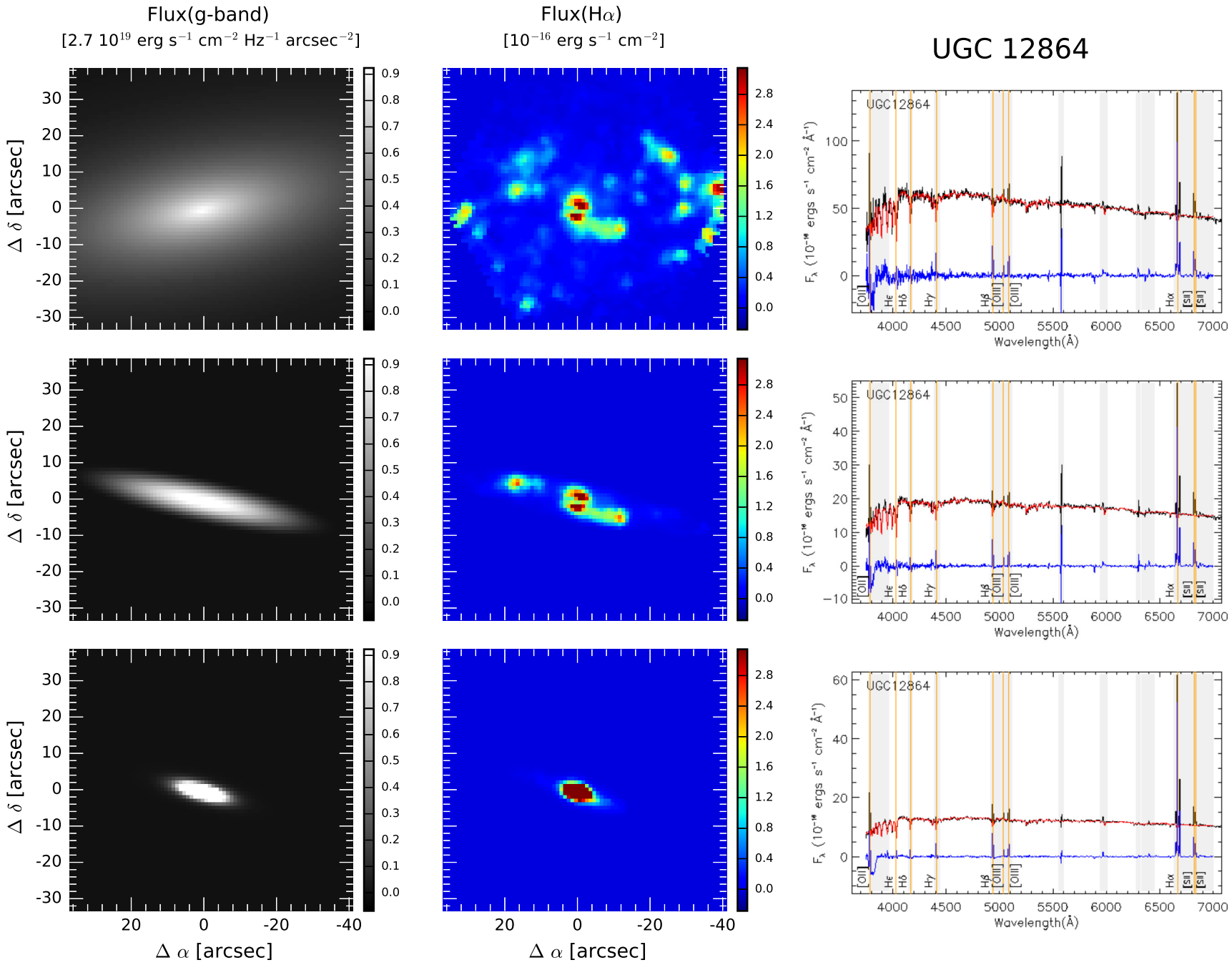
Flux(g-band)
[2.7 10^19 erg s^-1 cm^-2 Hz^-1 arcsec^-2]
Flux(Hα)
[10^-16 erg s^-1 cm^-2]
UGC 12864
Δ δ [arcsec]
Δ α [arcsec]
Wavelength(Å)
F_λ (10^-16 ergs s^-1 cm^-2 Å^-1)
[OII]
Hε
Hδ
Hγ
Hβ
[OIII]
[OIII]
Hα
[SII]
[SII]

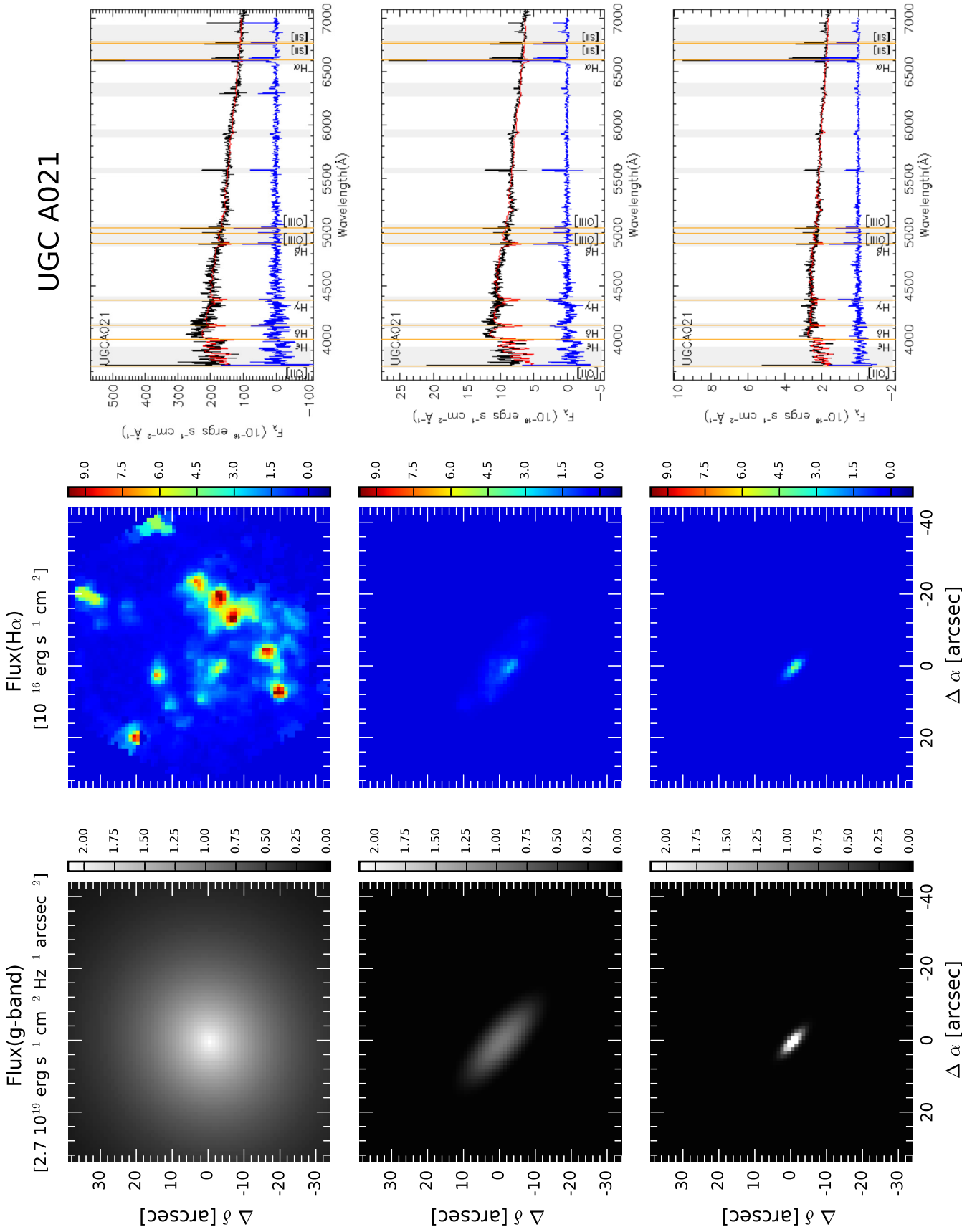
UGC A021
Flux(g-band)
[2.7 10^19 erg s^-1 cm^-2 Hz^-1 arcsec^-2]
Flux(Hα)
[10^-16 erg s^-1 cm^-2]
Δ δ [arcsec]
Δ α [arcsec]
Wavelength(Å)
UGCA021
[OII]
Hε
Hδ
Hγ
Hβ
[OIII]
[OIII]
Hα
[SII]
[SII]

Glossary

2MASS Two Micron All Sky Survey. Survey of the whole sky in the J, H and K_S bands (1.2 μm, 1.6 μm and 2.2 μm, respectively).

A&A Astronomy and Astrophysics.

AGN Active Galactic Nucleus. An unusually bright compact source in the center of a galaxy.

ApJ Astrophysical Journal.

B/D Bulge-to-disk ratio.

BLR Broad Line Region.

CALIFA Calar Alto Legacy Integral Field Area Survey.

CAHA Calar Alto Hispano Alemán Observatory.

DR Data Release.

D25 D25 refers to the isophote major axis at 25 magnitudes per square arcsecond in the SDSS r-band.

EW Equivalent Width. A measure of the total amount of energy subtracted from the continuous spectrum by an absorption line on a graph of relative intensity versus wavelength.

FIR Far-Infrared (from 25-40 μm to 200-350 μm).

FOV Field of view.

FUV Far-Ultraviolet (1350-1750 Å).

FWHM Full Width at Half Maximum. Measurement of the width of a function (such as a spectral line or a PSF) at half-maximum intensity.

GAMA Galaxy And Mass Assembly. A project to exploit the latest generation of ground-based and space-borne survey facilities to study cosmology and galaxy formation and evolution.

GALEX Galaxy Evolution Explorer. Space telescope that observes in the FUV and NUV bands.

GASP2D A new algorithm to perform the multi-component photometric decompositions.

GTC Gran Telescopio de Canarias

IC Index Catalogue.

IFS Integral Field Spectroscopy. Technique that allows gathering spatially resolved spectra of extended objects.

IFU Integral Field Unit. Instrument designed to perform two-dimensional spectroscopy.

IMF Initial Mass Function. Function describing the distribution of initial masses of newly born stars in terms of number of stars per mass interval.

IRAF Image Reduction and Analysis Facility. Software to analyze astronomical data.

IRAS Infrared Astronomical Satellite. An infrared space observatory that performed an all-sky survey at 12 μm, 25 μm, 60 μm and 100 μm.

IRX Infrared excess.

IRX-β Relation between the total-infrared to UV ratio (or infrared excess, IRX) and the slope of the UV spectrum (β).

IRSA Infrared Science Archive.

ΛCDM Lambda Cold Dark Matter. Cosmological model that includes dark energy and non-baryonic dark matter moving at non-relativistic speeds.

LINERs Low-Ionization Nuclear Emission-line Region galaxies

LIRG Luminous Infrared Galaxy. Galaxy whose total infrared luminosity is larger than 10^{11} solar luminosities.

LLAGN Low-luminosity active galactic nuclei.

LOS Line-of-sight (here refers to the LOS stellar velocity dispersions)

MaNGA Mapping Nearby Galaxies at APO.

MC Monte Carlo Simulations.

MCG Morphological Catalogue of Galaxies.

MIR Mid-Infrared (from 5 μm to 25-40 μm).

MS Main Sequence of galaxies. Relation between the SFR and the stellar mass of the galaxies.

NASA National Aeronautics and Space Administration.

NED NASA/IPAC Extragalactic Database. Database that compiles positions, basic data and bibliographic references for millions of extragalactic objects.

NGC New General Catalogue.

NIR Near-infrared (from 0.7-1 μm to 5 μm).

NUV Near-Ultraviolet (1750-2750 Å).

PA Position Angle. Angle between a galaxy's major axis and the north celestial pole, measured counterclockwise when north is up and east is left.

PMAS Postdam Multi-Aperture Spectrophotometer mounted on the 3.5m telescope at the Calar Alto observatory (Spain).

PPaK Pmas fiber PAcK. Integral field unit integrated within PMAS that consists of an hexagonal bundle with 331 optical fibers.

RC3 Third Reference Catalogue of Bright Galaxies. Catalog of thousands of nearby galaxies in the optical range.

SAURON Spectroscopic Areal Unit for Research on Optical Nebulae Project at WHT.

SAMI Sydney university AAO MOS IFU.

SDSS Sloan Digital Sky Survey. A survey that has provided optical and imaging spectra of more than a quarter of the sky.

SED Spectral Energy Distribution. The distribution of an object's luminosity among various wavelengths.

SF Star-forming galaxy.

SFR Star Formation Rate. Mass of gas transformed into stars per unit of time.

S/N Signal-to-noise ratio.

sSFR Specific Star Formation Rate. Ratio of the SFR and the total stellar mass.

SSP Simple Stellar Population. It consists of a number of stars born at the same time and having the same initial element composition.

TIR Total Infrared (3-1100 μm).

TF Tully-Fisher. Empirical relation between a galaxy's luminosity and its rotational velocity.

UGC Uppsala General Catalogue.

ULIRG Ultra-Luminous Infrared Galaxy. Galaxy whose total infrared luminosity is larger than 10^{12} solar luminosities.

WISE Wide-field Infrared Survey Explorer. It surveyed the entire sky at MIR wavelengths 3.4, 4.6, 12, and 22 μm.

This page was left intentionally blank.

Bibliography

Abadi, M. G., Moore, B., & Bower, R. G. 1999, MNRAS, 308, 947

Abazajian, K. N., Adelman-McCarthy, J. K., Agüeros, M. A., et al. 2009, ApJS, 182, 543

Abramson, L. E., Kelson, D. D., Dressler, A., et al. 2014, ApJ, 785, L36

Aguerri, J. A. L., Elias-Rosa, N., Corsini, E. M., & Muñoz-Tuñón, C. 2005, A&A, 434, 109

Alexander, D. M. & Hickox, R. C. 2012, New A Rev., 56, 93

Alonso-Herrero, A., Colina, L., Packham, C., et al. 2006a, ApJ, 652, L83

Alonso-Herrero, A., Rieke, G. H., Rieke, M. J., et al. 2006b, ApJ, 650, 835

Athanassoula, E. 1992, MNRAS, 259, 345

Bacon, R., Accardo, M., Adjali, L., et al. 2010, in Proc. SPIE, Vol. 7735, Ground-based and Airborne Instrumentation for Astronomy III, 773508

Bacon, R., Copin, Y., Monnet, G., et al. 2001, MNRAS, 326, 23

Baldry, I. K., Balogh, M. L., Bower, R. G., et al. 2006, MNRAS, 373, 469

Baldwin, J. A., Phillips, M. M., & Terlevich, R. 1981, PASP, 93, 5

Barnes, J. E. & Hernquist, L. E. 1991, ApJ, 370, L65

Barton, E. J., Geller, M. J., & Kenyon, S. J. 2000, ApJ, 530, 660

Beichman, C. A., Neugebauer, G., Habing, H. J., Clegg, P. E., & Chester, T. J., eds. 1988, Infrared astronomical satellite (IRAS) catalogs and atlases. Volume 1: Explanatory supplement, Vol. 1

Bershady, M. A., Andersen, D. R., Harker, J., Ramsey, L. W., & Verheijen, M. A. W. 2004, PASP, 116, 565

Bershady, M. A., Andersen, D. R., Verheijen, M. A. W., et al. 2005, ApJS, 156, 311

Bershady, M. A., Verheijen, M. A. W., Swaters, R. A., et al. 2010, ApJ, 716, 198

Bialas, D., Lisker, T., Olczak, C., Spurzem, R., & Kotulla, R. 2015, A&A, 576, A103

Bigiel, F., Leroy, A., Walter, F., et al. 2008, AJ, 136, 2846

Binggeli, B., Sandage, A., & Tammann, G. A. 1988, ARA&A, 26, 509

Blanc, G. A., Heiderman, A., Gebhardt, K., Evans, II, N. J., & Adams, J. 2009, ApJ, 704, 842

Blanc, G. A., Weinzirl, T., Song, M., et al. 2013, AJ, 145, 138

Bland-Hawthorn, J. 2015, in IAU Symposium, Vol. 309, Galaxies in 3D across the Universe, ed. B. L. Ziegler, F. Combes, H. Dannerbauer, & M. Verdugo, 21–28

Blanton, M. R., Hogg, D. W., Bahcall, N. A., et al. 2003, ApJ, 592, 819

Book, L. G. & Benson, A. J. 2010, ApJ, 716, 810

Bouwens, R. J., Illingworth, G. D., Franx, M., & Ford, H. 2007, ApJ, 670, 928

Bouwens, R. J., Illingworth, G. D., Oesch, P. A., et al. 2011, ApJ, 737, 90

Bouwens, R. J., Illingworth, G. D., Oesch, P. A., et al. 2015, ApJ, 803, 34

Bower, R. G., Benson, A. J., & Crain, R. A. 2012, MNRAS, 422, 2816

Brammer, G. B., van Dokkum, P. G., Franx, M., et al. 2012, ApJS, 200, 13

Brinchmann, J., Charlot, S., White, S. D. M., et al. 2004, MNRAS, 351, 1151

Brocklehurst, M. 1972, MNRAS, 157, 211

Brown, M. J. I., Moustakas, J., Smith, J.-D. T., et al. 2014, ApJS, 212, 18

Brown, T. M., Ferguson, H. C., Davidsen, A. F., & Dorman, B. 1997, ApJ, 482, 685

Bruzual, G. & Charlot, S. 2003, MNRAS, 344, 1000

Bryant, J. J. & Bland-Hawthorn, J. 2016, in Astronomical Society of the Pacific Conference Series, Vol. 507, Multi-Object Spectroscopy in the Next Decade: Big Questions, Large Surveys, and Wide Fields, ed. I. Skillen, M. Barcells, & S. Trager, 291

Buat, V., Iglesias-Páramo, J., Seibert, M., et al. 2005, ApJ, 619, L51

Bundy, K., Bershady, M. A., Law, D. R., et al. 2015, ApJ, 798, 7

Burgarella, D., Buat, V., & Iglesias-Páramo, J. 2005, MNRAS, 360, 1413

Calzetti, D. 1997, in American Institute of Physics Conference Series, Vol. 408, American Institute of Physics Conference Series, ed. W. H. Waller, 403–412

Calzetti, D. 2013, Star Formation Rate Indicators, ed. J. Falcón-Barroso & J. H. Knapen, 419

Calzetti, D., Armus, L., Bohlin, R. C., et al. 2000, ApJ, 533, 682

Calzetti, D., Kennicutt, R. C., Engelbracht, C. W., et al. 2007, ApJ, 666, 870

Calzetti, D., Wu, S.-Y., Hong, S., et al. 2010, ApJ, 714, 1256

Cano-Díaz, M., Sánchez, S. F., Zibetti, S., et al. 2016, ApJ, 821, L26

Cappellari, M. & Copin, Y. 2003, MNRAS, 342, 345

Cappellari, M., Emsellem, E., Krajnović, D., et al. 2011, MNRAS, 413, 813

Cardelli, J. A., Clayton, G. C., & Mathis, J. S. 1989, ApJ, 345, 245

Carles, C., Martel, H., Ellison, S. L., & Kawata, D. 2016, MNRAS, 463, 1074

Carniani, S., Marconi, A., Maiolino, R., et al. 2016, A&A, 591, A28

Castillo-Morales, A., Gallego, J., Pérez-Gallego, J., et al. 2011, MNRAS, 411, 1819

Castro, A., Miyaji, T., Shirahata, M., et al. 2014, PASJ

Catalán-Torrecilla, C., Gil de Paz, A., Castillo-Morales, A., et al. 2015, A&A, 584, A87

Chabrier, G. 2003, PASP, 115, 763

Charlot, S. & Fall, S. M. 2000, ApJ, 539, 718

Chary, R. & Elbaz, D. 2001, ApJ, 556, 562

Cheung, E., Athanassoula, E., Masters, K. L., et al. 2013, ApJ, 779, 162

Chilingarian, I. V., Cayatte, V., Durret, F., et al. 2008, A&A, 486, 85

Chung, A., van Gorkom, J. H., Kenney, J. D. P., Crowl, H., & Vollmer, B. 2009, AJ, 138, 1741

Cid Fernandes, R., Stasińska, G., Mateus, A., & Vale Asari, N. 2011, MNRAS, 413, 1687

Cid Fernandes, R., Stasińska, G., Schlickmann, M. S., et al. 2010, MNRAS, 403, 1036

Cluver, M. E., Jarrett, T. H., Hopkins, A. M., et al. 2014, ApJ, 782, 90

Coelho, P. & Gadotti, D. A. 2011, ApJ, 743, L13

Conselice, C. J. 2003, ApJS, 147, 1

Cortese, L., Boselli, A., Franzetti, P., et al. 2008, MNRAS, 386, 1157

Cortese, L., Catinella, B., Boissier, S., Boselli, A., & Heinis, S. 2011, MNRAS, 415, 1797

Cowie, L. L., Songaila, A., Hu, E. M., & Cohen, J. G. 1996, AJ, 112, 839

Croom, S. M., Lawrence, J. S., Bland-Hawthorn, J., et al. 2012, MNRAS, 421, 872

Daddi, E., Dickinson, M., Morrison, G., et al. 2007, ApJ, 670, 156

Dale, D. A. & Helou, G. 2002, ApJ, 576, 159

Dalla Vecchia, C. & Schaye, J. 2008, MNRAS, 387, 1431

Dalton, G., Trager, S., Abrams, D. C., et al. 2014, in Proc. SPIE, Vol. 9147, Ground-based and Airborne Instrumentation for Astronomy V, 91470L

de Jong, T., Clegg, P. E., Rowan-Robinson, M., et al. 1984, ApJ, 278, L67

De Propris, R., Colless, M., Driver, S. P., et al. 2003, MNRAS, 342, 725

de Souza, R. E., Gadotti, D. A., & dos Anjos, S. 2004, ApJS, 153, 411

de Vaucouleurs, G., de Vaucouleurs, A., Corwin, Jr., H. G., et al. 1991, Third Reference Catalogue of Bright Galaxies. Volume I: Explanations and references. Volume II: Data for galaxies between 0^h and 12^h. Volume III: Data for galaxies between 12^h and 24^h.

de Zeeuw, P. T., Bureau, M., Emsellem, E., et al. 2002, MNRAS, 329, 513

Dekel, A., Birnboim, Y., Engel, G., et al. 2009, Nature, 457, 451

Devereux, N. 1987, ApJ, 323, 91

Díaz-Santos, T., Alonso-Herrero, A., Colina, L., et al. 2010, ApJ, 711, 328

Díaz-Santos, T., Alonso-Herrero, A., Colina, L., et al. 2008, ApJ, 685, 211

Domínguez Sánchez, H., Bongiovanni, A., Lara-López, M. A., et al. 2014, MNRAS, 441, 2

Draine, B. T. & Li, A. 2007, ApJ, 657, 810

Dressler, A. 1980, ApJ, 236, 351

Driver, S. P., Norberg, P., Baldry, I. K., et al. 2009, Astronomy and Geophysics, 50, 5.12

Duarte Puertas, S., Vilchez, J. M., Iglesias-Paramo, J., et al. 2016, ArXiv e-prints

Efremova, B. V., Bianchi, L., Thilker, D. A., et al. 2011, ApJ, 730, 88

Elbaz, D., Daddi, E., Le Borgne, D., et al. 2007, A&A, 468, 33

Elbaz, D., Dickinson, M., Hwang, H. S., et al. 2011, A&A, 533, A119

Ellison, S. L., Nair, P., Patton, D. R., et al. 2011, MNRAS, 416, 2182

Emsellem, E., Cappellari, M., Krajnović, D., et al. 2011, MNRAS, 414, 888

Emsellem, E., Cappellari, M., Krajnović, D., et al. 2007, MNRAS, 379, 401

Erwin, P. 2015, ApJ, 799, 226

Faber, S. M. & Jackson, R. E. 1976, ApJ, 204, 668

Falcón-Barroso, J., Lyubenova, M., van de Ven, G., et al. 2017, A&A, 597, A48

Falcón-Barroso, J., van de Ven, G., Peletier, R. F., et al. 2011, MNRAS, 417, 1787

Ferrarese, L. & Merritt, D. 2000, ApJ, 539, L9

Fisher, D. B. 2006, ApJ, 642, L17

Fisher, D. B. & Drory, N. 2008, AJ, 136, 773

Fisher, D. B. & Drory, N. 2016, Galactic Bulges, 418, 41

Florido, E., Zurita, A., Pérez, I., et al. 2015, A&A, 584, A88

Folkes, S., Ronen, S., Price, I., et al. 1999, MNRAS, 308, 459

Förster Schreiber, N. M., Genzel, R., Bouché, N., et al. 2009, ApJ, 706, 1364

Förster Schreiber, N. M., Shapley, A. E., Erb, D. K., et al. 2011a, ApJ, 731, 65

Förster Schreiber, N. M., Shapley, A. E., Genzel, R., et al. 2011b, ApJ, 739, 45

Fumagalli, M., Patel, S. G., Franx, M., et al. 2012, ApJ, 757, L22

Gabor, J. M. & Bournaud, F. 2014, MNRAS, 441, 1615

Gadotti, D. A. 2009, MNRAS, 393, 1531

Gallego, J., Zamorano, J., Aragon-Salamanca, A., & Rego, M. 1995, ApJ, 455, L1

Gallego, J., Zamorano, J., Rego, M., Alonso, O., & Vitores, A. G. 1996, A&AS, 120, 323

García-Benito, R., Zibetti, S., Sánchez, S. F., et al. 2015, A&A, 576, A135

García-Lorenzo, B., Márquez, I., Barrera-Ballesteros, J. K., et al. 2015, A&A, 573, A59

García-Rojas, J., Peña, M., Flores-Durán, S., & Hernández-Martínez, L. 2016, A&A, 586, A59

Gebhardt, K., Bender, R., Bower, G., et al. 2000, ApJ, 539, L13

Genzel, R., Burkert, A., Bouché, N., et al. 2008, ApJ, 687, 59

Genzel, R., Förster Schreiber, N. M., Rosario, D., et al. 2014, ApJ, 796, 7

Gil de Paz, A., Boissier, S., Madore, B. F., et al. 2007a, ApJS, 173, 185

Gil de Paz, A., Boissier, S., Madore, B. F., et al. 2007b, ApJS, 173, 185

Gil de Paz, A., Gallego, J., Carrasco, E., et al. 2016, in Astronomical Society of the Pacific Conference Series, Vol. 507, Multi-Object Spectroscopy in the Next Decade: Big Questions, Large Surveys, and Wide Fields, ed. I. Skillen, M. Barcells, & S. Trager, 103

Gil de Paz, A. & Madore, B. F. 2005, ApJS, 156, 345

Gomes, J. M., Papaderos, P., Kehrig, C., et al. 2016, A&A, 588, A68

Gómez, P. L., Nichol, R. C., Miller, C. J., et al. 2003, ApJ, 584, 210

González Delgado, R. M., Cid Fernandes, R., Pérez, E., et al. 2016, A&A, 590, A44

González Delgado, R. M., García-Benito, R., Pérez, E., et al. 2015, A&A, 581, A103

Gonzalez-Delgado, R. M., Perez, E., Diaz, A. I., et al. 1995, ApJ, 439, 604

Gordon, K. D., Clayton, G. C., Witt, A. N., & Misselt, K. A. 2000, ApJ, 533, 236

Gültekin, K., Richstone, D. O., Gebhardt, K., et al. 2009, ApJ, 698, 198

Gunawardhana, M. L. P., Hopkins, A. M., Bland-Hawthorn, J., et al. 2013, MNRAS, 433, 2764

Gunn, J. E. & Gott, III, J. R. 1972, ApJ, 176, 1

Hao, C.-N., Kennicutt, R. C., Johnson, B. D., et al. 2011, ApJ, 741, 124

Hao, L., Jogee, S., Barazza, F. D., Marinova, I., & Shen, J. 2009, in Astronomical Society of the Pacific Conference Series, Vol. 419, Galaxy Evolution: Emerging Insights and Future Challenges, ed. S. Jogee, I. Marinova, L. Hao, & G. A. Blanc, 402

Hashimoto, Y., Oemler, Jr., A., Lin, H., & Tucker, D. L. 1998, ApJ, 499, 589

Hill, G. J., Gebhardt, K., Komatsu, E., et al. 2008, in Astronomical Society of the Pacific Conference Series, Vol. 399, Panoramic Views of Galaxy Formation and Evolution, ed. T. Kodama, T. Yamada, & K. Aoki, 115

Hirashita, H., Buat, V., & Inoue, A. K. 2003, A&A, 410, 83

Ho, L. C., Filippenko, A. V., & Sargent, W. L. W. 1993, ApJ, 417, 63

Hopkins, A. M. & Beacom, J. F. 2006, ApJ, 651, 142

Hopkins, P. F., Quataert, E., & Murray, N. 2012, MNRAS, 421, 3522

Hopkins, P. F., Torrey, P., Faucher-Giguère, C.-A., Quataert, E., & Murray, N. 2016, MNRAS, 458, 816

Hoyle, F. & Ellis, G. R. A. 1963, Australian Journal of Physics, 16, 1

Hubble, E. P. 1926, ApJ, 64

Hubble, E. P. 1936, Realm of the Nebulae

Huchra, J. & Sargent, W. L. W. 1973, ApJ, 186, 433

Hummer, D. G. & Storey, P. J. 1987, MNRAS, 224, 801

Hunter, D. A., Elmegreen, B. G., & Ludka, B. C. 2010, AJ, 139, 447

Husemann, B., Jahnke, K., Sánchez, S. F., et al. 2013, A&A, 549, A87

Iglesias-Páramo, J., Boselli, A., Gavazzi, G., & Zaccardo, A. 2004, A&A, 421, 887

Iglesias-Páramo, J., Buat, V., Takeuchi, T. T., et al. 2006, ApJS, 164, 38

Iglesias-Páramo, J., Vílchez, J. M., Galbany, L., et al. 2013, A&A, 553, L7

Iglesias-Páramo, J., Vílchez, J. M., Rosales-Ortega, F. F., et al. 2016, ApJ, 826, 71

Inoue, A. K., Hirashita, H., & Kamaya, H. 2001, ApJ, 555, 613

Ishibashi, W. & Fabian, A. C. 2012, MNRAS, 427, 2998

Jarrett, T. H., Chester, T., Cutri, R., et al. 2000, AJ, 119, 2498

Jarrett, T. H., Masci, F., Tsai, C. W., et al. 2013, AJ, 145, 6

Johnson, B. D., Schiminovich, D., Seibert, M., et al. 2007, ApJS, 173, 377

Jonsson, P., Groves, B. A., & Cox, T. J. 2010, MNRAS, 403, 17

Kauffmann, G., Heckman, T. M., Tremonti, C., et al. 2003, MNRAS, 346, 1055

Kawata, D. & Mulchaey, J. S. 2008, ApJ, 672, L103

Kelz, A., Verheijen, M. A. W., Roth, M. M., et al. 2006, PASP, 118, 129

Kennicutt, R. C. & Evans, N. J. 2012, ARA&A, 50, 531

Kennicutt, Jr., R. C. 1998a, ARA&A, 36, 189

Kennicutt, Jr., R. C. 1998b, ApJ, 498, 541

Kennicutt, Jr., R. C., Armus, L., Bendo, G., et al. 2003, PASP, 115, 928

Kennicutt, Jr., R. C., Calzetti, D., Walter, F., et al. 2007, ApJ, 671, 333

Kennicutt, Jr., R. C., Hao, C.-N., Calzetti, D., et al. 2009, ApJ, 703, 1672

Kewley, L. J., Dopita, M. A., Sutherland, R. S., Heisler, C. A., & Trevena, J. 2001, ApJ, 556, 121

Kong, X., Charlot, S., Brinchmann, J., & Fall, S. M. 2004, MNRAS, 349, 769

Kormendy, J. & Ho, L. C. 2013, ARA&A, 51, 511

Kormendy, J. & Kennicutt, Jr., R. C. 2004, ARA&A, 42, 603

Koyama, Y., Smail, I., Kurk, J., et al. 2013, MNRAS, 434, 423

Kroupa, P. 2001, MNRAS, 322, 231

Lamastra, A., Menci, N., Fiore, F., & Santini, P. 2013, A&A, 552, A44

Lang, P., Wuyts, S., Somerville, R. S., et al. 2014, ApJ, 788, 11

Larson, R. B., Tinsley, B. M., & Caldwell, C. N. 1980, ApJ, 237, 692

Lee, J. C., Gil de Paz, A., Tremonti, C., et al. 2009, ApJ, 706, 599

Lee, J. C., Veilleux, S., McDonald, M., & Hilbert, B. 2016, ApJ, 817, 177

Lee, N., Sanders, D. B., Casey, C. M., et al. 2015, ApJ, 801, 80

Leroy, A. K., Bigiel, F., de Blok, W. J. G., et al. 2012, AJ, 144, 3

Leroy, A. K., Walter, F., Brinks, E., et al. 2008, AJ, 136, 2782

Leslie, S. K., Kewley, L. J., Sanders, D. B., & Lee, N. 2016, MNRAS, 455, L82

Li, Y., Crocker, A. F., Calzetti, D., et al. 2013, ApJ, 768, 180

Lilly, S. J., Le Fevre, O., Hammer, F., & Crampton, D. 1996, ApJ, 460, L1

Lin, L., Patton, D. R., Koo, D. C., et al. 2008, ApJ, 681, 232

Ly, C., Lee, J. C., Dale, D. A., et al. 2011, ApJ, 726, 109

Ly, C., Malkan, M. A., Kashikawa, N., et al. 2007, ApJ, 657, 738

Madau, P. & Dickinson, M. 2014, ARA&A, 52, 415

Madau, P., Ferguson, H. C., Dickinson, M. E., et al. 1996, MNRAS, 283, 1388

Madden, S. C., Rémy-Ruyer, A., Galametz, M., et al. 2013, PASP, 125, 600

Magnelli, B., Lutz, D., Saintonge, A., et al. 2014, A&A, 561, A86

Maíz-Apellániz, J. 2004, PASP, 116, 859

Maíz Apellániz, J. 2012, CHORIZOS: CHi-square cOde for parameterRized modeling and characterIZation of phOtometry and Spectrophotmetry, Astrophysics Source Code Library

Marino, R. A., Gil de Paz, A., Castillo-Morales, A., et al. 2012, ApJ, 754, 61

Marino, R. A., Rosales-Ortega, F. F., Sánchez, S. F., et al. 2013, A&A, 559, A114

Mármol-Queraltó, E., Sánchez, S. F., Marino, R. A., et al. 2011, A&A, 534, A8

Martig, M., Bournaud, F., Teyssier, R., & Dekel, A. 2009, ApJ, 707, 250

Martin, D. C., Fanson, J., Schiminovich, D., et al. 2005, ApJ, 619, L1

Massey, P., Olsen, K. A. G., Hodge, P. W., et al. 2007, AJ, 133, 2393

Masters, K. L., Nichol, R. C., Haynes, M. P., et al. 2012, MNRAS, 424, 2180

Masters, K. L., Nichol, R. C., Hoyle, B., et al. 2011, MNRAS, 411, 2026

Meert, A., Vikram, V., & Bernardi, M. 2015, MNRAS, 446, 3943

Meert, A., Vikram, V., & Bernardi, M. 2016, MNRAS, 455, 2440

Méndez-Abreu, J., Aguerri, J. A. L., Corsini, E. M., & Simonneau, E. 2008, A&A, 478, 353

Méndez-Abreu, J., Debattista, V. P., Corsini, E. M., & Aguerri, J. A. L. 2014, A&A, 572, A25

Méndez-Abreu, J., Ruiz-Lara, T., Sánchez-Menguiano, L., et al. 2017, A&A, 598, A32

Meurer, G. R., Heckman, T. M., Leitherer, C., et al. 1995, AJ, 110, 2665

Mo, H. J. & White, S. D. M. 2002, MNRAS, 336, 112

Moles, M., Marquez, I., & Perez, E. 1995, ApJ, 438, 604

Monreal-Ibero, A., Relaño, M., Kehrig, C., et al. 2011, MNRAS, 413, 2242

Moore, B., Katz, N., Lake, G., Dressler, A., & Oemler, A. 1996, Nature, 379, 613

Moore, B., Lake, G., & Katz, N. 1998, ApJ, 495, 139

Morisset, C., Delgado-Inglada, G., Sánchez, S. F., et al. 2016, A&A, 594, A37

Morselli, L., Renzini, A., Popesso, P., & Erfanianfar, G. 2016, MNRAS, 462, 2355

Moshir, M., Kopman, G., & Conrow, T. A. O. 1992, IRAS Faint Source Survey, Explanatory supplement version 2

Moshir, M. et al. 1990, in IRAS Faint Source Catalogue, version 2.0 (1990), 0

Muñoz-Mateos, J. C., Gil de Paz, A., Boissier, S., et al. 2009, ApJ, 701, 1965

Mulchaey, J. S. & Regan, M. W. 1997, ApJ, 482, L135

Nelson, E. J., van Dokkum, P. G., Brammer, G., et al. 2012, ApJ, 747, L28

Nelson, E. J., van Dokkum, P. G., Momcheva, I., et al. 2013, ApJ, 763, L16

Neugebauer, G., Habing, H. J., van Duinen, R., et al. 1984, ApJ, 278, L1

Noeske, K. G., Weiner, B. J., Faber, S. M., et al. 2007, ApJ, 660, L43

Oey, M. S. & Kennicutt, Jr., R. C. 1997, MNRAS, 291, 827

Oey, M. S., Meurer, G. R., Yelda, S., et al. 2007, ApJ, 661, 801

Ohishi, Y., Sorai, K., & Habe, A. 2012, PASJ, 64, 74

Oppenheimer, B. D., Davé, R., Kereš, D., et al. 2010, MNRAS, 406, 2325

Osterbrock, D. E. 1989, Astrophysics of gaseous nebulae and active galactic nuclei

Page, M. J., Symeonidis, M., Vieira, J. D., et al. 2012, Nature, 485, 213

Papaderos, P., Gomes, J. M., Vílchez, J. M., et al. 2013, A&A, 555, L1

Pascual, S., Gallego, J., Aragón-Salamanca, A., & Zamorano, J. 2001, A&A, 379, 798

Pellegrini, E. W., Baldwin, J. A., & Ferland, G. J. 2010, ApJS, 191, 160

Pellegrini, E. W., Oey, M. S., Winkler, P. F., et al. 2012, ApJ, 755, 40

Peng, C. Y., Ho, L. C., Impey, C. D., & Rix, H.-W. 2002, AJ, 124, 266

Peng, Y., Maiolino, R., & Cochrane, R. 2015, Nature, 521, 192

Peng, Y.-j., Lilly, S. J., Kovač, K., et al. 2010, ApJ, 721, 193

Pérez, E., Cid Fernandes, R., González Delgado, R. M., et al. 2013, ApJ, 764, L1

Pérez-González, P. G., Gil de Paz, A., Zamorano, J., et al. 2003, MNRAS, 338, 525

Pérez-González, P. G., Kennicutt, Jr., R. C., Gordon, K. D., et al. 2006, ApJ, 648, 987

Pérez-González, P. G., Rieke, G. H., Villar, V., et al. 2008, ApJ, 675, 234

Poggianti, B. M., Fasano, G., Omizzolo, A., et al. 2016, AJ, 151, 78

Prescott, M. K. M., Kennicutt, Jr., R. C., Bendo, G. J., et al. 2007, ApJ, 668, 182

Ramos Almeida, C., Levenson, N. A., Rodríguez Espinosa, J. M., et al. 2009, ApJ, 702, 1127

Relaño, M., Kennicutt, Jr., R. C., Eldridge, J. J., Lee, J. C., & Verley, S. 2012, MNRAS, 423, 2933

Relaño, M., Monreal-Ibero, A., Vílchez, J. M., & Kennicutt, R. C. 2010, MNRAS, 402, 1635

Renzini, A. & Peng, Y.-j. 2015, ApJ, 801, L29

Rich, J. A., Persson, S. E., Freedman, W. L., et al. 2014, ApJ, 794, 107

Rieke, G. H., Alonso-Herrero, A., Weiner, B. J., et al. 2009, ApJ, 692, 556

Robaina, A. R., Bell, E. F., Skelton, R. E., et al. 2009, ApJ, 704, 324

Rosales-Ortega, F. F., Kennicutt, R. C., Sánchez, S. F., et al. 2010, MNRAS, 405, 735

Roth, M. M., Kelz, A., Fechner, T., et al. 2005, PASP, 117, 620

Saintonge, A., Kauffmann, G., Kramer, C., et al. 2011, MNRAS, 415, 32

Saintonge, A., Tacconi, L. J., Fabello, S., et al. 2012, ApJ, 758, 73

Sakamoto, K., Okumura, S. K., Ishizuki, S., & Scoville, N. Z. 1999, ApJ, 525, 691

Salim, S., Rich, R. M., Charlot, S., et al. 2007, ApJS, 173, 267

Salo, H., Laurikainen, E., Laine, J., et al. 2015, ApJS, 219, 4

Salpeter, E. E. 1955, ApJ, 121, 161

Salvatier, J., Wiecki, T. V., & Fonnesbeck, C. 2016, PeerJ Computer Science, 2, e55

Sánchez, S. F., García-Benito, R., Zibetti, S., et al. 2016, A&A, 594, A36

Sánchez, S. F., Jahnke, K., Wisotzki, L., et al. 2004, ApJ, 614, 586

Sánchez, S. F., Kennicutt, R. C., Gil de Paz, A., et al. 2012, A&A, 538, A8

Sánchez, S. F., Rosales-Ortega, F. F., Iglesias-Páramo, J., et al. 2014, A&A, 563, A49

Sánchez, S. F., Rosales-Ortega, F. F., Jungwiert, B., et al. 2013, A&A, 554, A58

Sánchez, S. F., Rosales-Ortega, F. F., Kennicutt, R. C., et al. 2011, MNRAS, 410, 313

Sánchez Almeida, J., Elmegreen, B. G., Muñoz-Tuñón, C., & Elmegreen, D. M. 2014, A&A Rev., 22, 71

Sánchez-Blázquez, P., Peletier, R. F., Jiménez-Vicente, J., et al. 2006a, MNRAS, 371, 703

Sánchez-Blázquez, P., Peletier, R. F., Jiménez-Vicente, J., et al. 2006b, MNRAS, 371, 703

Sánchez-Blázquez, P., Rosales-Ortega, F. F., Méndez-Abreu, J., et al. 2014, A&A, 570, A6

Sanders, D. B., Soifer, B. T., Elias, J. H., et al. 1988, ApJ, 325, 74

Schawinski, K., Urry, C. M., Simmons, B. D., et al. 2014, MNRAS, 440, 889

Schechter, P. 1976, ApJ, 203, 297

Schiminovich, D., Wyder, T. K., Martin, D. C., et al. 2007, ApJS, 173, 315

Schmidt, M. 1968, ApJ, 151, 393

Schreiber, C., Pannella, M., Elbaz, D., et al. 2015, A&A, 575, A74

Schruba, A., Leroy, A. K., Walter, F., et al. 2011, AJ, 142, 37

Scoville, N., Aussel, H., Brusa, M., et al. 2007, ApJS, 172, 1

Seibert, M., Martin, D. C., Heckman, T. M., et al. 2005, ApJ, 619, L55

Sersic, J. L. 1968, Atlas de galaxias australes

Sharples, R., Bender, R., Agudo Berbel, A., et al. 2013, The Messenger, 151, 21

Sharples, R. M., Bender, R., Lehnert, M. D., et al. 2004, in Proc. SPIE, Vol. 5492, Ground-based Instrumentation for Astronomy, ed. A. F. M. Moorwood & M. Iye, 1179–1186

Sheth, K., Vogel, S. N., Regan, M. W., Thornley, M. D., & Teuben, P. J. 2005, ApJ, 632, 217

Shimizu, T. T., Mushotzky, R. F., Meléndez, M., Koss, M., & Rosario, D. J. 2015, MNRAS, 452, 1841

Silk, J. 2005, MNRAS, 364, 1337

Silk, J. 2013, ApJ, 772, 112

Silk, J. & Mamon, G. A. 2012, Research in Astronomy and Astrophysics, 12, 917

Singh, R., van de Ven, G., Jahnke, K., et al. 2013, A&A, 558, A43

Skelton, R. E., Whitaker, K. E., Momcheva, I. G., et al. 2014, ApJS, 214, 24

Smith, B. J., Giroux, M. L., Struck, C., & Hancock, M. 2010, AJ, 139, 1212

Smith, B. J., Struck, C., Hancock, M., et al. 2007, AJ, 133, 791

Somerville, R. S. & Davé, R. 2014, ArXiv e-prints 1412.2712

Speagle, J. S., Steinhardt, C. L., Capak, P. L., & Silverman, J. D. 2014, ApJS, 214, 15

Stasińska, G., Vale Asari, N., Cid Fernandes, R., et al. 2008, MNRAS, 391, L29

Steinhardt, C. L., Speagle, J. S., Capak, P., et al. 2014, ApJ, 791, L25

Steinhauser, D., Schindler, S., & Springel, V. 2016, A&A, 591, A51

Strateva, I., Ivezić, Ž., Knapp, G. R., et al. 2001, AJ, 122, 1861

Stringer, M. J., Bower, R. G., Cole, S., Frenk, C. S., & Theuns, T. 2012, MNRAS, 423, 1596

Taylor, E. N., Hopkins, A. M., Baldry, I. K., et al. 2011, MNRAS, 418, 1587

Taylor, P. & Kobayashi, C. 2015, MNRAS, 448, 1835

Tempel, E., Saar, E., Liivamägi, L. J., et al. 2011, A&A, 529, A53

Terashima, Y., Ho, L. C., & Ptak, A. F. 2000, ApJ, 539, 161

Tonnesen, S. & Cen, R. 2014, ApJ, 788, 133

Tran, H. D. 2001, ApJ, 554, L19

Tran, H. D., Lyke, J. E., & Mader, J. A. 2011, ApJ, 726, L21

Treyer, M., Schiminovich, D., Johnson, B., et al. 2007, ApJS, 173, 256

van Breugel, W., Fragile, C., Croft, S., et al. 2004, in IAU Symposium, Vol. 222, The Interplay Among Black Holes, Stars and ISM in Galactic Nuclei, ed. T. Storchi-Bergmann, L. C. Ho, & H. R. Schmitt, 485–488

van Zee, L. 2000, AJ, 119, 2757

Vazdekis, A., Sánchez-Blázquez, P., Falcón-Barroso, J., et al. 2010, MNRAS, 404, 1639

Walcher, C. J., Lamareille, F., Vergani, D., et al. 2008, A&A, 491, 713

Walcher, C. J., Wisotzki, L., Bekeraité, S., et al. 2014, A&A, 569, A1

Wang, J., Kauffmann, G., Overzier, R., et al. 2012, MNRAS, 423, 3486

Weinberger, R., Springel, V., Hernquist, L., et al. 2017, MNRAS, 465, 3291

Weinzirl, T., Jogee, S., Khochfar, S., Burkert, A., & Kormendy, J. 2009, ApJ, 696, 411

Westra, E., Geller, M. J., Kurtz, M. J., Fabricant, D. G., & Dell'Antonio, I. 2010, ApJ, 708, 534

Whitaker, K. E., Franx, M., Bezanson, R., et al. 2015, ApJ, 811, L12

Whitaker, K. E., Franx, M., Leja, J., et al. 2014, ApJ, 795, 104

Whitaker, K. E., van Dokkum, P. G., Brammer, G., & Franx, M. 2012, ApJ, 754, L29

Wisnioski, E., Förster Schreiber, N. M., Wuyts, S., et al. 2015, ApJ, 799, 209

Wright, E. L., Eisenhardt, P. R. M., Mainzer, A. K., et al. 2010, AJ, 140, 1868

Wuyts, S., Förster Schreiber, N. M., Nelson, E. J., et al. 2013, ApJ, 779, 135

Wuyts, S., Förster Schreiber, N. M., van der Wel, A., et al. 2011, ApJ, 742, 96

Yamamura, I., Makiuti, S., Ikeda, N., & Fukuda. 2010, AKARI/FIS All-Sky Survey Bright Source Catalogue Version 1.0 Release Note

Yi, S., Demarque, P., & Oemler, Jr., A. 1997, ApJ, 486, 201

York, D. G., Adelman, J., Anderson, Jr., J. E., et al. 2000, AJ, 120, 1579

Zinn, P.-C., Middelberg, E., Norris, R. P., & Dettmar, R.-J. 2013, ApJ, 774, 66

Zwicky, F. 1942, Physical Review, 61, 489